JPL PUBLICATION 80-38, VOLUME II

(NASA-CR-163571) SEASAT. VOLUME 2: FLIGHT SYSTEMS Final Report (Jet Propulsion Lab.) 369 p HC A16/MF A01 CSCL 05B

N80-32829

Unclas
G3/43 28762

Seasat Final Report
Volume II: Flight Systems

Edited by
E. Pounder

September 1, 1980

National Aeronautics and
Space Administration

Jet Propulsion Laboratory
California Institute of Technology
Pasadena, California

JPL PUBLICATION 80-38, VOLUME II

Seasat Final Report
Volume II: Flight Systems

Edited by
E. Pounder

September 1, 1980

National Aeronautics and
Space Administration

Jet Propulsion Laboratory
California Institute of Technology
Pasadena, California

PREFACE

The Seasat satellite was launched at 01:12:44 GMT on 27 June 1978 from the Western Test Range at Vanderberg Air Force Base, Lompoc, California. The spacecraft was injected into Earth orbit to demonstrate techniques for global monitoring of the dynamics of the air-sea interface and to explore operational applications. To achieve these objectives, a payload of sensors emphasizing all-weather, active and passive microwave capabilities was carried on the satellite. The mission was prematurely terminated on 10 October 1978 after 106 days of operation by a catastrophic failure in the satellite power subsystem.

Major mission accomplishments were:

(1) Demonstration of the orbital techniques required to support the mission and sensor operations.

(2) Demonstration of the simultaneous operation of all sensors for periods of time significant to global monitoring.

(3) The collection of an important data set for sensor evaluation and scientific use.

The early mission termination precluded:

(1) Demonstration of the planned operational features of the end-to-end data system.

(2) Collection of a global data set to meet overall geodetic and seasonal objectives and plans.

This report, in four volumes, includes results of the sensor evaluations and some preliminary scientific results from the initial experiment team activities. Scientific and applications studies will continue through FY 80, and will be included in the final version of this report.

ABSTRACT

The Seasat Project was a feasibility demonstration of the use of orbital remote sensing for global observation. The satellite was launched in June 1978 and was operated successfully until October 1978. At that time, a massive electrical failure occurred in the power system, terminating the mission prematurely.

Volume II of the Final Report treats the Flight Systems used in the mission. Included are descriptions of the satellite and launch vehicle and a discussion of the satellite test program, the GFE plan, and launch operations. This is followed by a system performance section and a contract summary. Finally, each sensor and the associated algorithms are described, and the techniques for sensor management are explained.

CONTENTS

Figures

Tables

SECTION I

INTRODUCTION

This volume contains descriptions of the elements that formed the Seasat flight systems. Included are sections devoted to a description of the satellite, details of the satellite development and acceptance test program, and information concerning the utilization of the Government Furnished Equipment (GFE). Also part of this volume are descriptions of: (1) Seasat launch operations; (2) performance of the satellite after launch; (3) sensors that collected data for the Seasat experiments; and (4) the launch vehicle that placed the satellite into Earth orbit.

The Seasat flight vehicle (Figure 1-1) was launched from Space Launch Complex-3 West (SLC-3W) at the Vandenberg Air Force Western Test Range (VAFBWTR) at 01:12:44 Greenwich Mean Time (GMT) on 27 June 1978. The flight vehicle configuration consisted of a modified Atlas F booster, a mission-peculiar interstage adapter, a refurbished 305-cm (120-in.) diameter nose fairing, and the Satellite Vehicle System (SVS). The SVS (Figure 1-2) included a booster adapter, Agena, sensor module, and Sensor Module Support Structure (SMSS). The Agena functioned as the upper stage of the launch vehicle and also as the satellite bus.

The launch vehicle objective was to deliver the SVS to a pre-determined state vector, separate itself and the booster adapter from the remainder of the SVS, and then back safely away. All aspects of the launch vehicle objective were successfully accomplished.

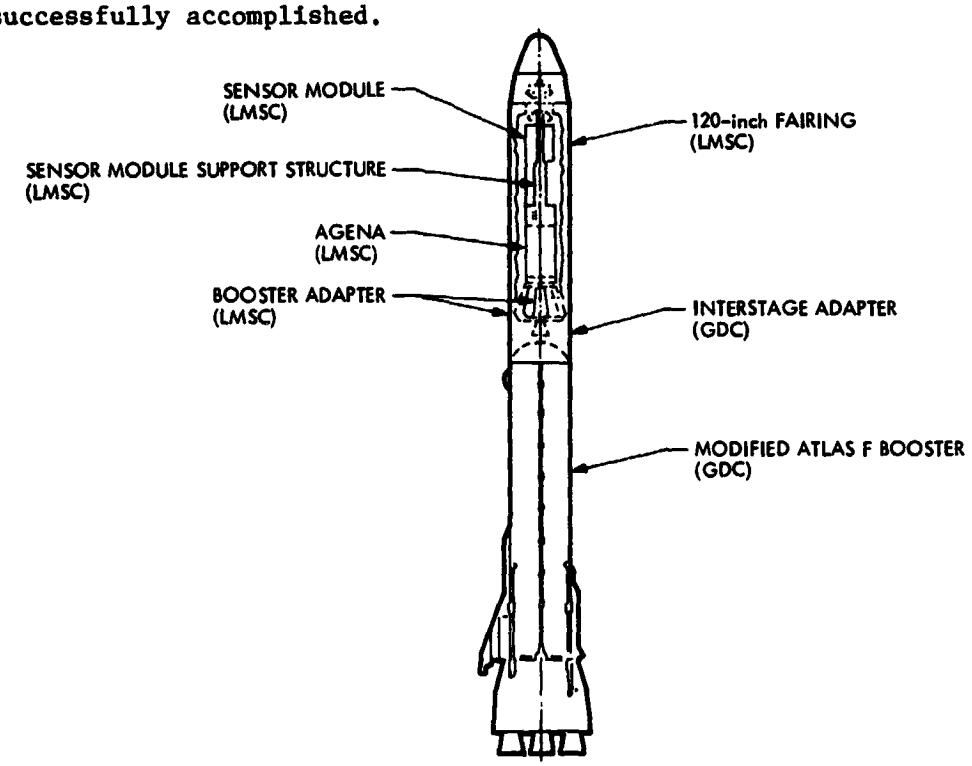

Figure 1-1. Flight Vehicle Elements

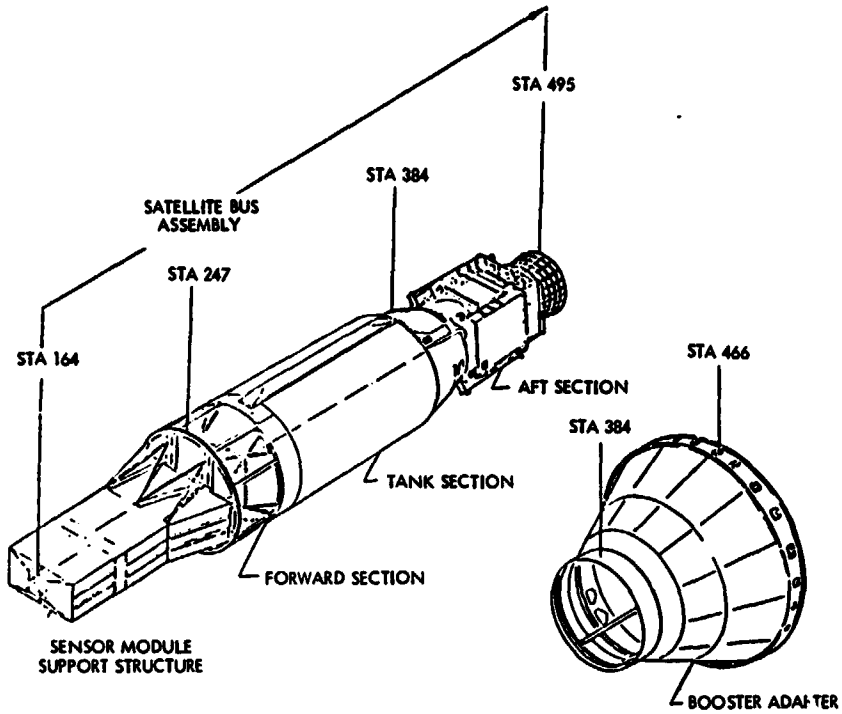

Figure 1-2. Booster Adapter, Agena, and Sensor Module Support Structure Details

The objective of the Agena orbit injection system was to deliver the SVS from the separation state vector to the desired final orbit conditions in the correct orientation (Figure 1-3). This objective, which required a 90-deg roll maneuver and two burns of the Agena main propulsion system, was also successfully accomplished.

The Seasat nominal orbit was selected to completely survey the Earth's surface in 5 month's time with a near-repeat of the orbit trace on the Earth's surface every 3 days. On-orbit attitude control was provided by a combination of gravity gradient stabilization, horizon scanners, and momentum wheels with magnetic desaturation. The mission objectives included: (1) demonstration of techniques for global monitoring of oceanographic phenomena and features from space; (2) provision of oceanographic data for application and scientific users; and (3) determination of key features of an operational ocean dynamics monitoring system. These Seasat objectives were derived from overall National Aeronautics and Space Administration (NASA) applications objectives and, in particular, from the objectives of the NASA Earth and Ocean Dynamics Applications Program (EODAP).

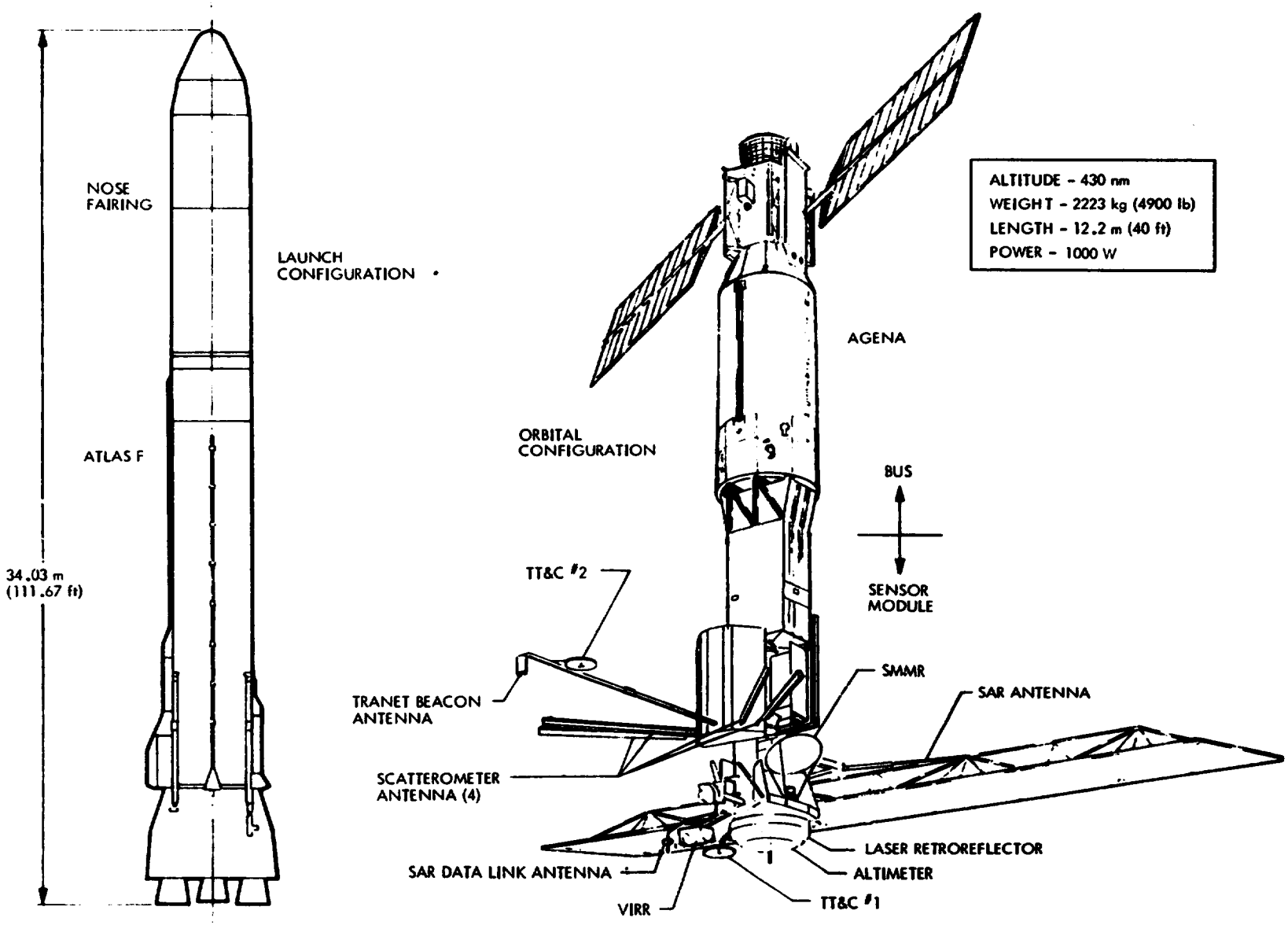

Figure 1-3. Satellite Configuration

To accomplish the stated objectives, the Seasat spacecraft carried five sensors. With their individual objectives, these sensors were as follows:

(1) The Radar Altimeter (ALT) measured wave height at the subsatellite point and the altitude between the spacecraft and the ocean surface. The altitude measurement was precise to within ±10 cm (4 in.). The altitude measurement, when combined with accurate orbit determination information, produced an accurate image of the sea surface topography.

(2) The Seasat Scatterometer System (SASS) measured sea surface wind speeds and directions at close intervals from which vector wind fields could be derived on a global basis.

(3) The Scanning Multichannel Microwave Radiometer (SMRR) measured wind speed, sea surface temperature to an accuracy of ±2°C, and atmospheric water vapor and liquid water content.

(4) The Synthetic Aperture Radar (SAR) was an imaging radar that provided images of the ocean surface from which could be determined ocean wave patterns, water and land interaction data in coastal regions, and radar imagery of sea and fresh water ice and snow cover.

(5) The Visual and Infrared Radiometer (VIRR) objective was to provide low-resolution images of visual and infrared radiation emissions from ocean, coastal, and atmospheric features in support of the microwave sensors. Clear air temperatures were also measured.

The sensors and their mounting structure comprised the sensor module. The sensor module was supported above the Agena by the SMSS. The Agena functioned as the upper stage of the launch vehicle and as a bus for the satellite. The Agena included provisions for furnishing electrical power, attitude control, and orbit adjust capabilities for the SMSS for the duration of the mission.

The Seasat launch was scheduled to permit the collection of data coincident with a variety of oceanographic research activities using ships, aircraft, and instrumented buoys. Data from these various sources were correlated in a "surface truth" operation to verify the accuracy of the Seasat data and to assist in the development of appropriate algorithms for converting the Seasat measurement data into useful physical information.

While the horizon scanners experienced sensor anomalies, pointing accuracy was maintained to the degree required to meet most sensor requirements most of the time. The SASS requirements were met more than 60 percent of the time. Flight anomalies included:

(1) Failure of two pairs of thermostats.

(2) A power management problem that resulted in battery voltages below acceptable levels for a portion of an orbit.

(3) Failure of the VIRR at the end of 52 days of operations.

(4) The flight-terminating failure that appears to have originated in, or near, the solar array slip rings.

Other activities of this project are documented in separate volumes of these sources:

Volume I	Program Summary
Volume III	Ground Systems
Volume IV	Attitude Determination

Abbreviations and acronyms used in this volume are defined in the appendix.

SECTION II

SATELLITE DESCRIPTION

A. GENERAL

This description has been grouped into four parts: (1) the spacecraft or bus (basically the Agena and SMSS with attendant subsystem elements); (2) the sensor module (exclusive of the sensors); (3) the SAR antenna; and (4) the fairing. The sensors and other payloads, including the ALT, SASS, SMMR, VIRR, SAR, SAR data link, Tranet (tracking network) beacon, and Laser Reflectometer Assembly (LRA) are described in the GFE plan presented in Section IV. Although the NASA standard transponder was also GFE, its functional description is given in this section. Each sensor is also individually described in Section VII.

The spacecraft bus used an Agena to perform the ascent propulsion and attitude control functions. Orbital functions were provided by appropriate structural, communications, command, data handling, attitude sensing, attitude control, electric power, and thermal control subsystems for long term support of the sensor payloads (Figure 2-1). The basic Agena is a multistart upper stage vehicle using a pump-fed liquid bipropellant rocket motor. Figures 2-2 through 2-4 show the major components of the Orbital Insertion System (OIS), Ascent Control System (ACS), and Orbit Adjust System/Reaction Control System (OAS/RCS), respectively. Two Agena rocket motor burns were required for this mission. The booster was an Atlas F strengthened to accommodate the heavier upper stage loads. A 3-m (10 ft) diameter fairing was used that covered the complete payload/Agena upper stage. The Atlas used radar tracking and radio guidance to correct a pre-programmed autopilot and to provide various guidance discretes.

The Agena used a pre-programmed sequence of events with first and second burns terminated by a velocity meter. The first burn placed the Agena into a Hohmann-type transfer orbit with the perigee at 185 km (100 nm) and the apogee at 790 km (426 nm). The second burn, at transfer orbit apogee, essentially circularized the orbit. The ascent sequence was a pre-launch nominal sequence that was stored in and executed by the Command Processor and Central Timing Units (CTUs), both of which were used for active redundancy. Operation of the CTU was initiated in flight by an Atlas discrete to compensate for pre-launch uncertainties in flight-time-to-booster apogee. The satellite remained in the pre-launch-stored CTU command control during the first approximately 4000 s on orbit. During that time, the satellite was maneuvered from the ascent horizontal attitude to the vertical orbital attitude and the planned deployments completed (see Section V). Subsequent satellite control was achieved by commands transmitted from the ground.

Figure 2-5 is a functional block diagram that shows the major components of the Atlas F, booster adapter, fairing system, bus, and sensor module. In general, the GFE components were mounted on the sensor module with the two NASA standard transponders (NSTs) being mounted on the SMSS (a part of the bus). The two Ithaco scanwheels (orbit attitude sensors) and the two orbit antennas, although a part of the bus, were mounted on the sensor module.

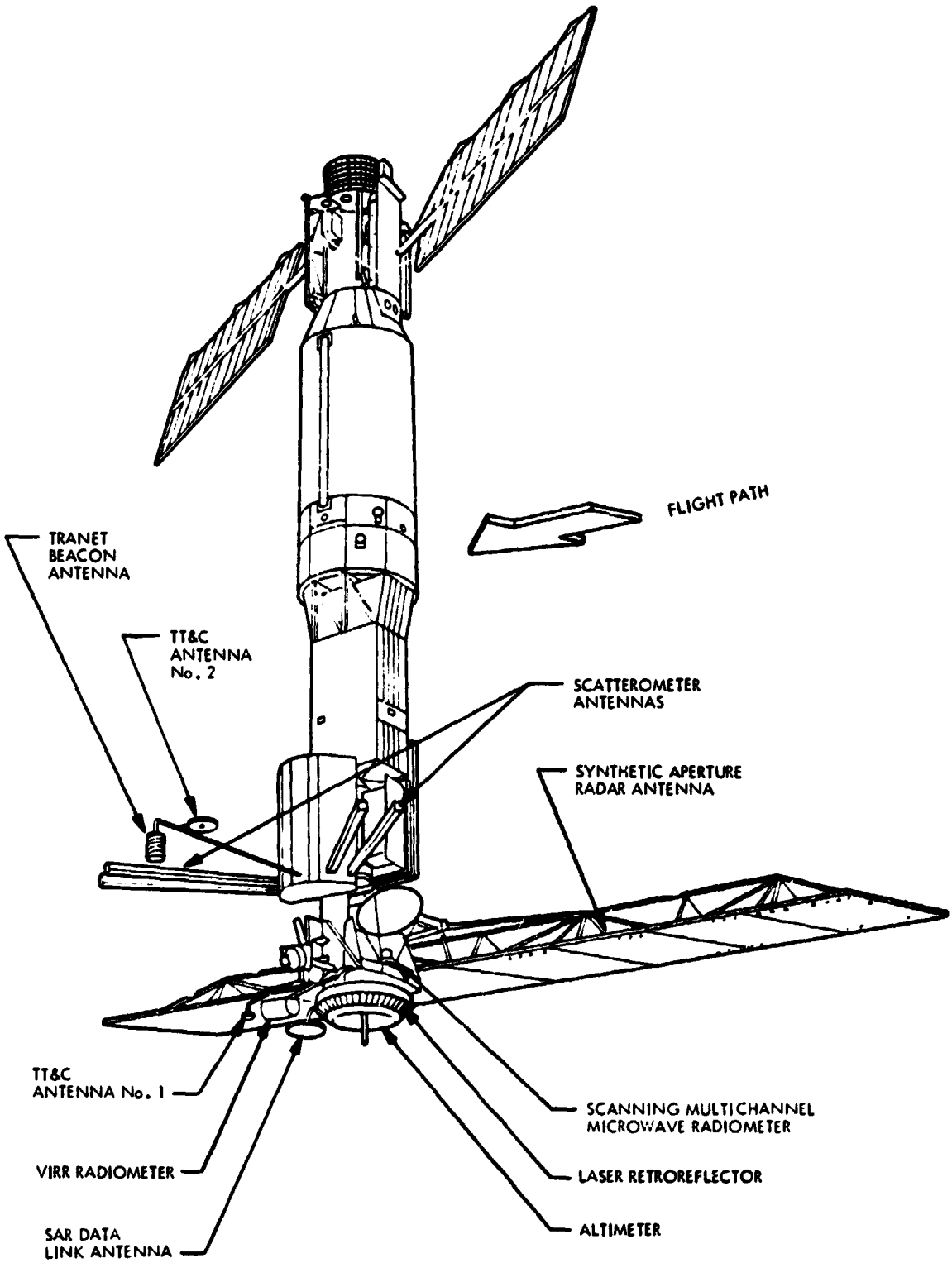

Figure 2-1. Seasat On-Orbit Configuration

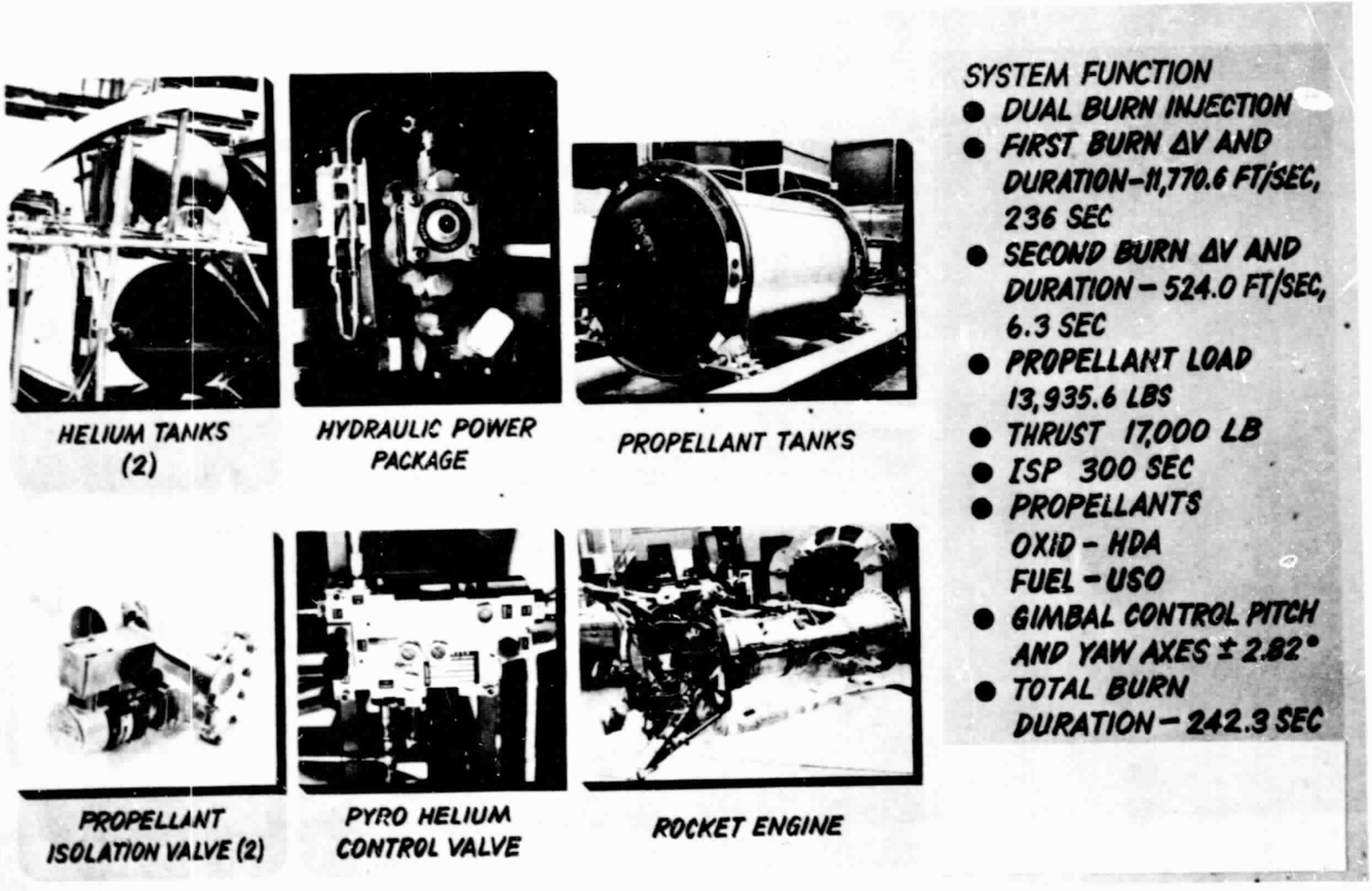

Figure 2-2. Orbital Insertion System

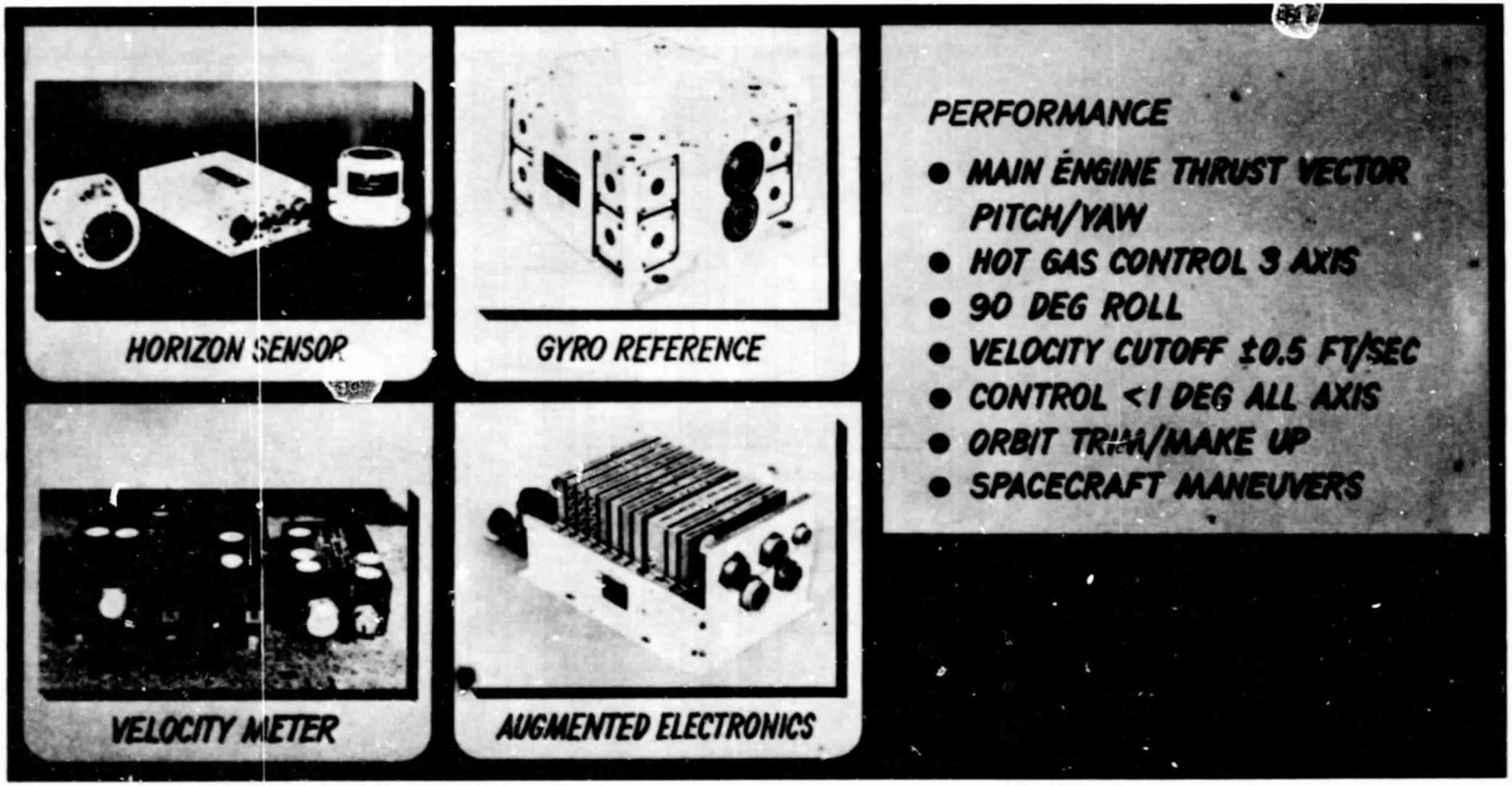

Figure 2-3. Ascent Control System

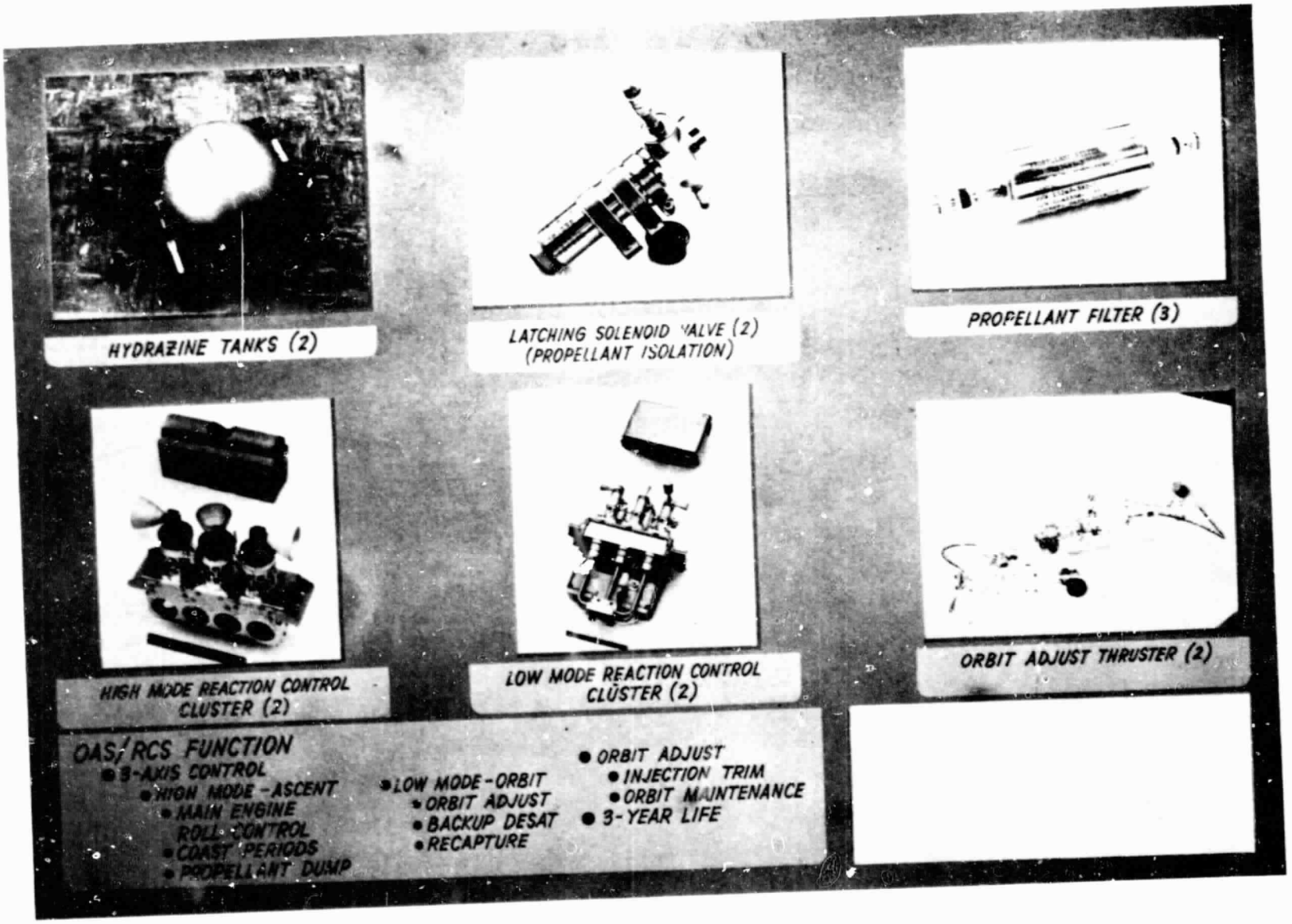

Figure 2-4. Orbit Adjust and Reaction Control Systems

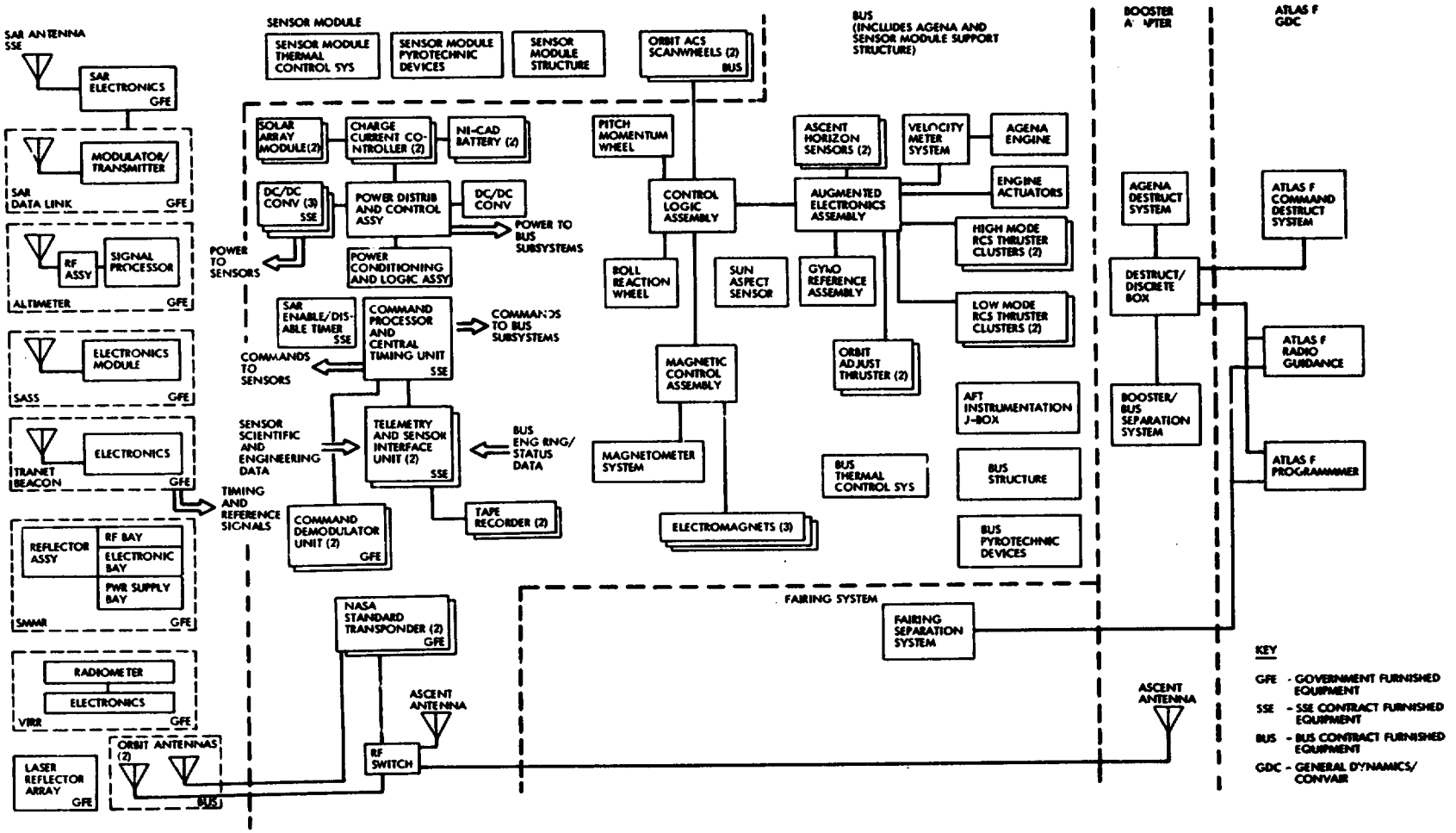

Figure 2-5. Satellite Functional Block Diagram

B. BUS

The following paragraphs describe each of the bus subsystems. In general, the bus consisted of that structure and equipment that extended from the Agena engine cone forward to, but not including, the sensor module (Figure 2-1). The major structural components were the aft rack, tank section, forward rack, and SMSS.

1. Electrical Power Subsystem

This subsystem consisted of the following major components:

(1) Solar array assembly (2).

(2) Solar Array Drive Electronics Unit (SADE).

(3) Main Power Control and Distribution Unit (MPCDU).

(4) Charge controllers (2).

(5) Batteries (2).

(6) Power Conditioning and Logic Assembly (PCLA).

(7) Aft control and instrumentation box.

(8) Bus pyro control unit.

(9) SMSS pyro control unit.

These components are discussed in the following paragraphs. Photographs of selected components are shown in Figure 2-6.

a. General Description. Electrical power of from 24.5 to 32 V dc was provided to the satellite subsystems and sensors using solar arrays and rechargeable batteries. Figures 2-7 and 2-8 are block diagrams of the power system and MPCDU, respectively. During ascent, satellite power was totally provided by the two batteries. Once normal vehicle orbital attitude was achieved, the two solar arrays were deployed on command and assumed the load, including battery charging until eclipsing occurred. A Charge Current Controller (CCC) was provided for each battery to control the charging rate and maximum voltage as a function of battery temperature. Commands were available to provide manual charge control. Solar tracking by the array was powered by the Solar Array Drive Electronics (SADE), which used the error signal generated by the sun sensor on each wing to control the array drive motor speed.

Power, instrumentation, and sun sensor signals were brought in from each solar array wing through a slip ring assembly (power transfer unit), which was coupled with the drive motor assembly. Commands controlled the rotation direction, dark angular rate, and initiation of fast rate. Power to the satellite subsystems and sensors was distributed, fused, and controlled in the main power

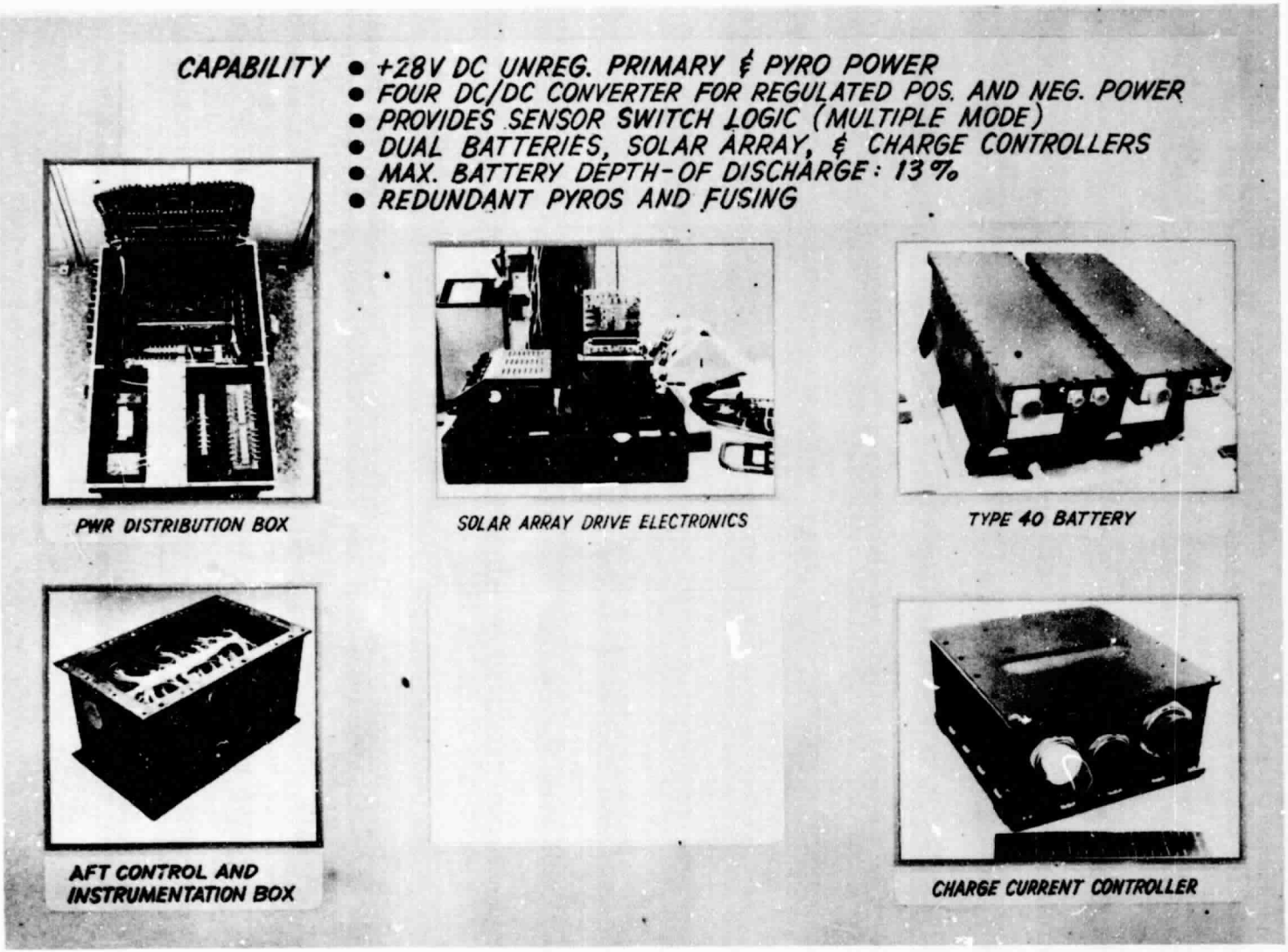

Figure 2-6. Power System Components

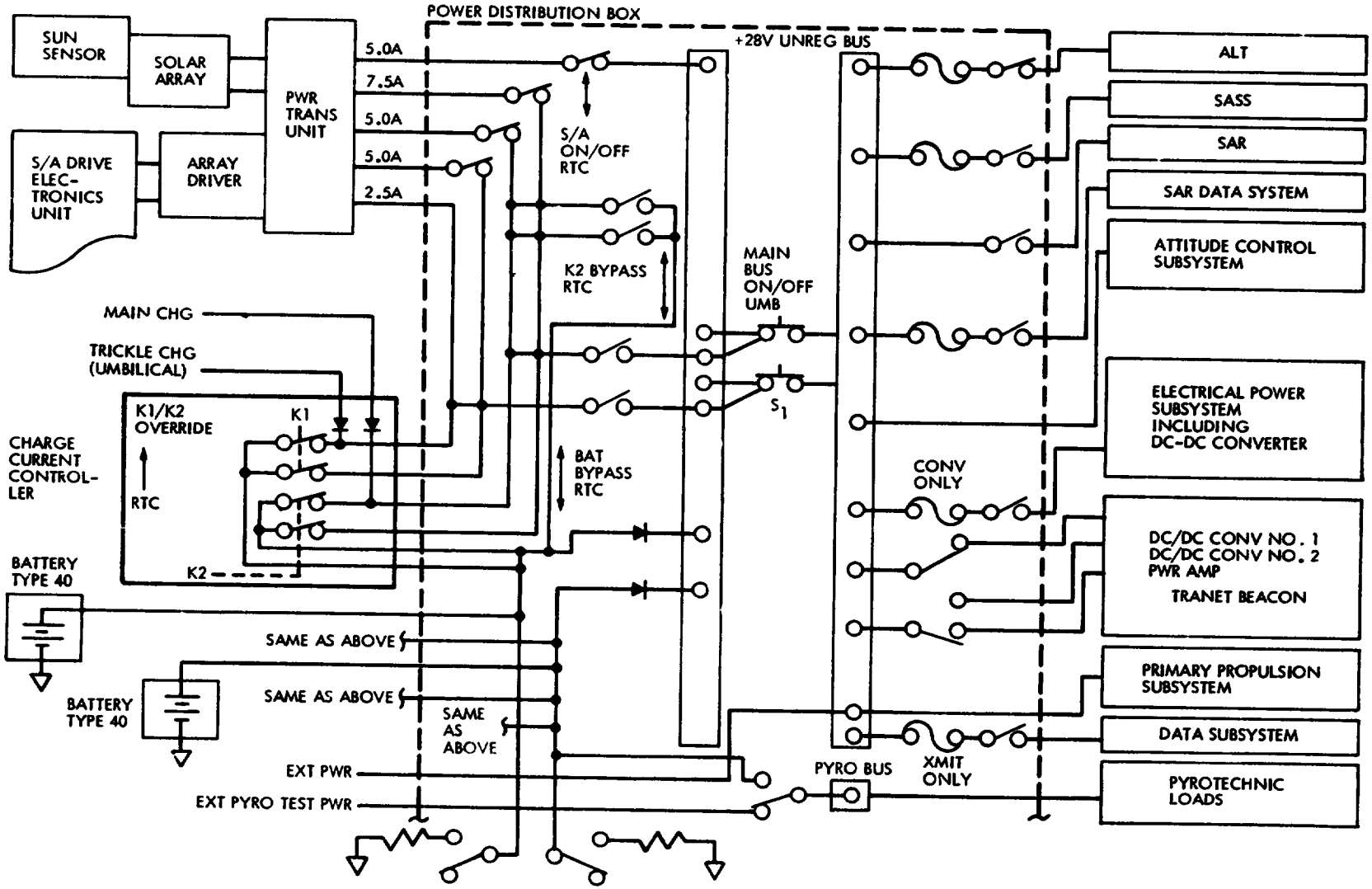

Figure 2-7. Power System Block Diagram

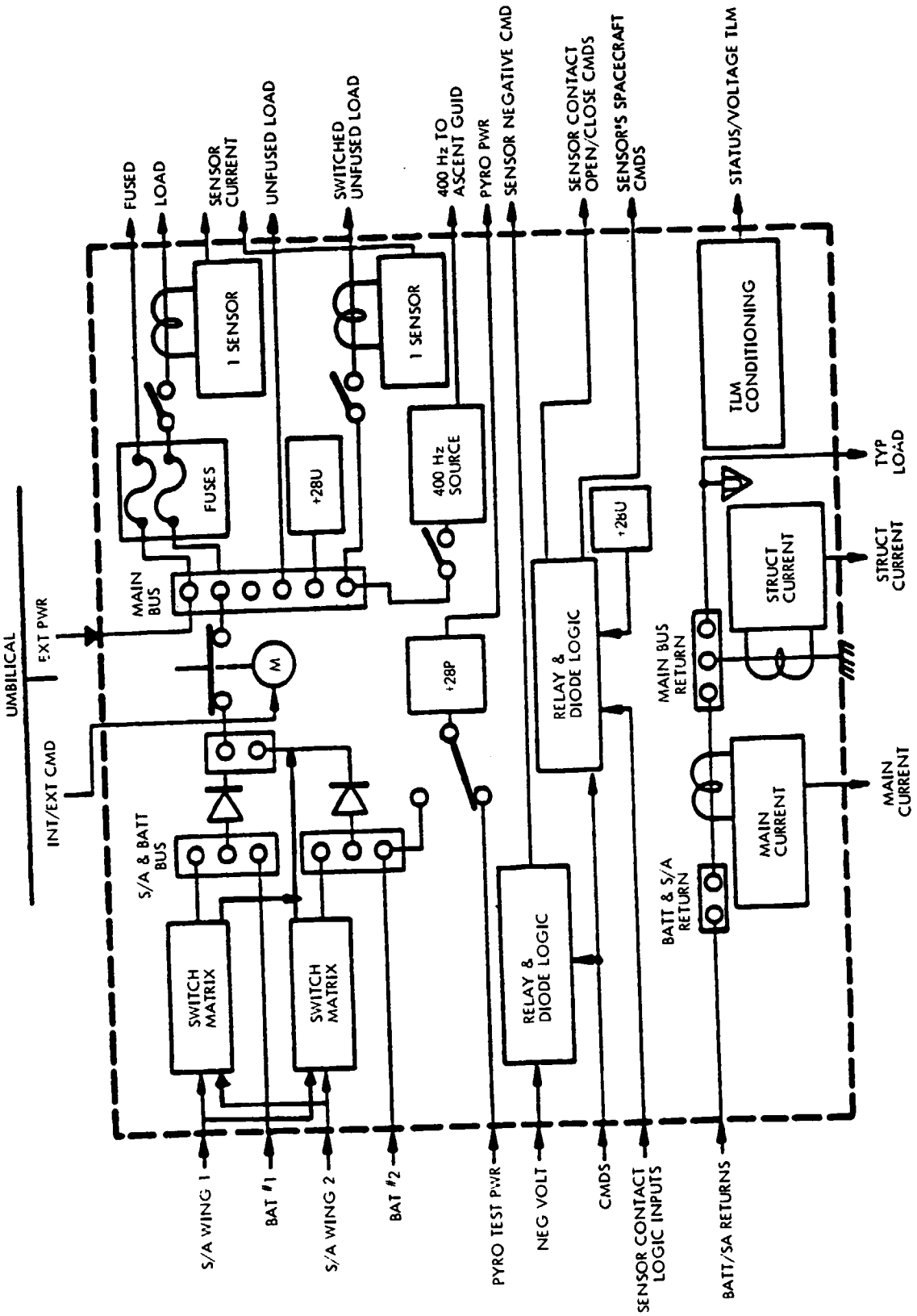

Figure 2-8. Main Power Control and Distribution Unit Block Diagram

transfer switch, which connected the batteries to the 28 V dc bus, the 115-V rms, 400-Hz, single-phase inverter for the velocity meter counter and the necessary current and voltage monitors. Also located in the MPCDU were the solar array panel disconnect relays and the CCC backup manual charge control relays. Regulated ±28 V dc power for the ascent guidance system, sensors, and instrumentation was provided by four dc-dc converters. The control logic for these units was also in the MPCDU. The converter distribution and control logic is shown in Figure 2-9.

The aft control and instrumentation box contained the engine control logic and instrumentation signal conditioning. It also contained the engine start can pyro control logic, fusistors, and safe/arm plug. The bus pyro control unit contained the pyro control logic, fusistors, and safe/arm plugs for the solar array deployment pin pullers, fuel and oxidizer dump valves, helium control valve, Tranet beacon antenna and orbit antenna 2 deployment pin pullers and the VIRR deployment pin pullers, pin pullers for the four SASS antennas, SAR data link antenna deployment pin pullers, and the SAR antenna deployment restraint and rotation release mechanism pin pullers.

The PCLA contained signal conditioning circuits to provide compatibility between the satellite analog and bilevel instrumentation and the Telemetry and Sensor Interface Unit (TSU). The instrumentation included sensor external temperature monitors, other non-sensor temperature monitors, deployment position potentiometer outputs for antennas and solar arrays, voltage monitors, and bilevel monitors for command verification of satellite housekeeping functions. The PCLA also contained the tape recorder control logic steering diodes and the SAR data link power relays controlled by the SAR Enable/Disable (SED) 3-day timer.

b. Primary Power System. The primary power source for the satellite was the solar array, which consisted of two modules (wings) mounted on either side of the aft rack. With the vehicle in the normal orbital attitude (sensor module pointing toward Earth) and the solar array deployed in the X-Y plane, the wing axes were aligned 40 deg ahead (toward the direction of flight) of the +Y axis and 40 deg behind the -Y axis (see Figure 2-10). The wings tracked the sun through 360 deg about each axis and, in addition, could be commanded to rotate either clockwise or counterclockwise.

Each wing contained 11 panels (Figure 2-11). The average power output capability of the solar array was expected to vary during the life of the satellite because of the seasonal intensity of the sun, the angle to the sun (beta angle), eclipse periods, and various factors that would tend to degrade the power output capability of the solar cells. During full sun the solar array supplied power to all the loads as well as charging the two Type 40 nickel-cadmium batteries. The batteries supplied the total satellite load requirements during eclipse and also supplied the surge loads that exceeded the solar array instantaneous capability. As the charging process was approximately 90 percent efficient, the solar array had to provide for this additional loss. All of these factors were considered in the solar array design. Figure 2-12 shows the power system's average load support capability during the 1-year mission.

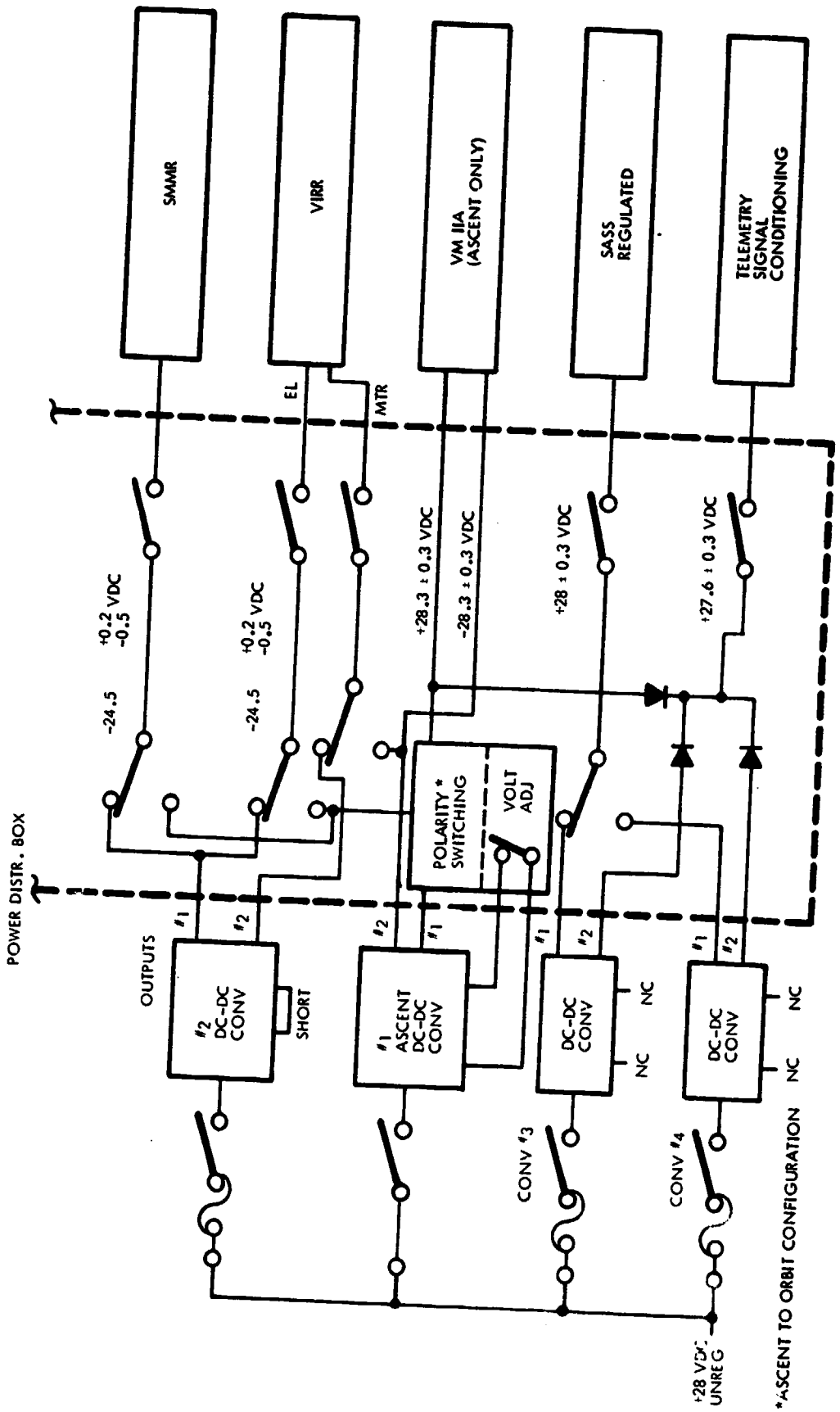

Figure 2-9. Converter Block Diagram

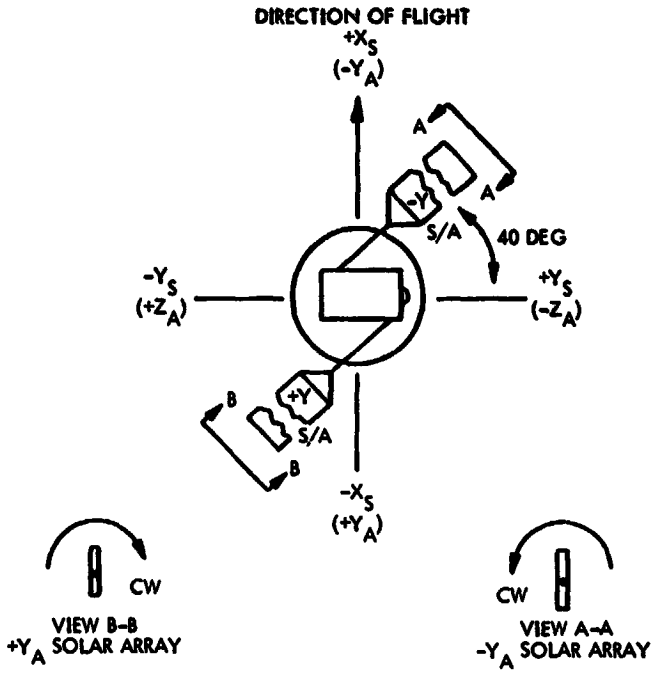

Figure 2-10. Solar Array Rotation Definition

Charging for each battery was controlled by the corresponding CCC, which was configured to charge at two rates by the use of two relays, K1 and K2. Relay K1 connected a maximum of four solar array panels to the battery and relay K2 connected a maximum of five panels to the battery. Each relay had a driver circuit that sensed battery temperature and terminal voltage. The relays were normally closed, permitting the battery to charge. The relay K2 circuit was set to open at a lower voltage than that of relay K1, decreasing the charge rate as the battery approached full charge. The relay K1 circuit was set to interrupt all charging at a slightly higher voltage. The temperature-sensing circuit had the effect of lowering these voltage set points as the battery temperature increased, so that at cooler temperatures the battery could be charged to a higher voltage without excessive oxygen generation with its attendant pressure and heat buildup.

The maximum operating temperature was 98°F and a separate temperature-sensing circuit terminated charging irrespective of voltage. A similar relationship existed for relay drop-out (resumption of charging). When the spacecraft entered an eclipse, the batteries would assume the load and start to discharge, and the voltage would drop. First relay K1 would close and, as the discharge continued to drop the voltage, relay K2 would also close. As the spacecraft emerged from the Earth's shadow, the solar array became illuminated, charging was initiated, and the cycle repeated. Figure 2-13 shows the CCC operating curve and the temperature/voltage relationship for the operating points of relays K1 and K2.

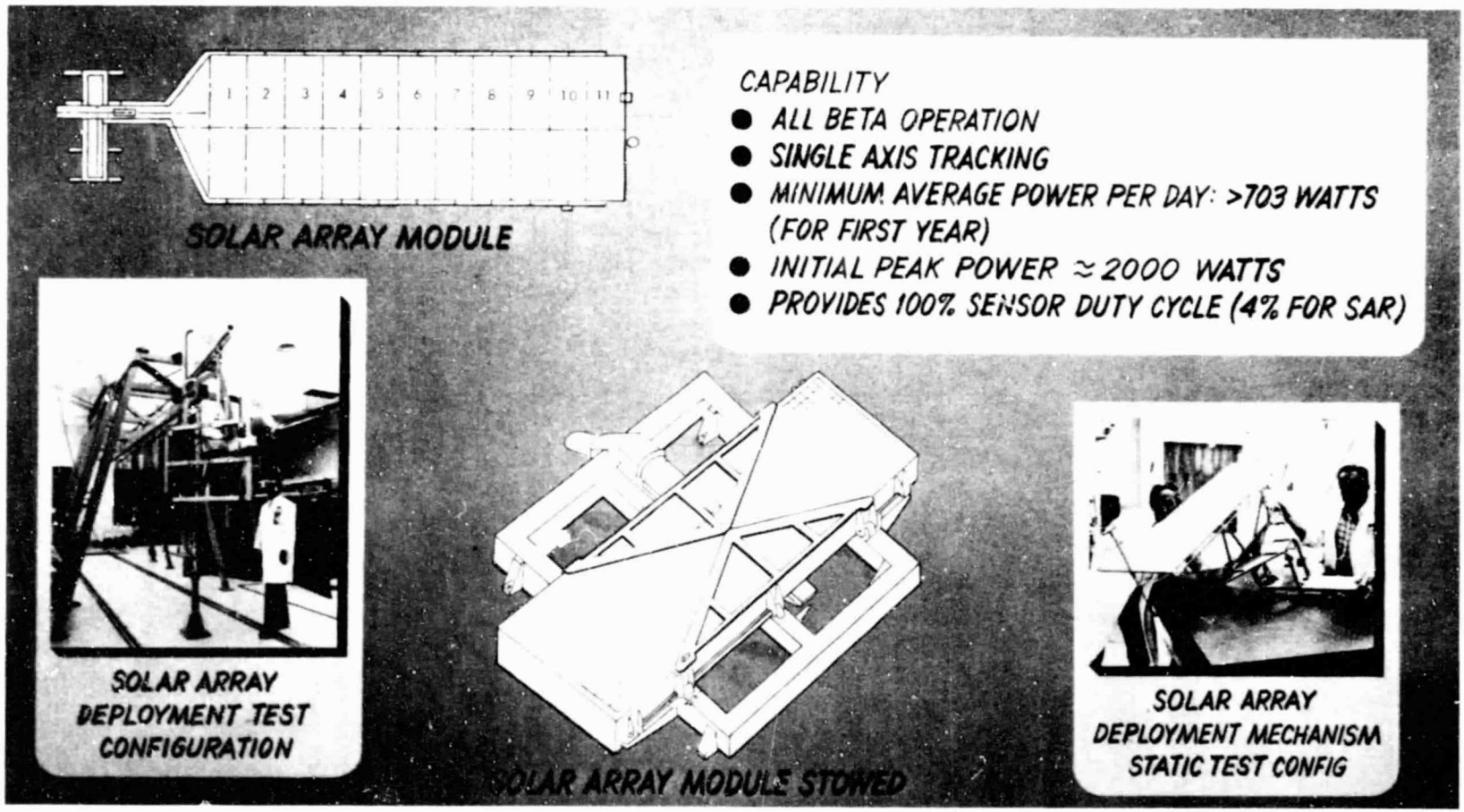

Figure 2-11. Solar Array

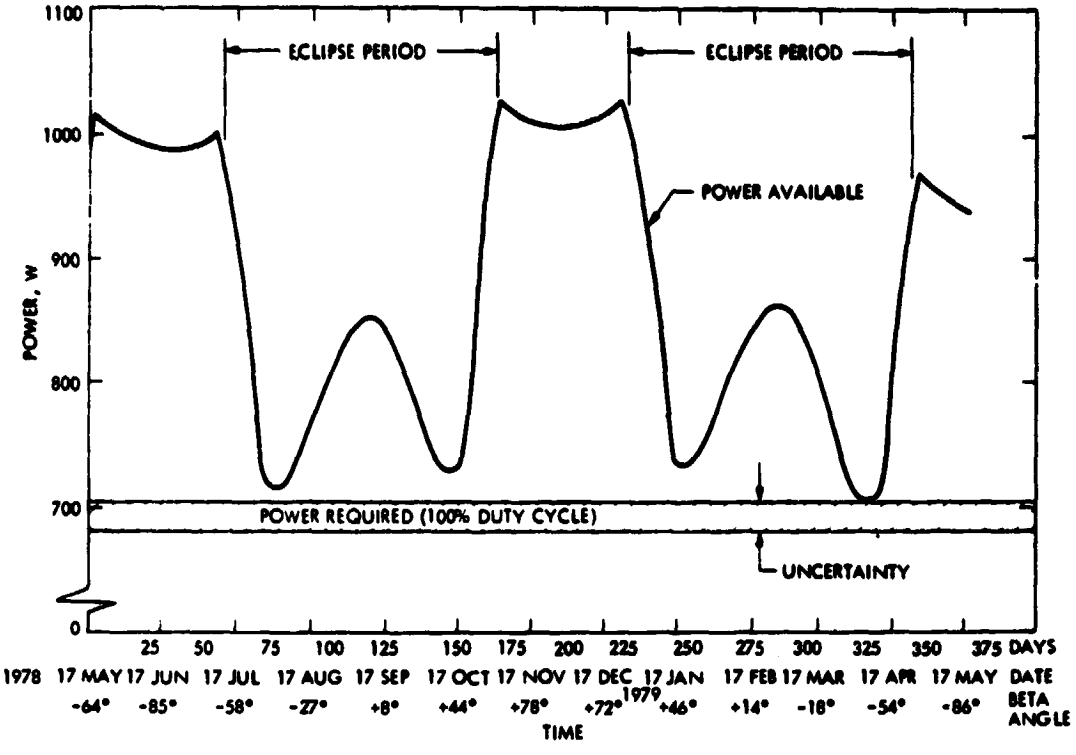

Figure 2-12. Representative Variation of Power Available

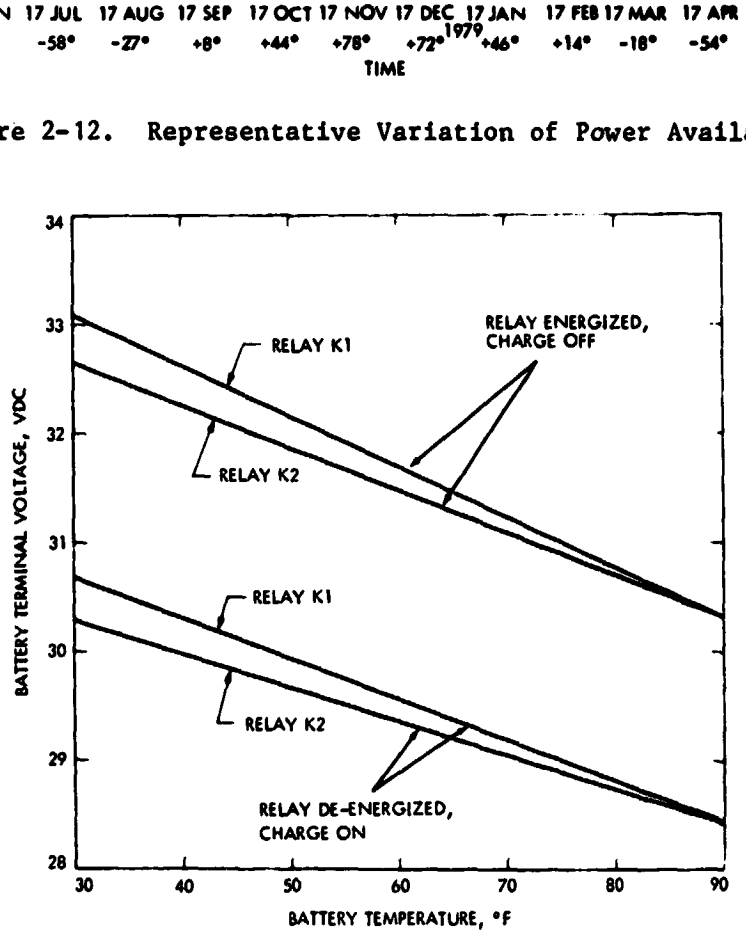

Figure 2-13. Charge Controller Characteristics

Figure 2-14 is a simplified schematic diagram of the primary power control system (solar arrays, batteries, CCCs, and power switching logic). The assignment of solar array panels to the K1 and K2 relays of each CCC is shown. It can be seen that panel 1 of each solar array was connected directly to the K1 relay of its CCC, while panels 9 and 10 were wired through separate disconnect relays (K28 and K34) directly to the battery diode bus, bypassing the CCC and the battery isolation diodes. The latter four panels furnished power to the satellite loads (unless their relays were open), but could not charge the batteries. Of the remaining eight panels that were controlled by both the CCC and disconnect (on/off) relays, four plus panel 1 were from one array and five were from the other. The net result was that in each CCC, relay K1 controlled from one to four panels and relay K2 controlled from zero to five panels, depending on the position of disconnect relays K29, K30, and K37 for CCC 1 and K31, K35, and K36 for CCC 2. In this way, part of each solar array supplied each battery.

Because the solar array output could vary over its 1-year mission by as much as 37 percent of its beginning of life (BOL) output, the solar array was configured to generate at BOL 1.37 times as much power as was actually required. This excess power could charge the batteries at an excessively high rate and cause them to reach maximum voltage too early. For this reason, the panel disconnect relays were provided. Using these relays, it was possible to reduce the number of panels supplying the K1 and K2 relays early in life, during the season of high sun intensity and periods of low load demand. In this manner, the disconnect relays could effectively trim or balance the power available with the load. The design intent was for the batteries to reach essentially full charge just before going into an eclipse. During eclipse, the batteries would normally be discharged by an additional 12.5 percent of capacity.

c. Power Management. Analysis techniques, augmented by real-time (R/T) and full-revolution flight data, were the basis of power management. Satellite activities were pre-planned based on analytical results that determined the sensor duty cycles that could be safely maintained, as shown in Figure 2-15. The power profile program was used to calculate the maximum load that could be supported as a function of solar beta angle (date), as shown in Figure 2-12. Satellite and sensor orbit average loads were determined by on-orbit measurements. The criterion for satellite operation was that the power available was to exceed the power required by the margin of the combined uncertainties of both calculations. In actual practice, this system of management experienced critical limitations that resulted in an undervoltage condition during the first low power period. This situation is discussed in the following paragraphs.

Battery State-of-Charge Determination. The R/T statusing of satellite voltage and current, and battery voltage, current, and temperature measurements provided only a coarse check of the battery capacity. This was because of a characteristic of nickel-cadmium batteries where voltage does not appreciably change as a function of battery capacity unless the battery is almost fully charged or discharged, as shown in Figure 2-16. For example, the difference in battery voltage from a 25- to a 75-percent discharged battery was approximately 1.0 V. The change in voltage for a change in load from 7 to 15 A at a constant capacity was 0.5 V. For a change in temperature, a different set of curves was required, as was the case for batteries being charged. Also,

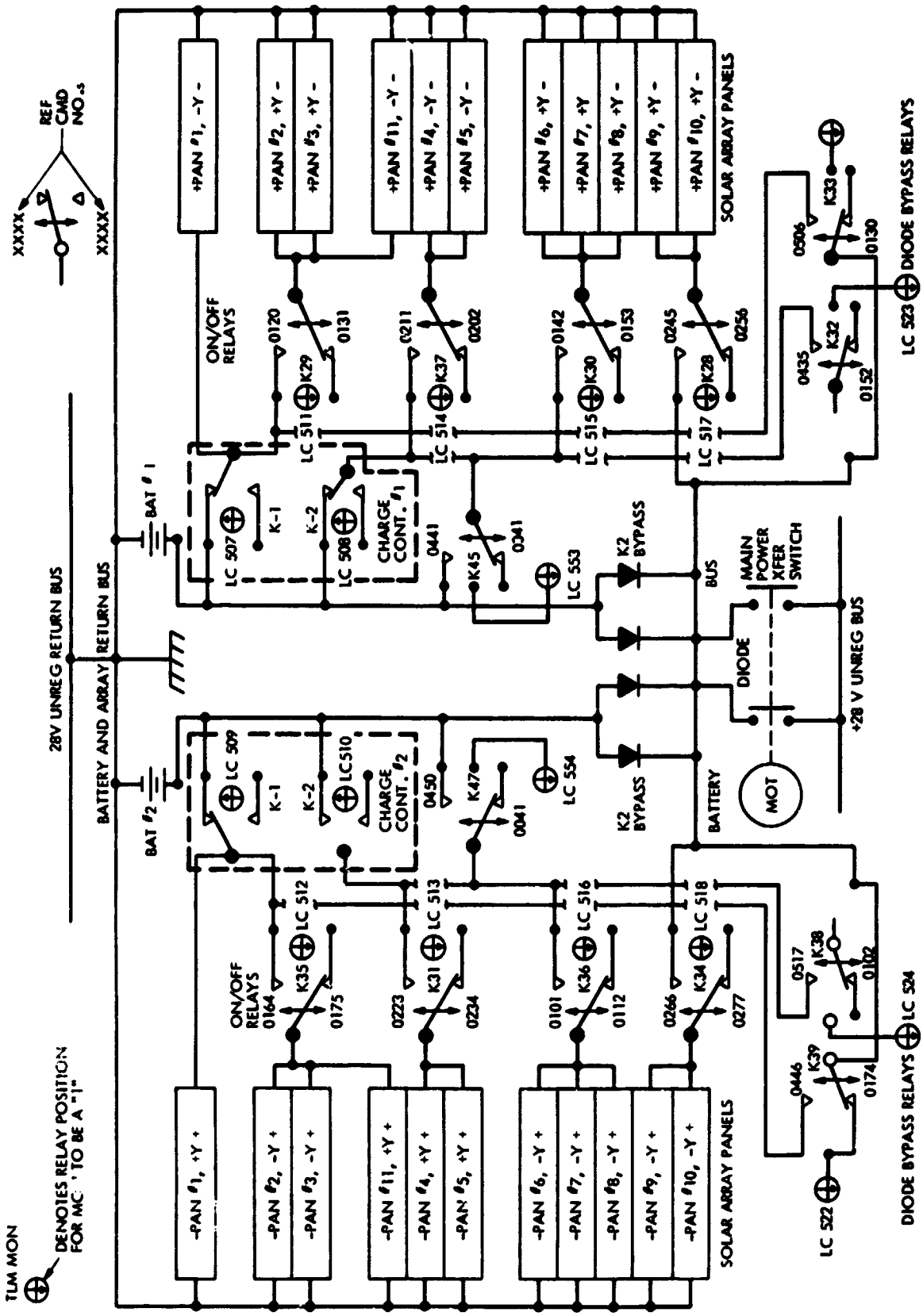

Figure 2-14. Primary Power Control, Simplified Schematic Diagram

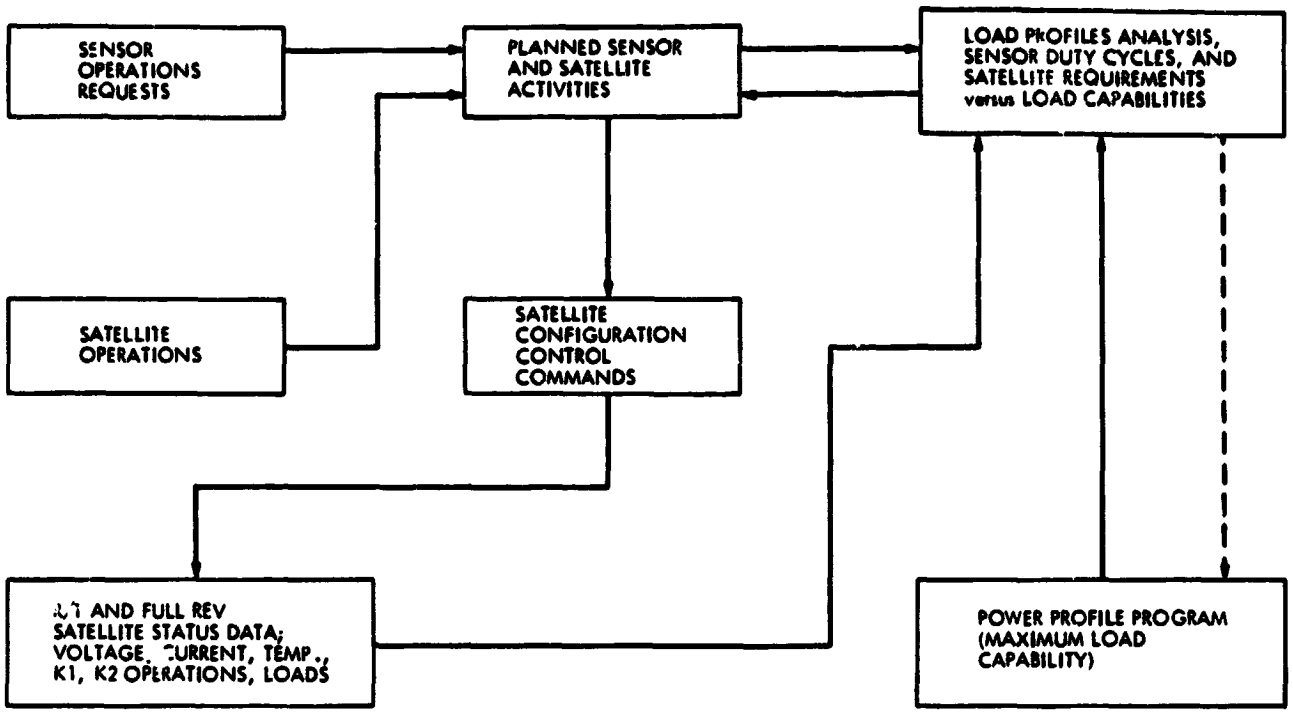

Figure 2-15. Power Management Functional Flow Diagram

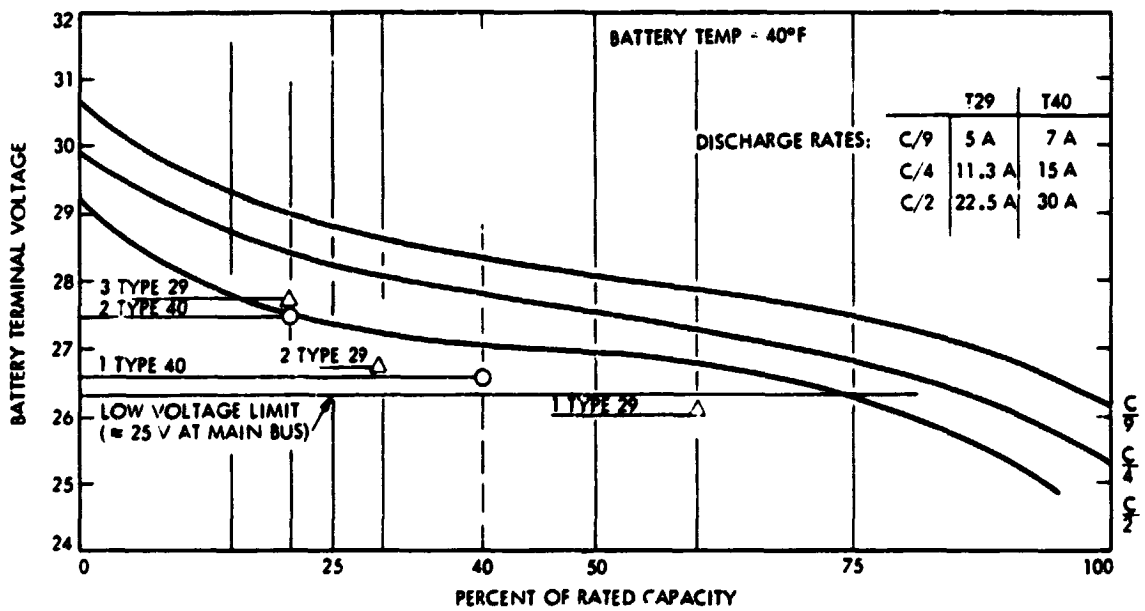

Figure 2-16. Main Bus Surge Load Characteristic Versus Battery Configuration

after a battery had been operated over a certain capacity interval for a period of time, the state-of-charge for a given voltage generally decreased, resulting in overall lower capacities as a function of voltage. However, if a K2 relay was open during a R/T pass, a more accurate estimate of capacity was possible and, in fact, this condition prior to eclipse entrance would indicate a normally operating system. Because, however, the R/T passes often did not cover the period just prior to eclipse entrance, quick turnaround data was required on a daily basis during critical power times (e.g., low power periods and satellite maneuvers. The availability of this data was planned for within 6 h of ground capture.

K1 and K2 Set Points. The opening and closing set points for relays K1 and K2 are shown in Figure 2-13 for a battery temperature range of from 30°F to 90°F. These set points were changed from the originally proposed design, which had the minimum operating temperature of 40°F. The batteries were to be maintained at or above this temperature by heaters. Subsequent analysis of maximum voltage effects, power consumption, and thermal design showed the following:

(1) The maximum voltage at the sensor interface could exceed 32.0 V (specification limit) by approximately 0.2 V for the ALT, SAR electronics, and Tranet beacon at 40°F at the K1 open set point.

(2) Power consumption essentially matched power availability at the fourth low power point (Figure 2-12).

(3) Power could be saved by lowering the battery operating temperature to 30°F, reducing the heater duty cycle.

The decision was made to extend the CCC operating range to 30°F using the K1 and K2 set points originally set for 40°F, and to maintain the same slope for all four curves. This approach had the advantage of requiring a minimum change to the existing CCCs that were planned for the program. It was additionally shown that for most solar beta angles, the expected battery temperatures were greater than 40°F, and that battery temperatures less than 40°F, which would require a larger battery heater duty cycle, would occur when excess power was available. Finally, operating temperatures of 30°F were never expected, eliminating the concern for overvoltage conditions. However, the result of shifting the K1 and K2 curves and maintaining the same slope was that at the expected operating range of 40°F to 45°F, the maximum state-of-charge possible was reduced from the proposed values. The original intention was that relay K2 would open at 90 percent state-of-charge at 40°F. For the adjusted conditions, the corresponding state-of-charge was 80 to 85 percent with relay K1 opening at approximately 90 percent.

Power Profile Program. This program had been originally used in the power subsystem design analysis, which determined the need for addition of the eleventh panel to each solar array wing. This program was rewritten to incorporate a

battery model that had been developed from initial development funds by the Electrical Power Systems Department at LMSC. This model used the latest laboratory-measured battery characteristics to determine charging and discharging efficiencies as a function of battery temperature and charge current. Power system conditions were calculated for 2-deg steps around the orbit. Energy was added to or taken from the batteries depending on the calculated power available, with satellite loads specified as variable. Array tracking was simulated for each step to provide correct available power. The operation of relays K1 and K2 was also simulated. By an iterative process starting with a condition of excess power, it was possible to determine for a specified date (the correct solar beta angle was automatically calculated) the maximum capability of the system; i.e., that load which would result in relay K2 opening just at eclipse entrance. Iteration (using an increasing load) was necessary as it had been determined that calculated available power was reduced as the load increased and approached capability (less power was available as the average system voltage decreased, all other things being equal).

2. Attitude Determination and Control Subsystem

The attitude determination and control subsystem consisted of the following:

(1) Scanwheels (2).

(2) Gyro Reference Assembly (GRA).

(3) Augmented Electronics Assembly (AEA).

(4) Reaction Control System (RCS).

(5) Control Logic Assembly (CLA).

(6) Roll Reaction Wheel (RRW).

(7) Pitch Momentum Wheel (PMW).

(8) Magnetic Control Assembly (MCA).

(9) Electromagnets (3).

(10) Magnetometer.

(11) Sun aspect sensor assembly.

Attitude control required two modes of operation: (1) a mass expulsion system for ascent and orbit adjust and (2) a gravity gradient and momentum bias system with magnetic desaturation for long term orbital use. Attitude determination for sensor data use was obtained by ground processing of the appropriate attitude control inputs and the sun aspect sensor outputs. The two attitude control modes are discussed in the following paragraphs. Attitude determination

for sensor use is described in Volume I of this report. A block diagram of the attitude control system is shown in Figure 2-17.

a. Ascent and Orbit Adjust. This mode of operation used hydrazine thrusters for attitude control. A description of the hydrazine thruster modes and control during Agena main engine burn-in is given in Paragraph 4. Attitude determination for control purposes was provided by the horizon scanners, which output a continous pitch and roll error signal. As shown in Figure 2-17, these signals (error voltages) were input to the AEA along with the output signals from the GRA (roll, pitch, and yaw attitude errors). The AEA also provided the scanwheel pitch and roll errors to the respective gyros as gyro torquing commands. The roll error was summed with the roll gyro output and with the sign reversal, and was input to the yaw gyro as a torquing command. This gyro compassing mode provided a bound on yaw gyro drift because roll and yaw errors were coupled, when the vehicle was pitching over at a constant rate (the orbit rate) necessary to keep one coordinate of the vehicle pointed to the center of the Earth. The vehicle response to these commands provided for removal of these errors. This response was obtained by the AEA, which received the gyro error signals as inputs and provided pulse commands as outputs to the appropriate hydrazine thrusters (Figure 2-18). The AEA integrated the horizon sensors (outputs), GRA (inputs and outputs), and the hydrazine thrusters (inputs). Mode change commands and manual hydrazine commands (e.g., orbit adjust thruster burns) were also provided from the Command Processor Unit (CPU) through the AEA. Figure 2-19 is a sketch of the guidance module assembly.

b. Orbit Attitude Control. Orbit attitude control was performed by a momentum management system that used wheels and electromagnets (Figure 2-20) to maintain the orbit attitude of the satellite with the long axis locally vertical, providing gravity gradient restoring torques about the pitch and roll axes (Figure 2-21). Disturbance torques caused the vehicle to accumulate angular momenta. These were absorbed by massy wheels, oriented with their spin vectors along orbit axes, executing rotation speed changes (Figures 2-22 and 2-23). Photographs of selected components are shown in Figure 2-24.

Seasat carried a 20.3 n-m/s (15 ft-lb/s) momentum wheel on the orbital pitch axis (Figure 2-22). The PMW rotated at 2210 rpm in a direction that extended its momentum vector in the minus pitch direction; i.e., the same sign as the orbit rate vector. The PMW was modulated ±10 percent about the 2210 rpm point to dampen pitch disturbances.

Pitch and roll attitude errors were detected by a combined conical-scan horizon sensor and momentum wheel termed a scanwheel. Two scanwheel assemblies were used, designated as the Left Scanwheel Assembly (LSWA) and the Right Scanwheel Assembly (RSWA). These assemblies were mounted and operated so that their spin vectors were in the plane containing the pitch axis and additive in the negative pitch direction. The vehicle pitch momentum bias was therefore the sum of that created by the PMW and the pitch components of the scanwheels. The term component is appropriate since the scanwheels were canted 26 deg down from the local horizontal. The momentum vector of each scanwheel therefore could be resolved into a pitch and yaw component. Because of the cant angle and the rotation direction that created a common pitch vector, the scanwheel

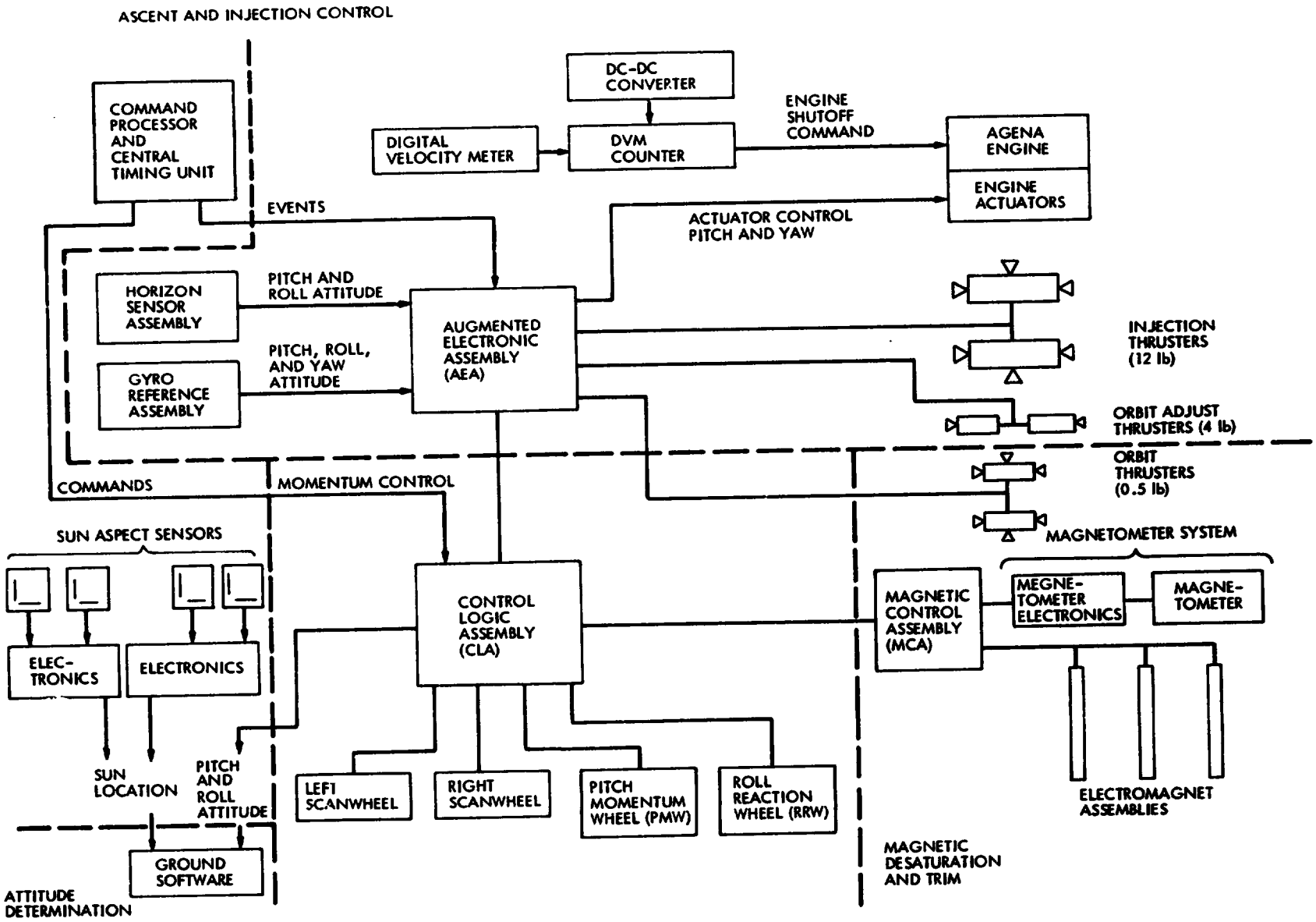

Figure 2-17. Attitude Control System

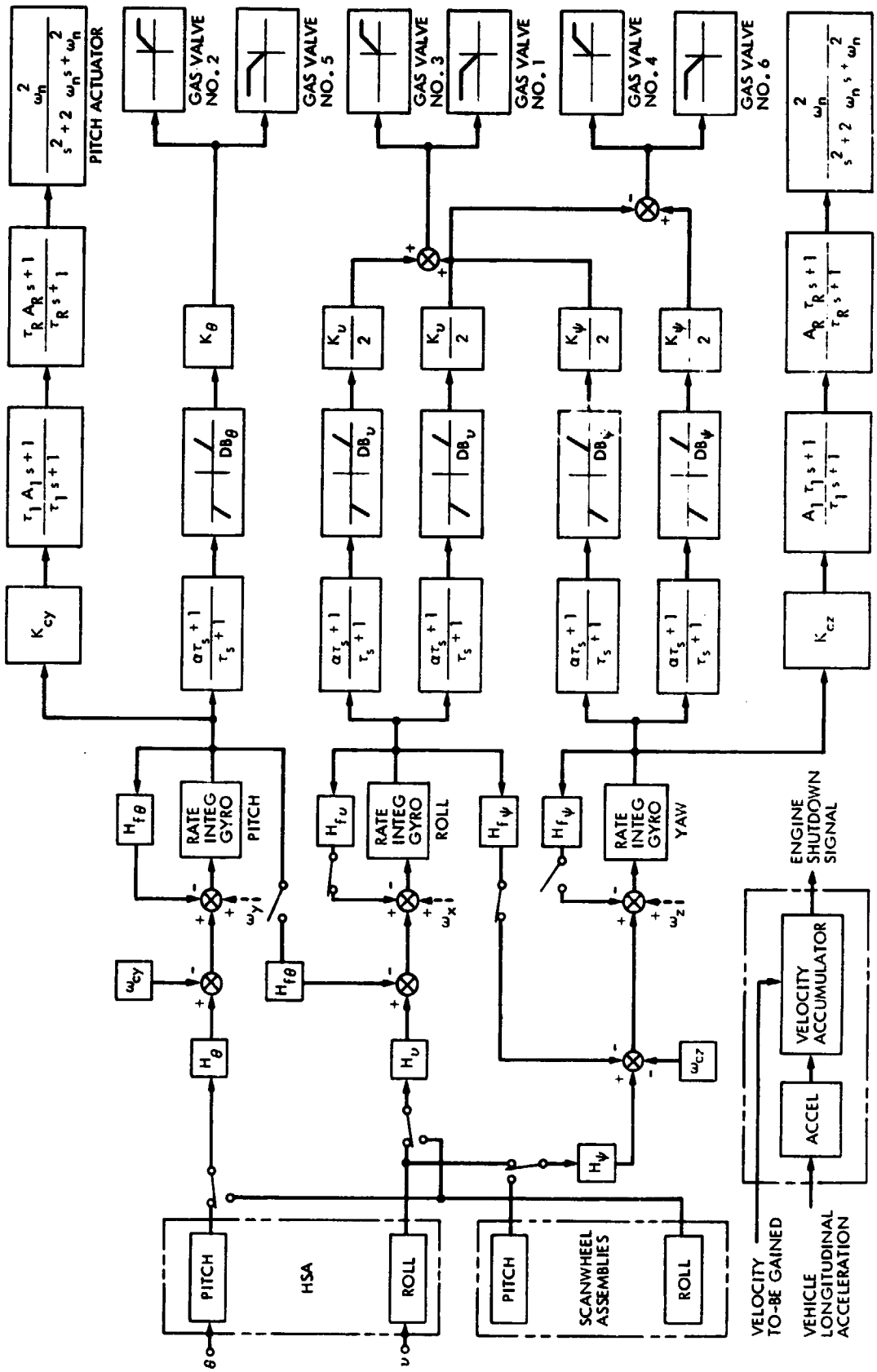

Figure 2-18. Ascent Control System

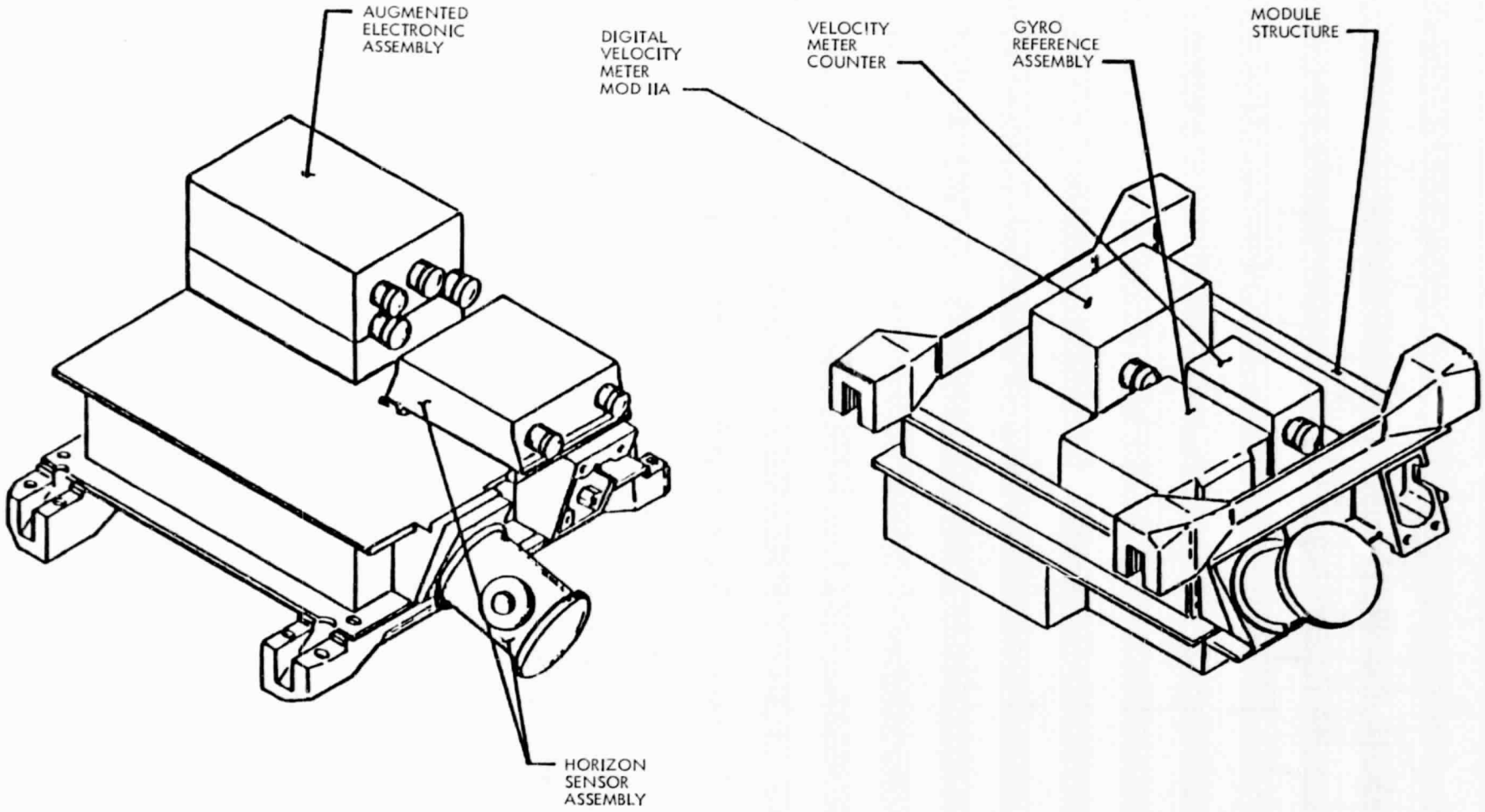

Figure 2-19. Guidance Module Assembly

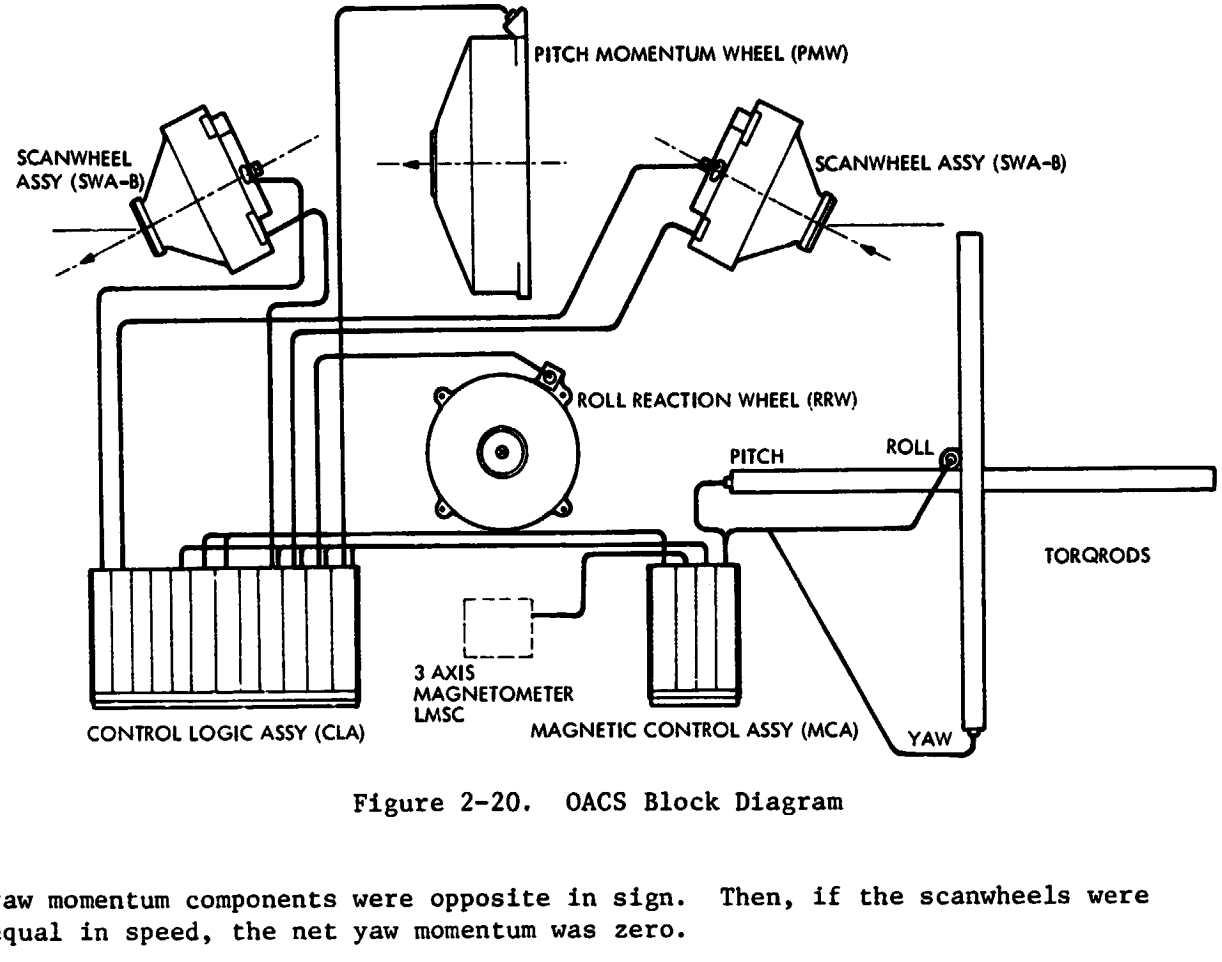

Figure 2-20. OACS Block Diagram

yaw momentum components were opposite in sign. Then, if the scanwheels were equal in speed, the net yaw momentum was zero.

To optimize their attitude determination functions, the scanwheels had an operating point of 900 rpm, and the nominal excursion was +300 rpm with a 500-rpm lower limit. At 900 rpm the scanwheels each had 2.6 n-m/s (1.9 ft-lb/s) of momentum. Given the 26-deg cant, each wheel developed 2.3 n-m/s in pitch and 1.1 n-m/s in yaw.

Roll torques were produced by speed changes in a reaction wheel (2.3 n-m/s (1/7 ft-lb/s) at 1800 rpm) sited with its spin axis along the vehicle orbital roll axis. In an ideal vehicle, the RRW would be at zero rpm for zero roll attitude error, and would accelerate in either direction as appropriate if an error was detected. The Seasat RRW was intended to operate at a biased operating point of 300 rpm counterclockwise (as viewed by an observer looking in the +X direction) to compensate for an expected principal axis offset. Fifteen other pre-set bias speeds were available and could be commanded in flight to compensate for possible other bias torques.

As previously stated, pitch and roll attitude errors were detected by the horizon scanner function of the scanwheels and were automatically used in the control of the vehicle, as well as being telemetered. The sun sensor system was only used as telemetered data to provide a ground computation of yaw attitude.

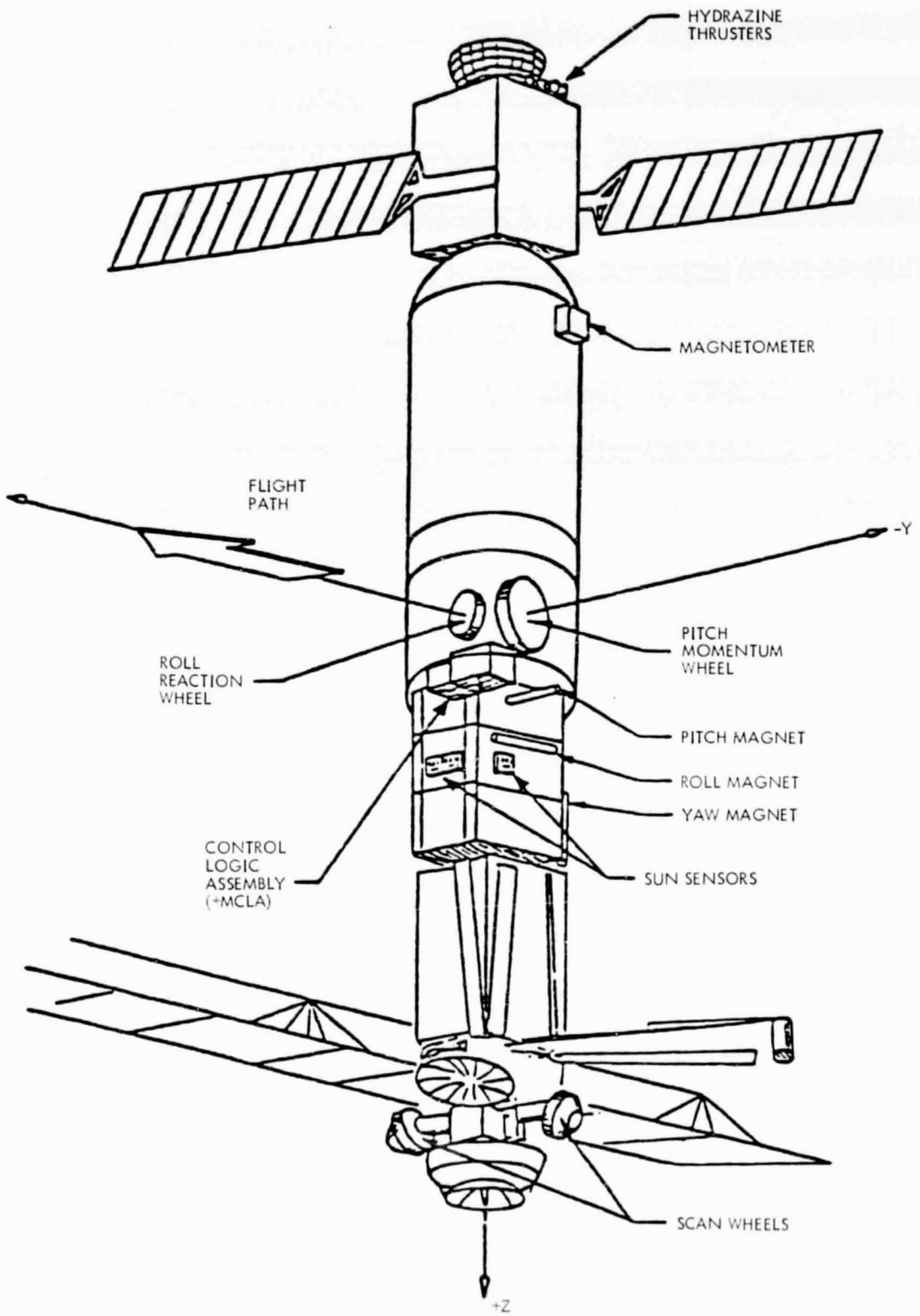

Figure 2-21. OACS Component Configuration

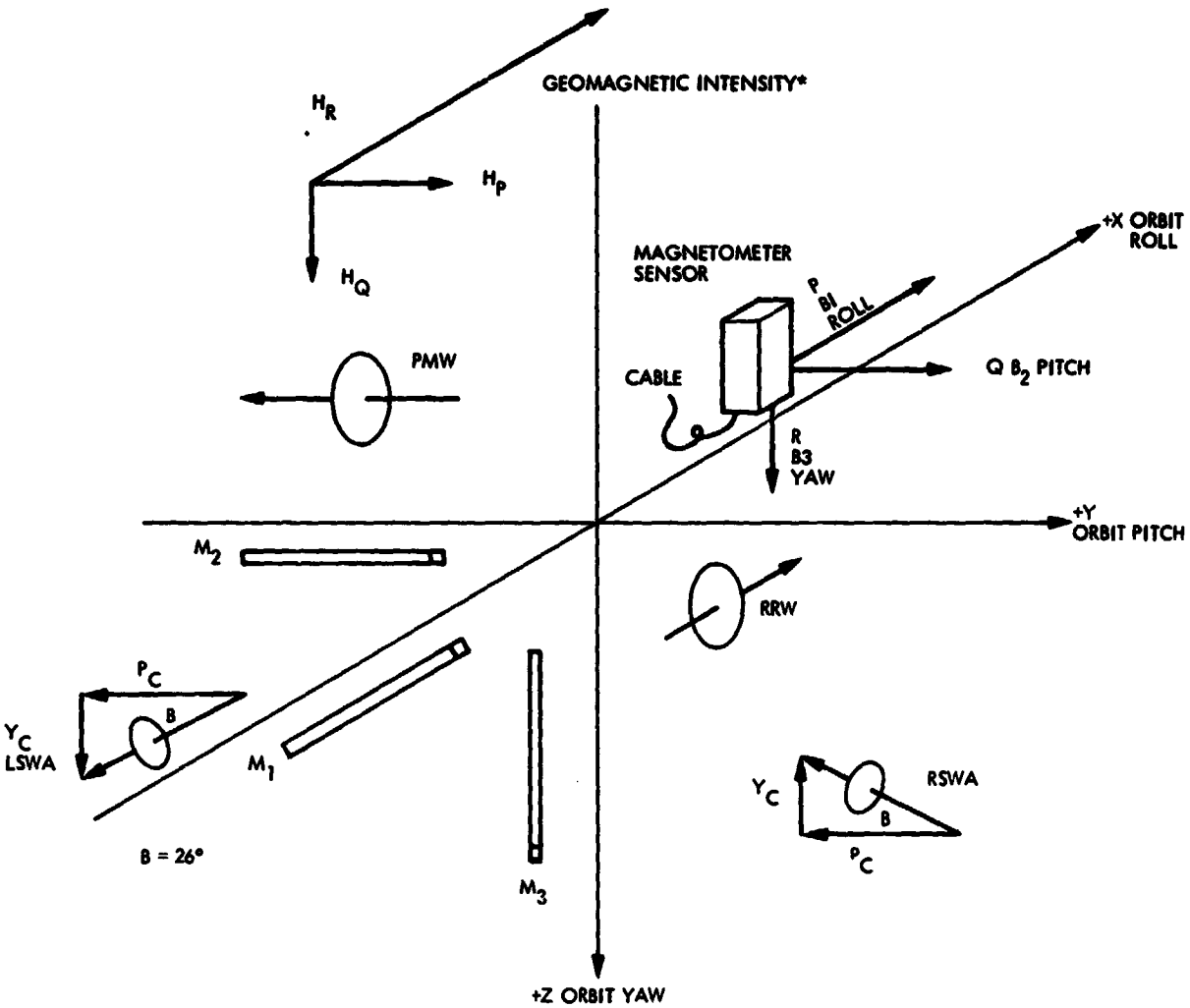

*H_Q, WHILE ORBITING SOUTH TO NORTH, IS NEGATIVE IN THE SOUTHERN MAGNETIC HEMISPHERE, CHANGING SIGN AT THE GEOMAGNETIC EQUATOR.

H_P, H_R WHILE ORBITING NORTH TO SOUTH, ARE NEGATIVE; H_Q IS POSITIVE IN THE NORTHERN MAGNETIC HEMISPHERE, CHANGING SIGN AT THE GEOMAGNETIC EQUATOR

Figure 2-22. Electromagnetic and Wheel Conventions, Right Hand Rule; Northern Hemisphere, Moving South to North

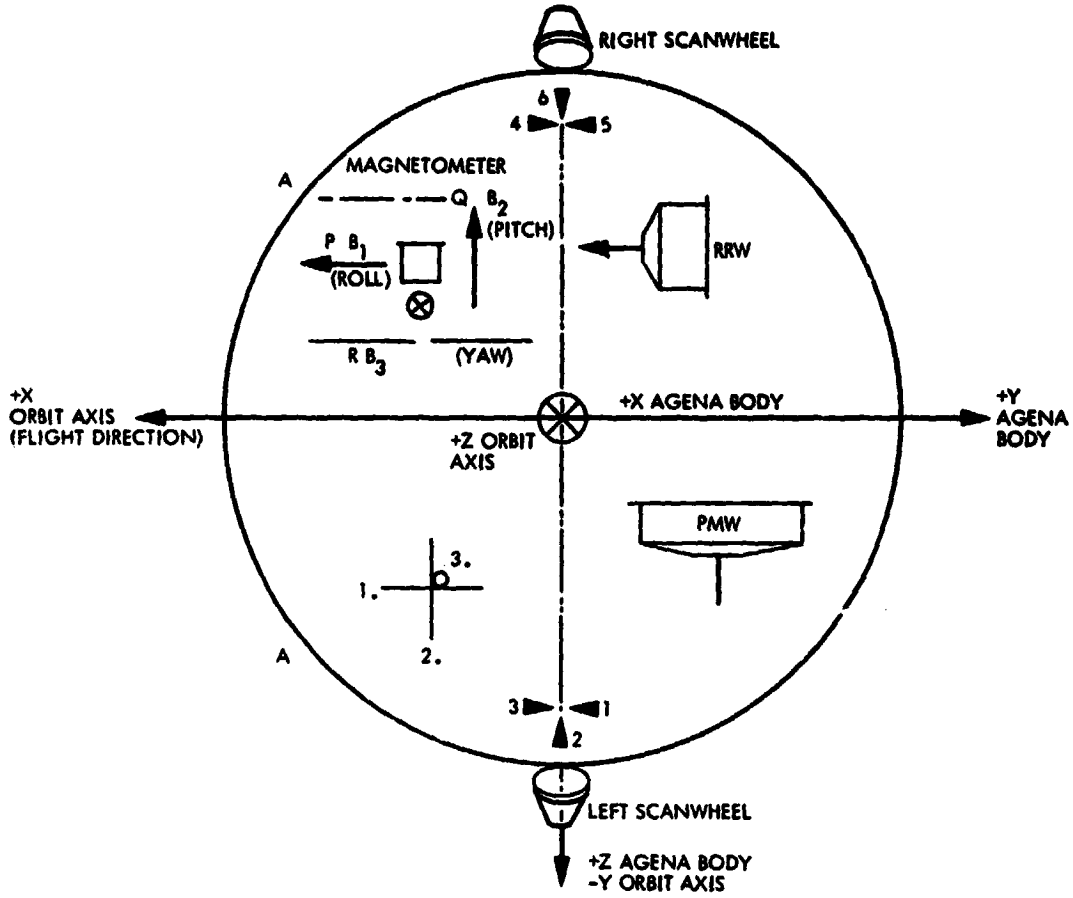

ELECTROMAGNETS
ASSEMBLY TRIAD

1. ORBIT ROLL AXIS MAGNET
2. ORBIT PITCH AXIS MAGNET
3. ORBIT YAW AXIS MAGNET
4. CONNECTORS AT POSITIVE AXIS END

THE SPIN AXES OF THE PMW AND THE RRW ARE PARALLEL TO THE SATELLITE ALIGNMENT REFERENCE AXES AS SHOWN WITHIN 0.07 degree. THE MAGNETS AND THE MAGNETOMETER ARE MOUNTED WITH THEIR AXES PARALLEL TO THE VEHICLE AXES WITHIN 0.5 degree. IDEALLY, THE MAGNETS SHOULD BISECT EACH OTHER AND BE ORTHOGONAL. THE MAGNETOMETER AND MAGNETS MUST BE AT LEAST 150 inches APART.

THE CONVENTION FOR THE WHEEL SPIN DIRECTION IS: WITH THE OBSERVER LOOKING INTO THE FLAT FACE WITH THE MOUNTING FEET, CW ROTATION OF THE WHEEL IS POSITIVE. IN ACCORD WITH THIS CONVENTION THE PITCH MOMENTUM WHEEL SPINS CW, THE ROLL REACTION WHEEL IS SHOWN CW (IT CAN SPIN EITHER WAY), THE RIGHT SCANWHEEL ROTATES CCW, AND THE LEFT SCANWHEEL ROTATES CW.

Figure 2-23. Orbit Attitude Control System Component Orientation

Figure 2-24. Orbital Attitude Control System

Twelve electronics modules, wired together and physically bolted together, formed the Control Logic Assembly (CLA) as shown in Figure 2-20. The name of each electronics module indicated its function:

(1) Signal processor 1 (left scanwheel).

(2) Signal processor 2 (right scanwheel).

(3) Attitude computer.

(4) Pitch shaping logic.

(5) Roll/yaw command logic.

(6) Power supply 1.

(7) Power supply 2.

(8) Command and interface.

(9) Left scanwheel motor driver.

(10) Right scanwheel motor driver.

(11) Roll reaction wheel motor driver.

(12) Pitch momentum wheel motor driver.

The signal processors conditioned the horizon scanner outputs for the attitude computer, which generated analog voltages representative of pitch and roll attitude information. These signals were applied to the telemeter, ascent system gyros, and pitch shaping logic and roll/yaw command logic. A detailed description of the function of these logic elements is available for reference.*

Referring to Figure 2-25, the pitch attitude angle and rate of change was processed into a signal applied to the PMW motor driver. The signal was proportional to a corrective torque required to remove the sensed pitch attitude error. The ability of the pitch wheel to accumulate or absorb vehicle pitch momentum was limited by electrical design parameters of the motor driver electronics. Total pitch momentum was maintained within wheel limits by the magnetic desaturation system. Because of gyroscopic effects, vehicle roll attitude errors resulted in a yaw displacement proportional to the torque and inversely proportional to the gyroscopic stiffness provided by the spin vector of the PMW and scanwheels. The roll attitude error from the attitude computer was simultaneously applied to two separate integrators in the roll/yaw control logic. Each integrator output was applied back through an orbit period (100 min) T network to the input of the other. The integrator output for the RRW motor driver was of opposite sign to the roll attitude error and represented a torque command to

*Weiss, R., Rodden, J. J., and Hendricks, R. J., "SEASAT-A Attitude Control System," AIAA Paper 77-1057, Hollywood, Florida, August 1977.

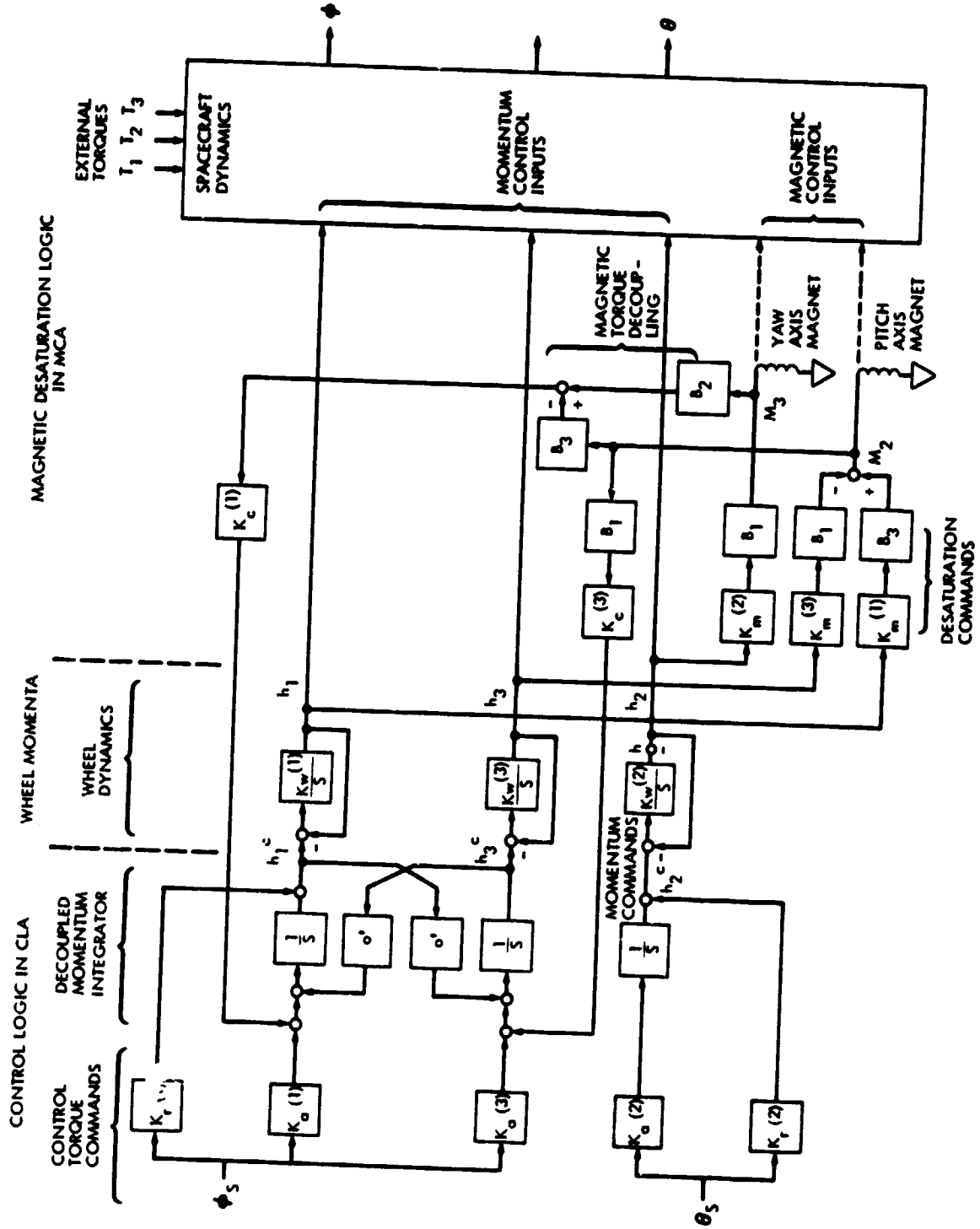

Figure 2-25. On-Orbit Control System

the RRW motor driver of 0.005 ft-lb/deg. The output connected to the scanwheel motor drivers was the same sign as the roll error and represented a torque command to the motor drivers of 0.001 ft-lb/deg. At the LSWA motor driver, this signal was applied so that a plus voltage caused a decrease in speed below 900 rpm; at the RSWA motor driver, a plus voltage caused a speed increase. Summaries of the wheel systems' response to attitude errors and the electromagnetic system's response to wheel speed are shown in Tables 2-1 and 2-2, respectively.

Two power supplies were carried for redundancy, although one was sufficient for CLA operation. The unused power supply could be left off for power saving; the outputs were hard-wired through isolating diodes. Each power supply was a dc-dc converter that produced regulated ±10 V for operating the electronics on the circuit cards and ±45 V for biasing the bolometers in the scanwheels. Specified power supply performance was obtained with a vehicle bus voltage between 24 and 33 V.

The command and interface module facilitated operation of the control system, although in a degraded mode, if the RRW failed; i.e., stopped operating or had to be turned off, or if one of the scanwheels ceased to function. Only one such component failure could be sustained. A backup mechanization was also available for the case of the PMW failing. No command and interface circuits were involved. The scanwheels would be commanded to operate at a 1700-rpm bias point to augment their contribution to the pitch momentum vector, and the output of the pitch shaping logic would be applied directly to the scanwheel motor drivers. A ±300-rpm excursion was still maintained for yaw momentum management, as the output of the roll/yaw command logic was also applied.

The previously assumed RRW failure would have been compensated for by controlling the scanwheels through a different control law to provide sufficient changes in yaw momentum to absorb roll errors. For the one scanwheel out case, the gain to the remaining scanwheel would be doubled and a bias applied to the attitude computer. This would provide a nominal roll attitude reference, sufficient for control purposes, even with the vehicle at the 1.13-deg roll attitude caused by the unbalanced yaw momentum from the remaining wheel. None of the reconfiguration for a failed wheel was automatic, as commanding was required.

The motor driver circuit cards for each wheel were inverters, changing the vehicle 28-V dc power into the ac energy required to operate the squirrel cage induction motor of the PMW (800 Hz) and the RRW and scanwheels (650 Hz). All of the wheels were equipped with electromagnetic tachometers. These signals were used in the motor drivers for internal speed feedback and also applied to the Magnetic Control System (MCS) and the telemeter, as they were an indication of wheel momentum.

It was a characteristic of the MCS that the momentum absorbing wheels reached a speed limit determined by the design of the motor driver electronics. This speed limit was the synchronous speed, where the wheel was rotating at the same rate as the magnetic field of the motor windings. Because the motor could not go faster than its synchronous speed, the wheel could not absorb more momentum and was saturated or loaded. The wheel was desaturated or unloaded by driving it in the opposite direction. This, of course, created a torque on the

Table 2-1. Wheel Systems Response to Attitude Errors[1]

Vehicle Attitude Error (Orbit Axes)	Left Scanwheel		Right Scanwheel		Pitch Momentum Wheel Speed	Roll Reaction Wheel Speed
	Speed	Scanner Output	Speed	Scanner Output		
+ Pitch	No response	+ Volts	No response	+ Volts	Decreases (step + ramp)	No response
- Pitch	No response	- Volts	No response	- Volts	Increases (step + ramp)	No response
+ Roll	Decreases (ramp)	+ Volts	Increases (ramp)	+ Volts	No response	Increase CW (step + ramp)
- Roll	Increases (ramp)	- Volts	Decreases (ramp)	- Volts	No response	Increase CCW (step + ramp)

[1]See Figure 2-22 for electromagnetic-wheel polarity convention and relation to reference axes. Component orientation is shown in Figure 2-23.

Note: There is no yaw attitude sensor in the control system.

Table 2-2. Electromagnet System Response To Wheel Speed

Wheel Momentum (Orbit Axis Convention)	Orbital Pitch Axis (M2) Magnet Excitation Sense	Orbital Yaw Axis (M3) Magnet Excitation Sense	D1 Desaturation Torque Compensation Command Sense	D3 Desaturation Torque Compensation Command Sense
Plus roll. Roll reaction wheel (CW above bias speed)	N to S: -YN +YN; S to N: +YN -YN	No response	- (RRW slows to zero or bias point)	+ Sign of B1 x B3 (SWA speeds change as function of roll axis field direction)
Minus roll Roll reaction wheel (CCW above bias speed)	N to S: +YN -YN; S to N: -YN +YN	No response	+ (RRW slows as above)	- Sign of B1 x B3 (Same note as + case above)
(+), Pitch momentum wheel below bias speed	No response	N to S: +ZN; S to N: -ZN	No command (PMW responds to attitude error caused by magnet torque)	No command (PMW responds to attitude error caused by magnet torque)
(-), Pitch momentum wheel above bias speed	No response	N to S: -ZN; S to N: +ZN	No command (PMW responds to attitude error caused by magnet torque)	No command (PMW responds to attitude error caused by magnet torque)
+Yaw, LSWA at higher speed than RSWA	N to S: -YN; S to N: +YN	No response	+ Sign of B1 x B3 (affects RRW speed as function of roll axis field direction)	-, LSWA speed decrease, RSWS speed increase to maintain average of both wheels at 900 rpm, normal mode

Table 2-2. Electromagnet System Response To Wheel Speed (Continuation 1)

Wheel Momentum (Orbit Axis Convention)	Orbital Pitch Axis (M2) Magnet Excitation Sense		Orbital Yaw Axis (M3) Magnet Excitation Sense	D1 Desaturation Torque Compensation Command Sense	D3 Desaturation Torque Compensation Command Sense
	N to S	S to N			
-Yaw, LSWA at lower speed than RSWA	+YN	-YN	No response	- Sign of B1 x B3 (same note as + case above)	+, RSWA speed decrease, LSWA speed increase to maintain average of both wheels at 900 rpm, normal mode

vehicle that had to be overcome if unacceptable rates were to be prevented. These necessary counter torques were generated by solenoid-wound magnets reacting against components of the geomagnetic field. Three magnets were carried, one for each axis. The roll axis magnet was used only to nullify the magnetic momenta of vehicle residual magnetism. This function was also performed by the pitch and yaw axis magnets, along with wheel desaturation. All three magnets were true electromagnets with the core material chosen for minimum retentivity.

Setting of the magnets to neutralize the effects of residual momenta was a ground command function. Each magnet, once selected, was stepped 200 pole-cm for each command, to a limit of 12,800 pole-cm. At the 65th step, the magnetization changed sign and decreased with subsequent steps. Reset or initialization was achieved by deactivating the MCS. A machine program had been devised to assist the setting of the magnets, based on observed attitude behavior.

The MCS was composed of the following four modules:

(1) Momentum shaping and power supply.

(2) Magnetic control logic 1.

(3) Magnetic control logic 2.

(4) Electromagnet drivers.

In addition to the MCS, a 3-axis fluxgate magnetometer was carried as an essential part of the desaturation function. It was a self-contained subsystem, requiring only the vehicle 28-V dc power for operation. It operated continuously and applied its outputs (the magnitude and direction of the components of the local field) to the magnetic control logic 1 module.

The momentum shaping and power supply module provided the switchable interconnect between the magnetic control logic 2 and electromagnet drivers circuit cards to enable and inhibit wheel desaturation. It also contained a dc-dc converter to provide regulated 10 V dc for the other modules in the MCS. The 10-V busses of the CLA could be switched to those of the MCS if the MCS power converter failed.

Magnetic control logic 1 conditioned the magnetometer outputs to 0- to 5-V dc levels for the telemeter, and also converted them to 5-kHz square waves for use in the magnetic control logic 2 module. It was here that the signals representing the natural field (B1, B2, and B3) and the wheel momenta (H1, H2, and H3) were combined as solid-state analog multiplers to generate desaturation commands (Vm2 and Vm3) to the pitch and yaw magnet drivers. The subscripts 1, 2, and 3 refer to roll, pitch, and yaw, respectively. Additional manipulations were performed, using the Vm2 and Vm3 commands and the natural field and wheel momenta signals to create feedback to the RRW and scanwheels.

The electromagnet driver module contained the solid-state counting modules for the stepping of each magnet, as required to counter residual momenta. Each solenoid was driven by a power amplifier, which was itself driven by the

step-level output from the counting register. The pitch and yaw magnet drivers also received an analog signal (Vm2 and Vm3) when desaturation was enabled.

At 800 km (431 nm) above Earth, the geomagnetic field in a near-polar orbit varies between 150 and 300 milliGauss. All three electromagnets (also referred to as "Torqrods", a trade name) reacted against the components of this natural field to create torques on the vehicle. In addition to the 12,800-pole-cm static magnetization capability, the pitch and yaw magnets could be driven, in an analog mode, an additional ±50,000 pole-cm. The torques created during desaturation were of the same magnitude as the disturbance torques, and served to restrain the vehicle deceleration or to position the vehicle to an attitude that caused a saturated wheel to be commanded to an unloaded state.

Specifically, the yaw axis magnet operated in the north-south flux of the terrestrial field to cause torques about the pitch axis. The excitation of this magnet was determined by the product of the pitch wheel momentum (H2), given by the speed, and the roll axis field (B1), the north-south flux found by the magnetometer. Because rotations about the pitch axis did not gyroscopically transfer into the other axes, the PMW was unloaded by exciting the yaw axis magnet so that the torque about the pitch axis caused a pitch attitude error which, when detected by the horizon scanners, commanded the wheel from its saturated state. This latter process also removed the pitch error. The system had time constants on the order of 1000 s.

Also, the yaw axis magnet would react against the east-west component of the natural field and cause undesired roll axis torques. This action was designated D1, and caused the RRW to change speed in such a manner as to create a counter torque to that caused by the yaw magnet. The objective was to have zero net torque about the roll axis, and therefore zero disturbance to roll attitude.

The command to the pitch axis magnet (Vm2) was the sum of the product of roll wheel momentum (H2) (speed) and the vertical or yaw axis field component (B3) with the product of the yaw wheel momentum (H3) (an algebraic summation of the scanwheels' speeds) and the roll axis field component (B1). The command to the pitch magnet (Vm2) was then multiplied by the yaw axis field (B3) to develop a speed command to the roll wheel; that is, another D1. The magnet command (Vm2) was also multiplied by the roll axis field (B1) to generate a feedback speed control command to the scanwheels, and it was designated D3. The function of D3 was to have the scanwheels change speed sufficiently to balance the disturbance to the yaw axis caused by the reaction of the pitch magnet to the roll field.

Both D1 and D3 were injected into the summing junction of the respective integrators for the roll wheel and the scanwheels in the roll/yaw command logic module. The design anticipated that the performance of the magnets could have been affected by their environment in the vehicle. Ideally, the magnets should have bisected each other in a cruciform array, which was not possible in the envelope of the bus and SMSS. Instead, the magnets were located at least one magnet length (63.5 cm) (25 in.) from each other and away from ferrous material. Also, the D1 and D3 signals were each applied through a stage where the gain could be selected by command. Eight gain settings were available, ranging from 1.29 to 0.55.

The purpose of the D1 and D3 feedback was to obtain a minimal disturbance to the vehicle while the roll wheel or the pitch wheel, or both, were being unloaded. To recapitulate, unloading the pitch wheel was done by causing actual vehicle pitch attitude change with the yaw magnet; the response of the system to this error commanded the wheel in the direction required to remove the error and unload the wheel. Because the yaw magnet reacted against the other cross component, an undesirable roll torque was created. This was countered by application of an electrical signal (D1) that commanded the roll wheel to accelerate, creating a counter torque.

Unloading of the roll wheel was effected by the D1 signal, with the pitch axis magnet creating a counter torque to the wheel speed change. The scanwheels were not directly unloaded. D3 commanded scanwheel speed changes to counter undesirable yaw axis torque created when the pitch magnet reacted to the roll field. It was undesirable to directly unload the scanwheels with the roll axis magnet because of the large yaw attitude excursions that would be created, as the yaw axis was the axis of minimum inertia. Also, as there was no yaw attitude sensor in the control system, closed loop operation could not be mechanized. However, because of gyroscopic effects involving the orbit rate vector, accumulated yaw momentum was transferred to roll momentum in one-quarter of an orbit. Subsequently, roll error was developed, detected, and the roll/yaw logic received an input. The T network interconnect caused both the roll wheel and the scanwheels to respond appropriately.

Had the MCS failed so as to disable the desaturation function, a backup mechanization could have been commanded. The 0.5-lb force hydrazine thrusters of the ascent system were pulsed by a circuit in the command and interface module to create pitch or roll attitude motion that would have commanded the pitch or roll wheel from the unloaded state. A threshold circuit monitored H1 and H2 and commanded the appropriate thruster to pulse only once when the wheel was at 80 percent of its capability. The authority of the thrusters was such that only 1 short (30-ms pitch, 60-ms roll) pulse was required. As an additional precaution, a timer prevented pulse repetition for 330 s.

From what was known of the variations of the terrestrial field, it was expected that at times in an orbit sufficient flux to permit a wheel to be adequately unloaded would not be sensed. An attitude error would therefore have been maintained in the integrator. A limiting circuit had been placed about all integrators to prevent them from accumulating an error that would have required more time to remove than was available in the expected period of the system's response.

Adjustments for trimming or failure compensation could have been effected by ground command. Table 2-3 provides a summary of this performance adjustment capability. The appropriate ground commands were to be sent after analysis of full-revolution data.

Yaw attitude information could not be measured directly, but had to be computed on the ground, based on scanwheel horizon-sensed pitch and roll data and the solar vector direction as measured by the sun aspect sensor system. This system consisted of two identical modules, each of which contained two sun sensors and an electronics package, as shown in Figure 2-26. Only one of the

Table 2-3. OACS Performance Adjustment Capability

Command	Function
1. Select pitch magnet Select roll magnet Select yaw magnet Step magnet up Step magnet down	(a) Magnetic trim of satellite residual magnetic field (b) 200 pole-cm steps
2. Roll wheel speed bias step	(a) 16 steps (b) Adjust for principal axis misalignments due to non-deployments. Improves yaw performance (c) Capability for compensation for 2 times nominal cross-products
3. D1 gain adjust D3 gain adjust	(a) 16 steps (b) Correct for mismatch between torque created by magnet and speed command to wheels. Greater than 20 percent mismatch can create out of tolerance performance
4. Roll bias to signal processor	(a) Afford roll attitude information with failed (inert) scanwheel, and trim out roll bias
5. Scanwheel processor signal disconnect	(a) Afford pitch and roll attitude information from one scanwheel only (b) Full momentum control in effect

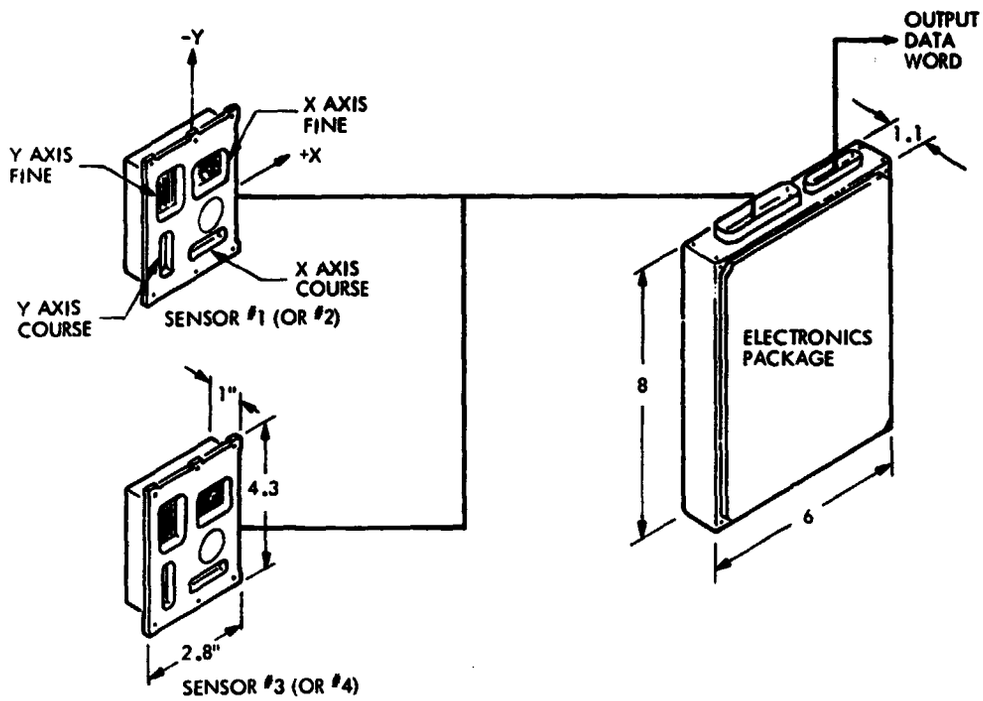

Figure 2-26. Sun Aspect Sensor System

sensors for each module could be monitored at any time; i.e., either sensor 1 or 3 and 2 or 4. The sun sensors were mounted to provide the maximum coverage possible (Figure 2-27). During high solar beta angles, the sun was viewed continuously by either sun sensor 1 or 2. During low beta angles (less than approximately ±60 deg), the sun was viewed only during approximately one-sixth of an orbit except at near beta angle zero when for 4 to 6 days the sun was visible for two intervals nearly opposite each other of approximately one-sixth of an orbit each. Because yaw could only be computed when the sun was in the field-of-view of a sun sensor, for most of the mission direct-measured yaw data was available only one-sixth of each orbit, extrapolation being required during the remainder of the time.

3. Data Subsystem

The data subsystem provided for the following requirements:

(1) Compatibility with Spaceflight Tracking and Data Network (STDN).

(2) Receive uplink ranging tones and retransmit the tones using coherent frequency carriers.

(3) Receive uplink command data.

SENSOR NO.	CLOCK (DEG)	CONE (DEG)	ROTATION (DEG)
1	+90.0	96.5	0.0
2	+23.5	98.0	0.0
3	+203.5	96.5	0.0
4	+270.0	96.5	0.0

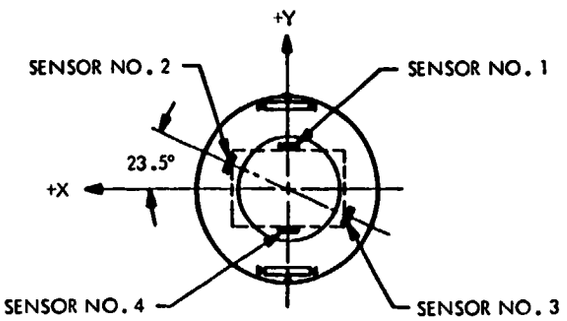

Figure 2-27. Sun Sensor Orientation

(4) Provide R/T and stored program commands.

(5) Provide a timed inhibit of SAR data transmission.

(6) Provide GMT satellite timing.

(7) Provide sensor timing signals.

(8) Provide engineering and status data multiplexing.

(9) Provide customized sensor interfaces.

(10) Transmit R/T and tape recorder (T/R) daca.

The subsystem consisted of two each of the following components:

(1) NASA Standaıd Transponder (NST).

(2) Command Demodulator (CDU).

(3) Command and Timing Unit (CTU).

(4) Telemetry and Sensor Unit (TSU).

(5) Tape Recorder (T/R).

(6) SAR Enable/Disable Unit (SED).

(7) Orbit antenna.

(8) Ascent antenna.

(9) Tranet beacon oscillator.

The SAR data link components were considered to be part of the SAR system and are described in Paragraph D.

Figure 2-28 is a functional block diagram of the data subsystem. Photographs of selected data subsystem components are shown in Figure 2-29. Not shown in Figure 2-28 is the SED, which interfaced with the SAR electronics subsystem. Complete cross-trapping was provided between the NST, CDU, CTU, Tranet beacon oscillator, TSU, and T/R. Generally, redundant equipment required manual commanding from the ground. Two exceptions were that: (1) the internal 1.6- MHz oscillator of the selected CTU would automatically provide spacecraft timing control for a detected Tranet beacon oscillator failure, and (2) the receiver and CDU units were in active redundancy.

a. Telecommunications. The telecommunications equipment consisted of the NSTs, CDUs, and the ascent and orbit antennas. The characteristics of this equipment were as follows:

Uplink Commanding.

(1) Frequency: 2106 MHz, phase modulated.

(2) Modulation: 2-tone non-return-to-zero-L (NRZ-L), frequency-shift keyed (FSK) with amplitude modulation (AM) clock deviation, 1.4 radian peak.

(3) Command rate: 2 kb/s

(4) Tone frequencies: 8 and 12 kHz.

(5) Squelch: -105 dBm.

(6) Command word length: 64 bits.

(7) Real time command (RTC) rate: 0.5-s spacing.

(8) Stored program command (SPC) rate: block-loaded with no spacing.

(9) Either NST accessed either CTU section.

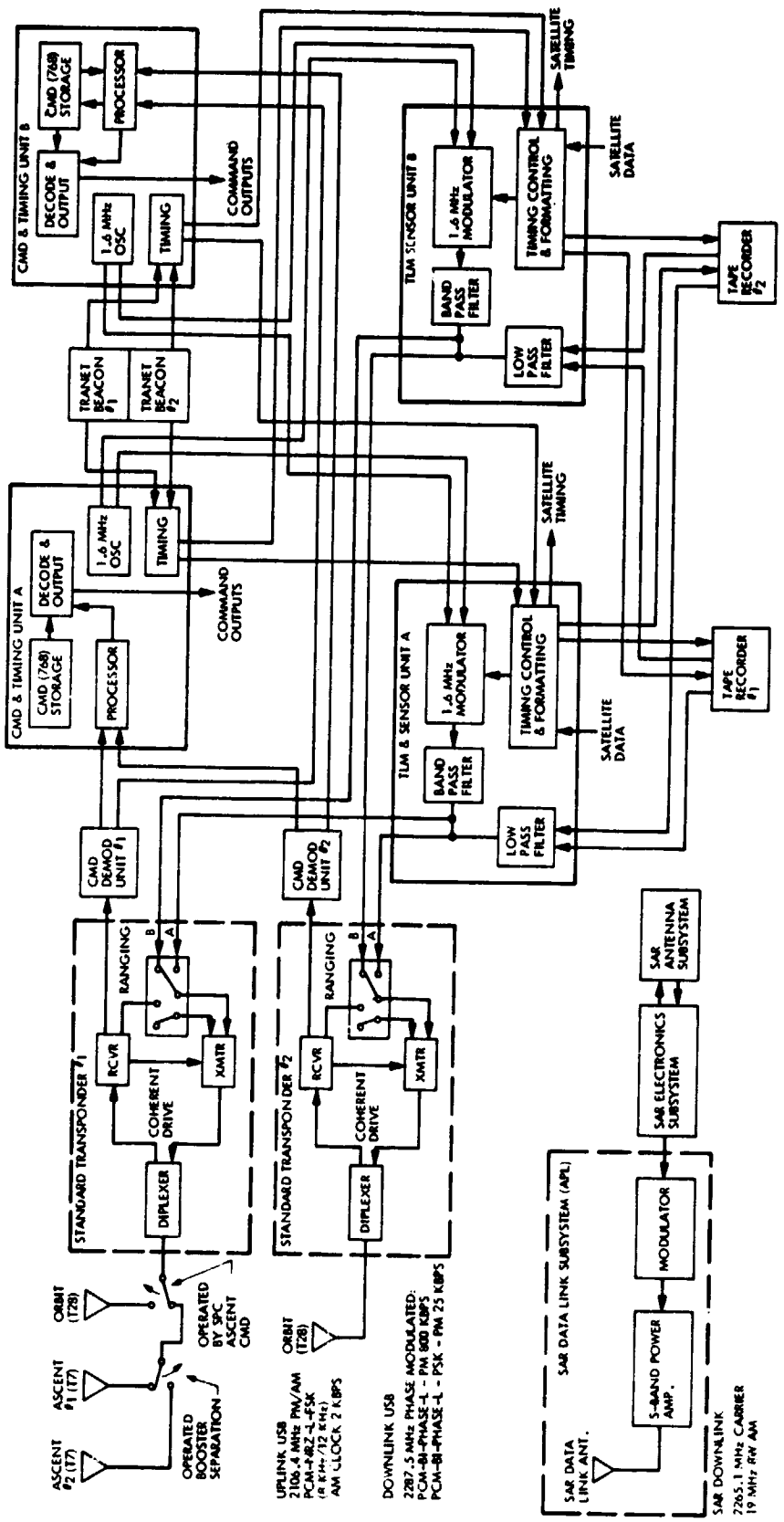

Figure 2-28. Data Subsystem Functional Block Diagram

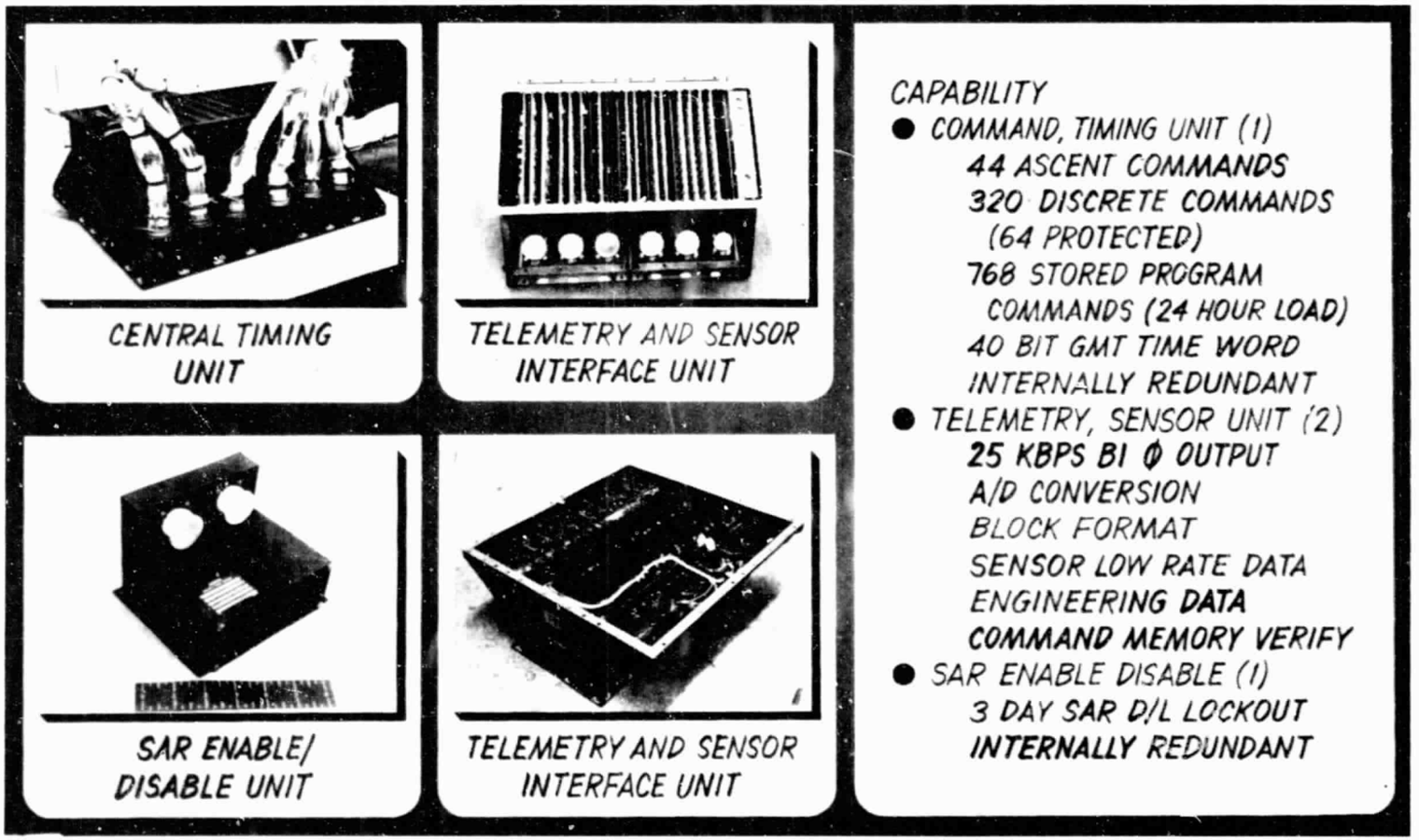

Figure 2-29. Low Rate Data System

Ranging.

(1) Tone frequencies: 500 kHz, 100 kHz, 20 kHz, 4 kHz, 800 Hz, 160 Hz, 40 Hz, and 10 Hz.

(2) Deviation: 0.6 one-tone, 1.2 two-tones radian peak.

(3) Turnaround deviation: 0.85 radian rms sine wave equivalent.

(4) Time-shared on downlink with T/R playback.

Downlink.

(1) Frequency: 2287.5 MHz (non-coherent) phase modulated.

(2) Coherent at 240/221 times uplink frequency.

(3) Power: 1 W

(4) R/T telemetry (T/M), 1.6 MHz SCO-modulated at 25 kb/s with Bi-Ø-L coding; deviation, 0.7 radian peak.

(5) T/R playback: 800 kb/s with Bi-Ø-L coding; deviation, 0.85 radian rms.

(6) High gain deviation: 2 times normal.

(7) T/M bit error rate (BER): 1 in. 10^5

Antennas.

(1) Two Type 7 ascent antennas used sequentially, 0-dB gain, linear polarization.

(2) Two Type 28 orbit antennas; 4 dB at 63 deg off axis, -4 dB at 0 deg off axis, right-hand circular polarization.

Both receiver CDUs were always energized and either was capable of receiving and processing all commands for either CTU.

b. Command and Timing Unit. The functions of the CTU were as follows:

(1) Accept and validate uplink data.

(2) Output R/T commands.

(3) Store and output SPCs.

(4) Provide GMT satellite timing as follows:

(a) Time reference for executing SPCs.

(b) Output to TSU for time-tagging block T/M data.

(c) Reference frequency for TSU and sensor timing.

(d) One-Hz output to SED.

The two CTUs were completely redundant. The reference frequency for GMT time generation was provided by one of two redundant Tranet beacon oscillators. In addition, each CTU had an internal 1.6- MHz oscillator for backup use for a detected Tranet beacon oscillator failure. Figure 2-30 is a block diagram of the CTUs. The two redundant CTUs are designated Section A and Section B in Figure 2-30.

Memory: The memory and control block diagram is shown in Figure 2-31. The total memory capacity was 768 command words grouped into 3 banks of 256 words each. Each bank could be separately enabled. Commands could only be executed once, as an execute bit was set. The memory scan timing system rolled over after approximately 6 days.

Timing Control. The time word had a magnitude of 40 bits, which included 26 binary seconds and 14 binary subseconds. The 19 least significant bit (LSB) binary seconds were used for SPC scan and execute control. The timing block diagram is shown in Figure 2-32. Three types of timing adjustment were possible, as follows:

(1) Pre-set time (initialization): this command set the counter to any selected count with a 1.0-s granularity.

(2) Load fine adjust (incremental): this command provided for an incremental adjustment to the counter from ±10 μs to ±10 s.

(3) Load offset (drift): this command permitted drift correction by inserting a ±10 μs count at a selectable interval of from each 2 s to each 9 h.

For the ideal clock, the value of the LSB should be 61.03515625 μs. The basic clock control frequency was approximately 10 μs (99,995 kHz input), thereby requiring an occasional "seven count" before an LSB change of state.

c. Telemetry and Sensor Unit. The TSU functions were as follows:

(1) Accept and multiplex analog, bilevel, and serial digital engineering and status data.

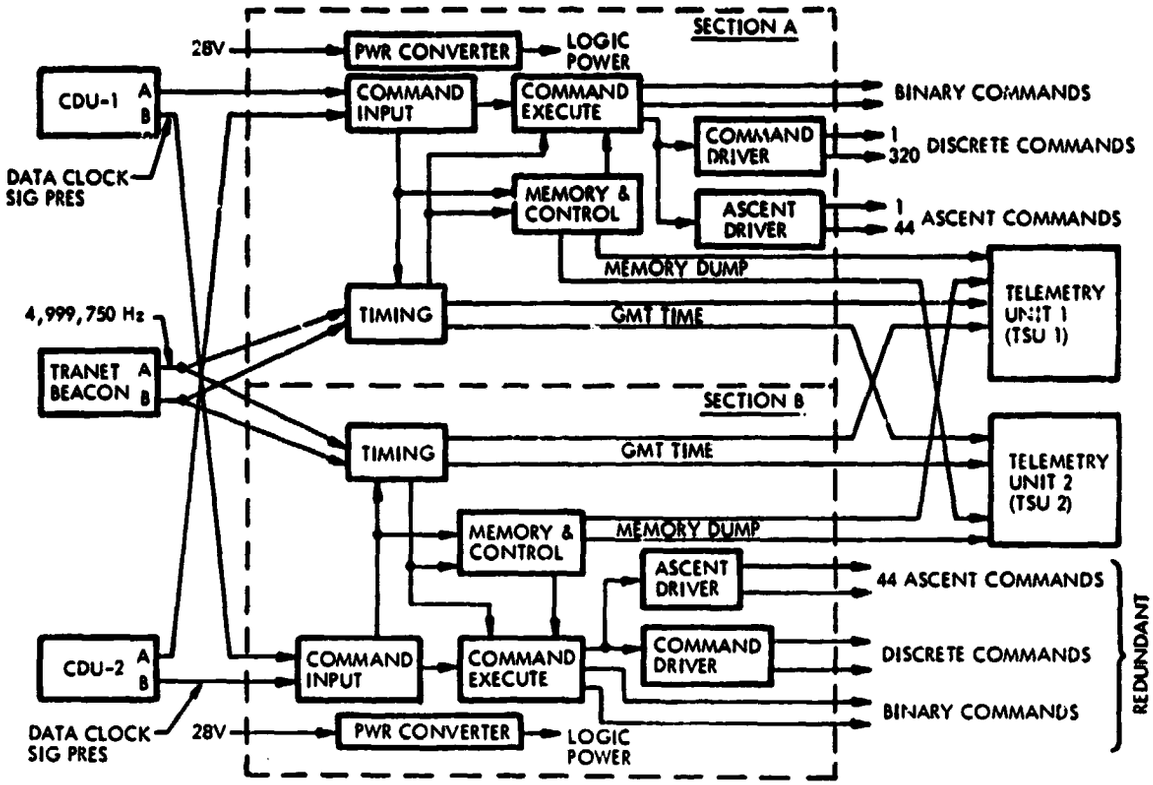

Figure 2-30. Command Processor and Central Timing Unit

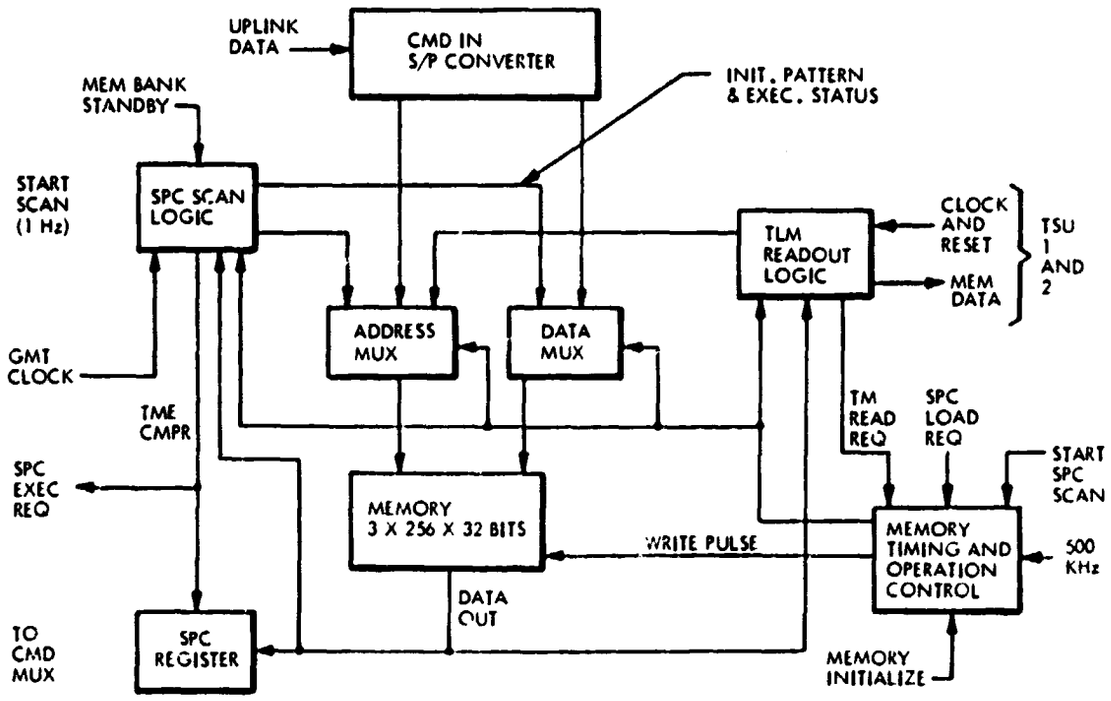

Figure 2-31. Memory and Control Block Diagram

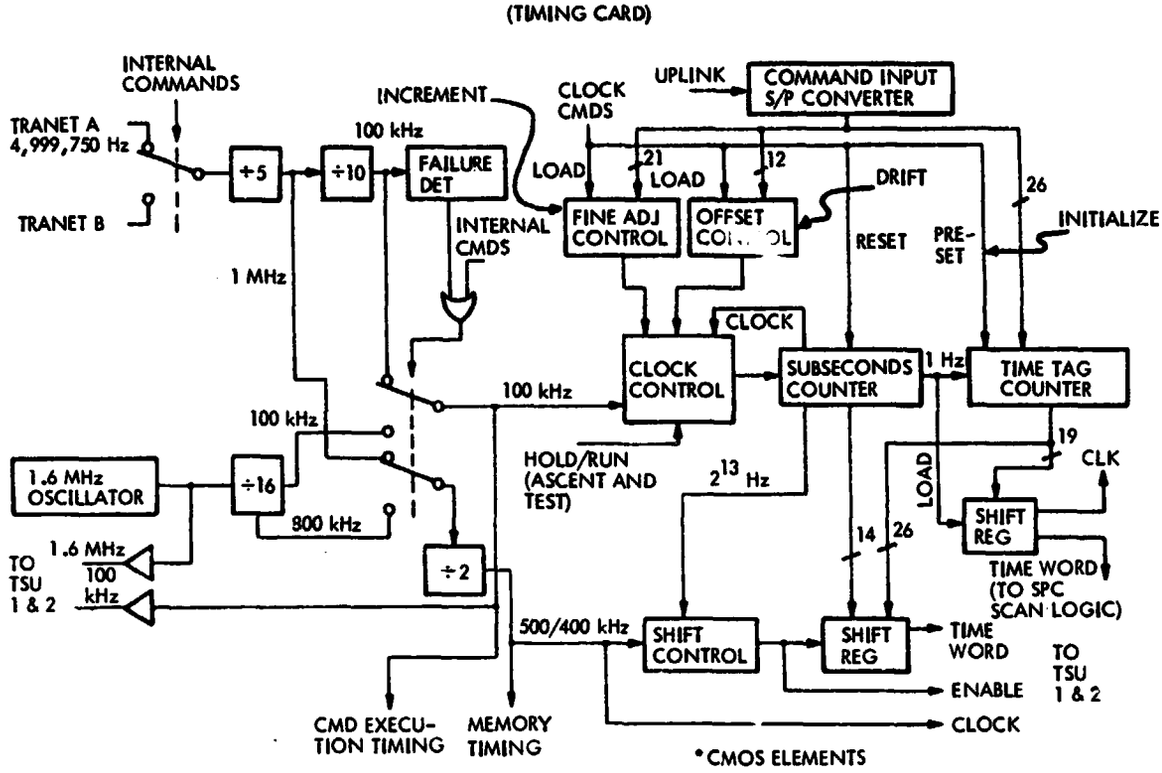

Figure 2-32. CTU Timing Block Diagram

(2) Provide a customized interface for data from the SAR, ALT, SASS, SMMR, and VIRR.

(3) Provide a block T/M formatter for the above data.

(4) Provide a mode control logic.

(5) Provide a T/R interface for read-in (R/I) and read-out (R/O).

(6) Provide a composite R/T and T/R R/O data output to a transponder.

The TSU transmitters were configured in cross-strapped redundancy with only one TSU operable at any time (Figure 2-28). A functional block diagram for TSU operations is shown in Figure 2-33.

Block Telemetry: A customized block telemetry format was provided for each sensor and for engineering status modes, as shown in Figure 2-34. These blocks were read-out on a priority and availability basis with the priority logic scanning the block channels from top to bottom until finding a "ready" block. After each block transfer, the scan was reinitiated. The primary

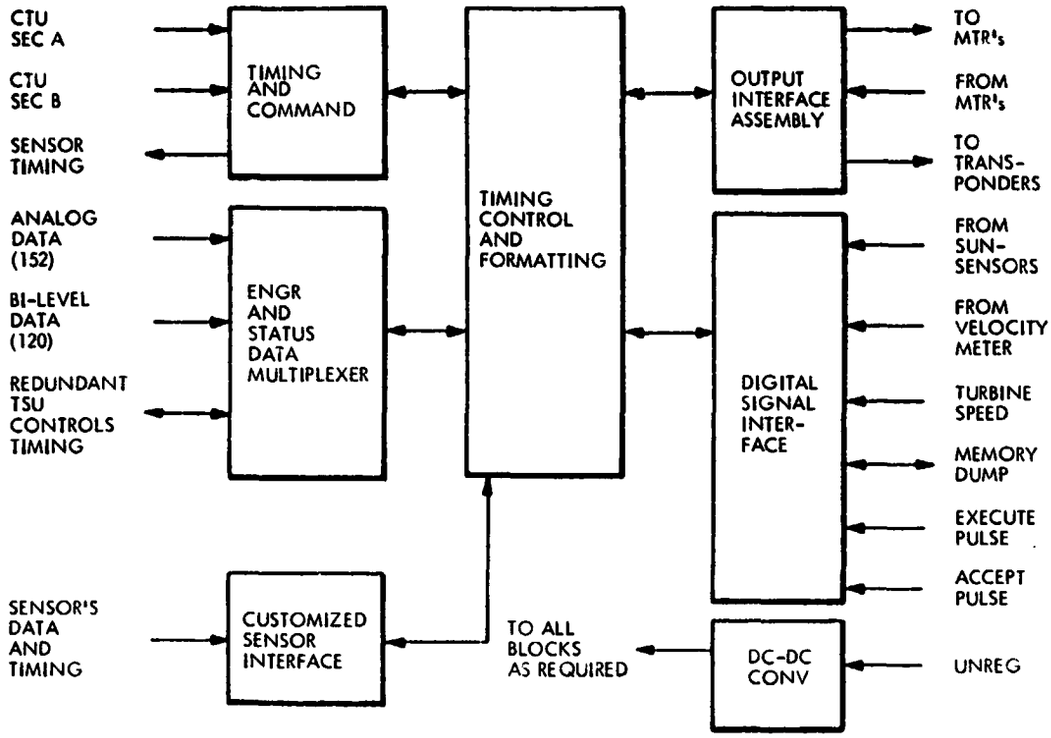

Figure 2-33. Telemetry and Sensor Unit Block Diagram

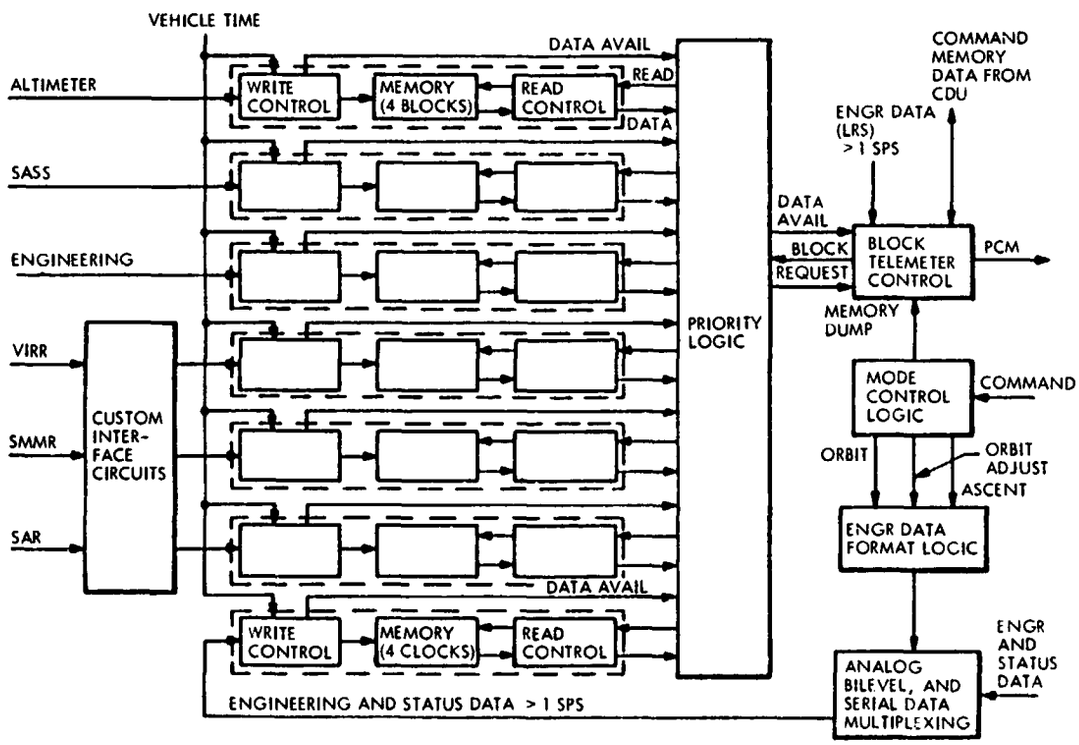

Figure 2-34. Sensor Block Telemetry Format

engineering and status block, designated the low rate sample (LRS) block, was output by wired-in logic each 25 blocks, regardless of other priority/availability logic status. Each block contained a unique time tag (referenced to when the block was filled) and a block counter indicating transmission order.

d. Tape Recorder. Two Odetics tape recorders (Figure 2-35) were used in a non-redundant alternative mode to provide for continuous T/I coverage. Each recorder had a R/I capacity of at least 230 min. The recording was in a continuous direction with no track switching required. Record speed was 1.67 in./s with a minimum of 2000 ft of tape. The R/O to R/I tape speed ratio was 32:1, resulting in a R/O data rate of 800 kb/s. A fast forward mode at the R/O speed could provide, for example, repositioning of the tape for an additional R/O if a previous R/O had not been captured; the erasure of existing data only being performed in the R/I mode. Because both T/Rs were required for continuous R/I coverage, there was no standby redundancy on board the satellite; however, with a single T/R, the P/T data lost during a R/O could be captured in R/T by the ground station as R/T and T/R data could be simultaneously downlinked.

e. SAR Enable/Disable Unit. A redundant binary counter timer provided, on command, a disabling function to the SAR data link, as shown in Figure 2-36. The timing interval counter of $2^{18} \pm 1$ timing period was driven by a 1-Hz source, providing an interval of 3 days, 49 min, and 4 s. Each timer could be reset at any time to initiate a full disabling interval. If one timer failed "open" (would not clock-out), SAR data link operation could be restored by initiating the other timer because, at the clock-out of either timer, operation was restored.

4. Propulsion Subsystem

The functions of the propulsion subsystem were as follows:

(1) Main propulsion.

(a) Impulse to transfer the satellite from the booster separation conditions to orbit injection.

(b) Pitch and yaw control during main engine burns.

(c) Main propellant tank pressurization.

(d) Dumping of excess propellants after orbit injection.

(e) Propellant isolation from turbine pump assembly between burns.

(2) Reaction Control System (High Mode).

(a) Roll control during two Orbit Injection System (OIS) burns.

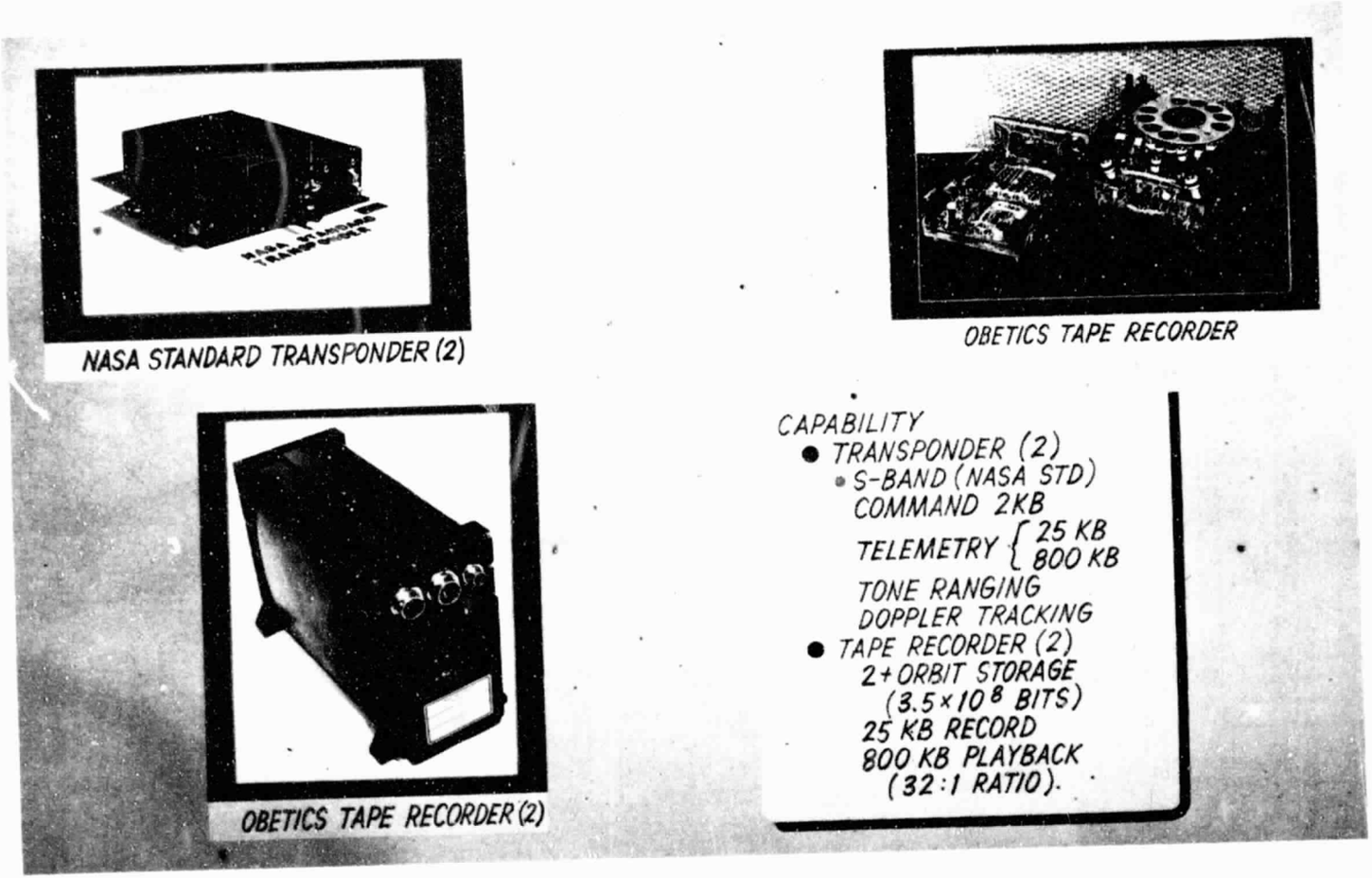

Figure 2-35. Telcommunications and Data Storage Components

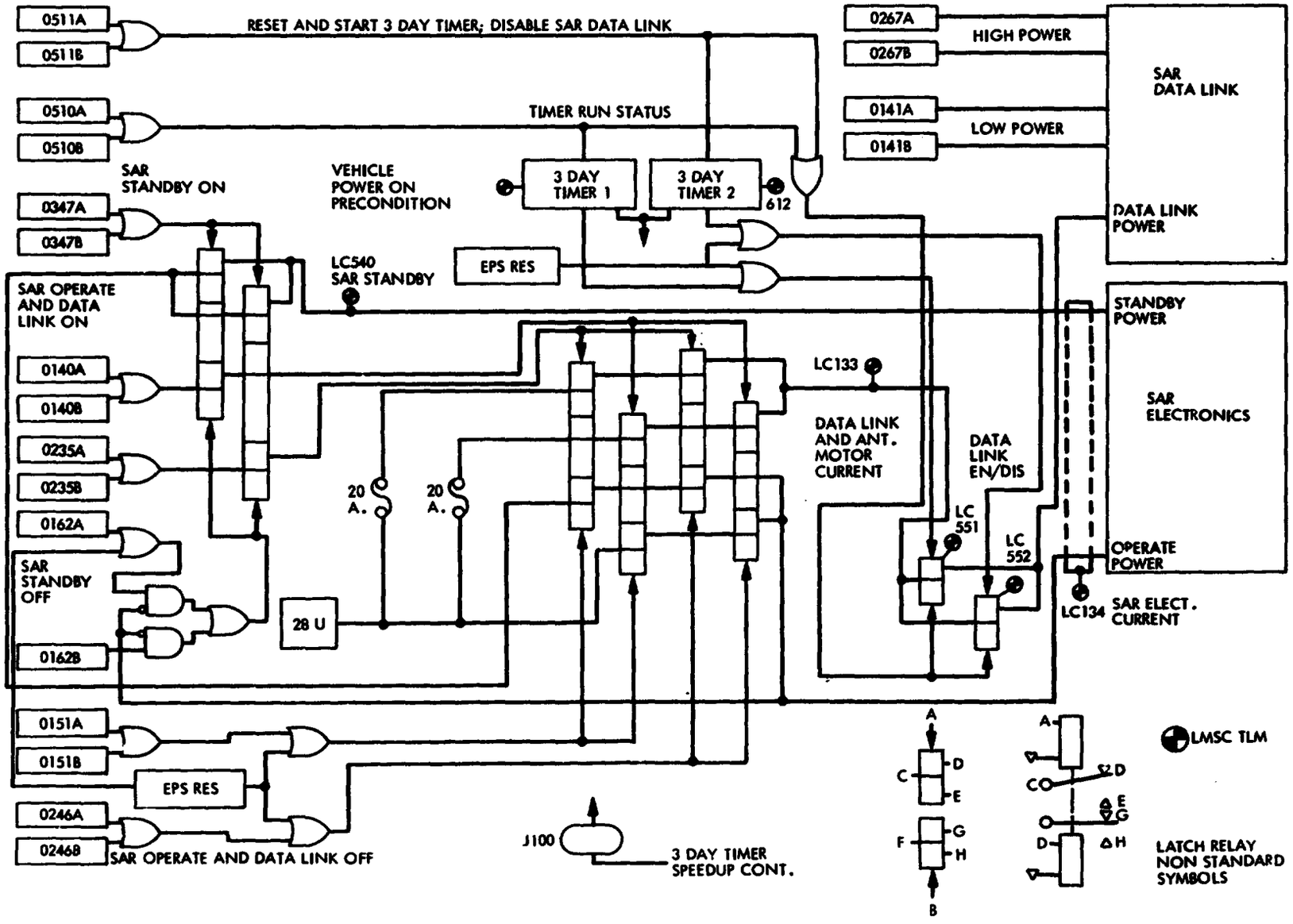

Figure 2-36. SAR Electronics/Data Link Command Logic Diagram

(b) Three-axis control during coast between OIS burns.

(c) Three-axis control during OIS propellant dump.

(3) Reaction Control System (Low Mode).

(a) Three-axis control during orbit adjust burns.

(b) Backup control during momentum wheel desaturation.

(c) Three-axis control during recapture operations.

(4) Orbit Adjust System.

(a) Injection error corrections.

(b) Orbit transfers.

(c) Orbit maintenance.

The propulsion subsystem consisted of the following components:

(1) Main engine and turbine pump assembly.

(2) Propellant Isolation Valve (PIV) (2).

(3) Propellant dump assembly.

(4) Propellant tanks, containment screens, and plumbing assembly.

(5) Helium pressurization system.

(6) Hydrazine tanks (2).

(7) Hydrazine isolation valves (2).

(8) OAS thrusters (2).

(9) Low Mode Reaction Control Cluster (LMRCC) (2).

(10) High Mode Reaction Control Cluster (HMRCC) (2).

(11) Hydrazine tank heaters and thermostats.

(12) Catalyst bed heaters.

(13) Time heaters and thermostats.

(14) Line filters (3).

(15) Fill valves (4).

A sketch of the orbital adjust and reaction control system is shown in Figure 2-37. Figure 2-38 shows the OAS/RCS flow schematic diagram. The OAS, LMRCC, and HMRCC were connected to the same hydrazine supply. Each of the two supply tanks was controlled by PIVs. The quantity of hydrazine was determined by tank pressure and temperature data.

A summary of the thruster performance is given in Table 2-4. Hydrazine was loaded so that pressure for full tanks was 300 psia and that for empty tanks was 110 psia.

5. Thermal Control Subsystem

The purpose of the thermal control system was to maintain the satellite and its components within specified temperature limits throughout the mission. This was done using the thermal design described in the following paragraphs. The thermal analysis on the satellite was computed for the following three groups of components: sensor module, SMSS/Agena forward section, and Agena aft section. Also, the thermal analysis was computed for the pre-launch, ascent, early orbit, and orbit phases of flight.

a. Pre-Launch. Thermal control during on-pad pre-launch conditions was accomplished using conditioned air supplied from the launch complex. The conditioned air maintained the satellite within allowable temperature limits over the variations in atmospheric conditions and pre-conditioned the spacecraft to withstand ascent heating and early orbit power requirements.

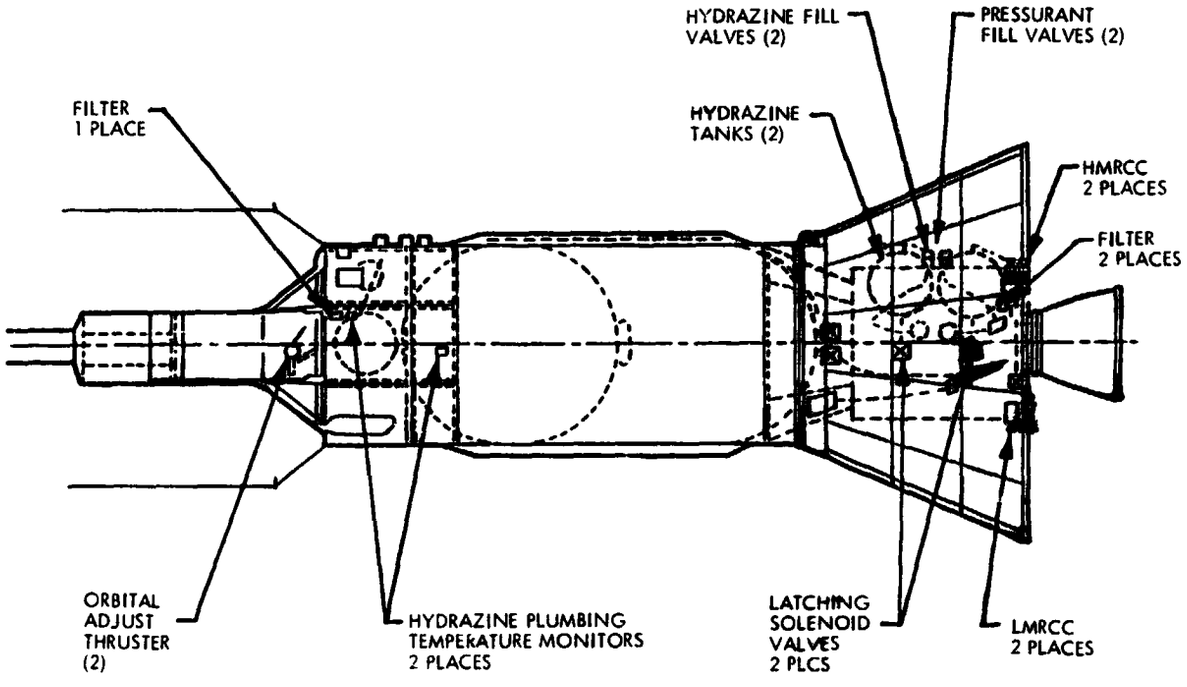

Figure 2-37. Orbital Adjust/Reaction Control System

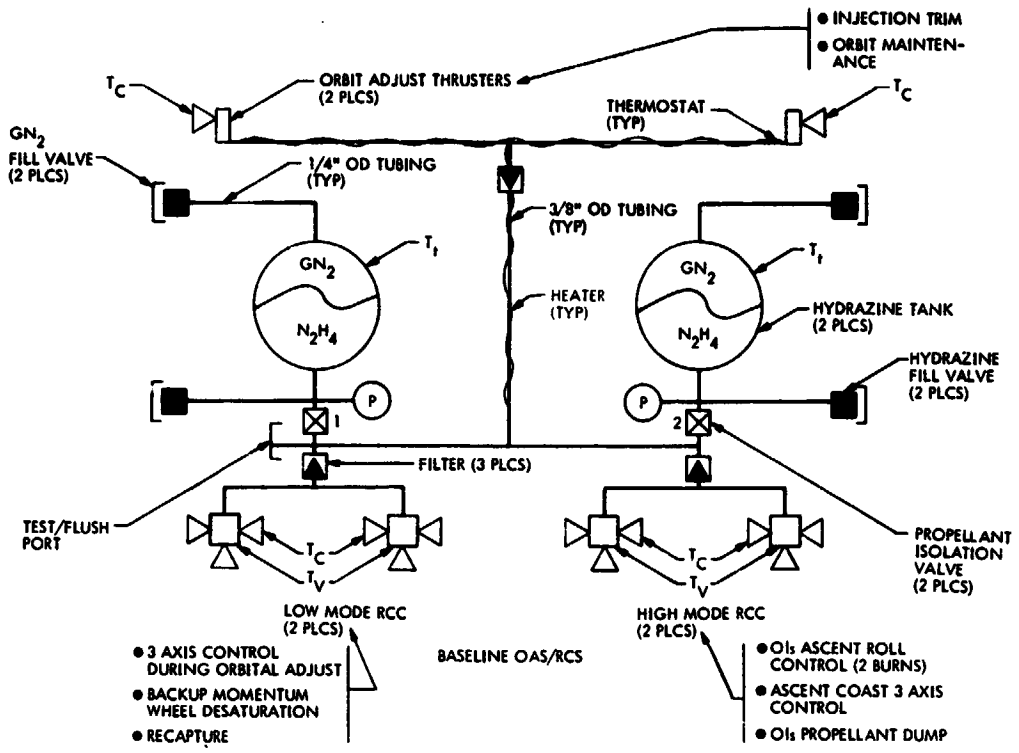

Figure 2-38. OAS/RCS Flow Schematic

b. Ascent. Thermal control during the ascent phase of flight was accomplished with a fairing, liners on the fairing, and the thermal capacity of the satellite. The fairing experienced significant heating, and the skin of the fairing reached 205°C in the area of the sensor module. An aluminum (low emittance) liner limited the heat load of the fairing on the sensor module to 57 ω/m^2. This heat load was small and caused a maximum temperature rise on components of 3°C, and a maximum temperature on the outer layer of the Multi-Layer Insulation (MLI) blanket of 37.8°C. The fairing was jettisoned at 128,400 m (419,840 ft) and 202 s after liftoff, after which the spacecraft was exposed briefly to free molecular heating.

c. Orbit. The orbital portion of flight began at the end of the Agena first burn at 612 s after liftoff, and consisted of the early orbit horizontal flight ($+Z_S$ axis aligned with the velocity meter) as well as the on-orbit operational mode.

The horizontal flight lasted approximately 5000 s. Because of the all-beta thermal design and brief duration, the spacecraft temperatures were relatively benign. Thermal design effort for this time was the control of the temperature gradients within the SAR antenna support structure, and the control of the temperature levels of the pyrotechnic devices and viscuous dampers used

Table 2-4. Thruster Performance Summary

Parameter	High Mode RCC		Low Mode RCC		Orbit Adjust Thruster	
	Requirement	Demonstrated	Requirement	Demonstrated	Requirement	Demonstrated
Thrust	7.4 lbf (110 psia) 15.2 lbf (300 psia)	9.7-10.0 at 170 11.1-12.0 at 210 12.5-14.0 at 258	0.23 lbf (110 psia) 0.56 lbf (300 psia)	0.3425 at 170 avg 0.415 at 250 all 0.495 at 250 REAs	2.6 lbf (110 psia) 5.7 lbf (300 psia)	To be verified during A.T.
Repeatability	±10%	<10% (all REAs) 170<pin <255	±10%	+10% (2 exceptions) -5.8% all REAs	±10%	11.8% qual test
Roughness	±15%	(All REAs) (3-9%, 3σ 170<pin<225 psig)	±30%	<30% (+12.5 TO +29.5% at 170 psig, 3σ limits)	±15%	9.4%
Total Impulse	6000 lb-s	>12,000 lbf-s	6000 lb-s	>11,000 lbf-s	22,000 lb-s	<40,000 lb-s
Minibit	<0.27 lb-s	0.14-0.18 at 15 ms at 210 psig	<0.014 lb-s	0.0065-0.008 at 15 ms at 170 psig	<6.0 lb-s	Analysis
Specific Impulse (steady-state)	>220 s	228 s, S.S.	>211 s	215 s mean S.S. (>211 s, min) (all RCCs)	>200 s	227&229 at 110 psia during A.T. Qual range 60 to 600 s

Table 2-4. Thruster Performance Summary (Continuation 1)

Parameter	High Mode RCC		Low Mode RCC		Orbit Adjust Thruster	
	Requirement	Demonstrated	Requirement	Demonstrated	Requirement	Demonstrated
Duty cycle	Unlimited	Unlimited	Unlimited	Unlimited	Steady State	Pulsing and S.S.
Pulse width	15 ms to S.S.	15 ms to S.S.	15 ms to S.S.	15 ms to S.S.	1.0 to 600 s	0.67 s and 600 s
Frequency	0 to 16.5 cps	0 to 16.5 cps	0 to 16.5 cps	0 to 16.5 cps	N/A	0.5 cps
No. of cycles	30,000	>60,000 cycles	100,000	>1,000,000 cycles	2,000	8,418
Leakage						
External	5×10^{-6} SCCS He max	$<0.2 \times 10^{-7}$ SCC/s He	5×10^{-6} SCCS He max	$<0.2 \times 10^{-7}$ SCC/s He max	1×10^{-4} SCCS He max	4.0×10^{-6} & 5.6×10^{-6} SCCS He
Internal	10 SCCH GN2 max	0.12 to 0.54 SCC/h GN2	10 SCCH GN2 max	0.24 to 5.34 SCC/h GN2 max	10 SCCH GN2 max	0.12 & 0.6 SCCH GHe
Electrical						
Operating Volt	28 ±4 Vdc	23.9 to 32.18 Vdc	28 ±4 Vdc	23.9 to 32.1 Vdc	28 ±4 Vdc	23.85 to 32.09
Heater Power	10.5 W MAX at 24.5 V (cat. bed and valv) 21.0 W max total 2 X 5 W=cat. bed 2 X 5=vlv htr	9.78 to 10.0 W cat. bed 9.58 to 9.77 vlv htr 19.58 W total at 24.5 Vdc 36 Vdc, 5 min (non-operating)	2.1 W max at 24.5 V (cat. bed only)	1.91 W at 24.5 Vdc (cat. bed only) 36 Vdc, 5 min (non-operating)	4.0 W max at 24.6 W (cat. bed only)	3.63 to 3.70 W at 24.55 V

in the deployment mechanisms. The on-orbit operate mode began with the pitch down (90-deg pitch, 90-deg yaw) maneuver to achieve final orbit attitude. Antennas, sensors, and solar arrays were deployed between 5550 and 6140 s. The initial orbit was an 800 km (431 nm) circular orbit with a beta angle of -62.5 deg and an orbit period of 100 min. Because of its expected mission life, the spacecraft was expected to experience a beta angle of +86 to -88 deg over the 1-year mission.

The thermal design was based on a direct solar irradiation between 1317 to 1397 ω/m^2 albedo based on an average Earth reflectance of 0.38, and an Earth emission based on a blackbody with a surface temperature of 248 K. Surfaces facing the $-Y_s$ and $+Y_s$ directions received continous one-sun irradiation in beta angle +90 and -90 deg orbits, respectively. Surfaces facing the $\pm X_s$ directions received no direct solar irradiation for beta angles of ±90 deg and a sinusoidal input for a beta angle of 0 deg.

The spacecraft thermal control system used passive thermal control techniques to control the temperature of the spacecraft and components with thermostatically controlled electric blankets on components with narrow temperature limits. As previously stated, the analysis for the thermal design was done in three sections.

d. Sensor Module. The sensor module thermal design, as listed in Table 2-5 and illustrated in Figure 2-39, used MLI, thermal shields (silver Teflon), radiators, Flexible Optical Surface Reflectors (FOSRs), thermal control surfaces, louvers, thermal capacity, and heaters. The sensor module consisted of the structure, the five sensors and antennas, guidance scanwheels, and the Tranet beacon. The scanwheels were part of the Agena guidance system, and the Tranet beacon was the master timing unit.

The structure thermal design was planned to minimize circumferential temperature gradients. Consequently, the mast and sensor support fittings were insulated with MLI in areas where they would otherwise view space. The surface finish was alodine, except in the vicinity of the SASS, SAR, and SAR data link electronics, where the structure was painted black to enhance radiation.

The sensor module thermal design was complex because of the mechanical design that thermally isolated the sensors. Therefore, each sensor required a separate thermal design.

ALT/Laser Retroreflector Assembly. The ALT consisted of an RF section and a signal processing section. The ALT RF unit was attached to the nadir end of the mast by a tripod support fitting. The thermal design of the RF section was effected so that the structural support (honeycomb) panel conducted the energy from its components to an aluminum radiator, which was bolted to the perimeter of the panel. The radiator surfaces were black anodized along two 60-deg segments centered on the X_s axis, and were covered with 5-mil aluminum FOSR for two 120-deg segments centered on the Y_s axis. The radiator was larger than necessary for thermal control because of a requirement to support an RF absorber around the antenna; consequently, a portion of the Y_s axis radiator section was

Table 2-5. Sensor Module Thermal Control Design

Component	Thermal Control
Structure	MLI, thermal control surface
Altimeter (RF)	MLI, radiator, thermal control surface, heater
Altimeter (SP)	MLI, radiator, thermal control surface, heater
Scatterometer	MLI, radiator with louvers, heater
SAR Electronics	MLI, radiator with louvers, thermal capacitance, heater
SAR Data Link	MLI, radiator, structure thermal capacitance, heater
VIRR	MLI, thermal control surface, thermal capacitance, heater
SMMR	MLI, radiator with louvers, thermal control surface, heater
LRA	MLI, radiator with louvers, conduction isolation
Tranet Beacon	MLI, radiation coupling to SASS and SAR
Scanwheels	MLI, thermal control surface, heater

covered with MLI. The zenith (-Z) side of the cover over the electronics and the back of the antenna were also insulated with MLI.

The signal processing section was attached to an aluminum mounting plate, which was bolted to the SMMR support bracket and to an aluminum boom that extended from the mast. Three sides of the box and an aluminum fin attached to the mounting plate were used as spare radiators. The $+X_S$ and $+Y_S$ were insulated with MLI. The three sides of the box were covered with 5-mil silver FOSR, while the aluminum fin was covered with 5-mil aluminum FOSR.

Thermostatically controlled heater circuits were bonded to each unit (RF and signal processor). The RF unit had three thermostatically controlled heater circuits bonded to the electronics side of the honeycomb panel, and the signal processor had thermostatically controlled heater circuits bonded to the back

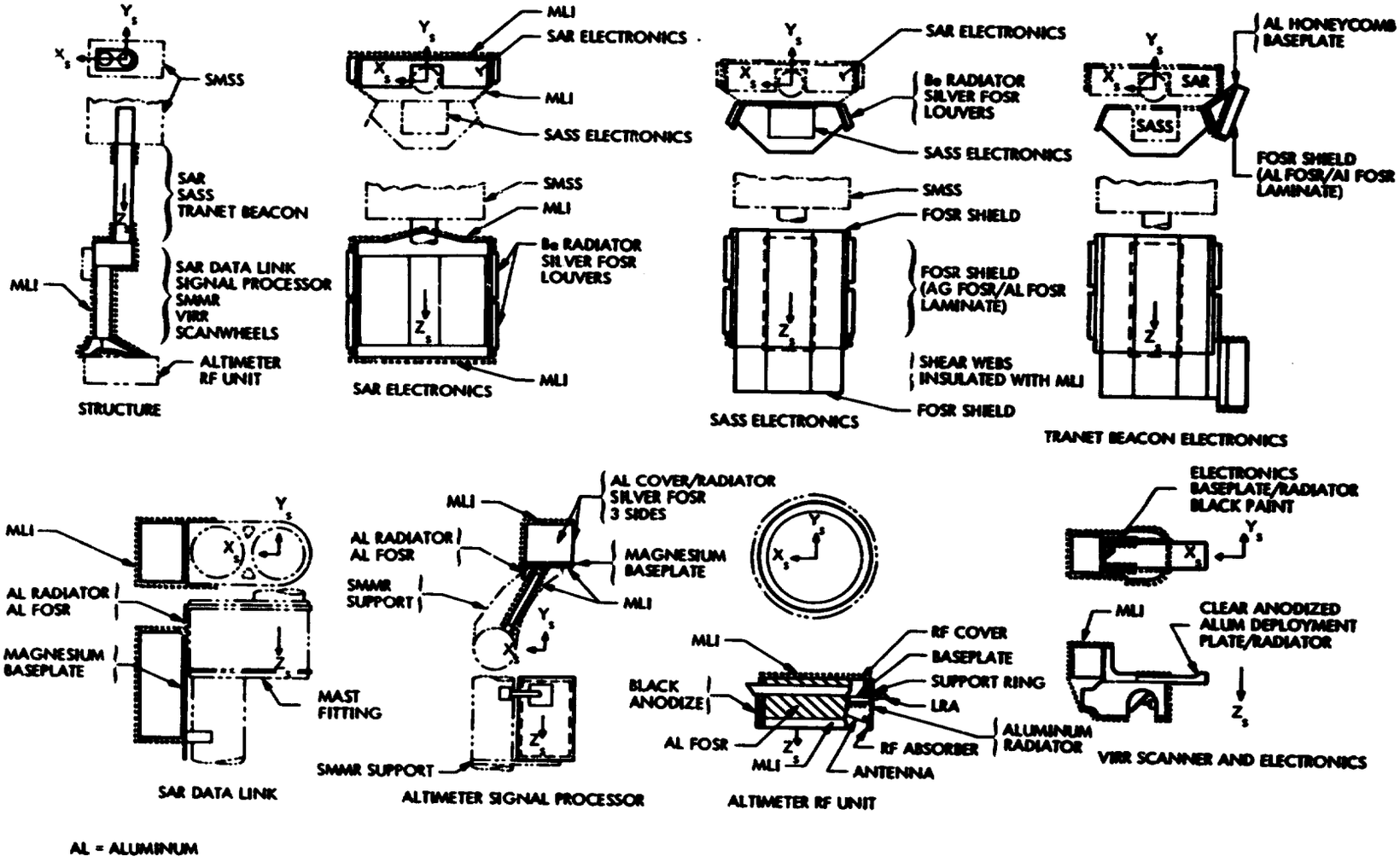

Figure 2-39. Sensor Module Thermal Control Design

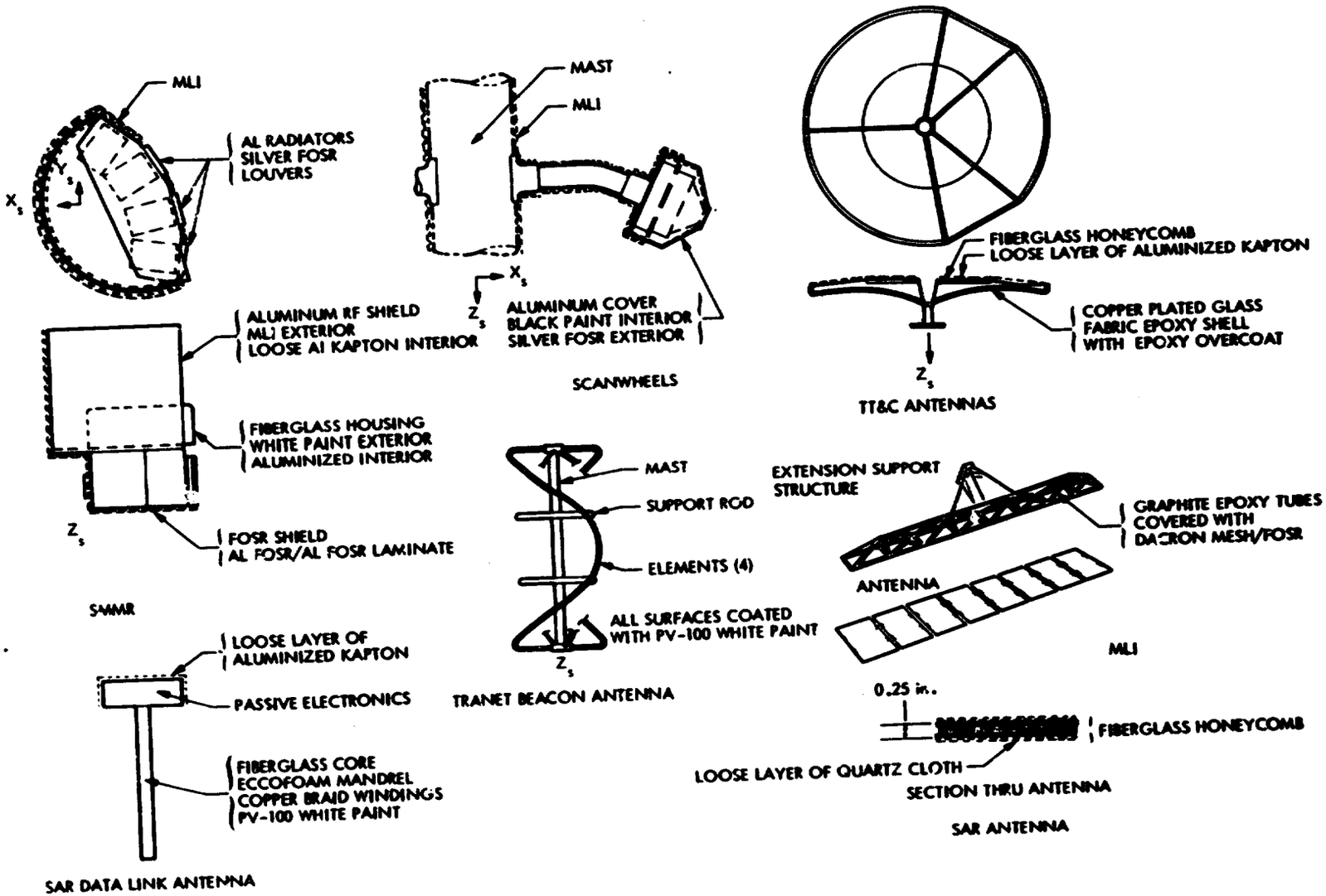

Figure 2-39. Sensor Module Thermal Control Design (Continuation 1)

face of the mounting plate. For both sets of heaters, two redundant circuits were used for thermal control when the ALT was operating. When not operating, these two circuits for each unit were deactivated by command, and temperature maintained by the third circuit on each unit, which had a lower thermostat setting.

The Laser Retroflector Assembly (LRA) was attached to the ALT support ring. Vespel insulators and a loose layer of Kapton that covered the back of the LRA mount ring thermally isolated the LRA from the ALT. Thermal control was passive, using the optical properties of the cubes and support tray to maintain temperature levels and gradients within design limits.

VIRR. The VIRR, consisting of a scanner and an electonics unit, was mounted on a deployment plate, and underwent a 90-deg rotation during deployment. Both units were attached to the outboard end of the deployment plate at its inboard side using phenolic washers. A single MLI blanket covered both units of the VIRR and the outboard end of the deployment plate. Areas exposed to space through the blanket were used as radiators, as were the base plate of the electronics unit, the scanner view openings (both painted black), and the inboard end of the deployment plate, which was clear anodized.

A thermostatically controlled heater circuit was bonded to the outboard end of the deployment plate, and provided thermal control for the VIRR. Two flexible conduction straps were used to thermally couple the scanner to the central portion of the deployment plate where the heaters were located.

Scanwheels. The scanwheels were mounted on booms, which were covered with MLI, near the forward end of the sensor module structure. With the exception of the coated germanium window, the scanwheel external surfaces were painted black. To minimize the effects of the external thermal environment on the scanwheel, each unit was surrounded by a low-temperature aluminum radiation shield. The shield had its exterior covered with 5-mil silver FOSR, and the interior was painted black. This shield provided a cold radiation sink for the scanwheel, regardless of sun angle; consequently, the major effect of the variation of the external environment was the variation of the external environment on the germanium window. Two redundant, thermostatically controlled heater circuits were bonded to the case of each scanwheel. Because of the narrow temperature range, heater power was required for one or both scanwheels throughout the mission.

SMMR. Each of the three SMMR electronics packages was installed using pressure plates to force one face against an aluminum radiator panel and another face against a side plate which was conduction-coupled to the radiator. A low outgassing thermal grease (Thermacoat 25I) was applied to the box-to-panel interface. Louvers were mounted on each of the three radiation panels, and were set to close at 16°C and to open fully above 32°C. The radiator surfaces were covered with 5-mil silver FOSR. Except for the louvers and the nadir (Z_S axis) surfaces, the three electronics bays were insulated with MIL. The nadir side was covered with a double FOSR shield to provide additional heat rejection. The scanner was covered with a fiberglass housing which had the external surface

painted white and the internal surface plated with aluminum. The SMMR antenna was covered on its zenith side with MLI, and on its nadir side with a controlled thermal optical surface.

The SMMR RF shield was insulated with an MLI blanket on the exterior surface and a single, loose layer of 2-mil aluminized Kapton on the interior surface. All of the support structure was insulated with MLI.

The SMMR heater circuit consisted of three heaters, wired in series, with redundant thermostats. One heater was bonded to a side wall of each electronics bay. Redundant circuits were not used because thermal analysis predicted that heaters were not required during normal operation.

Tranet Beacon Electronics. The Tranet beacon electronics boxes were installed on an aluminum honeycomb panel which was attached, by two triangular brackets, to structural rings located on the nadir end of the SASS enclosure. The rear side of the honeycomb panel was painted black and was coupled by radiation to the SAR electronics box and SAR mounting plate, and to the tip of the SASS beryllium radiator plate. The front side of the honeycomb panel and the electronics boxes were also painted black to enhance radiation exchange. The cover over the boxes was a double FOSR shield, similar to that which surrounded the SASS enclosure. Most of the $-X_S$ and $+Y_S$ sides, and all of the $-Y_S$ and $\pm Z_S$ sides were insulated internally with MLI. The uninsulated portions of the cover served as a cold radiation sink for the electronics. Approximately half of the heat dissipated by the Tranet beacon electronics was rejected to the SAR/SASS enclosure, and half was rejected through the FOSR cover. Because of its wide temperature limits and 100 percent duty cycle, heaters were not installed on the Tranet beacon electronics.

SASS Electronics. The SASS electronics box was mounted on a rib-stiffened aluminum panel which had beryllium radiator fins covered with louvers. However, where louvers were used on the SAR to accommodate high power and low duty cycle, they were used on the SASS primarily to conserve heater power when the SASS was turned off. Because of the long conduction path through the mount plate, the SASS louver set points were lower than those for the SAR; they closed at about -7°C and opened fully above 10°C.

The heat rejection capability of the SASS radiators was insufficient to maintain baseplate temperatures below the design limit of 35°C. Consequently, the SASS electronics box and mount plate were surrounded by a low temperature shield, which served as a radiation sink. The shield consisted of a layer of 5-mil silver FOSR and a layer of 5-mil aluminum FOSR, with metallized surfaces bonded together using a 2-mil acrylic adhesive. The silver FOSR had a lower solar absorptance and was outboard to ensure that the shield was considerably colder than the electronics box, even with the one-sun solar irradiation experienced in an orbit with a 90-deg beta angle. The inboard surface was the Teflon side of the aluminum FOSR, which had an infrared emittance of about 0.8.

The SASS mount plate was conduction-isolated from the primary structure by the SASS antenna alignment mechanism. Consequently, the only significant heat

paths for the SASS electronics were radiation to space through the radiator/louver system; radiation exchange between the box cover, mount plate, and FOSR shield; and radiation exchange between the SASS mount plate, SAR electronics, and mast. All of these surfaces had an infrared emittance of 0.8 or higher (black anodize, black paint, and 5-mil Teflon). A thermostatically controlled heater circuit was bonded to the Y_S side of the SASS mount plate. The heater was required for thermal control at large beta angles and when the SASS was turned off.

SAR Electronics. SAR electronics temperatures were maintained within design limits by use of space radiators with louvers. The thermal capacitance of the electronics package and adjacent structure was utilized to satisfy the temperature rise rate limit. The SAR electronics box was mounted on a rib-stiffened aluminum panel which had beryllium radiator fins attached to two edges. To minimize solar irradiation, the radiator surfaces faced in the $\pm X_S$ direction. Two louvers were attached to each radiator. They were set to close at about 2°C and to open fully above 18°C. The radiating surface was 5-mil silver FOSR, which was bonded to the beryllium radiator plate with 2-mil acrylic adhesive.

Except for the louvers, the SAR mount plate/radiator and the region between the SAR mount plate and SASS mount plate were insulated with MLI. Consequently, the only significant heat transfer paths for the SAR electronics were radiation to space through the radiator/louver system, conduction and radiation exchange with the mast, and radiation exchange with the SASS mount plate. The radiators were sized to maintain temperatures slightly above the lower design limit, based on average heat dissipation for a 4 percent duty cycle. During transient operation, temperatures were controlled using the box and structure thermal capacitance, and the variable heat rejection capability provided by the louvers.

Two redundant, thermostatically controlled heater circuits were bonded to the $+Y_S$ side of the SAR mount plate. These were primarily backup heaters for use when the SAR was not operated for an extended period; no heater power was required for a steady 4 percent duty cycle.

SAR Data Link Electronics. The SAR data link electronics box was attached to an aluminum mount plate which had small radiators located on the Z_S ends. Radiator surfaces were covered with 5-mil aluminum FOSR and were sized for a combined heat rejection of 10 W at 7°C. The box/mount plate assembly was installed on the mast fitting, which provided the supplemental thermal capacitance required to limit the baseplate temperature rise to the required 15°C per hour. The back face of the mount plate and the mast were painted black to promote radiation, although the primary heat transfer path was conduction through the three mechanical attachments. To ensure high thermal conductance, a silicone adhesive (Dow Corning DC-93-500) was applied between the magnesium baseplate and aluminum mount plate, and between the mount plate and the mast. With the exception of the two radiator areas, the electronics package and adjacent structure were insulated with MLI. Two redundant, thermostatically controlled heater circuits were bonded to the back face of the mount plate. These were required for thermal control throughout the mission because the SAR data link radiator was intentionally oversized. This was done to maintain the structure at a relatively constant, low temperature.

Antennas. The antennas were located at various positions on the spacecraft, and required different thermal control provisions because of design and temperature requirements.

The Telemetry, Tracking and Command (TT&C) antennas were deployable (one on the Tranet beacon boom and the other on a deploy plate), and had a loose, single layer of aluminized Kapton on the back face. The forward surface ($+Z_s$) was copper-plated and sprayed with an epoxy conformal coating. The remaining antennas were supplied to LMSC, and had the following thermal control surfaces:

(1) The SAR data link antenna was an aluminum housing with a fiberglass/eccofoam cylinder covered with copper braid. The zenith and side surfaces were insulated with a single, loose layer of 2-mil aluminum Kapton to minimize back face heat loss, while the other surfaces were coupled by radiation to the Earth. The eccofoam and copper braid were coated with PV-100 white paint to reduce the α_s/ε ratio for the copper.

(2) The Tranet beacon antenna had all surfaces painted with PV-100 white paint to achieve acceptable thermal control properties.

(3) The SASS antenna thermal control materials consisted of silver FOSR, white paint, and an anodized surface. These surfaces were used in a pattern to control temperature level and gradient. This was done to keep distortion because of thermal effects within allowable limits.

(4) The SAR antenna consisted of panels and the extension support structure. The nadir side of the panels was covered with a single, loose layer of quartz cloth, while the zenith side of these panels was insulated with MLI. The graphite epoxy tubes used for the extension support structure were covered with a single, loose layer of Dacron mesh and 1-mil silver FOSR.

Miscellaneous. To minimize gradients and to ensure moderate temperature levels, nearly all exposed surfaces which were not covered with MLI were wrapped with a single, loose layer of 2-mil aluminum Kapton, with the Kapton side outboard. The units wrapped in this manner were the SAR antenna support structure, the columns that supported the SASS antenna pin pullers, and the antenna booms.

SMSS/Agena Forward Rack. The SMSS/Agena forward rack thermal design used thermal shields, MLI, FOSR, thermal control surfaces, and heaters. The SMSS consisted of the SMSS structure and equipment located on the SMSS, while the Agena forward rack consisted of the forward rack structure, the forward half of the main propellant tank, and equipment.

SMSS. The SMSS structure (Figure 2-40) was a rectangular box, with the forward end containing the mast support for the sensor module while the aft end was attached to station 247 of the Agena. The SMSS thermal design was passive, using only thermal control surfaces, MLI, and shields. There were no heaters or louvers on the SMSS.

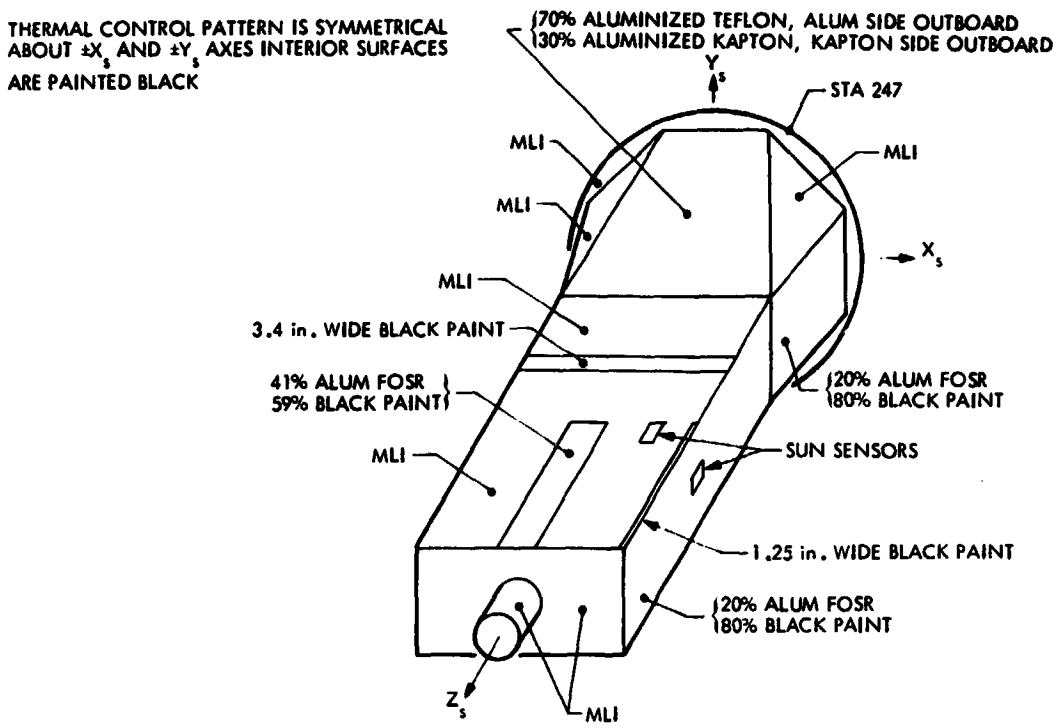

Figure 2-40. SMSS Thermal Control Design

All components were located within the structure, therefore the temperature control of the SMSS-mounted equipment was done with a thermal design on the SMSS structure. The interior surfaces were painted black to promote radiation. The external surface patterns were designed to minimize the variation in absorbed solar energy with beta angle, and by insulating external surfaces which were not required for heat rejection. The external surface finish on the $\pm X_s$ sides were 80 percent black paint and 20 percent aluminum FOSR, while the $\pm Y_s$ sides were primarily MLI.

Uninsulated areas on the $\pm Y_s$ sides were used to provide energy to bays which had low power components. The aft end (zenith) of the SMSS contained the momentum wheels and required thermal shields with patterns to control the temperature of the momentum wheels. The thermal shields were fabricated by bonding the aluminized side of 2-mil Kapton strips to the aluminized side of a sheet of 5-mil Teflon, using a 2-mil acrylic adhesive. The surface facing space was 70 percent aluminum and 30 percent Kapton. A MLI blanket at station 247 closed out the nadir end of the Agena forward rack, thereby thermally isolating the SMSS from the Agena. This isolation was necessary because of the difference in the thermal environment of the SMSS and Agena.

e. Agena Forward Section. The Agena forward section (Figure 2-41) consisted of the forward rack and the forward half of the main propellant tank.

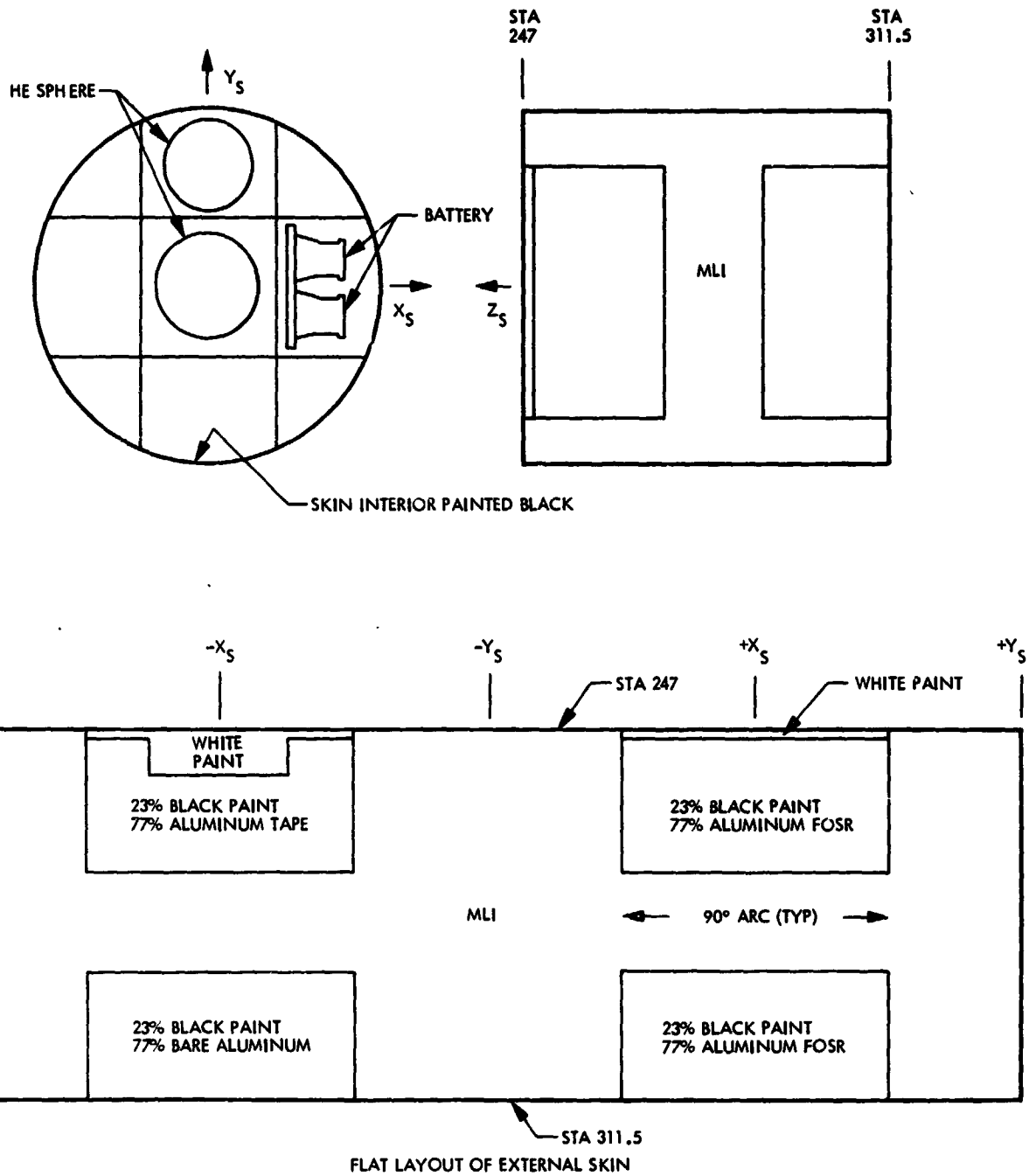

Figure 2-41. Forward Rack Thermal Control Design

The forward rack thermal design used the Agena forward rack cylindrical skin and the main propellant tank as its boundary to the external environment. The cylindrical skin pattern was selected to minimize the effect of beta angle on absorbed external heating. The external pattern consisted of MLI on the $\pm Y_S$ surfaces and a pattern of 23 percent black and 77 percent aluminum on the $-X_S$ and 23 percent black and 77 percent aluminum FOSR on the $+X_S$ surface. The $+X_S$ pattern had a lower α_S/ε ratio to provide a low-temperature environment for the batteries. The interior surface of the cylindrical skin and tank dome were painted black for maximum radiation interchange to forward rack-mounted equipment. Each battery was provided with redundant internal thermostatically controlled heaters as well as an external thermostatically controlled heater.

The Gyro Reference Assembly (GRA) also had thermostatically controlled heaters to keep the temperature of its gyros within allowable limits in the nonoperational case. The hydrazine lines through the forward rack were loosely wrapped with 12 layers of double-aluminized embossed Kapton, and were conductively isolated from the structure with standoffs. Redundant, thermostatically controlled heater circuits were used to keep the hydrazine lines above 7°C.

The orbit adjust thrusters were conductively isolated from the Agena and were covered with a shield. These shields had a thermal control pattern that was designed to keep the thrusters between 4 and 60°C. Further, these thrusters had catalyst bed heaters.

All components in the forward rack were passively controlled to interchange with the forward rack environment.

f. Agena Aft Section. The Agena aft section (Figure 2-42) consisted of the aft rack, thrust cone, and aft end of the main propellant tank. The basic thermal design approach was to insulate the aft rack and aft end of the thrust cone, where temperature-sensitive components were located, and apply thermal control patterns to the tank and thrust cone external surfaces to provide temperature control for the entire aft section. The insulation consisted of MLI blankets on four sides of the aft rack and portions of the thrust cone, and conduction-isolated, low emittance radiation shields on the aft bulkhead. Electronics boxes, the aft rack structure, the interior of the thrust cone, and the exterior of the propellant tank dome were all painted black to enhance internal radiation exchange. Thermal control finishes applied to the tank and thrust cone exterior surfaces were selected to provide a mean temperature of about 27°C for all beta angles. With good radiation coupling to this stable environment, and with the thermal capacitance of the structure and engine components used to damp orbital temperature swings, aft rack temperatures were relatively constant throughout the mission.

The hydrazine system was the most temperature-sensitive component in the aft rack, and consisted of two spherical tanks, propellant lines, and attitude control thrusters. The hydrazine tanks were conduction-isolated from the structure and covered with aluminum tape to minimize radiation. The lines were thermally isolated from the structure with insulating standoffs and loosely wrapped with 12 layers of double aluminized, embossed Kapton. Redundant heater circuits were used on the hydrazine system. Each tank had two circuits with

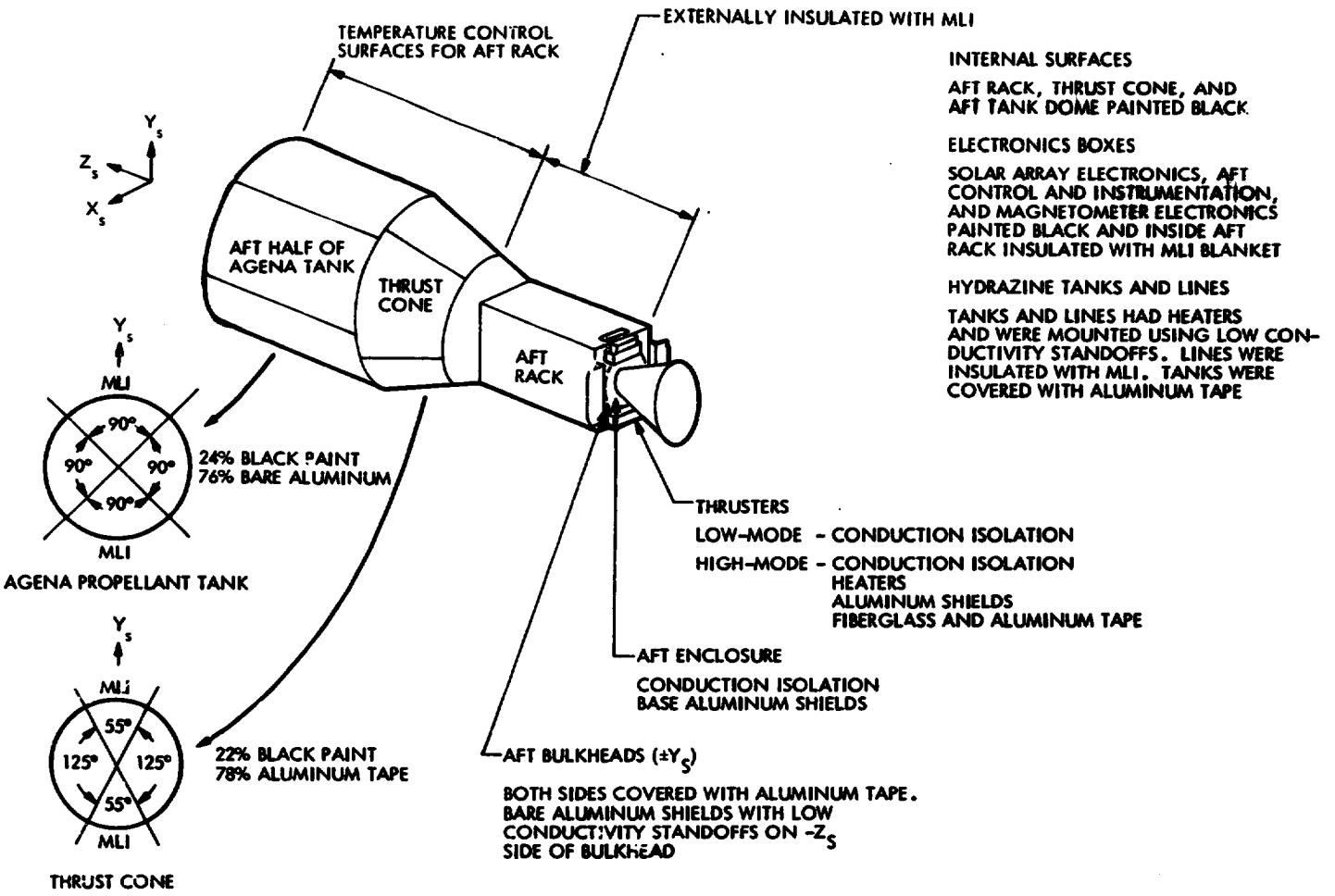

Figure 2-42. Aft Section Thermal Control Design

redundant thermostats. There were three redundant heater circuits on the lines with the thermostats located at the coldest locations on each of the three sections.

The attitude control thrusters were mounted on the aft bulkhead. These thrusters were conduction-isolated from the bulkhead and were enclosed by gold-plated aluminum covers. In addition, the high mode thrusters had an aluminum shield to protect them from Agena nozzle extension. The thruster cluster assemblies had catalyst bed heaters, and the high mode thrusters had valve heaters.

The solar array modules (Figure 2-43) were mounted on the aft rack and were stowed during ascent. The panels overhung the aft bulkhead and were isolated from the uncooled extension by gold-plated aluminum radiation shields. Temperature control prior to deployment was achieved by use of the radiation shields, a thermal control pattern on the launch restraint mechanism, and MLI blankets over the pin pullers and sun sensors. After deployment, temperature control was achieved by a high emittance coating on the rear side of the panels, and thermal control patterns on deployment hardware. The drive motor and slip rings were mounted inside the aft rack MLI blanket and were therefore exposed to a benign thermal environment.

g. Temperature Predictions and Heater Requirements. The thermal analysis for the spacecraft produced the temperature predictions and heater power requirements listed in Tables 2-6 through 2-12.

With two minor exceptions, predicted temperatures were within design limits. One exception was a SASS antenna temperature for a -90-deg beta angle orbit, when the antenna was shaded and received no direct solar or albedo irradiation. The predicted minimum temperature was -95°F, and the design lower limit was -89°F. No action was taken to resolve this discrepancy because a more detailed antenna thermal analysis performed by the manufacturer indicated that temperatures would be within design limits. The second exception was the SMRR reflector temperature for a -90-deg beta angle orbit when the reflector was shaded by the SAR antenna. The predicted minimum temperature was -41°F, and the design limit was -35°F. This discrepancy could not be easily resolved, and no design changes were made. The reflector had been qualified to -50°F.

The heater size and redundancy requirements were also determined from the analysis, and are shown in Figure 2-44. Several design considerations are worthy of note. The battery had two internal heaters, but a third external heater was added to keep the battery temperature above its minimum, as it was determined that in the worse case, with a failure of an internal heater, the other internal heater could not keep the battery above its minimum allowable temperature limit.

The ALT had three heater circuits, comprising primary and redundant operate mode heaters and a non-operate mode heater that maintained the ALT at a lower temperature to conserve power if the unit was turned off.

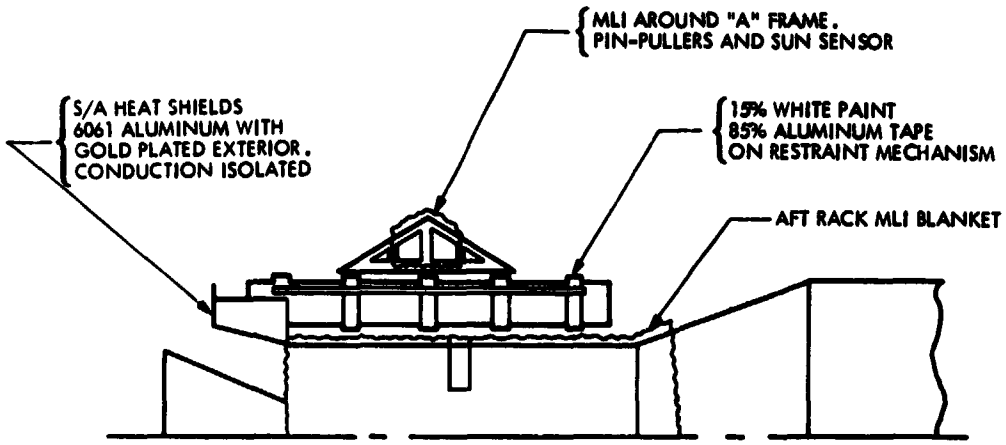

STOWED CONFIGURATION

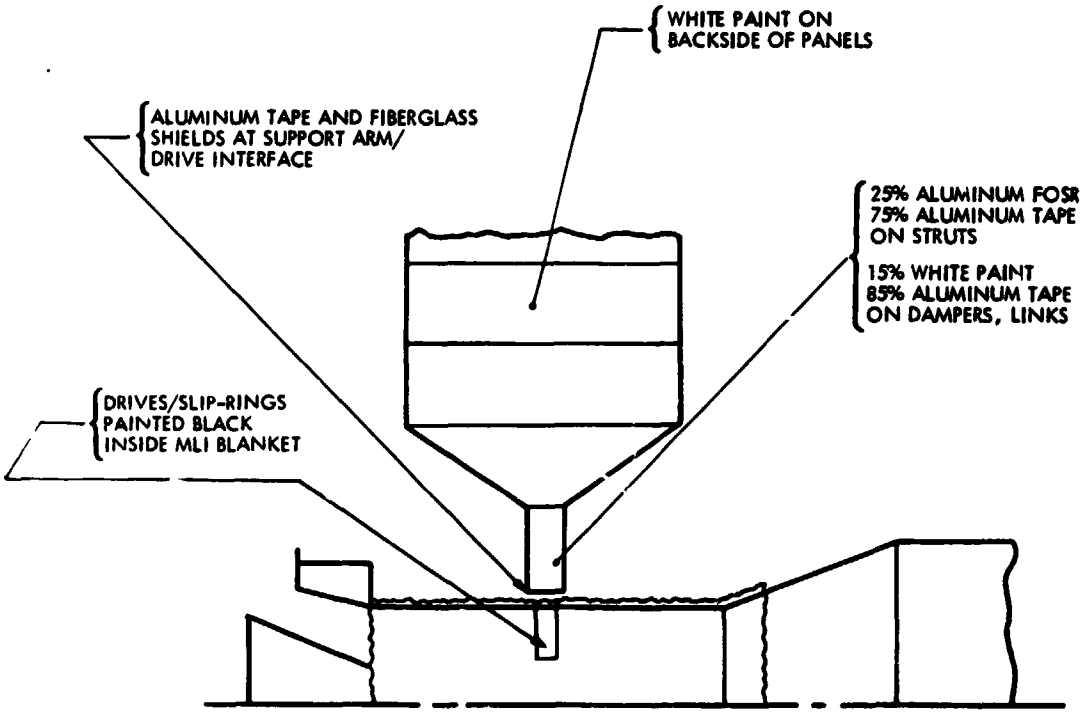

DEPLOYED CONFIGURATION

Figure 2-43. Solar Array Module Thermal Control Design

Table 2-6. Sensor Module Steady-State Temperatures

Component	Design Temp.(°F)		Predicted Temp.(°F)		Nominal Heater Power (W)					
	Min	Max	Min	Max	β=.70	β=.45	β=0	β=45	β=63	β=90
SAR Baseplate	32	95	42	67						
SAR Transmitter Baseplate	-	-	43	64						
SAR Mount Plate/Radiator	-	-	39	67						
SASS Baseplate	32	95	34	88	9.1					
SASS Mount Plate/Radiator	-	-	-14	87						
SASS Box Cover	-	-	-12	67						
Tranet Beacon Electronics	5	122	19	107						
Signal Processor Baseplate	32	95	42	70						
Signal Processor Cover	-	-	9	62						
SAR Data Link Baseplate/Radiator	32	95	35	42	5.6	2.1	2.3	1.2	1.5	2.0
VIRR Scanner	32	95	34	90	1.0		2.9			1.4
VIRR Electronics	23	104	29	90						
SMMR Electronics, Bay 2	59	95	68	75						
SMMR Electronics, Bay 1	59	95	73	86						
SMMR Electronics, Bay 18	59	95	75	92						
SMMR Scan Drive Assembly	59	95	63	89						
Scanwheel, +Y Side	59	95	60	67	0.9	3.9	6.1	7.4	7.8	8.2
Scanwheel. -Y Side	59	95	60	76	7.5	6.8	5.3	1.7		
Forward Mast	-	-	37	50						
Mast Fitting	-	-	37	52						
Aft Mast	-	-	39	73						
SAR Antenna	-67	180	-31	68						
SAR Data Link Antenna	-	-	-45	28						
SASS Antennas	-89	131	-95	28						
TT&C Antennas	-150	150	-25	88						

Table 2-7. ALT Steady-State Temperature Predictions

Component	Thermal Nodes	β=-63° Hot Case		β=0° Cold Case	
		T_{Min}(°F)	T_{Max}(°F)	T_{Min}(°F)	T_{Max}(°F)
Up-Converter Multiplier	800	75.5	75.5	43.5	43.5
TWTA Power Supply	801	84.3	84.3	53.0	53.0
DDL	802	78.1	78.1	37.6	37.6
Receiver	803	68.5	68.5	36.6	36.6
Microwave Transmission	804	59.5	59.5	34.6	34.6
TWT	805-807	85.8	96.7	58.7	66.5
Baseplate	200-312	58.6	88.0	33.6	58.7
RF Cover	110-174	52.1	79.9	29.5	48.3
Support Ring	43-106	40.4	81.3	22.6	47.2
Radiator	630-693	21.3	93.3	8.4	45.5
Antenna	700-724	50.8	100.4	50.9	53.9

Table 2-8. ALT Transient Temperature Predictions for Zero Beta Angle

Location	Thermal Nodes	Temperature (°F)			
		Average	Minimum	Maximum	ΔT
Up-Converter Multiplier	800	55.1	52.7	55.3	2.6
TWTA Power Supply	801	65.1	61.6	67.1	5.5
DDL	802	49.2	45.5	50.4	4.9
Receiver	803	47.9	43.2	51.0	7.8
Microwave Transmission	804	46.1	42.2	47.4	5.2
TWT Collector	805	83.2	76.4	89.8	13.4
Baseplate Hot Spot	261	71.5	64.8	77.8	13.0
Baseplate Cold Spot	290	45.3	41.3	46.6	5.3
RF Cover	110	50.3	47.4	51.1	3.7
Support Ring, +X Side	76	42.4	30.1	60.2	30.1
Support Ring, +Y Side	84	36.5	30.1	40.2	10.1
Radiator, +X Side	631	39.2	4.8	109.5	104.7
Radiator, +Y Side	647	23.3	13.9	29.0	15.1
Antenna	700	53.5	34.9	72.3	37.4

Table 2-9. SMSS Temperature Predictions

Equipment	Orbit β		β_0		β_{45}	β_{-45}	β_{63}	β_{-63}	β_{90}	β_{-90}
	Design		Cold[1]		nom[2]	nom	Hot[3]	Hot	Cold	Cold
	Min	Max	Min	Max	Min	Min	Max	Max	Min	Min
Sun Sensors, Operate	5	131	5[4]	60	21	14	38	84	57	54
Sun Sensors, Storage	-13	140	-3	26	15	12	40	42	0	2
Sun Sensor Electronics	5	131	37	50	56	58	94	92	29	28
Transponder	14	122	46	55	68	60	86	85	48	47
Command Processor & Timing	-12	142	46	55	68	60	86	85	47	47
Command Demodulator	32	104	42	69	57	57	94	94	41	41
Tape Recorders	32	95	47	58	51	61	87	87	46	46
DC Converters	-12	142	38	60	59	52	90	90	48	47
Torque Rods	-12	142	25	58	42	41	65	100	7	26
Power Distribution Box	-12	122	45	48	70	58	90	82	60	48
Power Control Logic Assy	-12	122	31	46	49	57	71	95	30	61
Telemetry Unit	-12	142	36	60	55	48	86	88	33	34
SED Timer	-12	142	35	45	54	49	75	80	36	41
Pyro Control Box	-12	142	30	31	34	42	45	68	23	46
Roll Wheel	9	111	46	48	58	56	80	85	55	61
Pitch Wheel	9	111	50	52	64	56	89	83	65	59
Control Logic Assy	-12	142	40	46	56	50	81	82	49	51
Magnetic Control Assy	-12	142	40	46	57	50	85	80	54	49

Notes:
1. Temperature readings are in °F.
2. Cold cases were based on 0.116 BTU/ft^2-s, nominal optical properties.
3. Nominal cases were based on 0.119 BTU/ft^2-s, nominal optical properties.
4. Hot cases were based on 0.123 BTU/ft^2-s, 1-year degraded optical properties.
5. Sun sensor warmed up at 4.5°F/min coming out of eclipse.

Table 2-10. Forward Rack Temperature Predictions

Equipment	Orbit		β_0		β_{45}	β_{-45}	β_{63}	β_{-63}	β_{90}	β_{-90}
	Design		Cold[1]		nom[2]	nom	Hot[3]	Hot	Cold	Cold
	Min	Max	Min	Max	Min	Min	Max	Max	Min	Min
Battery, Type 40	30	60	44	45	44	44	48	48	44	44
Charge Current Controller	-12	142	54	59	58	53	83	80	55	51
Pyro Control Box	-12	147	40	44	42	41	60	63	41	44
Attitude Control										
Augmented Electronics Assembly	-12	142	29	31	41	24	59	36	47	19
Gyro Reference Assembly	0	115	31	33	43	25	64	36	49	20
Velocity Meter, Model IIA	-12	142	30	31	41	23	62	33	48	18
Velocity Meter Counter	-12	142	32	33	43	25	64	37	50	20
Hydrazine Filter	40	120	45	45	45	45	45	70	45	53
Orbit Adjust Thruster Can	40	130	65	75	95	95	120	120	65	65

Notes:
1. Temperature readings are in deg F.
2. Cold cases were based on 0.116 BTU/ft^2-s nominal optical properties.
3. Nominal cases were based on 0.119 BTU/ft^2-s nominal optical properties.
4. Hot cases were based on 0.123 BTU/ft^2-s 1-year degraded optical properties.
5. Gra was protected by redundant heater circuits.
6. Hydrazine filter was protected by heater circuits.

Table 2-11. Agena Aft Section Temperature Summary

Component	Design Temp. (°F)		Predicted Temp. (°F)	
	Min	Max	Min	Max
Forward hydrazine tank	40	140	42	96
Aft hydrazine tank	40	140	42	96
Solar array electronics	-30	160	53	104
Aft control instrumentation	-30	160	50	101
Magnetometer electronics	-30	160	54	118
Low-mode thruster valves	40	250	42	99
High-mode thruster valves	40	250	40	212
Solar array panels	-150	175	-103	164
Solar array sun sensors	-150	240	-103	164
Solar array dampers	-30	100	-10	90
Solar array drives	-30	140	40	126
Solar array slip rings	-30	140	36	100

Table 2-12. Solar Array Module Temperatures at Deployment

Component	Design Temp. (°F)		Predicted Temp. (°F)	
	Min	Max	Min	Max
X_S Solar array panels	-70	225	-64	90
X_S Solar array sun sensor	-150	240	-64	-44
X_S Solar array pinpuller	-30	160	15	45
X_S Solar array damper	40	130	60	90
X_S Solar array drive motor	-30	140	60	90
$-X_S$ Solar array panels	-70	225	28	90
$-X_S$ Solar array sun sensor	-150	240	28	48
$-X_S$ Solar array pinpuller	-30	160	85	115
$-X_S$ Solar array damper	40	130	70	110
$-X_S$ Solar array drive motor	-30	140	60	90

Note: X_S SAM on shade side; $-X_S$ SAM on sun side.

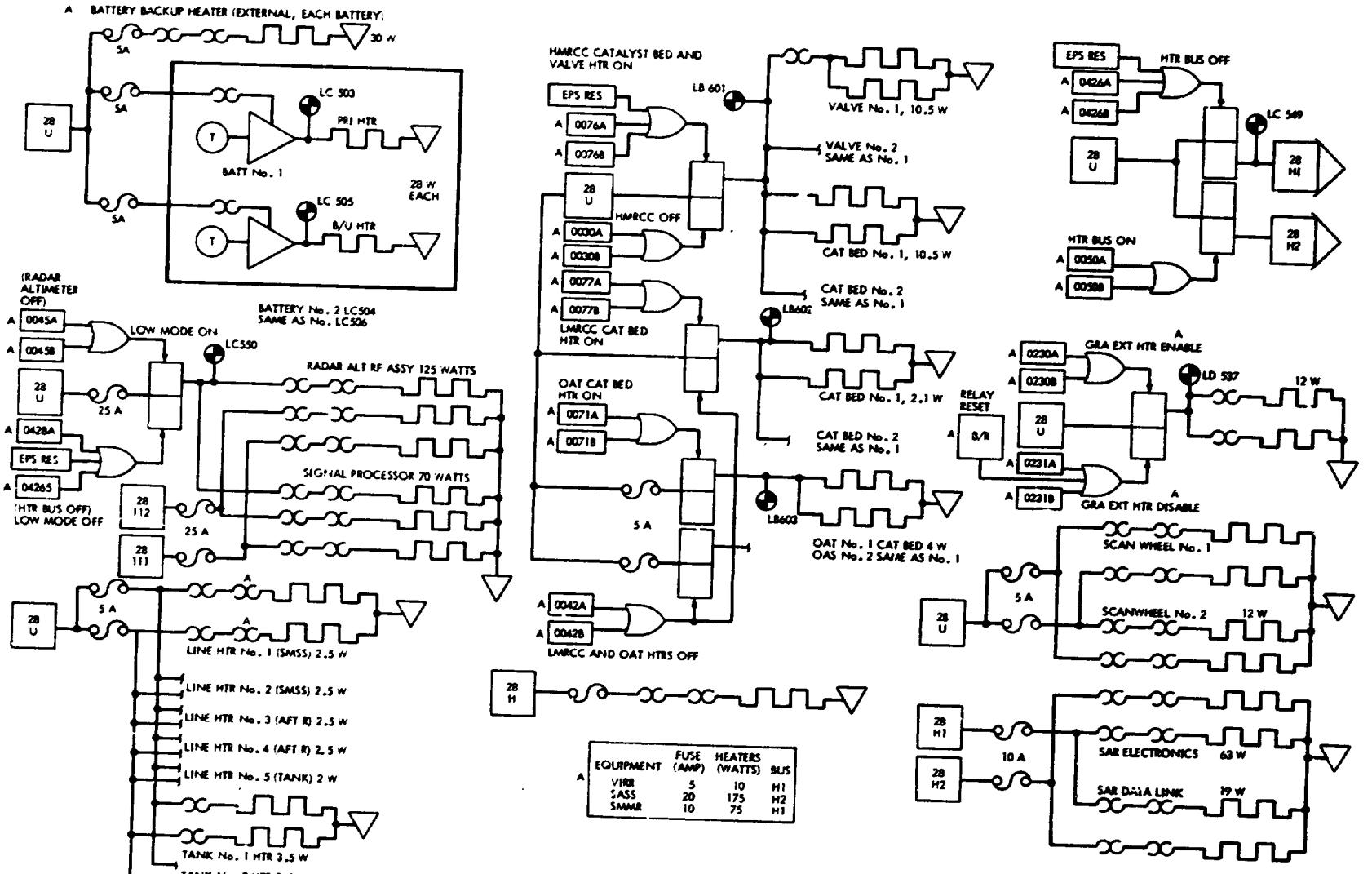

EQUIPMENT	FUSE (AMP)	HEATERS (WATTS)	BUS
VIRR	5	10	H1
SASS	20	175	H2
SMMR	10	75	H1

Figure 2-44. Heater Logic Diagram

The SASS, VIRR, and SMMR did not have redundant heaters, as the analysis showed that the heaters would be necessary only at specific beta angles or when the unit was turned off.

b. Flight Data. The spacecraft thermal control system maintained all sensors and spacecraft subsystems within allowable temperatures for the life of the mission. The spacecraft experienced ascent, early orbit, and orbital thermal environments. The orbital mode included orbital beta angle ranges of -86 deg to 0 deg. The launch beta angle was -62.5 deg, which was a 100 percent sun case. The spacecraft precessed to -86 deg and back to 0 deg. All thermal control system components operated as expected with the exception of the heater thermostats in the SASS and the ALT RF unit. Thermostats in all other circuits operated within specified limits. The thermostats used in all circuits had a current limit of 3 A. The heater circuits in the SASS and ALT exceeded this current limitation. The ALT RF and SASS current was 4.7 and 6 A, respectively. This high current caused the thermostats to fail in the "on" condition, therefore the heaters were dissipating power continuously. This condition could cause the sensor to overheat, therefore the heater power bus relay was cycled to reduce the thermal load on the sensors with the failed thermostats. This operational mode was initiated on day 207 and continued until the spacecraft power failure on 10 October 1978.

C. SENSOR MODULE

The sensor module was the forward section of the satellite, and carried all of the sensor equipments, including the antennas and deployment mechanisms. Figure 2-45 shows the major structural elements of the satellite and their relative locations. The sensor module structure basically consisted of two 10-in. diameter offset aluminum tubes firmly clamped together by an attach fitting with secondary structures to support the sensors, ACS scanwheels, and telemetry and command antennas. One of the aluminum tubes fitted firmly into the SMSS, which was attached to the forward end of the Agena forward section.

The sensors and other equipments were located on the sensor module as shown in Figure 2-46, which shows the antennas in the deployed configuration. The deployments were achieved using the standard deployment mechanism shown in Figure 2-47. Eleven deployment mechanisms were used: one for each of the four SASS antennas; one each for the VIRR, TT&C antenna 1, and SAR downlink antenna; two for the combined TT&C antenna 2 and Tranet beacon; and two for the biaxial SAR antenna deployment. Each deployment mechanism included an adjustable spring/damper assembly, an adjustable over-center latch mechanism, and a position readout potentiometer.

The field joint for the two parts of the satellite was the junction between the aft end of the SMSS and the forward end of the Agena forward section. The sensor module section was subjected to the EMI/RFI test in the anechoic chamber and to the thermal/vacuum (T/V) test in the High Vacuum Orbital Simulator (HIVOS) chamber.

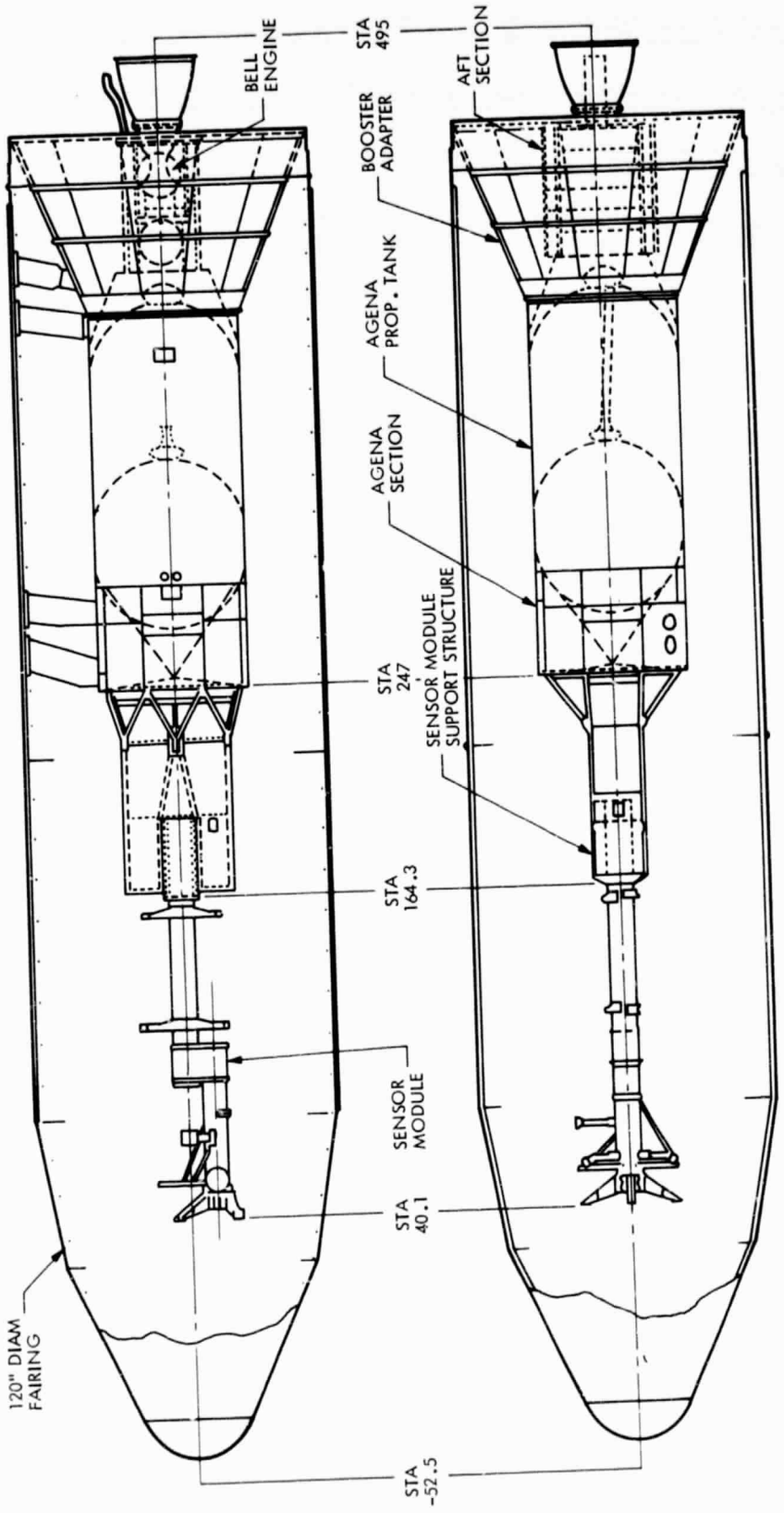

Figure 2-45. Seasat Structural Elements

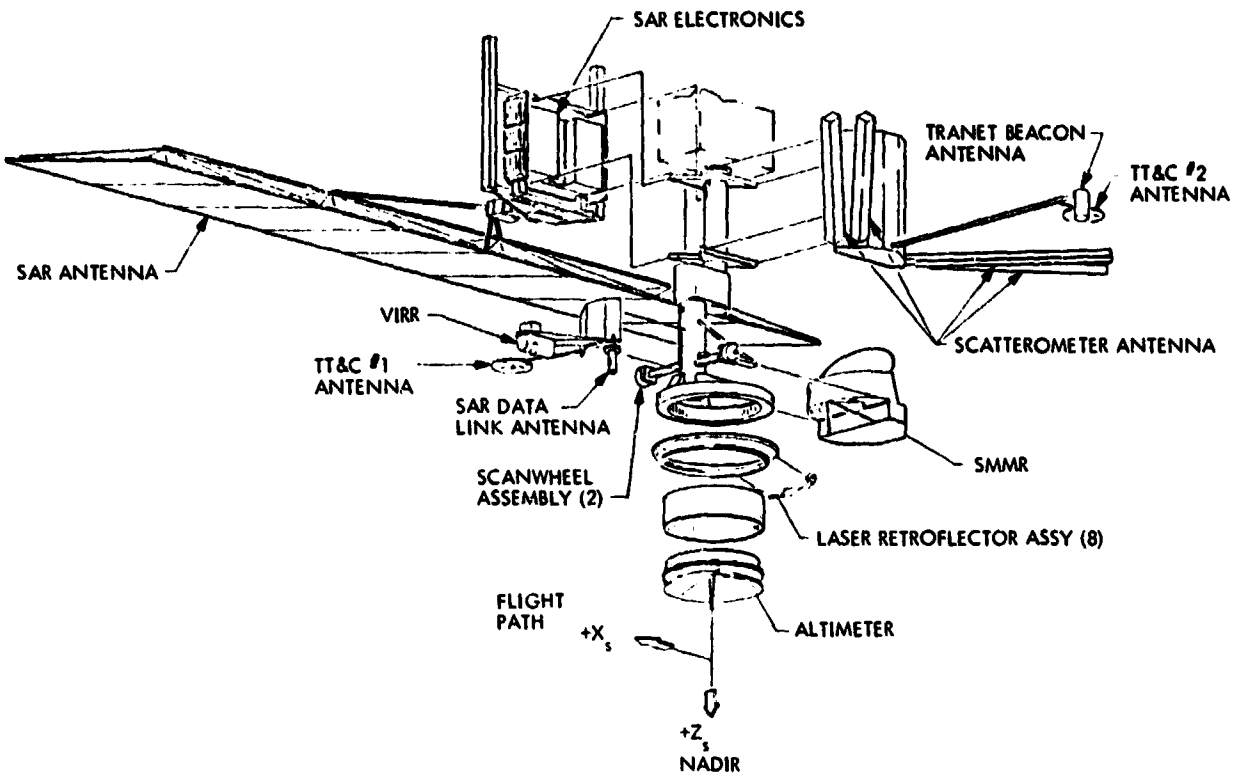

Figure 2-46. Sensor Module Equipment Installations

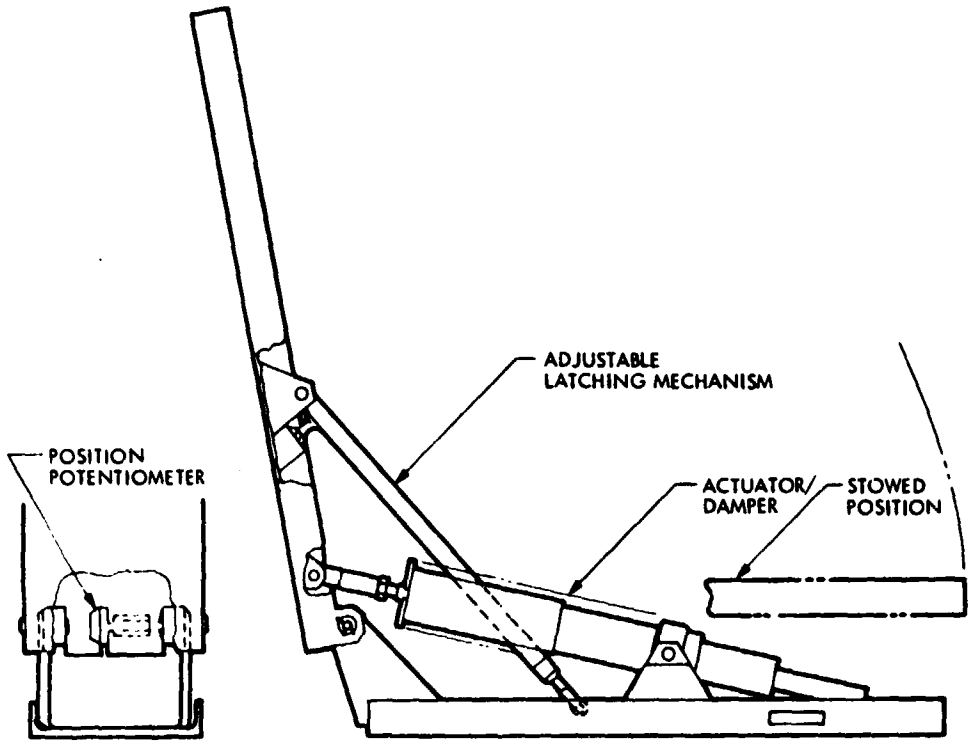

Figure 2-47. Deployment Mechanism

D. SAR ANTENNA

1. Introduction

The SAR antenna was always considered by LMSC to be a major extension of the state-of-the-art development effort for the Seasat program. At the start of the program, neither the final selection of the antenna configuration nor the supplier had been made by JPL. The LMSC proposal recommended the planar array designed by Ball Brothers Research Corporation (BBRC), which was an outgrowth of a recent research program conducted by BBRC for JPL. LMSC also proposed, as an alternative, a configuration consisting of a four-"flex rib" parabolic antenna array, an existing LMSC-qualified design. Although this latter configuration would not meet the swath wide requirement (100 km versus 95 km) (54 nm versus 51 nm), it was substantially cheaper and did meet the remaining design requirements. Subsequent to the start of the program, JPL commissioned LMSC to conduct another antenna competition with each competitor addressing identical but modified performance requirements.

The evaluation of this competition resulted in the selection of the BBRC planar array, with the wider swath width being a major factor. LMSC was directed to procure the antenna from BBRC as a subsystem.

LMSC authorized BBRC to start work on 9 April 1976. The contract was subsequently negotiated in August and deleted BBRC's responsibility for the biaxial deployment mechanism. This action was based on LMSC's concern with the marginal conceptual designs, which featured driving against mechanical stops and using the extension motor stall current as a method to remove power. The major contract milestones and activities are shown in Figure 2-48. SAR antenna electrical and mechanical development and acceptance activities are discussed in the following paragraphs, which also include descriptions of the systems test and orbit operations deployment of the SAR antenna. To indicate the relative size of the SAR antenna, the engineering development antenna is shown in Figure 2-49.

2. Electrical Development

BBRC's early efforts were directed to preparing for the Preliminary Design Review (PDR). The results of these efforts were reported to LMSC and JPL program personnel at a management review conducted in early July 1976. At this review the conceptual corporate feed and panel layout were described along with a review of the following major accomplishments:

(1) RFP and specification for the RF feed released.

(2) Completion of etching four half-panel arrays.

(3) Multiple four-by-four panel tests proved repeatability of results.

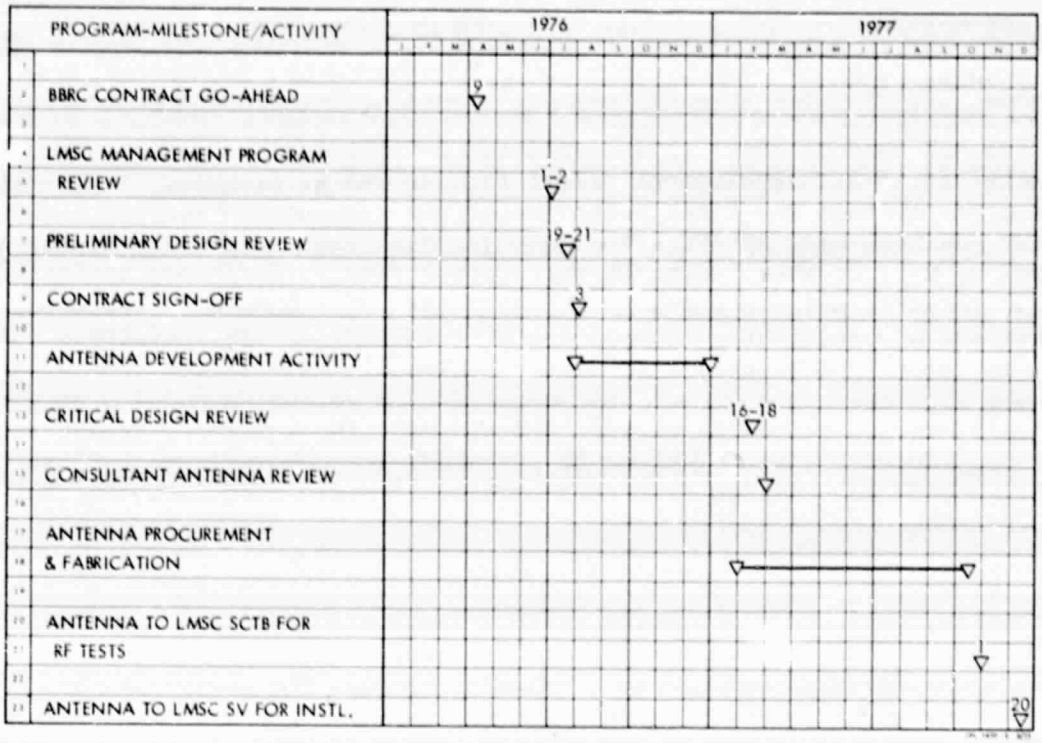

Figure 2-48. Synthetic Aperture Radar Antenna Schedule Plan

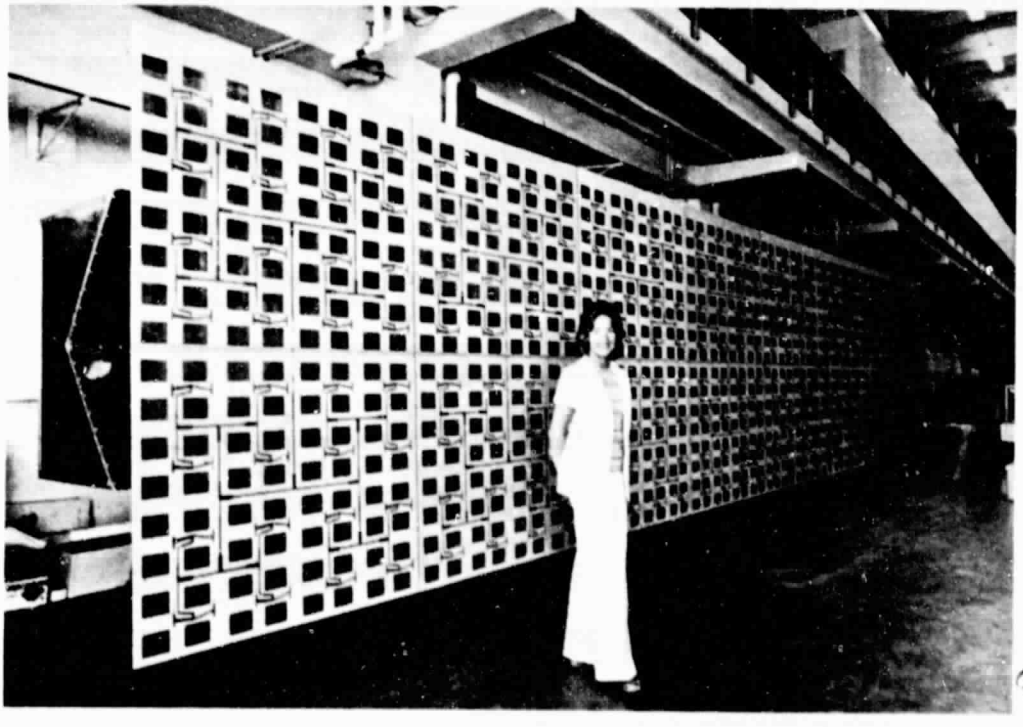

Figure 2-49. SAR Antenna Engineering Development Unit

It was also reported that an array tolerance analysis had been completed with the following conclusions:

(1) The Expandable Support Structure (ESS) flatness had to be held to ±0.635 cm (0.25 in).

(2) The antenna panel's flatness had to be held to ±0.635 cm (0.25 in.).

(3) The RF feed network phase shift had to be a maximum of ±1 deg at any output port.

These early efforts also included a detailed review of the antenna specification RF requirements. BBRC's analysis indicated all requirements except that for gain would be met or bettered. Original calculations indicated a theoretical gain figure for the antenna system of 35.03 dB versus a now-reported gain of 34.7 dB, or a change of 0.33 dB. This analysis had identified an additional loss of 0.17 dB because of the reduction of the antenna length from 11 m (36 ft) to 10.74 m (35 ft) and because of an error in calculating the H-plane taper loss. There were also small additional losses against the panel and the aperture with an additional 0.1 dB loss in the distributed cable assembly, which included the biaxial deployment mechanism.

At the PDR, held approximately 3 weeks after the management review, BBRC announced an additional reduction in the antenna gain figure. This was as a result of a worst-case study performed by BBRC using panel efficiency factors of 82 percent for the nominal value, 88 percent for the best case, and 76 percent for the worst case. These factors resulted in antenna assembly gains, respectively, of 34.46 dB, 35.00 dB, and 33.87 dB. As a result of these data, LMSC directed BBRC to initiate a development effort to increase this gain figure to the now-required value of 35.2 dB. This direction resulted in an additional 5 months of effort. Insertion of this much development effort after PDR made schedule considerations extremely critical and any misdirected effort had to be avoided.

Therefore, an LMSC team, along with JPL representatives, visited BBRC each week to ensure that the technical approach and progress were satisfactory. As this development phase progressed, larger test specimen results became more predominant in establishing BBRC's projected values. The maximum gain achieved from these test results were down 1.65 dB from the nominal specification value of 35.2 dB. Evaluation of these test data established the cause as substantial radiation loss attributed to the strip line feed network on the face of the panel. Subsequent redesign of the panel removed a major portion of this strip line design and replaced it with a coaxial feed on the rear of the panel. In late December, LMSC froze the production configuration with BBRC to permit the start of procurement for production no later than mid-January 1977 to avoid additional schedule delays.

The Critical Design Review (CDR) was conducted in mid-February with a detailed review of the various antenna configurations and the associated test results. The antenna development program had been designed to: (1) minimize parasitic losses; (2) eliminate radiation coupling losses for the high power transmission lines; and (3) substitute a new design, low-loss, state-of-the-art

corporate feed. Some of the approaches taken to reduce the dielectric and copper losses of the antenna were to: (1) mitre corners; (2) slot tees; (3) taper transformers; (4) selectively use lower impedance lines; (5) orient the ground plane internally; (6) use low-loss core material; and (7) reduce the quantities of a lower-loss adhesive. To reduce the RF coupling losses, there were experiments with various antenna circuit and radiating element spacing, and as previously identified, the higher powered lines were relocated to the back of the panels and the function accomplished with coaxial cable from the center feed point.

During the CDR, BBRC presented the fourth generation artwork (Figure 2-50) for the antenna panels, including the corporate feed. All of the above improvements to reduce the dielectric and copper losses had been incorporated. The core material of the panels was changed to Nomex phenolic honeycomb (Figure 2-51) which later attributed to a very serious bonding problem (see Paragraph 3). The Nomex-to-silver bonding of the panel was aggravated by the reduced use of adhesive to minimize RF losses. Also, the change to the coaxial feed on the rear of the panels intorduced multiple potential interferences with the ESS. To avoid these interferences, cut-outs were added to each panel to provide clearance.

To reduce the predicted gain losses in the corporate feed systme of the antenna, an effort was made to develop a suspended substrate corporate feed system with a predicted loss of only 0.8 dB instead of 1.5 dB with the original configuration. As shown in Figures 2-52 and 2-23, the suspended substrate corporate feed system was a sophisticated transmission line with a flexible motion of the antenna assembly.

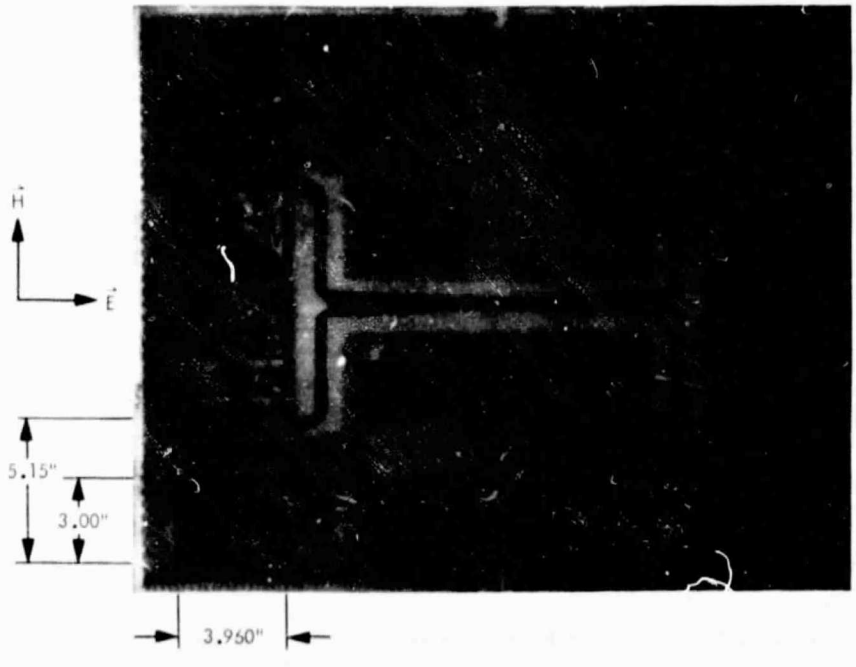

Figure 2-50. Fourth Generation Plan for Antenna Panels, Including Corporate Feed

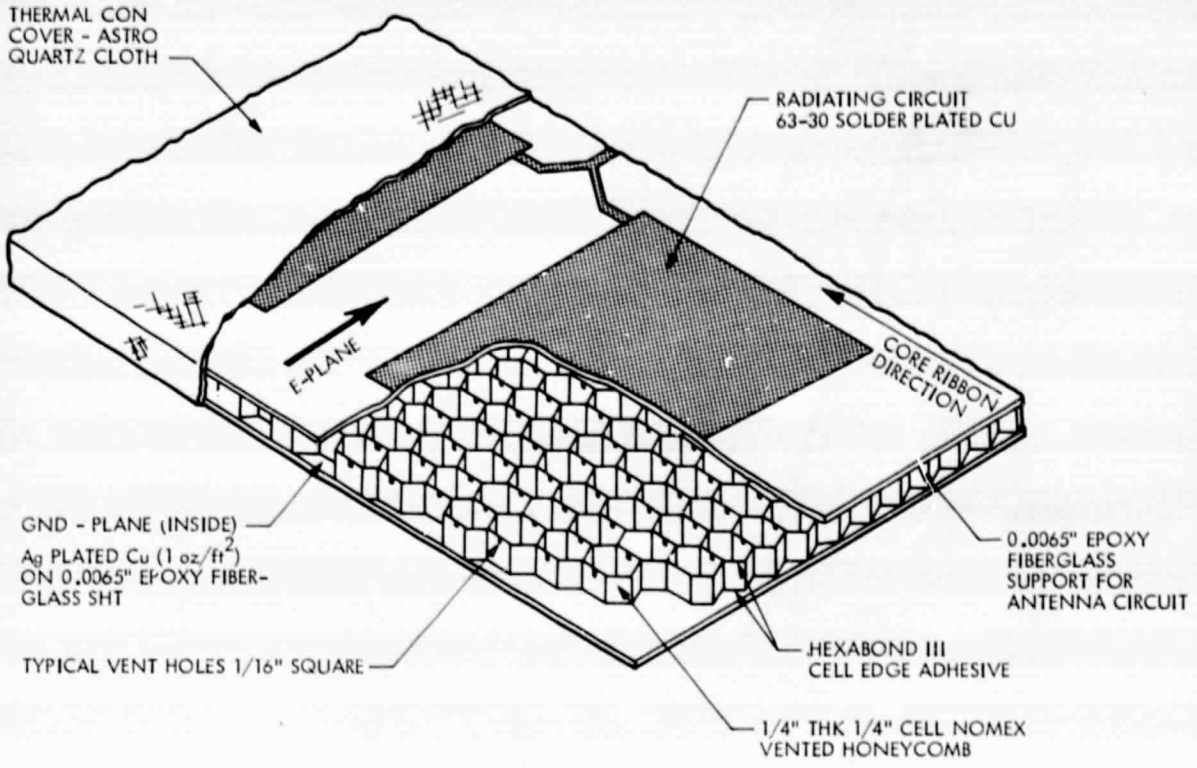

Figure 2-51. Construction of Nomex Phenolic Honeycomb Panel

The CDR specification compliance summary showed that the existing design met, or exceeded, all requirements except gain. BBRC's prediction based on measured data was now 34.77 dB versus the required 35.2 dB.

A detailed review and analysis of the design was conducted, and it was concluded that no more gain improvement was feasible. Therefore, a decision was made to proceed with the presented design.

3. Mechanical Development

The Astro Research Corporation (ARC) of Carpinteria, California, designed and constructed the ESS for BBRC. There were no major development or manufacturing problems associated with this major element of the SAR antenna assembly. In the latter half of June 1977, the ESS was shipped from ARC to BBRC, and in early July it satisfactorily passed torque margin testing.

As previously mentioned, the panel core material was changed to Nomex phenolic honeycomb and the amount of adhesive was reduced to improve the RF characteristics of the antenna. This subsequently created bonding problems between the Nomex core and the plated copper laminations. The "climbing drum"

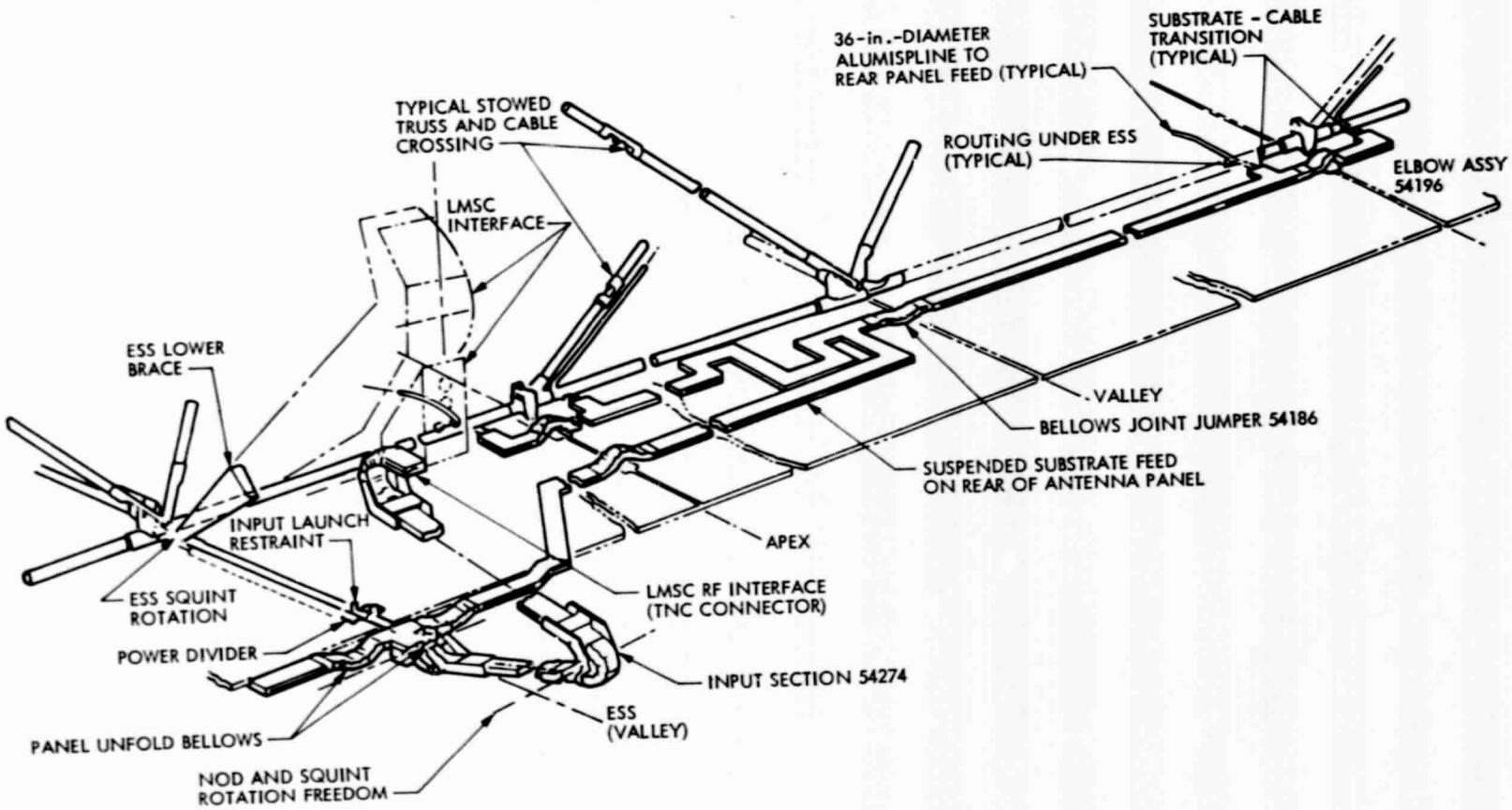

Figure 2-52. Suspended Substrate Corporate Feed System

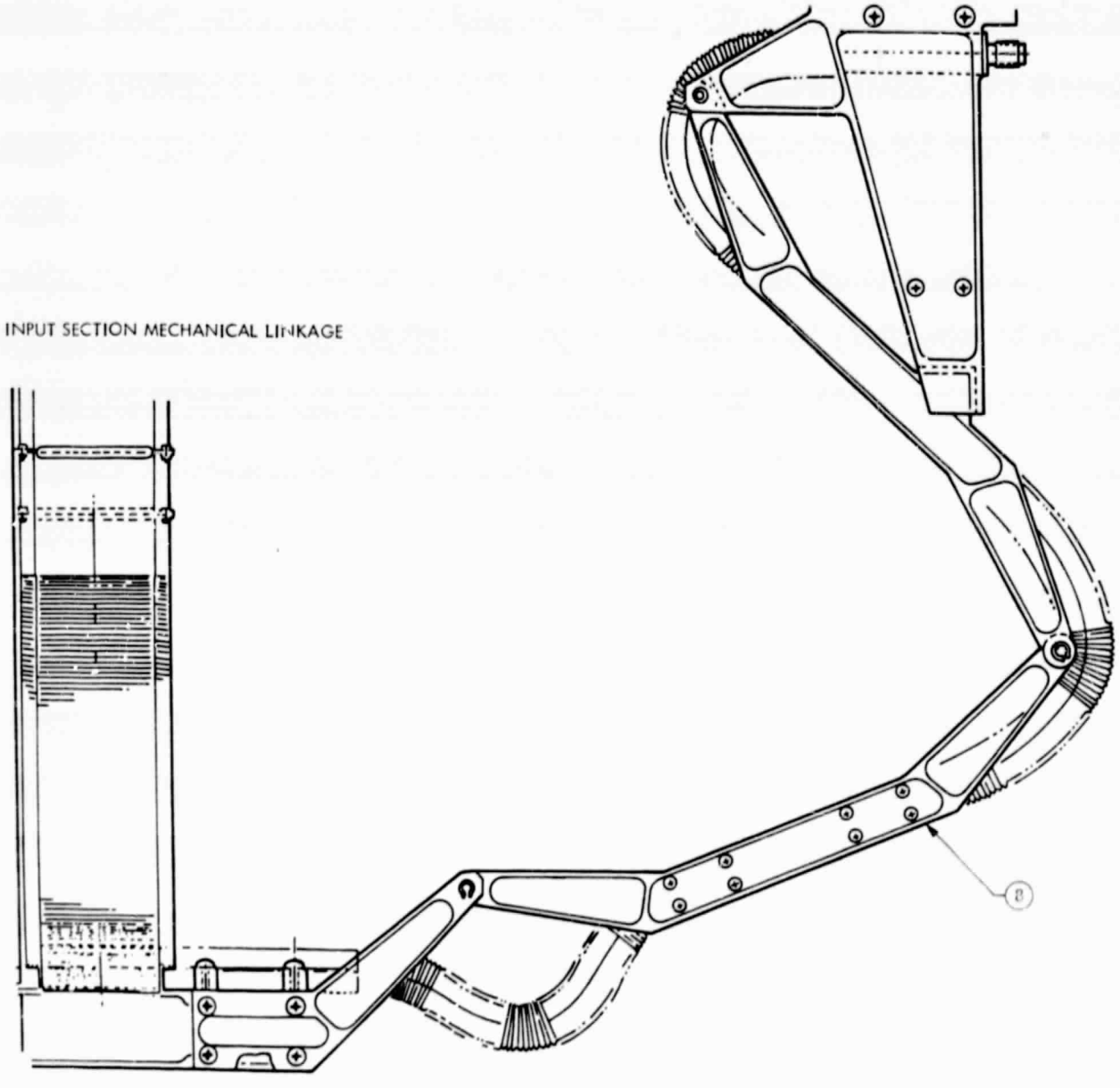

Figure 2-53. Input Section Mechanical Linkage

peel strength test was established as a method of evaluating the bonding characteristics. This became a major program concern because of the shortage of materials and because no timely resolution to the bonding problem was available. The materials and processes forces of both LMSC and JPL were organized to assist those of BBRC. Also, LMSC assigned a full-time management resident at BBRC for the duration of the processing of the flight hardware. These actions resulted in several processing improvements that were rigorously invoked in formal procedures. Even with these measures, the peel test results were unacceptably erratic. Finally, contamination of a very subtle and elusive airborne form was identified as the cause. With the additional contamination controls introduced, the peel test results became consistent and confirmed acceptable bonding strengths. Eight flight panels and three spares were fabricated in mid-August, and they met all requirements.

In early October, the qualification test program started with pre-test inspection and pre-environmental RF testing. The latter included voltage standing wave ratio (VSWR) and dc continuity tests. These tests were followed by an initial series of deployment tests that demonstrated flatness repeatability to be within specification limits. Then came 3-axes vibration tests, both low-level sine search and transient vibration on each axis. The lowest natural frequency observed was 8 Hz, which was a very adequate margin above the spacecraft's first mode. Amplification factors were not excessive and the Launch Restraint System (LRS) pre-load did not change significantly. No failures were encountered. Then, by the middle of the month, the antenna was moved to the Martin Marietta Company for the acoustic test, where it was exposed to 145 dB for 3 min without structural failure. Following the exposures to vibration environments, the SAR antenna was again checked for VSWR, dc continuity, and flatness.

The next test was a thermal exposure that concluded in the first days of November. The temperature extremes effected were 72°C and -80°C. After the thermal cycling tests, the package restraint system operated sluggishly with an apparent hesitation in panel separation during deployment, and a subsequent retest resulted in a complete malfunction. Investigation of the anomaly concluded that the malfunction was caused by a binding contact between the arm and the conical portion of the actuator. The modification shown in Figure 2-54 eliminated any possibility of metal-to-metal contact except at the mating faces. Ten releases were conducted to verify successfully the adequacy of this modification. The apparent hesitation in panel separation during the post-thermal deployment test was attributed to the adhesive not being properly cured. The curing of the adhesive was expected at the high temperature long-term stabilization periods of the thermal test and even though a "panel sticking" design modification was defined, it was decided to withhold its implementation to see if the hesitation would repeat with cured adhesives. The final planned deployment after the satellite system acoustic environmental testing, which followed a long term storage period, would determine if incorporation of the modification was required. Subsequent to the modification tests associated with the binding between the arm and the conical portion of the actuator, the first motion and pyro shock tests were completed without incident. The significant conclusions from these tests were that all launch restraint arms rotated without noticeable bounce-back and no interferences were revealed. Once again, VSWR, dc continuity, and flatness tests were verified to be satisfactory.

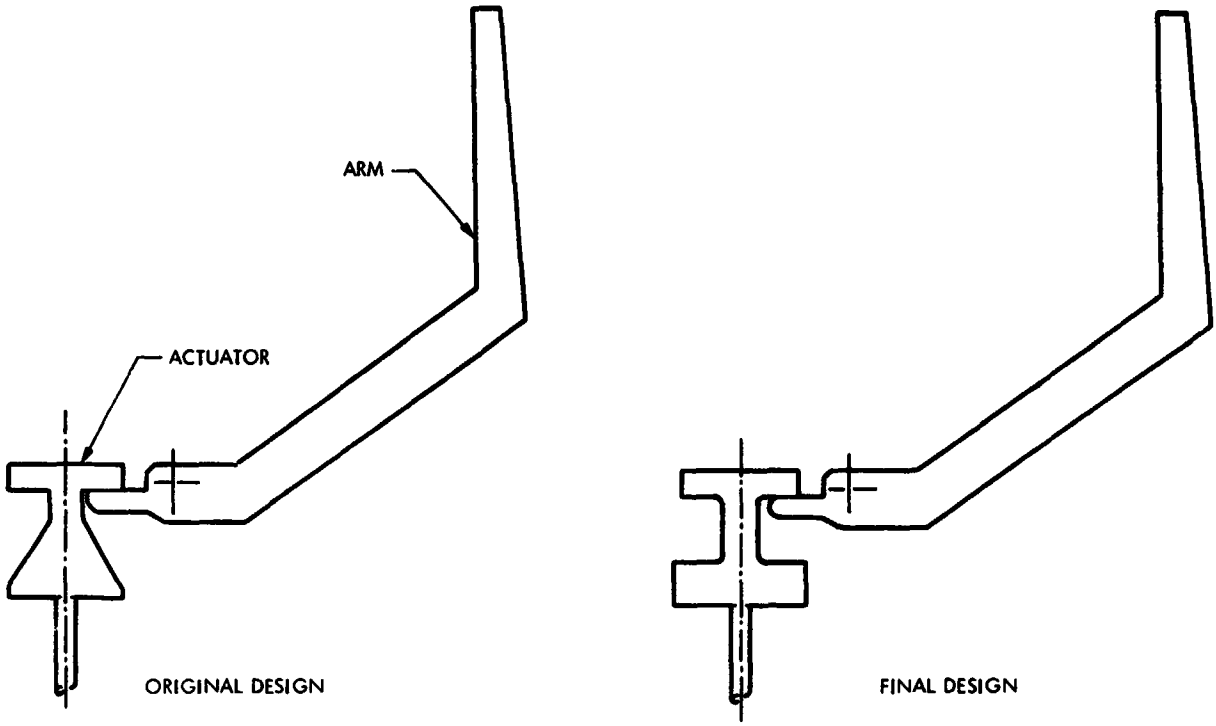

Figure 2-54. Package Restraint System

4. RF Acceptance Tests

In November 1977, the flight SAR antenna was shipped to LMSC's Santa Cruz Test Base (SCTB) large aperture antenna test range. This facility is located in the mountains near Santa Cruz, California, approximately 56 km (35 mi) from LMSC Sunnyvale. The natural topography of the test site at an elevation of 701 m (2300 ft) with heavily wooded areas, deep ravines, and orientation on the ocean side of the slope, provided maximum noise abatement and isolation. The SAR antenna was located in the 23-m (75 ft) diameter airhouse radome at the antenna test range, which was ideally suited for this type of test. The antenna was mounted on the gravity compensation fixture (Figure 2-55) and the following tests were performed: VSWR, dc continuity, and flatness. Then, the strongback was installed on the antenna and the combination was raised very carefully onto the airhouse pedestal (Figure 2-56) with its azimuth and elevation control capability. Once secured on the airhouse pedestal, antenna pattern measurements were performed using a receiving tower located 1564 m (5130 ft) across the canyon. The SAR antenna pattern measurement test configuration is shown in Figures 2-57 and 2-58. Special tests and analysis were performed to evaluate the effects of the 9-m (30 ft) diameter solid parabolic reflector located on the rear of the SAR antenna. Results of this evaluation determined that there was no effect. On completion of these procedures, the combination SAR antenna and strongback were removed from the pedestal and reinstalled on the gravity compensation fixture, where the strongback was removed. The antenna was inspected, carefully folded, and shipped to Sunnyvale, where it was placed in storage to await installation on the satellite.

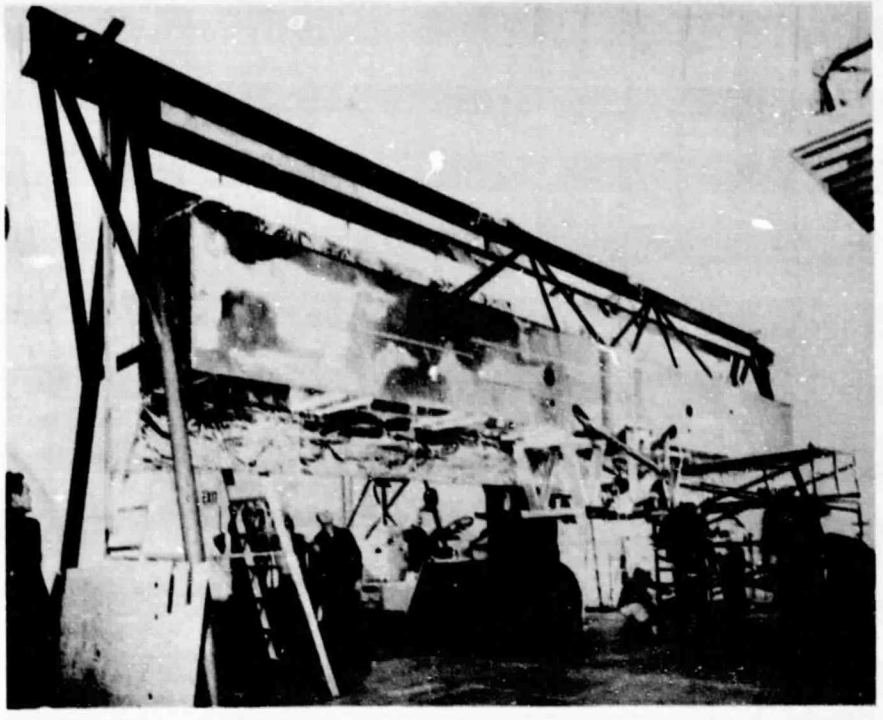

Figure 2-55. Gravity Compensation Suspension of SAR Antenna

The SCTB RF tests showed that the antenna complied with or exceeded, all of the specification requirements except gain. Peak gain was measured at 35.0 dB at one extremity of the bandwidth and varied linearly to 34.7 dB at the opposite extremity. As a result of analysis and negotiations with the Users Committee, LMSC had established with JPL that a nominal gain figure of 34.2 dB would be acceptable.

5. Systems Test and Launch Deployment

In February 1978, the SAR antenna was installed on the satellite in preparation for the system-level acoustic environmental test. The satellite was in a flight configuration with all antennas and thermal blankets installed. The acoustic environmental test was performed without incident and after removal of the satellite from the test chamber, the SAR antenna was removed and installed on the gravity compensation fixture for a post-environmental deployment test. The first attempt to deploy the antenna was terminated by the test conductor because of an interference between panels that could have caused damage to the flight hardware. The antenna was then commanded to its fully stowed (folded) position, and again deployment was attempted. This second deployment was completed successfully with no observed anomalies.

An in-depth analysis was initiated to investigate the cause of the first deployment interference. All potential failure mechanisms were identified and

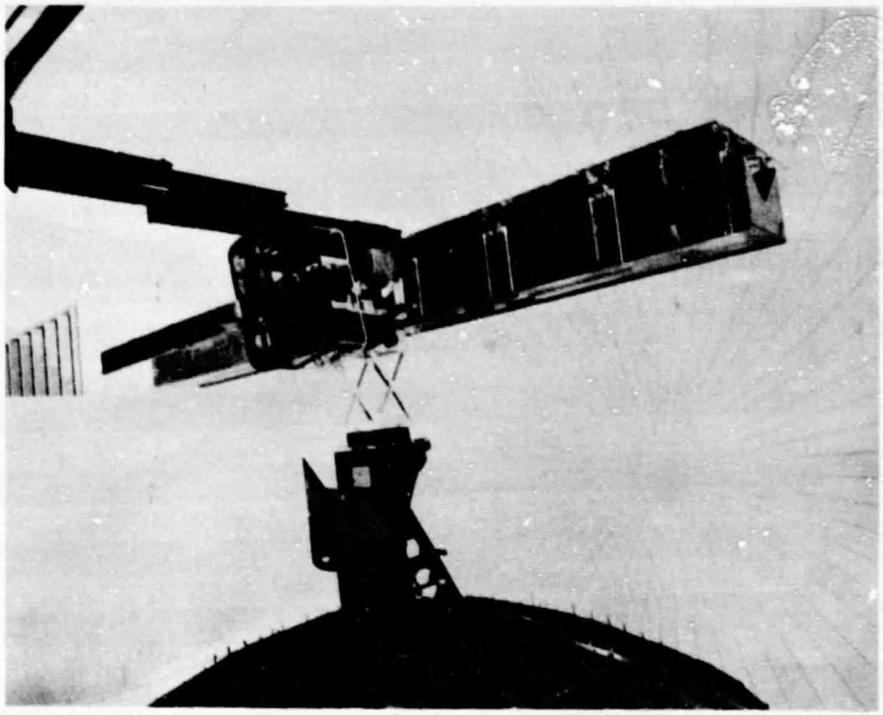

Figure 2-56. SAR Antenna and Strongback Assembly Installation on Airhouse Pedestal

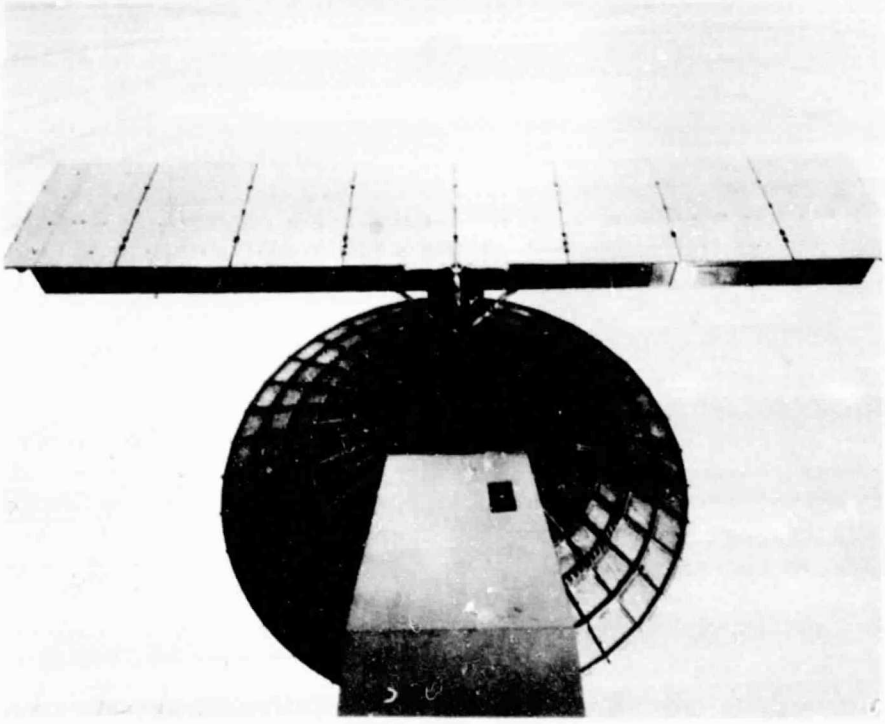

Figure 2-57. SAR Antenna Pattern Measurements Test Configuration No. 1

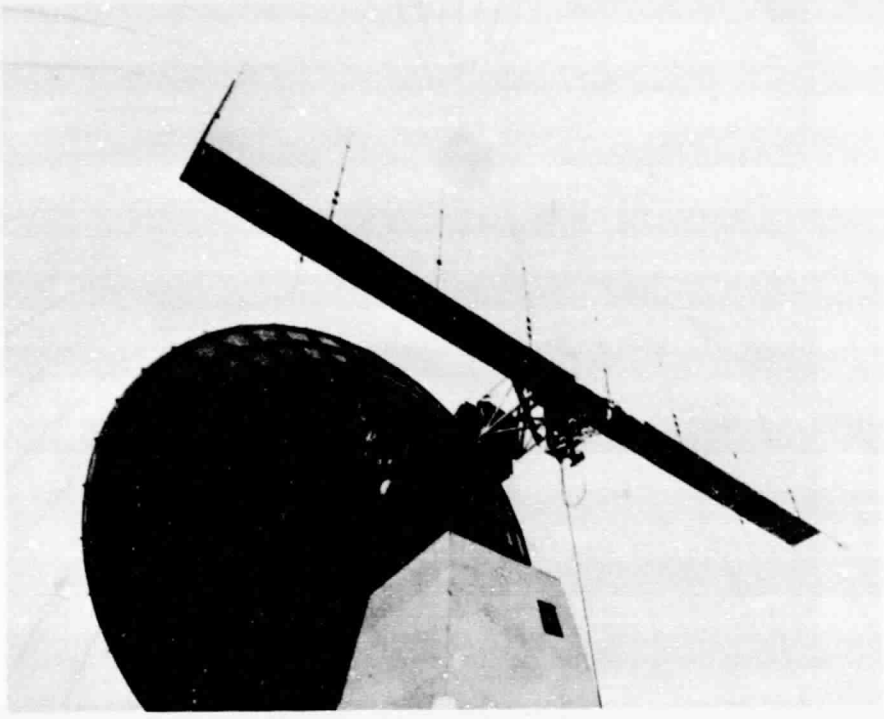

Figure 2-58. SAR Antenna Pattern Measurements
Test Configuration No. 2

all but one were eliminated by the data, inspection, and the subsequent normal extension. It was concluded that the hinge pin (Figure 2-59) had moved up and over so its exposed end was trapped in the open area in the longeron latching hinge. It should be noted that the distances that the hinge pin had to move are exaggerated in the exploded view of Figure 2-59, because actually the scissor members overlapped the longerons significantly. A design modification was performed to reduce the length of the hinge pin to avoid repetition of the malfunction.

After the modification, the antenna was stored in the stowed position for 8 days before another deployment test was performed to validate the modification. This deployment test was performed using the satellite power and command system, and provided excellent baseline data for orbit maintenance evaluation. There were no anomalies with this post-modification deployment test. The antenna assembly was removed from the gravity compensation fixture and prepared for final installation on the satellite.

The on-orbit deployment of the SAR antenna occurred later than planned because of tracking problems. However, the deployment was completely successful.

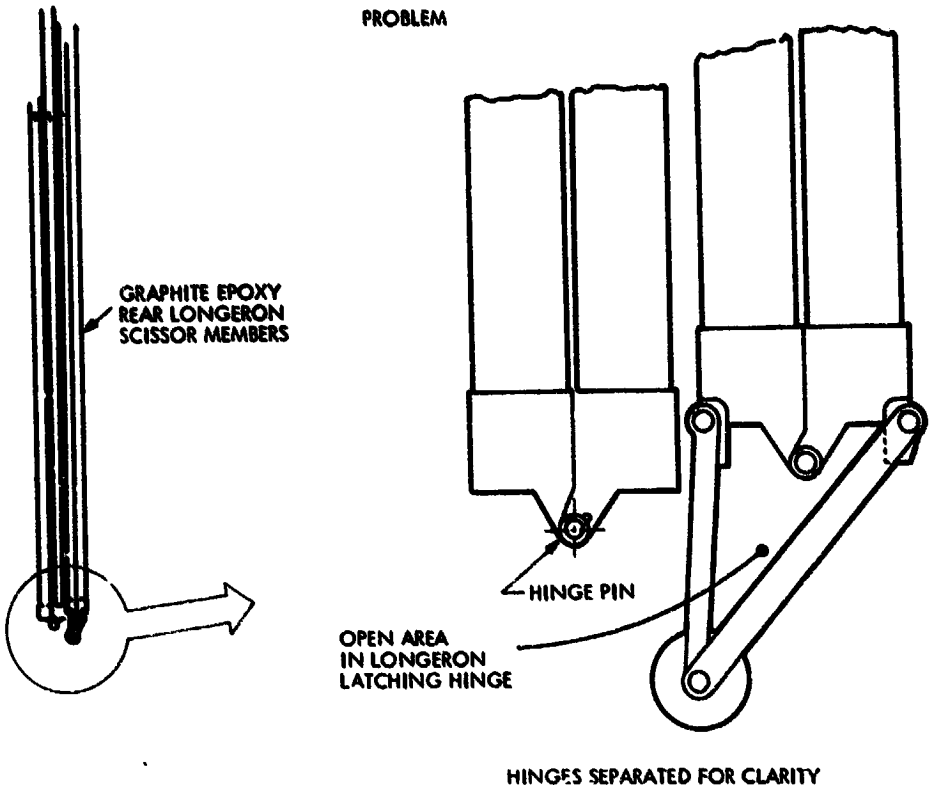

Figure 2-59. SAR Antenna Deployment Anomaly

E. FAIRING

In November 1976, NASA and JPL reviewed the design status of the protective nose cone fairing, which was to protect the Seasat payload during launch and ascent to 122,000 m (400,000 ft). The baseline design on Seasat was a "hammer head" configuration, with a 213-cm (84-in.) diameter fairing (manufactured by General Dynamics, Incorporated's Convair Division, San Diego, California) attached to a conical base structure that tapered down to the 152-cm (60-in.) diameter Agena. The concern was buffet load uncertainties because of the hammer head, and weight saving required by weight growth of the sensors and associated thermal control provisions. Accordingly, it was decided to investigate the procurement of a 305-cm (120-in.) diameter fairing, which would mate directly with the 305-cm diameter Seasat launch vehicle, the Atlas F, eliminating the hammer head configuration and some transition structures. However, the lead time for procurement of fairing forgings was over 1 year, and this lead time would not support the targeted launch data of 17 May 1978.

For over 10 years, LMSC had manufactured a 305-cm fairing used on USAF space programs using the Titan III launch vehicles, and there was an LMSC test fairing in storage (consisting of three cylindrical barrel sections and one conic section) that was available for Seasat. LMSC was instructed by NASA and JPL to form a study team to determine if this existing fairing, which included a center

barrel section length not required in the Seasat configuration (see Figure 8-4), could be refurbished and made flight worthy for the Seasat mission. The fairing was 7 years old and had been used in stack, static load, thermal/separation, and pressure tests in USAF qualification testing. There were over 200 discrepancies recorded (mostly minor nicks and scratches), including a missing skin panel and a bent ring, which was later replaced from a cannibalized part on the center barrel.

This fairing was retrieved from storage at LMSC in mid-November 1976. A 6-man multi-discliplinary team was organized to perform an in-depth inspection and engineering shakedown and to generate documentation of all discrepancies. The team completed its work on 15 December 1976 and informed the program office that the fairing was capable of being restored to flight status. During the same period, NASA headquarters designated Lewis Research Center (LeRC), Cleveland, Ohio, as the fairing procuring agency, with a complementary added role of launch vehicle integrator for Seasat. Therefore, the Seasat Atlas F launch vehicle was procured from GDC by the USAF Space and Missile Systems Organization (SAMSO), Los Angeles, California, with overall launch integration by LeRC. The Atlas F, originally a ballistic missile, received the standard Atlas E/F Vandenberg Atlas Modification Program (VAMP) by GDC at Vandenberg Air Force Base, California, converting it into a qualified space launch vehicle. LeRC agreed to the Seasat mission's use of this test fairing provided that the LMSC Senior Material Review Board concurred in the feasibility of refurbishment. The board was composed of the LMSC Space System Division Chief Engineer, the Chief of Product Assurance, and the Air Force Plant Representative's Office (AFPRO). This approval was obtained 14 January 1977 after extensive review of the documentation, including refurbishment requirements, on this fairing.

A contract was negotiated with LeRC for this fairing refurbishment and modification in February 1977 (No. NAS-3-20638), effective 1 March 1977. Refurbishment activities continued in conformance with the fairing master schedule (Figure 2-60). Refurbishment of the nose cone and aft and forward barrels was completed by May 1977, followed by successful LMSC inspection and local USAF quality assurance reviews. This work was completed without incident, although there was some difficulty in the welding of a small section on top of the nose cone (see Figure 2-59). The nose cone was manufactured from magnesium thorium (HM 21A), while the surface of the fairing barrel sections was 7075-T6 clad aluminum. The weight of the fairing was 1198 kg (2642 lb) and the height was 1268 cm (499.5 in.). The barrel rings were 2024-T aluminum while the interface ring was 7079 aluminum forging, providing the optimum mechanical properties of aluminum alloys.

The nose cone was made of magnesium thorium because of its light weight and better heat properties compared to aluminum. The small nose dome on top of the nose cone was replaced with a stainless steel cop. Steel was used because of its strength properties and ease of fabrication. Other significant changes and modifications were: (1) deletion of a nose cone air conditioning diffuser (not required on the Seasat mission); (2) replacement of new thermal liners with 2024-T# ALCAD (to protect the payload) in the nose cone and the forward barrel; (3) use of the proven S-500 thruster springs design; (4) use of proven Centaur Standard Shroud (CSS) program forward pyro joints; (5) use of the latest

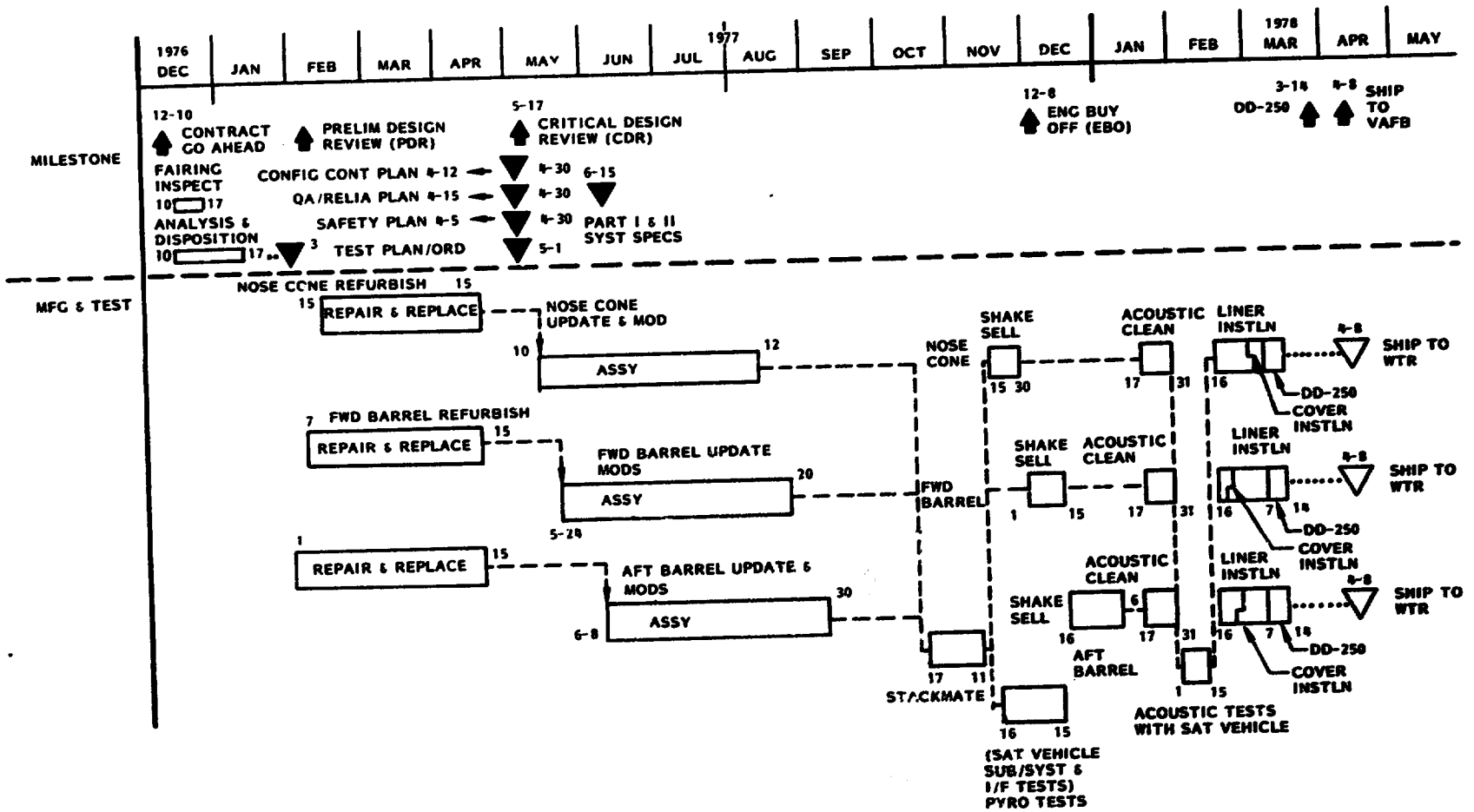

Figure 2-60. Fairing Master Schedule

electrical disconnect design; (6) incorporation of CSS-type detonator block, barrier, and clip configuration to improve reliability of the detonator; (7) deletion of nitrogen chute provisions; (8) addition of current nose dome ring and cross brace design; (9) installation of frangible doublers and superzip; (10) installation of new electrical harness; (11) nose cone modification to make an access door to enable access to the SAR data link antenna during the required launch pad test; and (12) triplex umbilical door modification. The forward barrel was painted white to meet thermal requirements.

These changes were made to bring this fairing, manufactured in 1970, up to the latest 1977 design technology, and to incorporate Seasat mission-peculiar modifications. These modifications were completed on the barrel assemblies in October and the following month on the nose cone. During this same time period there was considerable design and analysis performed in support of the refurbishment details and the integration with the Atlas F/Agena vehicle. All previous flights with this fairing design had been with another type of launch vehicle. These analyses included: (1) weight and mass properties studies; (2) separation and jettison analyses; and (3) structural dynamics and loads, including acoustic, aerodynamic, venting, thermodynamics, and stress analysis. These studies included interfacing with both the Atlas and the Agena/SMSS design and analysis.

There were also extensive studies, and tests at the SCTB, of the application of the superzip system, which is an LMSC-patented separation system. It could be compared to an "explosive can opener". Frangible doublers, manufactured by LMSC at Sunnyvale, connected the fairing's two clam shell sections longitudinally and horizontally. These sections contained explosive cords (mild detonating fuses) and 12 detonators (6 primary and 6 backup), both purchased items. The horizontal connection interface was to a booster adapter, an LMSC-manufactured item, which was connected to the Atlas and the Agena. There were both cord and detonator redundancies in the superzip system, which along with the associated frangible doublers, received extensive factory acceptance testing at SCTB. This testing included cycles of heating, cooling, wetting, and random vibration tests on a specially constructed Seasat test fixture. LeRC required higher levels of vibration testing than had been performed on similar USAF programs. The detonators and their mounts passed these higher vibration levels.

Another interesting feature of this program was the removal, or neutralization, of all major non-conducting areas on the fairing to prevent the possibility of an electrostatic buildup and discharge that could arc into and damage the payload.

During October and November 1977, the fairing was used to support an all-up vertical stack and alignment with the Agena. This was accomplished satisfactorily despite the fact that during this period there was a strike of the hourly workers at LMSC. Therefore, the stack was performed by salaried manufacturing quality assurance and program engineering personnel. All operations were completed within specifications despite the problems encountered.

Also, in December 1977, a team from LeRC and AFPRO conducted an engineering buy-off. This group statused close-out on the space technology analysis, and compared the as-planned configuration and design with the actual released

engineering specifications. Spot checks were also performed on the hardware to compare the as-designed and the as-built statuses, including the close-out of the original discrepancies discovered. In January 1978, acoustic cleaning was performed in LMSC's acoustic chamber. In February, the fairing was stacked with the Agena and the satellite, in a configuration closely resembling that required for launch, for the total-system acoustic testing. Safety, both for the hardware and operating personnel, received heavy emphasis throughout the fairing program. As a result, there were no reportable accidents either at Sunnyvale or at the launch site at VAFB. This fact was a tribute to the LMSC personnel involved, as with a large, bulky structure like the fairing, safety problems are not uncommon. After acoustic tests, the fairing was destacked and received DD 250 review and acceptance by the government representatives. Then, final wipe-down and special wrapping were performed. The fairing was shipped to VAFB without incident on 7 April 1978 on a USAF C-5A aircraft, which was loaded at Moffett Naval Air Station, adjacent to LMSC Sunnyvale.

SECTION III

SATELLITE DEVELOPMENT AND ACCEPTANCE TEST PROGRAM

A. INTRODUCTION

The Seasat test program was developed to provide an orderly sequence of tests and operations leading to the final acceptance of the satellite system. This approach was defined as a "factory-to-pad" sequence and has been successfully demonstrated on numerous LMSC programs.

Major emphasis was placed on the complete satellite systems test approach, with every reasonable attempt made to test the complete satellite system under as realistic conditions as were feasible. The Seasat test program objectives were to:

(1) Provide a complete flight-configured satellite system to the launch base on the required date that had successfully passed all ambient and environmental tests, including a launch-readiness simulation in the factory, where the same procedure events, software, test equipment, and personnel were used.

(2) Verify the satellite system design and compatibility.

(3) Demonstrate the satellite system design margins.

(4) Verify the satellite system performance in all operating modes.

(5) Provide a satellite system data baseline for mission operations support.

LMSC had developed and used on Seasat a comprehensive and perceptive test program that concentrated testing at the component level which would detect workmanship-type defects, and also identify incipient failures or infant mortality before subsystem or systems level testing. This planned test approach ensured progressive screening out of failures and anomalies from the component level through the systems environmental tests. This proved to be a cost-effective approach because failures at the component level did not involve or delay systems level support groups. The Seasat flight components were subjected to individual acceptance tests to demonstrate compliance with the individual component specification requirements before delivery to the system. Figure 3-1 shows the component acceptance test sequence and the minimum required tests for complex electronic components.

The rationale used in defining the component acceptance test program for Seasat was based on the results of a 5-year investigation into the cause of systems test failures. The results of this investigation were documented in "SSD Baseline Test Program Rationale for Flight Systems", LMSC document D381336 dated 1 April 1974. Data from systems test failure histories of 46 spacecraft were collected, categorized, and analyzed. These data indicated that workmanship

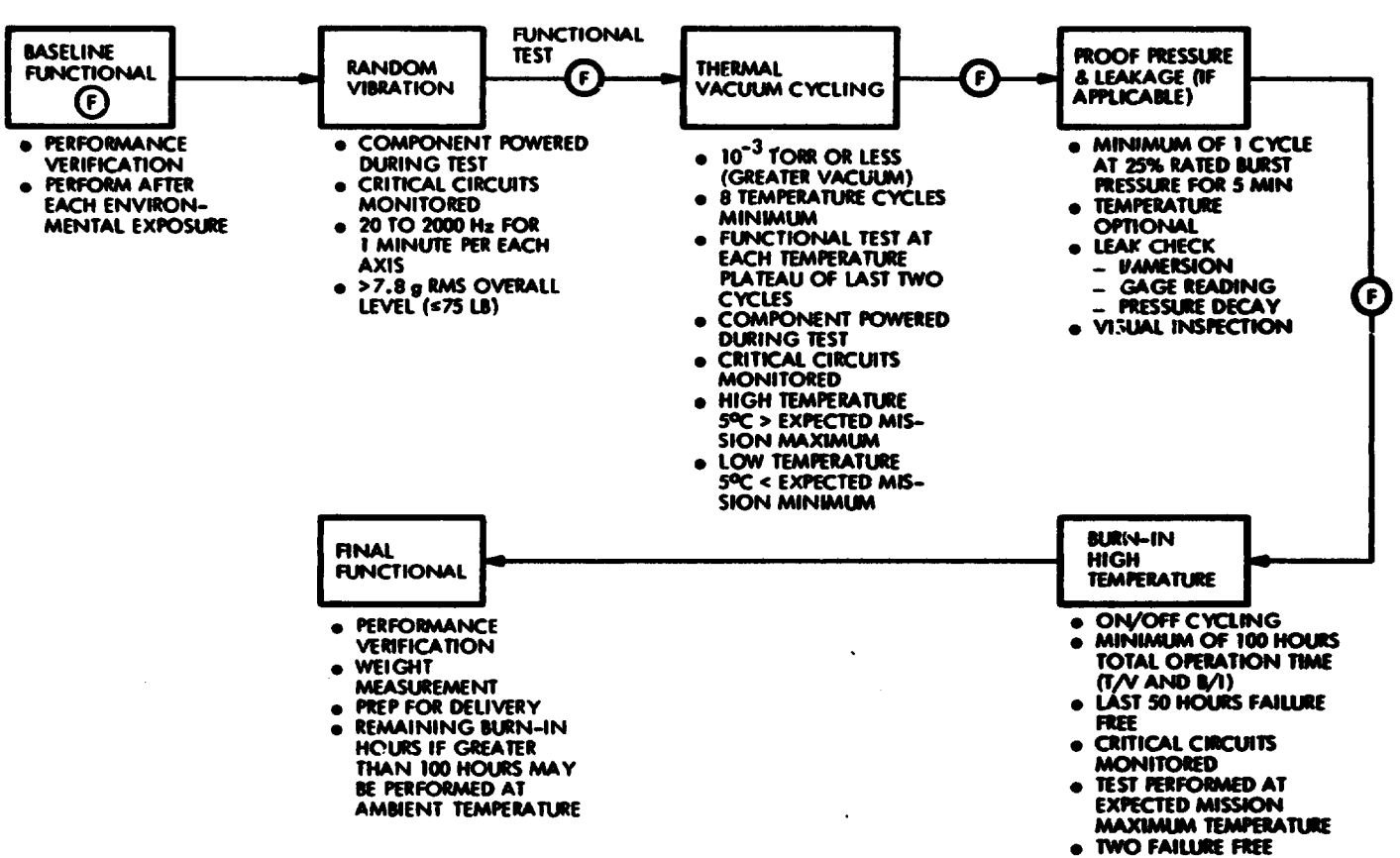

Figure 3-1. Minimum Required Acceptance Tests for Complex Electronic Components

was the most frequent cause of failure (47.2 percent), with parts problems (20.8 percent) constituting the second largest group of defects, followed by design errors (20.4 percent), and causes unknown (11.6 percent).

The Seasat test program was performed in two phases. Phase 1 consisted of the development tests performed on the SM/SMSS assembly that served the common goal of accumulating design and engineering data (not otherwise obtainable) required to complete or improve the proficiency of the design. This development test effort consisted of the following major procedures:

(1) Antenna coupling test.

(2) Static structural test.

(3) Modal survey test.

(4) SM/SMSS compatibility tests.

Phase 2 of the test program consisted of the systems acceptance testing of the SM/SMSS and the Agena bus in a total satellite configuration, followed by the launch operations. This activity consisted of the following major procedures:

(1) Satellite subsystem and sensor integration tests.

(2) Baseline systems test.

(3) EMI test.

(4) RFI test.

(5) Acoustic environmental systems test.

(6) Satellite STDN/POCC compatibility test.

(7) Thermal/vacuum environmental systems test.

(8) Final simulated flight test.

(9) Launch operations.

B. DEVELOPMENT AND TEST PROGRAM SCHEDULE

The Seasat program schedule shown in Figure 3-2 indicates the following major milestones and key events: (1) delivery of the GFE sensors; (2) Agena bus and SM/SMSS assembly and test; and (3) satellite integration and systems test procedures. A concentrated effort was initiated on the Seasat program coincident with the contract go-ahead on 12 February 1976.

Major emphasis was placed on defining the overall systems requirements, establishing interface agreements with the individual sensor representatives, and negotiating subcontracts. The first program milestone was the Preliminary

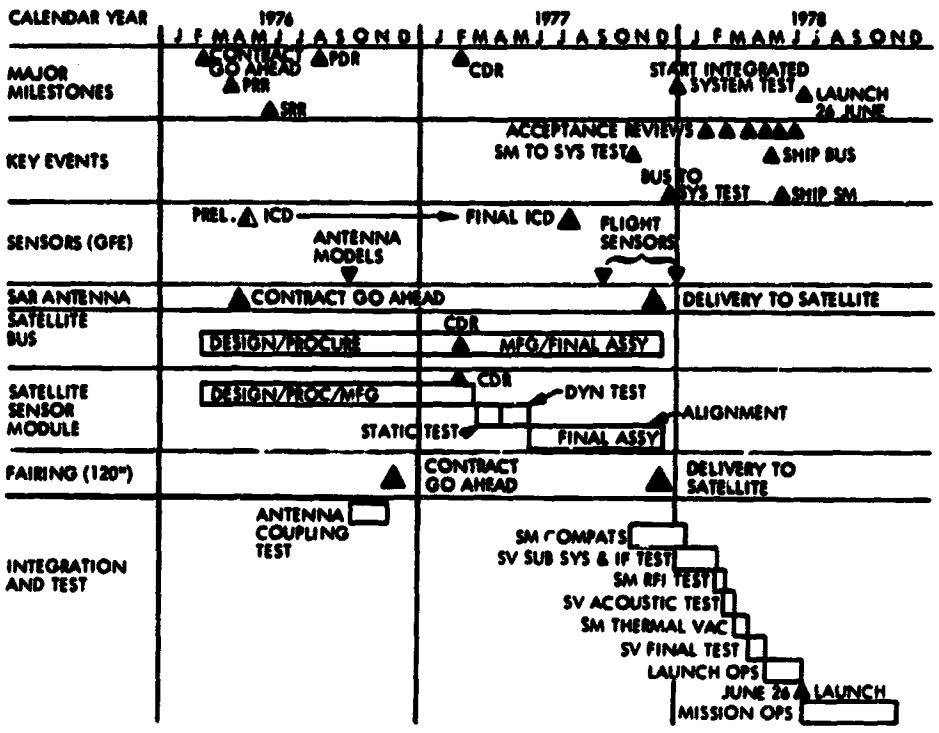

Figure 3-2. Development and Test Program Schedule

Requirements Review (PRR) conducted at LMSC from 30 March through 1 April 1976. This was a major review conducted with JPL, NASA headquarters, and sensor representatives with objectives to: (1) define the baseline mission, satellite system, and subsystem functional, performance, and design requirements; and (2) describe the current design concepts for compliance with established requirements. A significant revelation at the PDR was that, with the exception of the VIRR, the suppliers of the sensors and other GFE equipment were not prepared to make firm commitments on many of the key interface parameters, including space allocation and field-of-view (FOV), mass properties, power requirements, data and command formats, thermal provisions, etc. This situation reflected the fact that most of the sensors were still in an early phase of development and were not ready for detailed firm integration with the satellite. Therefore, many of the planned Interface Control Documents (ICDs) could not be completed at this time. In addition, a number of requests to improve the capability of the on-board data system were introduced by JPL. Detail definition and implementation of these changes placed great stress on the schedule, but were accommodated without serious impact.

The Systems Requirement Review (SRR) was held on 25-27 May 1976, where the baseline mission, satellite system and subsystem functional, performance, and design requirements were finalized. As a result of splintered working group sessions, preliminary agreements were achieved on some of the ICDs during this review. However, the complete area of system test was unresolved in terms of

basic policy and procedures, as well as detail agreements on sensor data formats, limits, apertures, alarms, and operating sequences. LMSC had proposed a factory-to-launch test philosophy that minimized direct access to the sensors, required the sensors to be flight-ready when delivered, and did not provide for extensive performance tests at the launch base.

The LMSC philosophy was adopted by JPL and, while it was new to the sensor suppliers, they adjusted appropriately and the test program proceeded accordingly with considerable success. To satisfy the desire of the associate contractors to test their equipment after shipping it to LMSC, a special area was prepared close to the Satellite System Test Facility so each could perform one final check before integration with the satellite. Later, this capability proved to be very useful in accommodating the several sensor removals, repairs, and reworks that were performed during the system test period. The Preliminary Design Review (PDR) was conducted at LMSC on 2-3 August 1976, where the Seasat baseline design and configuration were reviewed in detail. Estimated performance parameters were also reviewed with respect to program requirements. An in-depth review was conducted with the individual sensor representatives to ensure that the interface agreements and design criteria were fully understood by both LMSC and the representatives.

The last of the major design reviews was conducted on 1-2 February 1977 with the completion of the Critical Design Review (CDR). This milestone acknowledged the 90-percent release point for all of the engineering design documentation, and also was a detailed review of each subsystem to ensure system design compliance with the system specification. A significant result of the CDR was the announcement by the sensor representatives that delivery of the sensors could not support the planned pre-RFI compatibility testing at LMSC. The program test plan required the performance of a sensor compatibility test beginning the latter part of July 1977 and ending the first of September 1977. This was to be followed by the RFI compatibility test at the SCTB large aperture antenna test facility through the middle of October 1977. This announcement required a complete reassessment of the Seasat test schedule and planned test approach. As a result of this reassessment and the revised delivery schedule for the sensors, along with funding constraints imposed by JPL, the RFI compatibility test was rescheduled for completion during the satellite systems test period.

With the successful completion of the antenna coupling test in September and October 1976 (where the RF coupling characteristics were measured between radiating and receiving elements on a full-scale mockup at the SCTB test facility), technical credibility was provided for the decision to reschedule the RFI compatibility test. In addition, as a result of the antenna coupling test at SCTB, potential RFI incompatibility was additionally reduced by the required addition of RFI filters to the SAR system, altimeter, and SASS. This knowledge of sensor delays and the resultant rescheduling of the test program, which was then in-line with funding constraints imposed by JPL, also permitted a rescheduling of the manufacturing and test effort for the data system components and structural subassemblies.

The SAR antenna was assigned to LMSC under the Satellite System Engineering (SSE) contract at the beginning of the Seasat program. After a 3-month design

study of alternative approaches, where a planar array was compared to a multi-parabolic array, JPL selected the planar approach. A contract was then placed with BBRC to design and manufacture the array. Although this task proved to be considerably more difficult than anticipated, the array was completed in time to meet the satellite schedule. After delivery from BBRC, LMSC conducted performance tests of the antenna system at SCTB.

A major change in the satellite configuration was made in December 1976, just before the CDR, when the satellite fairing was changed from a 213-cm (84 in.) diameter to a 305-cm (120 in.) diameter design. This decision was made because of a NASA concern for the aerodynamic interactions between the 213-cm diameter fairing and the nose of the Atlas booster. This situation had been aggravated when the USAF changed the Atlas nose from the ogive-shaped Atlas F to the blunt-shaped Atlas D configuration. With the larger diameter fairing, more weight could be launched by the Atlas. The change in the Atlas configuration and the larger fairing size also required a change in the booster adapter configuration. This major change in structural configuration was accomplished without an impact on the program schedule.

The static and dynamic structural test program on the SM/SMSS was performed during March and April 1977, as originally scheduled at the start of the program. Minor design changes were made as a result of this test program, as discussed in Paragraphs C2 and C3, without significant effects on the program schedule.

Following the structural tests, the SM/SMSS was returned to the manufacturing area where the assembly was refurbished and final installations begun. This 5-month period included the detailed buildup and installation of the satellite harnesses and of the individual sensor submodules, followed by the SM/SMSS system alignments. All subsystem elements met the required delivery schedules with only minor workarounds and rescheduling of activities. Included in this time period was an hourly labor strike of one and one-half months in October and November 1977, along with late delivery of the SASS (14 November) and altimeter (29 November), which did impact the program schedule. These two sensors required "out-of-station" installations during the systems test span. The SASS was installed temporarily for initial integration tests, and required subsequent removal for a high voltage power supply replacement.

The final phase of the development test effort, which encompassed the satellite subsystem compatibility tests and the sensor integration tests, began with the transfer of custodial responsibility to systems test on 21 October 1977. In an attempt to make up the schedule loss (28 work days) caused by the labor strike and the late sensor deliveries, a second shift of test operations was initiated along with the use of selected overtime. It was emphasized by JPL that the original launch date of 17 May 1978 was still critical to the efforts of the sensor representatives to support other NASA meteorological activities. This development test effort was completed early in February 1978 after the demonstration of Agena bus subsystem performance testing and compatibility tests with the SM/SMSS. The Agena bus had completed its non-powered electrical, propulsion, and alignment subsystem tests and had been transferred to systems test on 14 December 1977. SAR and SMMR changeouts were also accommodated during the test span without serious impact by careful planning, coordination of workarounds, and intensive effort. It is also noted that the altimeter was delivered

with several discrepancies and in a non-flight status that was subsequently corrected.

The satellite systems test schedule is shown in Figure 3-3, and details the accomplished tasks and time periods for performance. This effort was performed on a nominal two-shift basis, except during the systems thermal/vacuum environmental test, where around-the-clock support was required. It was during the thermal/vacuum test that the SAR data link had a major failure and required subsequent removal from the satellite. It was returned to the Applied Physics Laboratory (APL) of Johns Hopkins University for repair and retest. This activity had a major impact on the program schedule. A launch date of 17 May 1978 required the shipment of the satellite system to the launch base by 5 April. It can be seen from Figure 4-3 that 16 of the original 28 work days were regained before the SAR data link failure, and it is believed that additional work days could have been made up.

The scheduling of operations at the launch base permitted the Agena bus to be shipped on 27 April 1978, followed by the mechanical integration to the Atlas booster on 2 May. The three separate fairing sections had been flown to the launch base by a USAF C-5A aircraft on 29 March 1978. The launch base detailed operations and schedule are shown in Figure 3-4. A concentrated launch base effort was initiated, targeting for a 10 June launch date. However, a concern was expressed by the USAF and LeRC about recent flight data on the Atlas booster associated with unexplained temperature increases in the boattail adapter section of the Atlas. A decision was made by JPL to delay the launch and determine the cause and possible effects (if any) on the Seasat mission. An extensive effort was made by GDC and their subcontractors in evaluating this problem and diagnosing the required rework to the suspect areas of the Atlas. The Mission Readiness Review (MRR) was conducted on 21 June, where final approval for the launch was given by JPL. A successful countdown and launch were made on 27 June 1978 (GMT). However, the final decision for launch was predicated on surface wind conditions and winds aloft, which were evaluated continuously during the countdown, and only moments before the required liftoff was this final approval given.

C. DEVELOPMENT TESTS

An antenna-to-antenna coupling test was performed early in the test program in October 1976 so that design changes could be incorporated in the individual sensors or in the sensor module electrical power or data subsystem equipments.

A structural static loads test of the sensor module primary structure and the SM/SMSS was performed on flight hardware (proto-flight test) to verify that the structural design strengths met the requirements for predicted flight loads.

A modal survey test was performed on the flight SM/SMSS to determine the dynamic model that was used for structural analysis.

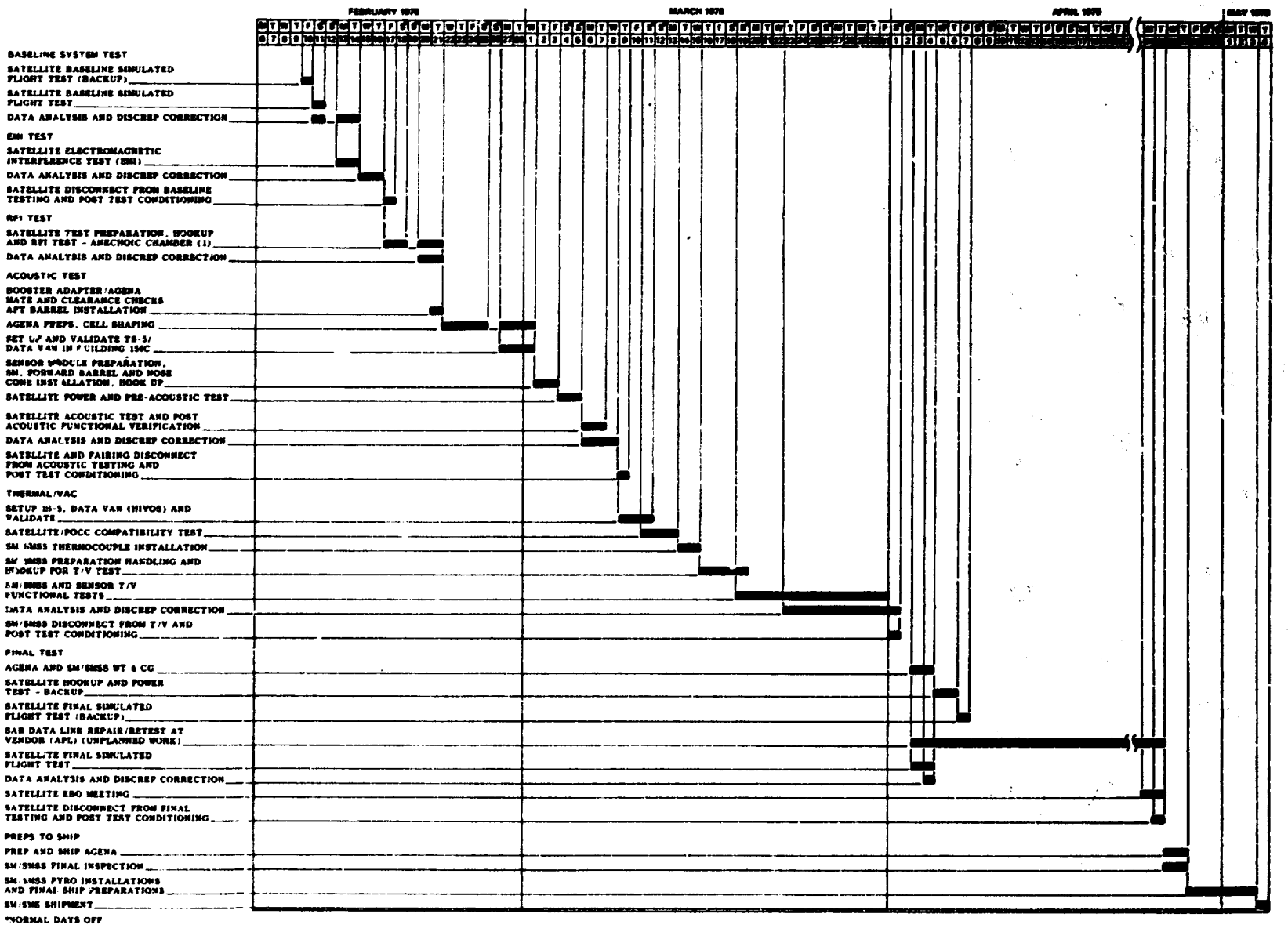

Figure 3-3. Detailed Systems Test Schedule

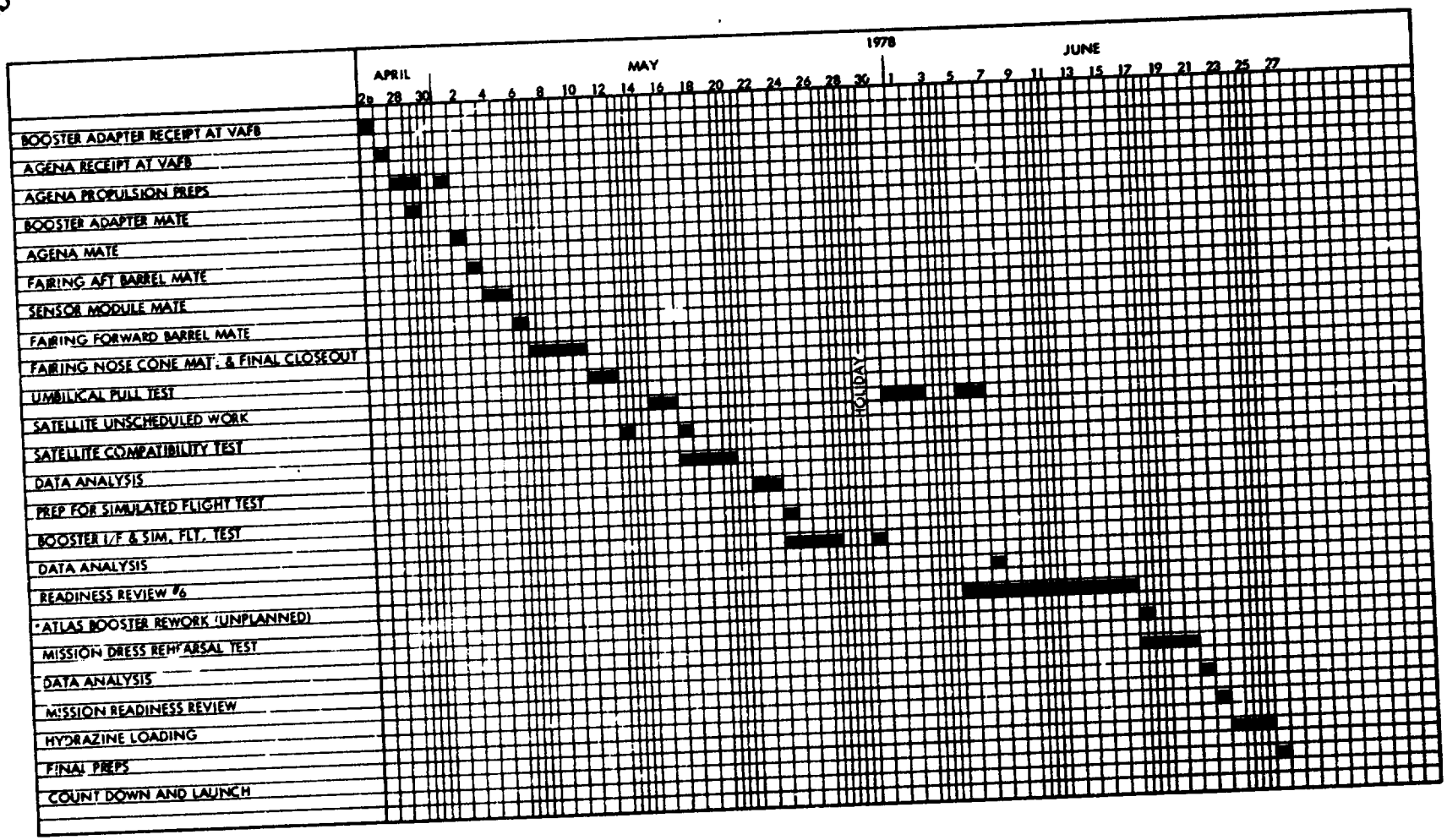

Figure 3-4. Launch Base Schedule

1. Antenna Coupling Test

a. Objective. The test objective was to verify that signal levels from each transmitting antenna were not high enough at the various receiving antennas to degrade the performance of any sensor. Additional objectives of this test were to validate the pre-test coupling predictions and to determine the peak RF field intensity in the vicinity of the VIRR and scanwheel assemblies.

Specific objectives for the SMMR were to determine if the in-band energy from any transmitter would cause a temperature bias, or if any out-of-band energy would cause a diode detector burnout.

b. Configuration. An engineering metal mockup of the sensor module was used along with prototype or simulated antennas in their respective locations (Figures 3-5 and 3-6). The mockup was considered electrically equivalent to the sensor module, and consequently any radio frequency coupling measurements made were representative of the coupling expected on the final flight configuration.

The antenna coupling test was performed at the SCTB large aperture antenna test range. The sensor module mockup was located in the 23-m (75 ft) diameter airhouse radome at the antenna test range.

c. Results. The mutual coupling between the various transmitting and receiving systems was determined by connecting a radio frequency source to the input terminals of a transmit antenna and making measurements at the input to the other transmitting and receiving antennas.

Prior to the coupling test, an evaluation of the test facility was made to ensure there would be no EMI caused by undesirable signals in the area or reflections from the walls of the facility that would invalidate the mutual coupling measurements. The results of this facility evaluation indicated no signals were present with a lever greater than -110 dBm and the RF signal reflections were not significant in the frequency spectrum of concern.

A total of 238 individual measurements were performed, involving 19 separate antenna locations and 26 different frequencies. The measured coupling values were in agreement with or were more conservative than the required values for the various sensors and subsystems to perform. All test objectives were accomplished.

2. Static Structural Test

a. Objective. The primary objective of the structural tests was to demonstrate the ability of the SM/SMSS to withstand limit and ultimate flight loads. Additional objectives were to obtain stress and deflection data to verify load paths and stiffness used in the structural and dynamic models.

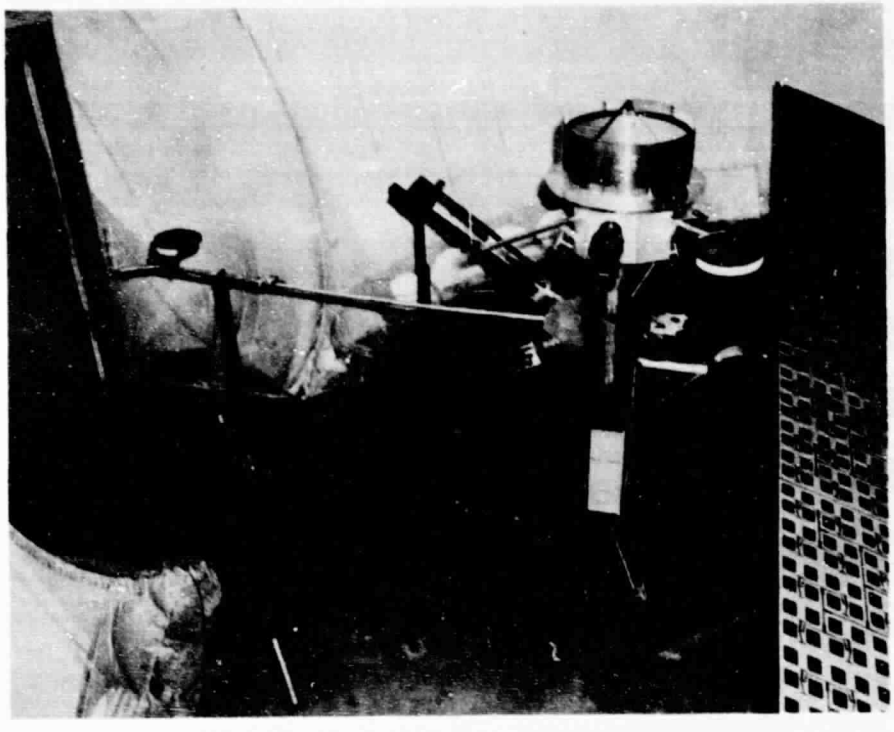

Figure 3-5. Antenna Coupling Test at SCTB (+X Overview)

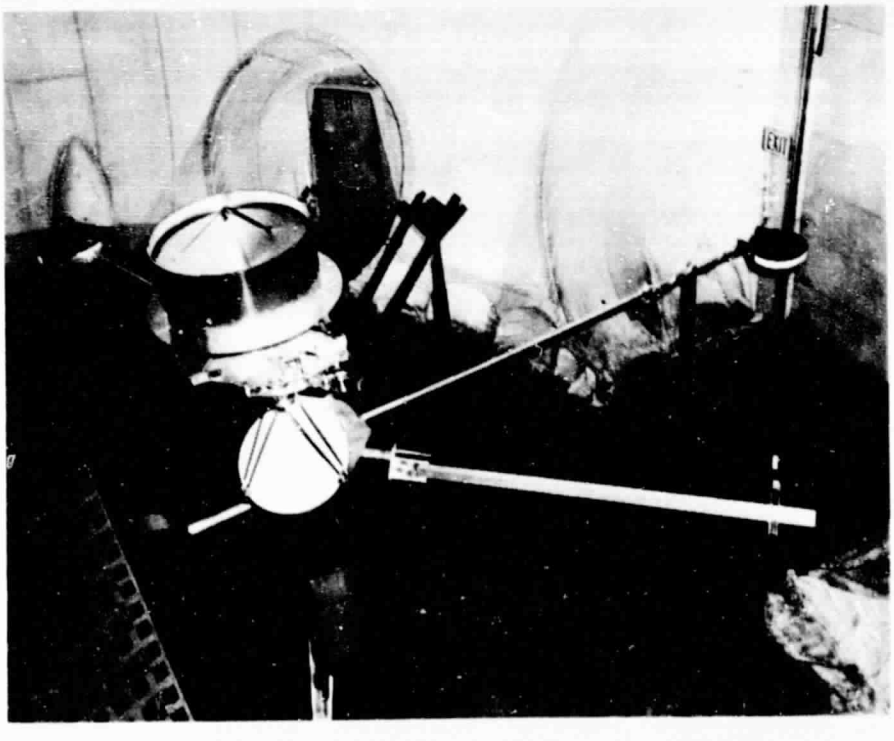

Figure 3-6. Antenna Coupling Test at SCTB (-X Overview)

b. Configuration. The flight sensor module and SMSS less all electronic equipments and associated harness assemblies were used for the static structural loads test. A non-flight Agena forward equipment section was used to support the SM/SMSS configuration (Figure 3-7).

Instrumentation requirements consisted of 30 strain gauges strategically located on the sensor module and SMSS. Fourteen deflectometers, referenced to ground, were used to measure the amount of bending in the structure and provided for up to a 15-cm (6 in.) deflection at the top of the SMSS (station 50). Loads were applied by four independent load programming systems. Each system had the capability of independent operation to permit application of a single loading system. All loads were applied by hydraulic force cylinders pressurized through hydraulic servo valves controlled by the load programming system.

c. Results. The static structural test program consisted of 3 distinct phases with a total of 14 different tests. Phase 1 testing applied 50 percent and 100 percent of design limit loads in the $-X_s$ direction, and was completed with no structural anomalies noted. However, residual structural deformation was observed in this and all subsequent tests.

Phase 2 testing was performed at 50 percent and 100 percent of the design limit load in the $+Y_s$ direction and produced cracks in the beryllium doors located on the SMSS. The doors were subsequently redesigned using aluminum, and the Phase 1 and Phase 2 tests were repeated.

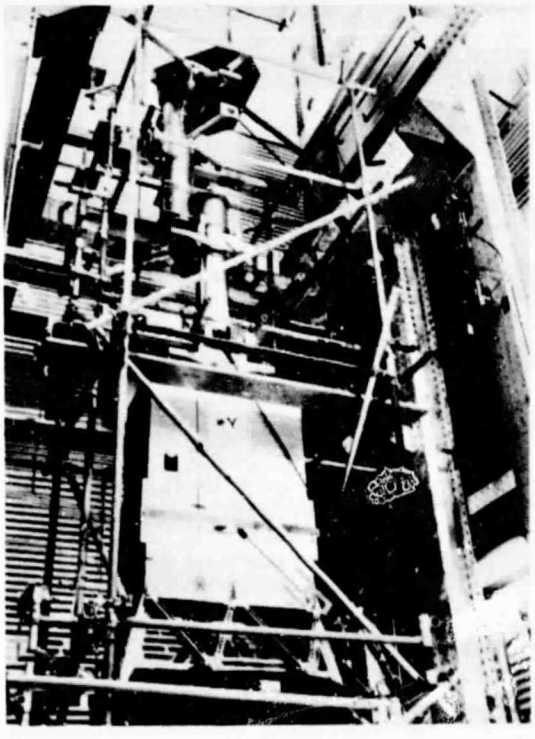

Figure 3-7. SM/SMSS Static Structural Test Configuration

The Phase 3 test was performed to assess the ability of a reverse shear load to reduce the accumulated residual deformations which had been observed during all phases of testing. The primary concern, relative to this residual deformation, was the alignment of the sun sensor and the forward end of the SMSS. The "alignment residuals" were attributable to motions at the junction of the forward and aft tubes of the sensor module. To eliminate the residual deformations at this junction, an epoxy "liquid shim" was inserted into the annulus between the mating components. Verification of the modified structure was obtained by testing to demonstrate that the residual deformations were within acceptable limits. The following table summarizes the various phases and associated tests of the static test program.

Phase	Load Direction	Load Percent
1	$-X_s$	50
1	$-X_s$	100
2	$+Y_s$	50
2	$+Y_s$	100
2-1	$+Y_s$	50
2-1	$+Y_s$	80
2-1	$+Y_s$	100
2-1	$+Y_s$	115
2-1	$+Y_s$	125
3	$-Y_S$	454 kg (1000 lb)
1-1	$-X_s$	50
1-1	$-X_s$	80
1-1	$-X_s$	100
2-2	$+Y_s$	454 kg (1000 lb)

The SM/SMSS, as modified during the static test program, demonstrated the ability to withstand maximum limit and ultimate flight loads.

3. Modal Survey Test

a. Objective. The purpose of the modal survey test was to verify the analytically-derived cantilevered modes for the SM/SMSS. This included the

determination of the number of modes existing in the 0- to 70-Hz frequency range by a series of broadband sweeps. Another requirement was the identification of the modal frequencies, modal damping, and mode shapes in the 0- to 55-Hz frequency range by processing the wideband sweep data or by a series of tuned narrowband sweeps. Emphasis was placed on the developing information on the vibration response characteristics of the SM/SMSS by measuring its vibration patterns when excited by small shakers (as low as a 0.45-kg (1 lb) force. These patterns are referred to as "normal modes" of vibration, and they determine the manner in which the structure responds to the transient flight environment. This data included the modal frequencies and the damping effects, and were used to compare with the analysis to confirm the flight worthiness of the structure.

b. Configuration. The complete SM/SMSS structural assembly with mass simulators was mounted in the vertical position as shown in Figure 3-8. The assembly was secured in a cantilevered position by bolting each of the eight interface attachment points to a massive base plate. Instrumentation for the modal survey test consisted of 71 accelerometers, 6 strain-gauge load cells, and 6 shakers strategically located on the SM/SMSS.

c. Results. The modal survey test was performed in the LMSC Mobile Dynamic Analysis Laboratory (MODALAB), which is a general purpose digital system consisting of an excitation system, a data acquisition system, and a data processing system. The excitation system is capable of independently controlling up to 16 shakers. The data acquisition system can acquire and convert 256 channels of analog data at a rate of 200,000 samples a second. The data processing system includes a minicomputer with 64,000 words of core storage and 2.5 million words of disk storage.

Pre-test analysis based on the finite element dynamic model predicted a total of five primary structural modes in the critical frequency range of 0-20 Hz. This frequency range has been identified as the critical region with respect to booster ascent loads. Test results indicated a total of 9 modes in this range of which 3 had earlier been identified as local modes with no influence on overall structural motion. Of the remaining six test modes, the first three (first and second bending and torsion) correlated very closely with analysis results with respect to both frequency and mode shapes. The fourth test mode was very close in frequency to the fourth analytical mode, but the mode shapes were out of plane with respect to each other. The fifth analytical mode corresponded reasonably well with the seventh test mode with respect to frequency and mode shape. The remaining test mode was a structural mode arising from local SAR dynamic motion. Structural damping was computed to be approximately 0.5 percent or less.

Post-test analysis of the modal survey test was limited to the 0-20 Hz frequency range with primary analysis involved in modeling the SMMR as a flexible subassembly to account for a 13.8-Hz predominant SMMR mode observed in test. Incorporation of this model into the full SM/SMSS model resulted in revised analytical modes that closely matched test results with respect to both frequency and mode shape.

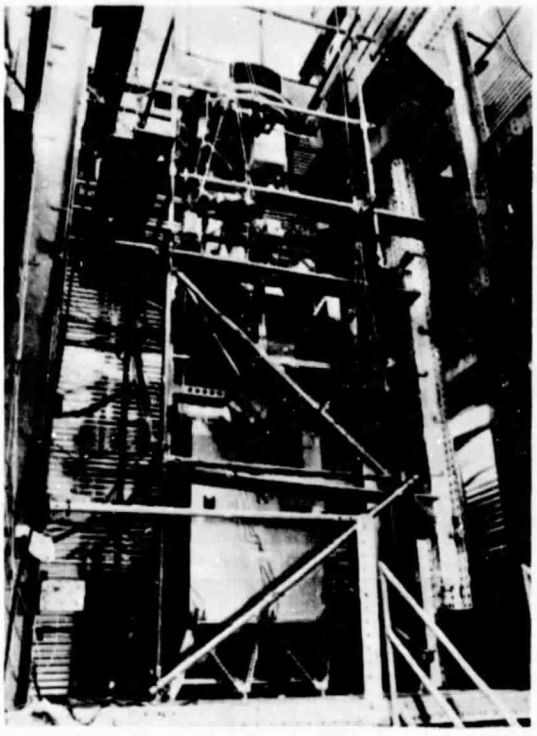

Figure 3-8. SM/SMSS Modal Survey Test Configuration

4. SM/SMSS Compatibility Tests

a. Objective. Subsequent to the final assembly of the SM/SMSS, a series of compatibility tests were performed to ensure that the power subsystem, data subsystem, and each sensor were compatible for power, functional command, and data response.

b. Configuration. The SM/SMSS was located in the systems test complex in the horizontal position on the specially designed handling dolly. The SAR antenna was not installed, and all RF connections to the data subsystem was by hardline coaxial cable. Figure 3-9 shows the SM/SMSS in the test complex from the aft end or Agena interface and with the SAR antenna holding frame on top.

c. Results. The compatibility verification tests were performed in a logical sequence beginning with pre-power and power-on checks, and culminating in a demonstration test of all sensors operating simultaneously into their respective RF loads, as applicable. After completion of the power and data subsystem tests, which demonstrated the operational performance of these components, sensor integration tests were performed to verify the capability of the individual sensors to function with the power and data subsystems.

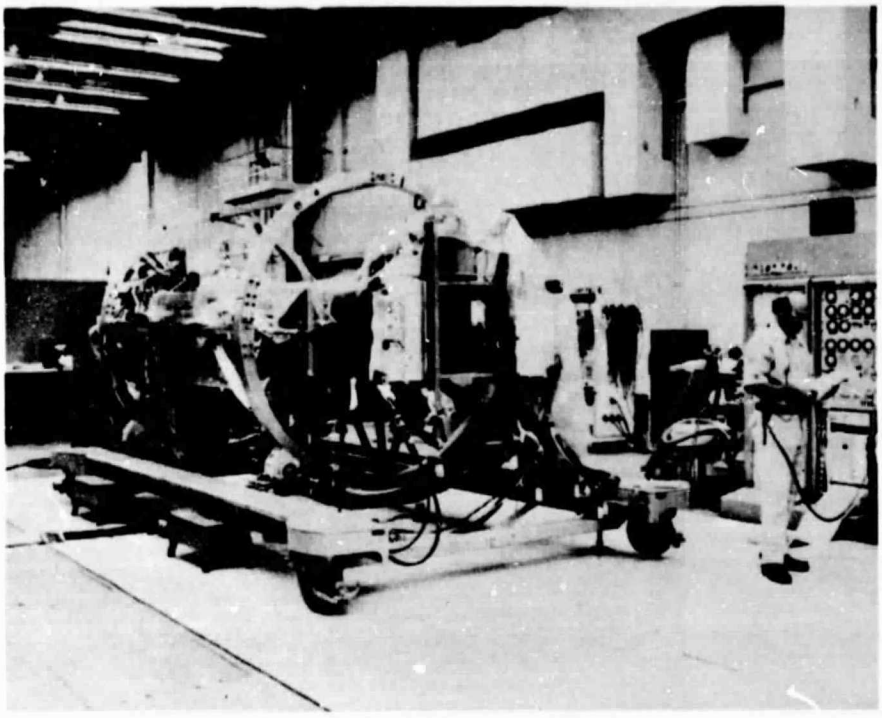

Figure 3-9. SM/SMSS Compatibility Test Configuration

During the integration tests of the altimeter, it was determined that the input capacity in the Low Voltage Power Supply (LVPS) command interface circuits was greater than ICD requirements and caused the overload protection circuits of the CPU of the data subsystem to activate. This condition was subsequently corrected by the addition of an external assembly to the altimeter signal processor that contained current limiting resistors in all LVPS command lines.

At the conclusion of the sensor integration tests, a pyrotechnic shock test was performed to supplement the analysis for pyroshock qualification of Seasat by firing pyrotechnic-actuated pinpullers, which were located adjacent to sensitive electronic equipment. This test was performed in two segments. The first test segment consisted of firing the pinpullers that constrained the SASS antenna booms, released the VIRR deployment mechanism, released the SAR data link antenna deployment mechanism, and released the Tranet beacon/orbit antenna 2 boom deployment mechanism. The test pinpullers used in test segment 1 were refurbished and used in test segment 2. The second segment consisted of firing the pinpullers that provided the SAR antenna restraints and released the orbit antenna 1 deployment mechanism. Fourteen accelerometers were used to monitor and record the shock levels at specific locations on the SM/SMSS.

Following the performance of the pyrotechnic shock tests, the sensor compatibility test was performed. The roadmap of sensor operation is shown in

Figure 3-10. This test sequence provided a demonstration of post-pyroshock performance verification of the sensors as well as individual and total sensor system compatibility. There were no major anomalies during this test program.

5. Orbit Attitude Control Development

The Orbit Attitude Control System (OACS) was developed under a subcontract to Ithaco, Incorporated. As described in Paragraph A2b, the system comprised 10 components, all but one of which were supplied by Ithaco to an OACS subsystem specification.

Each of the OACS components was of an existing design or was modified from an existing design to meet the required magnetic and control laws. A development test of the system was performed at LMSC using engineering units on a scanwheel, pitch momentum wheel, roll reaction wheel, electromagnet, control logic assembly, magnetic control assembly, and magnetometer. These assemblies were integrated with a SD-80 analog computer and other test equipment as shown in Figure 3-11, and simulation tests were conducted.

The objectives of this development test were to:

(1) Verify the OACS math model used in digital simulations of the system.

(2) Verify closed loop polarities and responses.

(3) Verify component interfaces.

(4) Test mode switching and system dynamic responses.

(5) Determine system sensitivity and margins.

(6) Evaluate on-orbit operating procedures.

(7) Obtain system test signatures.

The testing, which involved Ithaco and LMSC personnel, began on 1 December 1976 and was successfully completed 20 January 1977. The test results were presented at the ACS CDR at LMSC in late January 1977, and are documented in the OACS Critical Design Review Data Package, Ithaco document 91226, dated 18 January 1977.

6. Solar Array Development

The solar array system (described in Paragraph A1b) consisted of two deployable Solar Array Modules (SAMs) and a Solar Array Drive Electronics (SADE) unit. Each SAM included 11 solar panels, deployment mechanism with damper, a restraint mechanism, a slip ring assembly, and a drive motor.

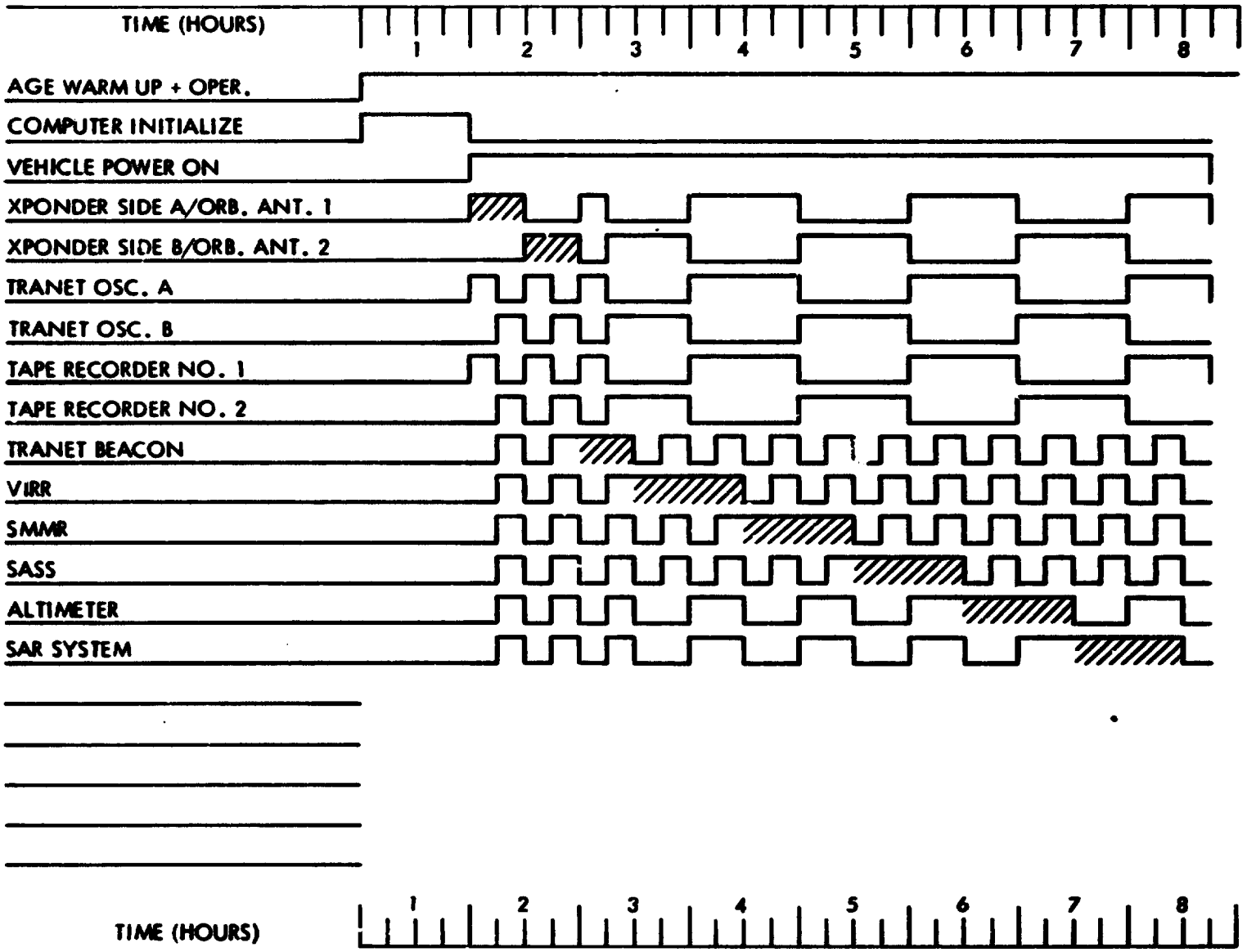

Figure 3-10. Sensor Compatibility Test Roadmap

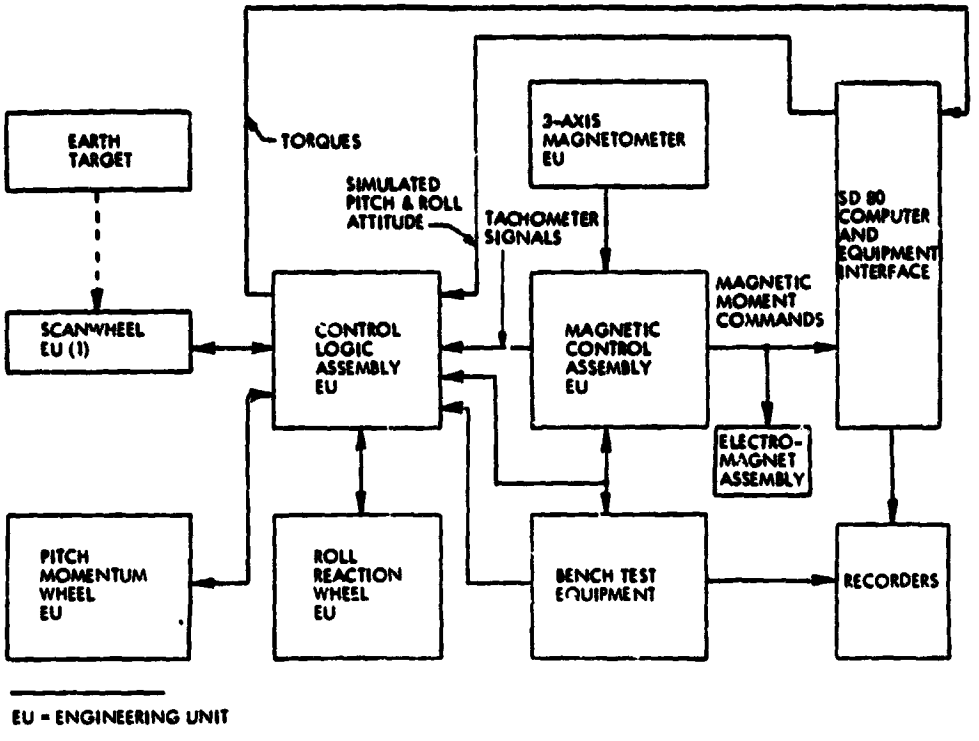

Figure 3-11. Orbital Attitude Control System Development Test Configuration

The design for each solar array element had been taken directly from or modified from that of another program where it had been previously flight-qualified. Also, each element of the system was subjected to complete acceptance testing according to program requirements before assembly of the system.

After assembly of the SAMs, acceptance tests were performed at either or both the module level and satellite level to verify electrical outputs, deployment rates and clearances, installed clearances, restraint release, end-to-end continuity and polarity, and proper rotation direction. During the acoustic chamber test of the complete satellite, the SAMs were installed and, after the acoustic test, were removed, tested for release, deployment, and continuity, and packed for shipment to the launch base.

In addition to these tests, certain elements of the solar array system, including the SAMs, were subjected to a series of development, proof, and confidence tests that are described in the following paragraphs.

a. Solar Cell Engineering Proof Test. This test verified the manufacturing process of solder-bonding the solar cells to the panels when 40 non-flight cells were bonded and pull-tested.

b. Deployment Mechanism Development Test. An engineering model of the SAM deployment mechanism was instrumented and tested under controlled conditions to verify deployment paths and clearances, to verify wire harness routing, to determine stiffness characteristics, and to verify functional performance. Loads were applied in both outboard and axial directions to simulate flight conditions while the deployment was executed.

c. Viscous Damper Development Test. An engineering model of the viscous damper was tested to determine fluid viscosity requirements, to verify performance at temperature extremes, to prove survival in the orbit thermal environment, to verify performance of the temperature compensation feature, and to determine acceptance test criteria.

d. Solar Array Drive Electronics Development Tests. An engineering breadboard model of the SADE was assembled and tested to verify design compatibility under conditions of a thermal/vacuum environment and under minimum and maximum voltage conditions. In addition, a flight design printed circuit board of the SADE was tested to verify functional performance under orbital conditions and at voltage extremes.

e. Solar Array Module Development Tests. A solar array module, comprising one flight panel with cells attached and nine dummy panels, was assembled and tested in a zero-g simulator along with a complete deployment mechanism, including damper, a complete restraint system, a full set of springs and outriggers, and a dummy drive motor and slip ring assembly. The objectives of these tests were: (1) to verify clearances, restraints, and actuator adjustments; (2) to select proper spring rates; and (3) to verify mounting and housing interfaces.

f. Solar Array Module Confidence Tests. After inspection and refurbishment where necessary of the SAM unit used in the development tests, the module was instrumented and tested for survivability under the vibration, shock, and acceleration environments expected in flight. Sine sweep, random vibration, and simulated pyro shock environments were applied to the stowed SAM configuration in all three axes and an acceleration test was performed in the axis representing the ascent. After the tests, the module was retested for suitable deployment, disassembled, inspected, refurbished where necessary, and reassembled as a flight unit.

Figure 3-12 illustrates the Seasat solar array power system testing from the part level to launch site assembly.

D. RELIABILITY AND QUALITY ASSURANCE

1. Reliability

a. Introduction. The Seasat reliability requirements were delineated in the "Project Plan for Seasat-A 1978 Mission," JPL document 622-3, November 1977,

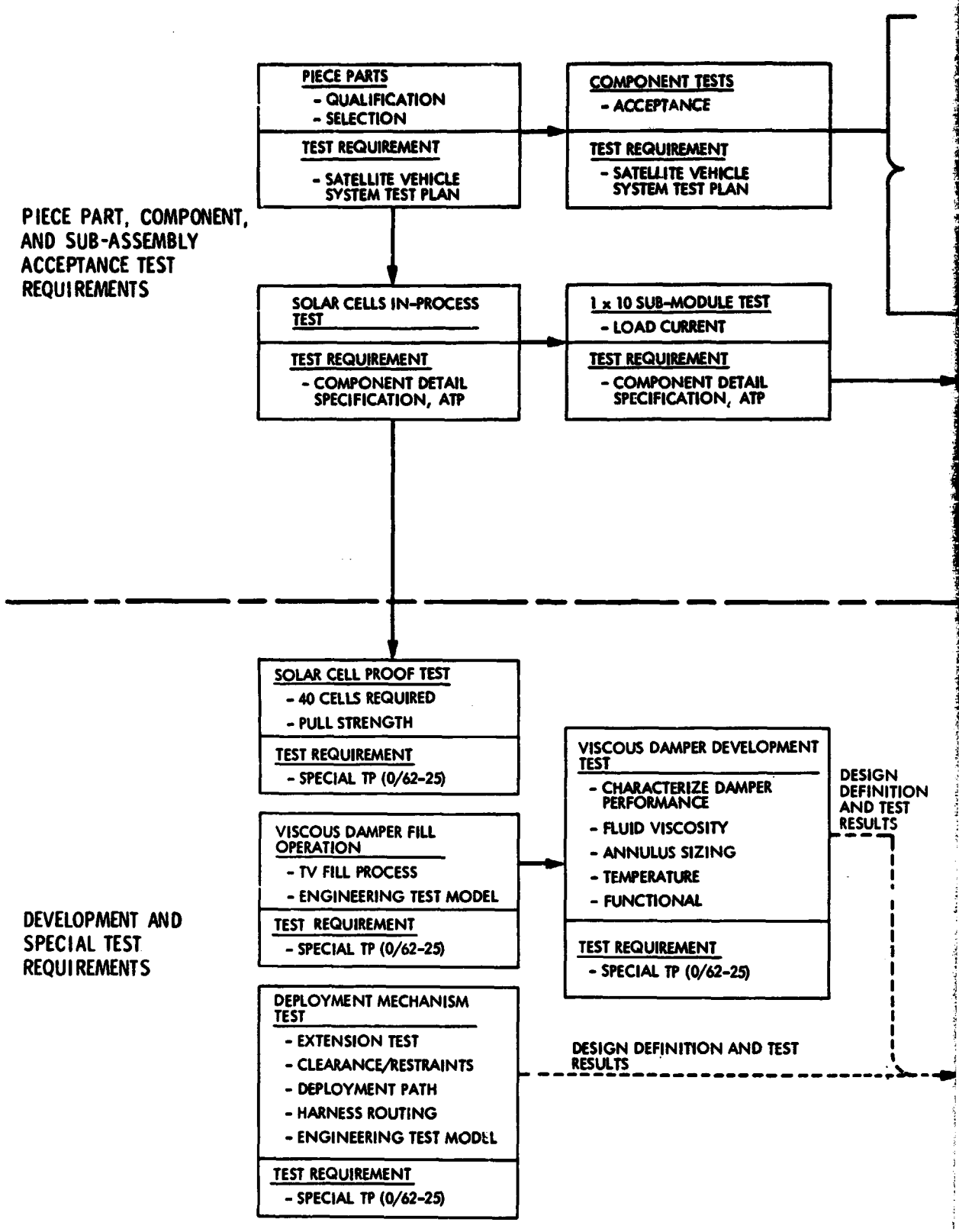
PIECE PARTS
- QUALIFICATION
- SELECTION
TEST REQUIREMENT
- SATELLITE VEHICLE SYSTEM TEST PLAN
COMPONENT TESTS
- ACCEPTANCE
TEST REQUIREMENT
- SATELLITE VEHICLE SYSTEM TEST PLAN
PIECE PART, COMPONENT, AND SUB-ASSEMBLY ACCEPTANCE TEST REQUIREMENTS
SOLAR CELLS IN-PROCESS TEST
TEST REQUIREMENT
- COMPONENT DETAIL SPECIFICATION, ATP
1 x 10 SUB-MODULE TEST
- LOAD CURRENT
TEST REQUIREMENT
- COMPONENT DETAIL SPECIFICATION, ATP
SOLAR CELL PROOF TEST
- 40 CELLS REQUIRED
- PULL STRENGTH
TEST REQUIREMENT
- SPECIAL TP (0/62-25)
VISCOUS DAMPER FILL OPERATION
- TV FILL PROCESS
- ENGINEERING TEST MODEL
TEST REQUIREMENT
- SPECIAL TP (0/62-25)
DEVELOPMENT AND SPECIAL TEST REQUIREMENTS
VISCOUS DAMPER DEVELOPMENT TEST
- CHARACTERIZE DAMPER PERFORMANCE
- FLUID VISCOSITY
- ANNULUS SIZING
- TEMPERATURE
- FUNCTIONAL
TEST REQUIREMENT
- SPECIAL TP (0/62-25)
DESIGN DEFINITION AND TEST RESULTS
DEPLOYMENT MECHANISM TEST
- EXTENSION TEST
- CLEARANCE/RESTRAINTS
- DEPLOYMENT PATH
- HARNESS ROUTING
- ENGINEERING TEST MODEL
TEST REQUIREMENT
- SPECIAL TP (0/62-25)
DESIGN DEFINITION AND TEST RESULTS

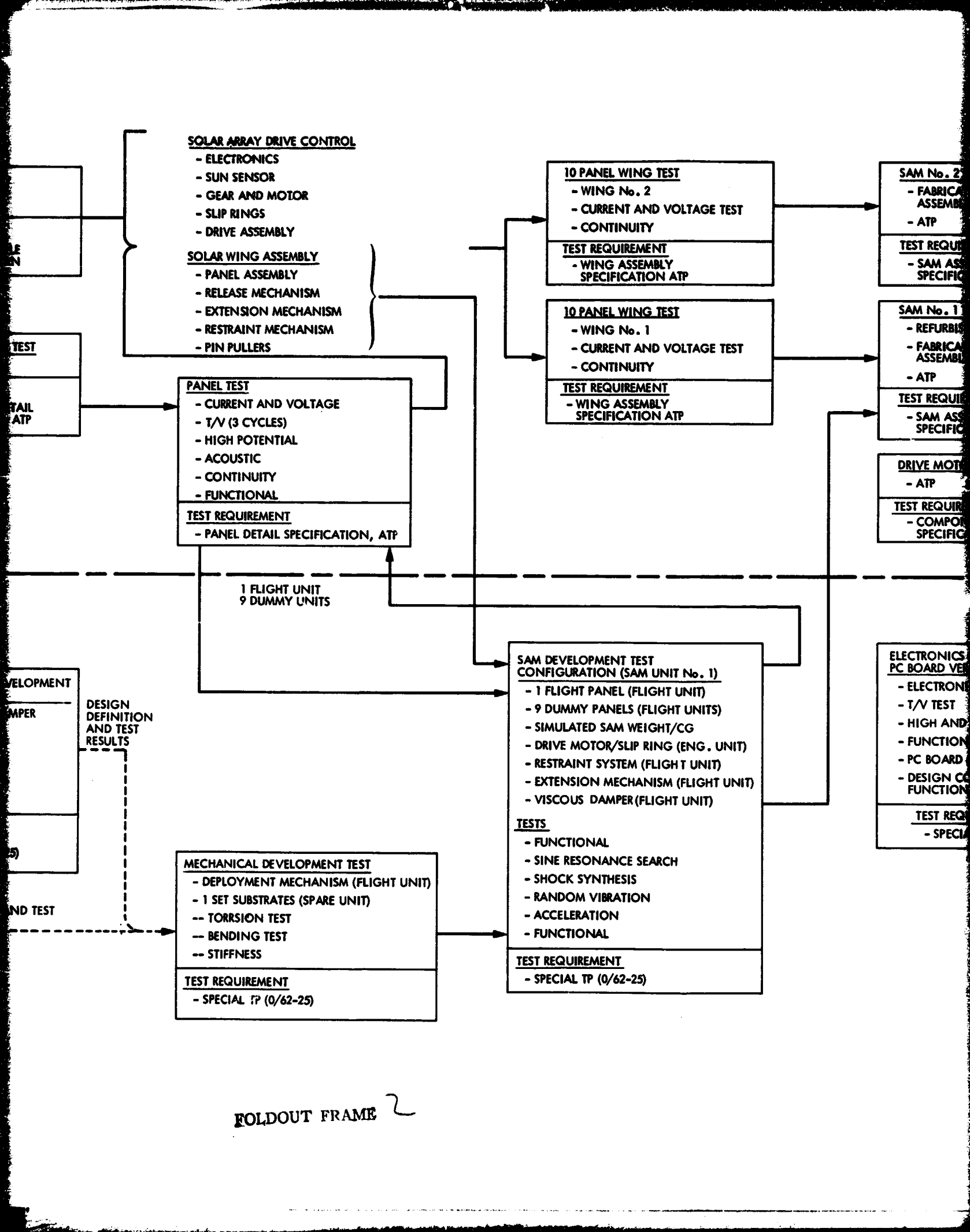

FOLDOUT FRAME 2

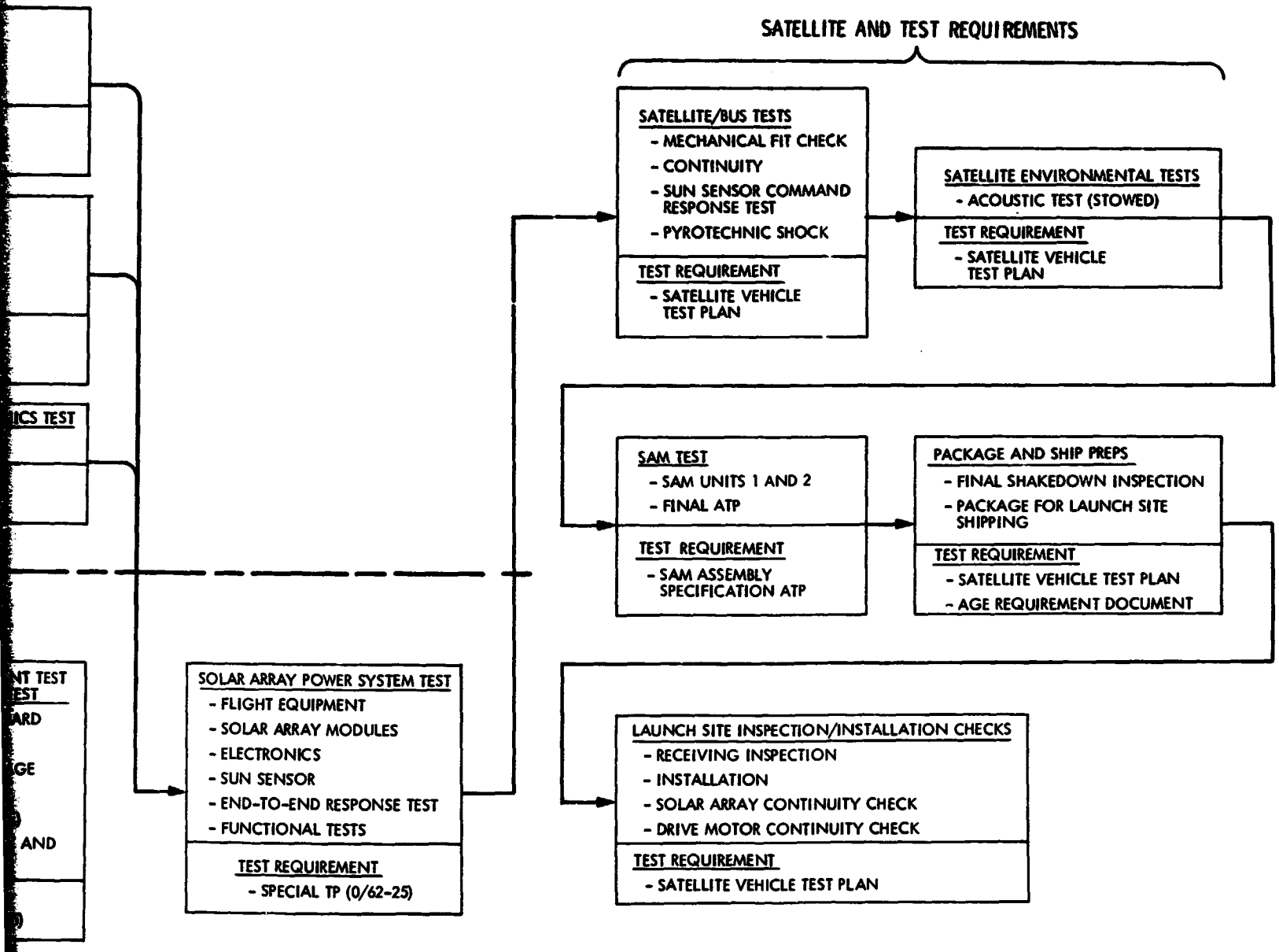

Figure 3-12. Solar Array Power System Development and Acceptance Test Program

FOLDOUT FRAME 3

requiring that the appropriate provisions of NASA document 5300.4(1A), April 1970, be selected by JPL Reliability Assurance for each element of the project and be specifically tailored to costs and risks associated with that element. Particular emphasis was placed on simple, conservative, and test verifiable design, and the appropriate utilization of redundancy. Failure reporting requirements were specified in a comprehensive program established by the "Seasat Failure Reporting Plan," JPL internal document 622-21, November 1977.

The major reliability activities were specified to be the satellite bus and sensor module procurement and the GFE sensors. The reliability requirements for the launch vehicle system were defined and implemented in References 3-1 and 3-2. JPL Reliability Assurance had only minor participation in these areas.

b. Reliability Plans. The satellite bus and sensor module were procured from LMSC. The reliability requirements were defined in "Reliability Assurance Program Plan, Seasat-A Bus and SSE/SM", LMSC document D427899, which was reviewed and approved by JPL Reliability Assurance. The reliability requirements were patterned after the basic LMSC high reliability program activities modified to meet specific Seasat reliability requirements. The plan detailed the requirements for: (1) reliability management and control; (2) failure modes, effects, and criticality analyses (FMECA); (3) design and interface analyses; (4) subcontractor/supplier reliability program; (5) reliable parts program; (6) design reviews; (7) AGE reliability program; (8) test support; (9) Non-Conformance Report (NCR) investigation and analysis; (10) satellite acceptance/readiness review support; (11) maintainability support; and (12) reliability reporting. Each of these major tasks was time-phased to the proper phase of the project schedule. It should be noted that the LMSC failure system, the NCR activity, was under the supervision of LMSC Quality Assurance and the reliability role was that of NCR investigation and analysis.

Reliability requirements for both the in-house and other sensors was imposed on each sensor organization through an individual reliability plan. The project plan specified that a comprehensive reliability plan be generated to meet the unique requirements of each sensor. The basic elements for each sensor reliability program consisted of: (1) worst case design and stress analysis; (2) failure modes, effects, and criticality analysis; (3) design review program; (4) failure reporting system; and (5) parts, materials, and processes control.

c. Review Participation. The Seasat Project had a comprehensive review program, consisting of a definitive series of reviews for the design phase, test phase, and for consent-to-ship and consent-to-launch. The individual reviews were the responsibility of the project element in charge of review activity. All major project reviews had the participation of both the presenting organization's reliability group and JPL Reliability Assurance.

d. Failure Reporting System. The Seasat Project used a systematic method for the identification, analysis, and correction of problems and failures encountered in each of its major hardware and operational system elements. Each major system element had an individual failure reporting procedure that identified its method of control.

Every attempt was made to use each participating organizational element's existing in-house failure reporting procedure and existing forms. No attempt was made to use a standardized failure reporting form. The total failure reporting system was designed for cost effectiveness. The failure reporting procedures of the various organizational elements stressed the following: (1) failure and problems to be identified in a timely manner and communicated to affecting interfacing organizations; (2) causes and effects to be analyzed and understood; (3) appropriate corrective taken; and (4) proper distribution of failure reporting documentation.

Formal failure reporting nominally commenced with the engineering model tests and mandatorily commenced with the start of acceptance tests of flight hardware. All failure reports and NCR listings were routed through the JPL Problem/Failure Report Center for JPL control and distribution, except for LeRC-controlled documentation. Failure reporting existed for flight equipment and associated ground support equipment.

Major system elements covered by the failure reporting system were the launch vehicle (L/V), satellite (Agena bus and sensor module), Spaceflight Tracking and Data Network (STDN), Mission Control and Computing Center (MCCC), and Project Operations Control Center (POCC). The governing procedures for these systems and subsystems were identified as follows:

System	Procedure	Issue/Date
Satellite	Q-400, LMSC Procedures	Issue No. 12
Project operations	JPL internal document 622-42, Seasat-A Space Flight Operations Plan	January 1978
Launch vehicle	LeRC Operating Instruction -19, LVD Procedures for Review and Disposition of Launch Vehicle System Quality and Engineering Problems	18 June 1975
Launch vehicle	GBJ 72-006, General Dynamics Mission Assurance Plan	1 December 1975
MCCC	1864-1, Revision A, MCCC Failure Accountability System (JPL internal document)	1 October 1975
POCC	OCD-2X-032-1, GSFC	12 December 1975
STDN	OCD-2X-032-1, GSFC	12 December 1975
Satellite	IOM, 513-RPS-230, JPL internal document	11 August 1977

Subsystem	Procedure and Issue Date	Problem/Failure Form	Transmittal Agency
SAR	JPL internal document 750-3 1 August 1967	JPL P/FR No. 1846	JPL
SMMR	JPL internal document 750-3 1 August 1967	JPL P/FR No. 1846	JPL
VIRR	SBRC Reliability Plan Itos, RCA 31 January 1974	SBRC 076B	GSFC
SASS	GE Reliability Plan Exhibit 4, S.O.W. 14 July 1975	GE FR	LaRC
ALT	APL/JHU SDO-4047 April 1975	JPL P/FR No. 1846	WFC
SAR data link	APL/JHU SDO-4157 January 1976	JPL P/FR No. 1846	APL
LRA	APL/JHU SDO-4157 January 1976	JPL P/FR No. 1846	APL
Tranet beacon	APL/JHU SDO-4611	JPL P/FR No. 1846	APL
NST	Motorola document 12-P16532A 28 February 1977	Motorola E2034	Motorola

The failure reporting interface between LMSC and JPL was unique. It merged two existing, highly effective institutional systems together without loss of efficiency. The two failure reporting systems were the LMSC NCR system and the JPL problem/failure reporting system. In the NCR system, a methodology existed for writing and processing of the NCR. All NCR information was entered in a LMSC corporate data bank that could be accessed in a flexible manner. JPL Reliability Assurance did not receive copies of the actual NCR in the routine failure reporting process, but obtained weekly transmittals of selected, specific information from the LMSC Corporate Computer Facility. The LMSC NCR was processed by the established NCR procedure and filed in a pedigree package for the appropriate hardware item. It was the JPL cognizant engineer's responsibility to review the pedigree package in real time and at specific review milestones.

Concurrent with this field review, the JPL cognizant engineer received from the JPL Problem/Failure Reporting (P/FR) Center key data about the NCR. It was the JPL cognizant engineer's additional responsibility to inform the JPL center of his concurrence with the LMSC NCR closure and rate the NCR for risk and closure certainty. Key NCR data was also forwarded weekly to LeRC flagging

ascent and shroud problems. In cases when more information was considered necessary by JPL, LMSC furnished the complete NCR package on demand. The JPL P/FR Center logged all data into its master data base and processed weekly status and management reports in a format similar to normal P/FR processing.

The composite system retained all the good features of both systems and created no additional demands on LMSC, resulting in a minimum cost failure report system implementation at LMSC. JPL cognizant engineers did not receive the usual full data package from the P/FR Center, but were informed about the existence and status of each NCR on a weekly basis. The requirement that the JPL engineer actually monitor the activity at the LMSC facility on a periodic basis was a positive reliability factor. The additional JPL reliability program workload was minimal and did not contribute to higher project costs.

The JPL P/FR Center transmitted to LeRC on a weekly basis a copy of the LMSC NCR listing and identified those problems concerned with active hardware associated with the ascent phase as well as interface problems with the launch vehicle. LeRC consulted with JPL on those problems and failures and provided constructive advice.

Each failure reporting center took the appropriate steps to identify the impact on its hardware and issued a failure report to its system as appropriate to make the problem or failure visible. All failure reporting systems processed the failure reports for closure in a normal manner according to their internal procedures.

Failure reports written on GFE flight equipment by the supplier and provider organizations (excluding the L/V system) were sent to the failure reporting center. The JPL control center was responsible for appropriate distribution of failure reports and NCR listings to appropriate JPL personnel and to any other Seasat organization, as appropriate.

JPL Seasat-cognizant personnel reviewed all open failure reports received and distributed by the JPL failure reporting center for adequate understanding of the problem or failure and worked toward an adequate resolution. JPL Seasat-cognizant personnel also reviewed all closed failure reports received by the P/FR Center and identified any residual deficiencies for additional corrective action. In addition to the JPL review of failure reports, WFC personnel reviewed altimeter failure reports, LaRC personnel reviewed all SASS failure reports from GE, and GSFC personnel reviewed all VIRR failure reports. JPL personnel reviewed failure reports on the Tranet beacon, LRA, SAR data link, and NASA standard transponder. A JPL in-house procedure was used for the SMMR and SAR. Project IOM 513-RPS-230 defined the JPL review of the LMSC NCR listings. Project IOM 153-RPS-104 defined JPL problem and failure review of the sensors and GFE. The failure reporting system was monitored by the JPL Seasat reliability representative.

e. Reliability Analysis. The required reliability analyses were performed by the cognizant project element and results reported at the appropriate design review. The analyses were either performed by the design

group and reviewed by the reliability organization or performed by the reliability organization with the support of the design group. Final acceptance was by the analysis organization project management and the pertinent review board.

JPL Reliability Assurance participation in monitoring the project reliability analysis activity ended at launch, with the exception of JPL reliability participation on the JPL anomaly team.

2. Quality Assurance

The quality assurance (QA) plan was developed according to the requirements of NASA document NHB 5300.4 1B. This contractually negotiated plan was the basis by which JPL QA monitored LMSC's quality control effort and efficiency.

a. Description. The QA activities on the Seasat Project were implemented by four separate activities:

(1) The contractor's quality assurance.

(2) The USAF quality assurance.

(3) JPL quality assurance at the contractor.

(4) JPL quality assurance at JPL and in residence at various science experiment suppliers.

The basic plan was that JPL would provide QA engineering and inspection support for selected science subsystems and associated GFE. The contractor would provide the first level of inspection coverage, and the USAF and JPL would share the surveillance of activities. The division of responsibility would be accomplished on a technical basis so that JPL would cover the electronics and the system level assemblies of the sensor module and the USAF would cover the remaining activities.

b. Performance. The general performance of the quality assurance effort was acceptable. There were many detailed problems, some of which will be discussed in subsequent paragraphs. However, when problems were revealed, the contractor and the USAF were responsive. In a general sense, the assembly and test of a single spacecraft in a production environment contributed to confusion and problems.

c. Management. The contractor assigned a full-time quality assurance engineer to the Seasat Project who initially reported to a line manager outside of the program. As a result of a major problem, the organization arrangement was changed so the manager reported directly to the deputy quality assurance manager of LMSC. This reporting arrangement provided effective backing for problem

resolution. The QA engineer obtained his inspection and QA support from the LMSC line organization.

The Air Force Plant Representative's Office (AFPRO) quality assurance was a typical AFPRO organization. That is, a civilian QA manager was assigned and reported directly to the commander.

The JPL quality assurance organization consisted of a resident QA manager supported by a staff of JPL inspectors. The JPL resident QA manager reported directly to the quality project representative/section manager.

The described organizations functioned fairly well with only minor changes as the spacecraft actively transitioned from subsystem to spacecraft assembly and launch.

d. Plan and History. Early in the Seasat program the QA section at JPL reviewed the potential contract to determine the management technique necessary to ensure a quality spacecraft. A pre-award survey was determined necessary to provide sufficient insight into the contractor's system and the USAF overview. The survey was conducted by JPL QA engineering. The survey results revealed that the contractor's system was adequate. However, discussion with the USAF indicated an inability of that organization to supply all of the manpower JPL QA felt necessary for this level of effort. It was therefore decided to divide the surveillance between the USAF and JPL QA.

Additional discussions with the USAF led to a review of the subcontract delegations from previous Agena programs. Agreement was reached with the USAF that where standard Agena hardware was in use, JPL would not change the delegation mode. However, JPL did require that for hardware peculiar to Seasat, JPL would be contacted and an individual assessment would be made concerning source requirements based on the hardware complexity.

3. LMSC Reliability and Qualification

Reliability design techniques were implemented from the beginning to the end of the system design effort. Electronic, electrical, and electro-mechanical circuit stress analyses were performed on all critical new designs and modifications to existing critical designs to ensure proper parts derating consistent with selected parts failure rates. Parts derating criteria were prepared for use in connection with electrical stress analyses and for distribution to the design engineering groups. Throughout the design period, recommendations for incorporation of redundancy were made to the program office and systems engineering when the reliability design analysis, trade-off studies, and associated evaluations indicated such action would result in significant system improvement. The objective of the reliability redundancy analysis of the system was to ensure the proper balance between effectiveness, the schedule, and the available resources.

A parts procurement program was established that took advantage of the existing LMSC high reliability parts program along with the requirement to use

existing parts where appropriate. The parts to be procured fell into two general categories; those for in-house manufactured equipment and those for subcontracted equipment. Existing designs and modified designs required the same specified parts. These were high reliability, 100-percent precap, visually-examined, screened, and burned-in parts. Where monitored line parts were specified on existing drawings, such parts were used if they were in inventory; otherwise, the equivalent LS non-monitored line parts were used.

For newly designed equipment, parts were selected from a preferred parts list (Reference 3-3). The selection, procurement, screening, control, and application were in conformance with specified parts control requirements (Reference 3-4). Substantiating data and technical rationale for the use of non-standard parts were reviewed and approved by program reliability and were made available to JPL for review on request. Preliminary and final engineering parts lists were reviewed and approved by program reliability for compliance with selection requirements. Parts selected were those with substantiated capability as demonstrated by one or more of the following criteria:

(1) Military or NASA qualification on same basic part.

(2) Military or NASA qualification on similar part (one with same design, materials, and construction).

(3) Qualification test by LMSC or other user to military type qualification requirements for same part type or similar part.

(4) Previous evaluation test by LMSC on similar part.

(5) Evaluation tests and configuration analysis by LMSC or subcontractor prior to use.

The parts supplier requirements were:

(1) The supplier must have been qualified for the device type being procured. If not, then qualified for a device of sufficient similarity in terms of design, construction, and processing.

(2) The supplier must have had significant previous successful experience in manufacturing the device type.

(3) The supplier must have an established and permanent testing and screening capability adequate for processing reliable parts.

(4) The supplier system and methods must be capable of approval through LMSC product assurance audits.

(5) The supplier must be listed in the LMSC Directory of Approved Suppliers for LMSC procured parts.

Subcontractors were required to use the same quality of parts as the LMSC-built equipment and program reliability reviewed and approved subcontractor parts

lists and control specifications for compliance with the requirements of LMSC document D427896.

A Program Preferred Parts List was prepared by the program reliability group that required new electronic parts to be qualified to levels commensurate with military specification requirements, and also specified that only qualified electronic and electrical parts would be used in flight hardware. Requirements for qualification for flight type mechanical parts were evaluated on a case-by-case basis, dependent on criticality. Qualification status determination performed by LMSC and its subcontractors used data from valid test sources, such as data from other contractors, GIDEP, and NASA reports and test data. The qualification program consisted of an environmental and life test and a configuration analysis according to LMSC document D427896.

Environmental and life tests generally conformed to normal military type qualification that was based on MIL-STD-202, MIL-STD-750, MIL-STD-883A, and other appropriate military test criteria. Qualification tests were normally conducted by the parts supplier on the initial procurement lot. Parts used in existing equipment were reviewed to determine their qualification status, based in part on prior testing of the parts at the part level, flight usage history of the same type of equipment, or qualification testing performed on the equipment.

Electronic parts used in modified or newly designed flight equipment were subjected to a sequence of non-destructive tests to eliminate non-conforming parts and early failures. The parts were subjected to stresses at levels known to be non-destructive to normal parts, but which would cause measurable characteristic changes in abnormal parts. Rejection of the part was based on specified changes in critical parameters or out-of-tolerance values. The type of screening tests, the parameters to be tested, and the accept and reject limits were specified on the parts procurement drawing. The testing was normally performed by the parts manufacturer and was in accordance with the requirements of LMSC document D427896.

Destructive physical analysis (DPA) was performed on lots of electronic parts designated for flight usage to determine lot acceptability. DPA was performed according to LMSC document D329716.

Traceability and lot control of parts was a firm reliability program requirement. Electronic and electrical parts were identified by the LMSC or subcontractor part number, manufacturer's name or trademark, and a lot-date code. LMSC and their subcontractors also established a traceability system for identifying part locations in the equipments. The system also permitted traceability back to the supplier for each specific lot by a lot-date code.

In-depth analysis was performed on part failures occurring during LMSC or subcontractor manufacturing or post-screening testing. This part failure analysis was integrated into the standardized failure reporting, analysis and corrective action system used for all system hardware. Failures were analyzed by the cognizant parts engineer and the program impact was determined along with appropriate corrective action.

FMECAs were performed on critical modified or new equipment and the satellite system. The effects of significant failure modes were traced to identify their influence on the operation of associated circuits, the effect on proper operation of the equipment, and single system catastrophic failure modes. A list of critical equipment was prepared and maintained throughout the program. Critical equipments were defined as those whose failure significantly affected the ability of the system or subsystem to perform its required function. Reliability FMECAs were used to identify these critical equipments. The list was used as the basic reference for special attention to testing, inspection, source surveillance, failure analysis, handling, and safety. For each item, reliability maintained a file of the special actions taken on failures to ensure timely and proper implementation of corrective action.

E. CHALLENGES AND PROBLEMS

1. Weight

During the initial design phase of the Seasat program the system weight increased rapidly, reducing the performance margin from over 272 kg (600 lb) to half that value in several months. The weight increase was due to several factors. Structure weight, principally of the new sensor module design, increased most. However, the thermal control system, electrical power system, and sensors (including the addition of the Global Positioning System (GPS) sensor), all increased in weight.

An intensive weight reduction and control program was initiated at LMSC and a performance improvement program was considered by GDC, the Atlas contractor. In spite of these programs, the performance margin continued to decrease slowly until in November 1976, after an allowance of 146 kg (322 lb) for contingencies and growth, the margin was near zero.

From that time, a number of factors took effect to alleviate the weight problem. Weight reductions through redesign of several structural elements were realized; a lighter wire (Kapton) was used for all cable harnesses; the GPS sensor was deleted; and, for aerodynamic reasons, the 218-cm (86 in.) diameter GDC nose fairing was replaced by the LMSC 305-cm (120 in.) fairing. The last item provided a 77-kg (169 lb) weight improvement.

As the design progressed and material was fabricated, more accurate weights were obtained and the contingencies could be reduced. Some of the resulting increase in performance margin was allocated to the Atlas as added propellants and to the Agena as excess propellants. Some of the costly weight reduction items were cancelled. The final performance report, based on actual weights, engine tag values, and the closed loop trajectory, predicted 116 kg (255 lb) of remaining Agena propellants at second burn cutoff. Therefore, a substantial payload margin was realized.

2. Thermal Control

LMSC designed the thermal control system for the complete Seasat satellite, including the sensors. Because the mission orbit was near-polar and not sun-synchronous, the sun would appear at any aspect except that for the 120-deg cone subtended by the Earth. Further, sun-eclipsing periods of up to 40 min would be encountered for significant periods of time during orbit life. The thermal control system had to control the sensor and bus equipment temperatures to within relatively narrow limits for almost any sun angle and, in the case of the sensors, whether the high powered radar equipment was operating, in standby, or off.

Most of the sensor equipment had a permissible temperature range of about from 0°C to 35°C when operating and from -20°C to 60°C when not operating. Some of the bus equipments had even closer temperature tolerances. For example, the scanwheels were limited to 15°C to 35°C, the batteries to 1°C to 16°C, and the hydrazine tanks and lines to 4°C to 32°C.

A comprehensive thermal design and analysis effort was conducted directed at achieving the maximum use of passive thermal control techniques. LMSC's thermal analysis computer programs were used to verify the design. Most of the external surfaces of the satellite structure and equipments were thermally protected by thermal control coatings, MLI, or FOSR. In addition, active thermal control in the form of electrical heaters were used for most of the sensors, and for the batteries, GRA, scanwheels, and hydrazine tanks, lines, and catalyst beds. In all cases redundant heaters and thermostats were installed. Thermal control louvers were used for three of the sensors (SASS, SMMR, and SAR electronics).

A full-scale thermal/vacuum test was conducted with the assembled sensor module, SM/SMSS, and all equipments and sensors except the SAR antenna in LMSC's High Vacuum Orbital Simulator (HIVOS). This test, described in detail in Paragraph F7, subjected the SM/SMSS, sensor module, sensors, and equipments to high vacuum thermal cycling, including simulations of various sun directions, Extensive temperature data were obtained that verified the thermal design and analysis, as well as validated the equipment installations when exposed to thermal stress.

3. TSU Piece Part

During the initial vehicle system test phase of the program, a potential piece part problem was revealed. The part was a complementary metal-oxide semiconductor (CMOS) expandable gate array that was also used on two other LMSC programs. Seventy-eight of these devices, 39 in each of 2 Telemetry and Sensor Interface Units (TSUs), were used in the Seasat data system. In July 1977, three devices failed at the circuit card level. In September 1977, one device failed at the assembly level, and in February 1978, two devices failed at the vehicle level.

In February 1978, a failure investigation team was organized headed by the LMSC manager of the Satellite Systems Division (SSD) System Effectiveness.

Actions taken by the team included: (1) dissection and analysis of the failed parts; (2) circuit analyses to determine proper part application; (3) process analyses to ensure proper part fabrication; (4) procedure analyses to ensure proper test, screening, installation, assembly, and protection of the part after assembly at the circuit card, assembly, and vehicle levels; and (5) an analysis of test conditions during each of the failures. In addition, 34 of the devices were subjected to a burn-in test at 120°C.

The failure analysis revealed that the failure was a short circuit between the field plate and substrate of the input gate protection circuit to the device. It was the type of failure that could be caused by a high electrostatic voltage on the input; however, the reason for the failure was not definitely established. It was determined that two of the failures at the circuit card level could have been caused by improper protective grounding when repair of the first failure was made. Also, at the vehicle level, prior to those failures, other circuit cards were removed from both TSUs without proper grounding procedures.

The analyses showed that the part manufacture was correct, the part application was correct, and protection against electrostatic damage was adequate at the assembly and vehicle levels. It was discovered that during burn-in screening of the device, the input gate was not voltage-stressed. That test has since been changed.

A reliability analysis based on the test history of the parts in the TSUs, on the special screening tests, and on the failures experienced showed a failure rate of 1.36×10^{-6} for each gate. Another analysis of the specific application of the devices in the satellite showed that of the over 200 telemetry data points passing through the devices, only 11 were considered critical to the mission and all of these were redundant. Therefore, mission failure would occur only if a limited number of specific pairs of the devices failed. The probability of this happening, considering the duty cycle involved, was calculated to be extremely small.

It was concluded that the installed units would not be changed, the units in accelerated burn-in test would be continuously monitored to vehicle launch, and strict grounding procedures would be adhered to during any additional disconnects, circuit card removals, or modifications to the flight hardware. No additional failures of the CMOS devices occurred prior to flight or during the subsequent mission.

F. SYSTEMS ACCEPTANCE TESTS

The satellite acceptance test program consisted of a comprehensive series of tests at the system level that lead to the final acceptance of the flight satellite system at the launch base.

After the successful completion of the development test program discussed in Paragraph C, the SM/SMSS was integrated with the Agena bus to form the satellite configuration, and the acceptance test program was initiated. However, before the performance of any satellite level tests, the Agena bus underwent a

series of manufacturing tests. These were standard tests that are performed on all Agena vehicles, and consisted of: (1) electrical installation tests; (2) propulsion system leak checks in the high pressure test cell; (3) equipment alignment and fit checks; (4) engine functional tests; (5) hydraulic system tests; (6) hydrazine RCS and OAS functional and leakage checks; and (7) Agena weight and center of gravity determination.

Beginning with the satellite acceptance test program, a detailed audit was performed comparing the satellite vehicle system specification requirements and the actual test data. This data was presented in tabular form (Reference 3-5). The data recorded in this document was evaluated for minimum values as well as trend analysis. A sample page from this document is shown in Table 3-1.

1. Satellite Subsystem and Sensor Integration Tests

a. Objective. With the addition of the Agena bus to the SM/SMSS to form the satellite system, the power and data subsystem tests associated with the Agena were performed to verify interface compatibility and functional performance. Subsequent to demonstrating proper satellite power and data subsystem performance, detailed performance evaluation tests were made on the ascent attitude control subsystem, orbital attitude control subsystem, and attitude determination subsystem, followed by a functional test of each sensor to verify compatibility and performance in the satellite configuration.

b. Configuration. The test configuration is shown in Figure 3-13. The SM/SMSS and Agena were aligned horizontally and joined temporarily to ensure proper fit, then were disconnected. During test the bus and SMSS were electrically interconnected with the flight harness assemblies and mechanical connections were made with bonding straps to avoid mechanical stress on the interface caused by structure flexure while in the horizontal position. The SM/SMSS was positioned with the SAR antenna on top and the SASS on the bottom. This permitted the Agena to be positioned with the hydraulic assembly down to avoid the effects of oil leakage and with the velocity meter positioned to provide a 1-g acceleration signal. Simulated horizon error targets were located on the scanwheel and horizon sensor assemblies. The sensors operated into either or both RF loads and target simulators with cable connections to their GFE support equipment. Satellite control and monitoring through the satellite data subsystem was effected by a coaxial cable connection to the systems test data van located outside the systems test complex. This was a standard configuration for all satellite system testing performed in the horizontal position in the systems test complex.

c. Results. The attitude determination and control system testing consisted of 3 different series of tests. However, evaluations were made to determine the influence, if any, of one area upon another. The three areas were the ascent attitude control subsystem elements, orbital attitude control

Table 3-1. Factory System Test Compliance Data

Spec Para		Test Plan Para (Bus)	Test Procedure		Test	Monitor Point	Requirements			Test Results			
3.X	4.X/5.X		#	Para			Min	Max	Unit	Base-line	Pre-T/V	Post T/V	Final
3.1.5.5	4.4.5.5	NR	NR	NR	Orbit EPS	-	-	-	-	-	-	-	-
3.1.5.5.1	4.4.5.5.1	3.4.7.3	Per drawing 124 1 of 2		Electrical power shall be provided by two type 40 batteries	-	As stated left			-	-	-	-
					Electrical power shall be provided by two single-axis tracking solar arays	-	As stated left			-	-	-	-
			S48058		Main bus, high voltage	LC101	29.8	32.0	Volt	31.09[a]	28.79[c]	30.08	30.15
					Main bus, low voltage	LC101	24.5	26.2	Volt	25.26	25.06	25.33	25.47
					Main bus current, typical orbit	LC104	NA	50	Amp	35.3[a] / 22.5	NA	NA	35.0[b] / 20.6
					Main bus current, SAR operate	LC104	NA	82	Amp	58.8[a] / 46.0	NA	NA	48.8[b] / 39.2
					Structure current	LC105	NA	1.0	Amp	1.0	0.2	0.00	0.40
			S48047	5.2.8	Main bus resistance	J100-26-1G	0.28	NA	Ohm	17	NA	NA	NA
			S48060	5.7.35	Main bus noise	C4P4	NA	0.5	VP-P	0.240	NA	NA	NA
			S48058	All	VIRR and SMMR regulated No. 2	LC115	-24.9	-24.2	Volt	-24.62	-24.62	-24.52	-24.67
			S48047	5.10.61	VIRR and SMMR regulated No. 1	LC114	-24.9	-24.2	Volt	-24.57	-24.57	-24.62	-24.57
			S48058	All	VIRR unregulated power No. 2	LC116	-28.0	-26.0	Volt	-26.75	-27.00	-26.87	-27.00
			S48047	5.10.27	VIRR unregulated power No. 1	LC116	-28.0	-26.0	Volt	-26.71	-26.95	-26.95	-26.95
			S48058	All	SASS regulated No. 3	LC117	28.0	28.6	Volt	28.32	28.32	28.32	28.32
			S48058	5.4	SASS regulated No. 4	LC117	28.0	28.6	Volt	28.32	28.32	28.32	28.32

[a]Voltage went to 32.24 V dc during 200-225 ms auto shutdown caused by test operator error increasing voltage.
[b]High/low current value with SASS pulses.
[c]Voltage incorrectly set low to avoid the auto shutdown occurrence of footnote a. (Not a vehicle performance anomaly.)

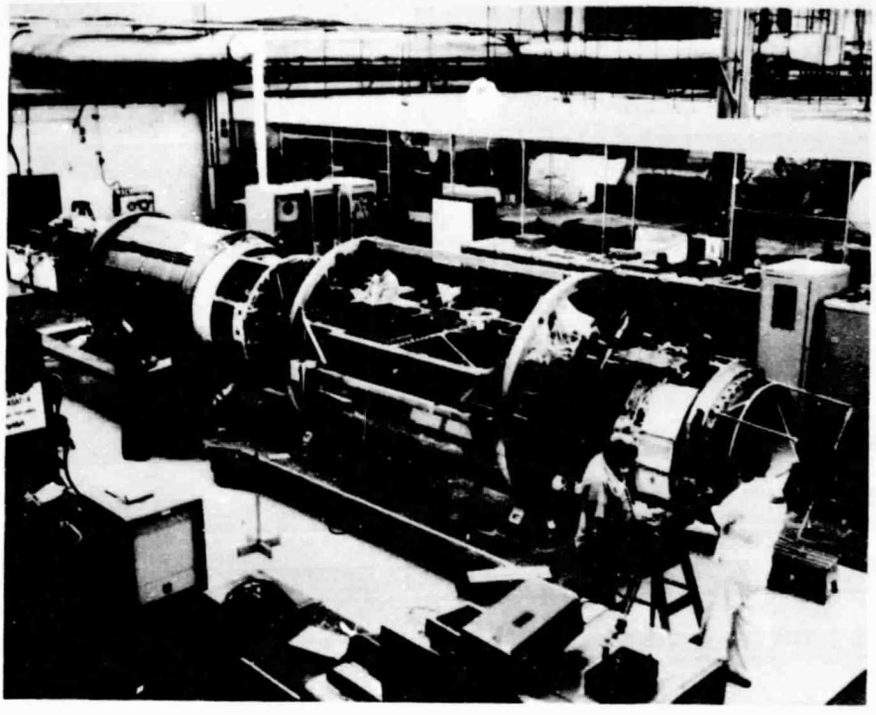

Figure 3-13. Satellite Systems Test Configuration in the Systems Test Complex (TS-5)

subsystem elements, and attitude determination subsystem elements. A summary of the ascent attitude control subsystem tests follows:

(1) Gyro Reference Assembly (GRA) drift and Spin Motor Revolution Detector (SMRD) checks.

(2) Horizon Sensor Assembly (HSA) polarity, rate gains, and gyro compassing loop checks.

(3) Scanwheel Assembly (SWA) polarity, rate gains, and gyro compassing loop checks.

(4) Reaction Control System (RCS) polarity, static gains, and rate gain loop checks.

(5) Velocity Meter (V/M) scale factor checks.

(6) Hydraulic system null and stability checks.

(7) Hydraulic system static gain and range checks.

(8) Hydraulic system step response test.

There were no major anomalies noted during this series of tests.

During the subsystem testing of the OACS in the vehicle, it was necessary to perform special open-loop response tests to obtain additional data to resolve testing discrepancies. These tests consisted of step response attitude error tests and recording scanwheel and magnet responses on an analog recorder. The responses were compared to digital simulations performed during the development testing. Problems were experienced because the scanwheel targets did not provide a stable attitude error signal over a sufficient period of time to make the necessary comparisons. A breakout box was used to assist in the injection of attitude error signals from a dc power supply downstream from the scanwheel bolometers to obtain the required responses. Identical comparisons were achieved with the OACS development test results. The scanwheel targets were subsequently reinstalled and end-to-end polarity checks and quantitative gain checks were satisfactorily conducted.

A summary of the orbital attitude control subsystem tests follows:

(1) Pitch momentum wheel, roll reaction wheel, and scanwheel attitude output polarity, null, saturation, and response checks.

(2) Speed bias adjust checks.

(3) Magnet intensity and response test.

(4) Magnetometer magnetic field polarity and response checks.

(5) Reaction control system backup mode response checks.

(6) Scanwheel backup mode response checks.

(7) Magnetic trim bias checks.

(8) Magnetic desaturation wheel speed feedback gain adjust checks.

The attitude determination subsystem tests consisted of verifying the output signal levels of the four solar aspect sensor heads to illumination energy within their respective fields-of-view.

Following the attitude determination and control system tests, a repeat test of the sensor compatibility test sequence described in Paragraph C4 was performed. This demonstrated compatibility between the SM/SMSS equipments when in a complete satellite configuration. After the post-test data analysis resulting from this in-depth subsystem testing, the satellite was ready for a pre-environmental baseline systems test.

2. Baseline Systems Test

a. Objective. An integrated system test was performed that demonstrated the total system compatibility between the SM/SMSS and the Agena bus and the readiness of the satellite for subsequent environmental testing. This test verified the functional performance of the system that would occur during a normal simulated flight.

b. Configuration. The satellite configuration was not changed from the previous subsystem testing.

c. Results. Testing sequences were performed that simulated actual ascent and orbit operations, but times were shortened and unusual (non-flight) sequences were used when necessary to verify the satellite design. All system elements were exercised and all redundant circuits were selected and operated, except for restricted deployments. Telemetry status monitors were the prime source for data analysis and formed a baseline for post-environmental data correlation. Systems operational characteristics were analyzed at both low and high voltage levels. No significant anomalies resulted from this major systems test.

3. Electromagnetic Interference Test

a. Objective. It was recognized early in the program that electromagnetic interference (EMI) between sensors and between sensors and the satellite equipment was a major concern. Therefore, a program was established to ensure system compatibility by control of interference emission and susceptibility at the equipment and subsystem levels and verification by performance of satellite system-level EMI and radio frequency interference (RFI) tests.

The EMI test consisted of transient and steady-state measurements of emissions and susceptibility in a test sequence that simulated launch orbit injection and orbit operations. The EMI test criteria were as follows:

Conducted Transient Emission (Ascent and Orbit). During the simulated satellite vehicle ascent and orbit sequence of events, the maximum allowable transient peak amplitude level for transients with rise times greater than 1 μs and durations from 1 μs to 50 μs had to be 12 volts above or below the nominal DC value. Transients with durations greater than 50 μs but less than 6 μs could not exceed 3 volts above or below nominal DC voltage.

Conducted Emissions (Ascent). While the satellite was operating in a steady-state condition typical of ascent, narrowband noise at selected critical test points had to be no higher than the following:

30 Hz to 10 kHz	0.6 V rms or 1.7 V p-p
10 kHz to 100 kHz	1.58 dB/decade roll-off to 0.5 V rms
100 kHz to 400 kHz	0.5 V rms or 1.4 V p-p

Ripple (Ascent). The total composite unregulated power bus ripple noise, consisting of frequency components between 30 Hz and 1 MHz had to be less than 500 mV p-p.

Conducted Emissions (Orbit). While the satellite vehicle was operating in a steady-state condition typical of orbit operation, narrowband noise at selected critical test points had to be no higher than 0.19 V rms or 0.5 V p-p in the range of 30 Hz to 400 MHz.

Ripple (Orbit). The total composite unregulated power bus ripple noise, consisting of frequency components between 3 Hz and 1 MHz had to be less than 500 mV p-p.

Radiated Susceptibility (Ascent). During the simulated satellite vehicle ascent sequence, when simulated booster and bus telemetry downlink RF irradiation of the bus was being performed, telemetry data was processed and analyzed in real time and post-test to verify that no malfunctions had occurred.

Radiated Susceptibility (Orbit). During simulated satellite vehicle orbit operation, when simulated SAR, ALT, and SASS RF irradiation of the bus was being performed, telemetry data was processed and analyzed in real time and post-test to verify that no malfunctions had occurred.

b. Configuration. The satellite vehicle system and test complex configuration for the EMI test was the same as for the baseline systems test, except that 3 special EMI breakout harnesses were installed at three critical test points.

c. Results. The same test sequences performed during the baseline systems test were repeated for the EMI test except that clock holds were added to provide time for real-time analysis and documentation. All transient and steady-state emissions were within acceptable limits. No degradation in systems performance was observed in real-time or post-test analysis because of radiation from CW RF signals simulating the Atlas booster signal and the calculated back lobe energy of the ALT, SASS, and SAR.

4. Radio Frequency Interference Test

a. Objective. As identified in the previous paragraph, RFI analysis was begun early in the program and the verification of corrective actions and design requirements was demonstrated by performance of a system-level RFI test. The test verified the following operational requirements with only the first considered to be mandatory:

(1) That the satellite system, including the NASA Standard Transponder (NST) and the Tranet beacon, operated successfully with any one sensor operating individually.

(2) That the satellite system, including the NST and beacon, operated satisfactorily with any two or more sensors operating at the same time.

(3) That the satellite system, including the NST and beacon, operated satisfactorily with all of the sensors operating simultaneously.

(4) That the satellite system and the sensors operated simultaneously without mutual interference, or if interference existed, sensor operational constraints could be identified.

b. Configuration. The RFI test was performed in the anechoic chamber located in building 104. The SM/SMSS was installed in the vertical position with all antennas except the SAR antenna deployed as shown in Figure 3-14. Substituting for the SAR antenna was a standard gain horn positioned where the center of the SAR antenna array would have been and pointing at the same angle that the SAR flight antenna would be when in orbit. A 10-dB RF attentuator was placed between the SAR transmitter and the SAR substitution antenna. The SAR test antenna, four SASS antennas, two telemetry downlink antennas, and the Tranet beacon antenna were all supported by wooden stands. Immediately above the ALT, a 2.44-m (8 ft) diameter wooden disc was suspended with RF absorbent material attached to the surface to prevent RF energy reflection from the crane support structure located in the chamber ceiling. A non-metallic 30-cm (12 in.) diameter plastic air duct was used to direct air on the SAR electronics unit and the SAR downlink transmitter.

Located in a corner of the anechoic chamber were two standard gain horn test antennas positioned approximately the same height above the floor as the two vehicle telemetry downlink antennas and the one vehicle SAR data link antenna. The SAR data link test antenna was connected to SSE equipment located outside the chamber by a 34-m (112 ft) coaxial cable. The telemetry data link test antenna was connected to the data van by a 29-m (95 ft) coaxial cable. All power wires and cables to the SMSS were placed on the floor of the anechoic chamber beneath RF absorbent material.

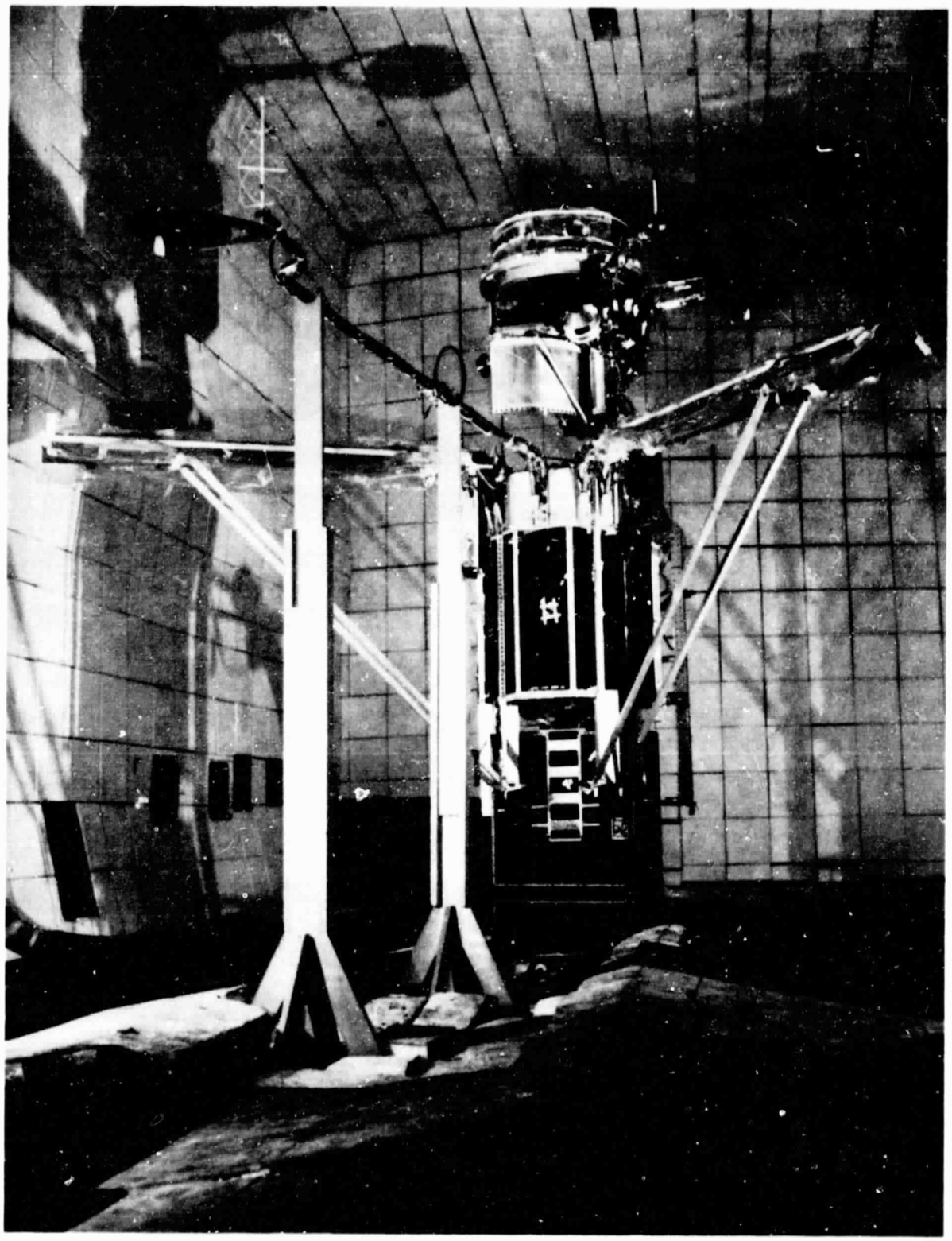

Figure 3-14. SM/SMSS RFI Test Configuration

c. Results. The sequence of satellite system and sensor operations during the test procedure was carefully planned to subject each element to combinations of other radiators as stimuli, permitting the thorough investigation of performance in the presence of one or more radiators at the same time. Figure 3-15 shows the sequence used in performing the RFI test.

The results from real-time and post-test data analyses of the RFI test show no significant interference among sensors or the satellite system. All test requirements were met. The results of the test demonstrated that the satellite system and the sensors could operate simultaneously with no interference. During the RFI test, it was observed that a sideband of the telemeter downlink at about 2275 MHz was present in the passband of the SAR data link Multi-Function Receiver (MFR), a part of the ground system. Subsequent analysis showed that the telemeter signal was 12 to 15 dB below the SAR echo signal and would not affect the SAR image processing.

5. Acoustic Environmental Systems Test

a. Objective. Acoustic environmental testing has been instrumental in detecting latent material and workmanship defects when exposed to a simulated launch dynamic environment. The primary objectives of the acoustic environmental test were to:

(1) Verify that the vehicle could perform as an end-to-end system during an ascent acoustic flight environment.

(2) Verify the random vibration test specifications used in testing of individual experiments and equipment and to verify the zone test specifications.

(3) Use the low-level acoustic test vibration data as a basis for modification of the full-level acoustic test so that flight equipment was not tested beyond its tested capability.

(4) Demonstrate individual equipment and experiments for the flight acoustic exposure.

(5) Provide a basis for development of random vibrations specifications for future similar vehicles.

(6) Complete the qualification certificates on several equipment items, including the solar array, sun sensor, and scanwheel.

(7) Obtain a "data baseline" of each sensor that could be used at the launch base to determine launch readiness.

b. Configuration. The Seasat vehicle acoustic test configuration was as near the flight configuration as possible with the exception of propellants in the tank section, which was empty and pressurized to ground handling pressure

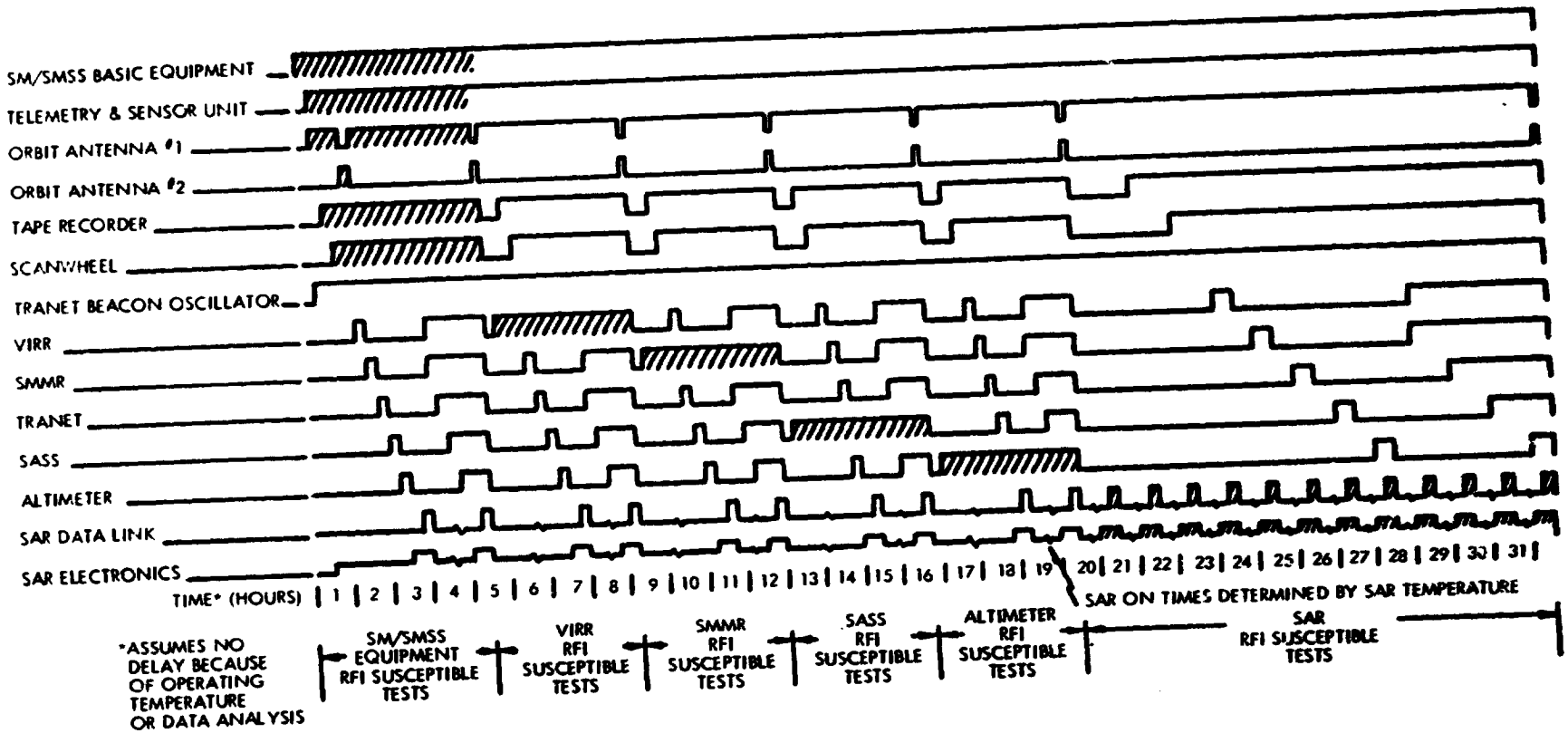

Figure 3-15. Sensor RFI Compatibility Test Sequence

levels. A non-flight Agena-to-Atlas adapter section was used to interface with the Maximum Access Booster Adapter (MABA) and the fairing aft section and to support the satellite system in the acoustic chamber. This adapter section was bolted to the chamber floor to provide stability. Figure 3-16 shows the buildup of the satellite in the acoustic test facility and Figure 3-17 depicts the final test configuration.

Instrumentation for the acoustic test consisted of 4 external and 6 internal microphones and 115 Endevco 2220 single-axis accelerometers.

c. Results. Subsequent to the buildup of the satellite in the acoustic test facility, a pre-environmental function test was performed to verify the satellite-to-Aerospace Ground Equipment (AGE) hookup and final test preparations. Included in this functional test was a series of tests that would also be performed at the launch base to ensure launch readiness. These tests provided a "data baseline" of each sensor for pre-launch status checks and established a method of verifying the solar array final electrical connections at the launch base. Before the application of the acoustic environment, the satellite equipments were conditioned to the launch configuration. The VIRR scan motor was energized, tape recorder 1 was reading-in, the SWA and horizon sensors were energized, and the command memories were loaded with the test ascent sequence of events.

During the acoustic testing, verifications were made that ensured no satellite equipments had changed configuration. Subsequent to the acoustic testing, performance verification tests were made, while still in the test chamber, that demonstrated satellite ascent performance along with sensor status checks.

Figure 3-18 compares the resultant acoustic levels with the required test levels. The final externally-applied field overall was 148.7 dB compared to the required external-flight overall of 148.7 dB. The externally-applied spectrum shape was maintained between the tolerance levels except for several frequency bands in the low frequencies where it was necessary to notch slightly below the minus tolerance to produce a flight-level internal acoustic field and prevent equipment overexposure.

The internal acoustic field was also maintained within the tolerance of ±2 dB with an overall level of 138.9 dB compared to the test goat of 140 dB. Comparison of previous flight and chamber data indicated that the shroud attenuation was nearly identical for chamber tests and flight fields in the high frequencies above 400 Hz.

As a result of the acoustic environmental test, two components (SED timer and destruct/discrete junction box) were exposed to acoustic levels greater than the component qualification specification. Although the SED timer survived the test and functioned properly after the test was completed, the installation was modified to improve its response characteristics and to prevent possible overexposure during flight. A tap test of the structure was performed before and after the modification to measure the structural frequency and damping

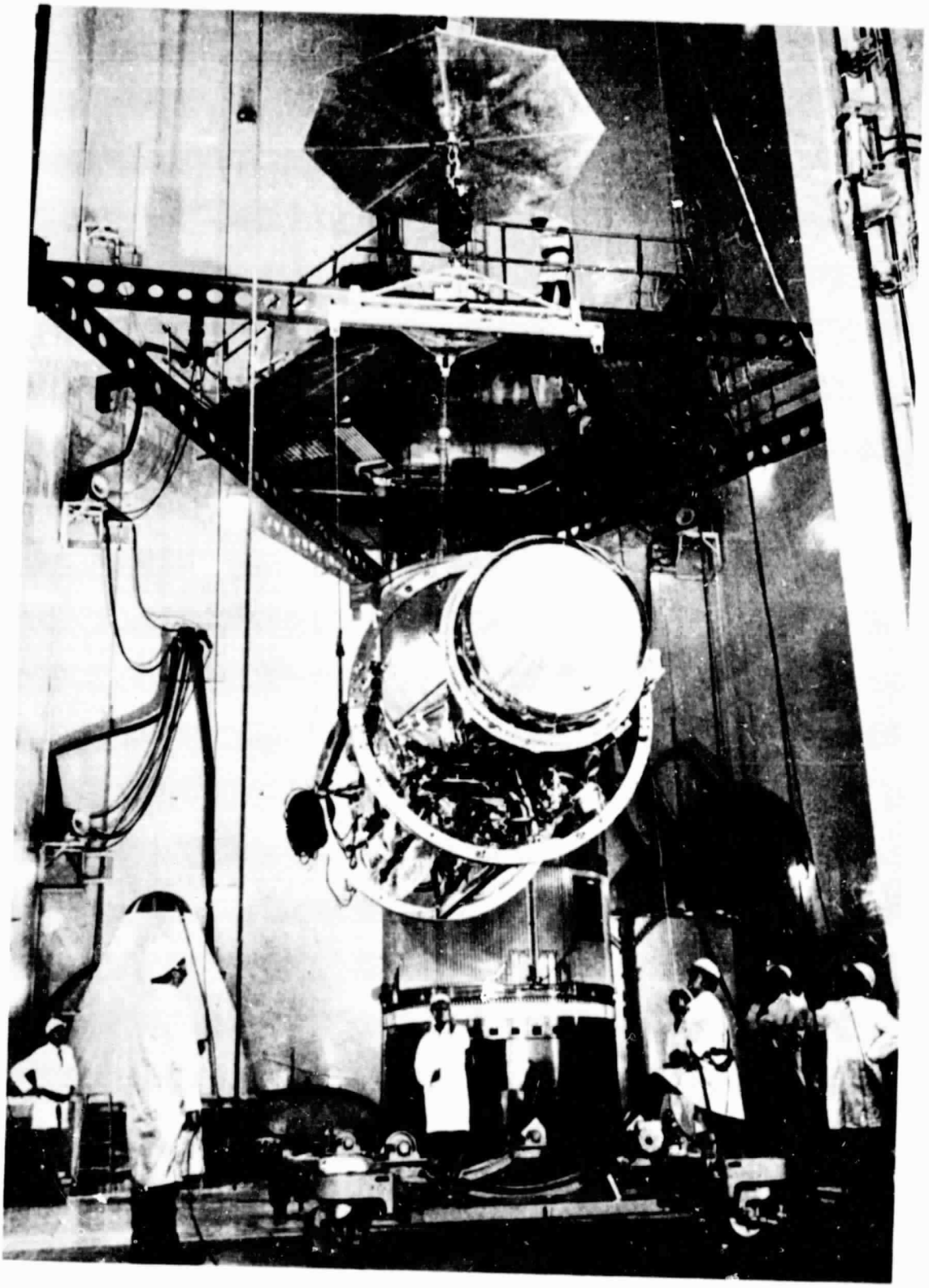

Figure 3-16. Satellite Buildup in the Acoustic Test Facility

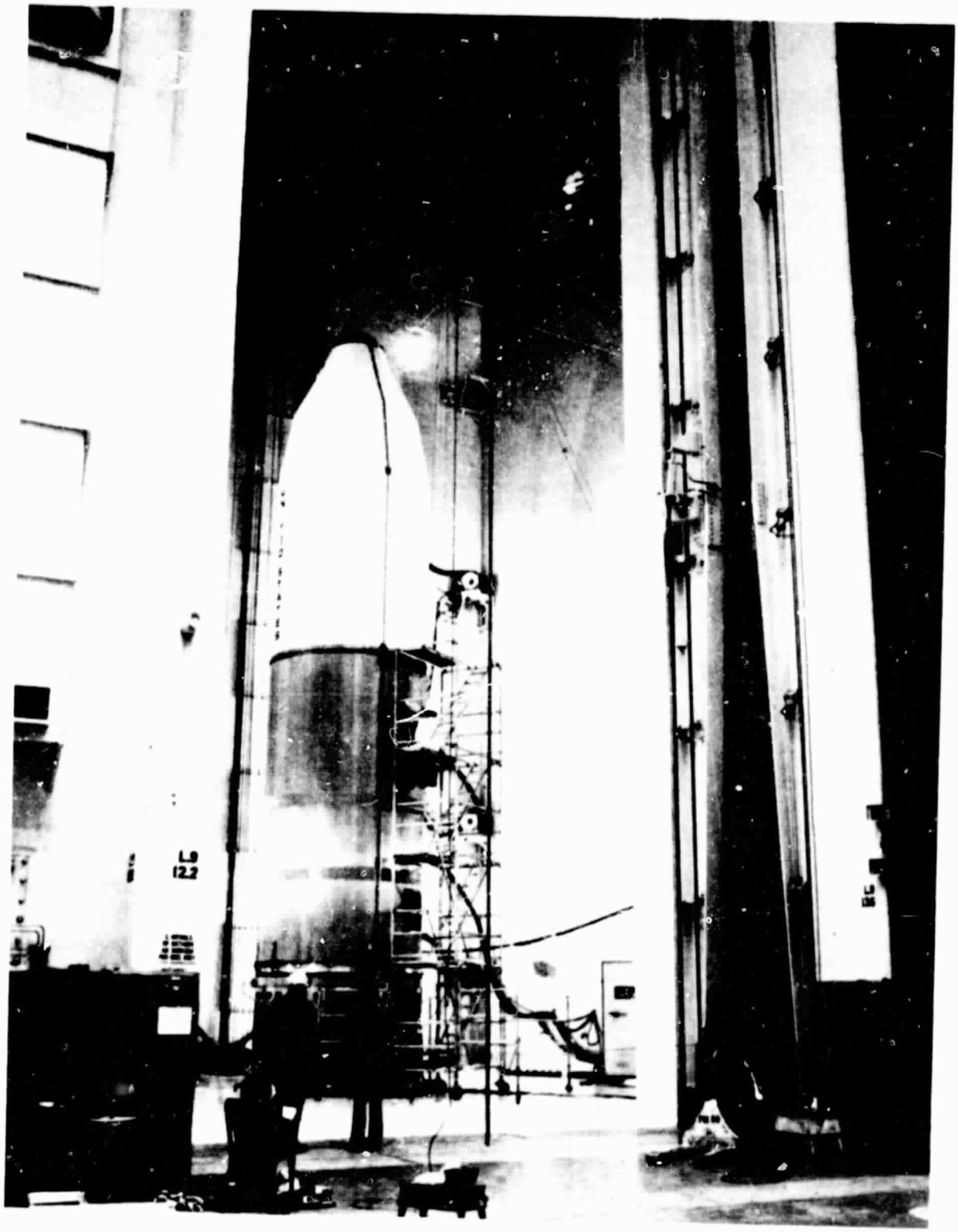

Figure 3-17. Acoustic Test Configuration

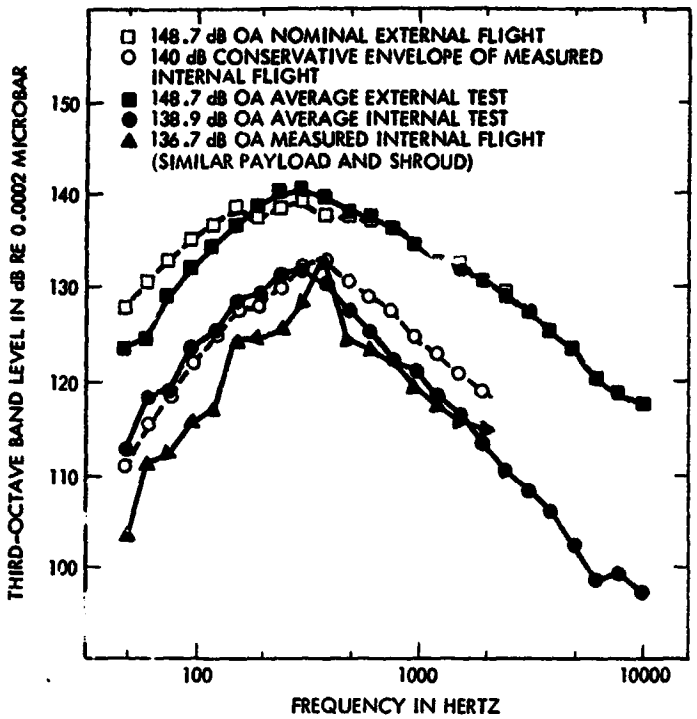

Figure 3-18. Comparison of Acoustic Test Levels with Requirements

characteristics. A prototype destruct/discrete junction box was retested at the higher vibration levels with internal relays monitored for chatter and transfer during the test. Functional performance tests were performed before and after the vibration tests and no anomalies were noted. The acoustic test demonstrated that the Seasat vehicle could survive the flight acoustics and random environments.

6. Satellite to STDN/POCC Compatibility Tests

a. Objective. Compatibility tests were performed to ensure that the STDN tracking, telemetry, and command parameters, as well as equipment configuration and operational procedures, could adequately satisfy the intended mission requirements. In addition, satellite performance data and magnetic tape recordings from these tests were used to prepare the network for operational support of the satellite.

The specific objectives of the STDN compatibility tests were to:

(1) Determine satellite-to-STDN tracking, telemetry, and command interface compatibility.

(2) Ensure compliance with certain aspects of the Aerospace Data Systems Standards (Reference 3-6).

(3) Verify support equipment configuration parameters.

(4) Provide the STDN with advance experience with the satellite under controlled conditions.

(5) Produce magnetic tapes, stripchart recordings, and other data, as applicable, suitable for verifying that the STDN outputs satisfied support requirements.

(6) Obtain data on satellite performance and characteristics applicable to signal margin studies and to the mission support by the STDN.

In addition to the STDN compatibility test, a satellite-to-Project Operations Control Center (POCC) compatibility test was performed to demonstrate the compatibility of the satellite with the ground data system that had been developed to support Seasat mission operations. The primary objective of this test was to verify the capability to operate and control the satellite from the POCC and to validate data flow through the end-to-end data system. This test followed the successful completion of the satellite-to-STDN compatibility tests.

b. Configuration. The satellite, as tested, had two redundant NASA standard S-band transponders, command demodulator units, command processor and central timing units, and telemetry sensor units. The redundant transponders had a receive frequency of 2106.4 MHz and a transmit frequency of 2287.5 MHz. The transponders used phase modulation, and were phase-lock or coherent type units; however, the systems were capable of operating in a non-coherent (internal VCXO) mode. Normal STDN ranging excludes non-coherent tracking.

The telemetry downlink system was composed of a 1.6 MHz PSK subcarrier, biphased-modulated by a real-time 25 kb/s split-phase PCM data stream and always present on the downlink carrier. In addition, either a 800-kb/s split-phase PCM data stream or "turned around" tone ranging signal (coherent from the uplink) could accompany the real-time data on the downlink carrier. If the ranging channel was enabled, uplink command modulation was turned around and modulated on the downlink carrier. The 800-kb/s PCM data was tape recorder playback data (reversed real time x 32). The real-time data, together with either the tape recorder playback or tone ranging signals, were combined into a composite signal that modulated either selected transmitter.

The uplink system was capable of receiving NRZ-PCM/FSK/AM command signals and tone ranging signals as required, both phase-modulated on the uplink carrier. Both receivers incorporated a command demodulator unit and were powered on, permitting the addressing of either command processor and central timing unit.

It should be noted that the SMMR was not installed for this test because of its removal for investigation of 2 suspect diodes and a suspect scanner drive belt.

c. Results. The satellite demonstrated compatibility with the STDN in the parameters tested. Various parameters normally validated during testing that should have been established to assist the STDN were not validated because of the non-availability of STDN equipments, the software configuration, software limitations, and satellite test time. These parameters were:

(1) PCM clock phase jitter.

(2) Telemetry transmitter transients.

(3) PCM frame sync pattern error analysis.

(4) Command response to false address.

(5) SRE operations using 100-kHz major range tone.

(6) Transponder acquisition threshold.

(7) Transponder tracking rate.

Reference 3-6 was used for the Seasat tests, of which 19 different detailed tests were performed that analyzed the 14 different modes of the satellite system. The satellite-to-STDN compatibility test anomalies were as follows:

(1) Spectrum photographs of the received downlink telemetry signal indicated spurious baseband harmonics of 25 kHz. Of concern was whether or not the ±100 kHz spurs that were 32 dB below the modulated carrier would interfere with the 100-kHz range signal when it was used as a major tone for coarse range measurements.

(2) Turned around noise severely degraded the tape recorder dump rate when the ranging channel was enabled with no range tones present on the uplink. Tape recorder dump plus ranging was not a Seasat operational mode.

(3) Uplink command operations indicated that the satellite was sensitive to over-modulation. For modulation indices exceeding 1.2 peak radians, commanding was not accomplished from the compatibility test van.

(4) Uplink signal acquisition occurred at sweep rates below 30 kHz/s over a frequency range tested at ±100 kHz of the specified frequency. Seasat acquisition was specified to occur over a frequency range of ±120 kHz of the specified frequency at a maximum 30-kHz/s sweep rate.

The satellite-to-POCC compatibility test demonstrated the capability to perform clock adjustments, exercised the real-time "wake-up" mode of the transponders, performed tape recorder data recording and dump sequences with data overlap, and the satellite memory load and dump sequence. Also included was a demonstration of the POCC ability to process the satellite block telemetry,

which consisted of orbit normal, ascent, orbit adjust, memory dump, SAR engineering, VIRR, SASS, and ALT blocks. (The SMMR data block was not available.) There were no reported anomalies from this test.

7. Thermal/Vacuum Environmental Systems Test

a. Objective. Following completion of the POCC compatibility test and the reinstallation of the SMMR sensor, the SM/SMSS was prepared for the thermal/vacuum environmental systems test while the Agena bus started the post-acoustic environmental test high pressure test cell tests, the SAR antenna underwent a deployment test, and the solar arrays received a deployment and functional test. Also, after the acoustic test, all deployment mechanisms were exercised to verify no galling or damage had occurred as a result of the environmental exposure.

The objectives of the thermal/vacuum environmental test were to:

(1) Ensure satisfactory performance of the SM/SMSS under thermal/vacuum conditions representative of those encountered in flight.

(2) Verify the thermal analysis math model.

(3) Detect latent material and workmanship defects that might not be detected in other test environments.

(4) Demonstrate that individual components and sensors would operate successfully at the systems level when exposed to simulated orbit and acceptance thermal/vacuum test conditions.

(5) Provide telemetry data to the POCC for SPAT training and familiarization with satellite responses to dynamic environments.

b. Configuration. The thermal/vacuum test configuration consisted of the SM/SMSS in a flight configuration, except that the SAR antenna, Tranet beacon, and 4 SASS antennas were not installed. Figures 3-19 and 3-20 show the test configuration on the HIVOS door and the heat flux array used to control the thermal environment.

The SMMR had an active stimulator over the cold horns and a passive stimulator over the main feed. The cold horn stimulator required a LN2 source, electrical power, and temperature monitoring and control.

The VIRR was provided a clear view of the chamber cold wall as a target source. Instrumentation for the test included 170 copper-constantan thermocouples and 20 colorimeters strategically located on the SM/SMSS. Three nude ionization gauge tubes were mounted on the heat flux array in close proximity to the altimeter signal processor, SAR electronics, and SASS electronics. These 3 gauges provided instantaneous pressure variations near the electronic flight hardware.

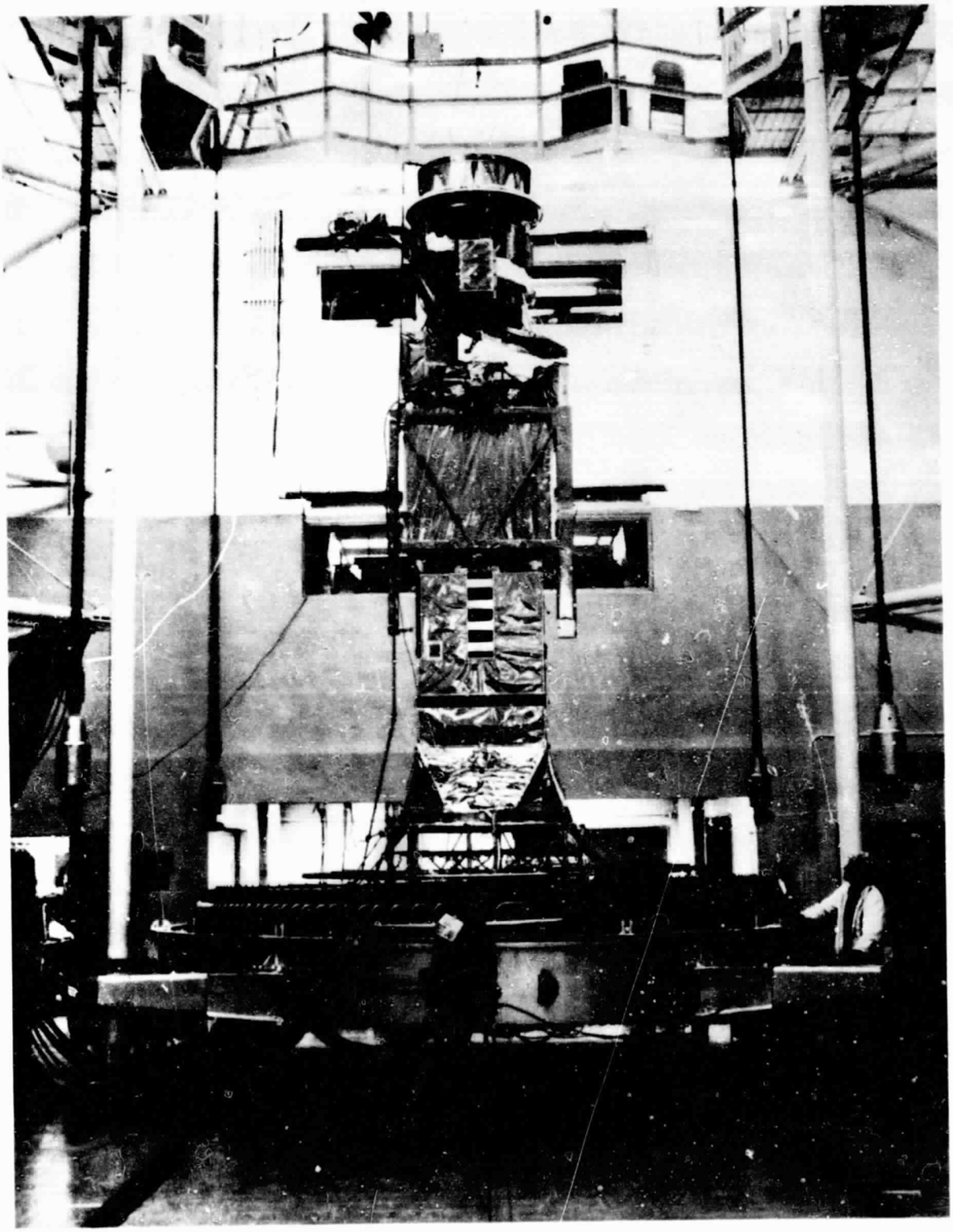

Figure 3-19. SM/SMSS Thermal/Vacuum Test Configuration

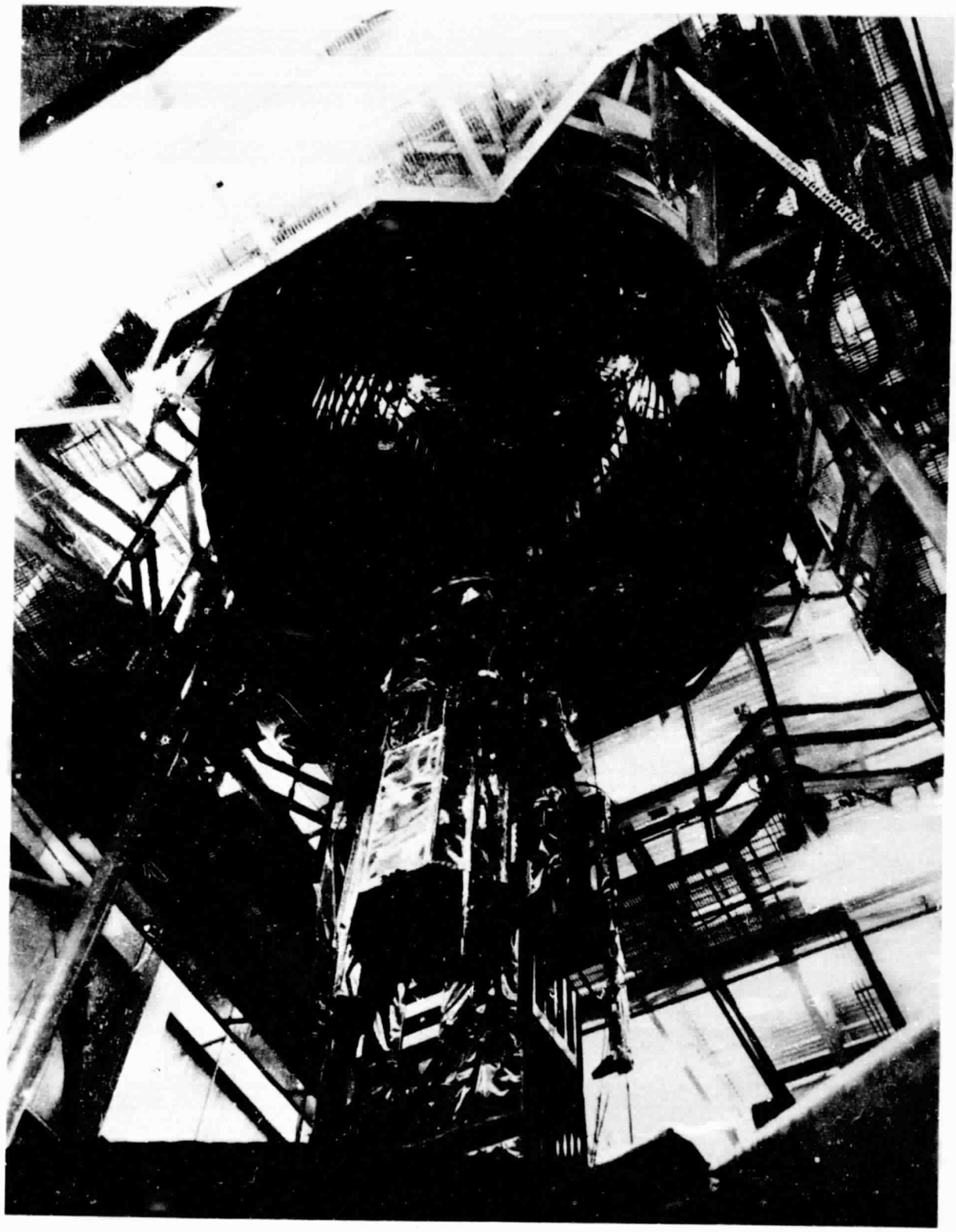

Figure 3-20. SM/SMSS and HIVOS Heat Flux Array

The heat flux array simulation was provided by 38 zones of quartz tubular lamps and 5 heater zones, all powered by variable transformers. The chamber was monitored for contamination throughout the test using a partial pressure analyzer and three aluminum foil witness plates. No significant amount of contamination was detected.

c. Results. The thermal/vacuum environmental systems test was the most comprehensive and detailed performance evaluation test of the on-orbit configuration performed during the Seasat program. A pre-environmental functional test was performed to verify test configuration, electrical hookups, and to obtain a data baseline for post-environment evaluation. Three thermal/vacuum cycles were performed as shown in Figure 3-21. There were four temperature cycles (acceptance tests) and four flux levels (thermal verification) during these three cycles. The extensive use of primary, redundant, and backup equipments along with the sensor operation is shown in Figure 3-22. The VIRR, SASS, and SMMR were operated continuously after initial turn-on just before cold test 1 until after hot functional test 3.

During the performance of the thermal/vacuum test, extensive thermal data were obtained that were subsequently used to verify the thermal math model of the satellite. No major changes were required to the model as a result of this data. Also, during the thermal/vacuum test, satellite telemetry data were transmitted to the POCC through NASCOM for training of the SPAT at GSFC. This data was used to verify display formats, certify software programs, and provide additional familiarization into the satellite's operational characteristics.

The only major anomaly observed during the performance of the thermal/vacuum test was associated with the SAR data link. During hot turn-on test 1 of the SAR data link, the pilot tone was down 23 dB from nominal. Subsequent to the thermal/vacuum test, the data link was removed and returned to the vendor for repair. The thermal/vacuum test at the system level was not repeated after return of the SAR data link. However, the SAR data link was subjected to a thermal/vacuum cycle at the vendor after repair.

8. Final Simulated Flight Test

a. Objective. Following the successful completion of the thermal/vacuum test, the SM/SMSS was returned to the systems test complex and was connected to the Agena bus for the final simulated flight test. The primary objective of this test was to demonstrate flight readiness of the satellite system following environmental exposure. Performance characteristics and results were compared with the data from the baseline system test to determine degradation.

b. Configuration. The satellite system configuration for this major test was the same as for the baseline systems test described in Paragraph 2.

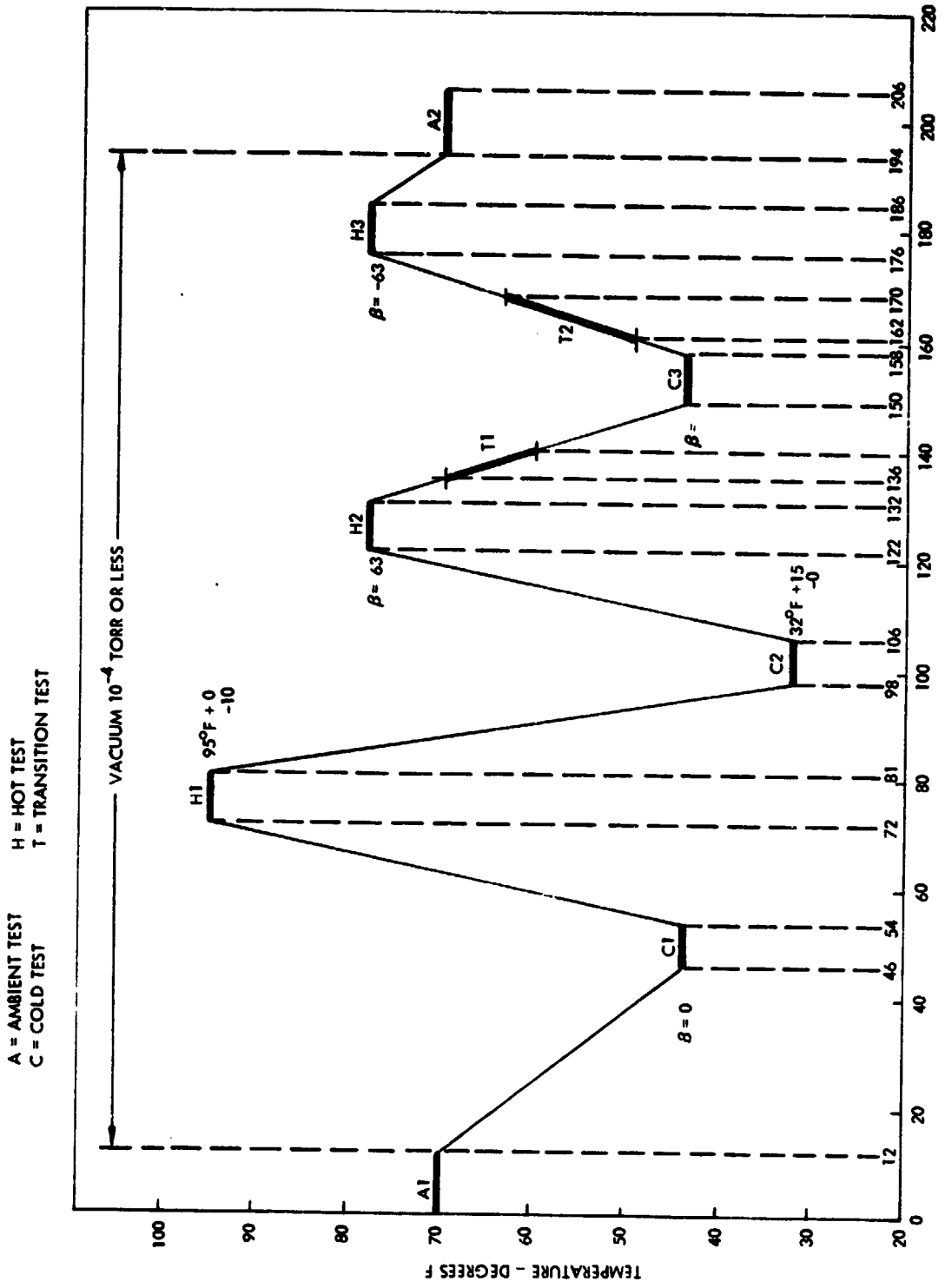

Figure 3-21. Thermal/Vacuum Systems Test Profile

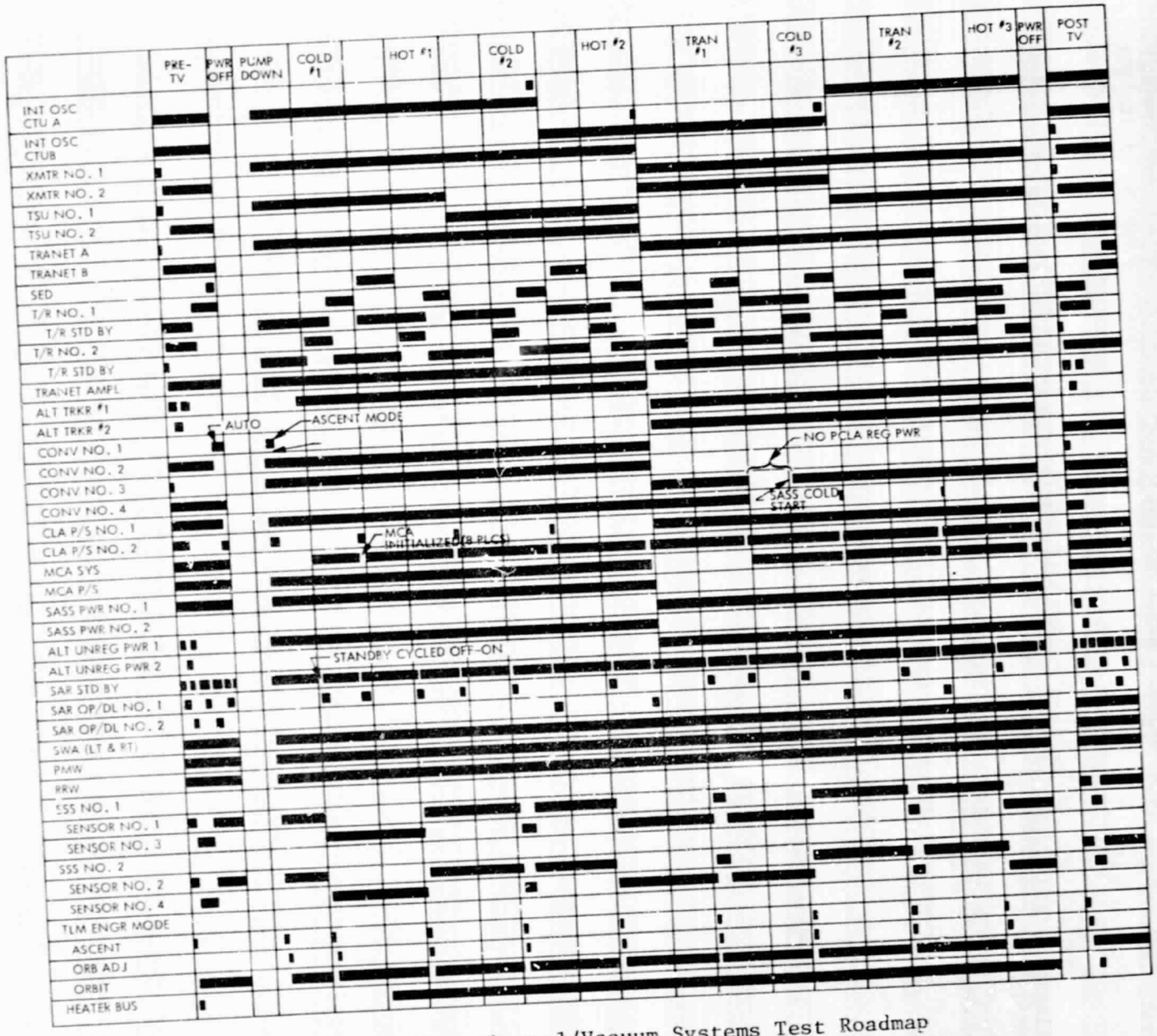

Figure 3-22. Thermal/Vacuum Systems Test Roadmap

c. Results. Systems performance tests were performed on all satellite subsystems and sensors and the resultant data were evaluated and compared with that obtained from the baseline systems test. Testing sequences were performed that simulated actual ascent and orbit operations, but times were shortened and special (non-flight) sequences were used where necessary to ensure equipment integrity. This test was also used to revalidate the reinstallation of the SAR data link at the system level after its repair and return to LMSC. There were no major anomalies resulting from this test.

Subsequent to the final simulated flight test, the final satellite preparations for shipping were performed. During the testing effort, the command memory load for the flight sequence of events was validated, the method of stimulating the SWAs for the launch base testing was validated, and the final coaxial and waveguide connections were certified. Following these final functional tests, the pyrotechnics were installed in all pinpullers and appropriately safed, the Agena bus was disconnected from the SM/SMSS and all system elements prepared for shipment to the launch base.

9. Acceptance Reviews

The QA system for Seasat ensured that end-item material complied with program requirements, as defined in end-item specifications, and that there was adequate objective evidence of end-item compliance. To meet these objectives, a system of incremental acceptance activities was initiated.

The acceptance process actually started at the lowest level of assembly at which inspection or test occurred and was carried on concurrently with the fabrication, assembly, and test of all levels of material, starting with piece part receiving tests and continuing through assembly level, subsystem level, bus assembly, and satellite final assembly. The documentation of lower level acceptances was maintained as a part of the corporate record in the closed order files where shop documents were impounded on completion of required work. These documents were reviewed by inspection supervision before closure to ensure completeness and accuracy.

QA documented all non-conformances to engineering requirements, impounded defective material until properly dispositioned for return to an acceptable condition, and provided documented evidence of actions taken. This discrepancy documentation was additionally used, through input to a computerized data bank, in determining and controlling quality trends and displaying this information for management and customer review.

To support satellite format acceptance, assembly level pedigree packages were prepared for critical equipment (as specified by the reliability representatives). Contents of these pedigree packages consisted of a thorough compilation of assembly and test documents as well as non-conformance history. All were reviewed by JPL cognizant engineers and by the reliability and CSE representatives of LMSC. These data packages were reviewed and approved before the first satellite-level incremental acceptance meeting.

LMSC responsibility for final acceptance (DD-250) of the satellite was discharged through a series of incremental acceptance meetings held at each major test milestone. There were a total of 6 meetings, as follows:

(1) After satellite integration and SM/SMSS compatibility tests.

(2) After baseline systems test.

(3) After acoustic environmental test and before thermal/vacuum test.

(4) After final systems test.

(5) At launch readiness review (pre-ship).

(6) At flight readiness review at WTR.

At each of these meetings, a joint decision of acceptability of actions to date was made by product assurance, engineering, and JPL, and was the basis for the decision to proceed with the next step of satellite processing. Before shipment to WTR, a preliminary DD-250 was presented for JPL signature, with final DD-250 signoff at WTR following the flight readiness review.

10. Equipment Qualification Summary

a. Introduction. LMSC policies and procedures require all mission-critical equipments to be qualified before flight. The Seasat implementation of these requirements was accomplished by issuance of a program qualification plan, which was incorporated into the program reliability plan (CDRL item) by revision, and then submitted to and approved by JPL.

b. Program Qualification Plan Summary. Qualification is a demonstration by test, similarity, analysis, or any combination of these, that equipments are capable of performing within specification requirements when subjected to simulated flight and operational environments. Therefore, the purpose of the plan was to establish the technical and administrative requirements for qualification of Seasat equipments and to provide a standardized method for documentation and certification. Because of the unique quality and complexity of the Seasat program with respect to the planned use of existing equipments and designs, modifications of previously qualified designs, and new designs, the program qualification plan provided for the establishment of a Senior Qualification Review Board.

c. Senior Qualification Review Board.

Membership. The Senior Qualification Review Board (SQRB) consisted of the program engineering manager, chief system engineer/systems manager, and the program reliability engineer. Additional support and advisory members were provided by technical representatives from aerodynamics, thermodynamics, and space technology.

Functions and Responsibilities. The SQRB had two primary functions: (1) to decide what Seasat flight equipments would be subjected to qualification-level testing during acceptance to establish design integrity and (2) to review and approve all qualification and certifications on equipments determined to be flight-mission critical.

The establishment of this SQRB was unique to the Seasat program. Previously, it was the responsibility of the Responsible Reliability Engineer (RRE) and the Responsible Equipment Engineer (REE) to establish the qualification status of flight equipments and to prepare and execute certifications.

This administrative technique was used on the Seasat program. However, the SQRB provided a second, in-depth technical review of the qualification status, certification and supporting tests, and either or both analytical data and technical rationale. This was accomplished at regularly scheduled SQRB meetings. In addition to the SQRB membership, the meetings were attended by and actively participated in, by JPL engineering representatives. On satisfactory completion of the review, a Seasat flight worthiness confidence statement was prepared by the SQRB chairman for signature by the SQRB members. (Of the 77 certificates initially presented to the SQRB for review, the approval of 26 was deferred until either or both additional test and analytical data were presented.)

Certification Technique. The standard techniques for qualification and certification of Seasat equipments were:

(1) Qualification by Test: satisfactory demonstration by test that the equipment specification design requirements were satisfied.

(2) Qualification by Similarity: an in-depth comparison of the equipment configuration and specification environmental qualification requirements to a similar equipment previously qualified by test to determine whether the requirements for both equipments were sufficiently similar to preclude retest. All differences, either or both of configuration and test, were summarized and addressed in the text as to the rationale for acceptance.

(3) Qualification by Test/Similarity and Analysis: a combination of test (for some conditions not satisfied by similarity) and similarity supported by substantive analytical data.

11. Qualification and Certification Summary

a. Introduction. The 11 critical flight equipments determined by the SQRB to require some testing to qualification levels were:

Equipment	Qualification Environmental Tests
Command timing unit	Random vibration, shock, T/V, EMI
Main power distribution unit	Random vibration, shock, T/V, EMI

Equipment	Qualification Environmental Tests
Power control logic assembly	Random vibration, shock, T/V, EMI
SAR enable/disable unit	Random vibration, shock, T/V, EMI
Telemetry sensor unit (1)	Random vibration, shock, T/V, EMI
SAR antenna	Sine, acoustic, pyro shock, T/V
Tape recorder	Shock
Solar array module	Random vibration, sine, shock, acceleration
Augmented electronics assembly	Random vibration
Control logic assembly	T/V
Magnetic control assembly	T/V

On successful completion of required testing, these equipments were issued Qualification by Test/Similarity and Analysis Certifications and Seasat Confidence Statements were executed.

b. Qualified by Test. On review by the SQRB, 17 equipments were determined to be qualified by previous test and Seasat Confidence Statements were executed. These equipments were predominately unmodified standard Agena components.

c. Qualified by Similarity. Thirty-seven equipments were determined to be sufficiently similar (either or both by configuration and prior environmental tests) to qualified equipments to warrant issuance of Qualification by Similarity certificates and Seasat Confidence Statements.

d. Qualified by Test/Similarity and Analysis. Twelve equipments were certified by comprehensive review of prior, or in-process, qualification test data on similar or identical equipments and analytical data.

Although the certification of equipments was progressive (as qualification packages were made available to the SQRB), some certifications were purposely deferred until vehicle post-acoustic test data could be reviewed. The intent was not to use this data as a mechanism for qualification, but rather to substantiate the credibility of the predicted levels and their translation into random vibration qualification levels. All equipments so deferred were established to have been either or both adequately tested and analyzed to support certification.

However, the review of the post-acoustic data indicated that the acoustic test level responses on seven equipments slightly exceeded the equipment specification levels in selected narrow frequency bands. Analysis by the SQRB, supported by space technology dynamics engineering, determined the equipment levels fell within the expected flight levels, and, in almost all frequency bands where an over-exposure occurred, the acoustic test levels were greater than the maximum expected in flight. This analytical data was attached to the applicable certification.

e. Certification Status and Reporting. The SQRB established a baseline schedule for completion, review, and approval of certifications. The schedule and changes thereto were administered by the SQRB chairman. As equipments were formally certified by the SQRB, copies of the certifications were distributed internally at LMSC and to the cognizant JPL participants.

During each of the five readiness (incremental acceptance) reviews, the equipment qualification current status was reported in a matrix format. Additionally, the schedule and constraints on equipment to be qualified were presented.

REFERENCES

3-1. GD/C Mission Assurance Plan, GD/C document GD/C-BCJ72-006.

3-2. Fairing Reliability and Quality Assurance Plan, LMSC document D570742.

3-3. Seasat-A Program Preferred Parts List, LMSC document D490723.

3-4. Seasat-A Parts Control and Standardization Requirements, LMSC document D427896.

3-5. Compliance Verification Document, LMSC document D615608.

3-6. STDN Spacecraft Compatibility Test Procedure and Data Sheets, Revision 1, NASA/GSFC document STDN 407.

SECTION IV

GFE PLAN

A. INTRODUCTION

The Government Furnished Equipment (GFE) on Seasat consisted of the 5 sensor systems, Laser Retroreflector Array (LRA), NASA Standard Transponder (NST), and Tranet beacon. The satellite system/launch vehicle interface and the launch vehicle are described in Sections II and VIII, respectively.

The plan for the integration and control of the GFE was simple in concept, as illustrated by the flow diagram shown in Figure 4-1, which shows the actions involved in the GFE system integration, interface control, and system compatibility. The task began with the satellite system specification, as first provided by JPL, and the respective GFE specifications. Interface responsibilities were defined, interface control documents prepared, and interface problems identified and resolved through the Interface Control Working Group (ICWG). The information was iterated through the requirements reviews and design reviews to ensure that the interface agreements were formulated, fully understood, and accurately documented.

At the same time, the Electromagnetic Compatibility (EMC) control plan was generated and the EMC requirements were established through the EMC Control Board working in cooperation with the ICWG. The EMC control plan established design and test requirements for the satellite system, as well as for the GFE and satellite subsystems. RFI analyses and tests were performed at both the subsystem and system levels.

The final systems tests were performed with no significant interference of any kind.

B. DESCRIPTION OF GFE

The 5 sensor systems were the: (1) Radar Altimeter; (2) Synthetic Aperture Radar; (3) Scatterometer; (4) Visual and Infrared Radiometer; and (5) Scanning Multichannel Microwave Radiometer. The overall configuration of the satellite and the sensors is shown in Figure 1-3.

The Radar Altimeter (ALT) was an active radar that achieved high resolution in range with a very short pulse that was synthesized from a chirp pulse, which was a time-rate-of-change FM pulse of 320-MHz bandwidth. The pulse was processed through a matched filter to obtain the equivalent of a 3-ns pulse. The ALT measured significant wave height of ocean waves to an accuracy of 1 m (3.3 ft) or 10 percent, and provided basic height tracking of the geoid to a 10-cm (4 in.) accuracy. The NASA Wallops Flight Center (WFC) was the agency responsible for the management of the development of the ALT. Principal contractors included the Applied Physics Laboratory (APL) of Johns Hopkins University and Hughes Aircraft Company.

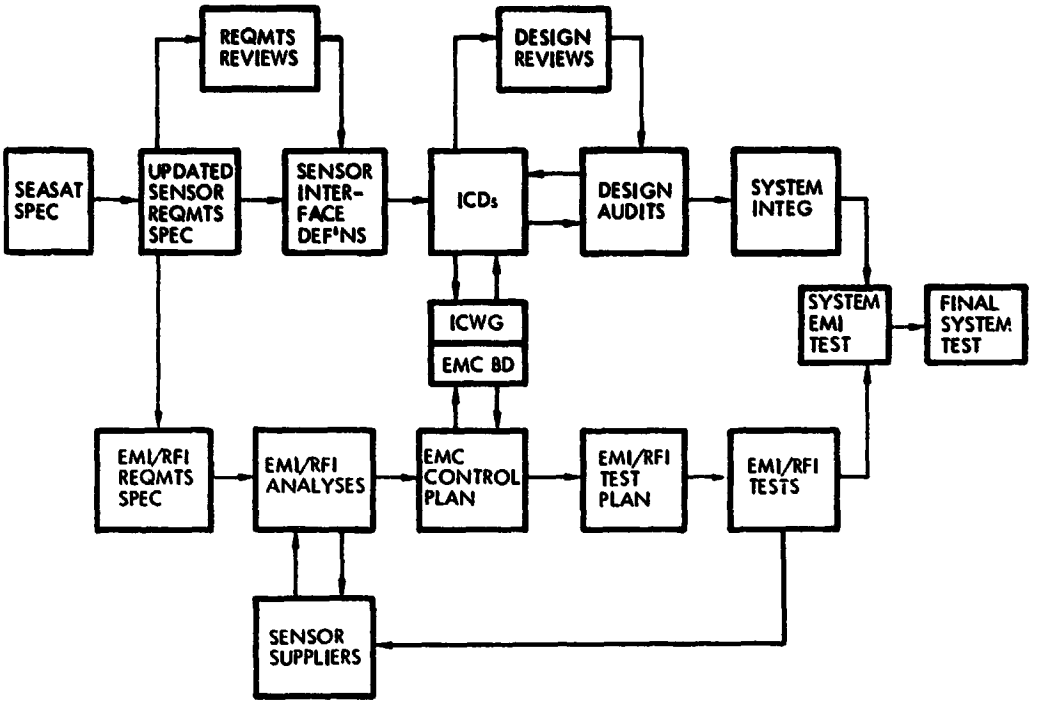

Figure 4-1. Sensor System Integration and Control

The Synthetic Aperture Radar (SAR) was an active side-looking radar that achieved very high azimuthal resolution by Doppler processing in exchange for integration time. The result was that the effective antenna length of the SAR was many times the physical length of the antenna on Seasat. Range resolution was determined by pulse length. Each transmitted pulse was chirped, and had an envelope of 32-μs duration and a 19-MHz bandwidth. Each return pulse was de-chirped to obtain fine range resolution by pulse compression in the ratio of 576 to 1. Because of the wide bandwidth and complex processing, all data was transmitted in real time to ground stations for later processing into radar images.

JPL was responsible for the SAR electronics system. The Westinghouse Corporation was a principal contractor. The self-extended planar array antenna was developed by BBRC under subcontract to IMSC. The wideband SAR data link system and antenna was developed by APL under management of NASA WFC.

The Scatterometer was developed under the management of the NASA Langley Research Center (LaRC). Principal contractors were the General Electric Company, Hughes Aircraft Company, and Aerojet Electrosystems Center. The Scattterometer, designated SASS for Seasat Scatterometer System, was an active calibrated radar by which the scattering coefficient of the ocean surface could be determined for comparison with empirical data to determine the local wind speed and direction.

A very narrowband 5-ms pulse was transmitted at approximately 33 p/s. The received pulse was processed through a Doppler filter bank into range cells approximately 50-km (27 nm) wide and calibrated against a known signal to obtain a measure of the scattering coefficient. The system used four dual-polarized linear array antennas to transmit and receive fan beams at ±45 deg and ±135 deg with respect to the line of flight.

The Visual and Infrared Radiometer (VIRR) was residual flight equipment from the Itos program. The unit used on Seasat was serial number F-27, provided by GSFC. The VIRR was a scanning two-channel optical radiometer. The scanner was a rotating mirror that provided 2-km (1.08 nm) and 4-km (2.16 nm) footprints in the visible and infrared regions at a scan rate of 48 rpm. The primary purpose of the VIRR was to provide a feature identification reference. Engineering and support for refurbishment and test was performed by the Santa Barbara Research Center (SBRC).

The Scanning Multichannel Microwave Radiometer (SMMR) was a five-frequency passive microwave receiver used to measure the brightness temperature of the observed surface. Experience in microwave radiometry has provided the basis for extracting from the multifrequency brightness temperatures such parameters as sea surface temperature, sea surface wind speed, sea ice coverage, and certain other parameters, when corrections are made for atmospheric opacity. However, opacity is strongly influenced by frequency. Therefore, radiometric measurements made at selected frequencies can be used to remove the atmospheric effects.

The SMMR was developed under the management of JPL. Principal subcontractors included the Microwave Research Corporation, Schaeffer Magnetics, Litton Systems, Electromagnetic Sciences, and Spacekom.

The LRA was a ring of 96 quartz corner cubes. The array ring was manufactured by APL under the contract management of GSFC.

The NST and Command Demodulator Unit (CDU) were supplied GFE to LMSC. The NST was manufactured by Motorola, the CDU by Cincinnati Electronics, and both units were integrated and tested as a set by Motorola. The NST was supplied in accordance with JPL design requirements and an LMSC ICD. The CDU was supplied in accordance with modified SAGE (Boeing) requirements and an LMSC ICD.

The Tranet beacon was also supplied GFE, and was used in connection with a Doppler tracking network. The beacon was supplied by APL to an APL specification and an LMSC ICD.

The organizational interfaces involved in the procurement, integration, and test of the GFE are shown in Figure 4-2. Physical, environmental, operational, and data interfaces were defined, controlled, and maintained through these channels. Each GFE subsystem was represented by an ICWG consisting of members from JPL and LMSC, the GFE manager, and 1 or more of the principal subcontractors.

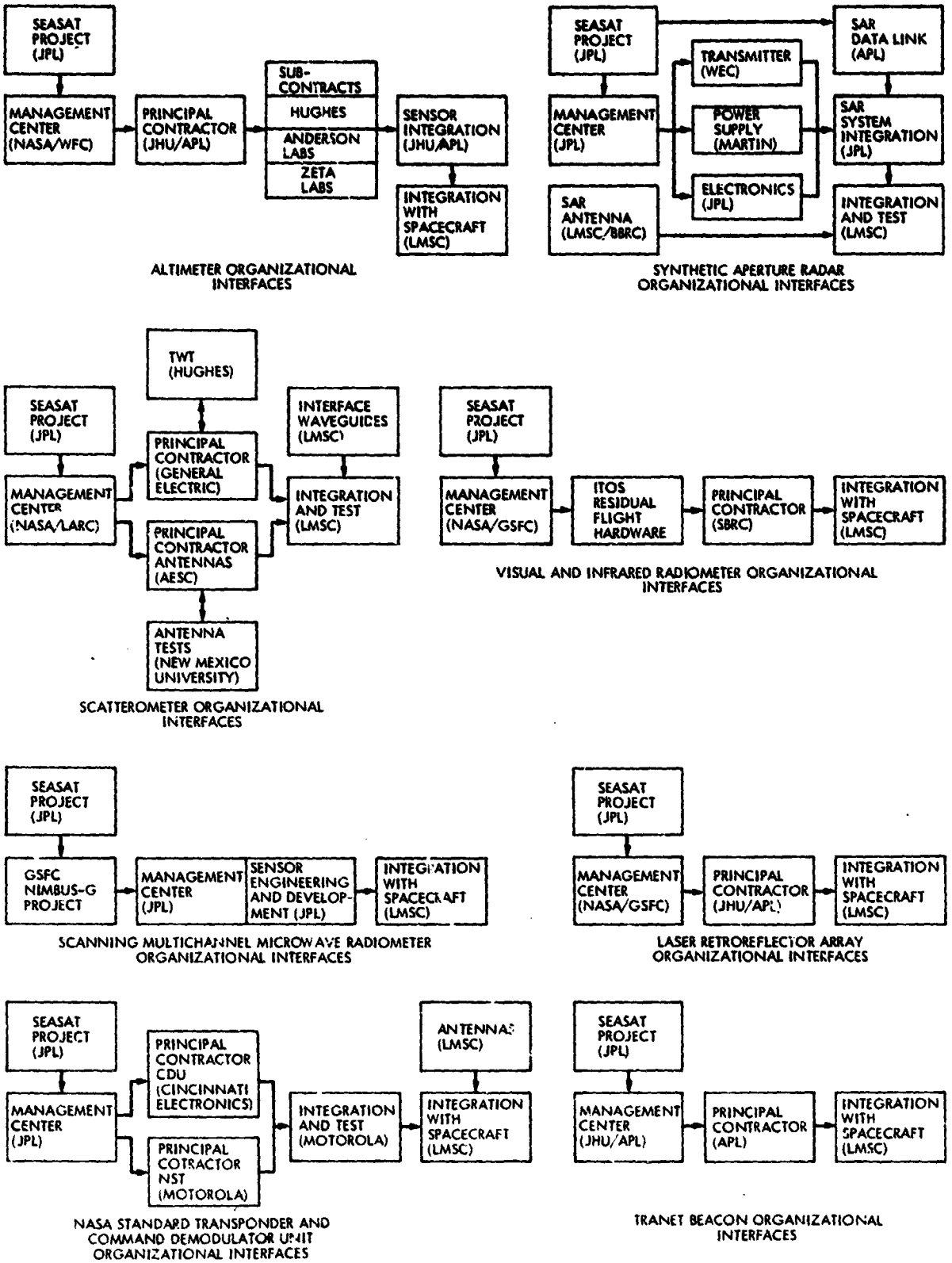

Figure 4-2. Seasat GFE Organizational Interfaces

C. INTERFACE DOCUMENTATION

The definition of interface requirements for the sensors and other GFE and the initiation of discussions of EMC and RFI control were undertaken early in the Seasat program. Arrangements were made for the first ICWG meetings on interface definition and EMC to convene at LMSC in December 1975, approximately 2 months before the start of the SSE contract. These first meetings began the process of integration analysis, interface definition, design and control, and EMC control.

Interface control ensured the compatibility and unimpaired operation of all elements of the satellite system. Frequent ICWG meetings were held to work out requirements and interface definitions for each of the sensors and for the other GFE. The goal of these meetings was to develop mutual understanding of the design details, required functions, constraints, environments, and other technical factors pertaining to each GFE subsystem. The mechanical, electrical, electronic, thermal, and environmental requirements were determined and defined in detail. Mutually acceptable interface agreements were worked out and documented. The Technical Interface Control Plan (LMSC document D490744) was prepared by LMSC and implemented in the development of the ICD for each of the sensors and other GFE. Twelve ICDs were prepared with the active participation of 28 organizations. These ICDs are listed in Table 4-1.

The Satellite System/Ground System ICD (LMSC document D523254) was prepared by LMSC and submitted to JPL, excluding the portions that applied to the JPL/GSFC interface. No final document was issued because JPL and GSFC were unable to resolve and complete certain items of the ICD early enough for the document to be useful.

Each item of GFE had unique interface requirements that made the task of integration a complex one. The key to success in the process of interface management accomplished on Seasat was the highly cooperative and mutually constructive approach by all participants to solve problems as they were discovered and to firmly agree on the course of action. Several studies were conducted during the program to improve certain interface conditions. In most cases, these studies resulted in design changes that were incorporated in the GFE or satellite design and documented in the ICDs.

D. UNIQUE REQUIREMENTS

An outstanding example of a unique and complicated interface requirement was the baseplate of the ALT. The baseplate incorporated a honeycomb sandwich construction with aluminum face plates, and was circular in shape. At the rim of the baseplate was an aluminum cylinder, which was surrounded by the LRA. The heat generated by the electronic assemblies of the ALT mounted on the baseplate could be dissipated only by conduction by the plate to the rim, and then radiated to space by the aluminum cylinder. By the same heat conduction path, the cylindrical radiator could cause the temperature of the baseplate to fall below safe operating limits if the ALT was not operating. After much study and some controversy, an agreement was reached by which LMSC performed a thermal analysis to determine the thickness of the face plate, the preferred alloy, and the

Table 4-1. Interface Control Documents

ICD No.	Type[a]	Custodian	Title	Principal Participating Organization/ Participating Organization(s)
LMSC D490728	1, 2	LMSC	Scatterometer/ Satellite System ICD	LARC/GE
LMSC D490729	1, 2	LMSC	Altimeter/Satellite System ICD	WFC/APL
LMSC D490730	1, 2	LMSC	Synthetic Aperture Radar Electronics/ Satellite System ICD	JPL/WEC MMC JPL
LMSC D490731	1, 2	LMSC	Synthetic Aperture Radar Data Link/ Satellite System ICD	JPL/APL
LMSC D490732	1, 2	LMSC	Synthetic Aperture Radar Electronic/ SAR Data Link ICD	JPL/JPL/APL
LMSC D490733	1, 2	LMSC	Scanning Multi-channel Microwave Radiometer/Satellite System ICD	JPL/JPL
LMSC D490734	1, 2	LMSC	Visual and Infrared Radiometer/Satellite System ICD	GSFC/SBRC
LMSC D499035	1, 2	LMSC	Laser Retroreflector Array/Satellite System ICD	WFC/APL
LMSC D490742	1, 2	LMSC	Tranet Beacon/ Satellite System ICD	DoD/APL

[a]Type 1, functional interface; type 2, physical interface; type 3, procedural interface.

Table 4-1. Interface Control Documents (Continuation 1)

ICD No.	Type[a]	Custodian	Title	Principal Participating Organization/ Participating Organization(s)
LMSC D523254	1, 2, 3	LMSC	Satellite System/ Ground System ICD	GSFC/JPL
LMSC D523289	1, 2	LMSC	Satellite System/ NASA Standard Transponder and Command Demodulator Unit ICD	JPL/Motorola/ Cincinnati Electronics

[a]Type 1, functional interface; type 2, physical interface; type 3, procedural interface.

location and type of heaters to mount on the baseplate. APL constructed the baseplate according to the recommendations, and mounted the heaters. This design was found to be completely satisfactory in subsequent thermal/vacuum tests.

Another unique interface condition involved the SASS and the eight waveguides that connected the SASS transmitter and receiver ports to the four dual-polarized linear array antennas. The SASS electronics assembly was developed, fabricated, assembled, and tested by the General Electric Company. The four dual-polarized antennas were developed, fabricated, and tested by Aerojet Electrosystems Center. The eight waveguides were procured, tested, and installed in the spacecraft by LMSC. Before integration on the spacecraft, none of these components of the SASS system had been operated together before.

The waveguides were conceptually simple but geometrically difficult. No two of the eight waveguides were alike. Each had a number of bends and twists to accommodate the installation, and each had a short section of flexible waveguide incorporated into its length to permit deployment of the antennas. As installed, they met all interface requirements, in spite of some early concerns about structural integrity and RF compatibility.

The SMMR presented another interesting interface situation. The problem arose from the fact that the SMMR for Seasat was identical to the system provided for the Nimbus-G spacecraft. For reasons of contract precedence, the SMMR electronic assemblies and the scanner had been designed to be compatible with the Nimbus-G. Therefore, LMSC designed a housing that duplicated a portion of the Nimbus-G specifically for installation of the SMMR antenna and scanner mechanism and three electronic assemblies. The resulting SMMR system was installed and integrated on the Seasat spacecraft.

Although many other examples of unique or special interfaces could be cited, one final example will suffice. This case involved the data system interface with the ALT, the so-called bit 7, 8, and 9 phenomenon. Because of a supposedly minor change made by the ALT supplier in the bit structure of the data command word that added 256 parameter select data commands and 256 dump control data commands, the resulting impact was widely felt, but particularly in the organization of the ALT test requirements and test procedures. No material changes were necessary, but the ICD was revised, the Altimeter Test Requirements Document (LMSC document EM No. S3.1-010) was revised, the command list was revised to add 512 data commands, and the systems test software was extensively rewritten to provide for verification of the 512 possible control words. This example is cited to show that a minor change in a minor function of the system could impact the complete area of interface control.

E. EMI AND RFI CONSIDERATIONS

It was recognized early in the Seasat program that potential EMI and RFI between sensors and between sensors and the satellite equipment was a major concern. Therefore, an EMC program was established to ensure the electromagnetic compatibility of the satellite system. The principal requirements of the EMC program were:

(1) To establish and coordinate the satellite system EMC requirements.

(2) To establish the Seasat EMC Control Board, consisting of representatives from LMSC and JPL, and the sensor equipment managers.

(3) To establish design and installation criteria based on proven EMC practices.

(4) To define EMC test requirements and coordinate test plans.

(5) To initiate early RFI analyses and testing of the sensor module.

(6) To resolve potential EMC problems.

The EMC program was planned to ensure system compatibility by control of interference emission and susceptibility at the equipment and subsystem levels and verification by satellite system EMI and RFI tests. The Seasat EMC Control Plan established design and test requirements for the satellite system as well as for the equipments and subsystems. The satellite system design requirements became the basis for the EMC control techniques used in the electrical and mechanical design of the satellite. (Refer to the Electromagnetic Compatibility Control Plan, LMSC document D490724.)

For example, criteria were established for cabling and wire harness design and installation, electrical power distribution, routing, grounding, and isolation, electrical bonding of structural members and components, and grounding of thermal blankets. Shielding was required on all AC wiring, electro-explosive device firing circuits, and critical analog data lines. RF and digital signals

required coaxial cables or twisted shielded pairs with the shield grounded to the structure at frequent intervals. DC and low frequency circuits were grounded to the structure at one point only, the single-point ground at the power distribution box.

Test requirements for the equipment and subsystems were based on MIL-STD-461A and MIL-STD-462. EMC test requirements and test levels were recommended to project management by the EMC Control Board, and the EMC tests listed in Table 4-2 were conducted by the equipment suppliers. Results of these tests were reviewed and approved by the EMC Control Board. Waivers were recommended by the board in those few cases in which test results did not fully satisfy the requirements of the EMC Control Plan, but did not threaten the successful operation of the system.

RFI analyses were initiated early in the Seasat project. Preliminary analyses of potential situations involving RFI were performed by APL before award of the SSE contract. APL continued to support EMI and RFI analyses throughout the period of the SSE contract.

RFI was recognized as one of the most serious challenges in the Seasat program. The system included among its sensors, beacon, and data links 7 transmitters, 10 receivers, 11 antennas operating at 13 different frequencies, and the VIRR. Three of the sensor systems were high power radars, transmitting pulses at widely different repetition rates. The spectrum of transmitter and receiver frequencies is shown in Figure 4-3. The six SMMR receivers were the most sensitive on the satellite. Nevertheless, it was imperative that the command receiver should not be interfered with by any other system, even at the cost of some possible interference with the sensors. Therefore, the first priority established was that the command receiver and Tranet beacon oscillator, which served as the central timing reference, should operate successfully in the presence of any single sensor, with the goal that all systems should operate simultaneously without interference.

The analyses of possible RFI problems were performed in three parts: (1) the determination of the RF energy and spectrum frequency generated by each of the transmitters, taking into account the radiated bandwidth, sidebands, and harmonics; (2) the determination of the antenna-to-antenna coupling coefficients at each radiated frequency; and (3) the calculation of the amount of RF power at each receiver compared to the sensitivity of that receiver to the particular frequency and bandwidth. A total of 42 possible interferences were found, and by calculation, 15 of these were identified as requiring additional investigation.

In addition, all intermodulation products that could be produced by the 13 frequencies, their sidebands, and harmonics were calculated. These were examined in a quantitative manner to determine if any could cause significant interference. It was found that the out-of-band signal levels would not support this type of interference, primarily due to the preselection filtering of all of the receivers except the SMMR.

Table 4-2. Sensor EMC Tests[a]

	SMMR	SAR	SAR D/L	VIRR	ALT	SASS	Tranet
CE-01, CE-03 Unregulated power lines ripple	A	A	A	A	W	W	A
CE-02 Signal and control lines ripple	O	W	W	A	W	A	A
CS-01, CS-02 Unregulated power lines susceptibility 30 Hz-50 MHz	A	A	A	A	A	O	A
CS-06 Unregulated power lines 50 volt spike	A	A	A	A	W	O	A
RE-02 Radiated emissions selected frequencies	A	A	A	O	A	O	A
RE-03, CE-06 Spurious/harmonics selected frequencies	A	A	A	O	A	A	A
RS-02 Magnetic induction 50 volt peak	O	A	A	A	A	O	A
RS-03 Radiated susceptibility selected frequencies	A	A	A	A	A	O	A
Transient in-rush current	A	W	W	O	W	A	O
Turn-on voltage transient	O	W	W	W	A	O	O
Bonding, 2.5 mΩ	W	A	O	A	W	A	W

[a]A = Acceptance test passed. O = No test performed. W = Waiver approved by EMC Board.

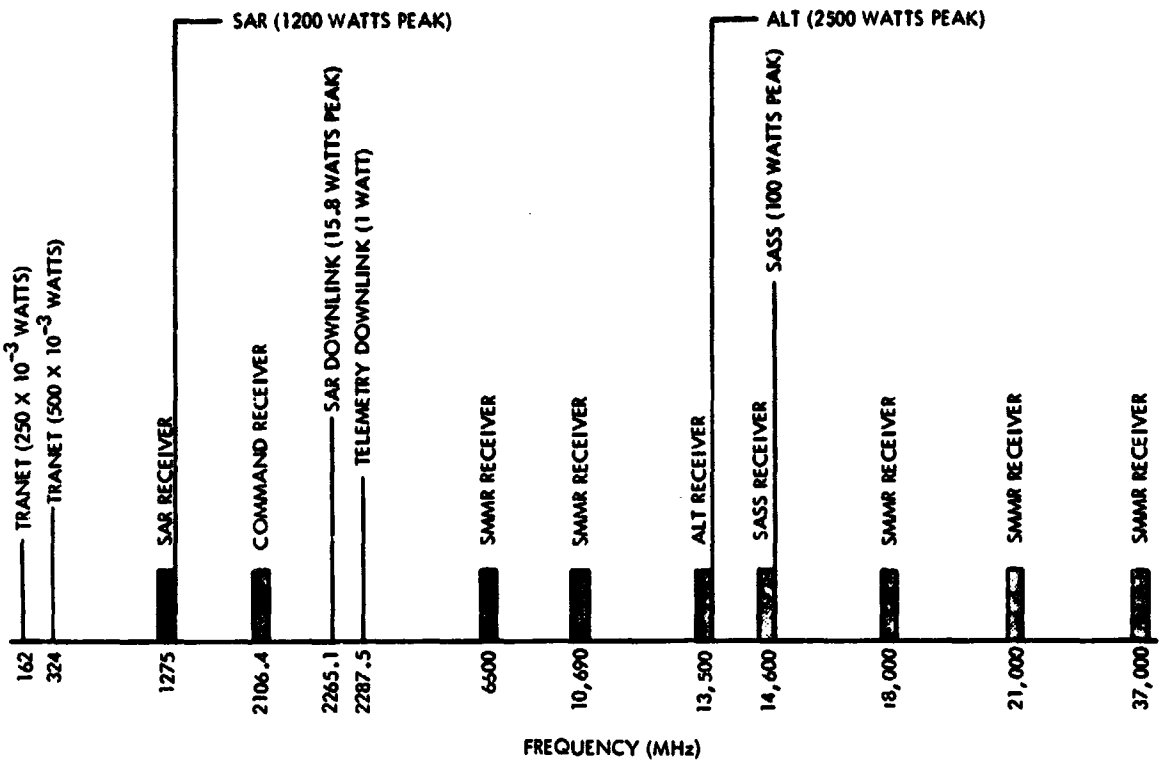

Figure 4-3. Sensor Module Frequency Spectra

The RFI analyses were augmented by actual antenna-to-antenna coupling measurements made with the aid of a full-scale mockup of the sensor module and the engineering models of the Seasat antennas. The mockup was positioned on a pedestal so that the local zenith corresponded to the nadir of the spacecraft in orbit. The measurements were made in the low-reflection airhouse at the SCTB. The test setup is shown in Figure 3-5.

The coupling measurements were made by connecting a signal generator to the input port of the selected antenna at the test frequency, and a spectrum analyzer was connected to the output port of another antenna. The difference in power level between the signal generator output and the detector represented the antenna-to-antenna coupling coefficient. A total of 238 separate measurements were made, encompassing 10 transmitting antennas, 13 receiving antennas, and frequencies ranging from 162 MHz to 37 GHz. Table 4-3 shows one set of such measurements between the NST, SAR, SAR data link, and SASS and the five SMMR channels. In each case, the transmitter frequency is listed in the left column and the corresponding coupling coefficients are listed for horizontal (H) polarization, vertical (V) polarization, and at the cold horn (C).

Table 4-3. Antenna Coupling Coefficients[a]

Transmitted Frequency (MHz)	Received (MHz)				
	SMMR 6.6	SMMR 10.69	SMMR 18	SMMR 21	SMMR 37
TLM 2 6600	H-90 V-99 C-89				
TLM 2 6862	H-96 V-92 C-88				
TLM 2 18300			H 95 V 85 C 92		
TLM 2 20587				H 92 V 103 C 100	
SAR 6600	H 94 V 91 C 101				
SAR 6374	H 103 V 105 C 95				
SAR 10690		H 104 V 104 C 104			
SAR data link 6600	H 83 V 101 C 93				
SAR data link 6795	H 92 V 91 C 98				
SAR data link 10690		H 102 V 99 C 104			

[a]H = horizontal polarization. V = vertical polarization. C = cold horn.

Table 4-3. Antenna Coupling Coefficients[a] (Continuation 1)

Transmitted Frequency (MHz)	Received (MHz)				
	SMMR 6.6	SMMR 10.69	SMMR 18	SMMR 21	SMMR 37
SAR data link 18121			H 97 V 99 C 100		
SASS 2 10690		H>104 V>104 C>104			
SASS 2 14599	H 98 V 90 C 94	H 108 V 102 C 90	H>110 V 102 C>110	H 100 V 100 C 106	
SAR 36970					>60

[a] H = horizontal polarization. V = vertical polarization. C = cold horn.

The measured antenna coupling coefficients were used in refinement of the RFI analyses. The resulting computations were documented in the Revised dB Tables for Seasat RFI Analysis (LMSC document EM No. S-14.2-006 dated December 1976). One example of such computation follows:

(1) Type of interference: harmonic 4 x 324 = 1296.0 MHz.

(2) Transmitter power: +26 dBm.

(3) Measured coupling: greater than -95 dB.

(4) Received power: less than -69 dBm.

(5) Sensitivity: -98 dBm.

(6) Required margin: +29 dB.

(7) Safety margin: 20 dB.

(8) Required rejection: less than +49 dB.

(9) Fourth harmonic loss: -70 dB (value that Tranet beacon will exhibit).

(10) Additional filtering: none.

In this case, the 4th harmonic of the Tranet beacon transmitter at 1.296 GHz fell near the center frequency of the SAR at 1.275 GHz. However, because the 4th harmonic was 70 dB down from the fundamental at 324 MHz, no interference was experienced.

Two other types of interferences were investigated. The first interference was gain compression at the SASS receiver caused by out-of-band signals radiated by the ALT. This problem led to a recommendation that a preselector filter be installed in the SASS, eliminating the interference. The second type of interference was potential burnout of the SMMR mixer diodes. In this instance, burnout was defined as a permanent 1-dB change in the noise figure of the diode. It was thought that the 14.6-GHz pulse of the SASS might cause burnout in the SMMR 18-GHz channel.

Calculations indicated there was a marginally adequate safety level between the radiated power and the power required to damage the diode. Subsequent tests showed that the receiver diode was safe from damage.

As a result of the RFI analyses, the installation of five filters were recommended:

(1) Low pass filter on SAR transmitter.

(2) Low pass filter on SAR data link.

(3) Band pass filter on ALT transmitter.

(4) Low pass filter on SASS transmitter.

(5) Preselector on SASS receiver.

After installation of these filters, all known interferences were eliminated.

Satellite system EMI and RFI tests were performed during February 1978. In the EMI tests, the procedure consisted of transient and steady-state measurements of emission and susceptibility in a test sequence that simulated launch, orbit injection, and orbit operations. The RFI test was conducted in the LMSC anechoic chamber with all antennas deployed, except that of the SAR, which was simulated by a standard gain horn located at the center of the SAR antenna in the fully extended and operational condition.

The Seasat EMI and RFI tests were completed with no indications of significant interference or EMC problems.

C-3

F. SPECIAL STUDIES

A number of special studies and analyses were conducted to resolve certain issues pertaining to critical interfaces. Among these studies were:

(1) Thermal analysis of the ALT baseplate. Concluded with the negotiated agreement for the thermal interface design.

(2) Study of weight reduction of the ALT baseplate. Concluded by accepting the design as recommended by APL.

(3) Mechanical analysis of the SASS baseplate. Found that the stiffness requirements were satisfied and the mechanical deflections under load were less than the basic requirement.

(4) Thermal analysis of the LRA mounting ring. Concluded that the thermal isolation mounts should be modified. The design was implemented and the thermal/vacuum tests confirmed the adequacy of the design.

(5) Study of relocation of one of the narrowband T/M antennas. Concluded that the antenna would affect the radiation pattern of one of the SASS antennas. The T/M antenna was relocated on the Tranet boom and the interference was eliminated.

(6) Study of the isolation of the SAR signal interface. Resulted in the design of magnetic isolation circuits for the SAR signal interface.

(7) Study of the obscuration of the SMMR cold horn by the SASS and SAR antennas. Concluded by analysis that the obscuration was negligible.

(8) Study of the spectral purity of the 5-MHz clock signal supplied to the SASS by the Tranet beacon oscillator. This analysis was specifically requested by the EMC Control Board. Concluded that the clock frequency and the spectral purity satisfied the requirements imposed by the SASS for the input to its solid-state local oscillator.

G. CONSENT-TO-SHIP AND COMPLIANCE REVIEWS

Before delivery of the GFE to LMSC for integration with the spacecraft, consent-to-ship meetings were held to ensure that the equipment was suitably qualified for flight. The subject of these reviews had been agreed on jointly by LMSC, JPL, and the GFE managers. The meetings were chaired by the JPL QA representative. The topics covered included:

(1) Configuration of system.

(2) Action item status.

(3) Design and performance verification.

(4) Hardware review certification requirements.

(5) Operating hours.

(6) Test performed.

(7) ICD performance verification.

(8) Problem and failure reports.

(9) Engineering changes and waivers.

(10) Support equipment

(11) Transportation plan.

This information was fully documented and supported by the necessary certifications, test reports, drawings, specifications, parts lists, and inspection reports. The information was submitted in the QA Acceptance Data Package on delivery of the equipment to LMSC.

An integral part of the Acceptance Data Package was the ICD Compliance Review, in which the item-by-item verification of the ICD requirements was presented and documented in a compliance list or matrix. A compliance matrix for the satellite system specification was presented by LMSC as part of the Seasat acceptance and readiness reviews.

H. TESTING AT SUNNYVALE

After shipment, but before formal delivery of the GFE sensors to LMSC, post-shipment tests and inspections were performed. Provisions had been made for test facilities for each of the sensors in an area adjacent to LMSC Systems Test Area 40. There the sensor equipments were inspected and given performance checks before delivery to LMSC for integration with the spacecraft.

Following delivery and installation on the spacecraft, a series of systems tests were performed to verify compatibility of each of the sensors and other GFE with the spacecraft, both individually and collectively. The series of tests with the spacecraft consisted of:

(1) Sensor module and sensor compatibility tests.

(2) Satellite vehicle and subsystem interface test.

(3) Baseline system test.

(4) EMI test.

(5) RFI test.

(6) Acoustic test.

(7) Thermal/vacuum test.

(8) Final system test.

The last test was followed by preparations for shipment of the satellite to AFWTR and subsequent pre-launch tests and operations. Refer to Paragraph 3F for additional discussion of the system integration tests.

I. DISCUSSION OF PROBLEMS

In view of the complexity of the Seasat satellite system, it is not surprising that a few problems were encountered in the process of GFE integration and interface control. Undoubtedly, the most pervasive problem was trying to maintain the schedule, both on the part of the GFE suppliers and LMSC, in regard to the original plan of integration and test as negotiated at the start of the contract.

At the outset, it was planned that engineering models or qualification models of the 5 sensors would be available to begin integration and compatibility tests with the sensor module by the middle of August 1977. As time went on, however, it became clear that both engineering models for integration tests and flight models of the sensors for final systems tests could not be supplied in accordance with the original plan. Accordingly, by mutual agreement among JPL, LMSC, and the sensor suppliers, the engineering models were deleted from the delivery schedule, and the satellite test schedule was revised to accommodate the delivery of flight models in November and December 1977. The exception to this practice was the VIRR, which was delivered ready for flight in June 1977. The baseline systems tests began on 26 January 1978.

The submittal of a number of calibration data inputs, distribution and review of the various test procedures, and availability of the test data printouts continued to plague the test operations throughout the first weeks of the systems test activities. However, by the time of the RFI test in mid-February, the test operations were accomplished rapidly and only minor difficulty was experienced in the receipt of test data for post-test analysis. Both the EMI and RFI tests were completed with no interference of any kind, in spite of a turn-off transient in the input line to the Tranet beacon that was later reviewed by the EMC Control Board and found to be of no consequence.

There were a number of other problems that occurred during post-shipment and compatibility tests that were corrected. In the case of the SASS, there was an inadvertent shutdown of the sensor system during integration tests. This problem was traced to the SASS high voltage power supply. With concerted effort, the SASS was removed, the defective unit was replaced, the complete system tested in a thermal/vacuum environment, the SASS was reinstalled, and the sensor module returned to satisfactory operation without substantial delay.

On delivery of the ALT, it was discovered that several items were in violation of the ICD: (1) the command interface circuit was at an incorrect value of input capacitance; (2) certain of the connector shells were cadmium-plated and not acceptable; and (3) certain cables were improperly covered. Corrective action was taken immediately and these discrepancies were properly resolved.

At the same time, the thermal control surfaces of the ALT processing unit was replaced to ensure that the proper materials and processing procedures had been followed.

Because of engineering changes made to the Nimbus-G unit of the SMMR, involving a diode failure, a failure in the analog-to-digital converter, and the scan drive belt failure in life tests, the SMMR was removed from the satellite and corrective action was taken according to the directives from JPL. The suspect diodes were replaced, and the scan drive belt modification installed. The unit was requalified by thermal/vacuum test.

Several problems occurred in the SAR system during integration and test that involved diagnostic studies and some corrective action. However, no major modifications or material changes were made.

The Tranet beacon suffered some inadvertent damage to its helix antenna during installation of thermal blankets to the satellite, the antenna cables were also damaged, and thermal grease was found migrating on the mounting plate surface. The grease was cleared and the thermal blanket covering the Tranet beacon was redesigned by LMSC. The antenna was reworked and replaced by APL, and new cables were provided by APL.

Following the detailed analysis of the satellite compatibility test data, the booster interface and simulated flight test was performed. The primary objectives of this next major test was to verify the Atlas booster-to-satellite interface connections, demonstrate final launch functional checks (R-1 day), and to verify the flight ascent sequence of events. This activity required the support of all normal launch facilities and personnel and resulted in successfully validating all interfaces and objectives with no significant problems.

Normally, the launch operations processing of the satellite would progress into the Mission Dress Rehearsal (MDR) test; however, concern was expressed by the USAF regarding the Atlas booster performance in recent flights. The performance data from these flights indicated temperature extremes in the boattail area of the Atlas not normally observed. An extensive investigation was conducted into this anomaly and resulted in approximately a 3-week delay in operations. Some modifications were made to the Atlas booster by GD/C along with special tests at vendors to alleviate the concern. After a review of the changes made and test results, final approval was received to continue the launch operations processing of the satellite.

This activity was resumed on 5 June, at a schedule position of launch minus 17 days, with the preparations for the MDR test. The objective of the MDR test was to rehearse the satellite launch preparations and selected abort sequences.

All objectives were satisfactorily fulfilled, and after the analysis of the resultant data, no satellite anomalies were observed. Following the MDR, launch preparations consisting of the umbilical quick-disconnect installation, the destruct system installation, and the helium pre-pressurization tests were conducted.

SECTION V

LAUNCH OPERATIONS

Subsequent to the final simulated flight test at Sunnyvale, the Agena bus was delivered to the launch base and located in the "root cellar" of Standard Launch Complex (SLC) -3 West for propulsion subsystem preparations and solar array installation. Following this activity, the Agena bus was transferred to the launch gantry and integrated with the Atlas booster. Figure 5-1 shows the Agena bus being lifted aloft for mating with the Atlas booster, which is shown in Figure 5-2. Following the Agena bus mating, the aft barrel section of the fairing was mechanically mated with the booster adapter assembly, and Figure 5-3 shows the aft barrel section being positioned in the gantry. Concurrently, the SM/SMSS was in final shipping preparations in Sunnyvale, and after the Agena bus to Atlas mating operations were completed, the SM/SMSS was delivered to the gantry and mated to the Agena. Figure 5-4 shows the SM/SMSS being lifted aloft for a mechanical mating with the Agena bus.

During the SM/SMSS to Agena mating operations, the systems test data van was located at the NASA facility (building 836) at South VAFB. This van, along with the 450-ft NASA antenna tower, was used as a remote site RF ground station and data processing facility for all launch base testing.

The satellite compatibility test was the first major test performed after completion of the mechanical mating operations. The primary objective of this test was to validate the satellite vehicle to AGE interfaces and to validate the Agena bus to SM/SMSS interface. This test encompassed functional subsystem and sensor system tests to verify that there was no handling or shipping damage. For the SAR, it was the final check before launch because of the need for a RF hat coupler over the SAR data link antenna to obtain status information that was subsequently removed during the satellite close-out operations. There were no significant problems resulting from the data analysis of this test.

The final launch conditioning followed with the actual launch taking place on 27 June 1978 GMT. Weather conditions on launch day were marginal with concern expressed about wind conditions, both ground winds and winds aloft. After a slight delay for a broken flame bucket water line, liftoff was achieved at 01:12:44 GMT (Figure 5-5).

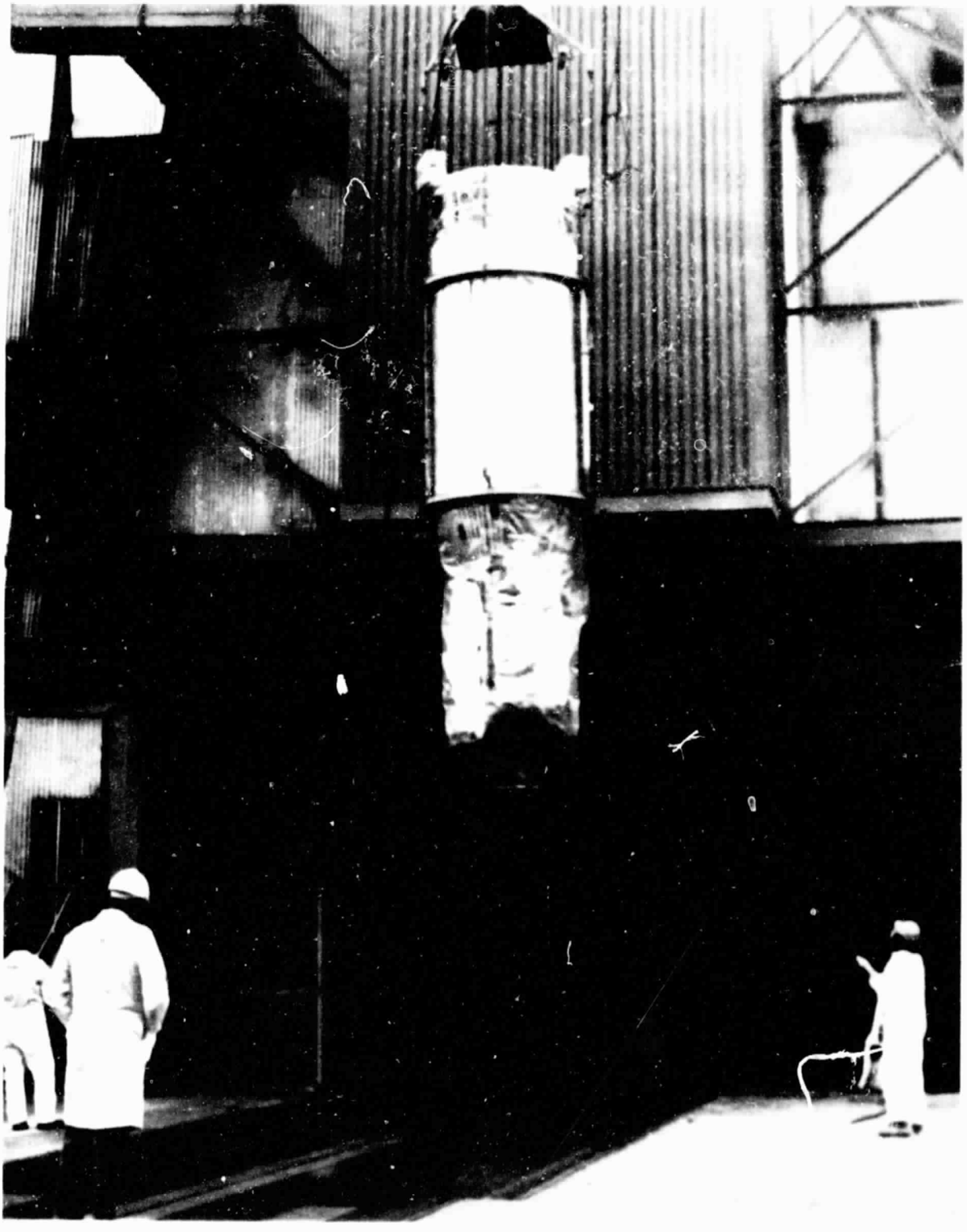

Figure 5-1. Agena Bus Vertical Lift for Final Mate with Atlas Booster

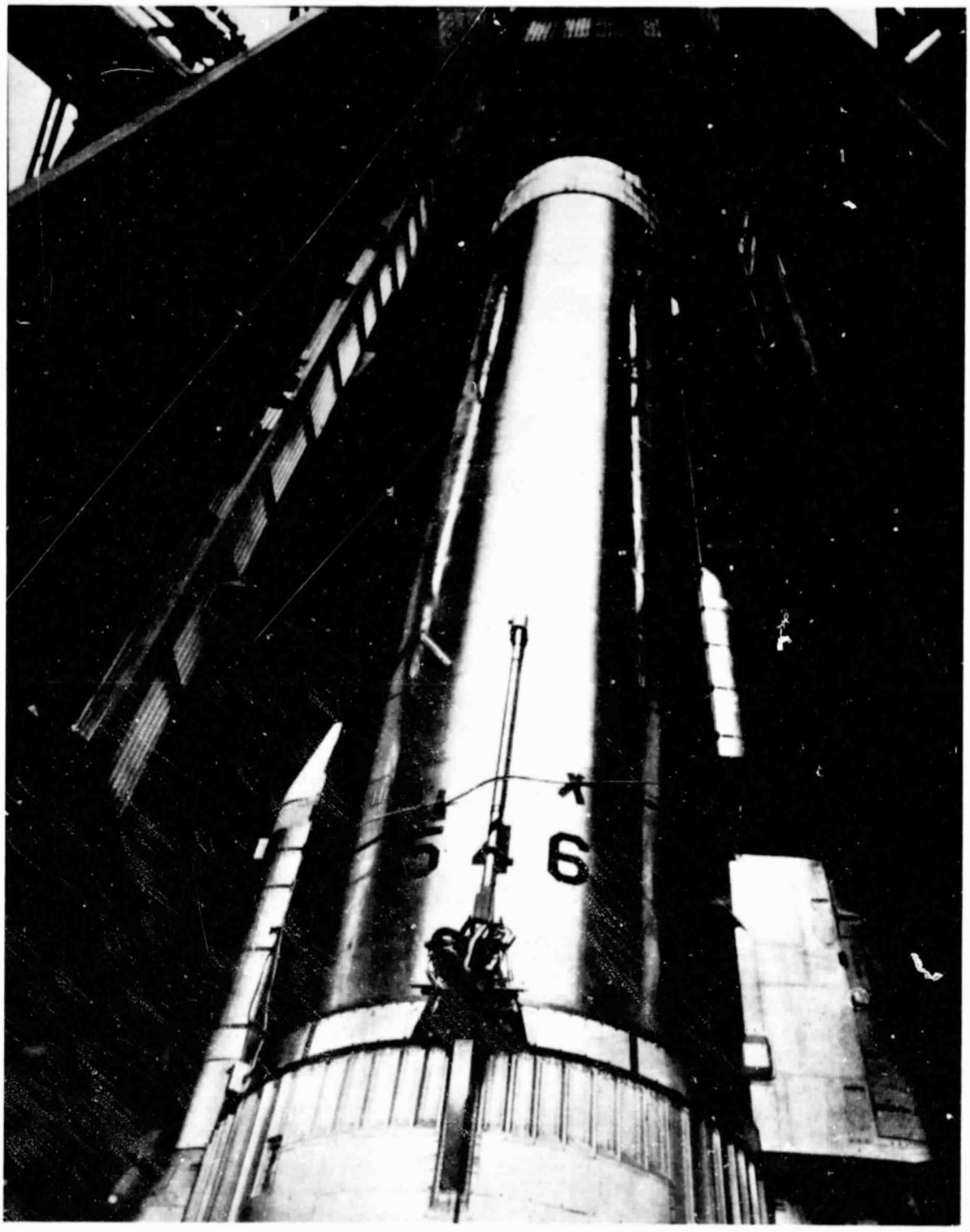

Figure 5-2. Atlas Booster in the SLC-3W Launch Complex

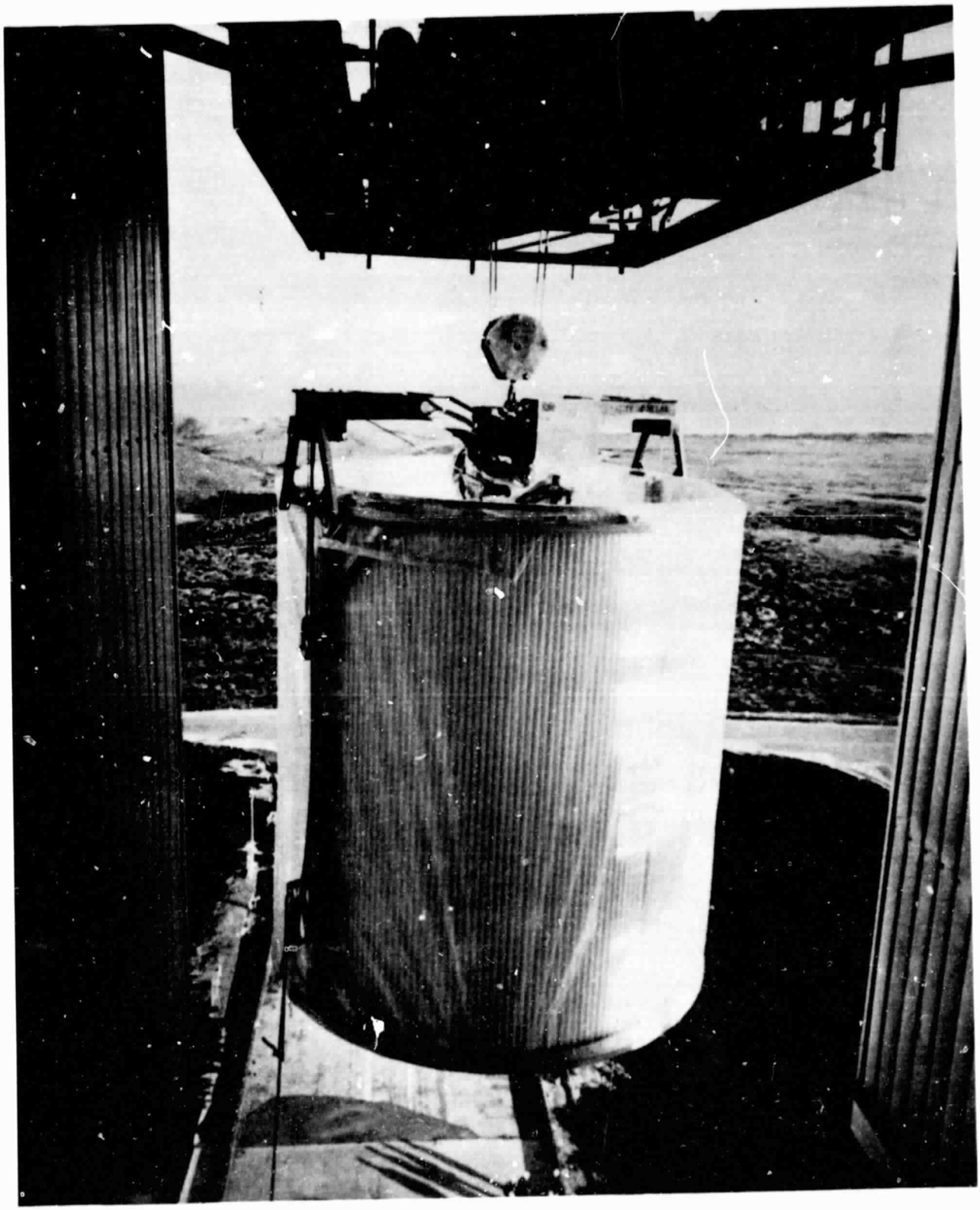

Figure 5-3. Fairing Section in the SLC-3W Gantry

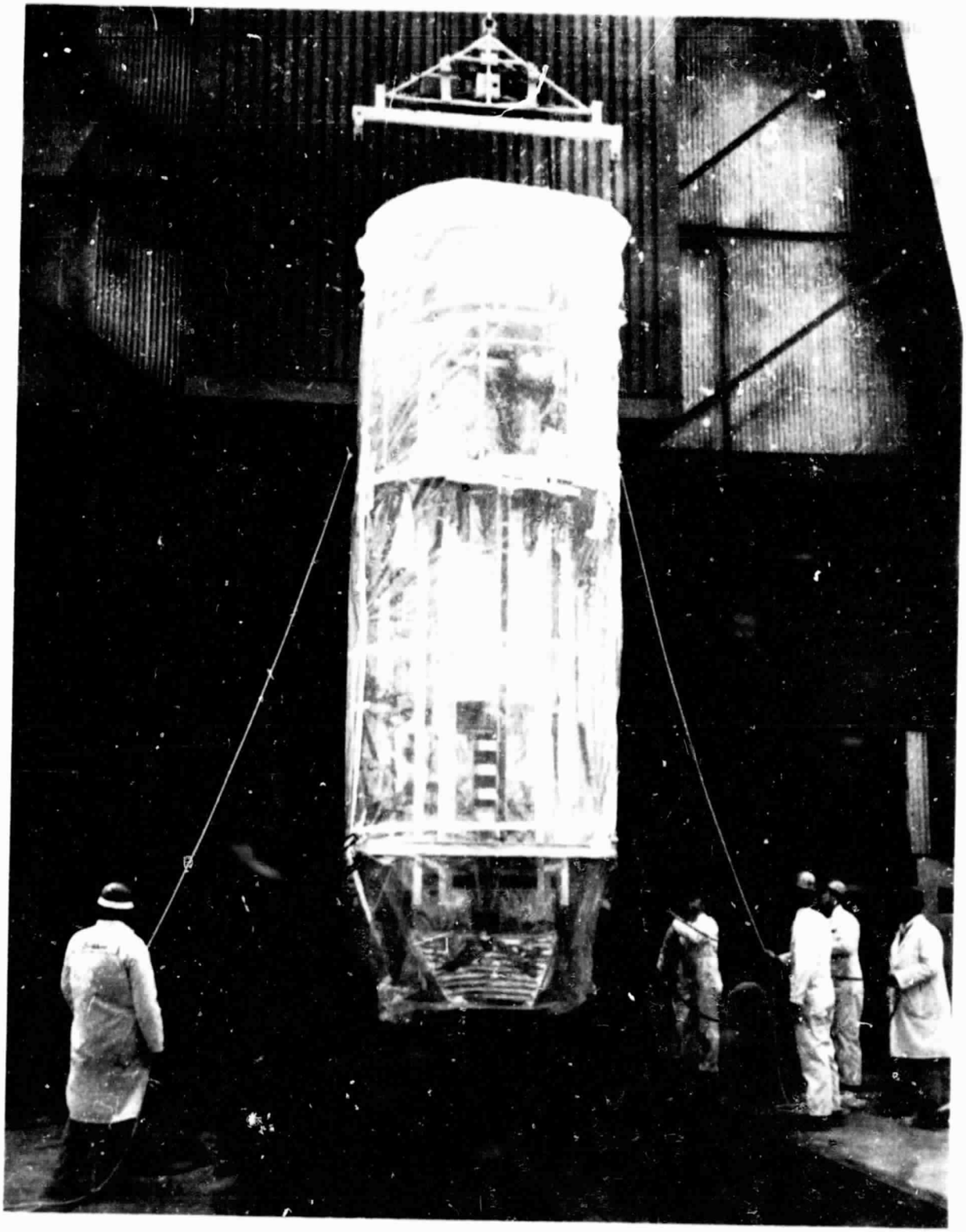

Figure 5-4. SM/SMSS Vertical Lift for Final Mechanical Mate with Agena Bus

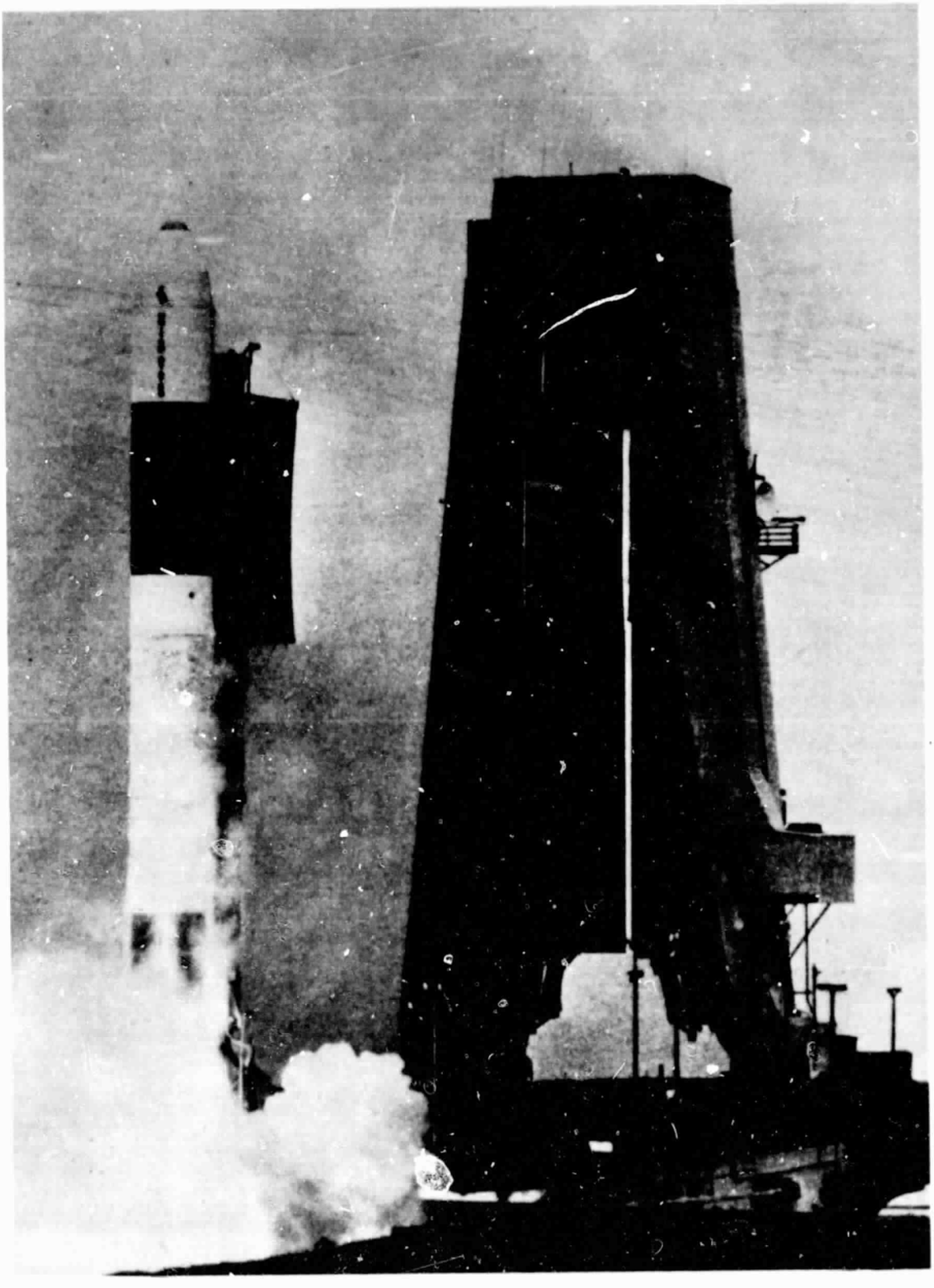

Figure 5-5. Seasat Lift-Off from SLC-3W
on June 26, 1978

SECTION VI

SATELLITE PERFORMANCE

A. INTRODUCTION

Seasat flight operations commenced at liftoff (1:12:44 GMT, 27 June 1948) and continued until the loss of all communications on 10 October 1978. The ascent sequence and the satellite orbit operations are summarized in Appendix A of Volume I of this report.

Satellite performance during ascent was completely nominal. Some problems in establishing the required attitude control performance were encountered at the beginning of orbital operations, but an acceptable workaround procedure was developed and the satellite was ready for sensor checkout by 3 July. The sensors, except for the SASS, were turned on one at a time on 3 July and satisfactory operation of sensor and satellite was demonstrated for each sensor. The SASS was not turned on at this time because the sensor representative preferred that the SASS remain on once it was turned on. SASS operation was successfully demonstrated on 6 July, and all sensors were successfully operated together on 7 July. The sensors were all left on at the conclusion of this demonstration and operated almost according to plan until flight termination. During the mission, several discrete failures occurred, resulting in a small amount of lost sensor data.

Perhaps the most significant achievement of the Seasat mission was the interference-free and simultaneous operation of all sensors and other RF transmitting and receiving equipment. Many combinations and modes were demonstrated with no indication of RFI or EMI between any sensor or satellite subsystem. Simultaneous EMI- and RFI-free operation of the sensors was only a system specification goal, not a requirements, and was considered one of the technical challenges of the mission.

In summary, the satellite support subsystems and sensors operated together to produce 99 days of microwave sensor data and 52 days of VIRR data. (The VIRR failed after 52 days in orbit.)

B. COMMAND AND DATA HANDLING

The equipment and performance for the Command and Data Handling (C&DH) subsystem are summarized in Table 6-1. The satellite ascent sequence was stored in both sections of the Command Processing and Central Timing Unit (CTU) at liftoff with the CTU clocks disabled. Telemetry and Sensor Interface Unit (TSU) 1 and NASA Standard Transponder (NST) 1 were selected and supplied ascent telemetry through the Type 7 ascent antenna, located on the booster adapter, from liftoff through Agena separation. Tape recorder 1 recorded data through liftoff and orbit injection (unfortunately, the data was improperly recorded at the ground station and was lost).

Table 6-1. Summary of Command and Data Handling Subsystem Equipment and Performance

Equipment	Performance
CTU Section A	Nominal
CTU Section B	Nominal (used on ascent only)
TSU 1	Nominal
TSU 2	Not used
NST 1	Nominal
NST 2	Not used
T/R 1	Nominal
T/R 2	Nominal
SED	Not used
Type 7 antenna (ascent)	Nominal
Type 7 antenna	Nominal
Type 28 antenna 1 (orbit)	Nominal
Type 28 antenna 2	Nominal
Type 14 RF switch	Nominal
Type 13 RF switch	Nominal

The CTU clocks were started by an Atlas radio discrete 20 s before separation. All Agena ascent events after separation were controlled, as planned, by the CTUs. There was same concern in the early design phases that storage of ascent commands in a volatile memory potentially sensitive to static charge (CMOS technology) might not be feasible. Analysis showed that with proper design precautions, which were taken, there would be no problems. The successful ascent of Seasat confirmed the analysis and design.

Type 28 orbit antenna 1 was deployed by stored command after second burn while the satellite was still horizontal. This was done so the orbit antenna could be used over the Alaska STDN station (ULA). Once the satellite pitched down, the ascent antenna would not provide enough gain to close the link. Completion of the reconfiguration required uplink of these three commands from ULA: (1) switch TSU to NST 2; (2) turn NST 1 off; and (3) turn NST 2 on. These

commands were not issued at ULA as planned because the tracking station did not have up-to-date pointing data and lock-in was not achieved. Acquisition prior to ULA at the Madrid, Spain STDN station (MAD) was also not achieved because of ground station procedural problems. Communication was, in fact, not achieved during the initial orbit operations, including the period when the satellite performed the planned pitch and yaw maneuvers to achieve vertical flight. By the time communications were re-established at the Ascension Island STDN station (ACN) on rev 2, orbit antenna 2 had deployed as planned. The Type 13 RF switch was ground-commanded to the orbit position, and no transponder switch was necessary, or made. Once the ascent phase was completed, CTU B was turned off and was not required for the remainder of the flight. All C&DH equipment performed as designed from liftoff to termination of operations with no failures or anomalous operation.

C. CONTROL SUBSYSTEMS SUMMARY

The ascent control, Orbital Attitude Control Subsystem (OACS), and Reaction Control Subsystem (RCS) equipment and performance are summarized in Table 6-2. The ascent attitude control system was a flight-proven Agena set. Reference signals were provided by two horizon sensors and a gyro triad. The control laws were implemented in the Augmented Electronics Assembly (AEA), which also controlled the hydrazine-fueled reaction control clusters.

Two sets of thrusters were available: (1) a high mode set rated at a nominal 22 kg (10 lb) for each thruster and (2) a low mode set rated at 1.1 kg (0.5 lb) for each thruster. Each set was capable of controlling satellite pitch, roll, and yaw. The high mode thrusters were sized to control satellite roll and pitch during Agena burns. The smaller thrusters provided controls at levels low enough to compensate the orbit adjust thrusters. The ascent control equipment also included a velocity meter counter to control Agena first and second burns.

The gyros were spun up before liftoff, and then enabled and uncaged by Atlas programmer and radio discretes, respectively, 1 s before nominal Atlas vernier engine cutoff. The high mode thrusters were activated by microswitches that sensed Agena clearance from the booster adapter. All subsequent ascent control commands were supplied from the CTUs.

A 90-deg roll was started approximately 10 s after separation to position the ascent horizon sensors for proper Earth viewing. It was completed in 36 s and the satellite then coasted until Agena first burn, which began at separation plus 75 s.

The ascent control system controlled the satellite through first burn, coast, second burn, orbit antenna 1 deployment, and satellite pitch down and yaw 90 deg, using the high mode thrusters. The remainder of the ascent sequence, including all deployments other than that for orbit antenna 1, were performed using the low mode thrusters and the scanwheel assembly horizon sensors. The ascent horizon sensors were disabled at the start of the satellite pitch and yaw maneuvers and these maneuvers were performed on gyro reference

Table 6-2. Summary of Control Subsystems Equipment and Performance

Equipment	Quantity	Performance
Ascent		
Augmented electronics assembly	1	Nominal
Horizon sensor assembly	1	Nominal
Gyro reference assembly	1	Nominal
Velocity meter	1	Nominal
Velocity meter counter	1	Nominal
Orbit		
Scan wheel assembly left	1	Anomalous
Scan wheel assembly right	1	Nominal except when sun in the FOV
Control logic assembly	1	Nominal
Magnetic control assembly	1	Nominal
Roll reaction wheel	1	Nominal
Pitch momentum wheel	1	Nominal
Magnetometer (3 axes)	1	Nominal
Electromagnets	3	Nominal
Dual sun sensor heads	2	Nominal
Sun sensor electronics	2	Some data anomalies with sun at edge of sensor FOV
Reaction Control System		
High mode reaction control clusters	2	Nominal
Low mode reaction control clusters	2	Nominal
Hydrazine tanks	2	Nominal
Latching solenoid valves	2	Nominal
Orbit adjust thrusters	2	Nominal

only. The scanwheels were on at liftoff, and the pitch and roll error signals were connected to the AEA at the same time that the low mode thrusters were enabled.

Two orbit adjust thrusters, oriented nominally colinear with the velocity vector and pointed in opposite directions, were mounted near the center of gravity to provide translation with minimum upsetting momenta. These thrusters were procured from Hamilton Standard and were rated at a nominal 2.3 kg (5 lb). The orbit attitude yaw determination reference was supplied for ground processing by two dual-head sun sensors from Adcole. Yaw on-orbit control was supplied by gyro compassing and roll error cross-coupling, and no explicit determination of yaw attitude was performed on board the satellite.

Once a stable nose-down attitude was achieved and the proper operation of the electrical power and command and data handling subsystems established, an attempt was made to transfer attitude control from the RCS to the momentum wheel configuration. The transfer was made on the ascending portion of rev 17 over MAD. The momentum wheel mode worked well from MAD, over the northern latitudes, and down until near fade at ULA, when errors became unacceptably large quite rapidly. A transfer back to the hydrazine system was made immediately at the Hawaii STDN station (HAW). Three other attempts at wheel capture were made between 27 June and 5 July. These attempts and analysis of the flight data led to the conclusion that the left scanwheel output contained anomalous spikes that appeared to be sun-related (glint or reflections), and that the right scanwheel data were erroneous when the sun was in the field-of-view (FOV) of the scanner. Long term successful capture, using only the right scanwheel, was achieved on 5 July 1978, when the sun no longer appeared in the FOV of the right scanwheel. During the interim, the RCS was used to provide nearly nominal control.

The planned magnetic trim of the OACS was successfully accomplished on 11 July. A roll reaction wheel speed bias adjustment was made on 13 July to improve yaw pointing performance. Near-nominal orbital attitude control was maintained from 13 July to 8 August, using only the right scanwheel signal processor and all momentum wheels.

A full day of definitive attitude determination data was obtained on 20 July for performance evaluation. The geocentric maxima in pitch, roll, and yaw were 0.458, 0.486, and 1.4 deg, respectively. Careful inspection of attitude data recorded during several later real-time passes indicated that this day of data was representative of single signal processor performance.

On 8 August 1978 sun interference was again experienced, as predicted, in the FOV of the right scanwheel. This problem required going to a mode of operation (Mode 5) in which the right scanwheel's signal processor output from the roll channel control loop was disconnected during expected sun interference periods, permitting the satellite to drift. The duration of Mode 5 was approximately 6 min, and the attitude excursions were typically 0.35, 0.65, and 2.1 deg for pitch, roll, and yaw, respectively. The satellite recovered from the open loop perturbation in 5 to 10 min.

On 4 September, with the sun on the horizon, 2 Mode 5 disconnects were required each revolution. However, real-time pitch and roll data indicated minimal attitude disturbances during the second disconnect. It is reasonable to assume that the same level of performance was experienced during the interval from 4 September to 17 September with two disconnects, as was experienced from 8 August to 4 September with one disconnect. Nominal operation using only the right scanwheel processor was resumed on 12 September and continued until mission termination.

A series of five orbit adjust thruster firings were performed during the period 15 August through 10 September. A very precise ground track was established over the Bermuda STDN station (BDA) so the ALT could be calibrated using the LRA. Each firing required switching from the momentum wheel to the RCS and

back again. The series was completely successful with the orbital parameters established well within tolerances, as follows:

Parameter	Desired	Actual	Allowable Error
Combined semi-major axis change (km)	+0.441	+0.438	±0.100
Combined eccentricity change	$+2.5 \times 10^{-5}$	$+2.5 \times 10^{-5}$	$\pm 5.0 \times 10^{-4}$
Combined argument of perigee change (deg)	+4.058	+4.014	±20.0

The result was a ground track that repeated within ±5 km (2.7 nm) of the nominal ground target point every 3 days until mission operations terminated.

D. ATTITUDE CONTROL SYSTEM PERFORMANCE

Most of the following detail on the in-flight performance of the Seasat Attitude Control System (ACS) was originally contained in LMSC document EM S2.1-008 dated 24 September 1978. This material was supplemented with data collected and analyses made after the EM release date and is included here because control system (ascent and OACS) performance was particularly important to the success of the mission, and anomalies were encountered.

Table 6-3 shows the different modes of operation that were successfully demonstrated in flight. Table 6-4 is a summary of the attitude performance for the Seasat mission. Overall, it can be stated that the ACS performed adequately, satisfying most mission requirements, and meeting the specification nearly all of the time for most of the scientific sensors. The SASS attitude control requirements were met 65 percent of the time.

1. Launch Phase

The launch phase began with liftoff and extended to satellite second burn cutoff. All initial orbit requirements were met. This portion of the flight successfully demonstrated that the ACS met the following requirements:

(1) Performance of the 90-deg roll maneuver after Atlas separation.

(2) Orienting the spacecraft and establishing the proper 3-axis attitude for first and second burn ignitions.

(3) Proper pitch and yaw thrust vector control during first and second burns.

(4) No adverse effects of vehicle bending or fuel slosh on control performance during burn periods.

Table 6-3. ACS Modes of Operation Demonstrated in Flight

Modes	Flight Demonstration
90-deg roll maneuver	Established correct attitude for first burn ignition
Ascent horizontal flight	Maintained 3-axis control with gyro-compassing in high gain operating mode utilizing hydrazine
Thrust vector control	Control of pitch and yaw attitude through hydraulic gimballing of engine during first and second burns
90-deg pitch-down and 90-deg yaw right	Established correct attitude for on-orbit operations in vertical mode
Vertical flight (hydrazine control)	Maintained proper 3-axis control with gyro-compassing in low gain operating mode utilizing hydrazine. Demonstrated low gas usage in this mode
Momentum control	Long term 3-axis control utilizing wheels for momentum bias and speed changes to maintain attitude control
Magnetic desaturation	Provided unloading of wheels with magnetic torques
Double scanwheel operation	Not demonstrated because of the anomalous behavior of the left scanwheel
Single scanner operation (alternate mode)	Provided pitch and roll attitude information as well as momentum control
Hydrazine desaturation (alternate mode)	Provided unloading of wheels by use of mass expulsion (hydrazine)
Orbit trims	Maintained 3-axis control during orbit trim periods
ACS trims	Improved ACS performance to provide in-specification performance most of the time through use of parameter estimator and in-flight magnetic trims, gain adjusts, and speed bias changes
Sun sensor system	Provided yaw attitude data.

Table 6-4. Attitude Performance Summary

Date	Day	Rev	Procedure	Pointing Control Percentages	Remarks
6/27	178	0	Revs 17, 30, 60, and 74 attempted wheel captures. 97.9% of interval between revs 17-114, pitch and roll was less than 0.6 deg and yaw less than 2.1 deg		Maintained adequate control for sensor turn-on and system checks
7/5	186	114	Start wheel operation (right scanner only)		
		200			
7/13	195	237	Complete ACS trims (right scanner operation only)	VIRR, SMMR, SAR, and ALT within pointing control requirements 100% of time. SASS, 68% of the time	ALT within pointing control requirements 97% of time; SMMR, 100% of the time; VIRR and SAR, 99% of the time; SASS, 82% of the time for interval between revs 237 and termination of operations
		400			
		600			
8/8	220	605	Start Mode 5 and Mode 2 switching to eliminate sun in FOV of right scanner	SMMR within pointing requirements 100% of the time; VIRR and SAR, 97-99% of the time; ALT, 91% of the time; SASS, 65% of the time	
8/13	225	682	Start Mode 5 only. Roll disconnect to wheels		
		800			
9/4	247	997	Start Mode 5A and Mode 5B to eliminate sun on horizon effects		
		1000			
9/12	255		Stop Mode 5 operation. Full rev single scanner operation	Pointing control same between revs 237-605	
10/12			Termination of operations		

(5) Precise measuring of spacecraft delta velocity during first and second burns and issuing of engine shutdown signals.

(6) Performance of gyro compassing function between first and second burn coast period to provide yaw gyro drift trim.

(7) Maintenance of proper 3-axis control during complete launch phase in high gain operating mode with hydrazine.

(8) Performance of sequence of events.

2. Orbit Insertion

The orbit insertion phase began at satellite second burn cutoff, and extended until momentum wheel capture. This portion of the flight successfully demonstrated the capability of the ACS to:

(1) Orient the satellite to a nose-down vertical flight attitude.

(2) Maintain 3-axis control in the low gain operating mode with hydrazine.

(3) Properly interface scanwheels with AEA and GRA.

(4) Demonstrate 3-axis attitude reference and gyro compassing control in a nose-down, yaw-right orientation.

(5) Maintain 3-axis control during deployments.

(6) Cause no anomalous structural interaction behavior between appendages and the hydrazine control system.

(7) Maintain 3-axis control during fuel and oxidizer venting phase.

(8) Dampen satellite rates with hydrazine control to within capture capability of the momentum wheel control system.

(9) Achieve 3-axis capture with the momentum control system.

(10) Perform special experiment using open-loop gyro control without use of scanwheels for two orbits.

(11) Successfully switch back and forth between hydrazine control and momentum control during anomaly investigation of scanwheels as well as orbit trim phases.

The ACS hydrazine system demonstrated the ability to maintain proper 3-axis attitude in performing the orbit trim functions. Disturbance torques from the orbit adjust thrusters were controlled as predicted.

3. Initial Observation Phase

The initial observation phase began when the satellite was in the momentum wheel attitude control mode and ended when the initial cruise parameters were achieved. During this phase of the operation, the scientific sensors were powered and checked out in a systematic manner. ACS wheel captures during this period were complicated by possible sun interference in both ACS scanwheels, causing anomalous roll and pitch attitude signals. During the period of 27 June to 5 July 1978, four wheel captures were tried of approximately 50-min durations each. However, because of sun interference, the capture attempts were aborted and control was switched back to RCS hydrazine control. During the wheel capture attempts (50-min periods average), the attitude errors were as follows: (1) pitch, less than 3.5 deg; (2) roll, less than 9.0 deg; and (3) yaw, 8 to 16 deg. During hydrazine control, the attitude errors were less than 0.6 deg for pitch and roll and less than 2.4 deg for yaw. This performance was achieved 97.9 percent of the time during the period of 27 June to 5 July (Table 6-4) and was calculated as follows:

$$\frac{114 \text{ rev} - 17 \text{ rev} \left(100 \frac{\text{min}}{\text{rev}}\right) - \left(4 \text{ wheel captures} \times 50 \frac{\text{min}}{\text{capture}}\right)}{(114 - 17) \left(100 \frac{\text{min}}{\text{rev}}\right.} = 0.979$$

Although problems were being experienced with attitude control during this period (27 June to 5 July), a large majority of the time (97.9 percent) reasonable control was being maintained that did not deter scheduled power-on of the sensors and their checkout sequences. On 5 July, the sun was no longer in the FOV of the right scanner, and a successful wheel capture was achieved with right scanner operation only.

4. Calibration/Observation Phase 1

During the period 5 July to 13 July 1978, a performance evaluation of the ACS wheel system was performed to gather data for ACS trims. At the beginning of wheel control prior to ACS trims, typical attitude errors were: pitch, -0.6 to +0.4 deg; roll, 0.6 to 1.0 deg; and yaw, -4.4 to +8.4 deg. The on-orbit trimming process consisted of estimating those control system and environment parameters that were subject to significant uncertainty, and commanding corresponding changes in those with on-orbit adjustment provisions. Parameters in the estimation process were:

(1) Magnetic momenta biases (3).

(2) Products of inertia (3).

(3) Magnetic desaturation compensation gains (2).

(4) Momentum decoupling gains (2).

Parameters with on-orbit adjustment provisions were:

(1) Magnetic momenta biases (3).

(2) Roll axis wheel momentum bias.

(3) Magnetic desaturation compensation gains (2).

The final trim settings were:

(1)	Pitch and roll magnet	3,000 pole-cm
(2)	Yaw magnet	5,000 pole-cm
(3)	Feed forward gain (D1)	1.28
(4)	Feed forward gain (D3)	0.64
(5)	Roll reaction wheel bias speed	200 rpm

ACS trims were successfully accomplished on 10 July and 13 July to improve ACS performance to -0.6 to +0.2 deg in pitch, -0.4 to +0.5 deg in roll, and -1.1 to +1.5 deg in yaw. The following trim capabilities were demonstrated:

(1) Satellite residual magnetic trim capability about 3 axes.

(2) Gain adjusts to reduce cross-coupling effects of magnetic desaturation torques.

(3) Roll wheel speed bias adjustments.

(4) Successful use of parameter estimator program to determine correct trim commands.

It should be pointed out that the residual magnetic field of the spacecraft was as predicted and well within the capability of the magnets. Also, no detrimental effects on magnetic control performance were observed as a result of sensor power switching.

5. Calibration/Observation Phase 2

ACS final trims were accomplished on 13 July 1978. A full day of definitive attitude determination data was obtained for day 201 (20 July) for performance evaluation.

The determined roll and pitch attitudes were relative to the geocentric reference frame. These were converted to the geodetic reference frame, using orbital ephemeris tables supplied by GSFC, for direct comparison with sensor pointing requirements as specified in the Seasat Satellite System Specification, LMSC document 1429000. For each scientific instrument, the geodetic roll, pitch, and yaw angles were transformed to cone, cross-cone, and rotation,

together with corrections to account for pre-flight measured sensor alignment errors. The determined values of cone, cross-cone, and rotation were computed at each of the local maxima of roll, pitch, and yaw during the complete day 201 interval. Table 6-5 documents the results of the computations, and it should be pointed out that the maxima shown for each experiment about each axis did not occur simultaneously. The geocentric maxima in pitch, roll, and yaw were 0.458, 0.486, and 1.4 deg, respectively, during this period. Careful inspection of attitude data recorded during real-time data passes indicates that day 201 was representative of typical performance during the interval between 13 July and 8 August 1978, and therefore Table 6-5 data is typical of control performance while on single scanner operation with the wheel and magnetic control system.

Note that Table 6-5 shows that four out of five of the experiments were within specification 100 percent of the time from 13 July to 8 August. In fact, the SMMR design goal was met.

6. Calibration/Observation Phase 3

On 8 August 1978, sun interference was experienced in the FOV of the right scanwheel, as predicted. This problem required going to a mode of operation (Mode 5) in which the right scanwheel's signal processor output from the roll control loop was disconnected during expected sun interference periods, permitting the satellite to drift. The duration of Mode 5 was approximately 6 min, and the attitude excursions were typically -0.6 to -0.3 deg in pitch, -0.6 to +0.6 deg in roll, and -1.4 to +3.1 deg in yaw. The satellite would recover from Mode 5 operation (to attitude control accuracy similar to day 201) in 5 to 10 min.

On 4 September 1978, with the sun on the horizon, two Mode 5 disconnects were required each revolution. However, real-time data indicated minimal attitude disturbances during the second disconnect. It was reasonable to expect that the same level of performance was obtained during the interval from 4 September to 17 September as with the single Mode 5 disconnects.

7. Calibration/Observation Phase 4

On 12 September 1978, the sun was no longer in the FOV of the right scanner, so Mode 5 disconnects were discontinued. Real-time pitch and roll data indicated attitude performance similar to that for the period from 13 July to 8 August (full single scanner operation). This flight interval demonstrated the following:

(1) Maintenance of 3-axis control through use of momentum bias and application of speed changes to wheels.

(2) Single scanwheel operation in providing pitch and roll attitude signals.

Table 6-5. Attitude Pointing Performance

Sensor	Flight Performance (Maximums)				System Specification Requirements				Design Goals			
	Cone (Deg)	Cross-Cone (Deg)	Rotation (Deg)	Rate (Deg/S)	Cone (Deg)	Cross-Cone (Deg)	Rotation (Deg)	Rate (Deg/S)	Cone (Deg)	Cross-Cone (Deg)	Rotation (Deg)	Rate (Deg/S)
VIRR	0.34	0.42	-	-	0.71	0.71	-	-	-	-	-	-
SAR	0.47	0.56	-	0.001	1.0	1.0	-	<0.[illegible]	0.5	0.5	-	<0.0001
SMMR	0.29	-	-	-	-	-	-	-	0.5	-	-	-
ALT	0.35	0.47	-	-	0.5	0.5	-	-	-	-	-	-
SASS[a] No. 1	0.43	0.94	1.03	-	0.35	0.60	0.64	-	-	-	-	-
No. 2	0.23	1.07	0.95	-	0.35	0.60	0.64	-	-	-	-	-
No. 3	0.44	0.83	1.13	-	0.35	0.60	0.64	-	-	-	-	-
No. 4	0.25	0.80	1.23	-	0.35	0.60	0.64	-	-	-	-	-

[a]Relative to antenna mounting surface.

Note: All values relative to geodetic reference frame. VIRR, SAR, SMMR, ALT includes 0.1 deg (RSS) for electrical boresight.

(3) Unloading of the wheels through use of magnetics without requiring expendables.

(4) Development of yaw attitude from sun sensor system data.

(5) Backup mode using hydrazine thrusters for unloading of the wheels.

(6) Proper 3-axis control during orbit adjusts.

(7) All-inertial mode with gyro reference only.

(8) Ability to disconnect roll signal to wheels.

(9) Ability to maintain reasonable control during scanwheel sun interference periods.

(10) No structural interaction effects between the wheel control system and deployed antennas.

Evaluation of data after the attitude control system trims showed that the pitch momentum wheel oscillated with the amplitude of ±0.25 ft-lb-s (±36.5 rpm) above and below a nominal operating speed of 2200 rpm. The roll reaction wheel was oscillating ±1000 rpm about the bias speed of -200 rpm. The right and left scanwheels were oscillating ±300 rpm about their bias speed of 900 rpm. These oscillations were primarily because of principal axis misalignment.

Data from the parameter estimator also indicated a principal axis misalignment of 0.5 deg on single scanner operation. This was because of scanwheel calibrations at the subcontractor's facility being accomplished with both scanners operating (normal mode of operation).

Analysis of the data indicates that the wheel speed excursions, the effectiveness of the magnetic desaturation in managing wheel speed, was as predicted for single scanner operation. Solar torques acting on the satellite were not directly measured from the data; however, it can be concluded that the solar torques were within approximately 15 percent of the predicted values, based on observation of measured variables (wheel speeds, sensed attitude, and magnet activity).

8. Evaluation of Orbital Attitude Control System Performance

a. General. The available data used for this analysis was for the entire day 213 and for the latter half of day 225. August 1 (day 213) was in the period after ACS trimming was completed and before horizon sensor interference resumed; data from this day is representative of the 13 July to 8 August period and presumably typical also of the post-12 September era. On day 225, revs 679 to 682 were subjected to sun interference with horizon sensors, but no special ACS commands were used to avoid these effects. For revs 683 to 686 on the same day, Mode 5 was used. For purposes of this analysis, revs 679 to 682 were considered typical of days 220, 221, and 225, and revs 683 to 686 were considered typical of Mode 5 performance.

Therefore, the following three classes of ACS behavior were investigated:

(1) Class 1. The trimmed-up undisturbed periods of days 195-219, 222-224, and 255-283.

(2) Class 2. Days 220, 221, and 225, which had sun interference with horizon sensors, but Mode 5 was not used.

(3) Class 3. Days 226-254, during which Mode 5 was used regularly.

Class 1 is 56 days, typified by day 213; class 2 is 3 days, typified by revs 679-682 of day 225; and class 3 is 29 days, typified by revs 683-686 of day 225.

Sensor requirements are given in geodetic cone, cross-cone, and rotation errors for each sensor boresight. To compute actual offsets in these terms, geocentric attitude was converted to the equivalent geodetic attitude for a truly polar orbit. The differences between this approximation and true geodetic attitude for the Seasat inclined orbit would not significantly affect the analytical conclusions.

b. SMMR. There was no control requirement placed by the SMMR. The design goal of less than 0.5-deg error in boresight cone angle was often achieved.

c. VIRR. During the 3-day class 2 period, pitch and roll were sometimes disturbed sufficiently to exceed the VIRR requirements of 0.7 for each axis (they coincided with cone and cross-cone). No more than 15 percent of each rev was out of tolerance, and no out-of-tolerance behavior was observed during classes 1 and 3 behavior. Therefore, ACS performance for the VIRR was within specification for 99.5 percent of the period from days 195-283, as shown by the following calculation:

$$(0.85 \times 3 + 1.0 \times 85) \div 88 = 0.995$$

d. SAR. To meet the SAR pointing control requirements, the SAR boresight had to be held within 1 deg in cone and cross-cone. The relationships of control error to boresight error are:

$$\Delta \text{ cross-cone} = (\Delta \text{ pitch}) \cos 20.5° - (\Delta \text{ yaw}) \sin 20.5°$$

$$\Delta \text{ cone} = -(\Delta \text{ roll})$$

Roll error exceeded 1 deg a negligibly small amount of the time, but the indicated mapping of pitch and yaw to cross-cone was out of tolerance 6.3 percent of the time for 3 revs in class 2 and 2.8 percent of the time for the four

analyzed revs of class 3 (Mode 5). Therefore, ACS performance was in tolerance 98.9 percent of the mission, as shown by the following calculation:

$$(1.0 \times 56 + 0.937 \times 3 + 0.972 \times 29) \div 88 = 0.989$$

The other SAR requirement was that the SAR boresight rate be less than 0.01 deg/s. The largest verifiable rate seen in the data was 0.002 deg/s, occasionally observable in yaw during all 3 classes of ACS behavior. This maps to less than 0.001 deg/s and the SAR boresight. So, apparently the design goal was achieved.

e. ALT. The ALT required pitch and roll (cone and cross-cone) each to stay within 0.5 deg. During four revs analyzed for class 2 behavior, either or both pitch and roll exceeded requirements an average of 584 s each rev, or 9.7 percent of the time. During the four revs of Mode 5, the average outage was 510 s, or 8.4 percent. Therefore, the ACS performance was in tolerance 96.9 percent of the time, as shown by the following calculation:

$$(1.0 \times 56 + 0.903 \times 3 + 0.916 \times 29) \div 88 = 0.969$$

f. SASS. For each of the 4 SASS boresights, the ACS control requirements were 0.50 deg, 0.35 deg, and 0.6 deg for cross-cone, cone, and rotation, respectively. Because of the ±45 deg and ±135 deg arrangement in clock and the constant 42-deg cone angle of the boresights, the requirements on the set of four can be simplified with respect to attitude deviations. Figure 6-1 shows these requirements as functions of two parameters: the absolute value of yaw, and the sum of the absolute values of pitch and roll. Control requirements for all SASS boresights are met only in the lower left (cross-hatched) area of Figure 6-1.

For class 1 behavior, two revs were analyzed in detail: rev 501 because of its relatively large yaw excursions, and rev 509 because of its relatively quiescent yaw behavior. The results showed 2680 s out of tolerance on rev 501 and 1155 s out of tolerance on rev 509. Average in-tolerance time was therefore 68.2 percent.

For class 2 behavior, again two revs were subjected to analysis: rev 681 had 4350 s out of tolerance and rev 682 had 2315 s out of tolerance. Average performance over the two revs was therefore 44.8 percent for in-tolerance time.

For class 3 behavior, the succeeding two revs were analyzed: rev 683 showed 2485 s out of tolerance and rev 684 showed 1695 s out of tolerance. The average in-tolerance time was therefore 65.4 percent.

Thus, ACS performance for the SASS was in tolerance 66.5 percent of the time, as shown by the following calculation:

$$(0.682 \times 56 + 0.448 \times 3 + 0.654 \times 29) \div 88 = 0.665$$

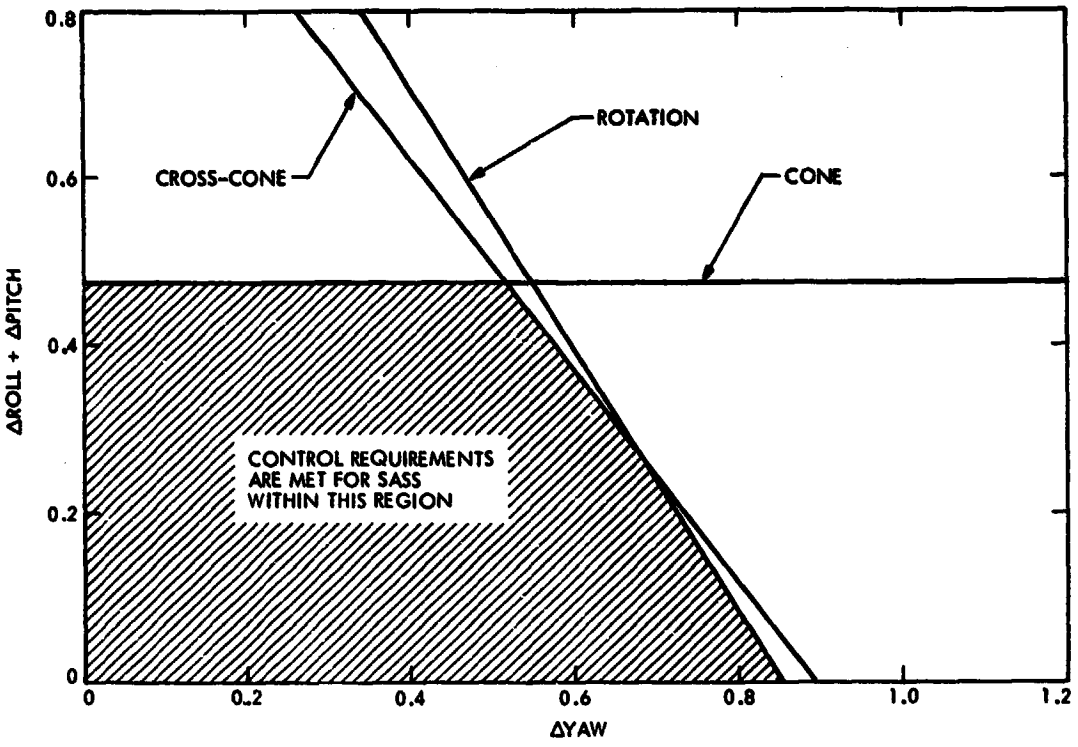

Figure 6-1. SASS Attitude Control Requirements

9. Orbital Insertion Propulsion Subsystem

The Orbital Insertion Propulsion Subsystem (OIPS) provided the satellite third stage propulsion for initial orbit injection, and then circularization. The OIPS equipments and performance are summarized in Table 6-6.

The rocket engine was the latest model of the Bell hypergolic rocket engine used on several hundred Agena flights. The propellants were high density nitric acid (HDA) and unsymmetrical dimethyl hydrazine with silicone oil (USO). The propellants were supplied to the thrust chamber by turbine-driven pumps. The turbines were initially spun up by pyro-activated cartridges, and then run on small amounts of diverted HDA and USO. The complete engine with nozzle extension was swiveled in pitch and yaw by hydraulic actuators controlled by the AEA.

The OIPS first burn was initiated by CTU command 75 s after separation. Shutdown was on velocity meter counter command just over 250 s later, and resulted in the planned elliptical orbit. The satellite then coasted for about 47 min. A second burn was initiated by the CTU at apogee and was terminated in approximately 7 s by the velocity meter counter. Subsequent to the second burn, the fuel and oxidizer tanks were dumped in sequence to avoid the possibility of slow leaks perturbing the orbit or a slow leak in the oxidizer tank causing bulkhead

Table 6-6. Orbital Insertion Propulsion Subsystem Equipment and Performance

Equipment	Quantity	Performance
Dual start engine	1	Nominal
Hydraulic power package	1	Nominal
Yaw hydraulic actuator	1	Nominal
Pitch hydraulic actuator	1	Nominal
Propellant isolation valves	2	Nominal
Propellant tank assembly	1	Nominal
Pyro helium control valve	1	Nominal
1612 in^3 He tank	1	Nominal
2760 in^3 He tank	1	Nominal

reversal between the fuel and oxidizer tanks, precipitating a hypergolic disaster.

All elements of the OIPS performed flawlessly and a very nominal satellite injection was achieved despite the somewhat "hot" Atlas. The resulting nominal versus achieved orbit parameters follow:

Parameter	Nominal	Achieved
Perigee (km)	793.7 (427.8 nm)	7.99.4 (430.9 nm)
Eccentricity	0.00078	0.00069
Inclination (deg)	107.93	108.02
Period (min)	100.68	100.55

10. Electrical Power Subsystem

The Electrical Power Subsystem (EPS) equipment and performance are summarized in Table 6-7. The EPS was transferred to internal power about 1 h prior to launch and performed as required throughout the ascent sequence. The inverter supplied 115 V ac to the velocity meter counter and was only used on ascent. A single dc-dc converter was used on ascent to provide regulated power

Table 6-7. Electrical Power Subsystem Equipment and Performance

Equipment	Quantity	Performance
Solar Array Modules (SAM)	2	Nominal
Solar Array Drive Electronics (SADE)	1	Nominal
Solar array drive motor	1	Nominal
Solar array slip rings	2	Probable failure
Main Power Control and Distribution Unit (MPCDU)	1	Nominal
Power Control Logic Assembly (PCLA)	1	Nominal
Converter Type 76	4	Nominal (only 3 used)
Inverter	1	Nominal
Type 40 batteries	2	Nominal
Destruct batteries	2	Not Used
Charge Current Controller (CCC)	2	Nominal
Pyro control unit	2	Nominal
Aft control and instrumentation box	1	Nominal
Destruct discrete box	1	Nominal
Harnesses	93	Nominal
Coaxial cables	15	Nominal

for the velocity meter, the signal conditioning, and to keep the VIRR motor operating. Once on orbit, this converter was reconfigured as a backup for VIRR and SMMR power. One of the other two converters was turned on once orbit was achieved to provide regulated power for the SASS and for signal conditioning. The fourth converter was available as a backup for SASS and signal conditioning power, but was never required. The inverter and the three dc-dc converters planned for use during the mission all performed as required and, in fact, maintained regulation within specification limits even during the period when regulated bus voltage dropped below the acceptable minimum.

Agena booster separation and deployment and the uncaging of all equipment was nominal, indicating proper functioning of the pyro control units and destruct discrete box.

The solar arrays were the first appendages deployed after a stable nose-down attitude was achieved. The solar arrays were identical in construction, stowed configuration, and deployment, so that when first deployed one array was not exposed to the sun and was oriented 180 deg about its axis of rotation with respect to the other array. A canned stored program sequence was immediately transmitted from the ground as planned, and resulted in coalignment of the arrays with each other and with the arrays facing the sun. Solar array auto track when the sun was available, and commanded dark rate array rotation during eclipse, was maintained as planned throughout the remainder of the mission.

All switching functions required of the MPCDU were executed as commanded throughout the flight. Similarly, there were no errors in engineering telemetry, indicating that the PCLA performed to requirements throughout the flight.

On rev 893 (28 August 1978) the satellite experienced a low bus voltage of 22.7 volts. The ALT, which had a low voltage protection circuit (the only device so equipped), switched to a lower power mode. At the time of this occurrence, it was believed that the ALT had experienced a failure, as the low voltage condition occurred out of tracking station coverage and R/T statusing did not indicate any undervoltage power condition. (However, battery voltages during charging were lower than they had been before.) A T/R dump and quick turnaround processing were requested; however, it was 36 h before these data were available for processing and analysis at the POCC. In the meantime, the usual satellite operations were continued, and it was noted that it had required approximately 10 to 12 h before a K2 was statused in the open position prior to an eclipse entrance.

The power profile program had predicted that a situation of a balanced condition would exist approximately 2 days later than that which occurred (approximately a 5-W difference in predicted power available). However, it was also believed that the program was conservative by approximately 50 W and, rather than reserve this as margin for error, it had been decided to use part of this as assumed power available and thereby keep all low-rate sensors operating. Voltage criteria that would require sensor shutdown were established for use during R/T statusing, but were never quite exceeded. Subsequent analysis showed that the power profile program predictions were essentially correct (an error of less than 5 W for a predicted load capability of 706 W) and, if followed, would have prevented this occurrence. The satellite was able to recover proper operation, and the ALT and all other sensors and satellite equipment were undamaged by the low voltage condition.

11. Thermal Control

The thermal control design for Seasat was particularly challenging because of the requirement for all beta operation (sun line to orbit plane would rotate through 360 deg over approximately 1 year), alternating periods of sunlight and shade (about 2 to 1 over the orbit period), high heat generation by the SAR when operated for up to 4 percent of a given day, and the desire to make the system as passive as possible. The resulting design made extensive use of MLI, louvers, thermostats and heaters, FOSR, tape, and paint. Specific thermal control equipments and performances for that equipment is summarized in Table 6-8.

In general, thermal control for the satellite was quite nominal with flight temperatures within predicted temperature ranges. However, on 6 July, two ALT RF assembly thermostats began operating erratically, indicating rapid cycling, extended periods of on time, and a shift in the set point from 0.4 to approximately 15°C. The net result was that the +Y side of the baseplate warmed up to its upper limit. Two SASS thermostats also failed closed at about the same time. (The ALT thermostats eventually failed closed and the SASS thermostats adopted a higher set point.) Nearly nominal temperature ranges were maintained throughout the flight for all equipments by cycling the heater bus on and off once each orbit, using ground commands. The duty cycle required at the time of failure was 20 percent, which was gradually reduced as the beta angle became more favorable.

12. Deployment Mechanisms

All Seasat deployments were performed using the same temperature-compensated actuator design, with damping rate set and attach fittings modified, as required for specific appendages. The only exception was the extension of the SAR antenna, which was performed by the electric motor delivered with the antenna.

The SAR antenna consisted of 8 panels stowed as a 2 by 4 by 1 stack. Deployment required a 90-deg rotation away from the satellite, a 90-deg rotation normal to the satellite, and then extension of the panels along the flight path.

Table 6-9 is a summary of the deployment actuators and their performance. All boom deployments and the SAR antenna deployment were completely nominal.

Table 6-8. Thermal Control Equipment and Performance

Equipment	Quantity	Performance
Louvers	11	Nominal
Blankets	120	Nominal
Heaters[a]	35	Nominal
Thermostats	68	64 nominal 4 failed

[a]Add on heaters only. Heaters such as those internal to the batteries or to the reaction control valves or catalyst beds are not included.

Table 6-9. Summary of Deployment Actuators and Performance

Deployed Equipment	Actuators	Performance
Orbit antenna 1	1	Nominal
Solar arrays	2	Nominal
SAR data link antenna	1	Nominal
SASS antennas 1 and 3	1	Nominal
SASS antennas 2 and 4	1	Nominal
VIRR/Tranet beacon antenna/orbit antenna 2	2[a]	Nominal
SAR antenna		
90-deg pitch out	1	Nominal
90-deg rotation	1	Nominal
Extension	1[b]	Nominal

[a]Two-jointed, folded boom with single latch point.
[b]Actuated by electric motor.

SECTION VII

SENSORS

A. GENERAL

Detailed descriptions of the five sensors are given in subsequent paragraphs. Engineerng assessments of the performance of the four microwave sensors (ALT, SMMR, SASS, and SAR) are also given, as well as a review of the lessons learned from their utilization. For the ALT, SMMR, and SASS, descriptions are also included of the algorithms required to translate their data into usable form.

B. RADAR ALTIMETER

1. General

The physical and functional characteristics of the ALT are shown in Figure 7-1. The ALT operated at 13.49932 GHz ±160 MHz (bandwidth was 320 MHz) with a pulse repetition frequency of 1020 p/s. The effective pulse width was 3.2 ns, and the pulse compression ratio or time bandwidth product was 1000. The ratio of transmit time to repetition time was 0.0033. The peak transmitted power was 2.0 kW, the average transmitted power was 6.5 W, and the average power input was 177 W.

The design of the traveling wave tube was based on that of GEOS-C, and the design of the ALT system was based on those of Skylab and GEOS-C and flown in the NASA Advanced Application Flight Experiment (AAFE) aircraft program.

The antenna pointed to the nadir or instantaneous sub-satellite point. The antenna had a conical beam of 1.5 deg. However, the spatial resolution at the surface was not determined by the antenna beam, but instead by the pulse width. The surface "spot" size was about 1.8 km (1 nm) by 7 km (3.8 nm) (across track by along track) over a calm sea, and increased to 8 km (4.3 nm) by 14 km (7.6 nm) over rough seas.

The return pulse or echo had the following two important characteristics:

(1) The slope of the leading edge of the echo varied as a function of sea state and could be used to infer significant wave height. The variation occurred because the outgoing radar pulse was reflected from all surfaces of the wave from crest to trough, so that the leading edge of the echo was stretched out according to wave height.

(2) The delay time to the mid-point of the leading edge of the echo gave a precise measurement of the distance from the satellite to the ocean surface.

The performance requirements for the ALT data output with appropriate ground processing were:

(1) Sixty-eight percent (1 sigma) of one-second altitude measurements had to lie within ±10 cm (3.9 in.) of the fitted mean.

(2) The real-time one-second significant wave height ($H_{1/3}$) measurement accuracy had to be at least ±10 percent or 0.5 m (1.6 ft), whichever was greater for $H_{1/3}$ from 1 to 20 m.

(3) The measurement accuracy of the oceanic backscatter coefficient had to be within ±1.0 dB.

The ALT was provided by the NASA Wallops Flight Center (WFC) under a Memorandum of Agreement (MOA) with JPL. The ALT was obtained by WFC from the Applied Physics Laboratory of Johns Hopkins University, who subcontracted the RF modules to Anderson Laboratories and Zeta Laboratories and the traveling wave tube amplifier to Hughes Aircraft Company.

A functional diagram of the ALT is shown in Figure 7-1, along with flow diagrams of the RF and signal processing sections, which contained the major elements of the system.

2. RF Section

Included in the RF section were the antenna unit, Traveling Wave Tube Amplifier (TWTA), Up-Converter/Frequency Multiplier (UCFM), Dispersive Delay Line (DDL), and receiver. The antenna was effectively a 1-m parabolic dish design. In addition to the dish, the unit consisted of a baseplate, support, and feed. The antenna assembly mounted to the RF electronics baseplate with provisions for alignment of the antenna beam to within 0.1 deg of the perpendicular to the RF electronics baseplate. The antenna dish was thermally insulated from the RF electronics. The antenna had the following characteristics over the frequency range of 13.5 GHz ±180 MHz.

(1) View angle: nadir looking

(2) Beamwidth: 1.5° (3 dB minimum)

(3) Power gain: 40 dBi minimum

(4) Side lobe level: -20 dB maximum within ±70° of beam peak, -50 dB maximum elsewhere

(5) Polarization: linear

(6) Cross polarization: -15 dB maximum

(7) Beam symmetry: at -3, -6, -9 dB points ±10%

(8) VSWR: 1.2: 1

RADAR ALTIMETER (ALT)

PACKAGE CONFIGURATION

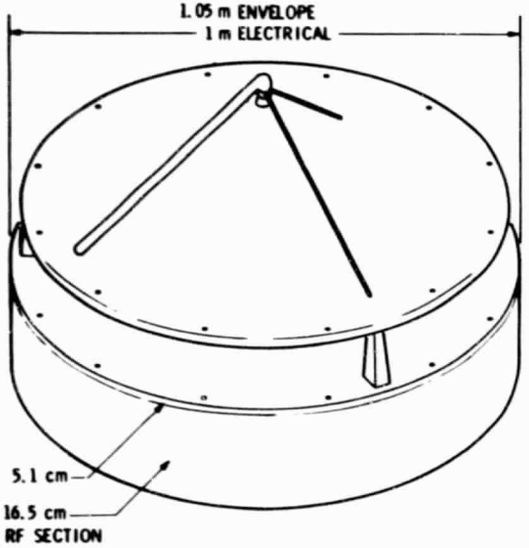

R F MODULE

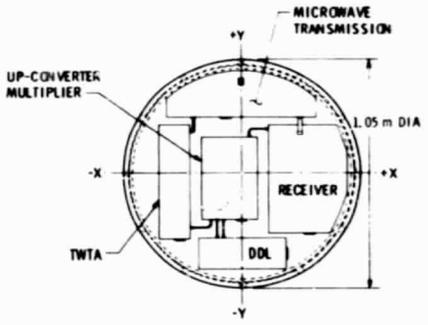

RF SECTION

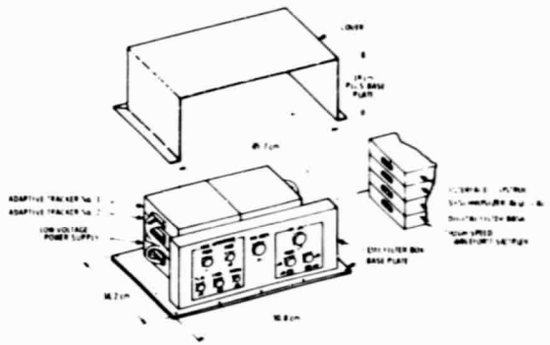

DIGITAL MODULE

FUNCTIONAL DIAGRAM

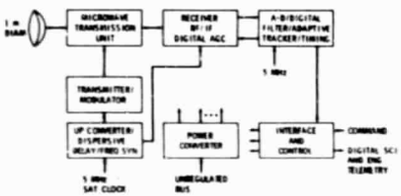

RF SECTION SIGNAL FLOW DETAIL

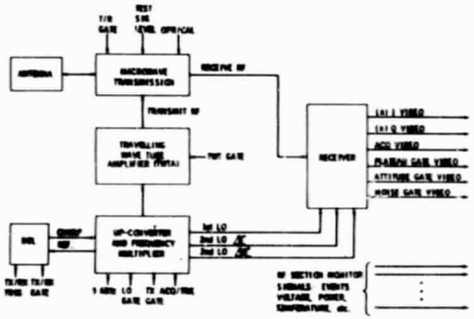

SIGNAL PROCESSING SECTION FUNCTIONAL DETAIL

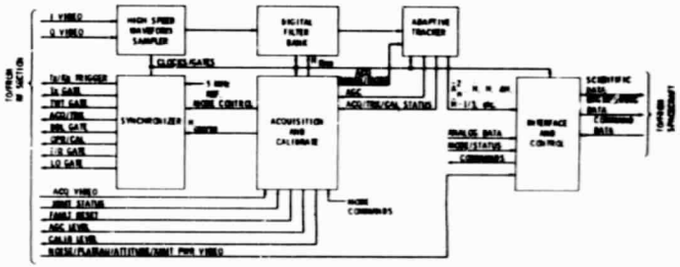

COVERAGE

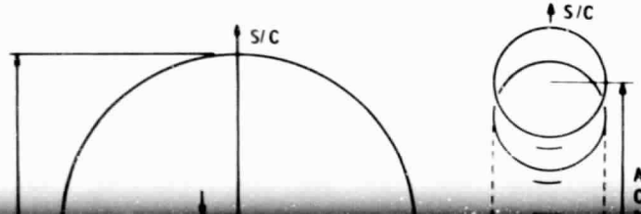

LINK EQUATION

$$SNR = \frac{P_T}{L_T} \frac{G_T^2 A \sigma^\circ \lambda^2}{(4\pi)^3 H^4 (KTB) F L_R L_P}$$

		+dB	-dB	
P_T/L_T	TRANSMIT POWER	62		dBm
G_T^2	ANTENNA GAIN (1m DISH)	80		dB
A	ILLUMINATED AREA (πHcτ)	63.8		dB m^2
σ°	SCATTERING COEFFICIENT (MIN)	6		dB

ALTIMETER HEIGHT PRECISION

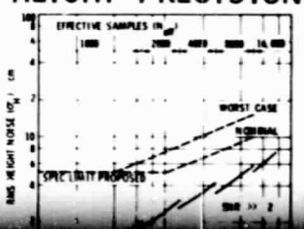

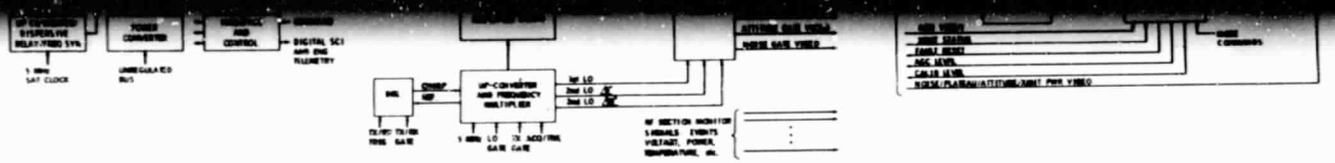

COVERAGE

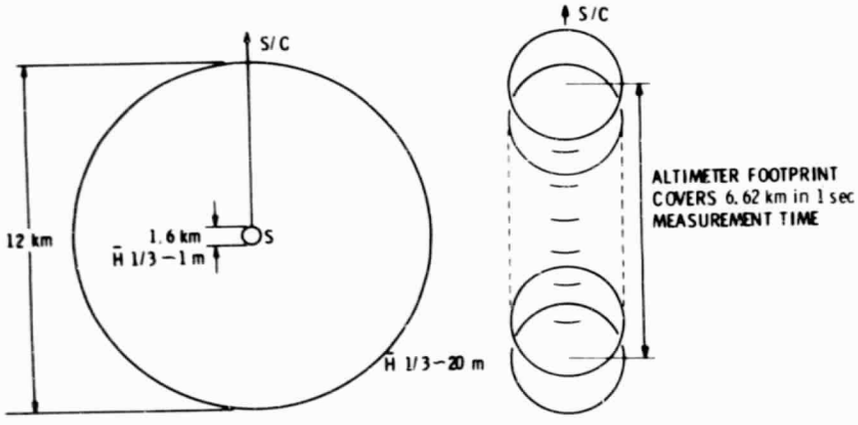

LINK EQUATION

$$S/R = \frac{P_T}{L_T} \cdot \frac{G_T^2 A \sigma^0 \lambda^2}{(4\pi)^3 H^4 (KTB)F L_R L_P}$$

		+dB	−dB	
P_T/L_T	TRANSMIT POWER	62		dBm
G_T^2	ANTENNA GAIN (1m DISH)	80		dB
A	ILLUMINATED AREA (πHcr)	63.8		dB m^2
σ^0	SCATTERING COEFFICIENT (MIN)	6		dB
λ^2	WAVELENGTH (λ = 2.22 cm)		33.1	dB m^2
$(4\pi)^3$			33	dB
H^4	HEIGHT (800 km)		236.3	dB m^4
KT	THERMAL NOISE (1 Hz)	174		dBm
B	BANDWIDTH (312.5 kHz)		54.9	dB Hz
F	NOISE FIGURE		11	dB
L_R	RECEIVE LOSS		2	
L_P	PROCESSING LOSS		1	
	TOTALS	(+)385.8	(−)371.3	

SIGNAL/NOISE (SNR) = 385.8 − 371.3 = 14.5 dB

OTHER LOSSES	ATTITUDE (2-WAY, 0.75°)	5 dB
	ALTITUDE (H), 856/800	0.75 dB
	PROPAGATION LOSS (2-WAY)	1 dB
		6.75 dB MAX

ALTIMETER HEIGHT PRECISION

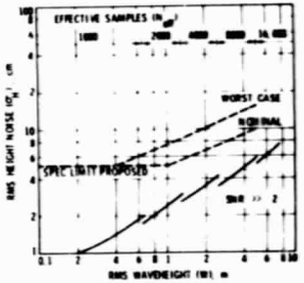

$$\sigma_H = \frac{C\tau}{4\sqrt{N_{eff}}}\left(1 + \frac{2}{SNR}\right)\sqrt{1 + \left(\frac{WH}{C\tau}\right)^2}$$

$C = 3 \times 10^8$ m/s

$\tau = 3.125$ ns

N_{eff} = EFFECTIVE SAMPLES AVERAGED

SNR = POWER SIGNAL-TO-NOISE RATIO

WH = RMS WAVEHEIGHT, m

PERFORMANCE

- SIXTY-EIGHT PERCENT (1σ) OF ONE SECOND ALTITUDE MEASUREMENTS TO LIE WITHIN ±10 cm OF THE FITTED MEAN
- REAL TIME ONE SECOND SIGNIFICANT WAVEHEIGHT (H 1/3) MEASUREMENT ACCURACY AT LEAST ±10% OR 0.5 m WHICHEVER IS GREATER FOR H 1/3 FROM 1 TO 20 m
- BACKSCATTER MEASUREMENT ACCURACY WITHIN ±1.0 dB

TECHNICAL CHARACTERISTICS

- FREQUENCY - 13.49932 GHz ±160 MHz
- BANDWIDTH - 320 MHz
- TRANSMIT TIME/TOTAL TIME - 3.3×10^{-3}
- PULSE WIDTH - 3.2 μsec
- CHIRP RATE - 100 MHz/μsec
- PULSE COMPRESSION - 1000
- TIME BANDWIDTH PRODUCT - 1000
- EFFECTIVE PULSE WIDTH - 3.2 nsec
- PEAK TRANSMITTED POWER - 2.0 kW
- PRF - 1020 PULSE/sec
- AVERAGE TRANSMITTED POWER - 6.5 W
- AVERAGE POWER INPUT - 177 W
- ACQUISITION SIGNAL - 3.2 μsec PULSE MODULATED BY CW SIGNAL
- SYSTEM NOISE TEMP FIGURE - 11 dB
- RECEIVER GAIN - 95 dB
- GAIN - AUTOMATIC, DIGITAL
- AVERAGE BACKSCATTER - 6 dB
- RECEIVER DYNAMIC RANGE - 63 dB
- RECEIVER POWER RANGE -
- ANTENNA PEAK GAIN - 40 dB
- ANTENNA POLARIZATION - LINEAR
- SCI DATA RATE - } 8.5 kbps TOTAL
- ENG DATA RATE - }
- WEIGHT - 90 kg

SPECIAL FEATURES

- REAL TIME ALTITUDE AND WAVEHEIGHT MEASUREMENTS
- SURFACE ACOUSTIC WAVE, DISPERSIVE DELAY LINE
- FULL DERAMP STRETCH CHIRP DEMODULATOR
- ADAPTIVE α - β TRACKER
- DIGITAL PROCESSING

INHERITANCE

- SKYLAB, GEOS-C, AAFE A/C ALTIMETER → SEASAT-A
- GEOS-C TWT → SEASAT-A TWT

SIGNIFICANT DEVELOPMENTS

- CHIRP MODULATOR
- HIGH VOLTAGE POWER SUPPLY
- DIGITAL PROCESSOR

Figure 7-1. Radar Altimeter Physical and Functional Characteristics

The function of the UCFM was to synthesize the transmitter drive, receiver local oscillator, and the DDL signals for the gated CW and chirp pulse operation of the ALT. Key interface signals between the RF and signal processing sections included a 5-MHz reference signal and a UCFM drive signal. The 5-MHz reference signal (locked to the spacecraft reference) was applied to the UCFM for coherent generation of all RF signals used in the conversion of an 80-MHz bandwidth DDL output pulse at 250 MHz to transmit drive and local oscillator pulses at 13.5 and 13.0 GHz, respectively. The UCFM drive signal was a trigger pulse applied from the synchronizer in the signal processing section to the DDL to generate both transmit and local oscillator chirped pulses. The chirp pulses derived from the DDL were used by the UCFM to develop transmit drive and receiver local oscillator signals during chirped pulse operation of the ALT.

3. Signal Processing Section

Included in the signal processing section were a High Speed Waveform Sampler (HSWS), Digital Filter Bank (DFB), Adaptive Tracker (AT), Synchronizer, Acquisition, and Calibrate Unit (SACU), and Interface and Control Unit (ICU). The HSWS sampled the I and Q video signals representing the ocean return from each transmit pulse, and converted the signals from analog to digital (A/D) form. The digital samples were then stored for subsequent processing during the interpulse period. The I and Q signals were each A/D-converted at a 20-MHz rate for 3.2 μs of each pulse return. A minimum of 5-bit quantization, including sign, was required. Storage was provided for 64 five-bit samples for each of the I and Q channels.

The DFB accessed these samples sequentially in the interval between receptions and, along with a sin/cos look-up table in a read-only memory (ROM), implemented a phase rotation algorithm and accumulated sums over the 64 samples to form a contiguous bank of filters. The filter bank spacing and overall tuning were determined by the manner in which the sin/cos memory was addressed during each read-out cycle. Addressing corresponded to a linear phase progression representative of both the center frequency of the filter being implemented, as well as a fine range offset derived from altitude tracking. Square-law detection was accomplished in a ROM addressed by the magnitude of the digital filter output.

Altitude tracking operations were conducted in the AT using detected outputs from the DFB. Operations of the AT were controlled by a microprocessor. Filter bank outputs were read out as serial 9-bit words and were accumulated (averaged) for 50 pulse repetition intervals to provide smoothed waveform samples. The samples were then accessed by the AT to close up the height tracking, receiver gain control, and waveheight estimation loops. The flexibility of the AT was also used to format and output basic measurement data (which included all waveform samples) to the spacecraft telemetry system through the ICU. Also, the AT interpreted ALT commands and controlled the sequencing of the ALT through acquisition, track, and calibration modes. Redundancy was provided by selection of either AT 1 or 2 for operation.

The synchronizer portion of the SACU provided the basic clocks and timing signals for the ALT operations. The timing functions were based on the spacecraft 5 MHz reference. Included in these functions were the transmitter PRF

control and transmit/receive gating and trigger signals. Time separation between the transmit and ocean return signals of at least 51.2 μs was maintained. Signals requiring more precise timing such as the receive DDL trigger and return signal had a precision of 12.5 μs.

The acquisition portion of the SACU contained the control and processing logic for the height detection process. Included in the acquisition circuits were a threshold detector and range counter to develop an initial height estimate and control logic for the basic timing and selection functions required for height detection.

The calibrate section of the SACU contained circuits used to determine ALT operability and to calibrate the characteristics of antenna measurements. Included in these were measurements of the ALT height bias and AGC characteristics over the receiver dynamic range and a determination of the input/output characteristics of the receiver/DFB combination. The ALT could be commanded to the calibrate mode by either real-time or delayed commands to initiate an automatic sequence of calibration tests, which consisted of calibration modes 1, 2, and 3.

In calibration mode 1, the transmit chirp waveform output of the TWTA was diverted to the receiver input through the calibration test signal path provided in the microwave transmission unit. Coincident with generation of the transmit waveform, the chirp first local oscillator signal was generated for reception of the test signal. The calibration procedure consisted of varying the test signal level with calibration attenuator settings from 0 to 60 dB in 6-dB increments. Four seconds was allotted for each calibration step. The signal processor processed the I and Q video signals the same as for a normal return, except that only fine height tracking was used with fixed gate selections for AGC and tracking purposes. The fine height readings obtained yielded the ALT height bias as a function of received signal level.

In calibration mode 2, the ALT was operated without the injected test signal but with noise only. There was no tracking in this calibration mode, but DFB data was obtained. Ground processing of this DFB data yielded the combined receiver/DFB response characteristics. The receiver AGC settings were established by normal AT processing for this mode. The completion of both of calibration modes 1 and 2 required no more than 60 s. As a commandable track mode option, the procedures of calibration modes 1 and 2 were initiated automatically once every hour for any track mode.

A third calibration sequence, calibration mode 3, was also available as a track mode option. In this mode, track and calibration data were integrated. Once every 4.6 s, a height bias measurement was taken for one of the eleven calibration mode 1 steps. This step was the one giving the closest match of the AGC between the calibration and ocean return signals. The resulting bias measurement was included in a subsequent telemetry frame.

The ICU portion of the signal processing section contained the logic and control circuits required to interface with the spacecraft data and command systems. The data interface consisted of a redundant digital channel that provided scientific and engineering data in a serial bit stream. The ICU command

interface accepted data commands from the redundant spacecraft command system, provided partial command decoding and AT reset as required, and input the command to the AT for additional processing. The ICU processed the noise, plateau, attitude, and transmit power video signals to provide a 100-sample average in digital form of the power level of these signals. These measurements were provided to the AT each ALT minor data frame.

The ICU conditioned all of the ALT engineering data parameters, converted them to a digital format as required, and provided commutation of these parameters to the AT at a rate of one parameter each ALT minor data frame. Selected parameters were provided each minor frame. The ICU conditioned 12 analog engineering parameters and provided these in a compatible analog form to the spacecraft for sampling and processing. In addition, the ICU provided "power on clear" initialization of the signal processor and indicated to the DFB and the SACU units which of the redundant ATs has been selected.

4. Algorithms

a. ALT Data Corrections. ALT data were received in raw form and therefore had to be corrected for instrument as well as geophysical effects. The algorithms for accomplishing these corrections are described in the following paragraphs. Instrument corrections applied to the raw data included blunder-point editing, timing corrections, track-mode corrections, and corrections for various rates and for significant wave height. These corrections, along with the raw data, were output on the ALT sensor file which, in turn, served as input to the geophysical correction processing.

The algorithms for geophysical corrections model known effects, due to the atmosphere, geodynamics, and tides, on the ALT data. Processing the ALT data through these algorithms resulted in the final geophysical file, which contains ALT data (raw and corrected), along with all applicable instrument and geophysical corrections.

The ALT algorithms are classified as either sensor file or geophysical. In the following algorithm listings, algorithms are tabulated in the order of processing.

b. Sensor File Algorithms. Sensor file algorithms (Table 7-1) relate to instrument and spacecraft characteristics as opposed to environmental effects. Figure 7-2 is a flow diagram of the sensor file algorithms.

c. Geophysical Algorithms. Geophysical algorithms are listed in Table 7-2. Figure 7-3 is a flow diagram of the geophysical algorithms.

Table 7-1. Altimeter Sensor File Algorithms

Algorithm Number	Name	Description
S-30	Operating mode	Determines whether or not the data are in track or not. If they are not in track, they are not processed. If they are in track, the data are passed along to the next algorithm.
S-33	Blunder point, h	Determines whether the processed point is a blunder point for h, and if so, flags it. It also provides a value of the variance of h to be used in algorithm S-31. The blunder point criterion is that the observed value of h differs by more than 30 cm (12 in.) from the predicted value of h.
S-35	Blunder point $H_{1/3}$	Determines whether the processed point is a blunder point for $H_{1/3}$, and if so, flags it. The blunder point criterion is that the observed value of $H_{1/3}$ differs by 9 m (30 ft) from the predicted value.
S-31	Engineering quality flags	Flags out-of-specification engineering parameters. The following parameters and their out-of-specification criteria are considered:
		altitude rate — 50 m/s (164 ft/s)
		noise gate — 0.5 V
		AGC — 0 (AGC) [illegible].5 dB
		tilt angle — 0.5 deg
		T (DFB) — >70°C
		T (SACU) — <-5°C
		T (MTU) — <10°C
		AGC gate — outside range 44 to 48
		T (TWTC) — >5[illegible]°C
		standard deviation — $H_{1/3}$ >0.5 m (1.64 ft)

Table 7-1. Altimeter Sensor File Algorithms (Continuation 1)

Algorithm Number	Name	Description
S-01	Time tag correction	Uses the corrections to the time tag from algorithms S-01.01 and S01.02 to adjust the time tag so that it refers to the time of signal reflection from the ocean (or land) surface.
S-01.01	Track mode correction to time tag	Computes a correction to time tag due to instrument time delay and to lag caused by transit time of the signal through wiring up to the telemeter.
S-01.02	Transit time correction to time tag	Adjusts the time tag for the light time from the footprint back to the antenna.
S-03	Computation of $\ddot{h}$	Uses the telemetered values of $\dot{h}$ to compute $\ddot{h}$.
S-03.01	Correction to h due to $\ddot{h}$	Computes the value of the acceleration correction to h; i.e., the tracker lag.
S-04	Data compress	Compresses the data, essentially by averaging. The telemetered 0.1 s data can be compressed up to 10 s.
S-05	Calibration correction to h	Uses the cal mode data obtained during flight to arrive at a correction to h.
S-06	Attitude/sea state correction to h	Uses the telemetered attitude and sea state information to infer a correction to h.
S-07	Center of gravity correction to h	Computes a correction to h, based on the distance between the electronic measurement point on the spacecraft and the spacecraft center of gravity.
S-09	Cal zone bias	Identifies the h-bias determined from cal-zone data analysis.
S-12	Edit	Edits the data on the basis of flags set in algorithms S-31, S-33, and S-35 and selected by the user.

Table 7-1. Altimeter Sensor File Algorithms (Continuation 2)

Algorithm Number	Name	Description
S-13	Sum instrument correction to h	Sums the instrument corrections to h and passes this sum to the sensor file. It also adds the raw value of h to obtain the corrected value of h (sensor corrections only) and passes this result to the sensor file.
S-14	Units change	Changes the units of h and $\dot{h}$ to meters.
S-15	Bias, $H_{1/3}$	Identifies the bias on $H_{1/3}$ as determined by a comparison with truth. This bias may be a function of wave height.
S-16	Correction $H_{1/3}$ for attitude and sea state	Obtains a correction considering attitude and sea state for $H_{1/3}$.
S-19	Sum instrument corrections to $H_{1/3}$	Sums the instrument correction to $H_{1/3}$, obtains an instrument-corrected value of $H_{1/3}$, and passes both the correction and the corrected value to the sensor file.
S-34	Correction to $H_{1/3}$ based on pre-launch evaluation	Corrects the real time value of $H_{1/3}$ on the basis of pre-launch calibration.
S-36	Backscatter coefficient	Computes the backscatter coefficient on the basis of AGC adjusted for height, tilt angle, and calibration.

5. Engineering Assessment Summary

The ALT was turned on for the first time on 3 July 1978, and was declared operational on 7 July 1978. During the next 30 days of operation, a detailed assessment of ALT performance was conducted. After this initial engineering assessment period, global ALT data continued to be collected until 10 October 1978, when a massive short circuit in the spacecraft power system prematurely terminated the Seasat mission after 99 days of sensor operations. However, because of the on-board data recording capability, some 1684 hours of high quality ALT data was collected. As a point of comparison, this represents about 90 percent of that collected by the GEOS-III ALT during its first 3-1/2 years of real-time operations.

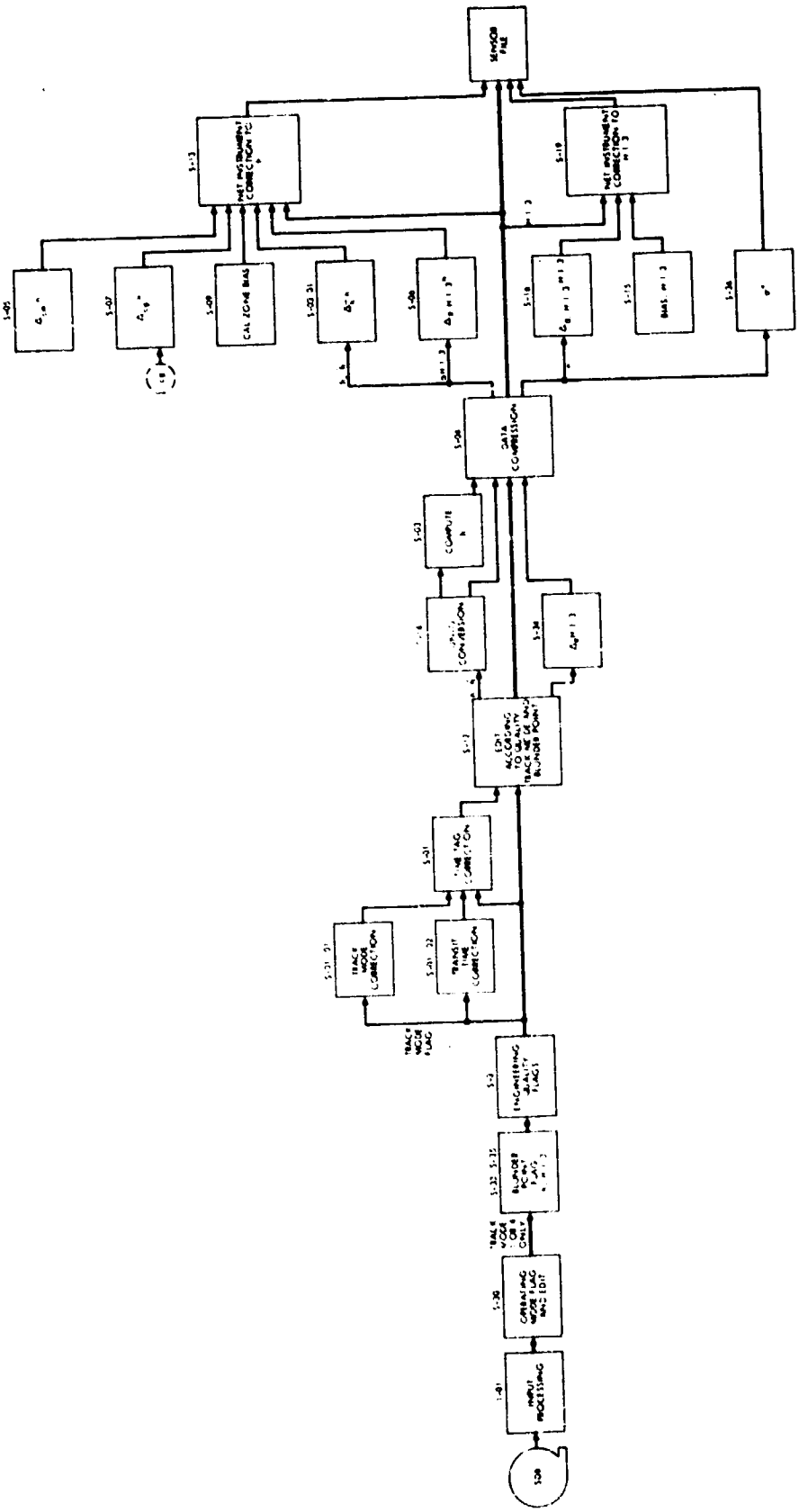

Figure 7-2. Altimeter Sensor File Algorithm Flow Diagram

Table 7-2. Altimeter Geophysical Algorithms

Algorithm Number	Name	Description
G-10	Ionosphere	Uses Faraday rotation data from the Deep Space Net stations to compute a correction to altimeter height, h.
G-11	Wet troposphere	Uses available weather information to determine the water vapor component of the atmospheric correction to h.
G-12	Dry troposphere	Uses available atmospheric pressure data to determine the dry component of the atmospheric correction to h.
G-17	Interpolation	Interfaces between the USN weather data and the ALT data processor. Accesses the tape containing the pressure data, obtains the pressure for the time and position of the spacecraft, and applies the results to G-12.
G-14	Net atmospheric correction to h	Sums the atmospheric corrections (including the ionosphere), applies them to h, and passes the results to the geophysical file.
G-1	Sea height above ellipsoid	Uses precision orbit information and the agreed-on Earth ellipsoid to convert ALT height (h) to the height of the surface above the ellipsoid.
G-4	Merge-interpolate	Reads the orbit tape and interpolates to obtain coordinates at the spacecraft time. These are used in algorithm G-1.
G-2	Barotropic effect	Obtains the sea-surface height above the geoid induced by atmospheric pressure differences.
G-3	Tides	Obtains the variation in sea-surface height due to tides, based on tide models. Three models are available for the algorithm: (1) Mojfeld model in the Bermuda calibration area; (2) Musen-Estes model, globally; and (3) Schviderski model, globally.
G-4	Steric anomalies	Obtains the variation in sea-surface height induced by ocean water density differences.

Table 7-2. Altimeter Geophysical Algorithms (Continuation 1)

Algorithm Number	Name	Description
G-5	Geoid	Obtains the height of the geoid above the reference spheroid (see also algorithm G-1). Various geoid models are available as input data.
G-8	Net geophysical corrections	Sums the geophysical perturbations of the ocean surface to obtain a net theoretical deviation from the spheroid. This result, when combined with the ALT sensor-corrected altitude measurement, yields a residual containing geophysical information accounted for in the models.
G-9	Optimal filter/ smooth	Filters the noise from the ALT data, leaving as clean a signal as possible for analysis.
G-10	Earth tides	Accounts for the deviation of the Earth (ocean) surface due to earth tides (solid-body tides as opposed to ocean tides).

Results of the ALT engineering assessment activity* indicate that, with minor exceptions, the ALT performed nominally throughout the life of the satellite. The ALT is felt to generally have performed in accordance with the original specification, and certainly in accordance with pre-launch expectations. This is despite the fact that the ALT occasionally had to operate in the presence of random attitude disturbances, outside its designed temperature range of operation, and at spacecraft bus voltages below its designed minimum. The only known ALT equipment anomaly was a transmitter power drop-out problem which, while it certainly was a cause for concern, in no way impacted the quality of the ALT data collected, since the transmitter drop-outs always occurred over land and for short durations (<5 s).

More specifically, it was determined that:

(1) The ALT responded to commands and operated in the minimal required experimental and calibration modes.

(2) The ALT engineering measurements were within design limits and were stable.

*SEASAT-1 Radar Altimeter Phase I Engineering Assessment Report, draft, dated December 15, 1978, prepared by NASA Wallops Flight Center, to be published as NASA TM-73279.

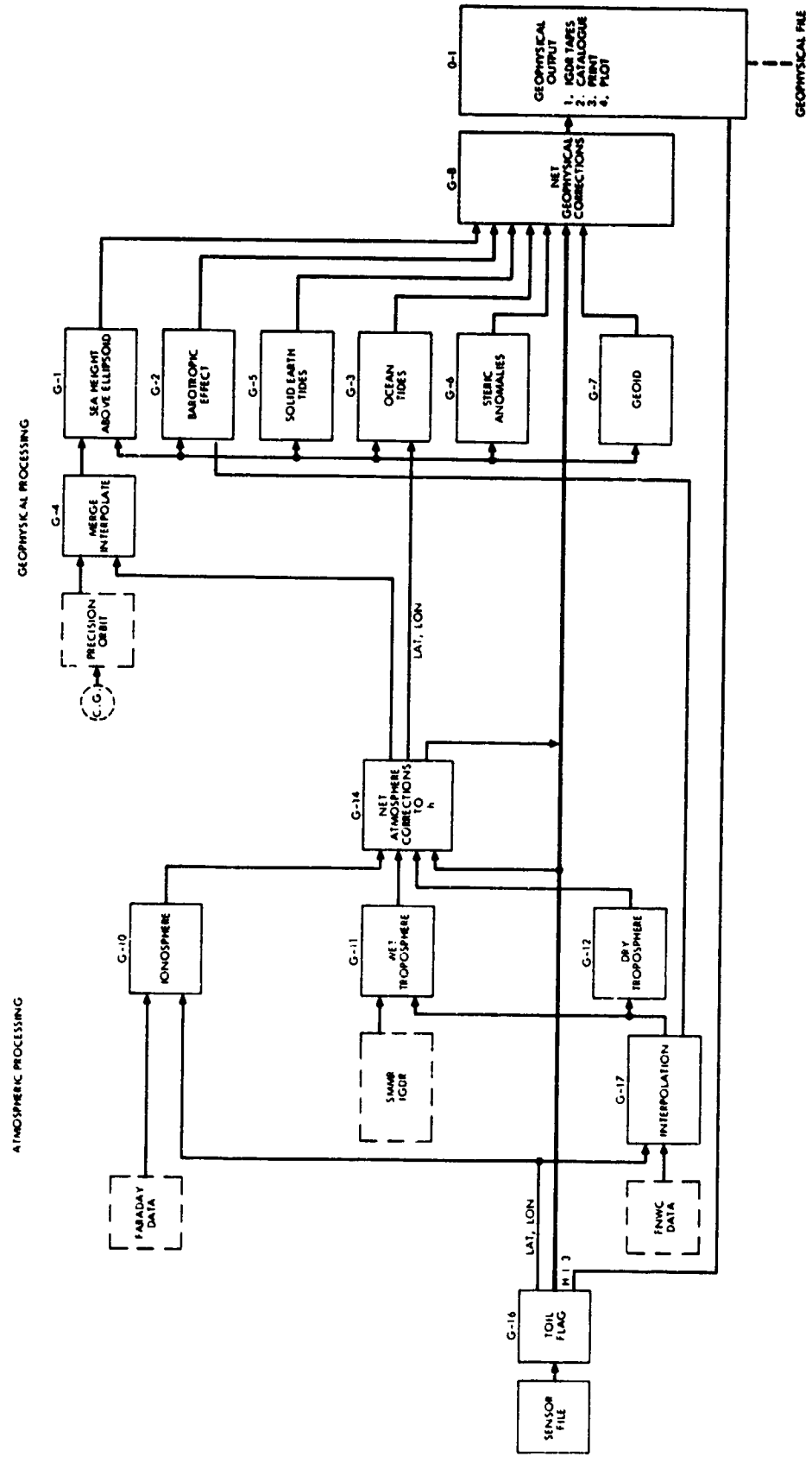

Figure 7-3. Altimeter Geophysical Algorithm Flow Diagram

(3) The ALT was not damaged by the various spacecraft-related anomalies that occurred during the mission, namely the 2 over-temperature conditions and the undervoltage condition, or by the ALT transmitter dropout problem.

(4) The height resolution achieved was as good as 2-3 cm (0.8-1.2 in.) at low sea states and no worse than 15 cm (5.9 in.) at high sea states, with the specification of 10 cm (3.9 in.) being met for sea states less than 10 m (33 ft) significant wave height (SWH).

(5) The ALT Sensor Data Record (SDR) is a valid data product suitable for release to the user community.

It is clear that 10-cm height resolution, as well as accurate, global, real-time measurements of sea state, were achieved by the ALT. Table 7-3 compares the ALT key parameter measurements made at APL, LMSC, and in-flight aboard the satellite with the specification requirements.

C. SCANNING MULTICHANNEL MICROWAVE RADIOMETER

1. Description

The Scanning Multichannel Microwave Radiometer (SMMR) operated in the microwave region of the spectrum in the frequency range of 6.6 to 37 GHz. The SMRR contained six radiometer receivers that operated simultaneously at five frequencies and with each frequency operating at both horizontal and vertical polarizations, a total of 10 receiving channels. The operating frequencies were: 6.6, 10.69, 18.0, 21.0, and 37.0 GHz. Each frequency and polarization performed a function in the measurement of oceanographic and atmospheric properties.

The physical and functional characteristics of the SMRR are shown in Figure 7-4. The instrument possessed a scanning antenna system that consisted of a 79-cm (31 in.) diameter collecting aperture and a multifrequency feed assembly. The antenna and feed assembly operated simultaneously at all frequencies within the operating frequency range. The antenna was mechanically scanned with a sinusoidal waveform over a 50-deg swath angle with a 4-s time period. The beams formed by the antenna produced contiguous footprints (Figure 7-5) that covered the sea surface in a ribbon-like pattern with a width of 600 km (323 nm).

At all frequencies and polarizations, the antenna beams were formed about the same central axis of the 79-cm collecting aperture. Passive radiation was received from the sea surface and atmospheric phenomena from which the geophysical properties were deduced. The scan pattern was offset from the vertical path to permit better coincidence between the beams formed by the SMMR and the SASS. The radiometers were basically superheterodyne receiving systems with RF switches at the input of the frequency converter (mixer unit) that served to modulate the received signal radiation and to introduce calibration temperatures.

The cosmic background radiation (2.7 K) provided a cold calibration temperature. A waveguide termination affixed to the RF switch assembly functioned as an ambient temperature calibration. Figure 7-4 shows the sky calibration horns.

Table 7-3. Altimeter Key Parameter Matrix

No.	Parameter	Specification	Measurement		
			T/V No. 6 at APL	T/V at LMSC	In-flight
	Key Performance Requirements				
1	Altitude noise	<10 cm RMS	3.5 cm @ 2.8 m	N/A	4.6 cm @ 2.8 m
		(1 m $\leq H_{1/3} \leq$ 20 m)	4.1 cm @ 3.4 m	4.3 cm @ 3.4 m	5.2 cm @ 3.4 m
			5.2 cm @ 5.1 m	N/A	6.5 cm @ 5.1 m
			6.4 cm @ 7.9 m	5.7 cm @ 7.9 m	8.5 cm @ 7.9 m
			11.1 cm @ 13.9 m	N/A	N/A
			14.7 cm @ 18.1 m	N/A	N/A
2	Sea state accuracy (real time)	Greater of ±0.5 m or ±10% of $H_{1/3}$ (1 m $\leq H_{1/3} \leq$ 20 m)	-0.05 m @ 2.8 m	N/A	Not part of engineering assessment. Reported on in Gulf of Alaska Workshop Report (JPL PD 622-101).
			+0.04 m @ 3.4 m	-0.2 m @ 3.4 m	
			-2.2% @ 5.1 m	N/A	
			+5.1% @ 7.9 m	+2.9% @ 7.9 m	
			+15.6% @ 13.9 m	N/A	
			+6.1% @ 18.1 m	N/A	

Table 7-3. Altimeter Key Parameter Matrix (Continuation 1)

No.	Parameter	Specification	Measurement		
			T/V No. 6 at APL	T/V at LMSC	In-flight
3	σ_o Accuracy (after ground processing)	±1 dB (1 m $\leq H_{1/3} \leq$ 20 m)	Not part of engineering assessment. Reported on in Gulf of Alaska Workshop Report (JPL PD 622-101).		
4	Acquisition time	Quality data within 5 s (1 m $\leq H_{1/3} \leq$ 20 m)	3.5 s @ 2.8 m	N/A	Not fully evaluated due to limited number of controlled acquisition attempts. However, generally in accordance with pre-launch test results. Note that due to a change in operating configuration, all acquisition attempts after start of day 268 are 2.8 s longer.
			3.4 s @ 3.4 m	3.4 s @ 3.4 m	
			3.4 s @ 5.1 m	N/A	
			3.4 s @ 7.9 m	3.1 s @ 7.9 m	
			4.1 s @ 13.9 m	N/A	
			5.1 s @ 18.1 m	N/A	
	Operational Characteristics				
5	Response to pulse commands	Functional	Yes	Yes	Yes
6	Response to data commands	Functional	Yes	Yes	Yes
	Data Characteristics				
7	Engineering data channels	Functional	Yes	Yes	Yes
8	Science data channels	Functional	Yes	Yes	Yes

Table 7-3. Altimeter Key Parameter Matrix (Continuation 2)

No.	Parameter	Specification	Measurement		
			T/V No. 6 at APL	T/V at LMSC	In-flight
9	Analog data channels	Functional	Yes	Yes	Yes
	Instrument Characteristics				
10	Antenna gain	>40 dB	40.8 dB	N/A	N/A
11	Antenna beamwidth	>1.5 deg	1.59 deg	N/A	N/A
12	Transmitter power	>2.0 kW	2.1 kW	2.1 kW	2.1 kW
13	Adaptive Tracker No. 1	Functional	Yes	Yes	Yes
14	Adaptive Tracker No. 2	Functional	Yes	Yes	Yes
15	Cal Mode	Functional	Yes	Yes	Yes
	Number of operating hours				
16	TWTA	N/A	326.4	183.6	1684.2
17	System	N/A	466.4	183.6	1684.2
18	Number of TWTA cycles dc power	N/A	87	--	12

Table 7-3. Altimeter Key Parameter Matrix (Continuation 3)

No.	Parameter	Specification	Measurement		
			T/V No. 6 at APL	T/V at LMSC	In-flight
19	Standby	102 W	105 W	105 W	105 W
20	Track	177 W	165 W	165 W	165 W
21	Weight	<90 kg	93.8 kg	N/A	N/A

Figure 7-6 shows the method of calibration and the functional relationship among the radiometers. The temperature of the SMMR was controlled by the thermal radiators provided by the spacecraft. The instrument itself was not thermostatically controlled.

Individual radiometers were provided for horizontal and vertical polarizations at 37 GHz. At all other frequencies the horizontal and vertical ports of the multi-frequency feed horn were connected to the radiometer input on alternate swaths.

The electrical properties of the antenna and the multi-frequency feed that illuminated the 79-cm reflector are given in Table 7-4. The spatial resolutions produced by the antenna beams at the sea surface are listed in Column 4 of Table 7-4.

Except that the radiometers were space-qualified, they were otherwise state-of-the-art equipment that are commonly used in radio astronomy and in other scientific observations.

The output of each radiometer was encoded with a 12-bit quantization accuracy by analog-to-digital converters which, in turn, were connected to the spacecraft telemetry system. Engineering quantities such as component temperatures and voltages were similarly encoded.

The volume and weight of the SMMR, less the antenna and scanning unit, was 0.03 m^3 (0.098 ft) and 30 kg (66 lb), respectively. The antenna and scanning unit weighed 25 kg (55 lb). The prime power consumption was 65 W, and the design lifetime of the instrument exceeded one year. During its orbital lifetime, the SMMR operated continuously.

2. Algorithms

a. Antenna Temperature Algorithms. The SMMR measured RF Earth radiation through a scanning antenna at 6.6, 10.7, 18, 21, and 37 GHz at vertical and horizontal polarizations. The received radiation was compared with the radiation from two calibration standards. One source of calibrated radiation was from a series of antennas which were directed toward cold space (2.7 K). These were referred to as the "sky horn" or cold calibration source. The second source of calibrated radiation was from a set of RF loads at the temperature of the instrument (300 K). This was referred to as the "ambient load" or hot calibration source. The temperature of this source and of various components of the receiver system were monitored. This data are part of the set of "housekeeping" data which includes monitors of the status of the instrument.

The general purpose of the antenna temperature algorithms is to convert raw spacecraft data (in the form of digital counts) to calibrated output antenna temperatures. These temperatures are not corrected for instrument-induced errors by these algorithms; this function is performed by the antenna pattern correction algorithms. The data flow of the set of antenna temperatures (T_A) algorithms is shown in Figure 7-7. The input processing algorithms unpack the data from the SMMR Sensor Data Record (SDR) and produce two sets of data. One set (consisting

FOLDOUT FRAME

SCANNING MULTICHANNEL MICROWAVE RADIOMETER

SMMR INSTRUMENT CONFIGURATION

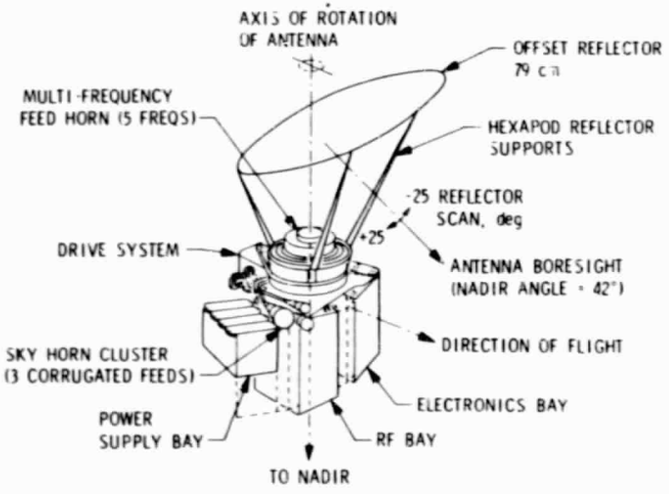

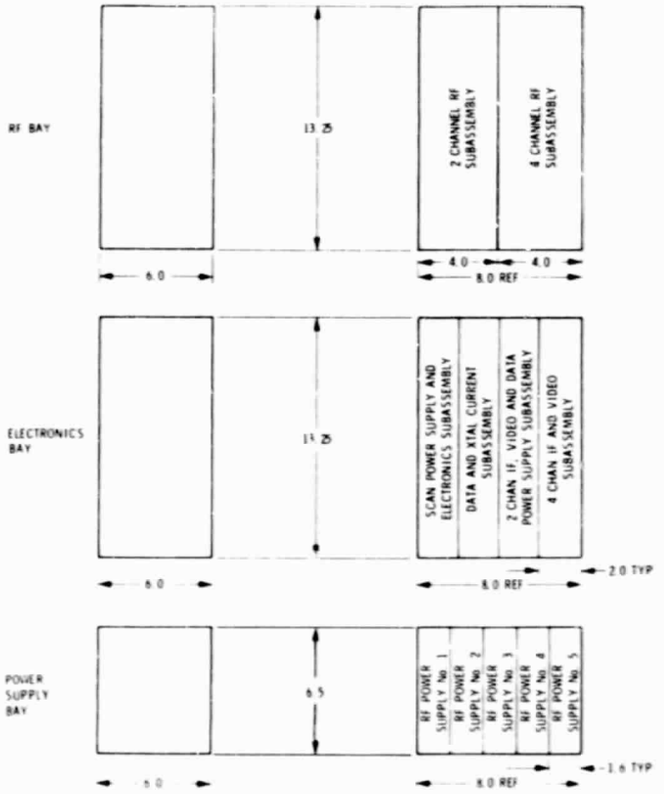

FUNCTIONAL DIAGRAM

SENSOR

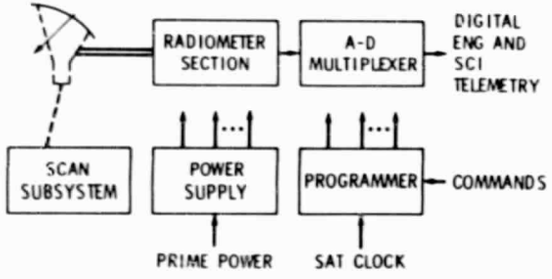

RADIOMETER SECTION DETAIL

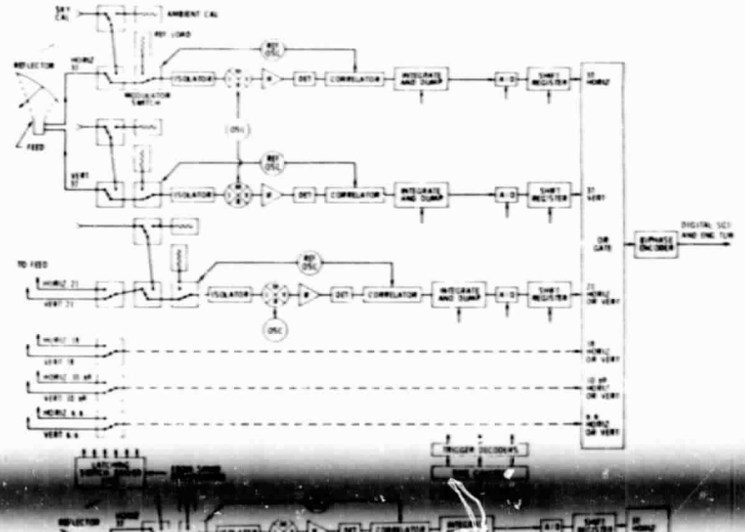

TECHNICAL CHARACTERISTICS

- CLOCK INPUTS - 1 Hz, 10 kHz, 1.6 MHz, SATELLITE TIME
- ENG AND SCI DATA RATE - 2 kbps
- WEIGHT - 53 kg
- PRIME POWER - 61 W (AVERAGE)
- FREQUENCY, GHz 6.63 10.69 18 21 37
- ANTENNA DIAMETER

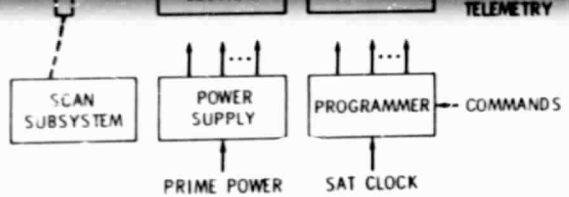

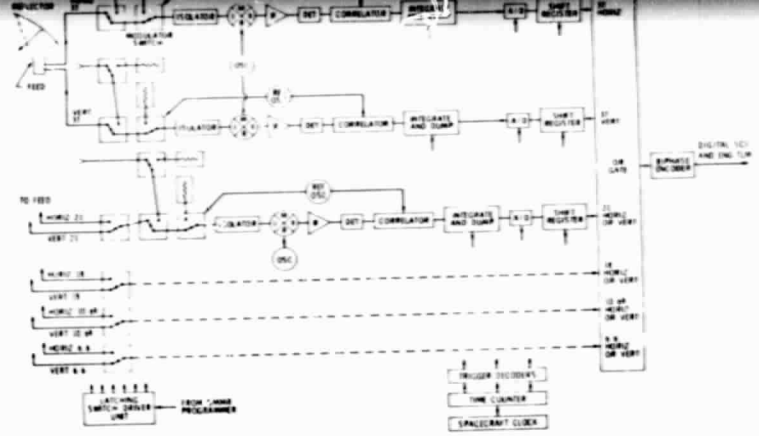

TECHNICAL CHARACTERISTICS

- CLOCK INPUTS - 1 Hz, 10 kHz, 1.6 MHz, SATELLITE TIME
- ENG AND SCI DATA RATE - 2 kbps
- WEIGHT - 53 kg
- PRIME POWER - 61 W (AVERAGE)

• FREQUENCY, GHz	6.63	10.69	18	21	37
• ANTENNA DIAMETER, m	←		0.79		→
• ANTENNA BEAMWIDTH, HALF-POWER, deg	4.2	2.6	1.6	1.4	0.8
• POLARIZATION	←		DUAL LINEAR		→
• FOOTPRINT DIMENSIONS (MAJOR AXIS / MINOR AXIS), km	121 79	74 49	44 29	38 25	21 14
• FULL SWATH ANGLE, deg	←		50		→
• SWATH ARC WIDTH, km	←		659		→
• INCIDENCE ANGLE OF BEAM CENTER AT SURFACE, deg	←		48.8		→
• ORBITAL ALTITUDE, km	←		794		→
• RF BANDWIDTH, MHz	←		250		→
• DISSIPATIVE LOSSES:					
(ORTHOMODE TRANSDUCER / WAVEGUIDES / SWITCHES AND ISOLATOR), dB	0.55 0.25 0.6	0.37 0.34 0.6	0.52 0.25 0.6	1.03 0.2 0.7	0.3 0.2 0.7
TOTAL DISSIPATIVE LOSSES, dB	1.4	1.21	1.37	1.93	1.2
• NOISE FIGURE (MIXER + IF AMP), DSB, dB	4	4	5	5	5
• SYSTEM NOISE TEMPERATURE (REFERRED TO PORT OF MODULATOR), DSB, K	490	490	692	703	728
• PREDETECTION BANDWIDTH, MHz	←		100		→
• INTEGRATION TIME CONSTANT, milliseconds	126	62	62	62	30
• TEMPERATURE RESOLUTION, K (1σ) (300K TARGET)	0.51	0.72	0.89	1.01	1.23
• ABSOLUTE TEMPERATURE ACCURACY, K (1σ)	←		2		→
• DYNAMIC TEMPERATURE RANGE, K	←		10-330		→

PERFORMANCE

- OCEAN SURFACE WIND SPEED FROM 7 m TO 50 m/sec ±2 m/sec OR ±10%, WHICHEVER IS GREATER
- OCEAN SURFACE TEMPERATURE TO WITHIN ±2°C ABSOLUTE AND ±0.5°C RELATIVE
- WIND AND TEMPERATURE RESOLUTION - 121 km
- ICE FIELD MAPS. RESOLUTION - 21 km
- MEASUREMENT OF INTEGRATED ATMOSPHERIC WATER VAPOR AND LIQUID MATTER IN A COLUMN ALONG THE SIGNAL VECTOR
- MEASUREMENT OF RAIN DROP SIZE AND DISTRIBUTION IN A COLUMN ALONG THE SIGNAL VECTOR

COVERAGE

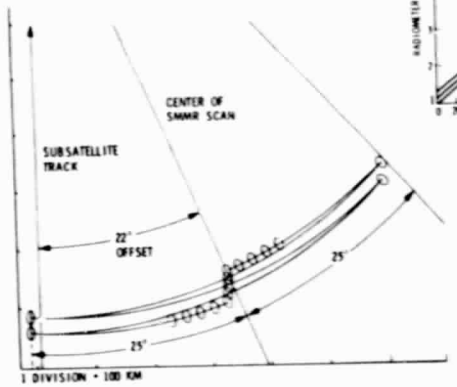

OUTPUT vs INSTRUMENT TEMP

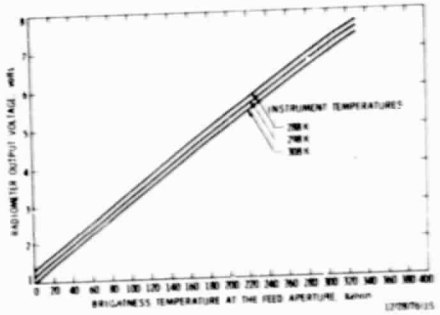

INHERITANCE

- NIMBUS-E (NEMS) → NIMBUS-G
  NIMBUS-F (SCAMS) → AND SEASAT-A (SMMR)
- SEASAT-A SMMR IS A ADD ON TO NIMBUS-G SMMR FLIGHT PRODUCTION

SIGNIFICANT DEVELOPMENTS

- ANTENNA FEED
- ANTENNA SCANNING MECHANISM INCLUDING MOMENTUM COMPENSATION

SPECIAL FEATURES

- OFFSET PARABOLIC ARRAY ANTENNA MECHANICALLY SCANNED ±25°
- MOMENTUM COMPENSATION TO OFFSET ANTENNA MOTION
- DUAL POLARIZATION, 5 FREQUENCY ANTENNA FEED

Figure 7-4. Scanning Multichannel Microwave Radiometer
Physical and Functional Characteristics

FOLDOUT FRAME 2

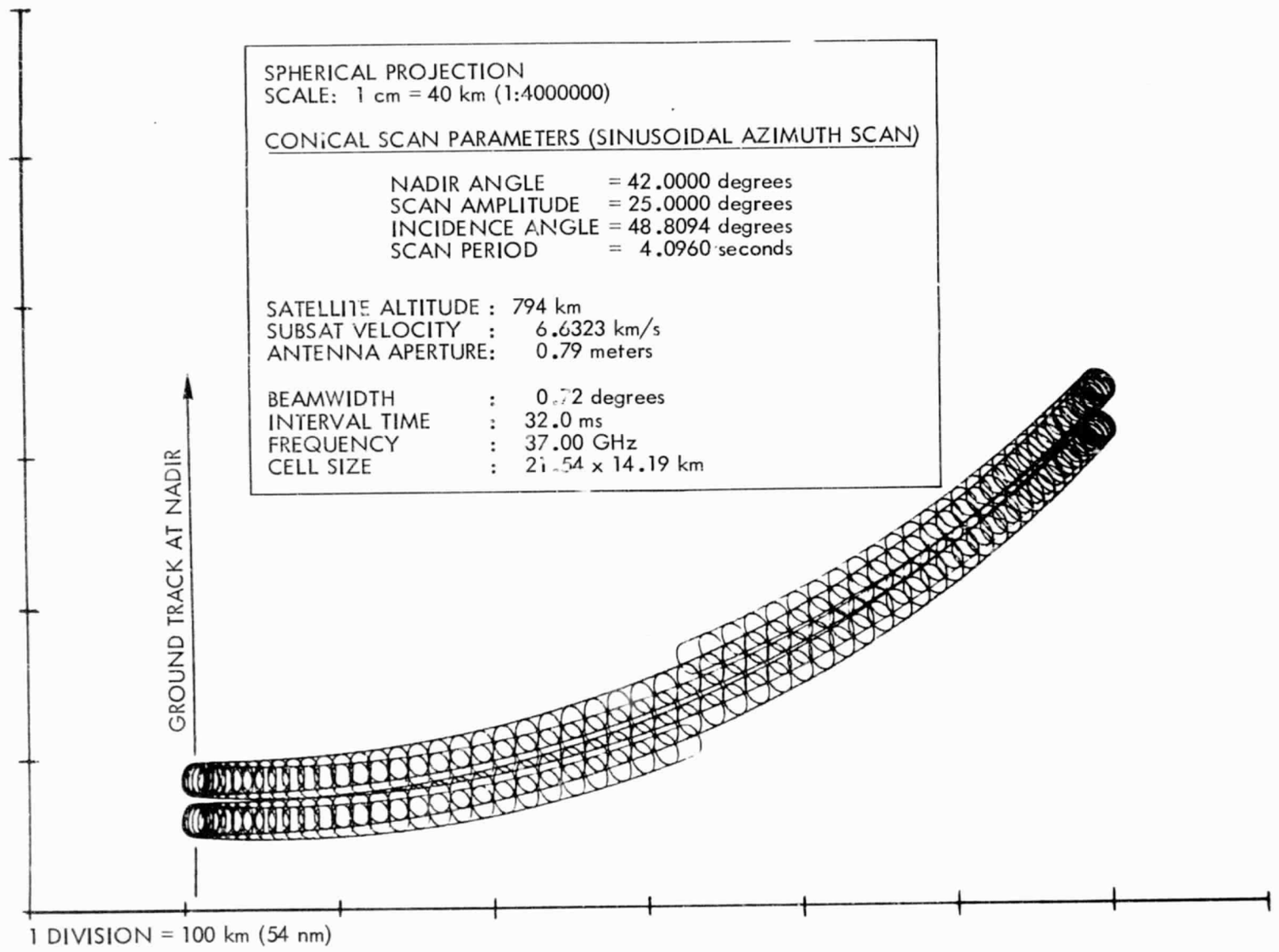

Figure 7-5. SMMR Scan Pattern at 37 GHz

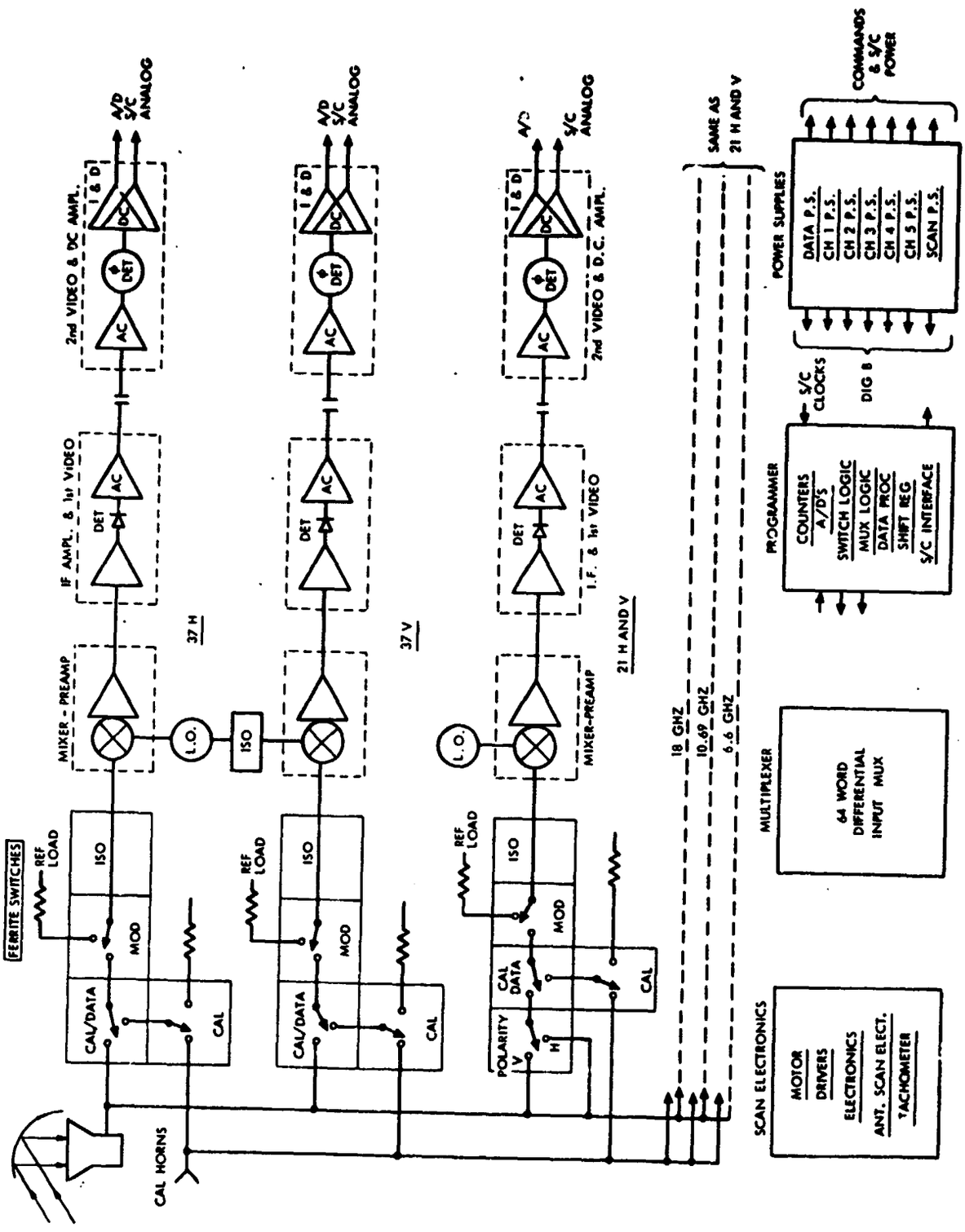

Figure 7-6. SMMR Functional Schematic Diagram

Table 7-4. SMMR Antenna Measurements Summary

Frequency (GHz)	Polarization	Half-Power Beamwidth in Degrees (Average of Transverse and Longi-tudinal Planes)	Sea-Surface Resolution Cell Dimension (km)	Beam Efficiency (2.5 x HP Beamwidth (%)	Cross Polarization Isolation (dB)	Dissipative Feed Loss (dB)
37	H	0.92	27	91.9	-17.0	0.7
37	V	0.92	(15 nm)	90.0	-17.6	0.7
21	H	1.48	54	90.0	-18.3	1.03
21	V	1.50	(30 nm)	87.0	-19.2	1.03
18	H	1.81	54	90.1	-20.0	0.52
18	V	1.80	(30 nm)	87.3	-21.6	0.50
10.69	H	2.90	85	90.2	-15.8	0.37
10.69	V	2.94	(46 nm)	86.1	-16.3	0.35
6.63	H	4.48	149	88.3	-19.4	0.55
6.63	V	4.56	(80 nm)	83.8	-21.7	0.55

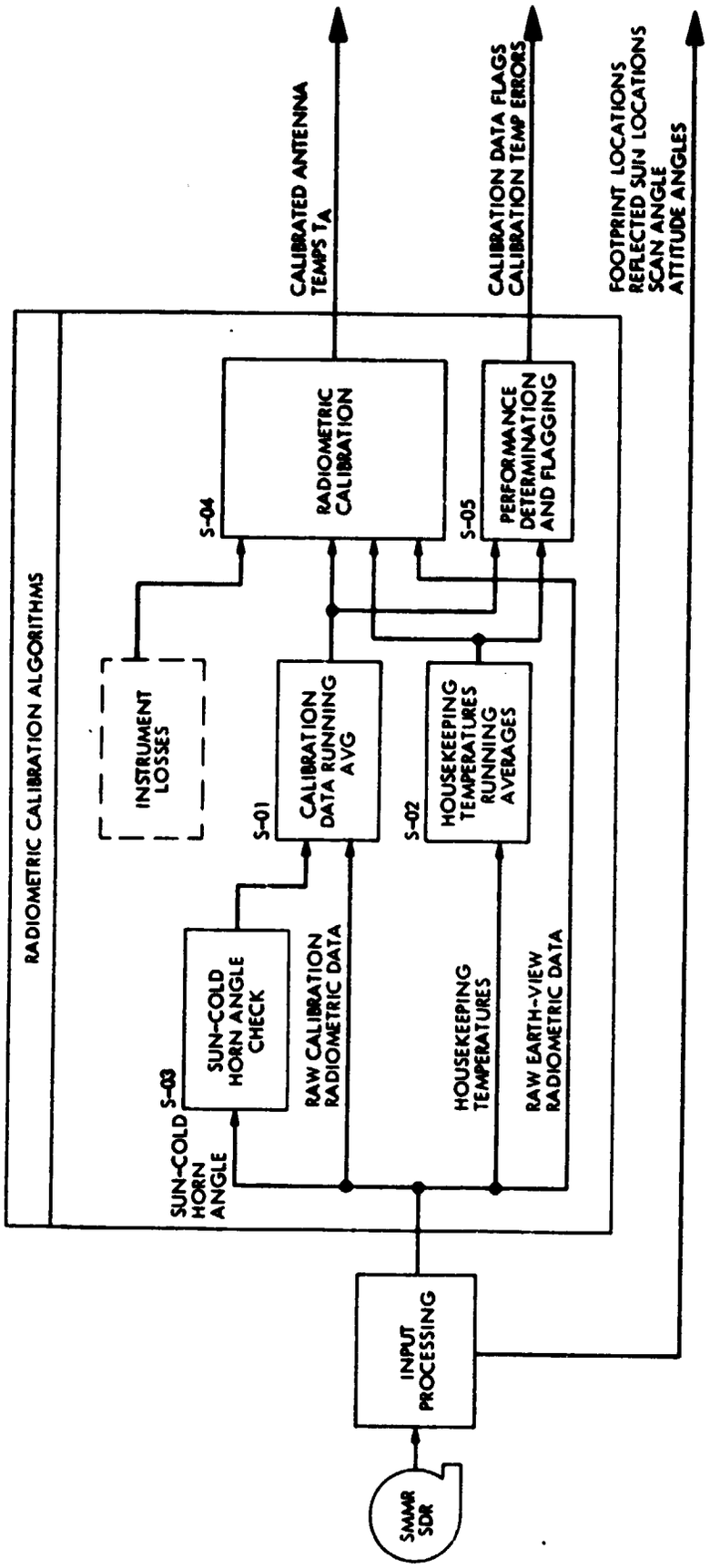

Figure 7-7. Radiometric Calibration Algorithm Flow Diagram

of spacecraft position, time, attitude, footprint locations, reflected sun locations, and scan angle) is passed through the algorithm with no change. The second set is used by the radiometric calibration algorithm and consists of:

(1) Raw radiometric Earth-view data.

(2) Raw radiometric calibration data from the horns.

(3) Housekeeping temperature data.

(4) Sun-cold horn angle data.

Both the raw calibration radiometric calibration data and the housekeeping data are applied to running average algorithms, which average over 52 samples. The sun-cold horn angle data is checked, and the averaged cold-horn radiometric calibration temperature output is not updated if the sun-cold horn angle is less than about 25 deg at 6.6 GHz and about 19 deg at 37 GHz. Intermediate angles are checked at the other channels. Running mean and standard deviation data are output from these algorithms and flags are set if these means and standard deviations are beyond certain limits.

The radiometric calibration algorithm provides calibration corrections to the radiometric Earth-view data and produces values of antenna temperature at each frequency. These calculations are based on the raw radiometric Earth-view data, the averaged calibration data, and the averaged housekeeping data. The algorithm used to produce the data for the Gulf of Alaska Seasat Experiment (GOASEX) Workshop is based on the following relation:

$$T_A = \frac{(C_t - C_a)\{\alpha_3 T_3 - \alpha_1 \alpha_2 \alpha_3 T_s + \alpha_2 \alpha_3 T_1 (1-\alpha_1) + \alpha_3 T_2 (1-\alpha_2)\}}{\alpha_6 \alpha_7 \alpha_8 (C_a - C_s)}$$

$$+ \frac{T_3 \quad T_8 (1-\alpha_8) + \alpha_7 \alpha_8 T_6 (1-\alpha_6) + \alpha_8 T_7 (1-\alpha_7) + \alpha_9 (T_3 - T_6)}{\alpha_6 \alpha_7 \alpha_8}$$

where

T_A = antenna temperature of the object being viewed

C_t = instrument digital counts from signal

C_a = instrument digital counts from ambient load

C_s = instrument digital counts from sky

T_s = temperature of the sky, normally 2.7 K

T_1, T_2, T_3, T_6, T_7, T_8 = temperatures of various parts of the instrument as read by the platinum resistance thermometers

α_1, α_2, α_3, α_6, α_7, α_8, α_9 = fractional transmission coefficients of various parts of the instrument

The coefficients, α, were derived from pre-launch component-transmission measurements, and in some cases, data fits.

A complete analysis of the algorithm errors has not been carried out, although initial analysis indicates that the errors are of the order of 1 K or less. It should be noted that an improved antenna temperature algorithm has been developed, and a change procedure initiated, to integrate this new algorithm into the set of radiometric correction algorithms. The errors in this new algorithm are expected to be the order of 0.3 to 0.4 K.

One error source in the SMMR instrument is radio frequency interference (RFI) from ground transmitters. It had been anticipated that this might occur at the 6.6 GHz frequency. Such RFI has indeed been observed at a number of places, although only tentative investigation of this problem has begun, RFI at 6.6 GHz has been observed over Europe, the coast of Africa, and Iceland. Furthermore, the GOASEX data set was scanned for RFI which was observed in three passes prepared for the GOASEX Workshop. Revs 1140, 1183, and 1298 show evidence of RFI in areas well isolated from the actual GOASEX areas. The RFI appears at the coast of California apparently radiating from the San Francisco area on Revs 1140 and 1183. Ground radiation appears in data from rev 1298 near the coast of Mexico. It appears that there was no corruption of the data received from the GOASEX area.

b. Antenna Pattern Correction (APC) Algorithm. The antenna temperature (T_A) measured by a radiometer/antenna system is the weighted integral of the brightness temperature (T_B) distribution over an all-solid angle. The weighting is provided by the antenna patterns which are peaked in the boresight direction, tapering off rapidly away from boresight to the lower sidelobe levels. For each radiometer channel there is a co-polarized and cross-polarized antenna pattern. The purpose of the APC algorithm is to invert the antenna pattern effects, deriving brightness temperatures from the antenna temperature measurements. In addition, the algorithm averages the data onto Earth-located grids suitable for geophysical processing. To meet the desired accuracy goals for sea-surface temperatures of 1 to 1.5 K, the APC algorithm must operate within an rms accuracy limit of less than 0.5 K in brightness temperature. This task is made more difficult by the relatively low beam efficiencies, high cross-polarization ratios, and polarization-rotation properties of the SMMR antenna.

The antenna pattern corrections are based on regular sub-satellite grids whose dimensions are approximately comparable to the antenna 3-dB footprints (Table 7-5).

To have an early data processing capability for the SMMR, an interim version of the APC was developed which contains all of the major operations of

Table 7-5. SMMR Grid Cell Dimensions

Frequency (GHz)	Grid Cell No.	Cell Dimensions (km)
6.6	1	149 x 149 (80 x 80 mm)
10.69	2	85 x 85 (46 x 46 mm)
18 21	3	54 x 54 (30 x 30 mm)
37	4	27 x 27 (15 x 15 mm)

the final version, except for sidelobe corrections within the Earth-viewing region. In open ocean, away from land regions, it was anticipated that results accurate enough for an initial data evaluation would be obtainable with the interim version. The interim version has been used for the GOASEX Workshop. It should be pointed out that even with the forthcoming final version of the APC, sidelobe corrections for data closer than approximately one or two cell distances away from land boundaries may have a reduced accuracy.

The major functional components of the APC algorithm are as follows (see Figure 7-8):

(1) Input of T_A data. The first portion of the APC algorithm:

(a) Reads the next SMMR scan from the T_A data file.

(b) Initializes processing for the first scan.

(c) Interpolates all scan data for small data gaps.

(d) Re-initializes processing for large data gaps.

(2) Interpolation to footprint locations. For each radiometer channel footprint location within the SMMR scan, this procedure:

(a) Interpolates location data along the SMMR scan to the position of each channel footprint.

1. Latitude.

2. Longitude.

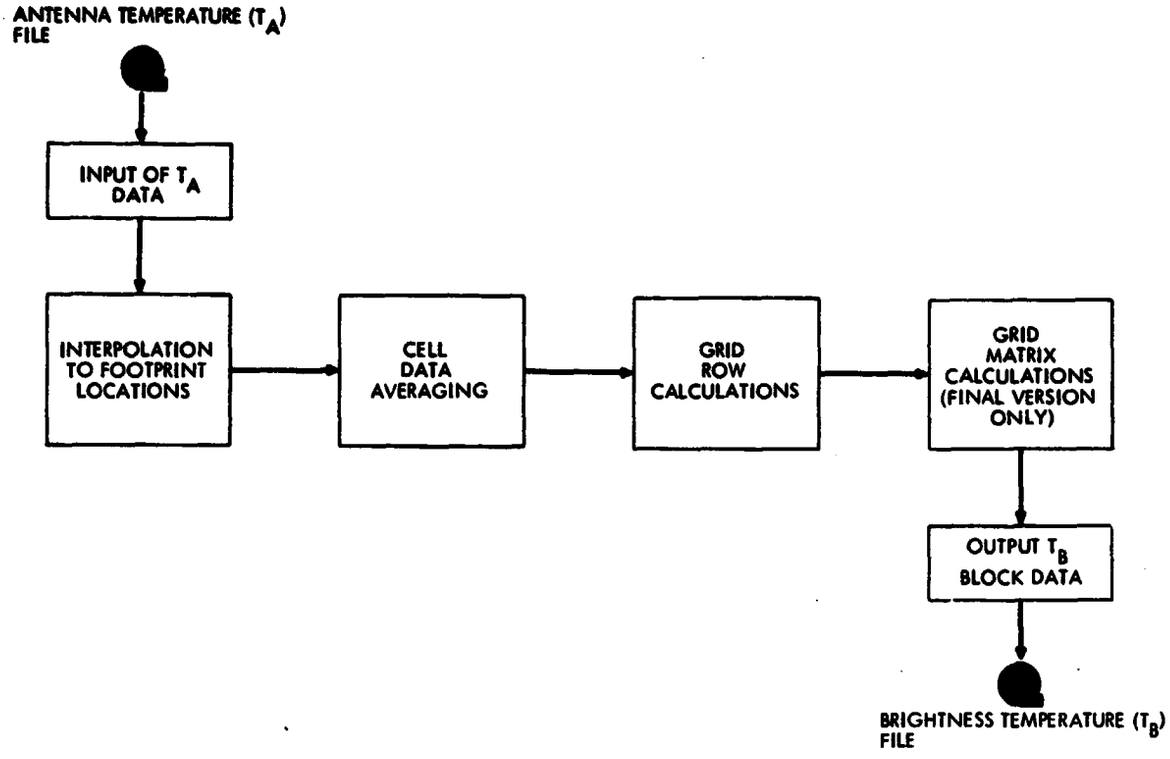

Figure 7-8. SMMR Antenna Pattern Correction Algorithm Flow Diagram

3. Incidence angle.

4. Sun angle.

(b) Computes a Faraday rotation angle for each 6.6 GHz footprint location.

(3) Cell data averaging. For each footprint within the SMMR scan, this procedure:

(a) Determines in which cell each footprint lies and computes a weight based upon its location.

(b) Calculates a weighted average for the data in each cell:

1. T_A data.

2. Incidence angles.

3. Sun angles.

4. Faraday rotation angles.

(4) Grid row calculations. For each cell within a completed row of grid cells, this procedure:

(a) Computes the cell center latitude and longitude.

(b) Corrects the cell T_A data for the space sidelobe contribution.

(c) Corrects the cell T_A data for polarization rotations due to Faraday rotation and non-nominal spacecraft attitudes.

(d) Corrects the cell T_A data for cross-polarization effects and polarization rotation due to scan motion. (Note that this is included only in the interim APC algorithm. In the final algorithm, this is replaced by the T_A to T_B conversion within the grid matrix calculations.)

(5) Grid matrix calculations. For each row of cells within a continuously updated matrix of grid cells, this procedure:

(a) Computes locations for accessing a stored Earth T_B map.

(b) Computes the far sidelobe contributions from the Earth outside the SMMR swath, using estimates from the T_B map.

(c) Converts the cell T_As to T_Bs by correcting for:

1. Cross-polarization.

2. Polarization rotation due to antenna scan.

3. Far sidelobe contributions from outside the SMMR swath.

4. Near sidelobe contributions from within the SMMR swath.

(6) Output T_B block data. When a T_B grid block is completed, then this last portion of the APC algorithm:

(a) Computes a block time tag.

(b) Sets missing data flags and surface-type flags for each cell with the block.[1]

(c) Computes T_B error estimates and instrument quality flags for the block as a whole.*

(d) Writes the T_B block as output to the T_B data file.

---

*Note that this operation is not included in the interim APC algorithm, but will be included in the final version of the algorithm.

c. Wentz SMMR Geophysical Algorithm. The Wentz SMMR geophysical algorithm is based on a theoretically derived function for computing the brightness temperature (T_B) observed by the SMMR. This function, denoted by $f(T_s, W, V, C)$, depends on the sea-surface temperature, T_s, the sea-surface wind speed, W, the columnar atmospheric water vapor, V, and the columnar liquid cloud water, C. A non-linear iterated, least-squares estimator operates on this function to locate the several environmental parameters sensed by the SMMR.

In the function, the atmosphere is modeled by a simplified radiative transfer equation which uses effective opacities computed from the molecular absorption lines for water vapor and oxygen, and from approximate Mie scattering by cloud and rain drops. The dependence of T_B versus sea surface temperature is based on Klein and Swift's equations for the dielectric constant for sea water (1977). The computed dielectric constant is then utilized in the Fresnel equation for sepecular emissivity. Surface-roughness effects are accounted for by assuming that emissivity increases linearly with wind speed. The following is a detailed description of the T_B function.

Brightness temperature measurements are made at five frequencies (6.6 GHz, 10.69 GHz, 18 GHz, 21 GHz, and 37 GHz) and two polarizations (vertical and horizontal). Frequency dependence is, in general suppressed from the notation; it is implicit that the model parameters are different for each frequency (although this point is duly noted).

(1) Instrument Parameters.

P = polarization, vertical or horizontal.

f = frequency (GHz). The frequencies are monotonically ordered; i.e., 6.6 GHz, 10.69 GHz, etc.

θ = Earth incidence angle (deg); angle of the SMMR boresight direction with respect to the logal surface normal.

(2) Unknown environmental parameters.

T_S = sea surface temperature (K).

U_* = logarithm of frictional velocity - $LOG_{10}\ U_*$. [log (cm/s)]

V = water vapor (g/cm^2).

R = liquid water (g/cm^2).

(3) Data base parameter set.

T_a = air temperature (K).

L = air-temperature vertical lapse rate (K/km); should be negative.

s = sea surface salinity (parts/thousand).

(4) Model parameters to be calculated from the data base parameter set.

γ = air-temperature difference between the surface and the top of the effective atmosphere (K).

$\bar{\alpha}_o$ = effective opacity of oxygen (nepers).

α_V = effective normalized opacity of water vapor (nepers/g/cm^2).

α_R = effective normalized opacity of liquid water (nepers/g/cm^2).

The parameters α, α_o, α_V and α_R are functions of frequency; and there is a set of values for each of these frequencies. Further, the parameters depend on the air-temperature vertical lapse rate, L, and the alphas depend in addition on the air temperature, T.

(5) Transmittance, τ.

$$\ln \tau = -\sec \theta \, (\bar{\alpha}_o + \alpha_V V + \alpha_R R)$$

(6) Emissivity, ε. The emissivity equation is:

$$\varepsilon = \varepsilon_{SP} + (b_1 \pm b_2 \theta) \, 10^u$$

where ε_{SP} - specular emissivity = $\varepsilon_{SP}(f, \theta, T_S, s, P)$, and the + (-) sign corresponds to horizontal (vertical) polarization.

(7) Constant parameters.

β_1 = first rain correction coefficient (dimensionless).

β_2 = second rain correction coefficient (dimensionless).

β_3 = third rain correction coefficient (cm^2/g).

b_1 = first coefficient for rough surface emissivity (dimensionless).

b_2 = second coefficient for rough surface emissivity (1/deg).

T_c = free space background radiation temperature, (K).

(8) Brightness temperature, T_B.

$$T_B' = T_a - \gamma\left(1 + \frac{1 - \tau}{1n\tau}\right) - \tau\,\varepsilon(T_a - T_S)$$

$$- \tau^2(1 - \varepsilon)\left[T_a - \gamma\left(1 + \frac{1 - \tau}{\tau 1n\tau}\right) - T_c\right]$$

$$T_B = T_B', \text{ freq} \neq 37 \text{ GHz}$$

$$T_B = \beta_1 + \beta_2 \exp\left(-\beta_3^2 R^2\right)) T_B', \text{ freq} = 37 \text{ GHz}$$

The estimation problem is formulated in terms of the SMMR measurement model. Let there be given M SMMR measured brightness temperatures,

$$T_B(m)(P_k, W_1)$$

$k = 1, 2$

$i = 1, \ldots, 5$

assumed to be accurate to within σK. Assuming the model (1) - (4), and the assumed model parameter values,

$$X^T = (T_s, U_*, V, R)$$

is found so as to minimize the weighted least squares likelihood function

$$J^2(X) = \left(\Sigma\left(T_B^{(m)}(P_k, \omega_i) - T_B\, p_k, \omega_i\right)\right)^2/\sigma^2 \qquad (1)$$

$i = 1, \ldots 5$

$k = 1, 2$

The T_B measurements are non-linear functions of X, and the purpose here is to document the strategy chosen to determine X so as to reduce $J^2(x)$ to less than M. Before processing to the strategy section, let us discuss the fit rationale.

Because of the non-linearity of the problem and the lack of knowledge of its underlying probabilistic structure, it is not critical that one truly minimize the performance functional $J^2(X)$. On the other hand, if the models were truly linear and the measurements independent (as we assume), then if one found the true value of X, X^*, it would turn out that

$$E\left(J^2(X^*)\right) = M = J^2_{min} \qquad (2)$$

Thus, it seems reasonable to accept an estimate, $\hat{X}$, which reduces the performance functional below its expected minimum. The strategy has been such that the estimates give performance functional values that are generally less than $0.75J^2_{min}$.

It is stated that modern estimation techniques are to be applied. The approach is, however, only formal; and it is inappropriate to claim rigorous statistical inferences from the results. Mathematically rigorous justification of the statistical implications of the results is, to say the least, an intimidating task. It should be noted that the function-minimization procedure (discussed in the next section) is dictated by estimation rationale and by physical interpretations. We close this problem formulation section with the observation that despite the disclaimer that one can make no rigorous statistical inference, numerical experiments show our estimate errors to be (with few exceptions) bounded by the 1-σ formal statistics of our non-linear estimator. There is an implication that the formal statistics are in fact upper bounds for the true statistics; and from an applications viewpoint, that is comforting.

Some comments in regard to programmatic considerations are in order. It is of value to review the prioritization involved with the design of the non-linear estimator. First, numerical reliability of the algorithm is of tantamount importance because we certainly do not want the validation of the physical models jeopardized by numerical difficulties. These criteria motivated our utilization of a square root information filter formulation (Bierman, 1977) and its testing under extreme conditions. Second, the requirement of physically meaningful results dictate the use of inequality constraints. Third, the desire to have estimate accuracy as an output further motivated the use of a linearized filter (although, the only justification for credence of the filter accuracy

estimates, the filter sigmas, are our numerical experiments). Fourth, the large amounts of SMMR data to be processed, together with the desire for a near-real-time economical processing capability, are of major concern. It is because of this concern that single-precision, compactness, and implementation efficiency are stressed.

Guided by extensive aerospace estimation applications experience, the non-linear optimization problem may be viewed, Equation (1), as a non-linear estimation problem. We briefly review the Gauss-Newton-type iterated weighted least squares algorithm often used to solve problems of this nature. Attention is then focused on the numerical, estimation-oriented techniques that are introduced to: (1) stabilize the iteration, (2) speed convergence, and (3) guarantee realizability of the results. To begin the review, let

$$J^2(X) = ||f_o - f(X)||_D^2 \equiv \sum_{i=1}^{m} f_o(i) - f(X,i)\ ^2D_i \tag{3}$$

where

$f_o^T = f_o(1), \ldots, f_o(m)$ - the observed values

$f(X)^T = (f(X,1), \ldots, f(X,m))$ - the non-linear vector functions

$D = \text{Diag}\ (D_1, \ldots, D_m)$ - the weights

The recursion, to minimize Equation (3) by iteration, is:

$$X_{j+1} = X_j + \Delta\hat{X}_j \tag{4}$$

where $\Delta\hat{X}_j$, subject to inequality and magnitude constraints to be discussed, is chosen to minimize the quadratic performance function $\tilde{J}_j^2$, where

$$\tilde{J}_j^2(\Delta X) = ||f_o - f(X_j) - A_j\ \Delta X||_D^2 \tag{5}$$

with $A_j = \partial f(X_j)/\partial X$. It is, of course assumed that f is smooth enough to guarantee continuous first derivatives. It is reasonable to expect, and not very difficult to prove, that if the recursion converges, then

$$J^2(X_{j+1}) \approx \tilde{J}_j^2(\Delta\hat{X}_j) \tag{6}$$

The recursion, based on equations (4) and (5), is as follows:

$$z_j = f_o - f(X_j) \quad \text{(predicted residuals)} \tag{7a}$$

$$A_j = \partial f(X_j)/\partial X \quad \text{(measurement partials)} \tag{7b}$$

Use composite Householder orthogonal transformations T_j (Bierman, 1978); form $\hat{R}_j$, upper triangular, and $\hat{z}_j$ such that

$$T_j D^{1/2} \left[\begin{array}{c|c} A_j & z_j \end{array}\right] \begin{matrix} \\ \} \end{matrix} m = \begin{matrix} \left[\begin{array}{c|c} \hat{R}_j & \hat{z}_j \end{array}\right] \} n \\ \left[\begin{array}{c|c} 0 & e_j \end{array}\right] \} m-n \end{matrix} \tag{7c}$$

Then (Bierman, 1977)

$$\Delta\hat{X}_j = \hat{R}_j^{-1}\, \hat{z}_j \tag{7d}$$

and $||e_j|| = \min \tilde{J}_j(\Delta X_j) = \tilde{J}_j(\Delta\hat{X}_j)$. A side attribute of this procedure, in the linear case with D as a measurement information matrix, is that R_j is an estimate error square root information matrix, i.e.,

$$E\left[(\Delta X_j - \Delta\hat{X}_j)(\Delta X_j - \Delta X_j)^T\right] = \hat{R}_j^{-1}\, \hat{R}_j^{-T} \tag{8}$$

When the function is only mildly non-linear, and A_j has full rank, the recursion, (7a) - (7d), works very well.

It turns out that sea surface temperature errors are of the order of 3.5 K. Our spatial correlation model, which is being prepared for testing, includes the effects of antenna overlapping measurement patterns at the 6.6 GHz and 10.69 GHz frequencies. Experience with a variety of other estimation problems has shown that properly accounting for model correlations can improve estimates by at least a factor of 2. If that be the case, we should be able to satisfy the sea surface temperature measurement accuracy design goal of 1.5 to 2 K.

d. Wilheit Geophysical Algorithm. The inversion algorithms which derive geophysical parameters from brightness temperatures rely on complete

representation of the forward problem; i.e., the dependence of brightness temperatures on geophysical parameters. This representation consists of a combination of theoretical and experimental models describing the microwave emission, absorption, and scattering characteristics of the Earth's surface and atmosphere.

The microwave water-vapor emission model is relatively well known, and is based on the resonance spectrum of the water vapor molecule, which has been verified and reported extensively in the literature. Water-vapor retrievals from microwave radiometers on Nimbus 5 and 6, using this model, have shown good correlation with surface truth radiosonde measurements.

The non-resonant emission and absorption from cloud liquid water can be well-modelled theoretically in the Rayleigh limit (droplet size << wavelength) where scattering is not significant. Although a good degree of confidence can be placed in this model and retrievals of cloud liquid water have been made with microwave radiometers on Nimbus 5 and 6, verification is difficult because of inadequate surface truth data on the water content of the different cloud types.

The emission and absorption properties of rain are difficult to model because droplet size is comparable to the wavelength, and multiple scattering occurs. Furthermore, rain cells may not fill the antenna footprint field of views, giving rise to ambiguities in the meaning of a rain rate retrieval. Because of this, rain rate retrievals may only be of qualitative accuracy. Furthermore, retrievals of the other parameters may be adversely affected if rain rates $\gtrsim$ 0.5 mm/hr occur.

The dependence of microwave emissivity on sea surface temperature is also well understood. The complex dielectric constant of water as a function of temperature and salinity is represented by the Debye relaxation expression, whose parameters have been obtained experimentally.

The dependence of microwave emissivity on wind speed is the major area in which an adequate model is lacking. Experimental and theoretical evidence indicates a dependence of emissivity on surface roughness and foam, which in turn are related to surface wind stress. However, the existing experimental data set is not sufficiently comprehensive and shows a lot of scatter. The current theoretical models cannot adequately account for the complexities of wave structure, spray, and foam. Moreover, the dependence of wave structure and foam on wind speed may not be unique, due to effects of wind fetch and duration. The Wilheit model uses a piece-wise linear relationship between emissivity and wind speed, with a break-point in slope at 7 m/s (23 ft/s), where foam streaks start to appear. This is an empirical relationship, based on the past history of aircraft and tower radiometric measurements, extrapolated to the frequencies and incidence angle of the SMMR.

The heart of the algorithm is a set of 7290 combinations of realistic sea surface temperatures, wind speeds, atmospheric temperature profiles, water vapor contents, and cloud models. From each member of this set, a vector of 15 elements is constructed, consisting of the sea surface temperatures, the surface wind speed, the integrated values of water vapor and cloud liquid water content, the ALT path length correction, and the corresponding 10-channel SMMR brightness temperatures calculated from the ocean (atmosphere emission models

discussed previously). From this set, a statistical relationship between any geophysical variable and the set of brightness temperatures can be generated, either for the full range of the variables or for a more restricted set.

The statistical relationships are generated by multiple linear regression, so two methods are used to reduce the non-linearities of the problem to negligible proportions. First, the opacity of the atmosphere is known to be linearly related to the water vapor and liquid water content, and the brightness temperature is related to the opacity in an approximately exponential fashion, so that the function ln (280. - T_B) is almost linearly related to the atmospheric water constituents. Since the three highest frequencies are the primary source of atmospheric water information, we use these log functions in place of the brightness temperatures themselves. Iteration is then used to reduce the non-linearities. A retrieval based on the full range of all the geophysical parameters may be used to derive initial approximate values. Then, using these approximate values, matrices generated over a more restricted range of the geophysical variables can be selected to obtain better estimates. Numerical simulations showed no consequential advantages, however, in reducing the range of any of the variables, except wind speed. The brightness temperature dependence on wind speed is linearly approximated in two segments; the slope of the effect is much greater for wind speeds greater than the 7 m/s threshold of foam generation than below. Therefore, the regression constants have significantly different values above and below this threshold.

The inputs to the geophysical algorithm are the set of 10 brightness temperatures and the boresight Earth incidence angle, located on four subsatellite grids whose dimensions are roughly equivalent to the 3-dB footprints of the lowest frequency. The algorithm consists essentially of four subalgorithms for: sea surface temperature; wind speed; atmospheric water vapor, liquid water, and altimeter path length correction; and rain rate. These parameters are derived independently for each cell.

Sea Surface Temperature (SMSST). This subalgorithm uses a vector of nine inputs on grid 1, consisting of four brightness temperatures (6.6 V&H, 10.69 V&H), four logarithmic brightness temperatures [ln (280-18V), ln (280-18H), etc., for 21 V&H], and the Earth-incidence angle. A set of wind coefficients is first used to derive the wind speed from a linear combination of the nine inputs. Depending on whether this wind speed is greater than or less than 7 m/s, one of two sets of temperature coefficients is then used to derive the sea surface temperature from a linear combination of the nine measurements. The sea surface temperatures are output on grid 1.

Wind Speed (SMWIND). This subalgorithm uses a vector of seven inputs on grid 2 consisting of 10.69 V&H T_B's, 18 V&H, and 21 V&H logarithmic T_Bs, and incidence angle. A general set of wind coefficients is first used to derive the wind speed from a linear combination of the seven inputs. Depending on whether this wind speed is greater or less than 7 m/s, one of two sets of wind coefficients specific to that wind range is used to derive a more refined wind speed. The wind speed is output on grid 2.

Atmospheric Water Vapor, Liquid Water, and ALT Correction (SMATMS). This subalgorithm uses a vector of seven inputs on grid 3, consisting of logarithmic T_Bs (18 V&H, 21 V&H, 37 V&H) and the Earth incidence angle. A separate set of coefficients is used to derive each of the three parameters: water vapor, liquid water, and ALT correction from linear combinations of the inputs. These parameters are output on grid 3.

Rain Rate (SMRAIN). This subalgorithm uses the 18H brightness temperatures on grid 3 and the 37H brightness temperatures on grid 4 to derive rain rate from a piece-wise linear fit to a model curve. The rain rate is output on grid 3.

3. Engineering Assessment Summary

The SMMR radiometers were energized on the second orbit after launch on 27 June, but the antenna scan mechanism remained caged until 6 July. The instrument operated continuously until October 10, when the prime power system of the spacecraft failed. The data record for the SMMR was continuous except for lacunas caused by data transmission failures and from imponderables. On or about day 146, a single command was transmitted to the SMMR from the STDN station at Fairbanks, Alaska, directing the instrument to read shaft angle encoder B instead of shaft angle encoder A. The command was sent to try to isolate a possible source of noise appearing in the spacecraft telemetry system. This was the only command sent to the SMMR during its operating lifetime with the antenna scan enabled.

Engineering and statistical information concerning the operation of the SMMR in orbit are available from the following three sources: (1) the real-time telemetry at the Program Operation Command and Control (POCC) facility operated by LMSC at GSFC; (2) the Sensor Performance Summary (SPS) record developed by JPL with data taken from the Sensor Data Record (SDR) tapes; and the SDR READ software developed by JPL, a hard copy record taken directly from the SDR data tapes.

The key parameter matrix (Table 7-6) documents the engineering performance of the SMMR at critical periods during development, pre-launch, and orbital phases. Tabulated in the key parameter matrix are temperature resolution, gain scale factor, and crystal current quantities. The discrete time periods shown in the matrix were taken during thermal/vacuum calibration, at the spacecraft integration facility at LMSC, and in orbit on day 195.

The temperature resolutions remained consistent throughout the development and lifetime of the SMMR in that the 90 percent confidence limits overlap for each channel when compared to the thermal/vacuum measurements and to those taken after three months in orbit. Table 7-7 shows the performance comparisons for the temperature resolution when the SMMR and the ambient calibration temperatures are uniformly at 300 K.

The gain scale factors are within statistical expectations for the thermal/vacuum and integration facility cases. The orbital values show a consistently

Table 7-6. SMMR Key Parameter Matrix

No.	Parameter	Specification	Measured Values		
			at JPL	at LMSC	In-flight (Day 195)
	Temperature Resolution: (Delta-T, kelvins)				
1	6.633 GHz horizontal	0.9	0.5	.59	0.60
2	6.633 GHz vertical	0.9	0.5	.59	0.60
3	10.69 GHz horizontal	0.9	0.74	.70	0.75
4	10.69 GHz vertical	0.9	0.74	.59	0.75
5	18.0 GHz horizontal	1.2	0.91	.78	0.85
6	18.0 GHz vertical	1.2	0.96	.77	0.85
7	21.0 GHz horizontal	1.5	0.94	.87	1.05
8	21.0 GHz vertical	1.5	0.91	.91	1.05
9	37.0 GHz horizontal	1.5	1.49	1.35	1.27
10	37.0 GHz vertical	1.5	1.48	1.31	1.59
	Gain Scale Factor: (DN/K[a])	(Not a specification requirement)			
11	6.633 GHz		8.5	8.52	8.33
12	10.69 GHz		8.4	8.50	8.26
13	18.0 GHz		8.3	8.36	7.85
14	21.0 GHz		8.0	9.10	8.75
15	37.0 GHz (H)		8.3	7.45	6.91
16	37.0 GHz (V)		8.7	7.97	7.69

[a] DN/K = dimensions, digital numbers per kelvin

Table 7-6. SMMR Key Parameter Matrix (Continuation 1)

No.	Parameter	Specification	Measured Values		
			at JPL	at LMSC	In-flight (Day 195)
	Crystal Current: (Units are digital numbers)	(Not a specification requirement)			
17	6.633 GHz (+)		2834	2800	2826
18	6.633 GHz (-)		2814	2800	2806
19	10.69 GHz (+)		1145	1058	1325
20	10.69 GHz (-)		1191	1101	1151
21	18.0 GHz (+)		922	889	901
22	18.0 GHz (-)		889	890	872
23	21.0 GHz (+)		1475	1489	1253
24	21.0 GHz (-)		1380	1379	1134
25	37.0 GHz (+H)		1194	1524	1466
26	37.0 GHz (-H)		1075	1482	1430
27	37.0 GHz (+V)		1368	1484	1990
28	37.0 GHz (-V)		981	1085	1921

smaller gain scale factor of about 2 percent. This result is not unexpected because the gain scale factor was computed from the 2.7-K sky temperature as opposed to the 100-K blackbody sky target used in the thermal/vacuum calibrations. Accumulated non-linearities over the extended dynamic range of sky temperatures are presumed to account for the difference in the orbital values. The assertions are reasonable, but recognizably inconclusive, because one-on-one comparisons of cold calibration temperatures are not possible because the 2.7-K sky temperature was not simulated during the thermal/vacuum tests.

Crystal current variations are evaluated within the limits of maximum and minimum expected values. The values shown in Table 7-7 are consistent with the expectations caused by the aging of the mixer diodes and from amplitude and frequency variations of the Gunn diode local oscillators.

Table 7-7. SMMR Temperature Resolution Summary

Frequency (GHz)	Thermal/Vacuum May 1978		After 3-Months in Orbit October 1978	
	Temperature Resolution (K)	90% Confidence Limits (K)	Temperature Resolution (K)	90% Confidence Limits (K)
37 H	1.35	(1.3 - 1.41)	1.44	(1.24 - 1.72)
37 V	1.50	(1.44 - 1.57)	1.47	(1.27 - 1.76)
21	0.94	(0.88 - 1.0)	0.97	(0.84 - 1.16)
18	0.84	(0.79 - 0.88)	0.91	(0.78 - 1.09)
10.69	0.73	(0.69 - 0.78)	0.76	(0.66 - 0.91)
6.6	0.66	(0.61 - 0.72)	0.65	(0.56 - 0.78)

Note: 300 K target and instrument temperatures

The SMMR was temperature-stabilized in orbit by the thermal louvers provided by the spacecraft. The instrument was not internally compensated or regulated. Moreover, the instrument was significantly thermally isolated from the other sensors on the spacecraft. A thermal shield enclosed the complete SMMR, except for the apertures of the multi-frequency feed and the sky calibration horns. The pods were thermally stabilized by aluminized foil wrappings. The back-up structure of the reflector had a radiatively cooled thermal blanket. Neither the pods or the reflector had temperature monitors or active temperature controls.

In the thermal/vacuum chamber, the SMMR was space-qualified over the instrument temperature range of from 268 to 318 K. In orbit, the mean temperature of the 37-GHz horizontal modulator switch assembly (defined as the representative instrument temperature) was 300.2 K with a standard deviation of 1.2 K and with a peak-to-peak range of 6.1 K. Figure 7-9 depicts the sampled thermometric history of the SMMR temperature from day 189 to day 283.

The orbital engineering record shows that all engineering temperatures remained within the temperature limits measured in the thermal/vacuum chamber. On day 221, the antenna scan motor slightly exceeded 45°C, which was the maximum value for any component in orbit, but within the limits observed in thermal/vacuum.

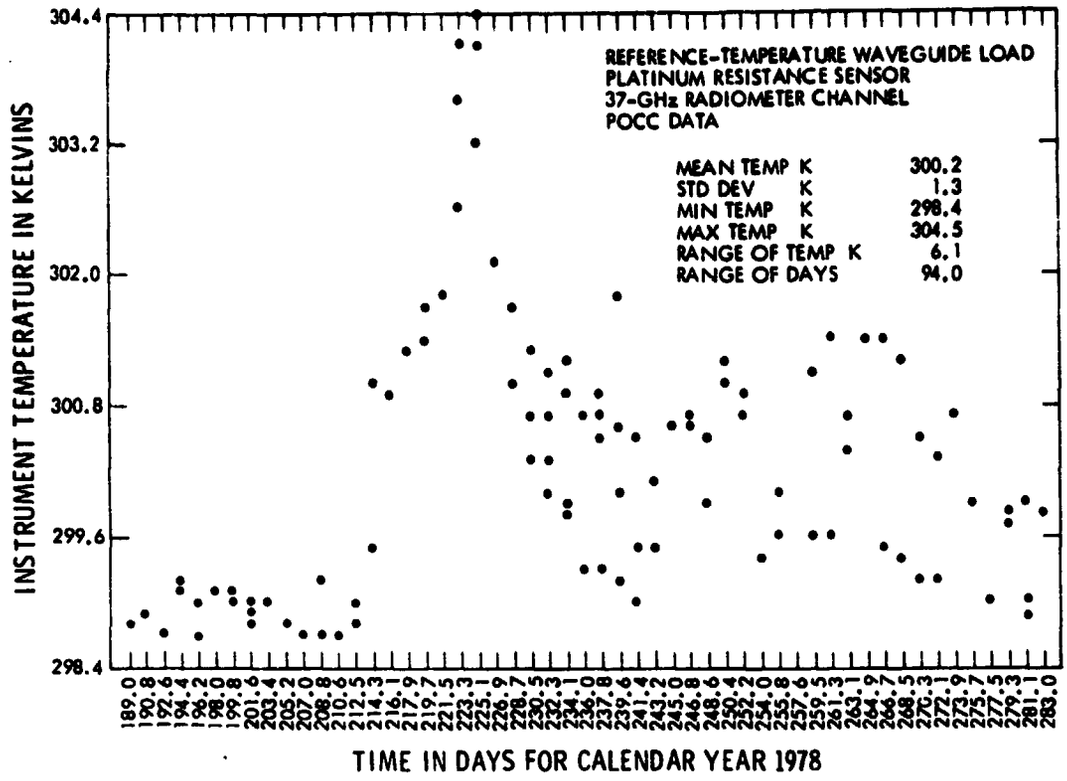

Figure 7-9. SMMR Orbital Temperature Summary

The electrical performance specifications for the SMMR are summarized in Table 7-8. The only technical specification that was rigidly verifiable in orbit was the temperature resolution, and this was demonstrated in the key parameter matrix shown in Table 7-6. The frequency tolerance was verified in the laboratory by measuring the leakage emission from the local oscillators through the multi-frequency feed horn. Antenna beam widths were measured on the antenna range at JPL. In general, the measured half-power antenna beam widths were approximately 10 percent higher than the specification. The polarization isolation specification was waived from 25 dB to 18 dB. Polarization isolation was verified by the antenna pattern measurements and certain frequencies exhibited isolations to -15 dB. Verification of the pointing accuracy was demonstrated at the spacecraft integration facility by optical alignment fixtures with the spacecraft. LMSC documentation shows the alignment to have been better than 0.1 deg. It did not seem feasible to rigorously determine the pointing accuracy specification from orbit to 0.1 deg. The solid angle beam efficiency was a calculated quantity derived from the antenna pattern measurements. The beam efficiency specification was a goal specification to exceed 87 percent. The measured beam efficiencies at 6.6 and 10.69 GHz are given at 86 and 84 percent, respectively. All other frequencies exceeded the specification. Table 7-4 summarizes the measured half-power beam widths, beam efficiencies, and polarization isolations. The absolute temperature accuracy was estimated to yield a secondary standard blackbody target at 0.36 K (1σ). The absolute temperature accuracy is embodied in the implementation of the temperature transfer

Table 7-8. SMMR Electrical Performance Requirements

Frequency (GHz)	6.633	10.69	18	21	37	37
Tolerance (1σ) (MHz)	5	8	14	16	28	28
Wavelength (cm)	4.52	2.81	1.67	1.43	0.81	0.81
Polarization	Vert. and Horiz.	Vert. and Horiz.	Vert. and Horiz.	Vert. and Horiz.	Vert.	Horiz.
Antenna Beamwidth, HP (deg)	4.2	2.6	1.6	1.4	0.8	0.8
Tolerance (1σ)	0.2	0.15	0.1	0.1	0.1	0.1
Polarization Isolation (dB)	>25					
Pointing Accuracy (deg) (1σ)	0.1					
Solid Angle Beam Efficiency (%)	>87					
Integration Time (ms)	126	62	62	62	30	30
Temperature Resolution (K) (1σ) (300 K Target)	0.9	0.9	1.2	1.5	1.5	1.5
Absolute Temperature (K) (1σ) Accuracy	2					
Dynamic Temperature (K) Range	10 - 330					
Temperature Stability (24 Hours) (K) (1σ)	1					

equation derived for the SMMR.* The dynamic temperature range was verified for signal and sky targets from 100 to 317 K in the thermal/vacuum chamber. The 2.7 K sky temperature observed in orbit was combined with the thermal/vacuum target temperatures to complete the calibration temperature range. The 24-hour temperature stability specification was effectively reconciled by the temperature transfer equation with respect to instrument temperature variations.

D. SCATTEROMETER

1. Description

a. General. The physical and functional characteristics of the SASS are shown in Figure 7-10. The SASS incorporated four antenna arrays, each with a 0.5- by 25-deg half-power beamwidth, producing a 761 km (410 nm) measurement swath on each side of the satellite. Wind speed measurements were made over a range of incidence angles from 25 to 65 deg. A minimum wind speed measurement of 4 m/s (13 ft/s) could be made for incidence angles of 33 to 53 deg (350 km (189 nm) swath on each side) and a 6-m/s (20 ft/s) measurement for incidence angles of 25 to 55 deg (500 km (270 nm) swath on each side). Slightly higher wind speeds were required for satisfactory measurements at the outer incidence angles.

A block diagram of the SASS is shown in Figure 7-11. The SASS used an integrated frequency synthesizer to generate all of the required RF signals at UHF and microwave frequencies used by the exciter, transmitter, mixers, and processor. The synthesizer consisted of a highly stable crystal-controlled oscillator from which all required frequencies were derived, ensuring coherency throughout the unit. The low-level microwave output of the synthesizer was amplitude-gated (on and off) by a pin-diode type switch to ensure high isolation (typically $\geq$60 dB) between the on and off states. The pulsed RF was amplified in the final output stage, which consisted of a TWT and integrated power supply. The 125-W peak power output pulse was directed to the stick antenna array through a series of waveguide components consisting of electromechanical waveguide switches, circulators, and a 1X5 waveguide diode switch. Each antenna had associated with it a switchable polarization circulator that was commanded in a preset mode by the timing and control electronics.

Received RF energy from the proper antenna was directed through the selected path of the 5-way switch, and was applied through the T/R circulator and receiver protection circulator to the low noise preamplifier, band pass filter, and first conversion mixer. In the mixer, a microwave signal derived from the stable oscillator in the synthesizer was added to the return signal to produce a coherent IF signal that was then applied to the processor. The processor consisted of IF amplifiers, amplitude control range gates, and processing channels. The processing channels for the data consisted of a bank of band-pass Doppler filters, detectors, dc amplifiers, and signal integrators. The timing and control for the processor was provided by the control unit.

---

*J. Stacey, L. Lyon, and P. Gloersen, Temperature Transfer Equations (A Hyperplane Regression), JPL Internal Document 622-103, 27 November 1978.

SEASAT-A SATELLITE SCATTEROMETER (SASS)

CONFIGURATION

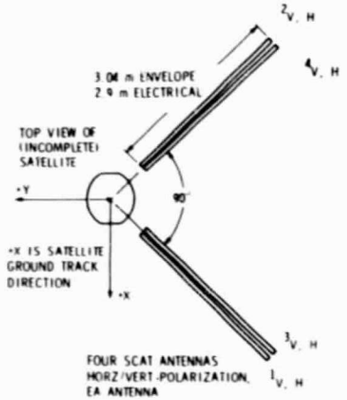

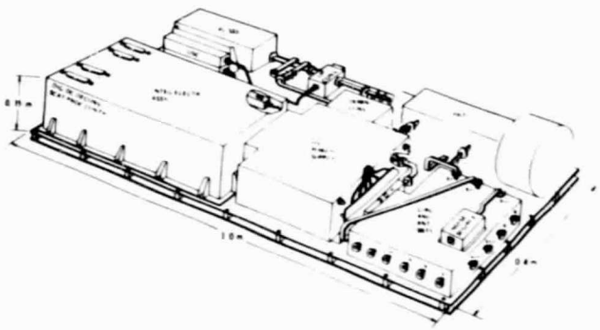

FUNCTIONAL DIAGRAM

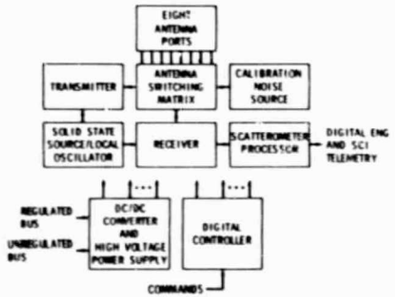

OPERATING MODES

MODE NO.	MEASUREMENT SEQUENCE PER BEAM	ANTENNA (1) BEAM SEQUENCE	TIME PER SEQUENCE (sec)*	SWATH WIDTH
1	VV	LF, RF, LA, RA	7.56	FULL
2	HH	LF, RF, LA, RA	7.56	FULL
3	VV, HH	LF, LA	7.56	1/2
4	VV, HH	RF, RA	7.56	1/2
5	VV, VV	LF, LA	7.56	1/2
6	VV, VV	RF, RA	7.56	1/2
7	HH, HH	LF, LA	7.56	1/2
8	HH, HH	RF, RA	7.56	1/2
9	CONTINUOUS CALIBRATE			

*INTEGRATION TIME PER MEASUREMENT = 1.89 sec

(1) LF = LEFT FORWARD
LA = LEFT AFT
RF = RIGHT FORWARD
RA = RIGHT AFT

LINK AND PERFORMANCE EQUATIONS

$$P_R = \frac{P_t \sigma^0 G_0^2 (G/G_0)^2 \phi L \lambda^2 L_s}{(4\pi)^3 R_c^3}$$

$$SNR = \frac{P_R}{KTB_c} \qquad K_p^2 = \frac{1}{B_c T_{SN}} \left[1 + \frac{1}{SNR} + \frac{1}{SNR^2} \frac{\tau_g}{\tau_s} (1 + \frac{\tau_g}{K_1 \tau_s}) \right]$$

PARAMETER	DEFINITION	+dB	-dB
P_t	TRANSMIT POWER	20.41	
σ^0	RADAR SCATTERING COEFFICIENT		16.00
G_0^2	ANTENNA PEAK GAIN	65.00	
$(G/G_0)^2$	ANTENNA PATTERN GAIN LOSS		15.40
ϕ	ANTENNA NARROW DIM. BW (ϕ = 0.5°)		20.59
L	DOPPLE CELL BASE DIMENSION, km		17.62
λ^2	WAVELENGTH (λ = 2.0535 x 10^{-5} km)		93.75
L_s	TRANSMIT AND RECEIVE LOSSES		3.6
$(4\pi)^3$	---		32.98
R_c^3	RANGE TO DOPPLER CELL		88.11
		+103.03	-270.43
P_R = 103.03 -270.43 = -167.4 dBW			
B_c	DOPPLER FILTER BW/CELL (1 BW = 25.65 Hz)		44.09
KT	THERMAL NOISE (1 HZ) T = 964°K	198.70	

SNR = -167.8 + 198.7 -44.43 = -12.79

FOR: T_{SN} = 292.8 msec, $K_1 = \frac{T_{SN}}{T_N}$ = 1.64, g = TOTAL RANGE GATE = 377 msec

$$K_p = \frac{1}{\sqrt{7513}} \left[1 + \frac{1}{0.53} + \frac{1.29}{0.003} \left(1 + \frac{1.29}{1.64} \right) \right]^{1/2} = 0.34$$

K_p = NORMALIZED STANDARD DEVIATION OF σ^0 MEASUREMENT

NOTE: ABOVE LINK CALCULATION IS FOR θ_i = 25°, W/S = 4 m/s

DOPPLER CELLS

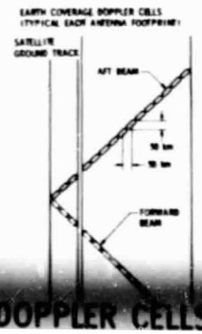

SWATH

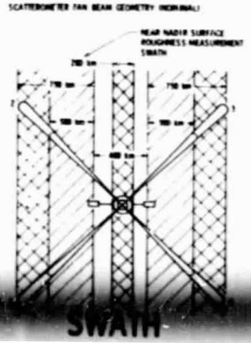

TECHNICAL CHARACTERISTICS

- BACKSCATTER/
RECEIVED SIGNAL, dBm = BACKSCATTER, σ^0 + RECEIVED SIGNAL, dBm

DOPPLER CELLS

SWATH

DOPPLER CELLS

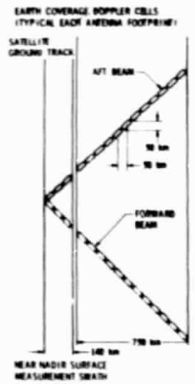

SWATH

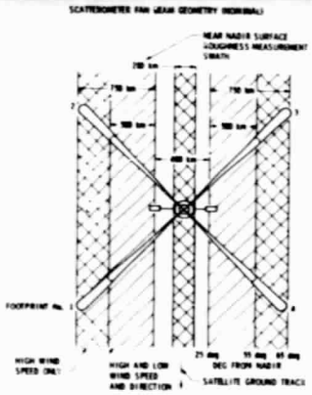

SNR = -167.8 + 198.7 -44.43 = -12.79

FOR: τ_{SN} = 292.8 msec, $K_1 = \frac{\tau_{SN}}{\tau_N} = 1.64$, q = TOTAL RANGE GATE = 377 msec

$$K_p = \frac{1}{\sqrt{7513}}\left[1 + \frac{1}{0.53} + \frac{1.29}{0.003}\left(1 + \frac{1.29}{1.64}\right)\right]^{1/2} = 0.34$$

K_p = NORMALIZED STANDARD DEVIATION OF σ^o MEASUREMENT

NOTE: ABOVE LINK CALCULATION IS FOR θ_i = 25°, W/S = 4 m/s

PERFORMANCE

- OCEAN SURFACE WIND SPEED - 4 TO >28 m/sec ±2 m/sec OR 10% WHICHEVER IS GREATER
- OCEAN SURFACE WIND DIRECTION - 0-360 ± 20
- SWATH - AS SHOWN IN COVERAGE FIGURE
- CELL RESOLUTION - 50 km
- CELL GRID SPACING - 50 km x 50 km
- MEASUREMENT INTEGRATION - 1.89 sec
- MODES: AS SHOWN ABOVE
- SCATTERING CROSS SECTION NORMALIZED STANDARD DEVIATION (Kp) - SEE ADJOINING CHART
- MAXIMUM BIAS ERROR ≤ ± 2 dB
- SYSTEM CALIBRATION ± 0.2 dB

CALCULATIONS

INCIDENCE ANGLE (deg)	4 m/sec WINDSPEED σ^o (dB)	4 m/sec WINDSPEED NOMINAL Kp (NUMERIC)	48 m/sec WINDSPEED HIGH σ^o (dB)	48 m/sec WINDSPEED NOMINAL Kp (NUMERIC)
25	-16	0.34	0	0.019
30	-21	0.25	0	0.013
40	-24	0.17	-3	0.014
50	-27	0.44	-6	0.019
55	-28	0.94	-7	0.023

σ^o = BACKSCATTER COEFFICIENT

BASED ON: NOMINAL ORBIT

40 POINTING ANGLE OF ANTENNA

TECHNICAL CHARACTERISTICS

- BACKSCATTER/RECEIVED SIGNAL:

BACKSCATTER, dB			RECEIVED SIGNAL, dBm		
WIND, m/sec	ANGLE, deg 25	55	WIND, m/sec	ANGLE, deg 25	55
4	-16	-28	4	-138	-143
25	-4	-13	25	-126	-128
48*	0	-7	48	-122	-122

*EXTRAPOLATED FROM LOWER WIND SPEED DATA

- FREQUENCY - 14.5927 GHz
- BANDWIDTH - ±500 kHz
- TRANSMIT TIME/TOTAL TIME - 0.2
- PULSE WIDTH - 4.8 msec
- PEAK TRANSMITTED POWER - 110 W
- PRF - 34 PULSES/sec
- AVERAGE TRANSMITTED POWER - 20 W
- AVERAGE RAW POWER - 80 W REGULATED
  - 85 W UNREGULATED
- RECEIVER NOISE TEMP 1250°K
- GAIN CONTROL - AUTOMATIC
- ANTENNA PEAK GAIN - 32.5 dB
- ANTENNA POLARIZATION - HORIZONTAL/VERTICAL
- SIZE - ANTENNA ≤ 3.04 m LONG
  - ELECTRONIC BAY ≤ 1.1 x 0.5 x 0.35 m
- DATA RATE - 540 bps
- WEIGHT - ANTENNA ≤ 13.6 kg EACH ANTENNA
  - ELECTRONICS BAY - ≤ 80 kg

SIGNIFICANT DEVELOPMENTS

- HIGH VOLTAGE POWER SUPPLY
- FAN BEAM ANTENNAS

SPECIAL FEATURES

- DOPPLER FILTERING
- FOUR ANTENNA ELECTRONIC SEQUENCE
- DUAL POLARIZATION (EACH ANTENNA)
- FAN BEAM ANTENNAS

INHERITANCE

- SKYLAB RADSCAT, AAFE A/C RADSCAT → SEASAT-A
- B-SAT TWT, B-SAT HVPS → SEASAT-A TWTA

Figure 7-10. Seasat - A Satellite Scatterometer (SASS)

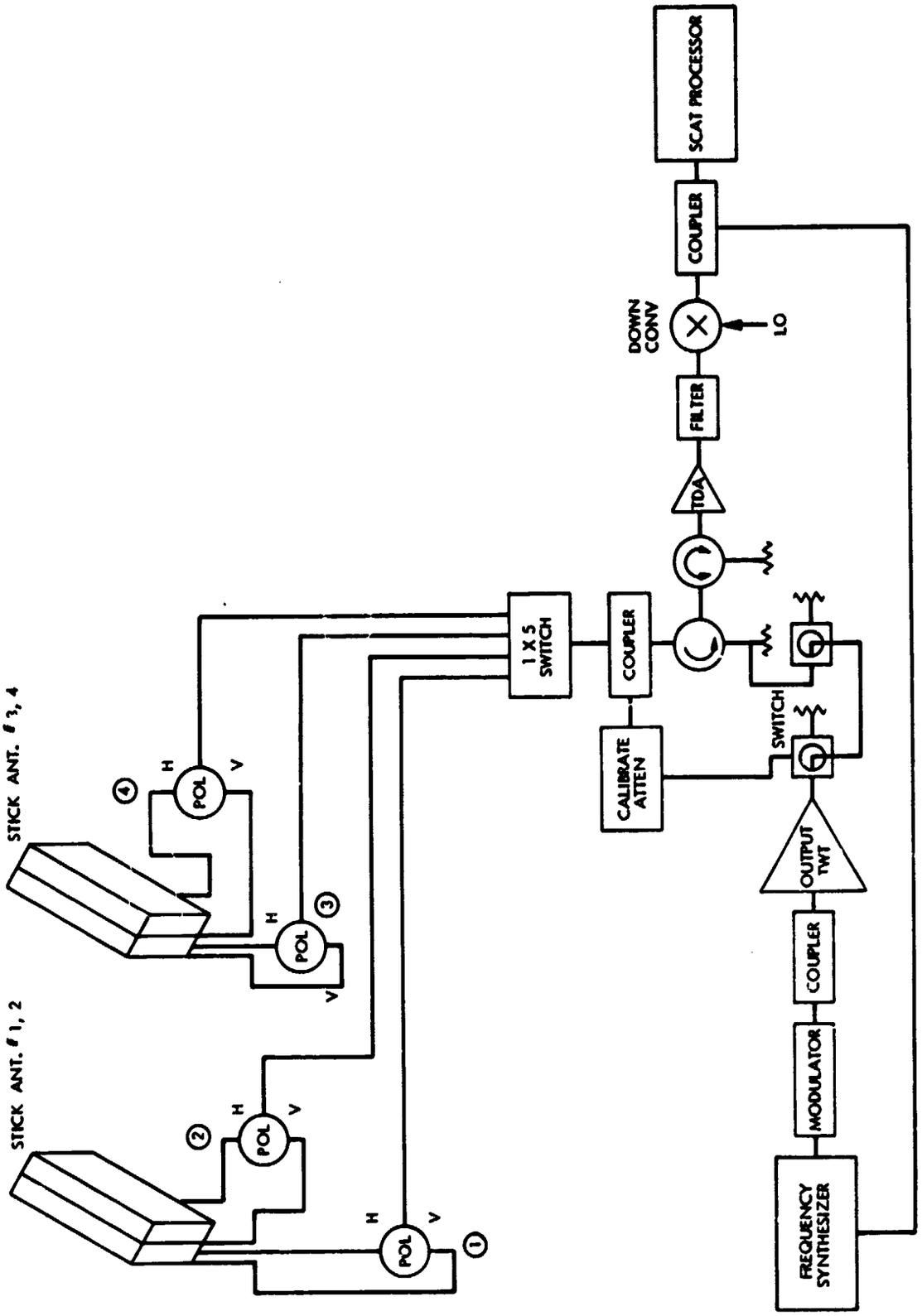

Figure 7-11. SASS Block Diagram

The function of the control unit was to accept spacecraft commands and power, and to generate the precise timing and control logic required by the SASS to form rf pulses and to operate the processor. In addition, the control unit accepted the output SASS data and instrument telemetry parameters and formatted them so they were compatible with the spacecraft data system.

b. Transmitter.

Integrated Frequency Synthesizer. Using an ultra-stable crystal oscillator, the integrated frequency synthesizer generated all required RF signals at vhf, uhf, and microwave frequencies for the SASS. Stabilities of better than 1 part of 10^8 over a few milliseconds and 1 part in 10^7 over a day could be obtained with proportionally controlled heated crystal oscillators. The oscillator frequency chosen depended on the final output frequency selected as well as the desired first and second RF frequencies, but would typically be 50 MHz below and use a third overtone crystal. The basic oscillator output was then buffered, amplified, and used to drive a harmonic generator that produced integer multiples of this frequency. Using stripline or combline filter techniques, the required VHF/UHF signals for down conversion were then obtained. Another portion of the crystal oscillator output was used to drive a phase-locked, solid-state multiplier that produced the proper microwave signal for the output.

Pin Diode Switch. This switch used a pair of pin diodes shunted across the waveguide structure that were driven into conduction or back-biased into the off state. Typical performances achievable in such a switch were a >35 dB on/off ratio, >2 dB insertion loss in the on state, ≤10-ns rise and fall time, and <2-ns rf pulse delay. These performance specifications ensured high fidelity pulses with ultra-sharp rise and fall times to provide proper SASS performance.

Output TWTA. The output TWTA amplified the pulses rf input from the pin diode switch, and had an output of 125-W minimum saturated power. Based on a TWT design derived from a Hughes tube (294-H) to be flown on the Japanese broadcast satellite, the TWTA could operate over a 200-MHz bandwidth with greater than 40 percent efficiency, including the power supply. The typical gain was 42 dB minimum at saturation, and an advanced cathode design would permit operation for over 3 years with little or no performance degradation. The TWTA required spacecraft power input, commands to turn on the heaters, and high voltage in addition to a pulse modulation input command. The TWTA provided telemetry outputs of critical temperatures, voltages, and currents to the SASS housekeeping telemetry data stream.

c. Receiver.

Input Circuits. The SASS receiver input circuits consisted of the 5-way waveguide diode switch that directed energy from the selected antenna to the T/R and receiver protection circulator. Both of these circulators together provided approximately 60 dB of isolation for the receiver when the pulse was being transmitted. In the receive state, the circulators exhibited less than 0.5 dB insertion loss. The low-noise device was a tunnel diode amplifier, which had a gain of 30 dB with a 6-dB noise figure. By minimizing losses from the amplifier to

the antenna, it was possible to maintain the total system noise temperature to approximately 1100 K (assuming a total loss of 3 dB).

The output of the tunnel diode amplifier was combined with a low-level microwave signal derived from the synthesizer in a low-noise, low-conversion loss diode mixer to produce the first i-f signal.

Processor. The processor amplified, detected, and integrated the samples of the backscattered energy and provided an indication of the total received power to the spacecraft data system. To accomplish, it was necessary for the system to amplify the first i-f signal, and then mix it once again with a signal derived from the synthesizer to bring the information down to a convenient second IF frequency. At this frequency, the range gating and Doppler filtering were accomplished that achieved the desired spatial resolution on the ground. After filtering, the selected element was detected, amplified, and integrated for a specific period of time. It was this integrated value, which represented an estimate of the received power, that was A/D-converted and applied to the data stream.

The processor was controlled through logic and switching commands provided by the digital control electronics to ensure the proper sequence of range gating and integration.

Control Unit. The control unit functioned as an interface between the spacecraft and the SASS, providing all required input voltages and accepting output data and housekeeping telemetry. Selected functions of the control unit were: (1) generation of pulses of the proper width and PRF for the transmitter; (2) generation of the proper sequence of commands for switching the antennas and antenna polarization; (3) generation of proper commands for operation of the processor, including the range gates and integration commands; (4) distribution of raw and processed voltages to the SASS components; (5) formatting, A/D-converting, and multiplexing the input data and telemetry; and (6) delivery of the SASS data stream to the spacecraft data processing system.

Antennas. Four antennas were used in the SASS system. Each antenna could operate in one of two linear polarization modes. The four antennas had an antenna bandwidth of 0.5 by 25 deg.

2. Algorithms.

a. Introduction. The SASS was a microwave radar that provided global day and night measurements of the synoptic scale ocean-surface wind vector. The physical basis for this technique is the Bragg scattering of microwaves from centimeter-length capillary ocean waves. The strength of radar backscatter (Normalized Radar Cross Section (NRCS) or σ^o) is a function of the capillary wave amplitude, which is proportional to the wind speed near the sea surface. Further, the radar backscatter is anisotropic; therefore, wind direction could be derived from SASS measurements at different azimuths. Specifications for the SASS required a wind speed measurement range of 4 to >26 m/s with an accuracy of ±2 m/s or 10 percent (whichever was greater), and a wind direction measurement range of 0 to 360 deg with an accuracy of ±20 deg.

The SASS incorporated four dual-polarized (vertical, vertically-polarized, horizontal, horizontally-polarized) antennas which produced an X-shaped pattern of illumination on the Earth (Figure 7-12). The satellite geometry required that both forward and aft looking antennas be used to obtain two independent radar measurements at the same ocean location. The Seasat implementation used antenna beams, each oriented 45 deg relative to the sub-satellite track, to yield observations that were separated in azimuth by 90 deg. Twelve Doppler filters were used to sub-divide electronically the broad antenna footprint into resolution cells approximately 50 km (27 nm) on a side. In addition, σ^o measurements from incidence angles near nadir provided coverage (wind speed only) along the subtrack.

The SASS Evaluation Task Group has three candidate geophysical algorithms for inferring ocean wind vector from radar backscatter measurements. Basic to all is the empirical model function which relates radar backscatter σ^o to wind vector as a function of incidence angle, azimuth angle, and polarization. The present model function was derived before launch using a limited data base of aircraft radar measurements and will be evolved using Seasat data with suitable surface wind measurements. Because of the harmonic nature of the model function, the geophysical algorithm recovers between one and four solutions for each grid point. These solutions are nearly equal in speed, but vary widely in direction. This result has been referred to as aliasing. Therefore, the data must be additionally processed to yield the correct solution. For the present time, a-priori knowledge of wind direction from surface observations, permit aliases to be removed.

b. Sigma Naught (σ^o) Algorithm. The value of radar scattering coefficient (σ^o) is determined by processing the Engineering Unit (EU) data from the Sensor Data Record (SDR). This process includes: (1) the determination of the SASS receiving system gain; (2) the determination of the mean value of power (P_R) reflected from the surface during a measurement period; (3) the determination of the antenna gain from the antenna gain function; (4) the determination of the measurement cell size; and (5) the calculation of σ^o from the radar equation.

The surface was sampled 61 times during a 1.89-s period. At the end of this period, 15 pairs of voltage measurements were obtained at 15 locations along one of 8 antenna beam illuminations. The antennas were arranged in pairs, one vertically polarized and one horizontally polarized. Each location and cell size was determined by the center frequency and bandwidth of 15 Doppler filters contained in the SASS receiver processor. Figure 7-12 illustrates the ground coverage patterns obtained. The 1.89-s sampling period was continually repeated, but with a different antenna being sampled each time. A different combination of antenna sequencing could be picked by the proper choice of one of eight modes.

After every 124 sample periods or science frames (approximately every four min), four calibration frames were processed in which known calibration signals were applied to the receiver. In the σ^o algorithms, the data from these calibration frames were processed to determine the gain of the system. These gain values were used for the next 124 science frames.

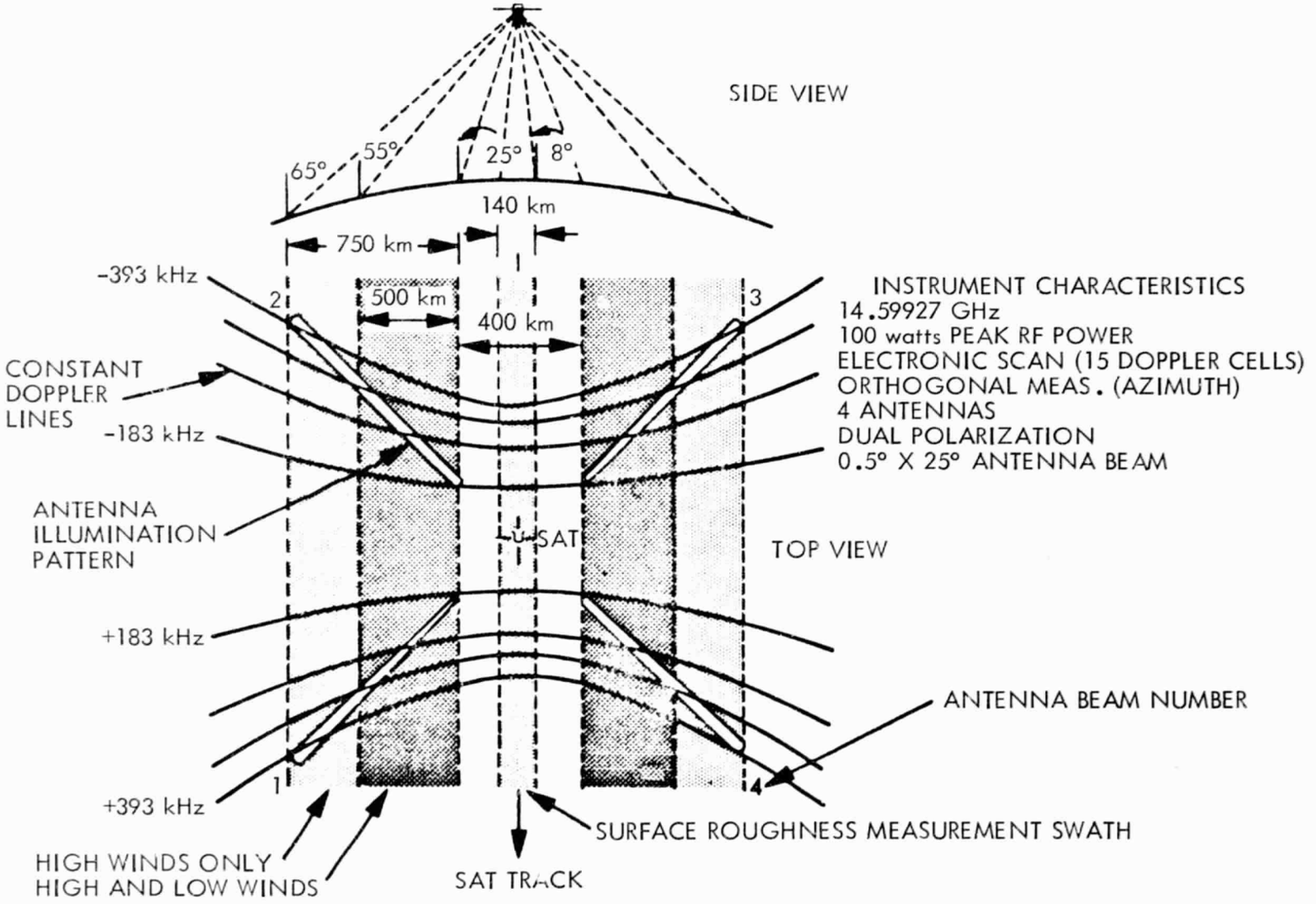

Figure 7-12. SASS Swath Gometry

The voltage pairs obtained for each of the 15 channels, during a science frame, were a measured of the signal reflected from the surface plus system noise (V_{SN}) and a measure of the system noise (V_N). Using these values plus the gain of the receiver obtained from the calibration frame, and known processing integration times, the power reflected from the surface were determined. This is illustrated in Figure 7-13. The pulse repetition period for one of the 61 samples is illustrated, along with a simplified diagram of the receiver processor system for one of the 15 Doppler channels. The 4.8-ms pulse is the transmitter "on" time. During the "off" period between pulses, the return signal and noise were integrated. At the end of the t_g integration period, the voltage V_{SNN} was obtained. At the end of the t_n integration period (integration dumped after t_g period), the voltage V_N was obtained. At the end of 61 samples (1.89 s), the mean value of V_{SNN} and V_N for all 15 channels was telemetered to the ground along with the measured transmitter power, various housekeeping data, and status information. The second part of the σ^o algorithms processes this information to obtain P_R.

The next step in the σ^o algorithm determines the antenna gain for each Doppler cell from a look-up table of antenna gain function, using the calculated antenna look direction for each Doppler cell. For each data sample of each Doppler channel, the look direction, footprint (Doppler cell) location, and various geometric parameters such as range (R), cell length (L), incidence angle (θ_i), etc. are determined in the Instrument Data Processing System (IDPS) and placed in the SDR along with the EU data. This determination utilizes the known spacecraft ephemeris data, spacecraft attitude data, spacecraft mounting angles for each antenna and its calculated electrical pointing direction, the known Doppler filter center frequencies (f_o), and the Doppler bandwidths (B_N).

The cell area of each Doppler cell is next determined by using the information from the footprint location processing.

Finally, the value of σ^o is determined by solving the radar equation. The derivation of this equation is as follows:

$$P_R = \left(\frac{P_T G_T}{4\pi R^2}\right)\left(\sigma^o A_e\right)\left(\frac{1}{4\pi R^2}\right)\left(\frac{G_R \lambda^2}{4\pi}\right) LS \qquad (1)$$

$$G_R = G_T G = G_o \left(\frac{G}{G_o}\right)$$

$$P_R = \frac{P_T \lambda^2 L_S G_o^2}{(4\pi)^3} \int_A \frac{(G/G_o)^2 \sigma^o n(f)}{R^4} dA \qquad (2)$$

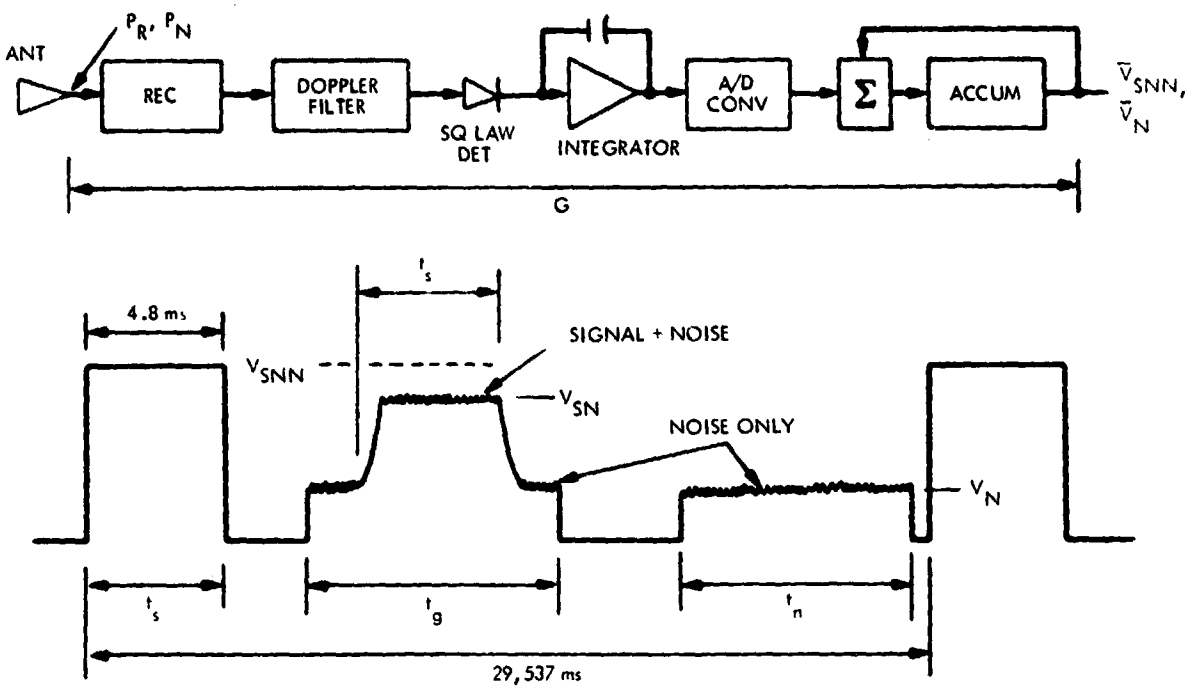

$T_S = 61 \times t_s = 0.2928$ (ALL CHANNELS)

$T_G = 61 \times t_g = 0.345$ TO 0.69

$T_N = 61 \times t_n = 0.4818$ (ALL CHANNELS)

$$V_S NN = T_S G (P_R + P_N) + (T_G - T_S) P_N G \quad (1)$$

$$\bar{V}_{SN} = \bar{V}_{SNN} - \frac{T_G - T_S}{T_N} V_N \quad (2)$$

$$P_{SN} = \frac{\bar{V}_{SN}}{T_S G} \text{ - SIGNAL + NOISE POWER} \quad (3)$$

$$P_N = \frac{\bar{V}_N}{T_N G} \text{ - NOISE POWER} \quad (4)$$

$$P_R = \frac{\bar{V}_{SN}}{T_S G} - \frac{\bar{V}_N}{T_N G} \text{ - SIGNAL POWER} \quad (5)$$

Figure 7-13. SASS Reflected Power Determination

WITH THE FOLLOWING ASSUMPTIONS:

$$h(f) = \begin{cases} 1 - f_\ell < f < f_u \\ o - \text{elsewhere} \end{cases}$$

R = RANGE TO CENTER OF CELL

G/G_o = GAIN LOSS RATIO TO CENTER OF CELL

σ^o = SCATTERING COEFFICIENT VALUE AT CELL CENTER

A = LR ϕ_A = CELL AREA

L = DISTANCE ON EARTH SURFACE FROM f_ℓ TO f_u

ϕ_A = NARROW DIMENSION ANTENNA BEAMWIDTH, radius

THEN: SOLVING FOR σ^o

$$f_\ell = f_o - \frac{B_n}{2}$$

$$f_u = f_o + \frac{B_n}{2}$$

A_e = effective surface area

B_n = noise bandwidth (Doppler filter)

f_o = center frequency

P_T = transmitter power

G_o = peak antenna gain

L_S = miscellaneous losses

P_R = measured receiver power

λ = transmit wave length

G_T = transmit antenna gain

G_R = receive antenna gain

$$\sigma^o = \frac{64\pi^3 P_R R^4}{P_{T\lambda}^2 L_S G_o^2 \left(\frac{G}{G_o}\right)^2 A} \quad (3)$$

Equation (1) gives the value of power reflected back from the surface. The first term in parentheses is the power density at the surface. The second term in parentheses is the effective radar cross section. The third term in parentheses is the rf spreading loss. The first, second, and third terms in parentheses, taken together, represent the power density at the receiving antenna, and the last term in parentheses is the antenna receiving aperture. The term L_S includes miscellaneous losses such as antenna switching matrix and waveguide losses. To obtain the true received power, certain parameters which vary over the cell area must be integrated over the area, as shown in Equation (2). However, certain approximations can be made which reduce the determination of σ^o to Equation (3). Minor correction factors are included in the calculation of σ^o to correct for differences between the approximate equation and the integral equation. This approach relieves the requirement, in the σ^o algorithms, for the inversion of the integral in Equation (2).

The value of σ^o is now obtained by substituting into Equation (3) the measured values for P_R and P_T, the values of G_o and (G/G_o) determined from the table look-up, and the calculated values of R and A. The pre-launch values of antenna switching matrix and waveguide losses are used for L_S.

The σ^o algorithms incorporate additional algorithms which provide supporting information for the value of σ^o. These are estimates of the normalized standard deviation (NSD) of the measurements, Doppler data cell geometric information, and the evaluation of status information. The status evaluation provides additional indicators for separating out bad data points. The geometric parameters include total integrated cell areas and the latitude and longitude of the four corners of a box which approximates the cell area. This information is useful for co-locating footprints from other instruments and for separating out measurements which fall on land.

An additional algorithm is incorporated in the σ^o algorithm which removes σ^o bias error. The heart of this algorithm is a bias table which will be generated when A/C underflight σ^o data are processed and compared to the SASS σ^o data. Initial analysis of the comparison of the SASS wind fields with surface spot observation and surface wind field analysis indicates that a bias of about 1 dB may exist.

Figure 7-14 is a sequence schematic of the σ^o processing algorithms and data flow for the ADF SASS software.

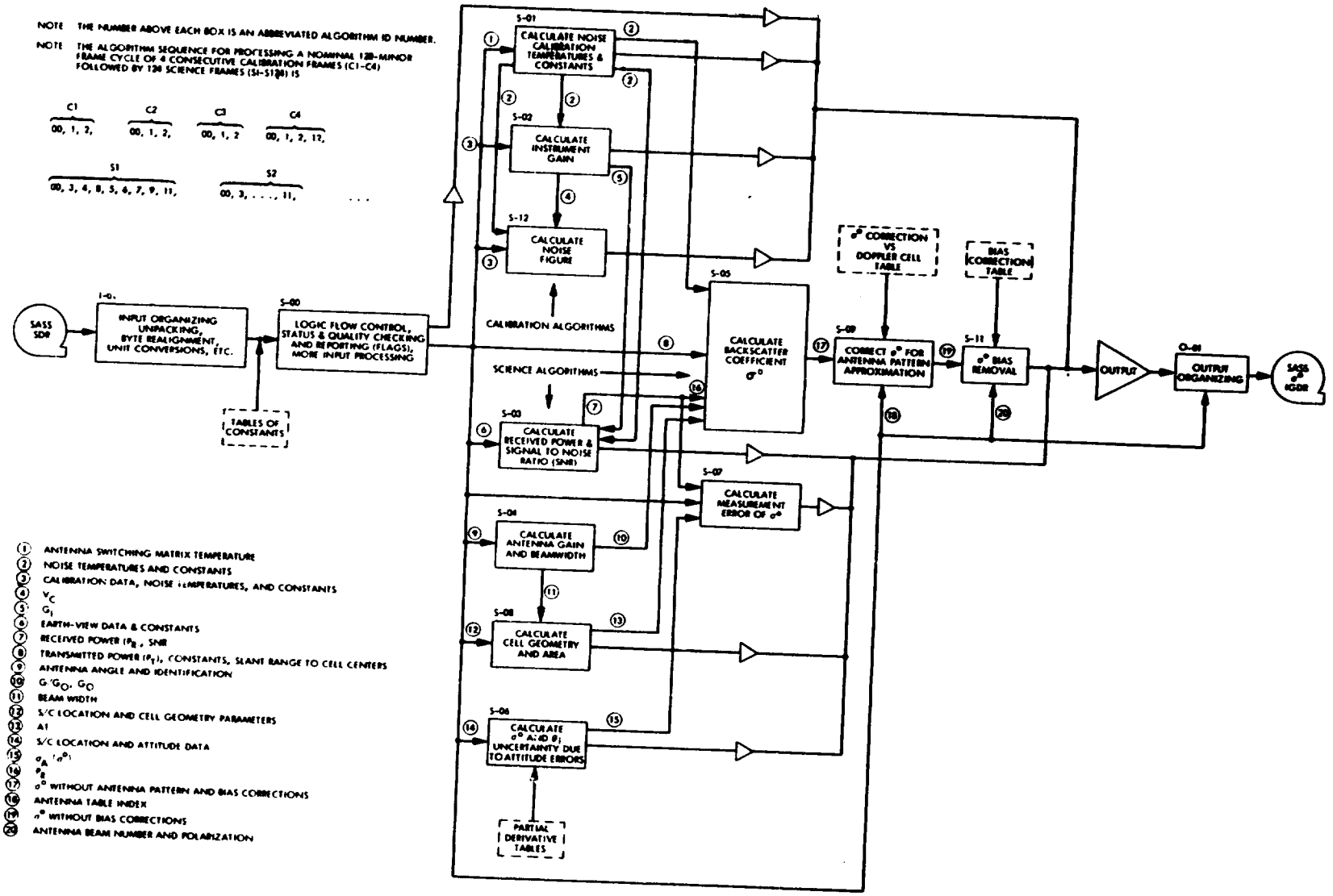

Figure 7-14. SASS ADF IGDR σ^o Processing Algorithms, Version 1

c. Wentz SASS Geophysical Algorithm. The Wentz SASS geophysical algorithm is based on a theoretically derived function for computing the NRCS or σ^o observed by the SASS. The parameters in the function were derived from the AAFE/RADSCAT aircraft NRCS measurements. A maximum likelihood estimator operates on this function to yield estimates of wind speed and direction. The following is a description of the estimation procedure.

Algorithm for Computing the Surface Wind Velocity. Consider the situation in which several NRCS measurements are taken of the same wind-sea state and it is desired to find the probability $P(W \mid \sigma_n^o)$ that the wind speed has a value W given the set σ_n^o of n measurements. The probability is given by the following extension by Bayes' equation:

$$P\left(W \mid \left\{\sigma_n^o\right\}\right) = \frac{P(W) \prod_{i-1}^{n} P\left(\sigma_i^o \mid W, \left\{\sigma_{i-1}^o\right\}\right)}{\int dW\, P(W) \prod_{i=1}^{n} P\left(\sigma_i^o \mid W, \left\{\sigma_{i-1}^o\right\}\right)} \qquad (1)$$

The term P(W) is the probability that the wind speed vector is W independent of the NRCS measurements. It is assumed that no other information on W is available and let P(W) be a uniform distribution over W space. Therefore, P(W) can be removed from the integral and cancels out.

The other term $P(\sigma_i^o \mid W, \sigma_{i-1}^o)$ in Equation (1) is the probability that the i^{th} measurement has a value of σ_i^o given the wind velocity vector is W and the first through i-1 measurements are the set σ_{i-1}^o. In order to specify $P(\sigma_i^o \mid W, \sigma_{i-1}^o)$, an analysis was performed of the fluctuations in the aircraft NRCS measurements. These fluctuations are caused by the microscale turbulence in the wind field and by the SASS noise. A χ^2 test indicated that the distribution of the measurements is closer to log-normal than normal. In view of this it is assumed that σ_i^o is log-normally distributed about the actual NRCS given by the NRCS function $f(\theta_i, \psi_i, W)$. The angles θ_i and ψ_i are the incidence and relative azimuth angles for the i^{th} measurement. Under this assumption, $P(\sigma_i^o \mid W, \sigma_{i-1}^o)$ is independent of σ_{i-1}^o and is given by:

$$P\left(\sigma_i^o \mid W, \left\{\sigma_{i-1}^o\right\}\right) = \left(2\pi\delta^2\right)^{-1/2} \exp\left\{-\left[\overline{\sigma_i^o} - \overline{f}_i(W)\right]^2 / 2\delta_i^2\right\} \qquad (2)$$

where $\bar{\sigma}_i^o = \log \sigma_i^o$, $\bar{f}_i(\theta_i, \psi_i, W)$, and δ_i is the standard deviation of $\bar{\sigma}_i^o$. Substituting Equation (2) into Equation (1) yields:

$$P\left(W \mid \left\{ \sigma_n^o \right\}\right) = \frac{\prod_{i=1}^{n} \exp\left\{ - \left[\sigma_i^o - \bar{f}_i(W) \right]^2 / 2\delta_i^2 \right\}}{\int dW \prod_{i=1}^{n} \exp\left\{ -\left[-\bar{\sigma}^o{}_i - \bar{f}_i(W) \right]^2 / 2\delta_i^2 \right\}} \qquad (3)$$

For a single, noise-free NRCS measurement, the possible wind velocity vectors lie on a line in W space. For the case of two orthogonal, noise-free measurements, i.e., $\psi_2 = \psi_1 + 90$ deg, the probability $P(W \sigma_1^o, \sigma_2^o)$ is non-zero only at the intersections of the two lines corresponding to the individual measurements. The number of intersections ranges from one to four depending on the value of ψ_1. The presence of noise spreads the region of possible W over areas in the neighborhood of the intersection points. When there are more than two measurements, the situation becomes more complicated with many such areas possible.

In order to obtain a best estimate of the wind velocity vector, we find the set of W corresponding to the local maxima of $P(W|\sigma_n^o)$. Some of the maxima may be much lower than the others and are discarded. If additional meteorological data of sufficient quality are available on wind direction then, in principle, all the remaining W can be eliminated except for the one corresponding to the actual wind velocity vector. The local maxima are found by first setting to zero the derivative of $P(W \mid \sigma_n^o)$ with respect to W for a particular wind velocity direction. Performing this operation on Equation (3) gives:

$$\sum_{i=1}^{n} \left\{ \left[\bar{\sigma}_i^o - \bar{f}_i(W) \right] / \delta_i^2 \right\} \bar{f}_i'(W) = 0 \qquad (4)$$

where the prime denotes differentiation with respect to W. We next use the property that for incidence angles greater than 20 deg, an approximate linear relationship exists between $\bar{f}_i(W)$ and log W. Taylor's expansion gives:

$$\bar{f}_i(W) = \bar{f}_i(W^o) + (\log W - \log W^o)\, \bar{f}_i'(W^o) + \Delta \qquad (5)$$

where W^o is a first guess for the wind speed vector and Δ is the remainder term. The prime now denotes differentiation with respect to log W. Setting the remainder term to zero and substituting Equation (5) into Equation (4) yields on the first iteration:

$$\log W = \log W^o + \frac{\sum_{i=1}^{n} \left[\sigma_i^o - \bar{f}_i(W^o)\right] \bar{f}_i'(W^o)/\delta_i^2}{\sum_{i=1}^{n} \left[\bar{f}_i'(W^o)\right]^2/\delta_i^2} \qquad (6)$$

On the second iteration W^1 replaces W^o in Equation (6) and a W^2 is found. The procedure continues until the desired convergence is reached. Generally, only one or two iterations are required for a convergence of 0.5 dB in low W.

Equation (6) is used to find a W_j for wind speed directions from 0 to 355 deg in 5-deg steps, yielding a set of 72 wind-speed vectors. The corresponding probabilities $P(W_j \mid \sigma_n^o)$ are searched for local maxima. If the jth probability is greater than or equal to the J-1 and j+1 probabilities, then W_j along with its probability are output. In this way we find the set of W corresponding to the local maxima of $P(W \mid \sigma_n^o)$.

3. Engineering Assessment Summary

a. Objective. The primary objective of the post-launch engineering assessment activity was to assure the JPL project office that the Scatterometer (SASS) SDRs contained a correct engineering data base and that the instrument was operating properly so that SDRs could be released for geophysical processing. The following constraints were applied:

(1) Data to be used was restricted to the first 30 days of operation.

(2) Hardware evaluation based on SDR products only and not P_R or σ^o.

(3) All location processing validation to be done independently from engineering assessment, since it is dependent upon σ^o computations.

b. Operations. The SASS antennas were deployed on the second orbit. The instrument was turned on 10 days after launch on 6 July 1978 (day 187) during Rev 139, and operated continuously throughout the first 30 days. Engineering assessment operations were completed on 6 August 1978 (day 218). Over the complete mission, the SASS operated for 2290 hours (95.5 days) and was only off for

21 hours for orbit adjust maneuvers. Between 23 August and 30 September, aircraft under-flights were conducted in conjunction with JASIN and GOASEX operations with surface winds up to 35 knots for calibration of the satellite instrument.

c. Software Evaluation. Excluding cell location, SDR processing has been evaluated with respect to status parameter handling and analog EU conversion. In addition, an SDR data quality analysis was conducted to estimate the probability of error in computing σ^o. The POCC processing was validated and SPS processing has been evaluated.

SDR processing itself, using software through 4.8C, was determined to be acceptable; however, after applying certain data filtering tests, the probability of an error in σ^o was estimated to be 1 in 2.3×10^3 measurements. Even though this may be considered acceptable, the error rate at the SDR output is surprisingly high. In fact, the raw data error rate was so high that both the maximum/minimum test in Standard Report 1's and a Special Report on SASS status were rendered useless, which was quite a deficiency in SPS processing. All data handling and EU conversion in POCC processing were acceptable. A data frame mixing problem on SASS ALL DATA SNAPSHOTS due to the absence of buffering at the printer was being corrected when the satellite failed. This was not a deficiency, given the original POCC plan, but it became a problem as POCC remained the sole source for engineering assessment data for the first three months. The conclusions on the software are that SDR processing beginning with 4.8C, and presumably thereafter, and POCC processing were acceptable. The deficiencies resulted from poor data quality and a data buffering limitation at POCC.

d. Hardware Evaluation. The hardware evaluation was concentrated in 3 areas: complete functional validation, receiver performance properties, and end-to-end instrument performance using SDR products (i.e., science voltages and gain state). The data base for this evaluation consisted of selected continuous data listings in each operating mode and SPSs over the first 30 days. Eighty-eight percent of the first 30 days of data were delivered in SPSs, which included 43 percent processed on 4.8C or later software.

The instrument operated flawlessly through the first 30 days with all electrical characteristics similar to those before launch, as seen in the key parameter matrix presented in Table 7-9. The minimum electronic package temperatures occurred with the altimeter thermostat failure (day 205); however, due to this failure and another apparaently erratic thermostat, SASS baseplate temperatures were marginal (at or barely above 0°C) for the remainder of the mission.

The continuous data listings confirmed flawless operation and that all receiver characteristics were normal. The usefulness of SDR products, however, for end-to-end performance monitoring is limited. The main conclusions regarding the hardware are that the instrument performed properly, but the thermal environment was marginal.

Table 7-9. SASS Key Parameter Matrix

Parameter	Design	SASS System	Sat. System	In Orbit
Electrical				
Transmit power	110 $^{+23}_{-23}$ W peak	99 W	100 W	99 ± 1 W
TWT cath. volt.	-8.0 ± 0.5 kV	-8.02 kV	-8.02 kV	-8.02 kV
TWT cath. curr.	58 mA nominal	57 mA	57 mA	55.5 mA
TWT body curr.	6 ±3 mA	5.7 mA	5.8 mA	5.7 mA
Ion pump curr.	< 5 μA	0 μA	0 μA	0 μA
HVPS input curr.	< 3.54 A	2.48 A	2.57 A	2.3 A
TWT filament curr.	1.55 A nominal	1.53 A	1.53 A	1.50 A
LO power	> + 10 dBm	13.8/12.2 dBm	13.6/12.0 dBm	13.3/11.4 dBm
Modulator power	> + 20 dBm	21.3 dBm	21.1 dBm	21.1 dBm
Trans. chan. power	> + 16 dBm	16.7 dBm	16.4 dBm	17.0 dBm
Upconv. bias	NA	.104 vdc	.105 vdc	.10 vdc
TDA stage 1 bias	NA	.135 vdc	.135 vdc	.16 vdc
TDA stage 2 bias	NA	.158 vdc	.160 vdc	.16 vdc
TDA stage 3 bias	NA	.167 vdc	.170 vdc	.17 vdc
DC/DC conv. +5 volt.	+5 ±7% vdc	5.17 vdc	5.11 vdc	5.08 vdc
DC/DC conv. +15 volt.	+15 ±1% vdc	15.02 vdc	15.05 vdc	14.97 vdc
DC/DC conv. -15 volt.	-15 ±1% vdc	-15.09 vdc	-15.09 vdc	-15.03 vdc
DC/DC conv. -6 volt.	-6 ±1% vdc	-6.05 vdc	-6.04 vdc	-6.04 vdc

Table 7-9. SASS Key Parameter Matrix (Continuation 1)

Parameter	Design	SASS System	Sat. System	In Orbit	
Electrical (contd)					
DC/DC conv. +6 volt.	+6 ±1% vdc	5.98 vdc	5.96 vdc	5.96 vdc	
Thermistor ref. No. 1	+5 ±7% vdc	5.10 vdc	5.10 vdc	5.10 vdc	
Thermistor ref. No. 2	+5 ±7% vdc	5.09 vdc	5.11 vdc	5.10 vdc	
Reg. bus voltage	28 ±0.28 V	NA	28.1 V	28.1 vdc	
Total input curr.	< 10 A	NA	8.96 A PEAK	< 9.0 A PEAK	
Unreg. bus voltage	28 ±4 V	NA	27.50 V	27.5-30 vdc	
Receiver NF	5.6 dB nominal	5.61 dB	5.70 dB	5.2 dB	
Thermal				Min.	Max.
Baseplate T1	0 - 36.5°C	28.6°C	33.3°C	-4.1	19.1°C
Baseplate T2	0 - 37.1°C	27.9°C	31.9°C	-4.1	19.2°C
Baseplate T3	0 - 37.1°C	25.4°C	32.7°C	-4.1	18.9°C
Baseplate T4	0 - 37.0°C	27.5°C	33.9°C	-0.8	21.6°C
Baseplate T5	0 - 37.7°C	27.0°C	32.1°C	-4.6	18.7°C
Baseplate T6	0 - 37.6°C	29.0°C	33.9°C	-3.7	18.5°C
TWT No. 1	0 - 48.0°C	28.0°C	32.6°C	-3.1	19.7°C
TWT No. 2	↓	26.2°C	32.7°C	-1.3	21.3°C
TWT No. 3	↓	26.2°C	33.3°C	1.5	23.4°C
Output ISO	↓	25.4°C	32.9°C	-2.8	19.5°C
HVPS	↓	26.8°C	34.2°C	-2.5	21.2°C

Table 7-9. SASS Key Parameter Matrix (Continuation 2)

Parameter	Design	SASS System	Sat. System	In Orbit	
				Min.	Max.
Thermal (contd)					
ASM	0 - 48.0°C	26.2°C	30.7°C	-8.5	13.8°C
SSS/LO		30.8°C	32.9°C	-4.4	18.4°C
Upconv.		26.5°C	33.0°C	-4.2	18.2°C
A/D conv.		40.7°C	42.8°C	12.1	32.8°C
Noise source		24.7°C	32.0°C	-7.3	14.4°C
Dir. det.		27.1°C	31.7°C	-5.2	17.3°C
1st mixer		29.5°C	34.7°C	-2.2	20.4°C
2nd mixer		34.8°C	39.6°C	9.3	31.2°C
TDA		35.3°C	36.3°C	31.8	35.7°C
Crys. fil. P6		35.4°C	40.7°C	13.7	34.5°C
Crys. fil. P1		37.7°C	42.3°C	18.1	38.6°C
Crys. fil. P10		37.4°C	42.8°C	19.2	38.4°C
Crys. fil. P12		37.3°C	42.2°C	16.9	37.3°C
Ant. 1 temp. 1	-67 - ±55°C	NA	NA	-78.8	-21.1°C
Ant. 1 temp. 2					
Ant. 1 temp. 3					
Ant. 1 temp. 4					
Ant. 1 temp. 5					
Ant. 1 temp. 6					
Ant. 1 temp. 7					
Ant. 1 temp. 8					

C-3

Table 7-9. SASS Key Parameter Matrix (Continuation 3)

Parameter	Design	SASS System	Sat. System	In Orbit	
Thermal (contd)				**Min.**	**Max.**
Ant. 1 temp. 9	-67 - +55°C	NA	NA	-78.8	-21.1°C
Ant. 1 temp. 10					
Ant. 2 temp. 1				-74.3	-18.2
Ant. 2 temp. 2					
Ant. 2 temp. 3					
Ant. 2 temp. 4					
Ant. 2 temp. 5					
Ant. 2 temp. 6					
Ant. 2 temp. 7					
Ant. 2 temp. 8					
Ant. 2 temp. 9					
Ant. 2 temp. 10					
Ant. 3 temp. 1				-80.7	-49.1°C
Ant. 3 temp. 2					
Ant. 3 temp. 3					
Ant. 3 temp. 4					
Ant. 3 temp. 5					
Ant. 3 temp. 6					
Ant. 3 temp. 7					
Ant. 3 temp. 8					
Ant. 3 temp. 9					

Table 7-9. SASS Key Parameter Matrix (Continuation 4)

Parameter	Design	SASS System	Sat. System	In Orbit	
Thermal (contd)				Min.	Max.
Ant. 3 temp. 10	-67 - +55°C	NA	NA	-80.7	-49.1°C
Ant. 4 temp. 1				-82.5	-49.9°C
Ant. 4 temp. 2					
Ant. 4 temp. 3					
Ant. 4 temp. 4					
Ant. 4 temp. 5					
Ant. 4 temp. 6					
Ant. 4 temp. 7					
Ant. 4 temp. 8					
Ant. 4 temp. 9					
Ant. 4 temp. 10					
Mount sur. T1	32 - 95°F	32 - 95°F	89.7°F		NA
Mount sur. T2	32 - 95°F	32 - 95°F	93.1°F		NA

E. SYNTHETIC APERTURE RADAR

1. Description

The SAR obtained high-resolution (25 m (13.5 mm)) radar imagery in two dimensions over a 100-km (54 mm) swath from a satellite altitude of 800 km (432 mm). The SAR obtained radar imagery data of ocean waves in deep oceans, over continental shelves and along coasts, and derived directional wave spectra in those regions. Also, the SAR obtained radar imagery data of sea and fresh water, ice, snow, and land surfaces. These imagery data were correlated to produce images for:

(1) Determining water-land interaction in coastal regions.

(2) Demonstrating Earth surface mapping.

(3) Estimating surface roughness.

(4) Identifying ice types.

(5) Differentiating surface materials, vegetation, and land forms.

(6) Demonstrating environmental monitoring.

(7) Demonstrating all-weather, day and night capability.

(8) Demonstrating fishing vessel surveillance.

(9) Designing future high resolution spaceborne radar systems.

The high resolution was obtained after processing by pulse compression in the range dimension and by synthesizing an aperture from the signal phase history in the azimuth dimension.

The physical and functional characteristics of the SAR are shown in Figure 7-15. The transmitter operated at 1.275 MHz using a linear FM (chirp) signal with a bandwidth of 19 MHz and a duration of 33.4 μs. The transmitted power level was 800 W. The pulses had an effective width of 53 ns (642:1 compression) at repetition frequencies of 1464, 1540, 1581, or 1647 p/ps. The radar antenna was a 10.7 by 2.2 m planar array consisting of eight panels, and had a 6.2 deg by 1.1 deg beamwidth. The long dimension was oriented along the satellite velocity vector, and the boresight was 20.5 deg from nadir and normal to the velocity vector. The transmitted pulse was derived from a phase-stable local oscillator and the returns were phase-referenced to the same oscillator. Upon reception, the echo at 1275 MHz was coherently translated up to 2265 MHz for telemetering to Earth. For synchronous demodulation on the ground, the stable local oscillator (STALO) was encoded in the 2265 MHz spectrum, as was the PRF pulse in PN-coded form. The composite signal containing the analog echo and timing signals was then transmitted at 5 W to one of three STDN stations by an omni-directional antenna.

2. Image Processing

Figure 7-16 is a block diagram of the SAR system. At the STDN station the radar echo was synchronously demodulated using signals derived from the pilot carrier. Analog-to-digital conversion of 288 μs of each echo occurred at five bits per word, controlled by a clock derived from the satellite STALO. The bits were buffered and recorded on a high density digital tape recorder (HDDTR) at a rate of approximately 107 mb/ps. The tapes were shipped from the STDN station by air to JPL for optical processing.

The tapes were converted to signal film using an optical recorder with appropriate electronics. For correlation, the signal film was illuminated with a coherent beam of light by an input mirror. A two-dimensional transform was first performed with a spherical lens. A Doppler tracking system was used that drove the input mirror to center the spectrum optically, because the antenna boresight changed with satellite attitude and its location was not accurately

SYNTHETIC APERTURE RADAR (SAR)

FOLDOUT FRAME

SENSOR CONFIGURATION

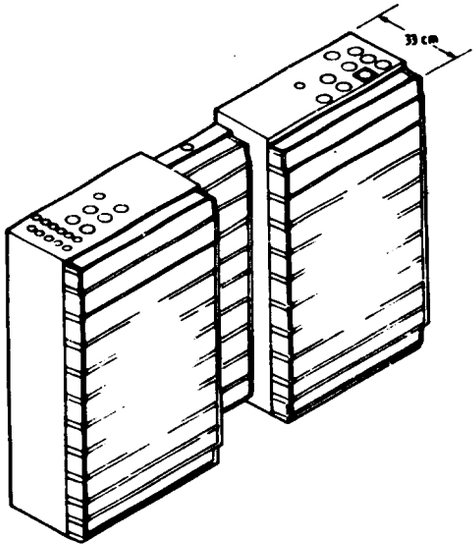

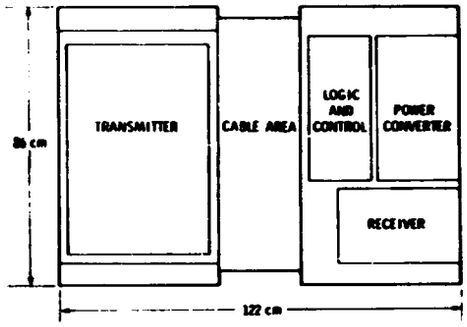

SAR SATELLITE SYSTEM

SAR SENSOR

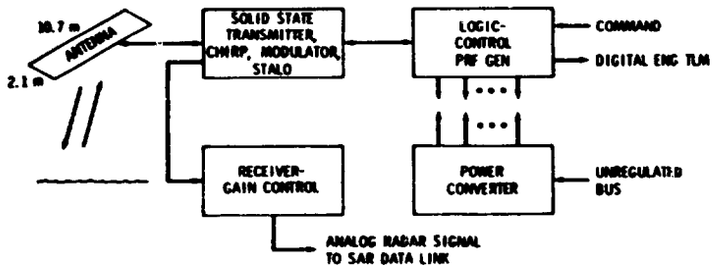

SAR FUNCTIONAL DIAGRAMS

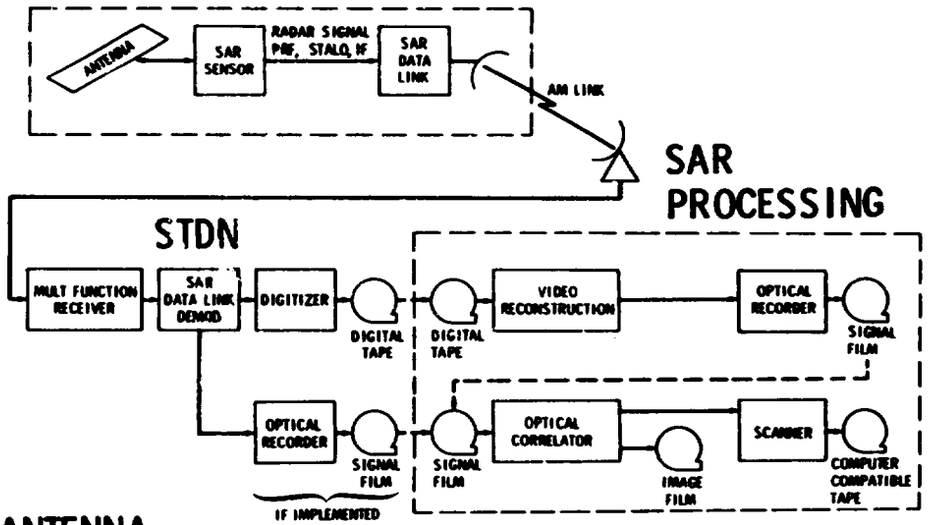

ANTENNA BEAMWIDTH

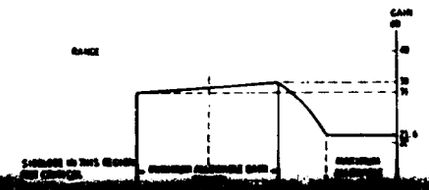

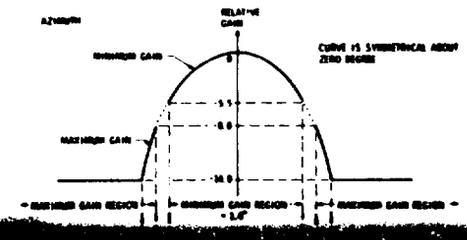

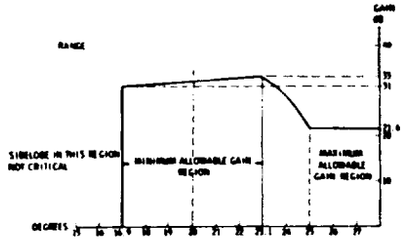

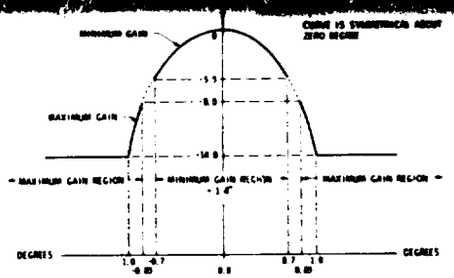

RESOLUTION CELLS

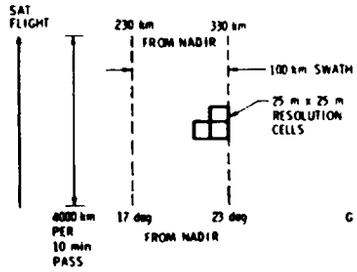

SIGNAL LEVEL vs SWATH WIDTH

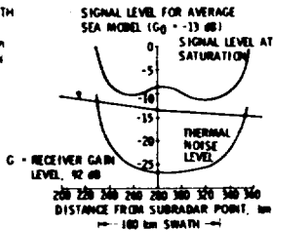

SIGNAL LEVEL vs SWATH WIDTH

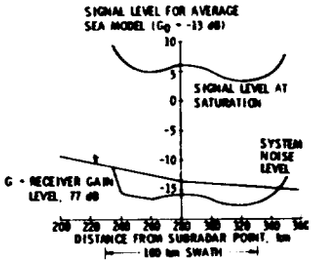

PIXEL SIGNAL TO NOISE RATIO vs SWATH WIDTH

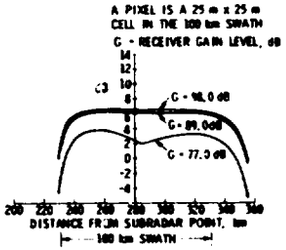

CONTRAST RATIO

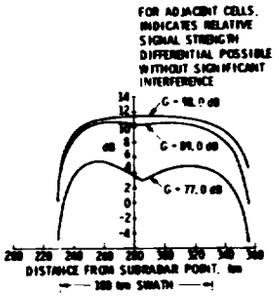

PERFORMANCE

- RADAR IMAGES AND INTENSITY SPECTRA OF WAVES IN DEEP OCEAN AND NEAR COASTS
- RADAR IMAGES OF SEA ICE AND FRESHWATER ICE
- RADAR IMAGES OF LAND AND SNOWCOVER
- 100 km SWATH WIDTH, 4000 km SWATH LENGTH IN 10 min PASS
- FOUR INDEPENDENT CELL MEASUREMENTS (4 LOOKS)
- 25 x 25 m CELL RESOLUTION (4 LOOKS)
- 0.5 sec INTEGRATION TIME PER CELL MEASUREMENT (PER LOOK)
- CELL SNR OF ≥5 db OVER 100 km SWATH (4 LOOKS)

TECHNICAL CHARACTERISTICS

- CENTER FREQUENCY - 1274.8 GHz
- BANDWIDTH - 19 MHz
- TRANSMIT TIME/TOTAL TIME - 0.35
- PULSE WIDTH - 33.8 μsec
- CHIRP RATE - 0.562 MHz/μsec
- PULSE COMPRESSION RATIO (TIME BANDWIDTH PRODUCT) - 642
- EFFECTIVE PULSE WIDTH - 53 nsec
- PEAK TRANSMITTED POWER - 1125 W NOM
- PRF's - 1464, 1540, 1580, 1647 Pulses/sec
- AVERAGE TRANSMITTED POWER - 55 W
- AVERAGE RAW POWER:

PEAK TRANS PWR, W	1125 NOM
1464	515
PRF 1540	533
1580	548
1647	558

- SYSTEM NOISE TEMP ≤ 600°K
- RECEIVER GAIN +77 TO 98 db
- GAIN - STC, AUTO, COMMANDABLE
- AVERAGE BACKSCATTER -13 db at 20°
- BACKSCATTER RANGE -26 TO 0 db
- RECEIVED POWER RANGE -97 TO -71 dbm
- ANTENNA PEAK GAIN - 34.5 db
- ANTENNA POLARIZATION - HORIZONTAL
- ENG DATA RATE - 494 bps
- SIZE 122 x 86 x 33 cm
- WEIGHT 125 kg

INHERITANCE

APOLLO 17 → SEASAT-A SAR
AAFE A/C RADAR → SEASAT-A SAR
AVAILABLE WESTINGHOUSE TRANSISTOR MODULE → SAR SOLID STATE POWER AMPLIFIER

SIGNIFICANT DEVELOPMENTS

SIGNIFICANT DEVELOPMENTS
- SOLID STATE TRANSMITTER POWER AMP
- CHIRP MODULATOR
- PHASED ARRAY ANTENNA

SPECIAL FEATURES

- RETURN OF RAW RADAR RETURN TO TRACKING SITE FOR RECORDING
- 19 MHz AM LINK FITS LANDSAT CHANNEL ALLOCATION
- SOLID STATE L-BAND TRANSMITTER
- DATA ACQUISITION: 10^{11} bits/10 minute PASS
- DATA RATE ≤ 120 Mb/s

Figure 7-15. Synthetic Aperture Radar Physical and Functional Characteristics

FOLDOUT FRAME 2

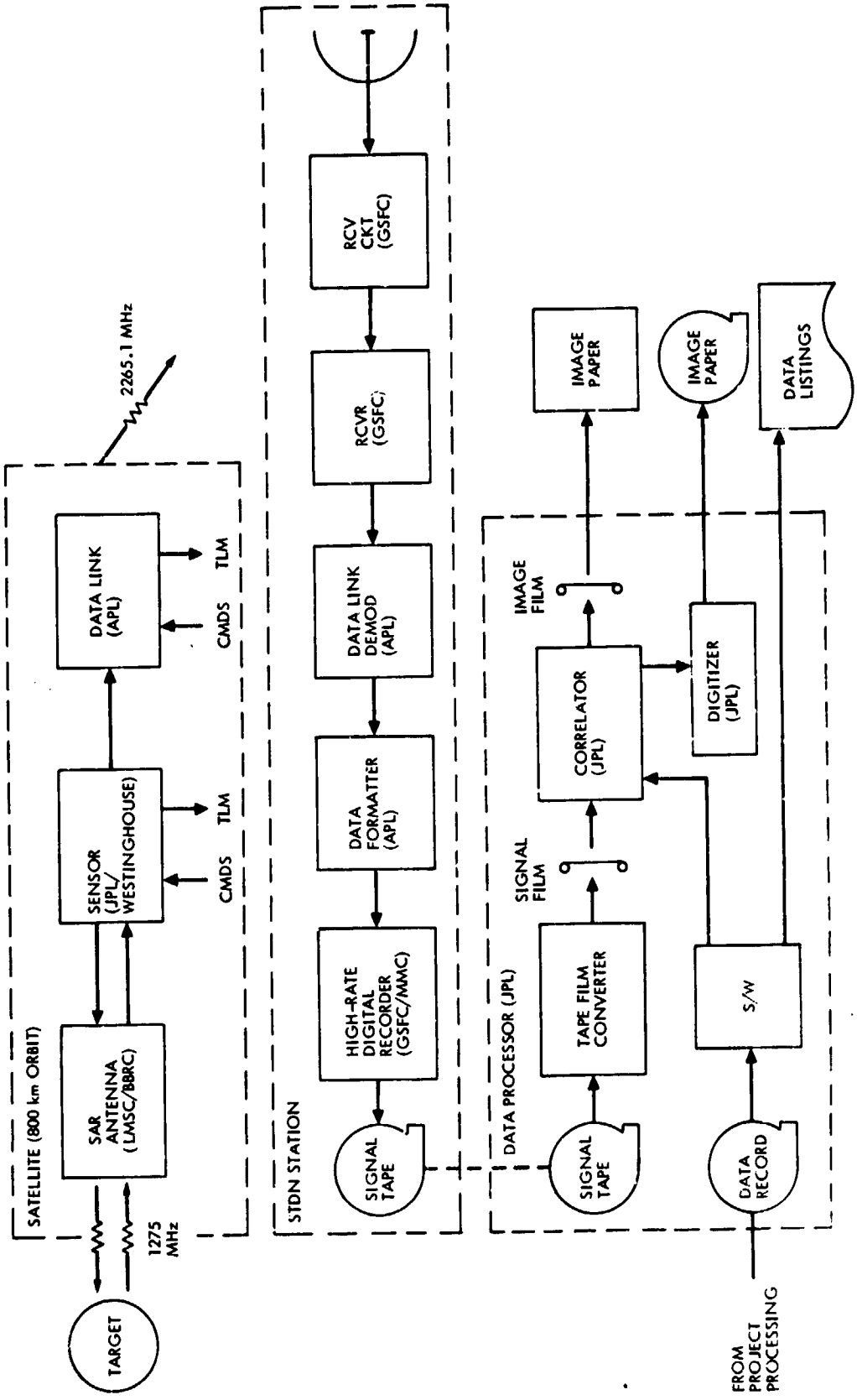

Figure 7-16. SAR System Block Diagram

known. Range migration corrections were then performed with lenses that deflected the light beams in proportion to the azimuth spatial frequency. A spectral weighting filter was kept centered on the phase histories.

The inverse transform was performed with a second spherical lens and light from targets at all ranges was focused by a set of cylindrical lenses at the output plane. Relay optics included a magnification lens to adjust the image scale factor to 500,000:1. The output film drive was tilted above the optical axis in synchronism with the input mirror to correct for azimuth skew from beam steering. The time code was detected from the signal film and transferred to the image film. The time code and film speed were adjusted to account for Doppler steering. In addition to the image film, correlated image data was provided on Computer Compatible Tapes (CCTs). The images were transferred to 9-track tape at 800 b/pi using an image dissector at the correlator output.

3. Engineering Assessment Summary

The Synthetic Aperture Radar (SAR) system pictorially represented the radar backscatter of the surface of the Earth. The performance of the imaging radar system can be described by three important image quality parameters: (1) the resolution of the system; (2) the detectable range of radar backscatter coefficients for distributed targets; and (3) the contrast ratio associated with imaging a strong region surrounding a perfectly black region.

The requirement of 25-m resolution on the ground for 4-look processing was to be met by using a pulse compression technique in range and the synthetic aperture technique in azimuth. Range resolution depends upon the local incident angle of the radar return and the radar bandwidth, while azimuth resolution depends upon the number of independent looks for each pixel and the processing bandwidth in azimuth. A array of corner reflectors of various sizes, each spaced 300 m apart, was deployed in the Goldstone Dry Lake area in California. The null-to-null width of the impulse response of these point targets was measured from the image film output. The preliminary measurements indicated a range resolution of less than 25 m and azimuth resolution of approximately 40 m for 4-look processing. The apparently excessive width in the azimuth direction was most likely due to irregularities in the film drive mechanism in the data processing system.

The radar backscatter σ_o is defined as the ratio of the reflected power per unit area to that which is incident on the terrain that is being illuminated. The range of detectable σ_o is that range of σ_o from a distributed uniform surface which is equal to the system noise to that σ_o which saturates the system, and is specified to be from -21 dB to +2 dB. The necessary system gain calibration was obtained by: (1) measuring the system receive-only noise; (2) verifying the antenna gain patterns by deploying portable receivers during selected passes; and (3) injecting calibrated noise into the input of the optical recorder to measure the gain of the optical system from the optical recorder input to the output image. The resulting relation between image film density and surface reflectivity is used to find the range of detectable σ_o. Measurements on the output image film for the Saline Valley area of California indicated a dynamic range of 16 dB,

limited by the output film. Measurements on the output image film for the ocean off the Baja Peninsula indicated variation in the range of detectable σ_o of 4 dB across the swath, and also indicated a noise equivalent σ_o of -26 dB to -17 dB.

Image contrast ratio is the ratio of energy contained in the main lobe portion of the system impulse response to the energy contained in the area outside the main lobe, and is specified to be greater than 7 dB. The effect is very noticeable at a sharp transition in radar reflectivity, such as that occurring at a land-to-water boundary. Measurements on the image of Charlton Lake, Oregon, indicated that the contrast ratio is greater than 7.5 dB. The techniques used in measuring the image quality parameters, the data base, and the specified, expected, and measured parameter values are shown in Table 7-10 for the above three image quality parameters as well as for additional parameters.

F. VISUAL AND INFRARED RADAR

The physical and functional characteristics of the VIRR are shown in Figure 7-17. The VIRR provided images of atmospheric conditions, cloud-coverage patterns, ocean and coastal features, and also provided sea-surface temperature maps. Visual-image resolution was 2 km (1 nm), and infrared resolution was 4 km (2 nm) over a 2100-km (1132 nm) surface swath. Radiation emitted from Earth was collected by an elliptically-shaped scan mirror that directed it into a dichroic beam splitter. Infrared radiation was applied to a bolometer detector, while visible radiation was applied to a silicon PV detector. The signals were amplified, filtered, and routed to the satellite telemetry system as analog signals. They were then digitized by the satellite data processing system for transmission to Earth for additional processing.

G. SENSOR MANAGEMENT

1. Management Responsibilities and Support Requirements

Sensor implementors were responsible to the Seasat project sensor manager for sensor design and development within the sensor allocations, including Institutional Management System (IMS) and contingency, as negotiated.

Sensor implementation tasks were managed by JPL pursuant to a Memorandum of Agreement (MOA) between the Seasat project office and WFC for the ALT, LaRC for the SASS, GSFC for the VIRR, the JPL Special Projects Office for the SMMR, and the JPL Telecommunications Science and Engineering Division for the SAR. These sensor implementation tasks included the following:

(1) Sensor design, development, procurement, fabrication, testing, and pre-launch calibration.

(2) Support to LMSC's system design, test planning, system test, and launch operations, and satellite EMI/RFI analysis and test, with this support to be performed as appropriate at JPL, LMSC, and VAFB.

Table 7-10. SAR Key Parameter Matrix

Parameter	Technique	Scene	Rev	Specification	Expected	Measured
Resolution	Measured null-null width of point target response.	Single 8-ft reflector	394	Range: 25 m Azimuth: 7 m (1 look)	25 m 7 m (1 look)	Range: <25 m Azimuth: 37 m ±10 m
Noise equivalent σ_o	Compare ocean return to that with transmitter off.	Ocean near Baja Peninsula	1294	-16.5 dB	>-16.5 dB	-26 dB to 17 dB
Contrast ratio	Measure transition response at edge of lake.	Charlton Lake, Ore.	394	7 dB	7 dB	>7.5 dB
Range of σ_o	Measure σ_o that saturates system and compare to NEσ_o.	Saline Valley	617	-25 to +5 dB	-21 to 2 dB	Dynamic range >16 dB. Limited by film dynamic range.
Ambiguities	Measure level of ambigious image of 9 m antenna return in sidelobe.	Goldstone area	394	Range: -22 dB Azimuth: -20 dB	-22 dB -20 dB	Range: correlated passes not available as yet Azimuth: no ambiguity image of point target observed
Number of looks	Compare auto-correlation width for single-look processing and multi-look processing.	Desert return	None	1 to 4	1 to 4	None. S/W for auto-correlation not available.
Swath width	Measure swath dimension in range for which contrast ratio >6 dB.	Full swath	407	100 km	100 km	~100 km. Imagery observed (qualitative).
Swath length	Measure swath dimension in azimuth for which contrast ratio >6 dB.	Entire pass	163	4,000 km	4000 km	5600 km. Imagery observed (qualitative).
Pixel location accuracy	Compare SDR-derived geodetic location of 26 m antenna in image film with known coordinates.	GDS 26 m antenna	None	Absolute: 50 m Relative: 10 m	100 m 50 m	None. Currently calibrating bias in S/W program from SDR information.
σ_o Knowledge	Compare the derived average σ_o of Death Valley location with known σ_o.	Death Valley area	None	Pixel relative to known σ_o: 0.5 dB System Transfer: 3.0 dB Relative σ_o over swath: 0.3 dB Digitization error: 0.3 dB	0.5 dB 3.0 dB 1.0 dB 0.3 dB	None. Required Death Valley surface truth information being prepared.

FOLDOUT FRAME

VISUAL AND INFRARED RADIOMETER (VIRR)

CONFIGURATION

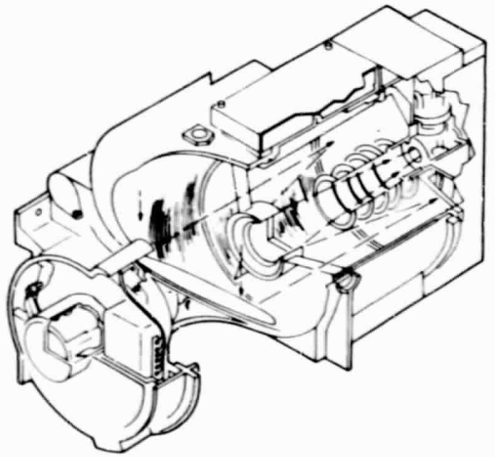

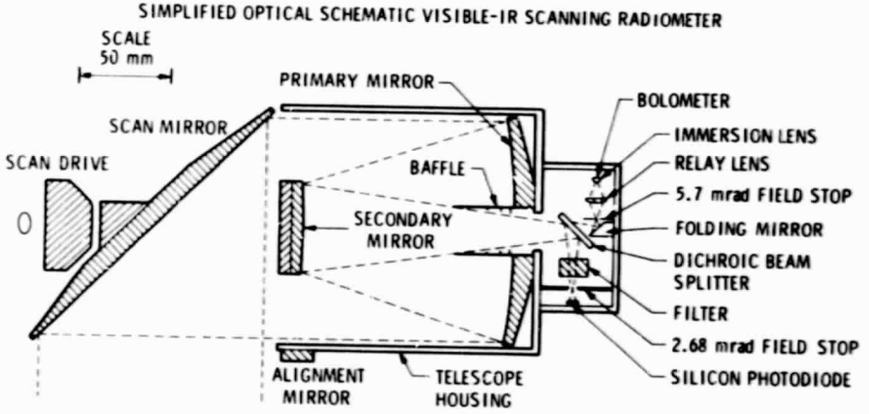

FUNCTIONAL DIAGRAM

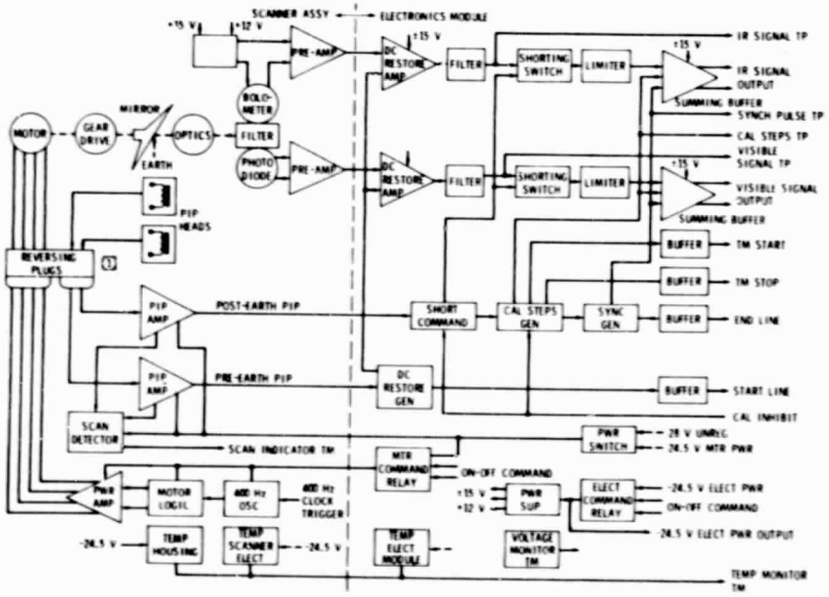

VIRR COMPOSITE VIDEO AND TIMING SIGNALS

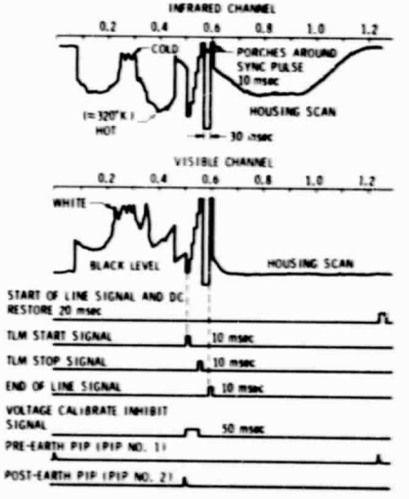

COVERAGE

SCAN ANGLE INFORMATION

GROUND COVERAGE

VISUAL AND INFRARED RADIOMETER (VIRR)

FOLDOUT FRAME

CONFIGURATION

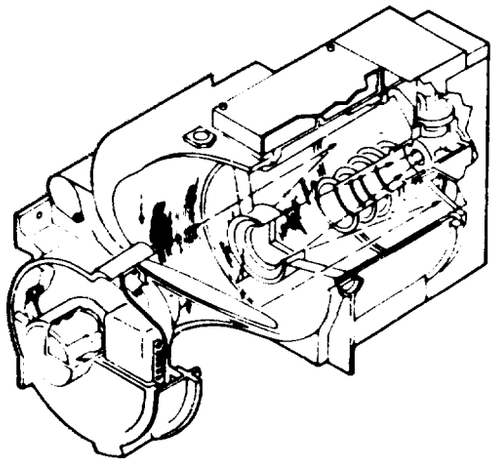

SIMPLIFIED OPTICAL SCHEMATIC VISIBLE-IR SCANNING RADIOMETER

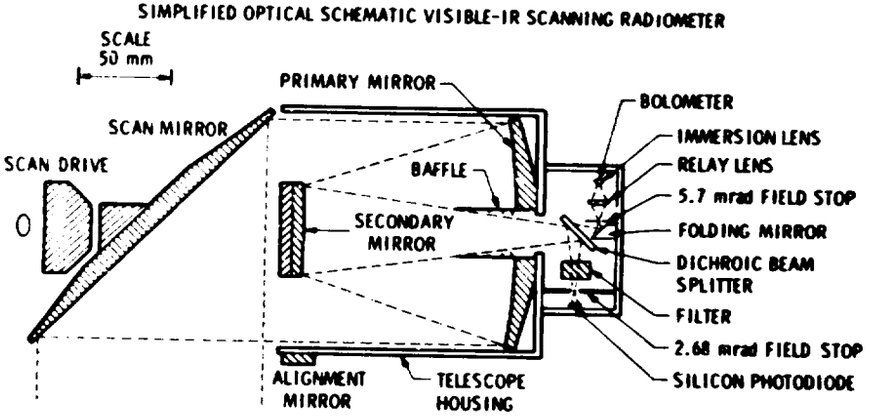

FUNCTIONAL DIAGRAM

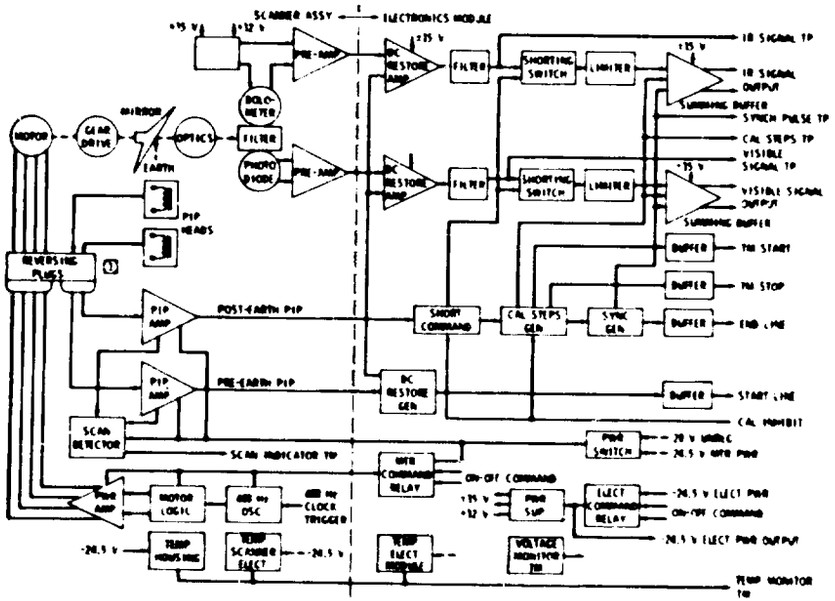

VIRR COMPOSITE VIDEO AND TIMING SIGNALS

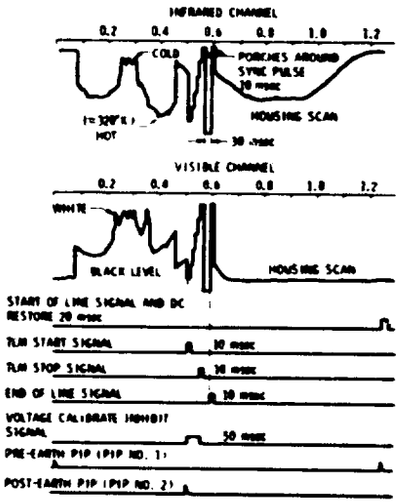

COVERAGE

SCAN ANGLE INFORMATION

GROUND COVERAGE

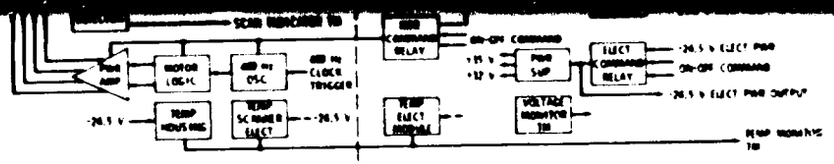

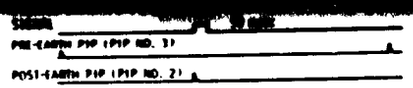

COVERAGE

SCAN ANGLE INFORMATION

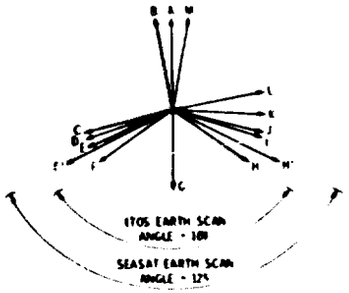

ITOS TIME (msec)	REFERENCE LETTER	ANGLE (deg)	SEASAT TIME (msec)	EVENT
	A	0	0	SATELLITE ZENITH
	B	50	54.7	RADIOMETER MOV SCANNER HOUSING
	C	105	164.6	RADIOMETER MOV JUST STARTING TO SEE ALL OF SPACE
0	D	148	375	SCAN MIRROR POSITION PIP NO. 1 (PRE-EARTH) OCCURS. RESTORE PERIOD AND START-OF-LINE SIGNAL PULSE BEGINS
29.1	E	111.0	[illegible]	[illegible] RESTORE PERIOD ENDS ; 70 msec DC RESTORE
30.1	F	117.1	408.3	SEASAT EARTH SCAN PERIOD BEGINS (432 mm ORBIT)
31.1	G	125.6	476.1	ITOS EARTH SCAN PERIOD BEGINS (910 mm ORBIT)
256	H	148	625	SPACECRAFT NADIR
438.6	H'	236.5	868.2	ITOS EARTH SCAN PERIOD ENDS (1470 mm ORBIT)
467.7	H''	242.7	882.7	SEASAT EARTH SCAN PERIOD ENDS
468	I	252	875	SCAN MIRROR POSITION PIP NO. 2 (POST-EARTH) OCCURS. TM VOLTAGE CALIBRATE SEQUENCE BEGINS. TM START PULSE BEGINS AND SPACECRAFT GATING SIGNAL FOR INHIBITING TM CALIBRATE SIGNAL (OR COMMAND) BEGINS
510.4	J	295	885.4	RADIOMETER MOV JUST STARTING TO SEE SCANNER HOUSING
550	K	298.4	925	TM VOLTAGE CALIBRATE SEQUENCE AND SPACECRAFT INHIBIT SIGNAL (IF SUPPLIED) ENDS. TM STOP BEGINS
580.9	L	277.6	961	END OF LINE SIGNAL PULSE OCCURS
848.5	M	356	1295	RADIOMETER NOW COMPLETELY SHIELDED BY SCANNER HOUSING
	A	360	1250	SATELLITE ZENITH

GROUND COVERAGE

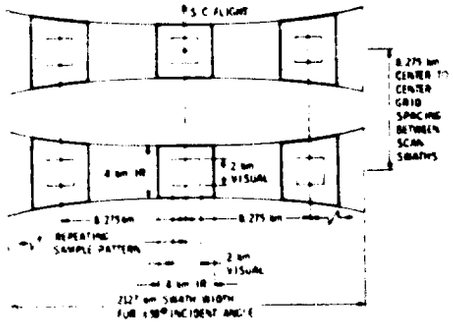

TECHNICAL CHARACTERISTICS

	VISIBLE CHANNEL	THERMAL CHANNEL
• SCAN RATE-48 RPM		
• IFOV (-6 db POINTS)	2.8 ± 0.3 mr	$5.3^{+0.5}_{-1.1}$ mr
• SPECTRAL REGION (-6 db POINTS)	0.47 ± 0.05 to 0.94 ± 0.05 μm	10.5 TO 12.5 μm (NOMINAL)
• INFORMATION BANDWIDTH		
UNFILTERED	1200 Hz	600 Hz
FILTERED (TEST)	900 Hz	455 Hz
• NEI (OVER OPERATING TEMPERATURE RANGE) FOR EXTENDED TARGET SOURCE	4.1×10^{-10} W/cm^2	4.2×10^{-10} W/cm^2
• NETD (AT INDICATED TARGET SCENE, OVER OPERATING TEMPERATURE RANGE) FOR EXTENDED TARGET SCENE	---	1.0°K AT 300°K 4°K AT 185°K
• OUTPUT VOLTAGE RANGE (NOMINAL)	-5.9 TO -0.3 Vdc	-0.25 TO -6.1 Vdc
• MAXIMUM OUTPUT VOLTAGE RANGE OVER TEMPERATURE FOR MAXIMUM CALIBRATED TARGET SCENE	-1.0 TO +0.1 Vdc (100% ALBEDO; 25°C SR TEMPERATURE REFERENCE)	-6.1 TO -5.8 Vdc (320°K TARGET)
• DC RESTORE LEVEL	-5.9 ± 0.095 Vdc	0.25 ± 0.05 Vdc
• OPERATING TEMPERATURE	-5°C TO +45°C	-5°C TO +40°C
• JITTER (SCAN LINE-TO-SCAN LINE, LONG TERM)	<2 msec	
• POWER (AT -24.5 Vdc)		
OPERATING	≤ 325 ma	
LAUNCH MODE	≤ 140 ma	
• RADIOMETER TOTAL WEIGHT	9 Kg	

VIRR DATA RATE

$$\text{DATA RATE} = \left(\frac{x}{2}\right)\left(\frac{2HS^2}{V_t}\right) Q R$$

- x = SAMPLING FACTOR = 2.5 PER IFOV
- S = SCAN SPEED = 0.8 REV/sec
- H = ORBITAL ALTITUDE = 800 km
- V_t = GROUND SPEED = 6.62 km/sec
- Q = SAMPLE QUANTIZATION = 8 bits/SAMPLE
- R = PERCENTAGE OF COMPLETE SCAN TO BE DIGITIZED = 0.3709

DATA RATE = 1830 bps (FOR EACH CHANNEL)

PERFORMANCE

- VISUAL AND INFRARED IMAGER
- OCEAN SURFACE TEMPERATURE ± 1.5 C AT 273 C
- CELL RESOLUTION (IFOV) - 4 km (IR), 2 km (VIS)
- GRID RESOLUTION (SCANNING) - 9 km x 9 km
- FEATURE LOCATION - 6 km

INHERITANCE

- ITOS C, D, F (SR) ⟶ ITOS-H, I, J (SR) ⟶ SEASAT-A (VIRR)
- WILL FLY A FLIGHT ITOS-J UNIT OBTAINED FROM NOAA

SPECIAL FEATURES

- INFRARED AND VISUAL ANALOG SIGNALS WILL BE DIGITIZED IN SATELLITE DATA SYSTEM

SIGNIFICANT DEVELOPMENTS

- NONE
- MAY NEED SPECIAL RFI/EMI OR STRAY LIGHT SHIELDING ON SEASAT SATELLITE

Figure 7-17. Visual and Infrared Radiometer Physical and Functional Characteristics

FOLDOUT FRAME 2

(3) Support of sensor experiment team meetings.

(4) Support of (data processing) algorithm development for system test and mission operations.

(5) Support of mission operations, including real-time operations at GSFC and sensor engineering assessment.

The remainder of this discussion summarizes, for each sensor, specific responsibilities, support, and delivery requirements which are additional to the above tasks.

a. Radar Altimeter. WFC was responsible for the ALT design, procurement, fabrication, subsystem testing, and calibration. WFC, through a Military Interdepartmental Purchase Request (MIPR), sub-contracted the sensor with APL. APL subcontracted the Dispersive Delay Line (DDL) design and breadboarding to Anderson Laboratories, the TWTA to Hughes Aircraft Company, and the up-converter to Zeta Laboratories, with total RF and sensor integration and test at APL. The digital processing units and development of the ground support equipment were done by APL.

b. Synthetic Aperture Radar. The SAR was designed, procured, fabricated, subsystem tested, and calibrated by the JPL Telecommunications Science and Engineering Division, which was responsible for the SAR end-to-end system design and for specification of the functional requirements of all SAR elements. Major sensor procurements were the transmitter from Westinghouse Corporation and the power supply from Martin-Marietta Corporation.

Elements and implementation of the SAR experiment, in addition to the sensor, were as follows: LMSC, as the bus contractor, furnished the SAR antenna; APL furnished a dedicated SAR data link; elements of the SAR data link were furnished by the STDN; interface agreements were developed by LMSC between the SAR data link and SAR sensor, SAR data link and bus, and SAR data link and STDN; a SAR data-handling group was responsible for developing the details of the STDN interface agreements; LMSC integrated the SAR antenna, sensor, and data link into the satellite system; and system compatibility and end-to-end performance tests were made prior to launch.

c. Scatterometer. SASS design, procurement, fabrication, and subsystem test and calibration responsibility was assigned to LaRC. Major subcontracts were between LaRC and the General Electric Company (GE) for the sensor, LaRC and Hughes Aircraft Company for the transmitter power amplifier (furnished to GE for integration), and between LaRC and Aerojet Electrosystems Company (AESC) for the SASS antenna. LMSC integrated the sensor and the antennas into the satellite system.

d. Scanning Multichannel Microwave Radiometer. The SMMR was designed, procured, fabricated, subsystem tested, and calibrated by JPL. The Seasat SMMR was an add-on to the Nimbus SMMR sensor flight production activity at JPL. The

Nimbus SMMR functional design and interfaces were used for the Seasat bus and sensor module. Major procurements were the antenna, antenna scanning motor, and RF subassemblies.

e. Visual and Infrared Radiometer. VIRR responsibility was assigned to GSFC. JPL obtained one ITOS-J Scanning Radiometer (SR) from the Tiros project. GSFC certified this unit for flight on Seasat. Upon certification, the designation was changed from SR to VIRR. Santa Barbara Research Center (SBRC), in a support contract with JPL, assisted GSFC in support of instrument retest and recalibration and supported LMSC in instrument integration. The Seasat bus and sensor module used the ITOS-J SR functional design and interfaces.

f. Sensor Delivery Requirements. The requirements for sensor delivery were as follows:

(1) Each sensor implementor provided one flight model, selected spares, associated documentation, and one set of support equipment and software.

(2) A SMRR engineering model was shared between the Seasat and Nimbus projects.

(3) An additional ITOS-J SR was made available from NOAA for use either in engineering model tests or as a flight spare.

g. Sensor Coordination Support. JPL provided sensor coordination support. The support coordination functions were to:

(1) Provide assistance in the development of sensor implementation plans and MOA's between the project and the implementing NASA center.

(2) Monitor and review development activities.

(3) Monitor, review, and coordinate sensor-related bus and sensor module activities as follows:

(a) Satellite system design and Interface Control Document (ICD) generation.

(b) Staellite system test planning and test operations.

(c) Satellite system Electromagnetic Compatibility (EMC) planning and tests.

(d) Launch operations and in-flight sensor engineering assessment.

(4) Manage SBRC support contract for VIRR integration and test.

2. Sensor Development

While the Seasat microwave sensors benefited from past sensor technology development,* major developments were necessary to achieve the Seasat sensor designs. In addition, integration of active radar sensors and sensitive multichannel radiometers into the satellite presented a major challenge. These developments were necessary to meet the ALT altitude and wave state measurements accuracies:

(1) A high voltage power supply design to drive the transmitter with a much faster than before pulse transmission rate and a narrower pulse width.

(2) A chirp modulator and frequency up-converter to provide the required pulse modulation characteristics.

(3) An adaptive tracker and linear FM/full-deramp waveform processing (using an Itel microprocessor) that permitted high resolution range tracking in the frequency domain, eliminating time variations.

For the SASS, these developments were necessary:

(1) Solid-state L-band, 1-kW peak transmitter to achieve the high quality, high resolution imaging requirements.

(2) Chirp modulator to provide for stable, coherent pulse modulation.

(3) A physically large, mechanically complex, planar array antenna (not a sensor development, but achieved under the satellite development contract).

SAR end-to-end system challenges were as follows:

(1) System design, performance modeling, system test planning, and test execution. Systems design techniques were developed to permit a rational transfer of system requirements, such as resolution and coverage, to subsystem parameter specifications, such as transmitter peak power, antenna gain, etc. The test challenge was related to the fact that to create a SAR image, the target had to be in motion relative to the SAR to create Doppler information used in SAR image processing.

(2) A dedicated SAR data link to relay the received SAR echo to Earth for digitizing and tape storage.

(3) SAR unique demodulator, digitizer, and formatter for use in the STDN stations for data acquisition and formatting.

*Skylab, GEOS-C, and AFFEE aircraft programs for the ALT; Skylab and AFFEE aircraft programs for the SASS; Apollo and AFFEE aircraft programs for the SAR; Nimbus program for the SMMR.

(4) Implementation of an optical correlator subject to severe cost constraints.

The SMMR presented a different development challenge to Seasat. The SMMR was developed by the Nimbus project, and its final development phase was accomplished during Seasat implementation. Seasat used the second flight model off the Nimbus fabrication line. A major Seasat challenge was to ensure that the SMMR design, still undergoing evolution in its final development phases on Nimbus, remained compatible with the sensor/satellite interface agreements and the Seasat SMMR experiment objectives. Seasat and Nimbus also shared the use of one engineering model and selected flight spares. The success of this arrangement required a close, cooperative working relationship with the satellite contractor and the Nimbus project, both of which were achieved.

Major SMMR developments were:

(1) A five-channel, dual-polarization antenna feed.

(2) A mechanical antenna scanning mechanism.

(3) Highly accurate antenna pattern and radiometer calibration techniques.

Two challenges existed in the integration of the sensors into the satellite: (1) sensor/satellite interface development, and (2) elimination of potential RFI. Microwave sensors are inherently large and require substantial bus power. Achieving compatible structure, thermal, and electrical interfaces were large, complex tasks. The development of data system interfaces and sensor/satellite systems test techniques were also major tasks. Much effort was devoted to the RFI problem. Three radars radiating wide spectrum to Earth posed a major interference threat to the radiometers and to the satellite communications system. A joint team, which included sensor, satellite, RFI, and EMC representatives, identified, through computer analysis, potential sensor-to-sensor and sensor-to-satellite interference paths as a function of frequency. Antenna coupling tests were conducted on a mock-up sensor module, and filters were placed in sensors to eliminate interference signals that were at a level sufficiently high to cause interference. Finally, a satellite RFI test was conducted which successfully verified that all RFI sources had been eliminated. The achievement of compatible sensor interfaces and the RFI-free environment, permitting simultaneous sensor operations, was only possible through the cooperative effort of a large satellite/sensor team.

3. Sensor Scheduling

Figure 7-18 summarizes significant sensor-related milestones grouped into those associated with development of the sensors themselves and those associated with sensor support to other project activities; primarily, the satellite integration and test activity and flight operations.

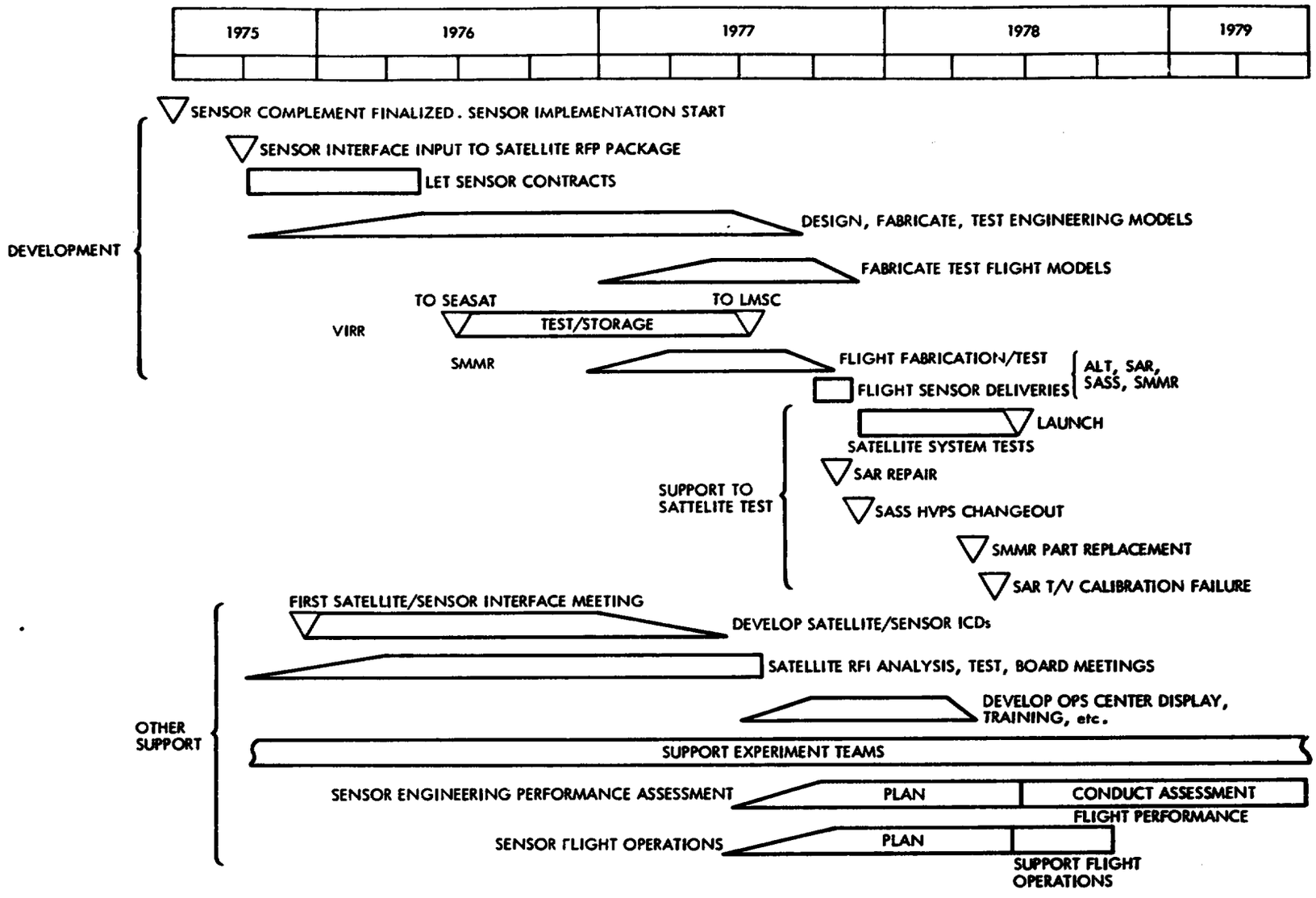

Figure 7-18. Sensor Task Schedule

The final sensor complement was defined in mid-1975, and sensor implementation began at that time. The fall of 1975 was dedicated to the development of MOA's between the Seasat project and the NASA centers responsible for sensor development, development of sensor development contracts with sensor developers, and establishment of sensor interface requirements to be placed into the satellite procurement documents. Sensor development began in the fall of 1975 and was completed in the fall of 1977, culminating with the delivery of the sensor to the satellite contractor for integration and test. A major task, the development of sensor/satellite interfaces, began at the start of 1976 and continued to the spring of 1977, culminating with signed-off sensor/satellite interface documents which contained hardware interface agreements, sensor/satellite system test requirements, and launch and flight support requirements.

Detailed planning for sensor engineering in-flight performance assessment and support of flight operations began in the fall of 1977.

4. Sensor Status at Key Periods in Time

Figures 7-19 and 7-20 and Table 7-11 contain data that summarizes the status of the sensors in July 1977. Tables 7-12 through 7-16 present sensor data pertinent to the consent-to-ship review of 24-25 April 1978. These data provide insights into the nature of sensor problems experienced, the level of sensor flight qualification achieved, the extent to which sensor engineering performance was achieved prior to launch, and the status of the in-flight engineering performance assessment during its conduct. Final reports of the sensor engineering assessment were given verbally in January 1979 at the GOASEX Workshop results presentation. Final drafts of written reports were issued in April 1979.

The performance of the microwave sensors, except for minor anomalies documented in the final reports, closely matched pre-launch performances and was within the specifications. All microwave sensor modes, sensor mode switching, and the telemetering of data were successfully accomplished. The VIRR, which was primarily a support instrument, operated successfully for approximately 60 days after launch, at which time the scan motor failed. Sufficient data were acquired for the VIRR to achieve the proof-of-concept mission objective, however. Additional visual infrared imaging in support of the microwave sensor data has been acquired from other satellites.

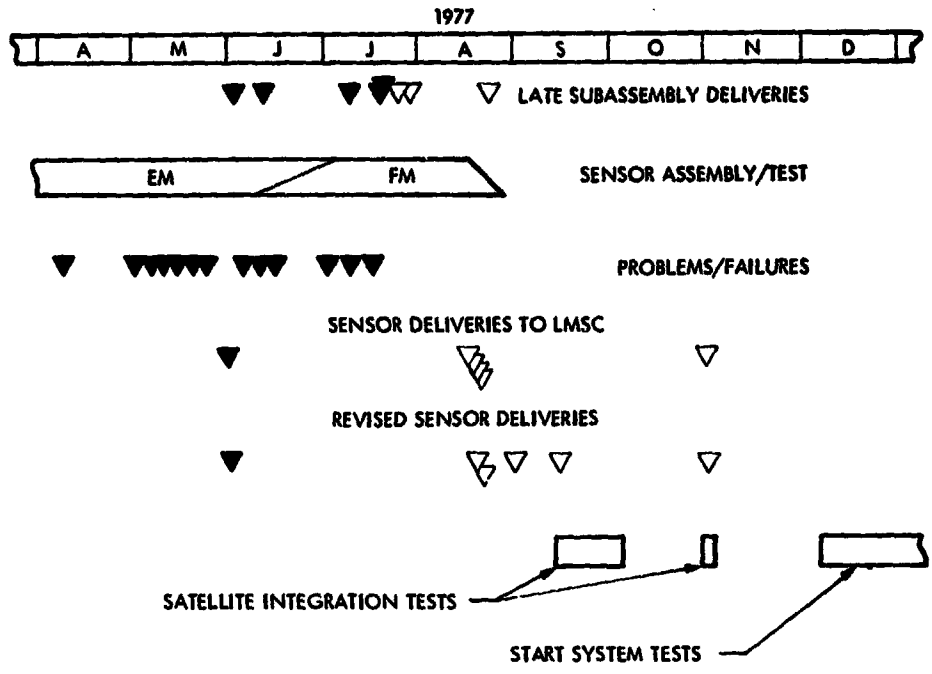

Figure 7-19. Sensor Summary Status (July 1977)

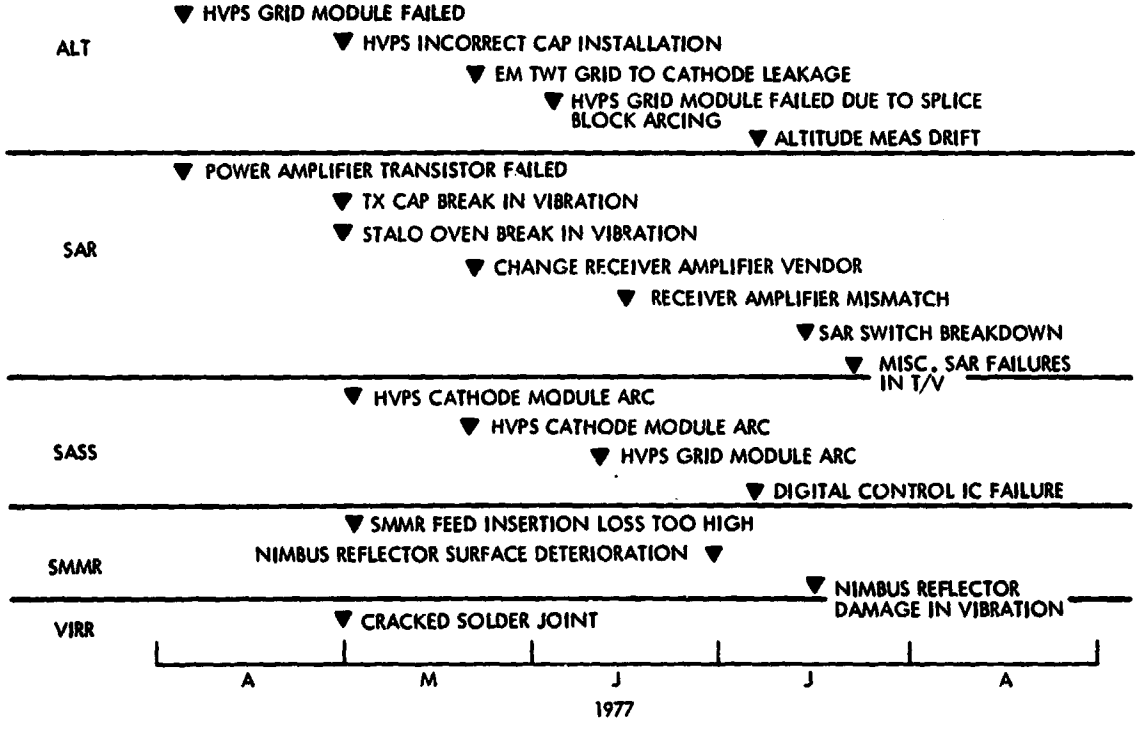

Figure 7-20. Major Sensor Problems/Failures Summary (July 1977)

Table 7-11. Sensors Weight and Power Status (July 1977)

Sensor	Total Allocated Weight (kg)	Current Weight Estimates (kg)	Total Allocated Power (W)	Operating Power (W)
ALT	436 (198 lb)	427 (194 lb)	177	173
SASS	504 (229 lb)	482 (219 lb)	165	130
SAR	726 (330 lb)	719 (327 lb)	749	668
SMMR	255 (116 lb)	255 (116 lb)	61	61
VIRR	40 (18 lb)	40 (18 lb)	8	7.3

Table 7-12. Project Overview of Sensor Problems

Sensor	Pre-Delivery	Post-Delivery	Present Status
VIRR	Microphonic IR channel	1. Noisy electrical interface with satellite 2. Satellite power converter No. 2 anomalies	Problems resolved
SASS	1. High voltage power voltage breakdowns 2. Solid state local oscillator component failed in vibration	Inadvertent shut-down during integration test	HVPS changed out. All problems resolved
ALT	1. High voltage power arc protection circuit malfunction and splice block voltage arcing 2. Contamination in cathode support structure of TWT 3. Inadequate venting in TWT output connector and TWTA housing 4. Erratic command response of ATU at high temperature test of RASP 5. Amplifier gain changes in receiver at low temperatures	1. Command interface incompatible 2. RASP temperature control surface defective 3. Connector shells cadmium plated 4. Cables improperly covered 5. Loose connector	Problems resolved. Temperature control surface repaired at LMSC on RASP
SMMR	1. A/D converter responded to noise input due to cable problems 2. Nimbus reflector corrosion 3. RF filter failure on nimbus SMMR	1. Nimbus diode failure 2. Nimbus A/D converter failure 3. Scan drive belt failure in life test 4. RF filter failure in TLM channel of SMMR 5. Satellite power converter No. 2 anomalies	A/D converter study near completion. Plan to use as-is. Belt test in progress. Problems are resolved.

Table 7-12. Project Overview of Sensor Problems (Continuation 1)

Sensor	Pre-Delivery	Post-Delivery	Present Status
SAR	1. RE switch failure in T/V - switch removed 2. Power transistor failed in transmitter in T/V	1. Decrease in pilot tone level 2. Calibration attenuator pad changeout required 3. Intermittent chirp retrigger in in-flight calibrator 4. Satellite/sensor interface anomaly with SAR engineering data procedures 5. Noisy TLM channels in SAR 6. Lock ambiguity 7. SAR/satellite over-flight results	All problems have been resolved. No additional SAR changes required.

Table 7-13. Sensor Environmental Test Summary Status

Environmental Test	VIRR		SASS		ALT		SMMR		SAR	
	Assy	Sub-Sys	Assy	Sub-Sys	Assy	Sub-Sys	Assy	Sub-Sys	Assy	Sub-Sys
Acoustics					X		X			
Random Vibration	X	X	X	X	X		X	X	X	X
Sinusoidal Vibration	X	X					X	X	X	X
Synthesized Shock			X	X	X					
Temperature Cycling at Ambient Pressure	X		X	X	X		X	X	X	
Temperature Cycling in Vacuum		X	X	X		X		X	X	X
Electromagnetic Interference (EMI)		X	X	X		X		X		X
Radio Frequency Interference (RFI)		X		X		X		X		X

Table 7-14. Sensor/Satellite System Test Results Summary

System Test	Sensor Passed/Failed Status	Test data[a] analysis
Sensor and satellite integration tests	Passed with ALT exception (altimeter command interface adapter required)	Complete
Baseline	Passed	Complete
EMI	Passed	Complete
RFI	Passed	Complete
Acoustic	Passed	Complete
Thermal vacuum	Passed with SAR exception (SAR in-flight calibrate circuit failure. Recommend use as-is.)	Complete
Final baseline	Passed	Complete
Final baseline (SMSS only)	To be performed	To be performed
WTR check	To be performed	To be performed

[a]Test data processed analyzed

1. LMSC sorts
2. LMSC analog recordings
3. Sensor GSE data processing
4. SASS stat. processing at NASA/LRC

Table 7-15. Sensor Problem/Failure and Non-Conformance Report Status

Sensor	Problem/Failure Reports		Non-Conformance Reports	
	Open PFRs	Risk Rated 3 or 4	Open NCRs	Risk Rated 3 or 4
VIRR	None	None	None	None
SASS	None	One PFR rated 3	None	None
ALT	None	One PFR rated 3 One PFR rated 4	None	None
SMMR	One	Two PFRs rated 3	None	None
SAR	One	Eleven PFRs rated 3 One PFR rated 4	None	None

Table 7-16. Sensor Operate Time Summary

Sensor	Hours of Operation		
	Pre-Delivery	Post-Delivery	Total
VIRR	250 scanner. 300 electronics	275 scanner. 240 electronics	525 scanner. 540 electronics
SASS	340	230	570
ALT	470	180	650
SMMR	360 electronics. 270 scanner mechanical	210 electronics. 200 scanner mechanical	570 electronics. 470 scanner mechanical
SAR	700	50	750

SECTION VIII

LAUNCH VEHICLE

A. INTRODUCTION

The Seasat launch vehicle was a unique one-of-a-kind configuration. The Atlas 23F booster was originally completed in 1961 as an intercontinental ballistic missile. When the Atlas system became obsolete, the 23F was removed from its underground silo and put into storage at Norton Air Force Base, California. Following its selection as the booster for Seasat, the Atlas 23F underwent extensive forward tank modifications, was equipped with appropriate mission-peculiar equipment, and was thoroughly inspected and refurbished. The interstage adapter (ISA) was a new, unique item, although its design was similar to that of the Centaur ISA. The 305-cm (120-in.) diameter nose fairing was a refurbished test fairing that was updated and configured specifically for Seasat. The Agena functioned as an ascent stage, using two main engine burns to achieve the desired final orbit conditions. A standard booster adapter provided the mechanical interface between the Agena, fairing, and ISA.

The flight vehicle incorporated significant configuration differences in comparison with previous Atlas F vehicle mission configurations. Seasat was the first Atlas F/Agena, the first vehicle to incorporate a 90-deg roll by an Agena, and the first vehicle to fly a 305-cm diameter fairing on the Atlas F.

B. DESCRIPTION

Significant Atlas F (including the ISA) and fairing system configuration specifics are summarized in the following paragraphs. The launch vehicle configuration comparison between the baseline Atlas F and Seasat is shown in Figure 8-1. The general arrangement of the Seasat booster is shown in Figure 8-2, and the B1 and B2 pod layouts are shown in Figure 8-3. The fairing system is shown in Figure 8-4.

1. Atlas F Modifications

The forward end of the LO2 tank was modified with new cylindrical skins, and also the 10-ft diameter SLV-type bulkhead and interface ring. The LO2 loading probe assembly, LO2 PU stillwell, LO2 tank pressurization line, diffuser line, and wiring tunnel were modified for compatibility with the SLV bulkhead and constant diameter tank.

The Phase II LO2 tank pressure was increased by raising the boiloff valve and airborne LO2 relief valve settings. This change permitted an increase of the ground wind placard to 19 knots.

The new ISA (approximately one-half the length of the Centaur's) incorporated the Centaur design, 15.75 cm^2 (40 $in.^2$) of venting area, access doors (same as on Centaur), and an insulation blanket over the Atlas forward bulkhead.

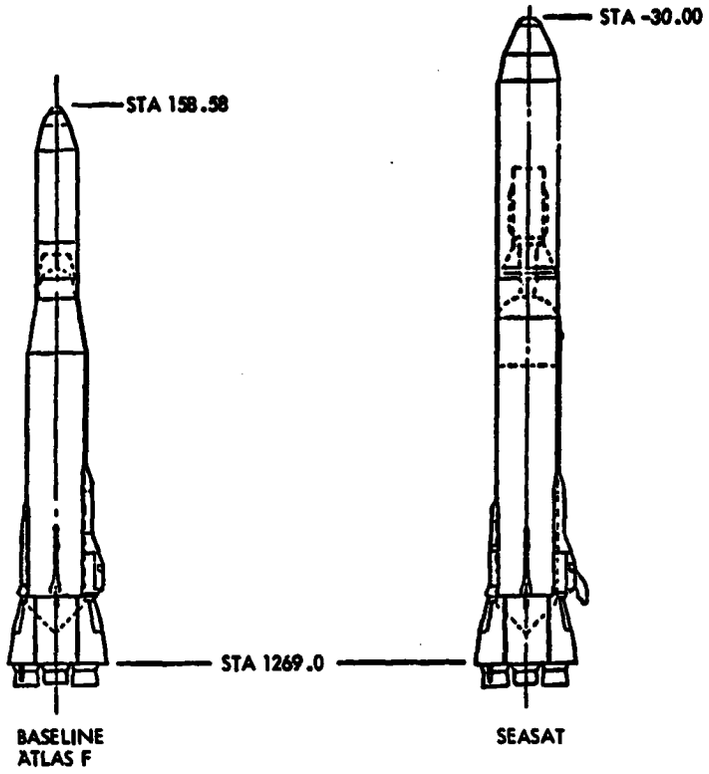

Figure 8-1. Launch Vehicle Configuration Comparison

Two Titan III retrorockets were installed in the vernier fairings. Chemseal was applied to the Atlas tank at the retrorocket thrust impingement area to protect the tank from erosion.

The flight control system was modified for mission specifics in the programmer, displacement gyro, and servo packages. The baseline rate gyro package was not modified, but relocated (see rate gyro fairing in Figure 8-2). The arm/disarm switch was also revised.

The guidance decoder relay assignments were revised for mission-peculiar discretes. The General Electric Company guidance horn antenna was installed at the base of the B-2 pod, and the range safety and telemetry antennas were repositioned.

Instrumentation and electrical modifications were incorporated. These included a delta P measurement at the ISA/booster interface, ambient temperature at the ISA, and a higher accuracy LO2 tank pressure transducer (landline). Also, monitors were provided for discrete commands across the Atlas/Agena interface, e.g., fairing separation. Mission-peculiar interface harnessing connectors (P/J106 and P/J107), and a retrorocket harness were provided.

The booster engine mixture ratio was increased by reorificing. The increase compensated for lower average vehicle acceleration that resulted in a lower LO2 flow rate and increased LO2 residuals.

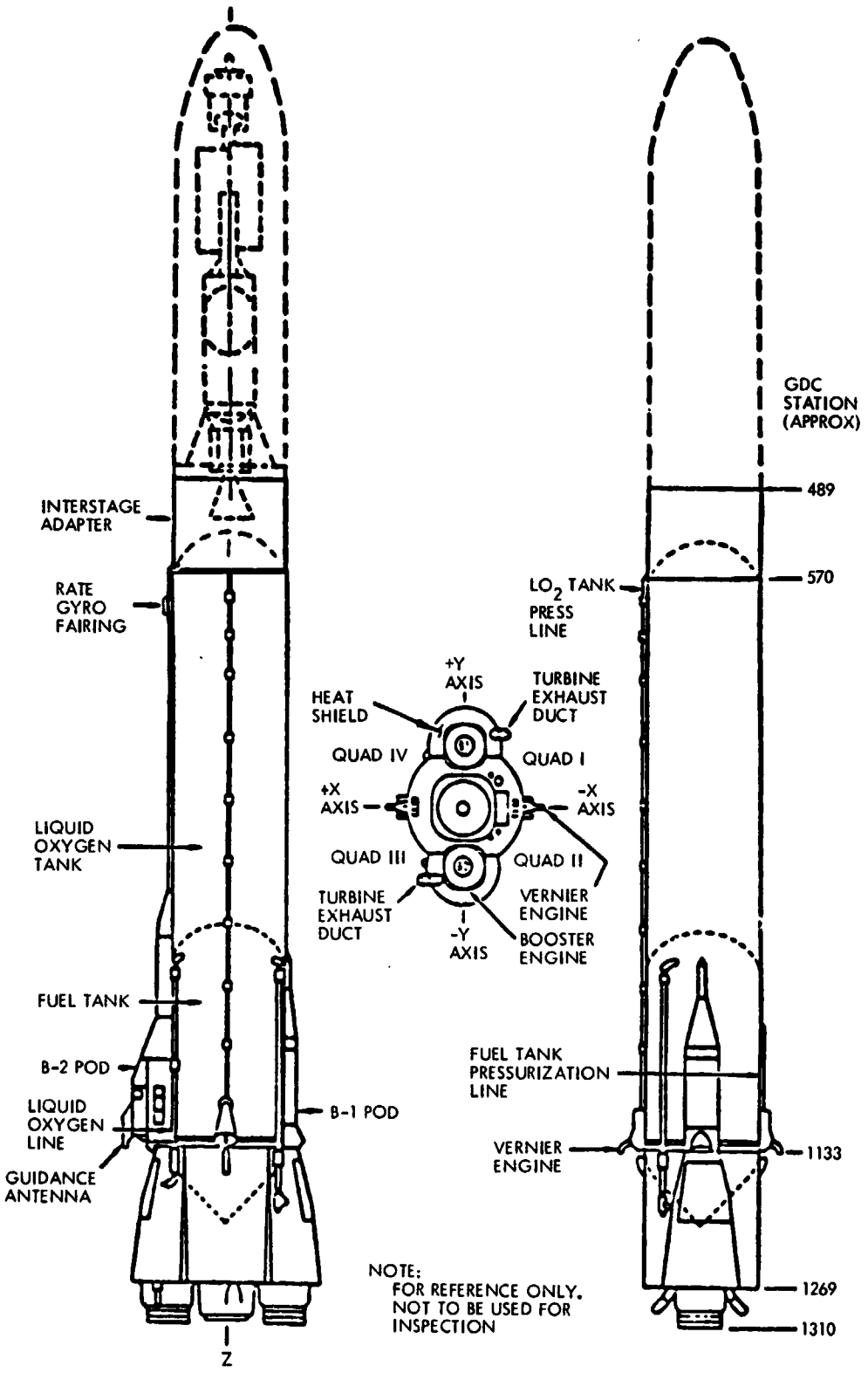

Figure 8-2. Sea- Booster General Configuration

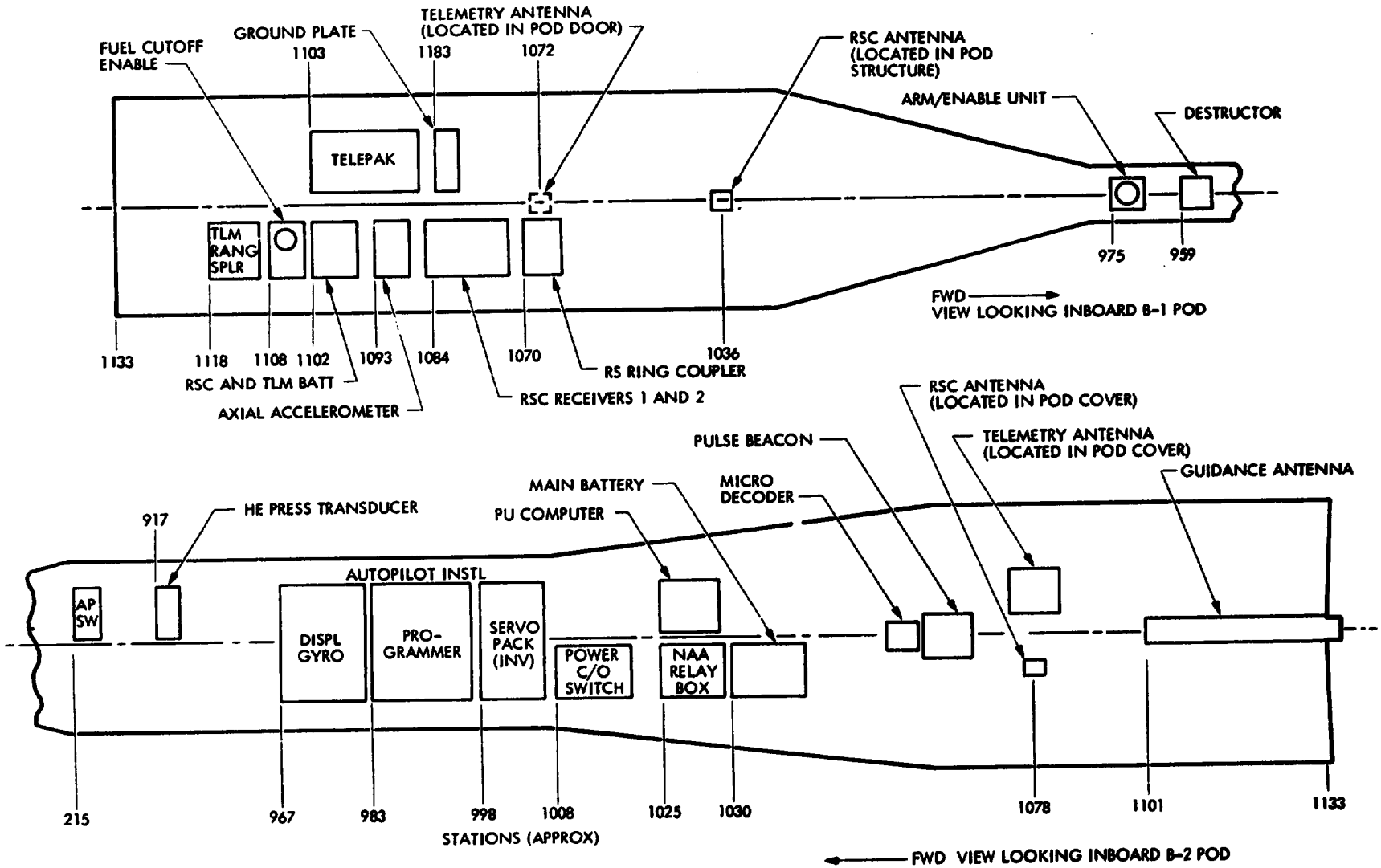

Figure 8-3. Equipment Pod Layout

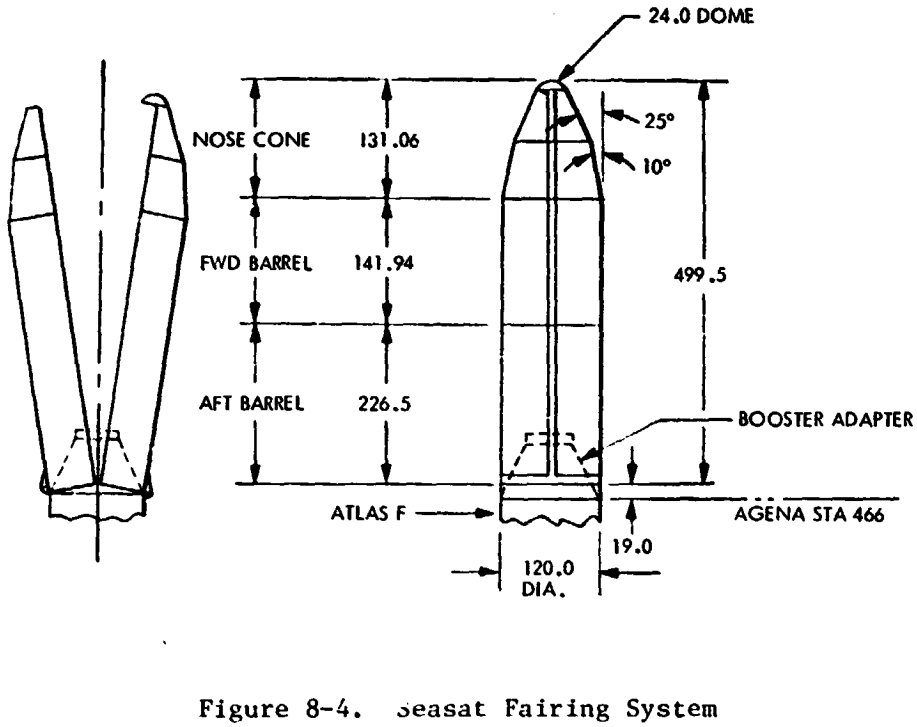

Figure 8-4. Seasat Fairing System

Booster and sustainer hydraulic pumps were installed that had had the SLV-3D vibration test.

The 600P/J12 booster staging disconnect installation was revised by reducing the lower lanyard length, providing a "hardpoint" on the harness for the secondary disconnect mode, and adding a tether to preclude impact of the plug on the sustainer engine.

2. Payload Fairing Configuration Modifications

To eliminate potential static charge buildup, a fiberglass panel in the forward conic section was replaced with a metal panel, the internal fiberglass air conditioning duct was covered with aluminum tape, and the triplex chute door skin was replaced with aluminum. The nose cone air conditioning diffuser (not required) was deleted. Thruster springs with a higher G level at separation were installed. For satellite SAR checkout, an access door was added in the aft conic section. The nose cone and forward barrel were painted white to reduce skin temperatures.

3. Trajectory and Performance

The Seasat spacecraft was successfully launched by the Atlas F/Agena launch vehicle from launch complex SLC-3W at Vandenberg Air Force Base on June 26, 1978, at 18:12:44.159 PDT (21:12:44.159 EDT or June 27 at 1:12:44.159 GMT). The launch vehicle placed the Seasat spacecraft into a highly accurate circular orbit inclined at 108 deg.

A comparison of the predicted and actual sequence of events is shown in Table 8-1. Liftoff (defined as 1-in. motion) occurred 7 min and 44.159 s after the designated launch window opening. This delay in liftoff was the result of 3 launch countdown holds as shown in Table 8-2. Beginning at 2 s after liftoff, the launch vehicle was rolled from a pad azimuth of 133.53 deg East of North to the design flight azimuth of 203.548 deg East of North. The roll maneuver was completed 15 s after liftoff, and a pre-programmed pitch and zero yaw program was executed from 15 s to booster engine cutoff (BECO). The pitch program was designed to give a near zero angle of attack during the booster phase of flight for a no-wind condition.

Booster engine performance was slightly higher than the pre-flight prediction. This high performance was expected based on post-flight reconstructions performed by the Aerospace Corporation for vehicles 64F, 65F, and 50F. The increased booster performance resulted in a 0.34-s early BECO, well within pre-flight estimated 3 sigma dispersion of one s. Approximately 3 s after BECO, the booster engines were jettisoned as planned.

The sustainer engine continued to perform nominally after booster jettison. Payload fairing separation occurred at T+200.8 s at a guidance predicted altitude of 122,000 m (400,000 ft), 6.72 s earlier than planned but within the 3-sigma estimate of 12.9 s. The primary reason for this early shroud jettison was the high booster performance. Sustainer engine cutoff (SECO) occurred at T+296.75 s and the separation retrorockets were fired 6 s after SECO. Both of these events were 6.63 s earlier than planned but within the 3-sigma limit of 15.5 s.

A planned 90-deg roll maneuver was performed by the Agena from T+313.8 to T+350.2 s. This was followed by a short coast phase to stabilize and reorient the satellite vehicle prior to the first Agena burn. Agena main engine ignited at T+379.0 s and continued to burn until T+613.4 s. This burn was 2.75 s longer than planned, which indicates lower than nominal engine performance. This is in agreement with previous Agena flights, which also showed a lower than expected engine performance. After a 2815.2 s coast phase, the Agena main engine ignited for the second time at T+3428.6 s into the flight. The second burn continued for 6 s, and placed the satellite vehicle into a highly accurate, nearly circular orbit.

The Seasat trajectory was targeted to a state vector at Atlas separation, because the Agena had no capability for real-time trajectory shaping. A comparison of the predicted and actual orbit parameters at Atlas separation is provided in Table 8-3. The apogee radius was 157 m (515 ft) higher than predicted, while the perigee radius was 785 m (2576 ft) lower. This resulted in a .0002 error in orbit eccentricity. Inclination, true anomaly, and longitude of the ascending node were all extremely close to the design values.

Table 8-1. Seasat Sequence of Events

Event	Time (T+Sec)		
	Predicted[a]	Actual	Difference
Programmer start (GMT on June 27)	1:05:00	1:12:44.468[b]	
Lift-off (1 in. motion)	T=0.0	0.0	
Booster engine cutoff	129.50	129.16	-0.34
Payload fairing separation	207.50	200.80	-6.70
Sustainer engine cutoff	284.38	277.75	-6.63
Vernier engine cutoff	303.38	296.75	-6.63
Fire retrorockets	309.38	302.75	-6.63
Start 90 deg roll	320.38	313.80	-6.58
Stop 90 deg roll	356.38	350.20	-6.18
Agena main engine start 1	385.38	379.00	-6.38
Agena main engine cutoff 1	617.03	613.40	-3.63
Agena main engine start 2	3435.38	3428.60	-6.78
Agena main engine cutoff 2	3441.48	3434.60	-6.88

[a]Obtained from the GDC Seasat final closed loop trajectory, March 1978.
[b]Represents receipt of programmer start signal at the GERTS guidance station. There is a 309-ms indicated transmission delay.

Table 8-2. Launch Countdown Holds

Time in the Count (min/sec)	Reason for Hold	Hold Time (min/sec)
T-13:00	To allow tasks to overtake the countdown clock.	3:18
T-4:00	To evaluate a water leak at the pumphouse.	4:12
T-1:40	To verify readiness for commitment by all agencies.	0:14
Total Hold Time		7:44

Table 8-3. Orbit Parameters at VECO

Parameter	Predicted[a]	Actual[b]	Difference
Radius (ft)	21,524,000	21,524,006	+6.0
Inertial velocity (ft/s)	14,708.09	14,705.68	-2.41
Flight path angle (deg)	7.6727	7.6954	0.0227
Perigee radius (ft)	4,171,007	4,168,431	-2,576
Apogee radius (ft)	21,618,310	21,618,825	+515
Eccentricity (nd)	0.6765	0.6767	0.0002
True anomaly (deg)	176.291	176.248	-0.043
Orbit inclination (deg)	106.136	106.135	-0.001
Longitude of the ascending node (deg)	48.051	48.047	-0.004

[a]Based on the GD/C Seasat final flight test trajectory (Revision B) quick look processor data.
[b]Based on guidance data quick look processor output.

A comparison of the predicted and final orbit parameters is given in Table 8-4. Design orbit requirements were defined in terms of semi-major axis, orbit inclination, eccentricity, and argument of perigee. The final orbit semi-major axis was 5.6 km (3 nm) lower than the design value of 7160.6 km (3870.6 nm), well within the ±17.9 km (±9.7 nm) range defined by the targeting specifications. Orbit inclination was 0.022 deg above the design value of 108 deg, but within the ±5 deg design range, while the orbit eccentricity was 0.0008 with a design constraint not to exceed 0.0052. The final orbit argument of perigee fell outside the Seasat design goal 90 ±20 deg, but remained within the pre-flight 3-sigma dispersion range of 18 to 275 deg. Argument of perigee is not defined for circular orbits, and it is very sensitive to small dispersions in injection conditions for nearly circular orbits. This error in argument of perigee was corrected during a planned orbit adjust maneuver.

A summary of the usable Atlas propellant residuals is given in Table 8-5. The residual fuel was 39 kg (85 lb) higher and the residual oxidizer 113 kg (250 lb) higher than predicted by the GDC pre-flight final closed-loop trajectory simulation. The estimated fuel outage of 42 kg (93 lb) was 0.9 kg (2 lb) below pre-flight prediction. This propellant residual data was derived from the actual SECO and ΔP port uncovered times and pre-flight estimates of propellant flow rates and tank volumes. Errors in tank volumes or actual propellant flow rates could have affected these residuals slightly.

4. Guidance Software

The Atlas 23F vehicle guidance was accomplished using the General Electric Radio Tracking System (GERTS) located in building 488, South Vandenberg, at Vandenberg Air Force Base. The system uses a ground-based radar to measure the range, azimuth, and elevation of the vehicle. This information was processed by the Radar Interface Unit (RIU) and applied to the ground guidance computer (Harris S-120). Guidance computer software transformed the radar data into vehicle position, velocity, and acceleration data, which was used to generate pitch and yaw steering commands and discretes. Steering commands and discretes were transmitted through the GERTS command link to the vehicle. Vehicle-borne equipment consisted of a beacon and a command decoder.

GERTS radar for the Seasat mission operated in the track-only mode. In this mode, only position measurements were made and there was no direct measurement of the vehicle acceleration along the trajectory. The track-only system operated in a wide-beam conical scan mode for beacon acquisition and a narrow beam monopulse mode for precision tracking. Acquisition in the conical mode occurred at 75.91 s after liftoff as the vehicle entered the first acquisition cube set at 76 s. Cube settings were based on the final GD C closed-loop trajectory simulation. Transfer to monopulse tracking mode occurred at 79.59 s and remained in this mode of operation until loss of signal at 458.84 s after liftoff.

The RIU data channel was an interfacing unit between the radar and guidance computer. This unit accepted radar data from the GERTS digitizer and supplied discrete and steering data to the GERTS command modulator. Synchronization with

Table 8-4. Mean Orbit Parameters Following Agena Blowdown

Parameter	Predicted[a]	Predicted Based on GERTS State Vector	Actual[b]
Perigee altitude (nm)	423.04	417.74	420.89
Apogee altitude (nm)	429.15	431.88	426.43
Orbit eccentricity (nd)	0.0007899	0.001828	0.000716
Orbit inclination (deg)	107.962	107.949	108.022
Longitude of the ascending node (deg)	7.3296	7.3460	--
Semi-major axis (nm)	3870.03	3868.74	3867.58
Orbit period (min)	100.774	100.629	100.550
Argument of pericenter (deg)	76.698	55.839	242.720

[a]Based on the LMSC closed loop Seasat trajectory simulation dated June 24, 1978.
[b]Best estimate of mean orbit elements as of June 30, 1978.

Table 8-5. Atlas Usable Propellant Residuals at SECO

Item	Predicted[a]	Actual
Oxidizer (lb)	1017	1267
Fuel (lb)	572	657
Time to deplete (s)	5.56	6.95
Fuel outage (lb)	95	93

[a]Obtained from the GDC Seasat final closed loop trajectory, March 1978.

the radar was provided through these units by input and output interrupts. Data were input from the RIU to the guidance computer at a rate of 10 samples a second and output at a rate of 50 samples a second.

The Harris S-120 computer contained all real-time flight software. This included data editing, navigation equations, logic for generating flight discretes, and a modified Kalman filter to provide nearly optimal estimates of vehicle position, velocity, and acceleration during the sustainer and vernier phases of flight. During the booster phase, the radar data were used to compute booster time-to-go (shown in Figure 8-5) as a linear function of slant range (distance between the vehicle and guidance antenna), rate of change in slant range, and elevation angle. Guidance-generated booster engine cut-off was issued when the time-to-go was zero. Payload fairing separation was commanded when the vehicle reached an altitude of 121,920 m (400,000 ft.). Guidance steering was nulled during the primary and backup shroud jettison sequences. Sustainer engine time-to-go function was determined by the desired angular momentum at separation. All other guidance-generated discretes were timed from BECO, payload fairing jettison time, or SECO.

For this mission, 10 guidance-commanded discretes were generated. Table 8-6 lists these discretes with the predicted and actual event times measured from liftoff. Liftoff was defined as a 1-in. motion. Differences in the event times were caused primarily by higher than expected booster performance. All flight events were accomplished by the primary guidance-generated commands.

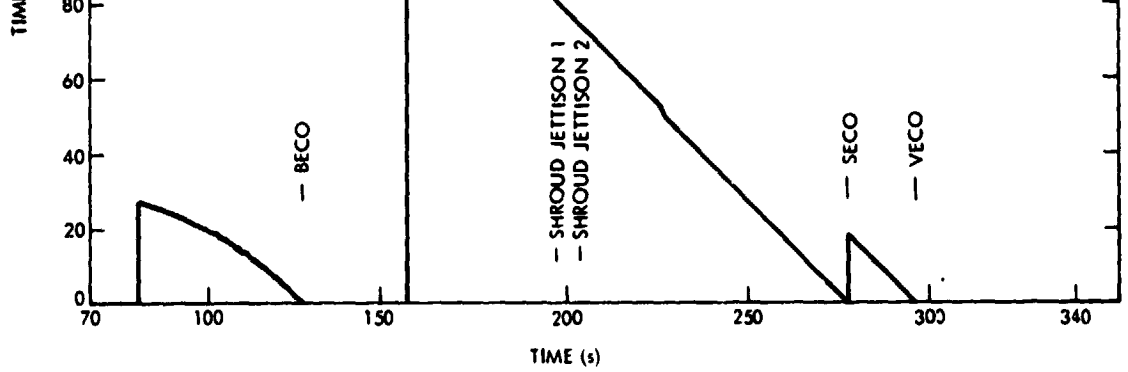

Figure 8-5. Time-to-go Function Generated by the GERTS Ground Guidance Computer

Table 8-6. Guidance Generated Discretes

Event	Time (T+sec)	
	Predicted[a]	Actual[b]
Booster engine cutoff	129.50	129.16
Payload fairing separation 1	207.50	200.80
Payload fairing separation 2	211.50	204.80
Sustainer engine cutoff	284.38	277.75
Premature satellite separation inhibit	286.38	279.75
Start Agena timing	289.38	282.75
Uncage satellite vehicle gyros	302.38	295.75
Vernier engine cutoff	303.38	296.75
Satellite vehicle separation	308.88	302.25
Fire retrorockets	309.38	302.75

[a]Based on the GDC Seasat final closed loop trajectory, March 1978.
[b]Quick-look post-flight guidance data processor output.

Seasat guidance consisted of pre-programmed open-loop booster steering and closed-loop sustainer and vernier steering. Closed-loop guidance steering was enabled at BECO +8.5 s, but all steering commands were pulled until the Kalman filter operation stabilized. The guidance equations used a numerical integration to predict SECO-state conditions. Equations of motion for a constant thrust, constant flow rate rocket vehicle, and a spherical Earth model were solved in the pitch plane using a simple Newton iterative technique to guide the vehicle to the desired end conditions. Pitch steering angle was assumed to be of the linear tangent form, where the coefficients are iterated. The steering coefficients were updated every third guidance cycle, or approximately every 1.5 s. Yaw steering angle was obtained from an optimal closed-form solution of the equations of motion to control orbit inclination at SECO. The actual pitch and yaw steering histories are shown on Figure 8-6.

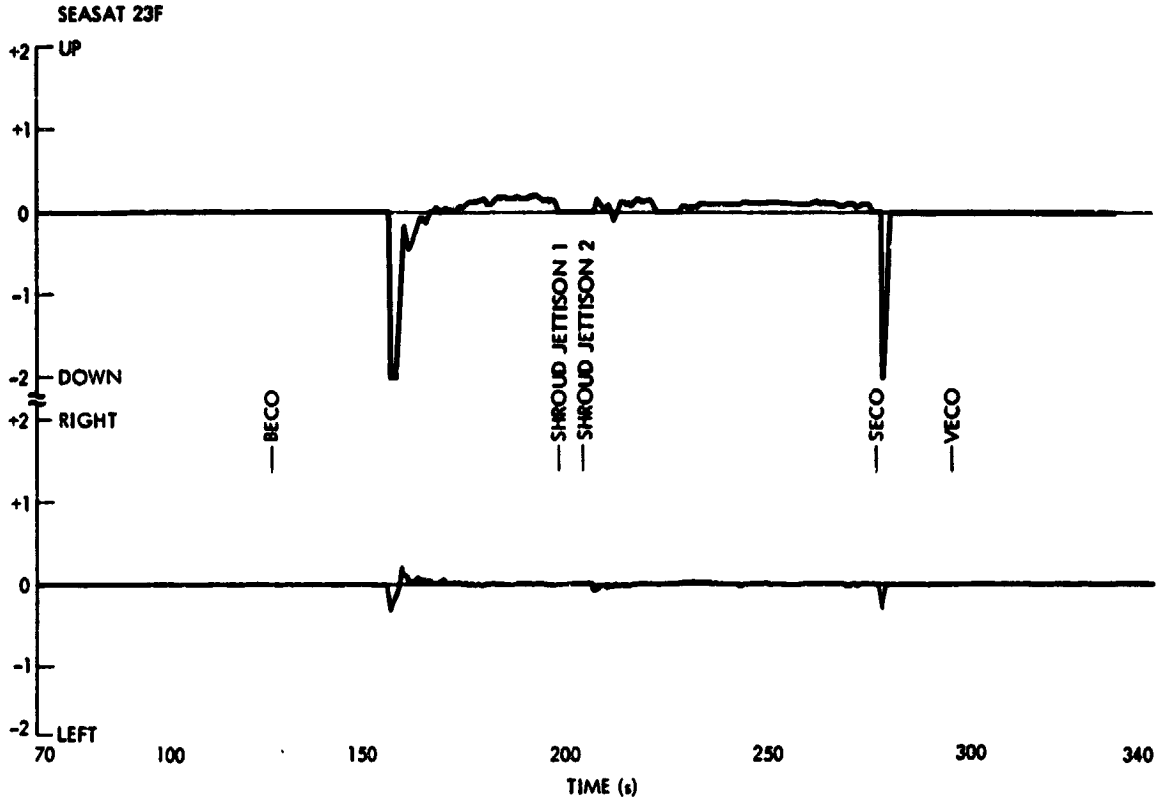

Figure 8-6. Pitch and Yaw Steering Commands

Maximum nose-down pitch rate (2 deg/s) was commanded at the start of sustainer and vernier steering for approximately 2- and 1-s periods, respectively. Following this initial reorientation of the vehicle, pitch steering was stable and less than 0.25 deg/s. Steering was nulled during primary and backup payload fairing separation sequences as planned. After a slight transient of less than 0.2 deg/s at the start of sustainer and vernier steering, yaw steering commands were extremely small. Sustainer closed-loop steering started at BECO +28.58 s, 1.08 s later than predicted, which implied slightly noisier radar data near BECO than predicted.

Seasat mission design requirements included a specified satellite vehicle pointing at separation. This included pitch, yaw, and roll orientation as well as residual rates of these parameters. Satellite vehicle pointing was accomplished during the vernier solo phase using guidance-generated attitude information at SECO. Table 8-7 shows the actual and 3-sigma design residual attitude errors and rates. All parameters were well within the 3-sigma design requirements.

Atlas separation was followed by a short coast phase (11.05 s) to stabilize the satellite vehicle system prior to a 90 deg roll maneuver. This roll reorientation was performed by the Agena attitude control system at a rate of approximately 2.5 deg/s. The Agena horizon sensors acquired as planned during the roll

Table 8-7. Pointing Accuracy at Satellite Vehicle Separation

Parameter	Actual[a]	3σ Requirement
Attitude error (deg)		
Pitch	-0.12	±2.46
Yaw	0	±2.02
Roll	0.37	±2.95
Attitude rate error (deg/s)		
Pitch	0.12	±0.60
Yaw	0	±0.50
Roll	0.48	±0.75

[a]Obtained from Atlas gyro data at VECO +5.5 s.

and maintained pitch and roll control during the Agena main burns. Both Agena main burns were terminated by an onboard velocity meter when the design delta velocities were reached. The delta velocities added by the first and second burns were 3613 and 167 m/s (11,855 and 549 ft/s), respectively.

Guidance equations, software, and GERTS hardware performed as designed. No anomalous behaviour was noted during the flight or after post-flight data evaluation.

5. Vehicle Dynamics

Close attention was paid to ground wind measurements and predictions during pre-launch operations, since vehicle ground wind restrictions were fairly low (approximately 18 kt, depending on tanking conditions). However, the meausred ground winds decreased steadily as the countdown progressed. At the time of launch, the measured wind at a height of 16 m (54 ft) above the launch pad was 5 kt at an azimuth of 300 deg from north.

The decision that winds aloft were acceptable for launch was based on a Jimsphere balloon released at 2315Z, June 26, 1978. The pitch and yaw components of this wind are shown in Figure 8-7. Pre-launch peak response to the 2315Z wind was calculated to be 92.5 percent of the weakest structural allowable. Including an allowance of 10 percent to account for possible extreme wind changes over the next 80 min. This peak response was calculated to occur at an altitude of 9.8 km

(32,175 ft). The product of dynamic pressure, Q, and total angle of attack at that altitude was calculated to be 1384 deg-lb/ft^2.

The wind measurement closest to launch was made by a Jimsphere balloon released at 0030Z, June 27, 1978. The pitch and yaw components of that wind profile are shown in Figure 8-8. Tracking of this balloon was terminated at 12.6 km (41,400 ft), as Atlas 23F/Seasat was launched. The 0030Z balloon reached 12.2 km (40,000 ft) about 3 min before vehicle liftoff. Peak calculated response for the 0030Z sounding was 80 percent of the weakest structural allowable after deletion of all allowances for extreme wind changes. The peak response was calculated to occur at 11.1 km (39,667 ft) and was associated with a Q-alpha total of 1091 deg-lb/ft^2. This peak corresponded to a flight time of 66.75 s.

The most direct measure of dynamic load response during flight was axial accelerometer U101A. A review of this acceleration measurement reflected a very nominal longitudinal acceleration history for both booster and sustainer phases of flight. Response to transient events was very moderate. Oscillations about steady-state acceleration levels were low, and no appreciable "pogo" (unstable thrust-coupled longitudinal vibration) was noted.

Dynamic behavior of the vhicle flight control system was evaluated through review of the measurements of booster engine actuator motion (S203D, S204D, S205D, S206D), vernier engine actuator motion (S222D, S223D, S233D, S234D), sustainer engine actuator motion (S256D, S257D), Atlas displacement gyros (S063D, S062D, S061D), and Atlas rate gyros (S054D, S053D, S052D). None of these measurements indicated any anomalous behavior of vehicle motion. Responses to commands and transients were normal.

a. Liftoff. Rate gyro responses at the liftoff event were maximum in yaw with predominate oscillations at 6 Hz with peak-to-peak amplitude of 1.9 deg/s. Small amplitude oscillations at 6 Hz persisted for about 20 s after liftoff. The programmed roll maneuver was verified by the roll rate gyro, which showed a mean roll rate of 5.1 deg/s from T+2 to T+15 s.

b. Atmospheric Ascent. At approximately T+15 s, the Atlas pitch rate gyro responded, verifying initiation of the pitch-over program. Peak rate in pitch was observed to be -1.2 deg/s at 64.1 s. Peak rate in yaw was +1.1 deg/s at 62.2 s. The yaw rate gyro exhibited prolonged low level oscillations at about 5 Hz from transonic speeds until the end of booster flight. This was believed to be second bending mode limit cycling. No excessive vehicle responses were noted during the maximum dynamic pressure region of flight. The largest booster engine gimbal angles measured were +1.8 deg in pitch at 76.2 s and -2.0 deg in yaw at 77.0, 78.4, and 82.5 s. Booster engine 1 appeared to operate with an average 0.2-deg positive yaw offset from start of the pitch program to booster engine cutoff.

c. Booster Engine Cutoff. The booster engine cutoff was observed at T+129.2 s. The sustainer engine, activated for control during the period

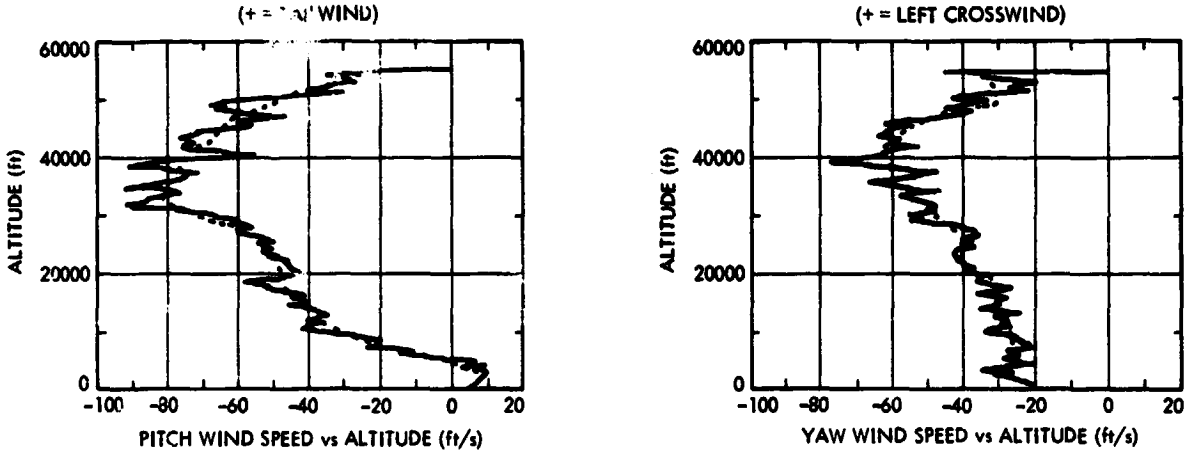

Figure 8-7. Pre-Launch Wind Components

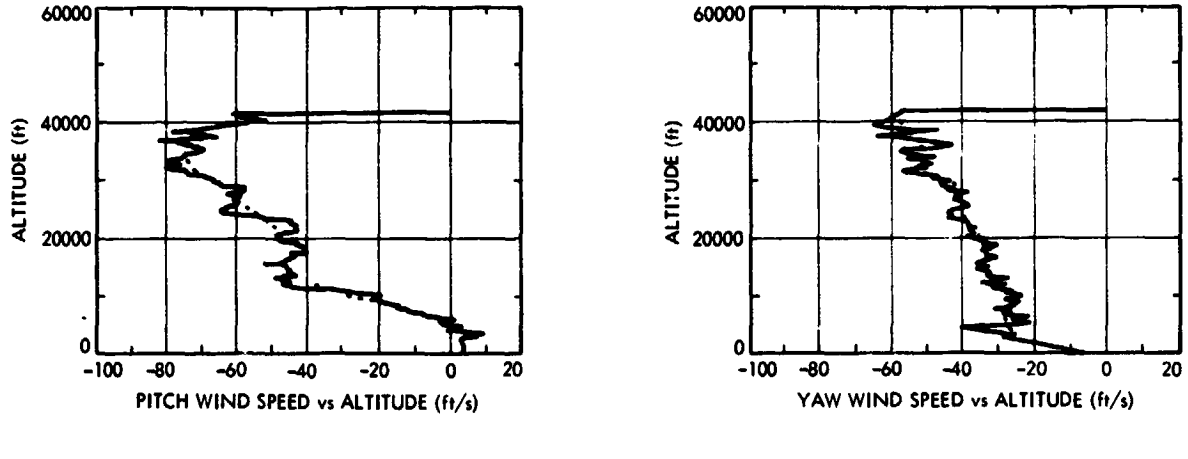

Figure 8-8. Launch Wind Components

between the BECO command and booster package jettison, required +0.4 deg pitch and +0.9 deg yaw to trim the vehicle.

d. Booster Package Jettison. The booster package jettisoned at T+132.4 s. This event initiated low level transient vibration responses on the pitch, yaw, and roll rate gyro measurements.

e. Sustainer Engine Cutoff. The instrumentation indicated sustainer engine cutoff at T+277.8 s. The yaw rate gyro measurement reflected a transient response which peaked at +1.0 deg/s, returning to null about 2 s after SECO.

f. Separation. The Atlas/Agena separation event was observed at T+302.2 s. The Atlas longitudinal accelerometer indicated that Atlas retro-rockets were fired 0.5 s later, as programmed.

6. Agena Astrionics Systems

a. Agena Avionics. The block diagram of the Agena avionics system is shown in Figure 8-9. The system consisted of the Augmented Electronics Assembly (AEA), Gyro Reference Assembly (GRA), Horizon Sensor Assembly (HSA), Digital Velocity Meter (DVM), DVM Counter, engine actuators, and hydrazine High-Mode Reaction Control Cluster (HMRCC). The Command Processor and Central Timing Unit (CTU) stored and recalled the entire ascent sequence of events, but this was

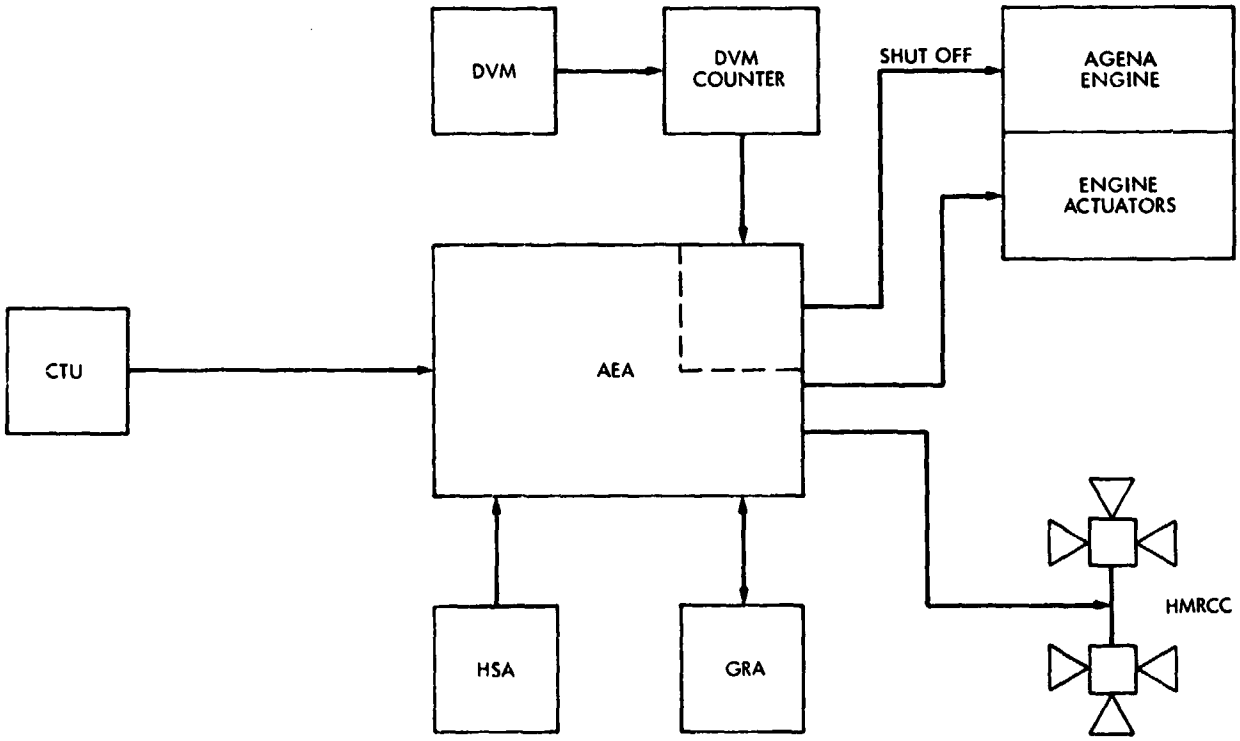

Figure 8-9. Agena Ascent Avionics System

only a part of its overall mission function; it is, therefore, regarded to be part of the on-orbit control system. The CTU issued redundant commands to the AEA with a granularity of 1 s. The AEA then activated all relays, control signals, and filter networks required to execute the command.

The ascent sequence of events is listed in Table 8-8. The sequence started with the ground guidance sending the start Agena timing command. The CTU started counting time upon receipt of this signal, nominally at SECO +5 s. All CTU commands were timed events based on this reference time. At SECO +18 s ground guidance sent the uncage satellite vehicle gyros command. VECO occured 1 s later. The retrorockets fired at VECO +6 s. After the Agena cleared the booster adapter, the separation switches activated the HMRCCs. During the next 9 s, the 3-axis-stabilized ascent controller (AEA, GRA, and HMRCC) arrested the separation rates and established an attitude with the pitch, roll, and yaw attitudes that existed before VECO. Beginning at a CTU time of 31 s, and for the next 36 s, the CTU commanded a 150-deg min roll rate for a total roll of 90 deg. At this point, the HSA acquired the horizon and established the proper pitch and roll references for the Agena first burn. The GRA provided the yaw reference.

After some additional maneuvering and settling, the CTU commanded an Agena engine burn at a CTU time of 96 s. The burn lasted about 210 s. An engine turn-off signal was generated by a signal from the DVM. This ensured that an exact pre-programmed velocity increment was imparted by the first burn. During the burn, the HMRCCs were deactivated in pitch and yaw, and the hydraulic integral circuits were enabled. Between the first and second burns, the vehicle was stabilized in a horizontal position. Just before the second burn, the CTU deactivated the HSA control and yawed the vehicles by torquing the yaw gyro in the GRA. The CTU commanded the second burn start after a coast time of about 46 min. Termination of the second burn occurred about 6 s later upon receipt of a signal from the DVM when this second pre-programmed velocity increment was reached. Following the burn, the HSA was again added to the control loop and the vehicle reoriented. This was the conclusion of the Agena ascent phase.

Review of the flight data shows that the ascent system performed as expected. Actual event times are given in Table 8-8.

b. Agena Instrumentation and Telemetry. The block diagram of the block telemeter is shown in Figure 8-10. There were seven independent, asynchronous inputs to the block telemeter. Each of the inputs was connected to an individual Sensor Data Assembler (SDA) module which consisted of a memory capable of storing four blocks of data, and associated read/write control logic. Each block of data stored in the memory included an 8-bit identification word, a 40-bit time word, and up to 944 data bits. The blocks were selected asynchronously based on full data block availability and priority for outputting as a time-multiplexed, pulse-code modulated (PCM) signal. The carrier frequency was 2287.5 MHz.

The formatting of the block sequence was accomplished by the block telemeter control function. The output bit rate was 25,000 b/s, and there were 1024 bits in each block. Therefore, a new output block occurred every 40.96 ms.

Table 8-8. Agena Ascent Events

Event	Signal Source	Nominal Time From Reference	Actual Time (GMT)
Start Agena timing (CTU=0)	Atlas guidance	SECO + 5	1:17:27.0[a]
Uncage S/V gyros	Atlas guidance	SECO + 18	1:17:40.0
VECO	Atlas guidance	SECO + 19	1:17:41.0
S/V separation	Atlas guidance	VECO + 5.5	1:17:46.5
Activate HMRCC	Separation switches	CTU = 22.5	1:17:49.0
Start 90-deg roll	CTU	31.0	1:17:58.0
Stop 90-deg roll	CTU	67.0	1:18:34.0
First burn start	CTU	96.0	1:19:04.1
Command engine shutdown	DVM	327.1	1:22:58.0
Transfer second burn DVM number	CTU	357.0	1:23:24.6
Second burn start	CTU	3146.0	[b]
Command engine shutdown	DVM	3152.1	[b]

[a] SECO at 1:17:22.0.
[b] Real-time data not available.

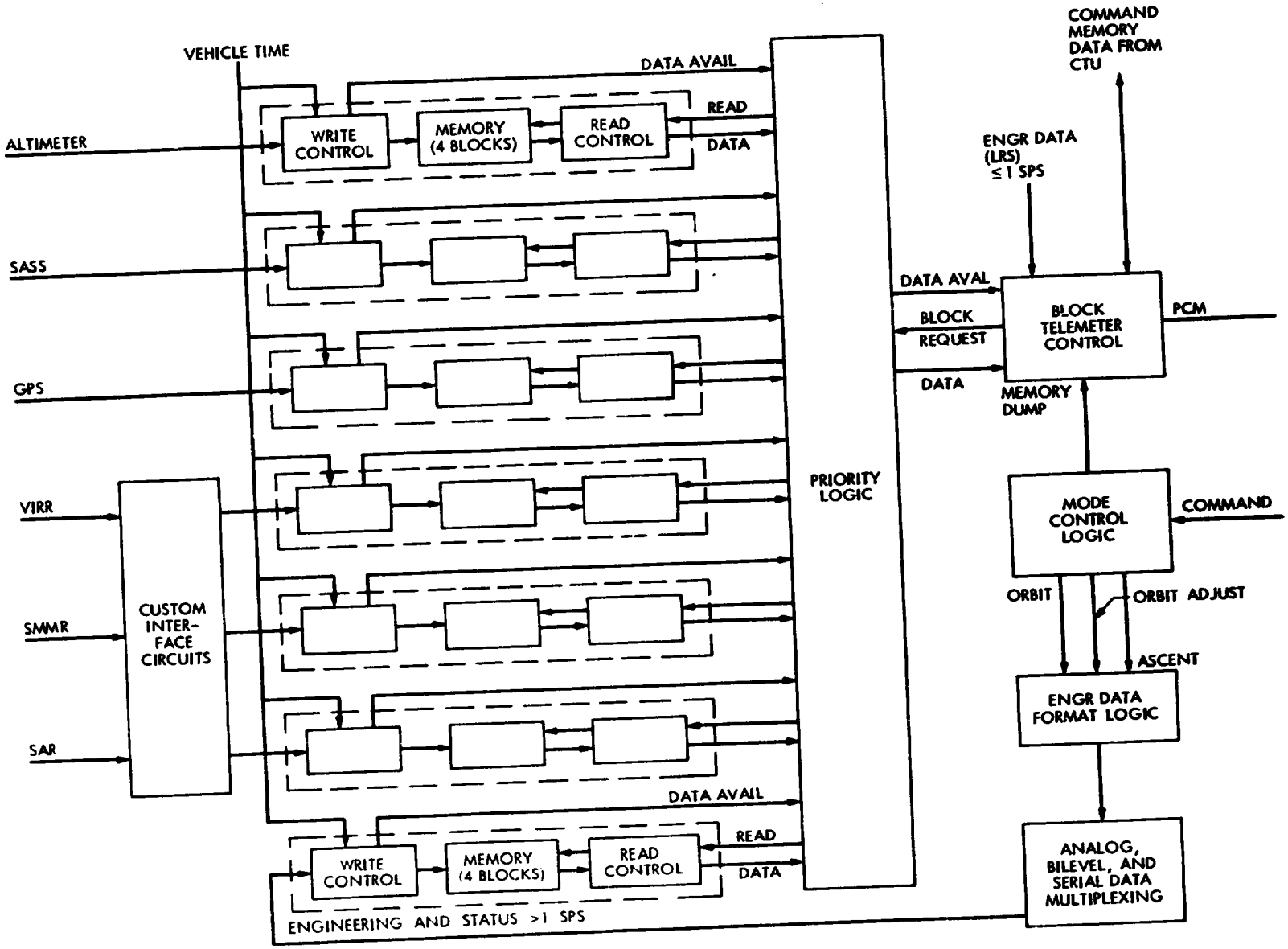

Figure 8-10. Block Telemetry Diagram

Every twenty-fifth block (every 1.024 s) the block telemeter control output a low rate sample (LRS) data block. This block was formatted and output in real time. There was no intermediate data storage for the LRS data block.

By definition, a block frame consisted of the LRS block and the succeeding 24 data blocks. When the LRS was not being output, an available data block was read out, and if more than one data block was available, the blocks were sequentially selected based on their priority ranking. By use of real-time commands, the engineering and status blocks (ascent, orbit, and orbit adjust blocks) could be selected for output.

The following telemetry blocks were assigned:

(1) Low Rate Sample (LRS) Block. The LRS block contained all engineering and status data with a sampling rate less than or equal to one sample a second.

(2) Ascent (ASC) Block. The ascent block contained engineering and status data with sampling rates exceeding one sample a second. This block contained all engineering and status data, including that contained in the orbit and orbit adjust blocks.

(3) Orbit (ORB) Block. The ORB block contained engineering and status data with sampling rates exceeding one sample a second and contained all engineering status data during the orbit mode.

(4) Orbit Adjust (O/A) Block. The O/A block contained engineering and status data exceeding one sample a second and contained all engineering data during the orbit adjust mode.

Measurement Designation. This was always composed of two letters followed by a three-digit number. The two letters identified the subsystem or sensor system from which the data originated. The conde for identifying the subsystem and sensor system is summarized below:

AL	Radar altimeter.
LA	LMSC structures and mechanics subsystem.
LB	LMSC orbit insertion system and OAS/RCS.
LC	LMSC electrical power system.
LD	lmsc ascent and orbit guidance and control subsystem.
LH	LMSC telecommunication and data system.
RA	Laser retroreflector.
SA	LMSC synthetic aperture radar antenna.
SD	SAR data link.
SM	Scanning multichannel microwave radiometer.
SR	SAR electronics.
SS	Scatterometer.
TR	Tranet beacon.
VI	Visible and infrared radiometer.

The 3-digit numbers following the letters could be used to identify the type of measurements. The codes for identifying the type of measurements are listed below:

LRS, Ascent, Orbit, and Orbit Adjust Data Block

01x		LRS word 11, bits 3 through 8.
1xx	2xx	Analog data.
4xx		Serial bit data.
5xx	6xx	Discrete data.

In the engineering blocks the interest was limited to LRS and ASC data. Similarly, in the measurement designation the interest was limited to LA, LB, LC, and LD. The analog data and serial bit data were recorded on 8-channel recorders while the discrete data was displayed on the event recorder. Of the 297 data signals available in these categories, 85 data signals were displayed at the NASA telemetry station in building 836.

Performance. Agena data reception at the NASA telemetry station was satisfactory through the Agena first burn. It had been anticipated that real-time data of the Agena second burn would be received, but this did not occur. Second-burn data was later relayed from another tracking station.

7. 305-cm Diameter Fairing

a. General. The Atlas F vehicle baseline configuration included a 213-cm (84-in.) diameter payload fairing. Marginal performance capability resulted in a configuration change to a 305-cm (120-in.) diameter fairing. An available fairing, 305-cm in diameter, that was the test specimen in an earlier test program, was inspected and found to be suitable. It was refurbished, updated, and modified for use with the Seasat launch vehicle.

The fairing protected the satellite vehicle system from aerodynamic forces and thermal effects during ascent through the atmosphere by complete encapsulation of the sensor module and the Agena stage. The aft end of the fairing interfaced with the launch vehicle at the booster adapter skirt through a bolted field joint. At a programmed point in flight, the fairing was separated by activation of a pyrotechnically-actuated system and jettisoned from the launch vehicle by spring thrusters.

b. Basic Design. The 305-cm diameter payload fairing (PLF), as shown in Figure 8-4, was a jettisonable structure consisting of an aft barrel, forward barrel, and biconic nose cone sections bolted together at their interfacing field joints. One section, the mid-barrel of the former test fairing, was not required for the Seasat vehicle configuration. An aft circumferential and two longitudinal joints separated the fairing into clamshell halves which pivoted on and jettisoned from separable type hinges.

The fairing basic structure was a ring stiffened aluminum and magnesium/thorium shell. Both the aft and the forward cylindrical barrel sections were constructed of two light gage sheet aluminum skins riveted together with the outer sheet corrugated for longitudinal stiffness as shown in Figure 8-11. The stiffening rings, doublers, and local framing and stiffening members in both barrel sections were aluminum.

Conventional rivet and bolted construction was used, composed of longitudinal half-shells joined by magnesium and thorium frangible doublers. The aft barrel section included a circumferential joint consisting of aluminum frangible doublers located immediately forward of the fairing-to-vehicle interfacing ring.

The biconic nose cone was a single-skin magnesium and thorium shell with stiffening rings of the same material. It was capped with a stainless steel nose dome. Similar to the barrel sections, the nose cone was composed of longitudinal half-shells joined by magnesium and thorium frangible doublers. The nose dome was attached to one half-shell and made a separable lap joint with the other half to permit separation at jettison.

Separation of the fairing from the launch vehicle was accomplished during the Atlas sustainer phase. Two stainless steel hinges on each half-shell were located at the aft end of the fairing, as shown in Figure 8-12. The hinges were designed to permit rotational motion only during the first 60 deg. The hinges would then separate and each fairing half would translate outward and aft away from the launch vehicle.

The fairing assembly had openings for ground support umbilical and service access as shown in Figure 8-13. In the forward barrel sections there was a port with a spring-loaded door for the payload air conditioning umbilical. The aft barrel had the following openings: Agena air conditioning port with door; triplex port and door for the electrical umbilical, oxidizer vent, and fuel vent; helium supply port; oxidizer fill port; and a fuel fill port. All of the aft barrel ports had chutes attached to the inside of the fairing and interfaced with the Agena by separable seals. In addition, there were service access doors for the separation system initiators and thruster springs.

Thin aluminum sheet liners were attached to the stiffening ring inner flanges in the forward barrel section and the biconic nose cone for thermal control of the payload sensor module area. The nose cone dome used thin aluminum conical liners with one inverted as illustrated in Figure 8-14.

The fairing was stack-mated in the factory for fit and alignment. It was acoustically cleaned to preclude payload contamination during assembly on the vehicle or in flight.

The fairing had been subjected to static test loads in an earlier program that were nearly twice the Seasat requirements. Dynamic and pressure loads margins were analyzed as adequate or greater. The flight instrumentation did not include structural load-sensing transducers.

c. Refurbishment. The fairing was completely refurbished. Test load application holes were repaired by patch plates and filler rivets. Corroded

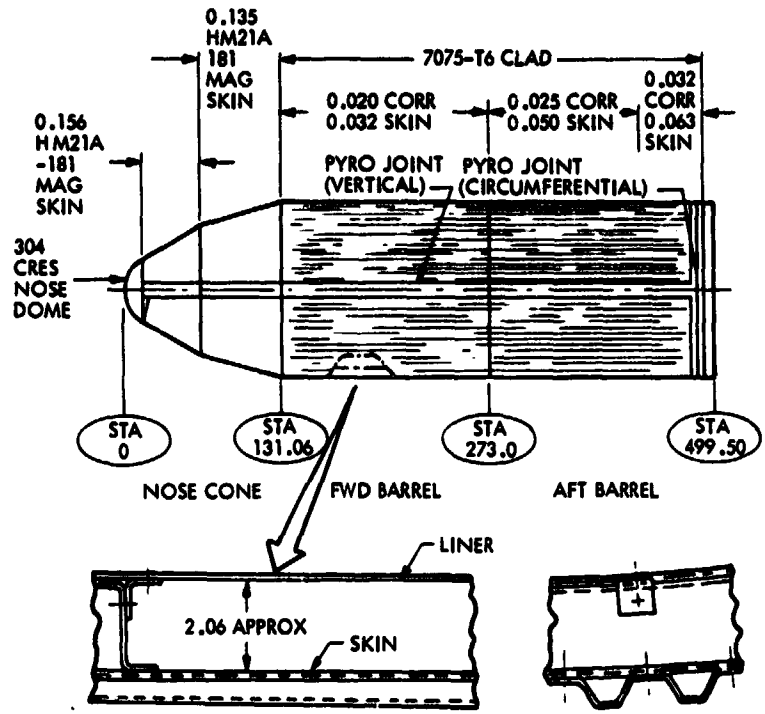

FAIRING MATERIAL

NOSE CONE
- DOME — STAINLESS STEEL
- SKIN — HM21 A-T31 MAGNESIUM THORIUM
- RINGS — HM21 A-T3 MAGNESIUM THORIUM AND HM31 A-T5 EXTRUDED BAR

BARREL
- CORRUGATIONS — 7075-T6 ALUMINUM
- SKIN — 7075-T6 ALUMINUM
- RINGS — 2024-T4 ALUMINUM

INTERFACE RING — 7079 ALUMINUM FORGING

PYRO JOINT (VERTICAL)
- FRANGIBLE DOUBLER — HM31A-T5 MAGNESIUM THORIUM
- TUBING — 347 STAINLESS
- DETONATION BLOCK — CRS 303 Se MIL-S-7720

PYRO JOINT (CIRCUMFERENTIAL)
- FRANGIBLE DOUBLER — 7075-T6 ALUMINUM
- TUBING — 347 STAINLESS

AREA	THERMAL LINER MATERIAL	REMARKS
NOSE DOME	0.016 6061 T6 ALUM	DOUBLE CONICAL LINERS SPACED 0.3 APART + SINGLE INVERTED
25° CONE	0.016 2024 T3 ALCAD	SINGLE CONICAL LINER SPACED OVER RINGS
10° CONE	0.012 2024 T3 ALCLAD	SINGLE CONICAL LINER SPACED OVER RINGS
CYLINDER SECTION TO STA 273	0.012 2024 T3 CLAD	SINGLE LINER SPACED OVER RINGS

Figure 8-11. Fairing Structural Components and Materials

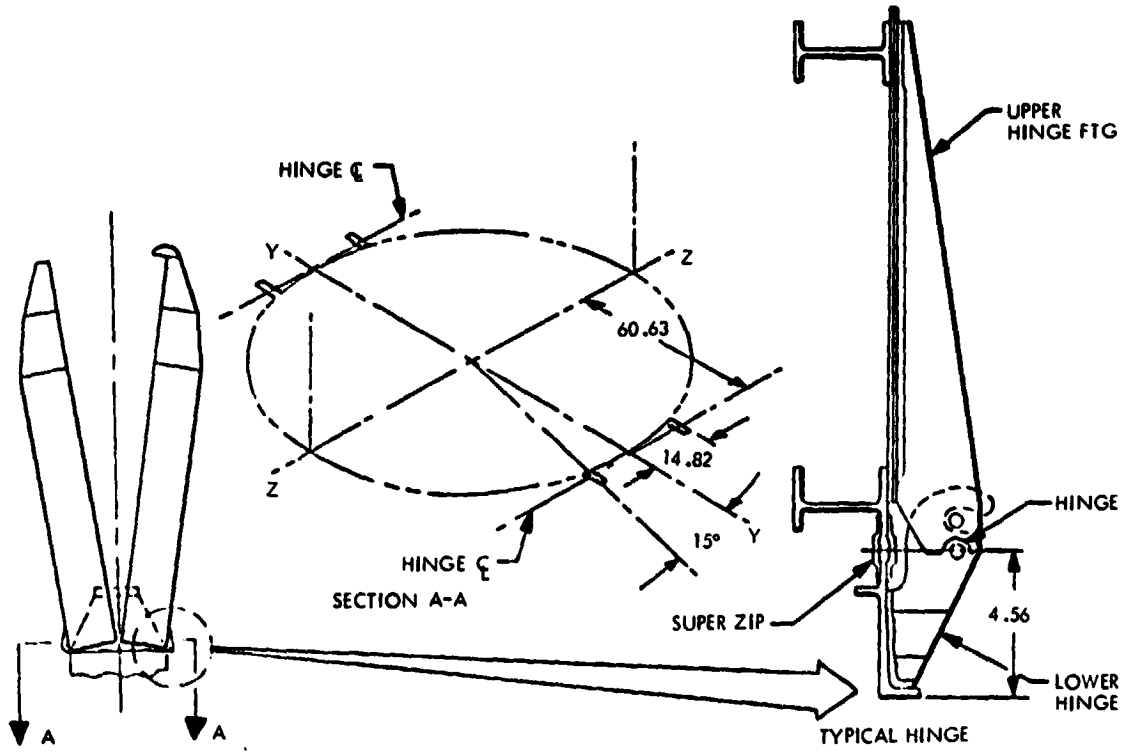

Figure 8-12. Fairing Hinge Assembly

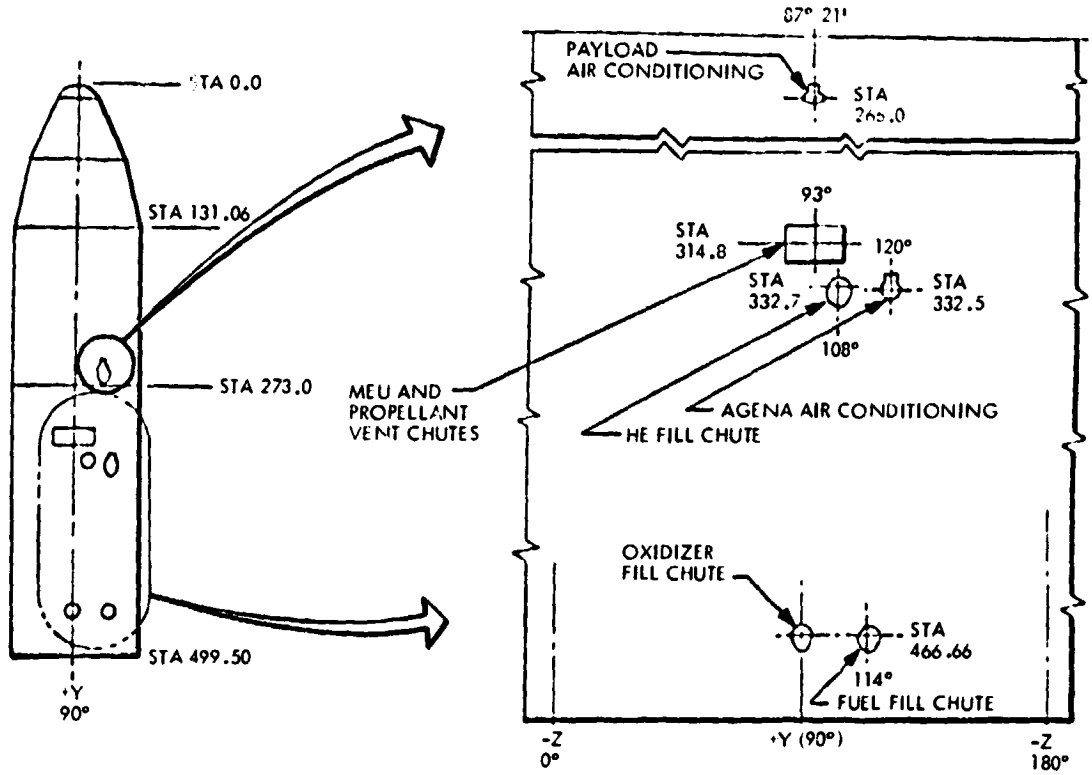

Figure 8-13. Access Openings in Fairing

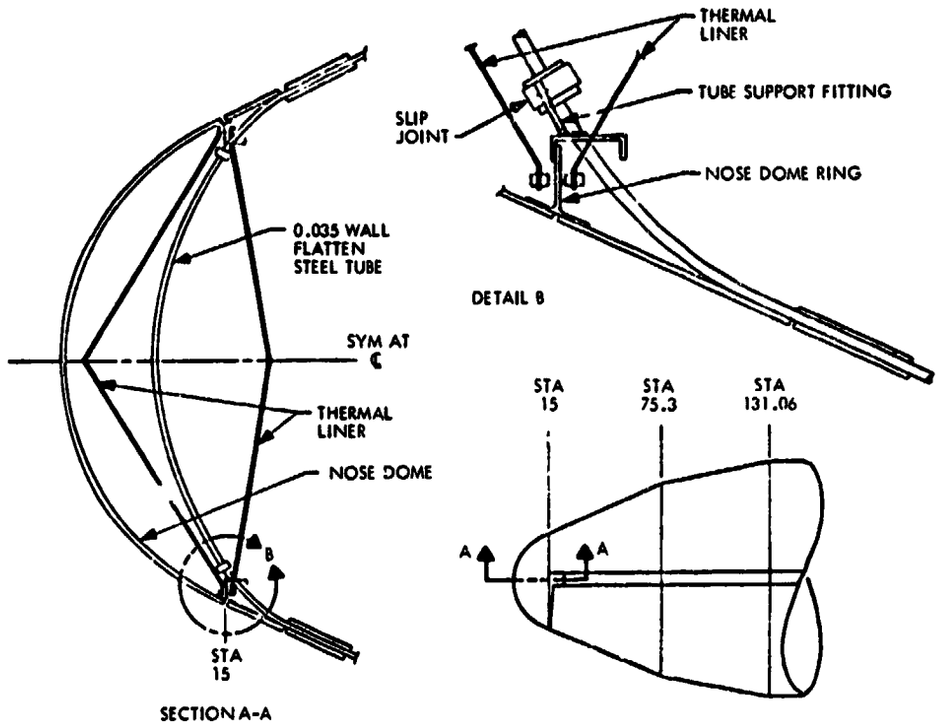

Figure 8-14. Nose Cone Thermal Liners

nose cone aft field joint fastener holes were cleaned, treated, and repaired. The forward end of the nose cone skin was repaired with a welded replacement strip. Black thermal test paint was removed from the nose cone. Forward and aft barrel section shell damages were repaired with standard structural doublers and patches. Damaged stiffening rings were repaired with splice plates or replaced with new rings. Missing parts replaced were: hinges; chutes; triplex and air conditioning doors; internal air conditioning doors; internal air conditioning duct; separation joint frangible doublers; thruster spring access doors; and separation system service door fairings.

d. Update and Modification. Design update improvements and modifications were incorporated. The latest design nose dome ring and cross bracing were added at the forward end of the biconic section. At the field joint between the forward and aft barrel sections, the latest design field joint/doubler configuration was added as shown in Figure 8-15. The electrical disconnects were replaced with the latest design units. At the circumferential separation joint, compression load support blocks were added at the separation doubler ends. The latest configuration hinge support struts were added at each hinge. The nitrogen supply opening was not required and was closed over and the umbilical chute provisions were deleted. In the separation system, the pyro joints at the nose cone-to-forward barrel section and at the nose dome were of the Centaur Standard Shroud (CSS) design. Also, the detonator blocks in the separation system incorporated CSS-type barrier and clip configurations as shown in Figure 8-16.

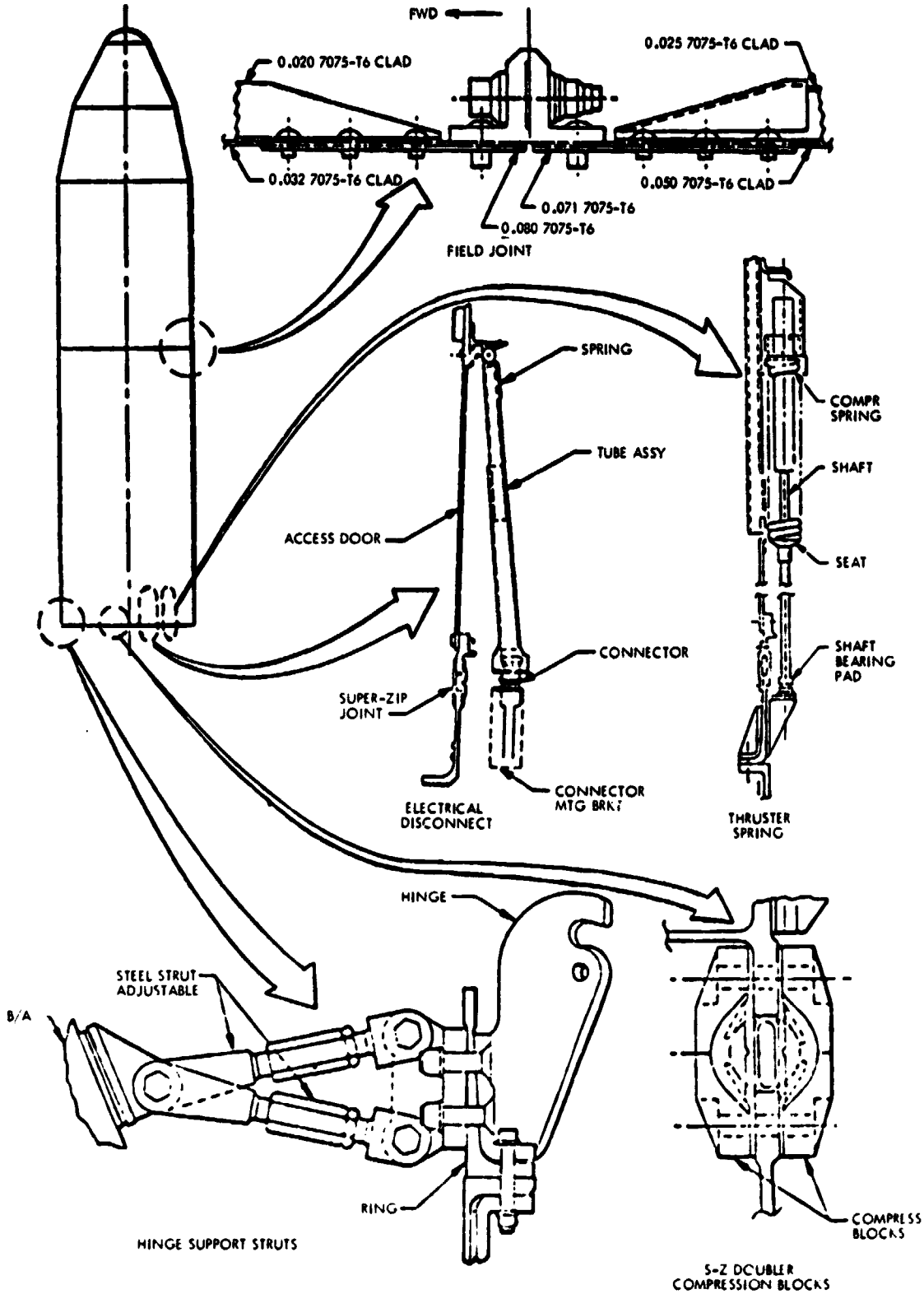

Figure 8-15. Component Details

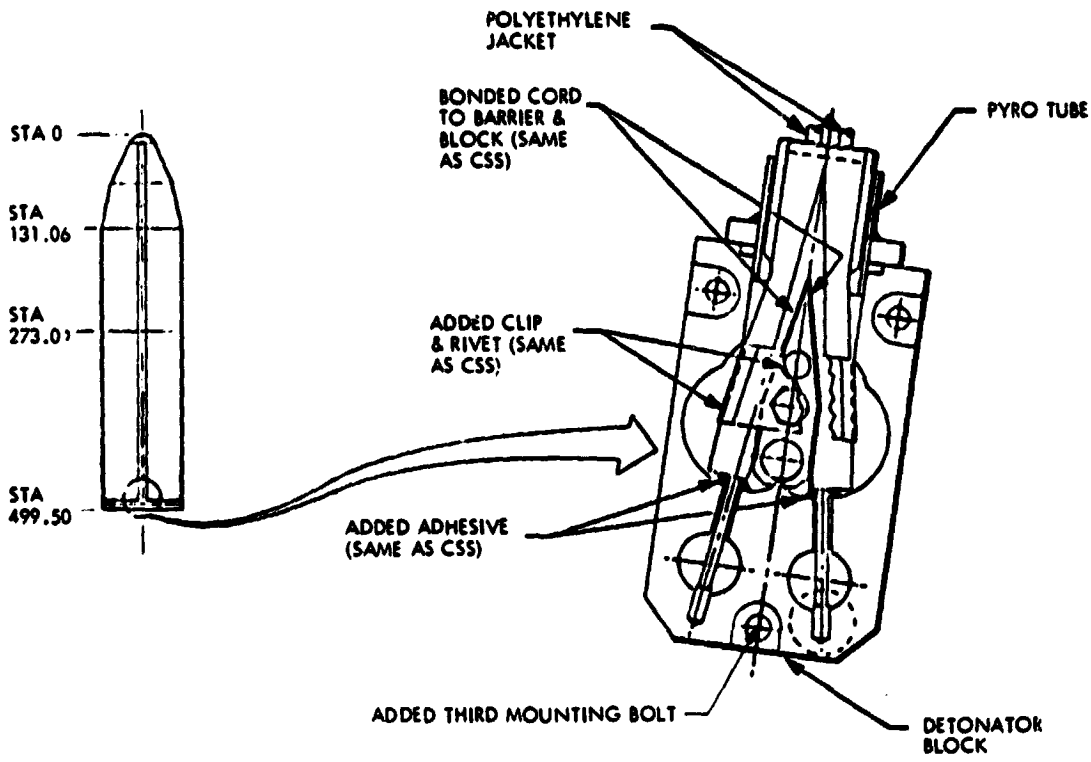

Figure 8-16. Detonator Block Barrier and Clip Modification

e. Mission Peculiarization. The air conditioning duct diffuser inside the fairing was not required with the Seasat payload and was deleted. Thruster springs assemblies with longer stroke length were incorporated into the fairing separation system as shown in Figure 8-16. Greater stroke length was required with the shortened fairing so that the applied spring force would act until the Center of Gravity (CG) of the fairing halves was beyond TDC during fairing rotation at jettison. A door was added in the aft section of the biconic assembly, as shown in Figure 8-17, to provide access to the satellite SAR for checkout. Both the biconic nose cone and the forward barrel were painted white for thermal control.

Static charge buildup on fiberglass components of the fairing, with subsequent potential discharge to the payload, was prevented by modifying those components as follows:

(1) The RF transparent panel in the forward section of the biconic nose cone was replaced with a metallic (magnesium and thorum) panel as shown in Figure 8-18, because an RF "window" was not required.

(2) The fiberglass skin on the triplex door in the aft barrel section was replaced with a metallic (aluminum) skin (Figure 8-19).

The internal air conditioning duct was covered with aluminized tape and grounded to the fairing shell by aluminum spacers on the supports.

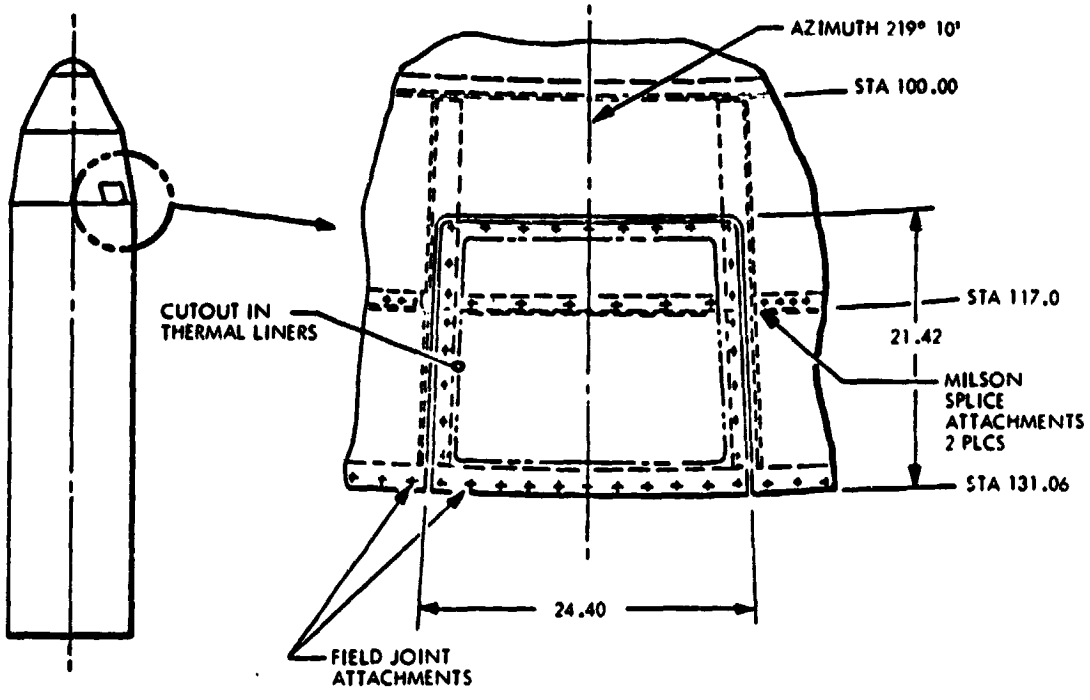

Figure 8-17. SAR Access Door

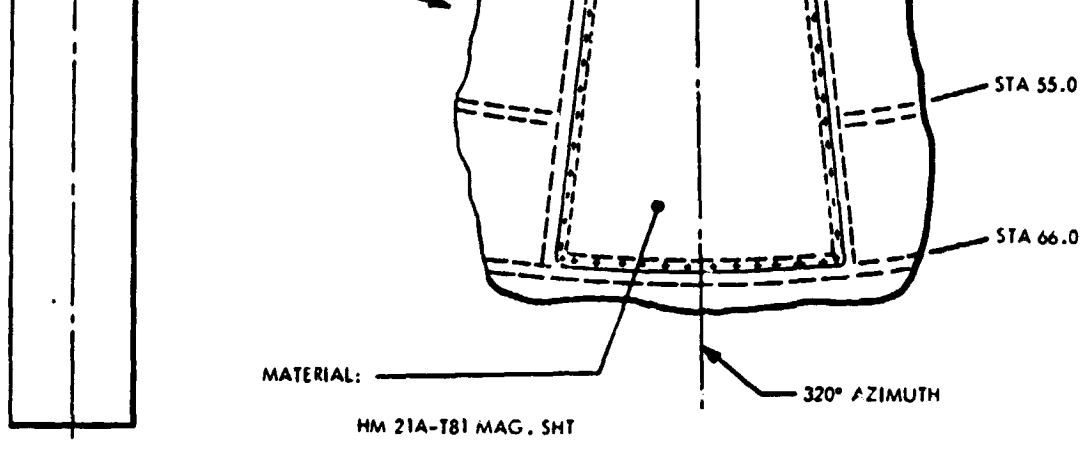

Figure 8-18. Nose Cone RF Transparent Panel Replacement

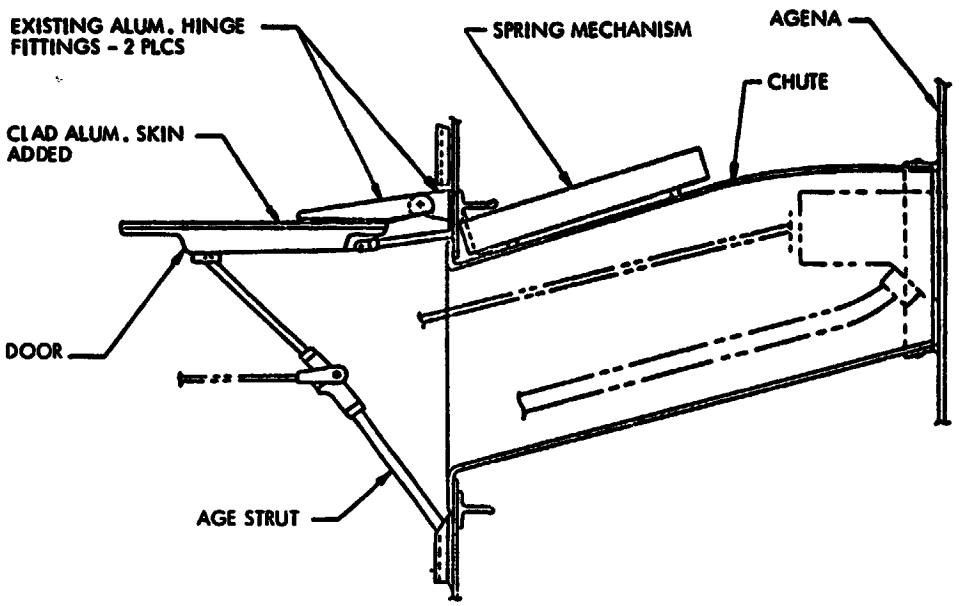

Figure 8-19. Triplex Door Skin Replacement

f. Super Zip Separation and Jettison. Super zip separation systems, both primary and secondary, are shown in Figures 8-20 and 8-21. The systems incorporated a longitudinal and circumferential joint consisting of two explosive cords in a stainless steel tube as shown in Figures 8-22 and 8-23. When either cord was ignited, the resultant pressure expanded the tube and fractured the frangible doublers.

The secondary system was fired 4 s after primary command only if the primary system failed to separate the shroud. Each joint was redundantly actuated by electric detonators as shown in Figures 8-24 and 8-25. Deactivation of the secondary system was accomplished by electrical disconnects located at the base of the shroud.

Jettison of the fairing following joint separation was accomplished by eight jettison springs located at the base of the fairing and two helper springs on the split lines, as shown in Figure 8-26.

At T+200.80 s the super zip primary system actuated and separated the fairing from the vehicle. The jettison springs rotated the fairing halves on the hinges until the shroud jettisoned free of the Atlas vehicle. Primary system separation of the fairing was verified by comparison of command times and breakwire and disconnect data.

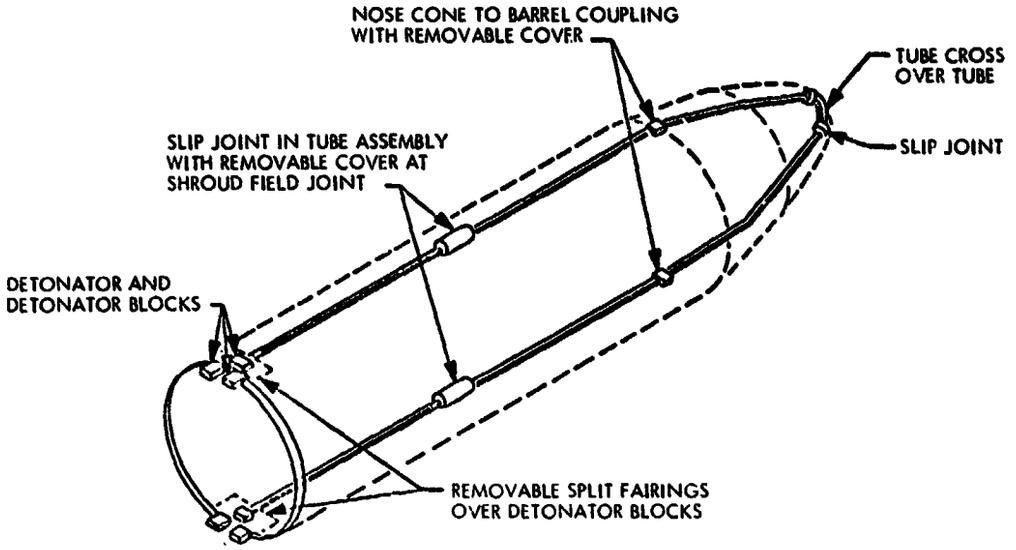

Figure 8-20. Fairing Super Zip Separation System

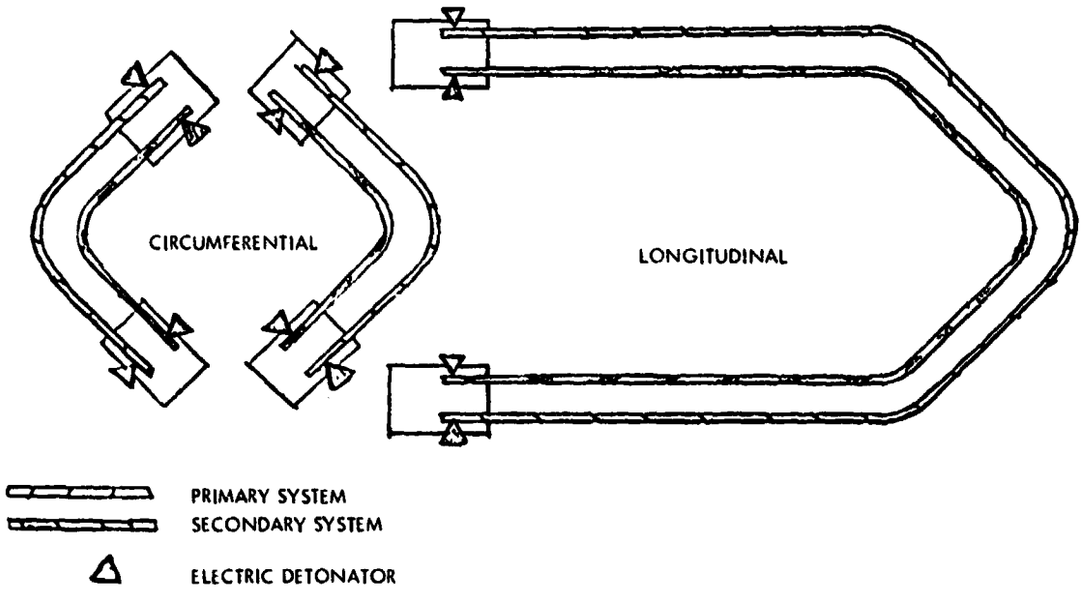

Figure 8-21. Super Zip Ordnance System Schematic

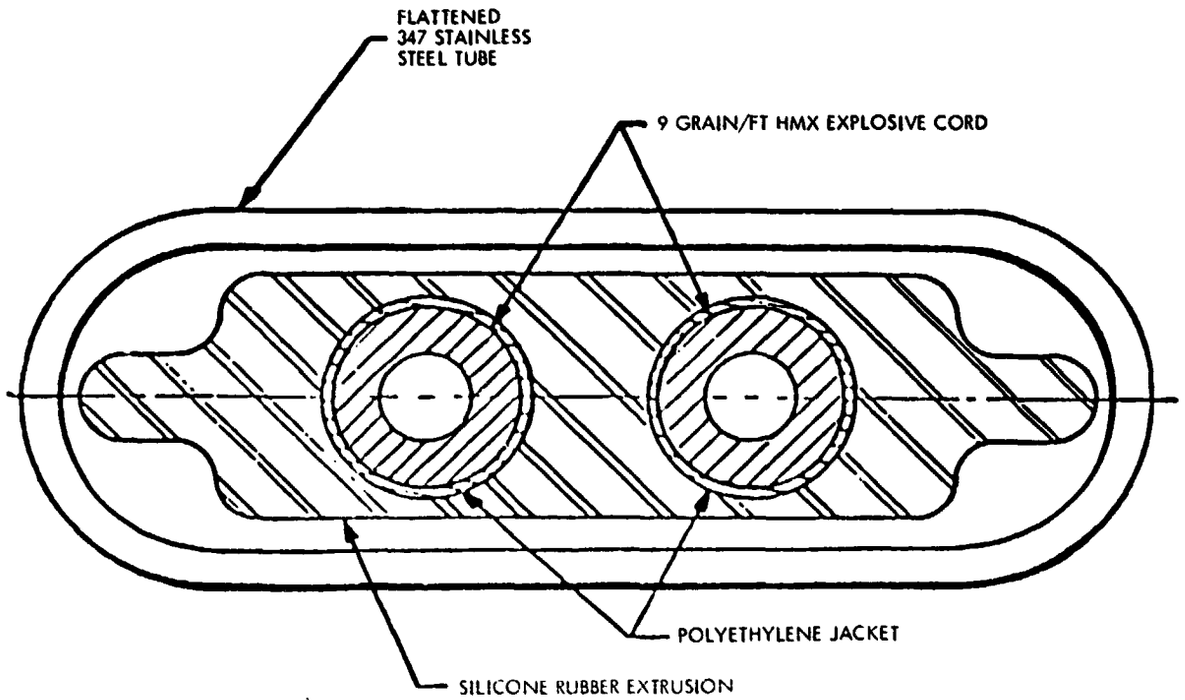

Figure 8-22. Super Zip Explosive Cord and Tube Assembly

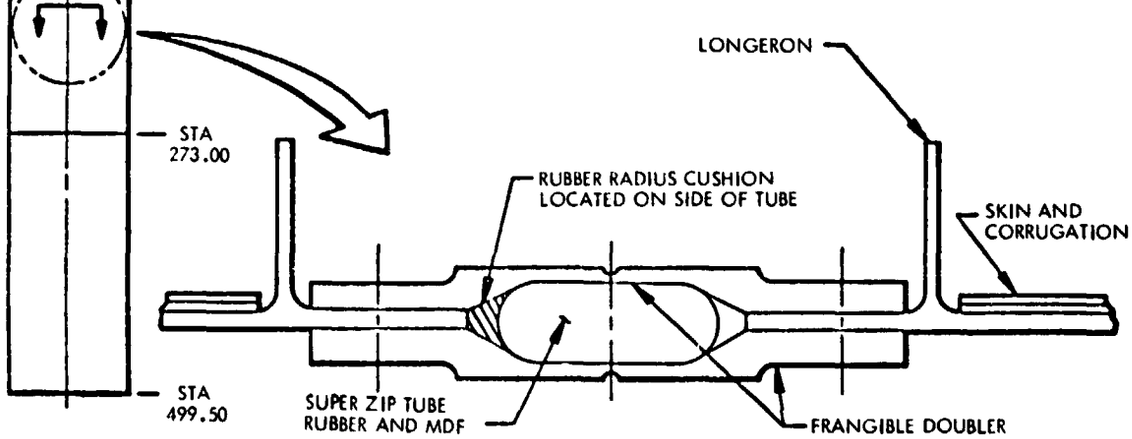

Figure 8-23. Super Zip Separation Joint

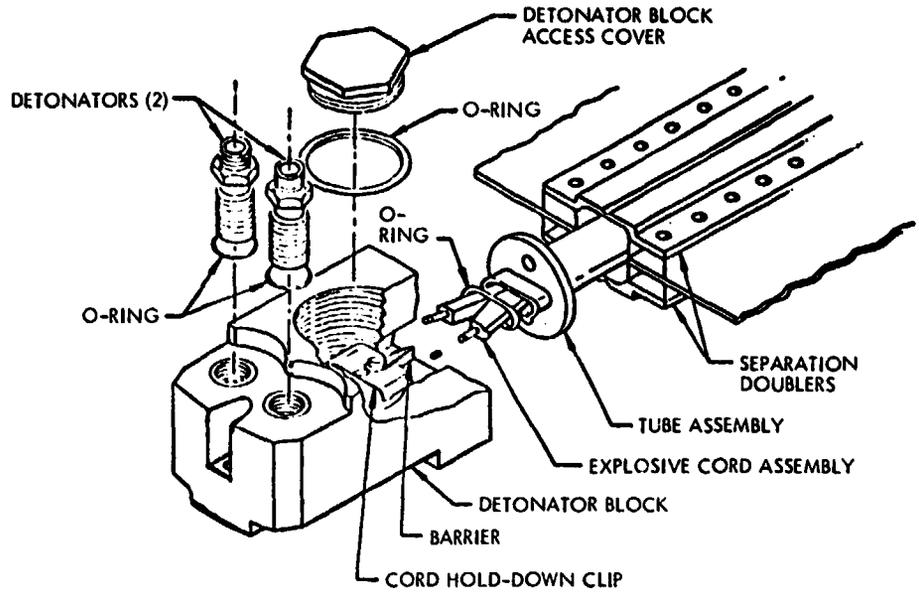

Figure 8-24. Super Zip Detonator Block Assembly

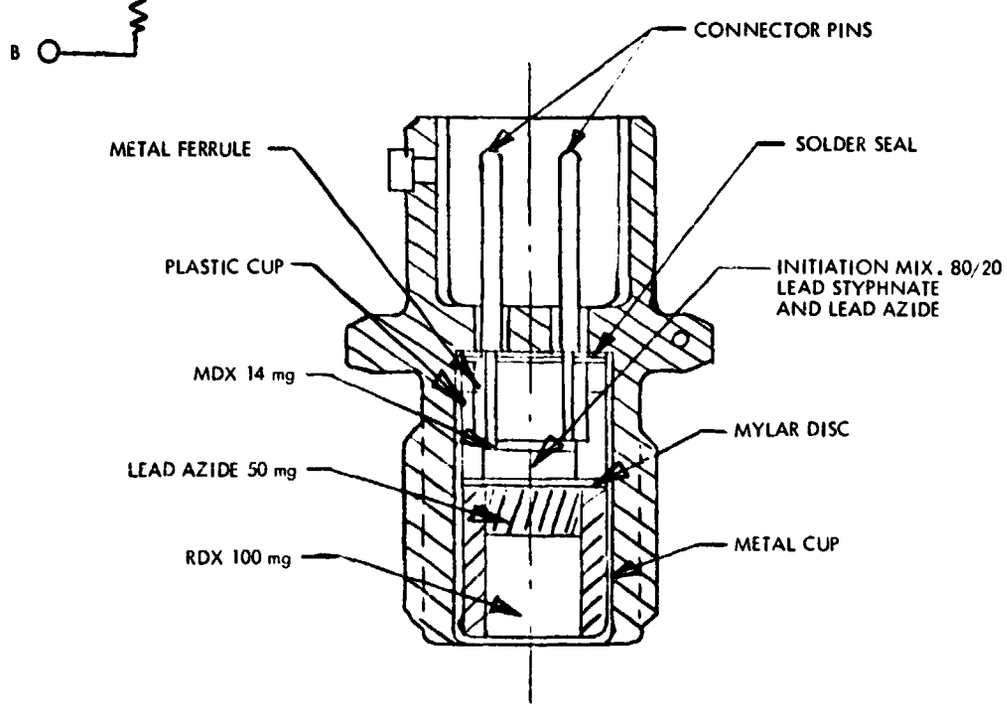

Figure 8-25. Super Zip Electric Detonator

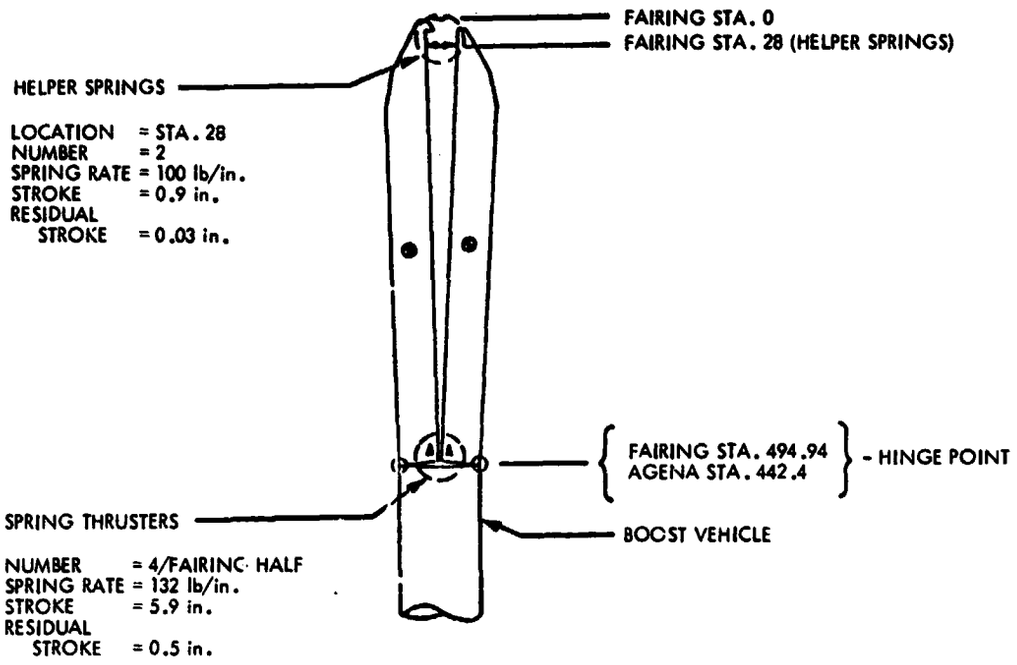

Figure 8-26. Fairing Jettison Spring System

8. Ground Support Equipment

a. General. Space Launch Complex Number 3 West (SLC-3W), Western Test Range (WTR), Vandenberg Air Force Base (VAFB), was the launch site for the Seasat launch vehicle. Extensive modification was required to accommodate the vehicle configuration. In particular, the larger diameter fairing and greater length of the vehicle, above that of the baseline Atlas F vehicle, required much structural alteration of the upper platforms and installation of an auxiliary crane.

The vehicle hold-down system was reworked for remote reengagement. The Atlas stretch sling and the Missile Service Tower (MST) support points were modified. Propellant, pneumatic, and electrical services were reinstalled and updated in the Umbilical Mast (UM) for the Agena. The air conditioning system for the payload and vehicle compartment conditioned air supply was refurbished. The UM wind deflector sails were enlarged. Cabling for mission-peculiar instrumentation and controls were added. Miscellaneous work-stands and supportive devices were added. Fairing handling and installation equipment such as slings, protective covers, and internal work platforms were provided.

b. Site Modifications. Seven tower platforms (folding-sliding sections) from Tower Stations (TS) 63 to 111, shown in Figure 8-27, were extensively reworked or replaced to accept the 305-cm diameter fairing. The vehicle opening

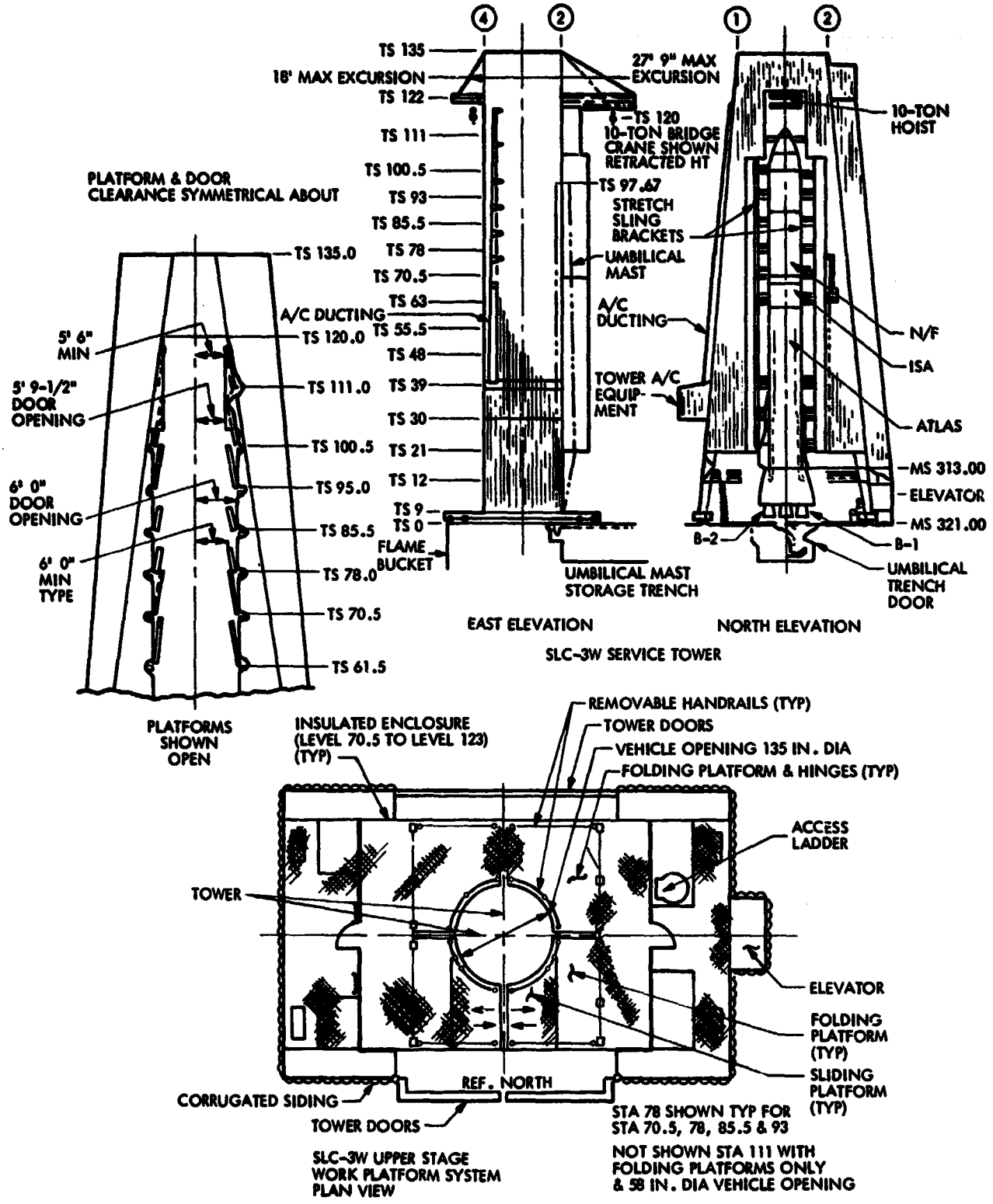

Figure 8-27. Missile Service Tower Platform Modifications

in these platforms was increased from 40- to 54-cm (102- to 138-in.) diameter, except at TS 111, which required a 23-cm (58 in.) diameter opening. The folding platforms were modified and insert pieces provided to return the MST to the original configuration following the launch of the Seasat. The sliding platforms were completely replaced with new sections and inserts were also provided for post-launch reconfiguration. TS 111 was totally replaced with a smaller and thinner platform to increase clearance in the folded-back configuration (the MST A-frame structure afforded progressively smaller clearances at the forward end of the vehicle fairing). Various platform cut-outs were incorporated for satellite and fairing handling equipment clearances. An auxiliary access platform was added to the TS 55 platform for vehicle rate gyro servicing. Minor protrusions in the area of the upper weather doors (TS 100.5 and TS 111) were removed or relocated to afford clearances for fairing handling. A guide rail system was provided for the tower upper platforms to facilitate removal of the payload handling fixtures from the tower.

A bridge crane and rails was installed above the main crane, shown in Figure 8-28, for increased hook height necessary to install the forward barrel and nose cone on the vehicle.

The Atlas stretch system was reworked by lowering the actuating cylinders to TS 86 from TS 89.5. This was required by the Atlas/ISA configuration. The stretch sling was rebuilt to fit the revised configuration.

Launch site air conditioning for the vehicle compartments and the launch services building was refurbished to supply conditioned air to the full capability of the system to provide the necessary quality and quantity of air. On the UT, the system had two runs. System I had a flow control valve, adapter, and flex duct provided at TS 69 to service the ISA. System II had two flow control valves and stub-outs installed for the umbilical connections to the sensor module and the Agena compartments at TS 96.6 and 90.4 respectively.

The Atlas holddown system was modified for remote engagement of the hooks in case of an aborted launch. The hook assembly was modified by installing hook guides, replacing the locking links with non-locking links, and adding unlatch indicator switches. The hydraulic system which activated the actuating cylinders was modified by the addition of four valves and the rework of a fifth valve to afford double isolation of the pressure source and the return as shown in Figure 8-29. Also, the existing cylinders were replaced with new units. The hook position indicators and the valve operating controls and indicators were wired to the launch operations building.

The wind deflector sails on the UT were enlarged both in height and width to accommodate the taller vehicle. Propellant lines, pneumatic lines, and electrical cables were installed and updated for servicing the Agena.

c. Handling GSE. The Atlas rotation sling and adapter were provided to hoist the Atlas off the launcher, when first erected, and to rotate it 180 deg for proper orientation (the transporter would not accommodate the desired orientation). An existing adapter was modified at the lift points and a new sling was provided for the Atlas rotation operation.

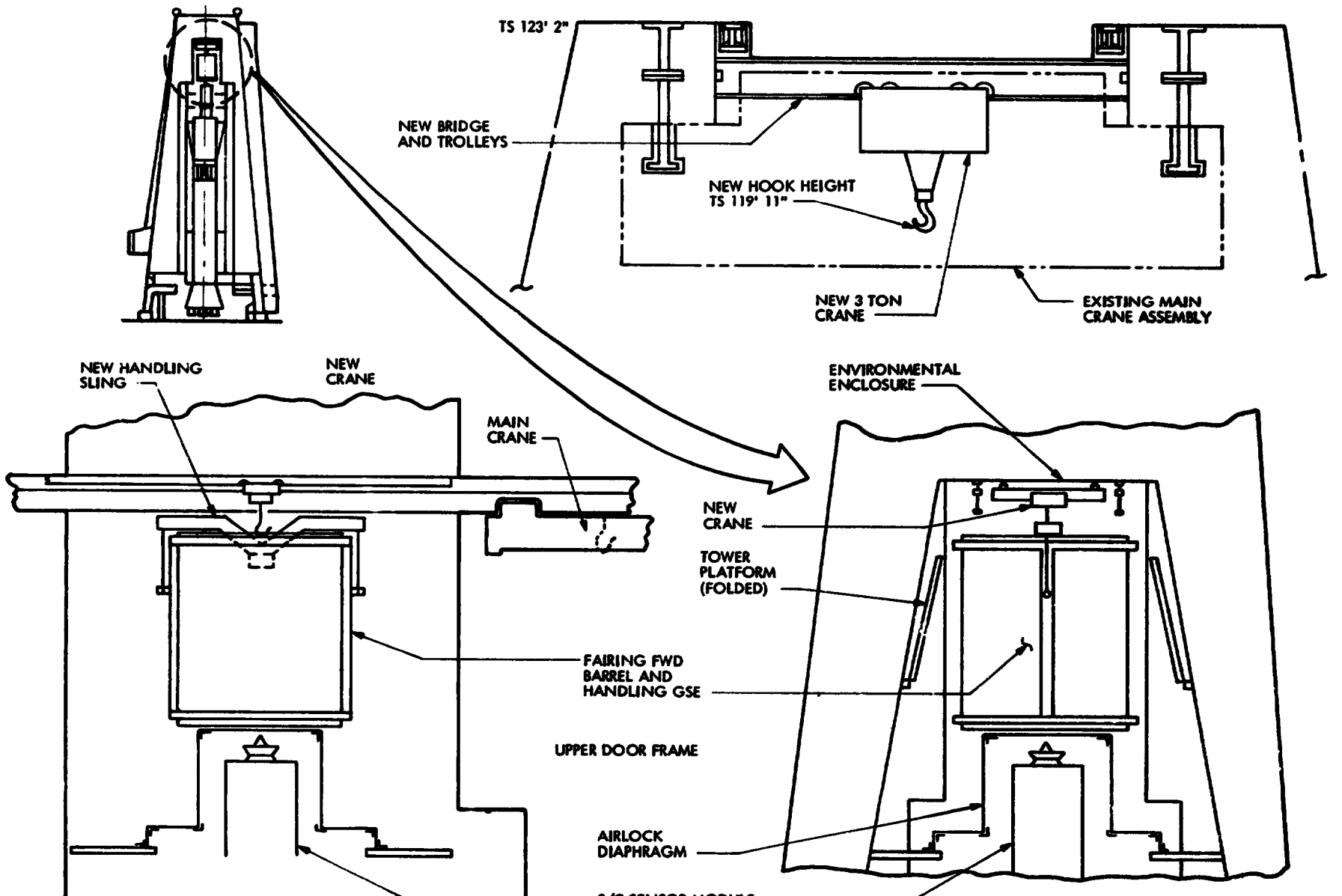

Figure 8-28. Bridge Crane Assembly

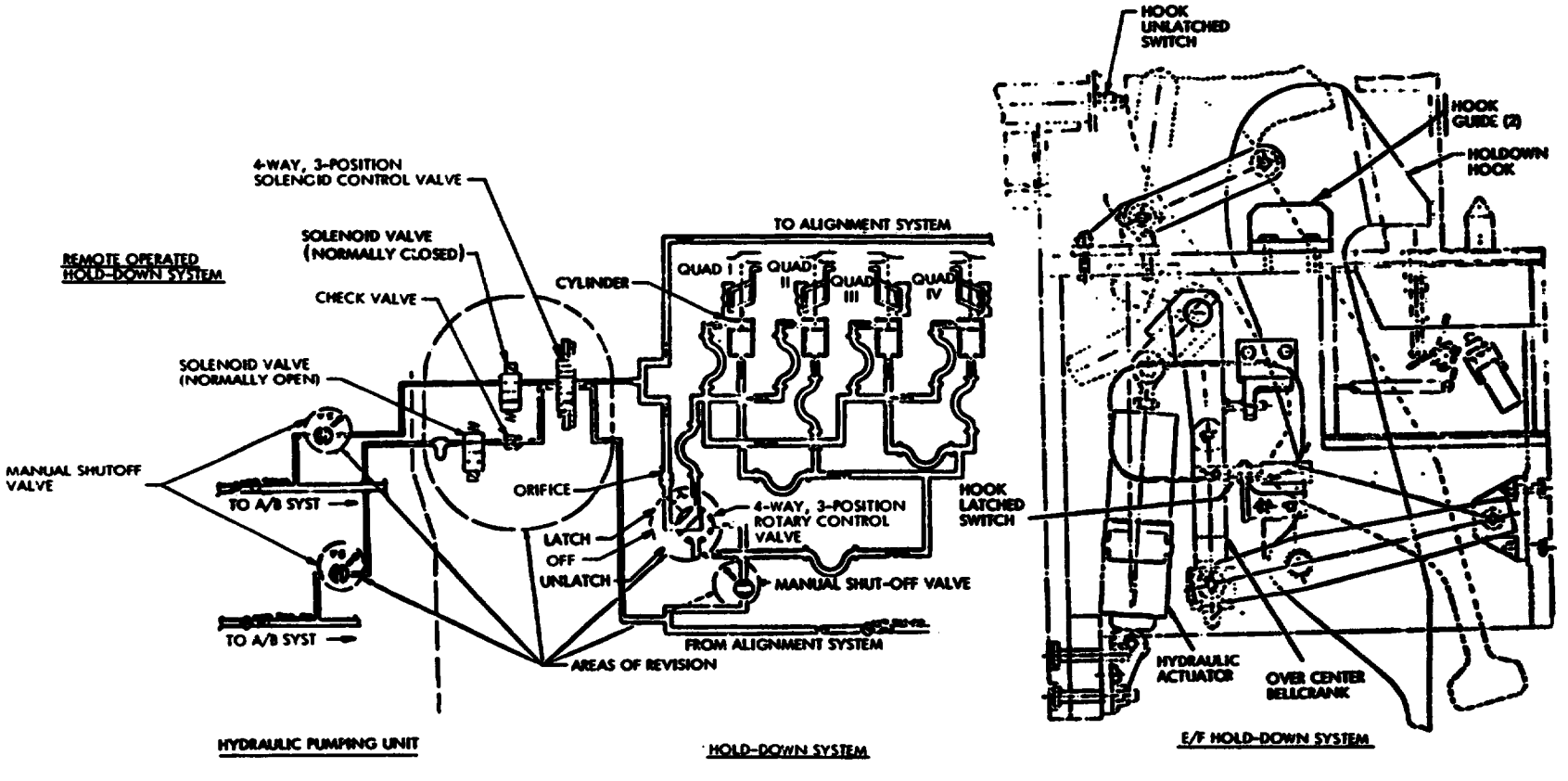

Figure 8-29. Hold-Down System

A new sling with built-in winches and a short coupling for hook attachment was designed and provided for the fairing forward barrel erection on the vehicle in the MST. The minimum clearance vertically in the MST required a minimum height design. An adapter for the fairing nose cone sling was required to install the nose cone in the MST.

A cover assembly called an airlock diaphragm was provided to enclose the forward end of the sensor module from the TS 100.5 platform. The airlock diaphragm sealed off the sensor module while the upper weather doors of the MST were opened for entry of the fairing forward barrel and nose cone preparatory to mating with the vehicle.

A booster adapter access platform was provided for servicing the Agena after mating to the vehicle at the booster adapter interface and prior to assembly of the aft barrel of the fairing.

For servicing the aft end of the Agena, an access platform was supplied for pre-flight use in the ISA. The platform was composed of small sections for handling within the ISA. Two platforms, also of several segments, were used inside the fairing aft barrel for service access to the Agena.

Six cantilever-type workstands were provided for use on the upper platforms of the MST for access to the Agena and sensor module during installation on the vehicle. The stands were keyed to the MST platforms for stability and ready mobility.

An adapter for use with the fairing thruster spring compression tool was provided to cock the longer springs used with the Seasat fairing.

Various covers and guards were used in the handling operations to enclose and protect sensitive components.

APPENDIX

ABBREVIATIONS AND ACRONYMS

AAFE	Advanced Application Flight Experiment
ACN	STDN station at Ascension Island, United Kingdom
ACS	Attitude Control System
A/D	Analog to Digital
ADF	Attitude Determination File
AEA	Augmented Electronics Assembly
AESC	Aerojet Electrosystems Center
AFB	Air Force Base
AFPRO	Air Force Plant Representative Office
AFWTR	Air Force Western Test Range (VAFB)
AGC	Automatic Gain Control
AGE	Aerospace Ground Equipment
ALT	Radar Altimeter
AM	Amplitude Modulation
APC	Antenna Pattern Correction
APL	Applied Physics Laboratory of Johns Hopkins University
ARC	Ames Research Center (NASA), Moffett Field, CA
AT	Adaptive Tracker
BBRC	Ball Brothers Research Corporation, Boulder, CO
BECO	Booster Engine Cutoff
BER	Bit Error Rate
BOL	Beginning of LIFE
BTU	British Thermal Unit
CATS	Computer Aided Test System

CCC	Charge Current Controller
CCT	Computer Compatible Tape
C&DH	Command and Data Handling
CDR	Critical Design Review
CDU	Command Demodulation Unit
CG	Center-of-Gravity
CLA	Control Logic Assembly
CMDS	Command Data System
CMO	Chief of Mission Operations
CMOS	Complementary Metal-Oxide Semiconductor
CPU	Command Processor Unit
CSE	Chief Systems Engineer
CSS	Centaur Standard Shroud
CTU	Central Timing Unit
CTU	Command and Timing Unit
DDL	Dispersive Delay Line
DELTA P, ΔP	Pressure Differential
DFB	Digital Filter Bank
DOY	Day of Year
DPA	Destructive Physical Analysis
DVM	Digital Velocity Meter
EDT	Eastern Daylight Time
EMC	Electromagnetic Capability
EMI	Electromagnetic Interference
EODAP	Earth and Ocean Dynamics Applications Program
EPS	Electrical Power Subsystem

ESS	Expandable Support Structure
EU	Engineering Unit
FM	Frequency Modulation
FMECA	Failure Modes, Effects, and Criticality Analysis
FOSR	Flexible Optical Surface Reflector
FOV	Field of View
FSK	Frequency-Shift Keyed
GD/C	General Dynamics, Inc., Convair Division, San Diego, CA
GDS	STDN station at Goldstone, CA
GE	General Electric Company
GEOS	Geodetic Earth-Orbiting Satellite
GERTS	General Electric Radio Tracking System
GFE	Government Furnished Equipment
GMT	Greenwich Mean Time (Zulu Time)
GOASEX	Gulf of Alaska Seasat Experiment
GPS	Global Positioning System
GRA	Gyro Reference Assembly
GSE	Ground Support Equipment
GSFC	Goddard Space Flight Center
HDA	High Density Acid
HDDTR	High Density Data Tape Recorder
HGOM	High Gain Operating Mode
HIVOS	High Vacuum Orbital Simulator
HMRCC	High Mode Reaction Control Cluster
HSA	Horizon Sensor Assembly
HSWS	High Speed Wave Sampler

HVPS	High Voltage Power Supply
ICD	Interface Control Document
ICU	Interface and Control Unit
ICWG	Interface Control Working Group
IDPS	Instrument Data Processing System
IMS	Institutional Management System
ISA	Incident Surprise Anomaly
ISA	Interstage Adapter
ITOS	Improved Tiros Operational Satellite (NOAA)
JASIN	Joint Air-Sea Interaction Experiment
JPL	Jet Propulsion Laboratory (NASA), Pasadena, CA
LaRC	Langley Research Center (NASA), Hampton, VA
LeRC	Lewis Research Center (NASA), Cleveland, OH
LMRCC	Low Mode Reaction Control Cluster
LMSC	Lockheed Missile and Space Company, Inc., Sunnyvale, CA
LN2	Liquid Nitrogen
LO2	Liquid Oxygen
LRA	Laser Retroflector Assembly
LRS	Low Rate Sample
LSB	Least Significant Bit
LSWA	Left Scan Wheel Assembly
L/V	Launch Vehicle
LVPS	Low Voltage Power Supply
MARA	Maximum Access Booster Adapter
MAD	STDN station at Madrid, Spain
MCA	Magnetic Control Assembly

MDR	Mission Dress Rehearsal
MFR	Multi-Function Receiver
MIL	STDN station at Merritt Island, FL
MIPR	Military Interdepartmental Purchase Agreement
MLI	Multi-Layer Insulation
MMC	Martin Marietta Corporation, Denver, CO
MOA	Memorandum of Agreement
MODALAB	Mobile Dynamic Analysis Laboratory
MPCDU	Main Power Control and Distribution Unit
MRR	Mission Readiness Review
MSR	Monthly Status Review
MST	Missile Service Tower
NASA	National Aeronautics and Space Administration
NASCOM	NASA Communications Network
NOAA	National Oceanic and Atmospheric Administration (DoC)
NRCS	Normalized Radar Cross Section
NRZ	Non-Return-to-Zero
NSD	Normalized Standard Deviation
NST	NASA Standard Transponder
N_2H_4	Nitrogen Tetroxide (Hydrazine)
OACS	On-Orbit Attitude Control System
OAS	Orbit Adjust System (LMSC)
OIPS	Orbit Insertion Propulsion System
OIS	Orbit Insertion System
PCLA	Power Conditioning and Logic Assembly
PCM	Pulse Code Modulation

PDPS	Project Data Processing System
PDR	Preliminary Design Review
PDT	Pacific Daylight Time
P/FR	Problem/Failure Report
PIV	Propellant Isolation Valve
PLF	Payload Fairing
PMW	Pitch Momentum Wheel
POCC	Project Operations Control Center (GSFC)
PPPL	Program Preferred Parts List
PRR	Program Requirements Review (LMSC)
PSK	Phase Shift Keyed
PST	Pacific Standard Time
QA&R	Quality Assurance and Reliability
RCS	Reaction Control System (LMSC)
R&D	Research and Development
REE	Responsible Equipment Engineer
RF	Radio Frequency
RFI	Radio Frequency Interference
RFP	Request for Proposal
R/I	Read-In
RIU	Radar Interface Unit
R/O	Read-Out
R&QA	Reliability and Quality Assurance
RRE	Responsible Reliability Engineer
RRW	Roll Reaction Wheel
RSWA	Right Scan Wheel Assembly

R/T	Radio Telephone
R/T	Real Time
RTC	Real Time Command
SACU	Synchronizer, Acquisition, and Calibration Unit
SADE	Solar Array Drive Electronics
SAM	Solar Array Module
SAR	Synthetic Aperture Radar
SASS	Seasat Scatterometer System
SBRC	Santa Barbara Research Center, Goleta, CA
S/C	Spacecraft
SCTB	Santa Cruz Test Base (California)
SDA	Sensor Data Assembler
SDL	SAR Data Link
SDR	Sensor Data Record
SECO	Sustainer Engine Cutoff
SED	SAR Enable/Disable
SLC	Space Launch Complex
SLV	Standard Launch Vehicle
SM	Sensor Module
SMMR	Scanning Multichannel Microwave Radiometer
SMRD	Spin Motor Revolution Detector
SMSS	Sensor Module Support Structure
SPAT	Satellite Performance and Analysis Team
SPC	Stored Program Command
SPS	Sensor Performance Summary
SQRB	Senior Qualification Review Board

SR	Scanning Radiometer
SRR	System Requirements Review (LMSC)
SSD	Satellite Systems Division (LMSC)
SSE	Satellite System Engineering
STALO	Stable Local Oscillator
STC	Sensitivity Time Control
STDN	Spaceflight Tracking and Data Network (GSFC)
SVS	Satellite Vehicle System
SWA	Scan Wheel Assembly
T_A	Antenna Temperature
T_B	Brightness Temperature
TELOPS	Telemetry On-Line Processing System (GSFC)
TLM, TM	Telemetry
T/R	Tape Recorder
Tranet	Tracking Network
T_S	Sea-Surface Temperature
TS	Tower Station
TSU	Telemetry and Sensor Interface Unit
TTE	Temperature Transfer Equation
T/V	Thermal Vacuum
TWT	Traveling Wave Tube
TWTA	Traveling Wave Tube Amplifier
UCFM	Up-Converter/Frequency Multiplier
ULA	STDN station at Fairbanks, Alaska
UM	Umbilical Mast
USAF	United States Air Force

USN	United States Navy
USO	Unsymmetrical Dimethyl Hydrazine with Silicone Oil
VAFB	Vandenberg Air Force Base, CA
VAMP	Vandenberg Atlas Modification Program
VECO	Vernier Engine Cutoff
VIRR	Visual and Infrared Radiometer
V/M	Velocity Meter
VSWR	Voltage Standing Wave Ratio
WFC	Wallops Flight Center (NASA), Wallops Island, VA
WTR	Western Test Range, VAFB, CA
XPDR	Transponder